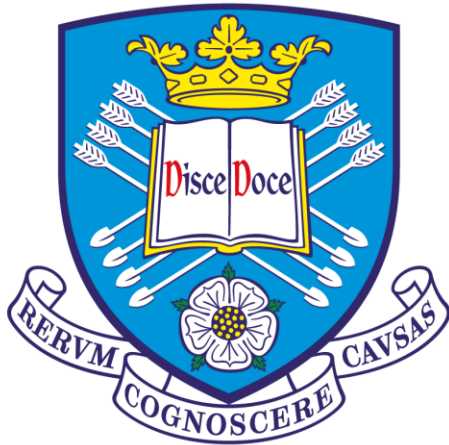


**Tribological, Electrochemical, and Tribocorrosion Behaviour of
New Titanium Biomedical Alloys**



**The
University
Of
Sheffield.**

**A thesis submitted to the University of Sheffield for the degree of
Doctor of Philosophy in the Materials Science and Engineering**

By: Zuheir Talib Khulief

Supervisor: Professor W. Mark Rainforth

Co-Supervisor: Professor Iain Todd

The Department of Engineering Materials

The University of Sheffield

Acknowledgements

It is with immense gratitude that I acknowledge my supervisor Professor Mark Rainforth, for his support, patience, encouragement, and guidance enabled me to finish my PhD. Thanks, are also due to Professor Iain Todd for his support throughout my PhD.

This study was sponsored by Ministry of High Education and Scientific Research, The Government of Iraq, I owe to you all.

The Embassy of the Republic of Iraq, Cultural Attaché, London, Representative of the Iraqi Ministry of Higher Education and Scientific Research (MOHESR) in the UK and Ireland, and the University of Babylon, College of Material Engineering, Metallurgy Department are kindly acknowledged.

I also wish to acknowledge Righdan Namus for all the support and assistance he has given me.

I would like to thank all the research student in G8 and H6- Department of Materials Science and Engineering, University of Sheffield, who providing a friendly environment, and supported me during my study.

I would like to express my thanks to Dr. Cheryl, Dr. Peng Zeng, and Dr. Le Ma in Sorby Centre for their training and timely help when necessary.

I would like to thank Dr. Lynne Newcombe an English teacher, department English language support for her advice and feedback.

Last but not least, I would like to thank my family for their unwavering support in my life.

Zuheir Talib Khulief

2018

Declaration

No portion of the work referred to in this thesis has been submitted in support of an application for another degree or qualification of this or any other university or institute of learning.

To
My Family

Abstract

Second-generation titanium biomaterials, β titanium alloys, particularly vanadium free titanium alloys, have become a focus of research due to their potential application in biomedical fields. Therefore, there is currently considerable interest in the tribocorrosion response of these alloys. In the present work, a systematic study has been completed to investigate and understand the degradation resulting from electrochemistry (corrosion) and mechanical (wear) in a range of vanadium free titanium alloys in 25vol% bovine calf serum. Five different β based titanium-based alloys, namely Ti-Mo₈-Nb₄-Zr₂, Ti-Mo₈-Nb₆-Zr₄, Ti-Mo₈-Nb₄-Zr₅, Ti-Ta₃₀, and Ti-Ta₂₇-Al₅ alloys (at%) were prepared using a non-consumable arc-melting furnace with inert argon atmosphere. Alloys were arc melted, homogenized, cold rolled and finally subjected to solution heat treatment and then quenched in water. Commercially pure titanium Cp-Ti with an α -phase microstructure and Ti-6Al-4V with α + β -phase microstructure was tested for comparison. Alloys were characterized before testing. Alloys were successfully fabricated using ingot metallurgy, including the Ti-Ta₃₀ alloy. The alloys exhibited excellent cold workability, except the Ti-Ta₃₀ alloy which needed an intermediate annealing treatment during thermo-mechanical treatment to increase the cold workability. XRD and microstructural analysis showed that the alloys except the Ti-Ta₂₇-Al₅ consisted of single phase β . All alloys had a lower elastic modulus than that of Cp-Ti and Ti-6Al-4V and had average Vickers micro-hardness values higher than that of Cp-Ti and lower than that of Ti-6Al-4V.

The coefficient of friction and wear increased with load. A tribological film was generated on the surface of the alloys in some cases. The film generation correlated with friction and wear by reducing and limiting the friction and wear. The tribological mechanism can be attributed to abrasive ploughing wear mechanisms. The precise tribological response was controlled by the microstructure, hardness, surface chemistry (tribofilm) in the wear track and load. Characterization of subsurface microstructures after tribology tests under different applied loads showed that grain refinement did occur adjacent to the rubbing surface. An increase in the extent of grain refinement was observed with an increase in load. For pure corrosion, alloys tend to form a passive film. The β -phase Ti-Ta₃₀ had a relatively low corrosion current density because the more stable Ta₂O₅ passive films strengthen the TiO₂ passive films. The corrosion potential under rubbing shifted cathodically and the current density increased compared with static corrosion. The current densities and mean corrosion rate increased after tribocorrosion tests, while the corrosion potential showed cathodic and anodic shifts, and this shifting

depended on the alloy composition and the electrochemical condition of the alloy under tribocorrosion tests. Tribocorrosion tests were carried out against an alumina counter face at OCP, cathodic (-0.5 V vs OCP) and anodic conditions (0.3 V vs OCP). The coefficient of friction was unaffected by the potential. No direct relationship between the mechanical properties of the alloys (hardness and elastic modulus) and wear volume could be found on the tribocorrosion responses of alloys. All alloys suffer from wear-accelerated corrosion at OCP and cathodic potential (-0.5V vs OCP). However, β -microstructure alloys benefit from corrosion-decelerated wear at anodic potential (0.3V vs OCP). All corrosive wear surfaces were free from corrosion products after tribocorrosion. All alloys exhibited a large total removed wear volume after cathodic rubbing conditions compared to OCP and anodic rubbing conditions. The wear tracks on β -microstructure alloys recovered their passivity during rubbing. However, β -microstructure alloys were more susceptible to mechanical wear. The nature and extent of deformation of subsurface after tribocorrosion tests was dependent on the applied potential, and the samples rubbed at anodic potential exhibited significantly less deformation than that of the samples rubbed at OCP and cathodic potential.

The results of this thesis have shown that the β -microstructure Ti-Mo₈-Nb₄-Zr₂ and Ti-Mo₈-Nb₄-Zr₅ are promising biomedical alloys for implants applications with relatively low elastic modulus and less material loss, comparable mechanical and tribocorrosion behaviour, and non-toxic alloying elements. The passive behaviour of the β -microstructure alloys did not have a positive influence on their tribocorrosion performance, but it was beneficial due to the suppression of the wear-accelerated corrosion process. The carbonaceous film did have a positive influence on reducing the friction and limiting wear on the alloys surface. The wear tracks on the β -microstructure alloys recovered their passivity during rubbing and this is a critical property for implants applications. The synergistic effect of wear accelerated corrosion was more pronounced in the α -microstructure, $\alpha+\beta$ -microstructure and $\beta+\alpha''$ -microstructure than the β -microstructure alloys. Though α -microstructure and $\alpha+\beta$ -microstructure have minimum some applications due to its super corrosion resistance. Thus, improving the wear resistance of β -microstructure by surface modification could lead to enhancing the tribocorrosion resistance and extending the service life of alloys.

Contents

Acknowledgements.....	I
Declaration	II
Abstract.....	IV
List of Figures	XII
List of Tables.....	XIX
List of Abbreviations and Symbols.....	XX
Chapter 1 MOTIVATION and RESEARCH AIMS.....	1
1.1 Motivation	1
1-2 Objectives of This Study.....	2
1-3 Thesis outline	3
Chapter 2 : Literature Review	4
2.1 Introduction	4
2.2 Biomaterials	4
2.2.1 Historical Developments of Metallic Biomaterials.....	7
2.2.2 Fundamental Considerations in Design and selection of Metallic Implants.....	10
2.2.2.1 Excellent biocompatibility	10
2.2.2.2 High corrosion resistance	12
2.2.2.3 Suitable mechanical resistance.....	13
2.2.2.4 High wear resistance	15
2.2.2.5 Osseo-integration	17
2.3 Titanium	17
2.3.1 General Properties of Titanium.....	17
2.3.2 Titanium Crystal Structure	18
2.3.3 Titanium Alloys.....	19
2.3.3.1 α - and near α titanium alloys.....	20
2.3.3.2 α - β titanium alloys	20
2.3.3.3 Metastable and stable β -titanium alloys	21
2.3.4 Titanium Alloys as Biomaterials.....	21
2.3.4.1 Biocompatibility of Alloying Elements	23
□ Titanium (Ti).....	23
□ Vanadium (V)	23
□ Niobium (Nb).....	24
□ Molybdenum (Mo).....	24
□ Tantalum (Ta)	24

□ Zirconium (Zr)	24
□ Aluminum (Al).....	25
2.4 Tribology.....	25
2.4.1 Friction	25
2.4.1.1 The coefficient of friction	26
2.4.1.2 Components of friction	26
2.4.2 Wear	27
2.4.2.1 Mechanisms of wear.....	27
2.4.3 Lubrication	28
2.4.4 Tribological Testing Systems and Characterization Techniques	30
2.4.5 Tribology of Titanium.....	31
2.5 Corrosion.....	33
2.5.1 Electrochemical Techniques for Corrosion Study	36
2.5.1.1 Open Circuit Potential (OCP)	37
2.5.1.2 Potentiodynamic polarization (PD).....	38
2.5.1.3 Potentiostatic Polarization (PS).....	39
2.5.1.4 Electrochemical Impedance Spectroscopy and Equivalent Circuits	40
2.5.2 Corrosion Mechanisms.....	43
2.5.2.4 Galvanic corrosion	43
2.5.3 Corrosion of Titanium and Titanium Alloys.....	46
2.6 Tribocorrosion.....	52
2.6.1 Factors Affecting Tribocorrosion Rate and Mechanisms	54
a). Materials.....	54
b). Mechanical/ operational parameters	54
c). Solution/environment.....	55
d). Electrochemical parameters	55
2.6.2 Tribocorrosion Approaches.....	56
2.6.2.1 The synergistic approach.....	56
2.6.2.2 The mechanistic approach.....	56
2.6.2.3 The third- body approach	57
2.6.3 Electrochemical Techniques for Tribocorrosion Study	58
2.6.3.1 Open circuit potential technique (OCP)	59
2.6.3.2 Potentiodynamic technique (PD)	59
2.6.3.3 Potentiostatic technique (PS)	60
2.6.4 Tribocorrosion test system	60

2.6.5 Tribocorrosion of Titanium and Titanium Alloys.....	62
Chapter 3: Experimental Procedure	66
3.1 Introduction	66
3.2 Arc Melting	67
3.2.1 Material and Methods.....	67
3.2.2 Alloy Fabrication.....	67
3.2.3 The Arc Melting Process.....	68
3.2.3.1 Ti-Ta based alloys	68
3.2.3.2 Ti-Mo based alloys.....	68
3.3 Thermal and Thermomechanical Treatment	69
3.3.1 Homogenization Heat Treatment	69
3.3.2 Cold Rolling and Recrystallization treatments	69
3.3.3 Solution heat treatment.....	70
3.4 Composition Analysis and Density of Alloys	70
3.5 Transformation Temperatures	70
3.6 Material Characterization.....	71
3.6.1 Microstructural Investigations.....	71
3.6.1.1 Sample Preparation	71
3.6.1.2 Optical Microscopy (OM).....	71
3.6.1.3 Scanning electron microscopy (SEM).....	71
3.6.1.4 X-ray diffraction (XRD).....	72
3.6.1.5 Transmission electron microscopy	72
3.6.2 Mechanical characterization.....	72
3.6.2.1 Nanoindentation Test	72
3.6.2.2 Micro-hardness testing	72
3.6.2.3 Elastic modulus measurement by ultrasound technique	73
3.6.3 Tribology, Electrochemical, and Tribocorrosion Tests.....	74
3.6.3.1 Samples Preparation.....	74
3.6.3.2 Lubricant and electrochemical media	74
3.6.3.3 Tribology test	75
3.6.3.4 Electrochemical test	75
3.6.3.4.1 Open circuit potential (OCP) measurements.....	76
3.6.3.4.2 Potentiodynamic measurements.....	76
3.6.3.4.3 Electrochemical parameters measurements	76
3.6.3.5 Tribocorrosion test	76

3.6.3.5.1 Open circuit potential (OCP) wear test	77
3.6.3.5.2 Potentiostatic wear tests	78
3.6.3.5.3 Electrochemical test of alloys during and after tribocorrosion test.....	78
3.6.3.6 Wear track analysis	78
3.6.3.6.1 Wear track profiles	78
3.6.3.6.2 Total materials loss rate.....	79
3.6.3.6.3 Surface characterization	80
3.6.3.6.4 Focused ion beam (FIB).....	80
3.6.3.6.5 Raman Spectroscopy	80
3.6.3.6.6 Wear-corrosion synergism	81
4.1 Introduction	83
4-2 Composition Analysis and Density.....	83
4-3 Microstructure and Phase Constitution of Titanium Alloys	85
4-4 Mechanical Characterization	100
4-4-1 Reduced Modulus and Nanoindentation Hardness.....	100
4.4.2 Elastic Modulus.....	104
4.4.3 Micro-Hardness	105
4.5 Summary	106
Chapter 5 Results: Tribological Behaviour of Titanium Alloys	107
5.1 Introduction	107
5.2 Lubricated Sliding Friction	107
5.3 Wear Track Morphology, Chemistry and Roughness	116
5.4 Wear Rate.....	132
5.5 Wear Tracks Subsurface Morphology.....	138
5.6 Summary	140
Chapter 6 Results: Electrochemical Behaviour of Titanium Alloys.....	141
6.1 Introduction	141
6.2 Electrochemical Behaviour of Starting Surface of Alloys	141
6.3 Electrochemical Behaviour during and after Rubbing.....	147
6.4 Summary	153
Chapter 7 Results: Tribocorrosion Behaviour of Titanium Alloys.....	155
7.1 Introduction	155
7.2 Tribocorrosion at Open Circuit Potential	155
7.2.1 Sliding Friction Response	155
7.2.2 Wear Morphology, Chemistry and Roughness under OCP conditions.....	160

7.2.3 Total Material Loss Rate	169
7.2.4 Subsurface Morphology	173
7.3 Tribocorrosion at Cathodic Potentiostatic (-0.5V vs OCP).....	174
7.3.1 Sliding Friction Response	174
7.3.2 Wear Morphology, Chemistry and Roughness under cathodic conditions.....	178
7.3.3 Total Material Loss Rate	187
7.3.4 Subsurface Morphology	191
7.4 Tribocorrosion Under Anodic Potentiostatic Conditions.....	192
7.4.1 Sliding Friction Response	192
7.4.2 Wear Morphology, Chemistry and Roughness under anodic conditions.....	197
7.4.3 Total Material Loss Rate for anodic conditions	207
7.4.4 Subsurface Morphology	211
7.4 Summary	212
Chapter 8: Discussion	214
8.1 Structural and Properties Characterization of Titanium Alloys	214
8.1.1 Introduction	214
8.1.2 Composition Analysis and Density	214
8.1.3 Microstructure and Phase Constitution	214
8.1.4 Mechanical Characterization.....	217
8.1.4.1 Reduced Modulus, Nanoindentation Hardness and Elastic Modulus	217
8.2.1 Introduction	219
8.2.2 Lubricated Sliding Friction	219
8.2.3 Wear Track Morphology, Chemistry, and subsurface Morphology	221
8.2.4 Wear Rate.....	223
8.3 Electrochemical Behavior of Titanium Alloys.....	224
8.3.1 Introduction	224
8.3.2 Electrochemical Characterization: Corrosion Resistance	224
8.3.3 Electrochemical Behavior During and After Rubbing.....	227
8.4 Tribocorrosion Behaviour of Titanium Alloys.....	229
8.4.1 Introduction	229
8.4.2 Sliding Friction Response of Titanium Alloys.....	229
8.4.3 Corrosive Wear Tracks, Surface and subsurface Morphology and Surface Chemistry	236
8.4.4 Total Material Loss Rate	239
Chapter 9: Conclusions and Recommendations for Future Work	244

9-1 Conclusions.....	244
9.1.1 Structure and Property Characterization of Titanium Alloys.....	244
9.1.2 Tribological Behavior of Titanium Alloys.....	244
9.1.4 Tribocorrosion Behavior of Titanium Alloys.....	246
9.2 Recommendations for Future Work.....	248
1- Tribological Behaviour	248
2- Electrochemical Behaviour of Titanium Alloys	248
3- Tribocorrosion Behaviour of Titanium Alloys	248
References	250
Appendix.....	269
Appendix A	269
Wear Track Roughness	269
Appendix A	272
Wear Track Surface Chemistry	272

List of Figures

Figure 2-1 The definition boundaries of biomedical materials, biomaterials, and biological materials [3]	5
Figure 2-2 The major applications of biomaterials in the human body [32]	6
Figure 2-3 Representation of different medical devices [33]	6
Figure 2-4 History of metals and various materials for biomedical applications[46]	8
Figure 2-5(a) The Harrington rod, (b) The stem of a total hip replacement [3]	9
Figure 2-6(a) A vascular stent, (b) an aneurysm clip [3]	9
Figure 2-7(a) Cytotoxicity of some pure metals, (b) the relationship between polarization resistances and biocompatibility of pure metals, cobalt-chromium alloy and stainless steels [73]	12
Figure 2-8 Fatigue strength at 10^7 cycles of biomedical, cobalt alloys, stainless steel, titanium and its alloys, and bone [80]	15
Figure 2-9 Two congruent joints in human bodies, (a) hip, and (b) shoulder [3]	16
Figure 2-10 Two artificial incongruent joints (knee) and (b) ankle [3]	17
Figure 2-11 The hcp α structure titanium, β structure titanium and their lattice parameters at (RT for α and 900 °C for β)[93]	19
Figure 2-12 Schematic diagrams showing the effect of alloying elements on the β -transus temperature [90]	20
Figure 2-13 The impact of roughness on friction [146]	27
Figure 2-14 Schematic of mechanisms of wear [149]	28
Figure 2-15 The Stribeck curve [148]	30
Figure 2-16 Schematic of wear test methods[7]	30
Figure 2-17 Materials factors affecting the tribological performance of titanium [160]	31
Figure 2-18 Schematic presents the electrochemical reactions involves in the corrosion of an active and a passive metal [33]	34
Figure 2-19 Typical polarisation plot for a passive material [176]	35
Figure 2-20 Scheme of the reactions occurring at a biomaterial metallic surface in contact with electrolyte [175]	36
Figure 2-21 A hypothetical polarisation of a passive metal [182]	39
Figure 2-22 Tafel plot that can be used to calculate the corrosion parameters [183]	39
Figure 2-23 Nyquist Plot for a Simple Electrochemical System [189].	42
Figure 2-24 Bode Plot for a Simple Electrochemical System[189]	42
Figure 2-25 Equivalent Electrical Circuit a) Compact oxide film, b) Porous passive layer [193]	42
Figure 2-26 Schematic represent the types of corrosion [181]	43
Figure 2-27 Scheme of Galvanic corrosion [198]	45
Figure 2-28 Galvanic series of various metal in salt water [198]	45
Figure 2-29 Schematic representation of two theoretically limiting galvanic coupling situations that can arise during tribocorrosion at OCP [196]	46
Figure 2-30 Schematic representation of two types of galvanic coupling mechanisms arising during tribocorrosion of 304SS in artificial seawater at OCP [195]	46
Figure 2-31 Types of corrosion taking place in implant [200]	47
Figure 2-32 Schematic illustration of the current -potential relationship for titanium in an acidic solution [190].	48
Figure 2-33 Basic concept and definition of tribocorrosion [179].	52

Figure 2-34 Schematic representation of tribocorrosion mechanism [200].....	52
Figure 2-35A spectrum of practical importance of tribocorrosion [179].	54
Figure 2-36 Factors influencing the tribocorrosion [179].....	55
Figure 2-37 Schematic diagram of material flows occurring during the formation of third bodies in a tribocorrosion experiment of passive metal [24].....	58
Figure 2-38 Basic methodology in a tribocorrosion study [179].....	61
Figure 2-39 Basic steps in tribocorrosion study [179].....	61
Figure 3-1 Schematic of cross sectional area of the wear track calculation via numerical integration [146].....	79
Figure 4-1 Density for titanium and titanium alloys used in this study.	84
Figure 4-2 Chemical distribution of the titanium alloys fabricated in this study, where for Ti- Mo alloys (red=Ti, green=Mo, Cyan=Nb, and green=Zr), for Ti-Ta alloys (red=Ti, green=Ta, and cyan Al).	85
Figure 4-3 Light micrographs showing microstructure of the titanium alloys.	86
Figure 4-4 SEM micrographs (BSE, orientation and composition contrast) of the microstructure of titanium alloys.	88
Figure 4-5 X-ray diffraction pattern of titanium alloys.	90
Figure 4-6 X-ray diffraction pattern of the Ti-Ta ₂₇ -Al ₅ alloy.....	90
Figure 4-7 DSC heating and cooling curves of the titanium alloys.	91
Figure 4-8 Combined DTA/TGA heating curves of the titanium alloys.	92
Figure 4-9 Combined DTA/TGA heating curves of Ti-Ta ₃₀ and Ti-Ta ₂₇ -Al ₅ alloys.	92
Figure 4-10 DSC heating and cooling curves of the Ti-Ta ₂₇ -Al ₅ alloy.	93
Figure 4-11 SEM (BSE) and Energy Dispersive X-ray (EDX) spectroscopy results of Ti-Mo ₈ - Nb ₄ -Zr ₂ obtained from the three spectra highlighted in SEM (BSE).....	94
Figure 4-12 SEM (BSE) and Energy Dispersive X-ray (EDX) spectroscopy results of Ti-Mo ₈ - Nb ₆ -Zr ₄ obtained from the seven spectra highlighted in SEM (BSE).....	95
Figure 4-13 SEM (BSE) and Energy Dispersive X-ray (EDX) spectroscopy results of Ti-Mo ₈ - Nb ₄ -Zr ₅ obtained from the four spectra highlighted in SEM (BSE).....	96
Figure 4-14 SEM (BSE) and Energy Dispersive X-ray (EDX) spectroscopy results of Ti-Ta ₃₀ obtained from the four spectra highlighted in SEM (BSE).....	97
Figure 4-15 SEM (BSE) and Energy Dispersive X-ray (EDX) spectroscopy results of Ti-Ta ₂₇ - Al ₅ obtained from the eight spectra highlighted in SEM (BSE).....	98
Figure 4-16 Bright field TEM image and the corresponding electron diffraction of solution treated titanium alloys.....	99
Figure 4-17 Reduced elastic modulus of titanium and its alloys measured by nano-indentation at different loads.	100
Figure 4-18 Reduced modulus of titanium and its alloys measured by nano-indentation technique as a function of the contact depth with different loads.....	101
Figure 4-19 Nanoindentation hardness of titanium and its alloys used in this study measured by nano-indentation at different loads.	101
Figure 4-20 Nanoindentation of titanium and its alloys used in this study measured by nano- indentation as a function of the contact depth with different loads.	102
Figure 4-21 Reduced modulus of titanium and its alloys measured by nano-indentation at constant load.	103
Figure 4-22 Nanoindentation hardness of titanium and its alloys measured by nano- indentation at constant load.	103

Figure 4-23 The average elastic modulus of titanium alloys.....	104
Figure 4-24 Microhardness of titanium alloys.....	105
Figure 5-1: The evolution of the coefficient of friction of titanium alloys at a normal load of 0.25 N under lubricated conditions.....	108
Figure 5-2: The evolution of the coefficient of friction titanium alloys at a normal load of 0.5 N under lubricated conditions.....	110
Figure 5-3: The evolution of the coefficient of friction of titanium alloys at a normal load of 1 N under lubricated conditions.....	112
Figure 5-4: The evolution of the coefficient of friction of titanium alloys at a normal load of 2 N under lubricated conditions.....	114
Figure 5-5 The mean friction coefficient values of titanium alloys under different loads in lubricated conditions.....	116
Figure 5-6: SEM micrographs of wear track of titanium alloys at a normal load of 0.25 N under lubricated conditions.....	118
Figure 5-7: SEM micrographs of wear track of titanium alloys at a normal load of 0.5 N under lubricated conditions.....	120
Figure 5-8: SEM micrographs of wear track of titanium alloys at a normal load of 1 N under lubricated conditions.....	122
Figure 5-9: SEM micrographs of wear track of titanium alloys at a normal load of 2 N under lubricated conditions.....	124
Figure 5-10: EDX element mapping of the wear track of titanium alloys at a normal load 0.25N under lubricated rubbing conditions.	126
Figure 5-11: Raman spectra of the wear track of titanium alloys under lubricated conditions.	128
Figure 5-12 Optical images of the alumina ball after wear tests.	128
Figure 5-13 SEM images of the alumina ball after wear tests.....	129
Figure 5-14 EDX element mapping of the alumina ball after wear tests.....	129
Figure 5-15 The average surface roughness titanium alloys at different loads under lubricated conditions.....	130
Figure 5-16: Surface roughness, 3D, X, Y profile, and 2D top view of the wear track at a normal load of 0.25N under lubricated conditions.	130
Figure 5-17: 3D images of wear track of titanium and titanium alloys fabricated in this study at a normal load of 0.25N under lubricated rubbing conditions.	133
Figure 5-18: 3D images of wear track of titanium and titanium alloys fabricated in this study at a normal load of 0.5N under lubricated rubbing conditions.	134
Figure 5-19: 3D images of wear track of titanium and titanium alloys fabricated in this study at a normal load of 1N under lubricated rubbing conditions.	135
Figure 5-20: 3D images of wear track of titanium and titanium alloys fabricated in this study at a normal load of 2N under lubricated rubbing conditions.	136
Figure 5-21: Wear volumes for titanium alloys at different loads.....	137
Figure 5-22: Specific wear rates of titanium alloys at different loads.....	137
Figure 5-23 Ion channelling contrast image of bulk Ti-Ta ₂₇ -Al ₅ alloy.	138
Figure 5-24 Ion channelling contrast image of a transverse cross-section of wear track formed at Ti-Mo ₈ -Nb ₄ -Zr ₂ under a normal load of 0.5N.....	138
Figure 5-25 Ion channelling contrast image of a transverse cross-section of wear track formed at Ti-Mo ₈ -Nb ₄ -Zr ₂ under a normal load of 2N.....	139

Figure 5-26 Ion channelling contrast image of a transverse cross-section of wear track formed at Ti-Ta ₂₇ -Al ₅ under a normal load of 0.5N.	139
Figure 5-27 Ion channelling contrast image of a transverse cross-section of wear track formed at Ti-Ta ₂₇ -Al ₅ under a normal load of 2N.	139
Figure 6-1 Variation of OCP with time for titanium alloys in bovine calf serum solution. ..	143
Figure 6-2 Potentiodynamic polarization curves of titanium alloys in new-born calf serum solution, the arrows indicates the formation of new passive region.	144
Figure 6-3 The surface morphology of titanium alloys after potentiodynamic polarization.	146
Figure 6-4 Tafel curves of titanium alloys.....	149
Figure 6-5 Tafel curves of titanium alloys during rubbing under OCP conditions.	150
Figure 6-6 Tafel curves of titanium alloys after tribocorrosion tests under OCP rubbing conditions.....	150
Figure 6-7 Tafel curves of titanium alloys after tribocorrosion tests under cathodic potentiostatic rubbing conditions.....	151
Figure 6-8 Tafel curves of titanium alloys after tribocorrosion tests under anodic potentiostatic rubbing conditions.....	152
Figure 7-1: The evolution of the coefficient of friction and the open circuit potential of Ti-Mo ₈ -Nb ₆ -Zr ₄ under OCP-rubbing conditions. The two graphs show the repeatability of the same test.....	156
Figure 7-2: The evolution of the coefficient of friction and the open circuit potential of Ti-Mo ₈ -Nb ₄ -Zr ₂ under OCP-rubbing conditions.	157
Figure 7-3: The evolution of the coefficient of friction and the open circuit potential of Ti-Mo ₈ -Nb ₄ -Zr ₅ under OCP-rubbing conditions.	157
Figure 7-4: The evolution of the coefficient of friction and the open circuit potential of Ti-Ta ₃₀ under OCP-rubbing conditions.	157
Figure 7-5: The evolution of the coefficient of friction and the open circuit potential of Ti-Ta ₂₇ -Al ₅ under OCP-rubbing conditions.....	158
Figure 7-6: The evolution of the coefficient of friction and the open circuit potential of Cp-Ti under OCP-rubbing conditions.	158
Figure 7-7: The evolution of the coefficient of friction and the open circuit potential of Ti-6Al-4V under OCP-rubbing conditions. The two graphs show the repeatability of the same test.	159
Figure 7-8 The mean friction coefficient and potential values of titanium alloys under OCP rubbing conditions.	159
Figure 7-9: SEM micrographs of wear tracks of the titanium alloys under OCP rubbing conditions.....	161
Figure 7-10: EDX element mapping of the wear track of titanium alloys under OCP rubbing conditions.....	163
Figure 7-11: Raman spectra of the wear track of titanium alloys under OCP rubbing conditions.....	165
Figure 7-12 Optical images of the alumina balls rubbing against the titanium alloys under OCP rubbing conditions.....	166
Figure 7-13 SEM images of the alumina balls rubbing against the titanium alloys under OCP rubbing conditions.	166
Figure 7-14 EDX element mapping of the alumina ball after rubbing against Cp-Ti under OCP rubbing conditions.....	167

Figure 7-15 The average surface roughness of titanium alloys under OCP rubbing conditions.	167
Figure 7-16: Surface roughness 3D and 2D top view of the wear track under OCP rubbing conditions.	168
Figure 7-17: 3D images of wear track of titanium alloys under OCP rubbing conditions. ...	170
Figure 7-18: (a) Wear volumes (b) Specific wear rate of wear track for titanium alloys under OCP rubbing conditions.	171
Figure 7-19 Tafel plots during rubbing at OCP.	171
Figure 7-20 Contribution of mechanical wear and electrochemical to total material loss rate volume of titanium alloys after tribocorrosion tests under OCP rubbing conditions.	172
Figure 7-21 Ion channelling contrast image of a transverse cross-section of wear track formed at Ti-Mo ₈ -Nb ₄ -Zr ₅ under OCP rubbing conditions.	173
Figure 7-22 Ion channelling contrast image of a transverse cross-section of wear track formed at Ti-Ta ₂₇ -Al ₅ under OCP rubbing conditions.	173
Figure 7-23: The evolution of the coefficient of friction and the current of Ti-Mo ₈ -Nb ₆ -Zr ₄ alloy under cathodic potentiostatic rubbing conditions. The two graphs are repeat of the same test.	175
Figure 7-24: The evolution of the coefficient of friction and the current of Ti-Mo ₈ -Nb ₄ -Zr ₂ alloy under cathodic potentiostatic rubbing conditions.	175
Figure 7-25: The evolution of the coefficient of friction and the current of Ti-Mo ₈ -Nb ₄ -Zr ₅ alloy under cathodic potentiostatic rubbing conditions.	176
Figure 7-26: The evolution of the coefficient of friction and the current of Ti-Ta ₃₀ alloy under cathodic potentiostatic rubbing conditions.	176
Figure 7-27: The evolution of the coefficient of friction and the current of Ti-Ta ₂₇ -Al ₅ alloy under cathodic potentiostatic rubbing conditions.	176
Figure 7-28: The evolution of the coefficient of friction and the current of Cp-Ti under cathodic potentiostatic rubbing conditions.	177
Figure 7-29: The evolution of the coefficient of friction and the current of Ti-6Al-4V under cathodic potentiostatic rubbing conditions. The two graphs are repeat of the same test.	177
Figure 7-30 The average friction coefficient and current values of titanium alloys under cathodic potentiostatic rubbing conditions.	178
Figure 7-31: SEM micrographs of wear tracks of titanium alloys under cathodic potentiostatic rubbing conditions.	179
Figure 7-32: EDX element mapping of titanium alloys under cathodic	181
Figure 7-33: Raman spectra of the wear track of titanium alloys under cathodic potentiostatic rubbing conditions.	183
Figure 7-34 Optical images of the alumina balls rubbing against the titanium alloys under cathodic rubbing conditions.	184
Figure 7-35 SEM images of the alumina balls rubbing against the titanium alloys under cathodic rubbing conditions.	184
Figure 7-36 EDX element mapping of the alumina ball after rubbing against Ti-Mo ₈ -Nb ₆ -Zr ₄ and Cp-Ti alloys under cathodic rubbing conditions.	185
Figure 7-37 The average surface roughness titanium alloys under cathodic potentiostatic rubbing conditions.	185
Figure 7-38: Surface roughness, 3D and 2D top view of the wear track under cathodic potentiostatic rubbing conditions.	186

Figure 7-39: 3D images of the wear track of titanium and titanium alloys fabricated in this study under cathodic potentiostatic rubbing conditions.....	188
Figure 7-40: (a) Removed wear volumes (b) Specific wear rates of wear track for titanium alloys under cathodic potentiostatic rubbing conditions.....	189
Figure 7-41 Contribution of mechanical wear and electrochemical to total material loss rate volume of titanium alloys after tribocorrosion tests under cathodic potentiostatic rubbing conditions.....	190
Figure 7-42 Ion channelling contrast image of a transverse cross-section of wear track formed at Ti-Ta ₂₇ -Al ₅ under cathodic rubbing conditions.	191
Figure 7-43 Ion channelling contrast image of a transverse cross-section of wear track formed at Ti-Mo ₈ -Nb ₄ -Zr ₅ under cathodic rubbing conditions.	191
Figure 7-44: The evolution of the coefficient of friction (COF) and the current of Ti-Mo ₈ -Nb ₆ -Zr ₄ alloy under anodic potentiostatic rubbing conditions. The two graphs show the repetition of the same test, which gives very consistent results.	193
Figure 7-45: The evolution of the coefficient of friction (COF) and the current of Ti-Mo ₈ -Nb ₄ -Zr ₂ alloy under anodic potentiostatic rubbing conditions.	193
Figure 7-46: The evolution of the coefficient of friction (COF) and the current of Ti-Mo ₈ -Nb ₄ -Zr ₅ alloy under anodic potentiostatic rubbing conditions.	194
Figure 7-47: The evolution of the coefficient of friction (COF) and the current of Ti-Ta ₃₀ alloy under anodic potentiostatic rubbing conditions.	194
Figure 7-48: The evolution of the coefficient of friction (COF) and the current of Ti-Ta ₂₇ -Al ₅ alloy under anodic potentiostatic rubbing conditions.	195
Figure 7-49: The evolution of the coefficient of friction (COF) and the current of Cp-Ti alloy under anodic potentiostatic rubbing conditions.	195
Figure 7-50: The evolution of the coefficient of friction (COF) and the current of Ti-6Al-4V alloy under anodic potentiostatic rubbing conditions. The two graphs show the repetition of the same test, which gives very consistent results.	196
Figure 7-51 The mean friction coefficient and current values of titanium alloys under anodic potentiostatic rubbing conditions.....	197
Figure 7-52: SEM micrographs of wear tracks of titanium alloys under anodic potentiostatic rubbing conditions.	199
Figure 7-53: EDX element mapping of the wear track of titanium alloys under anodic potentiostatic conditions.	201
Figure 7-54: Raman spectra of the wear track of titanium alloys under anodic potentiostatic conditions.....	203
Figure 7-55 Optical images of the alumina balls rubbing against the titanium alloys under cathodic rubbing conditions.....	204
Figure 7-56 SEM images of the alumina balls rubbing against the titanium alloys under cathodic rubbing conditions.....	204
Figure 7-57 EDX element mapping of alumina ball rubbing against (a) Ti-Mo ₈ -Nb ₆ -Zr ₄ and (b) Ti-6Al-4V under anodic rubbing.....	205
Figure 7-58 The average surface roughness of titanium alloys under anodic potentiostatic conditions.....	205
Figure 7-59: Surface roughness, 3D and 2D top view of titanium alloys under anodic potentiostatic conditions.	206

Figure 7-60: 3D images of wear track of titanium alloys under anodic potentiostatic conditions.....	208
Figure 7-61: (a) Removed wear volumes (b) Specific wear rates of wear track for titanium alloys under anodic potentiostatic conditions.	209
Figure 7-62 Contribution of mechanical wear and electrochemical to total material loss rate volume of titanium alloys after tribocorrosion tests under anodic potentiostatic rubbing conditions.....	210
Figure 7-63 Ion channelling contrast image of a transverse cross-section of wear track formed at Ti-Mo ₈ -Nb ₆ -Zr ₄ under anodic rubbing conditions.	211
Figure 7-64 Ion channelling contrast image of a transverse cross-section of wear track formed at Ti-Ta ₂₇ -Al ₅ under anodic rubbing conditions.	211
Figure 1 Surface roughness, 3D and 2D top view of the wear track at load of 0. 5N	269
Figure 2: Surface roughness, 3D and 2D top view of the wear track at load of 1N	270
Figure 3 Surface roughness, 3D and 2D top view of the wear track at load of 2N	271
Figure 4 EDX element mapping of the wear track of titanium alloys at load of 0. 5N	272
Figure 11: EDX element mapping of the wear track of titanium alloys at load of 1N.....	273
Figure 18: EDX element mapping of the wear track of titanium alloys at load of 2N.....	274

List of Tables

Table 2-1 Comparison of metallic implants used in the human body [7, 47, 68-70]	9
Table 2-2 Elements in the human body [3].....	11
Table 2-3 Roles of macro elements in the human body [3, 71].....	11
Table 2-4 Roles of trace elements in the human body [3]	11
Table 2-5 List of trace elements in the human body [3]	12
Table 2-6 The ionic concentrations (mM) of human blood plasma [74].....	13
Table 2-7 Mechanical properties of metallic biomaterials and cortical bone [76]	14
Table 2-8 Ranking of articulating surfaces for joint prosthetics in terms of wear-resistance [3]	16
Table 2-9 Impurity limits for Cp-Ti (wt%) [106]	22
Table 2-10 The mechanical properties of titanium alloys	22
Table 2-11 ASTM/UN standards for titanium and titanium alloys used for medical implants [3].....	23
Table 2-12 Advantages and disadvantages of various wear test methods [159]	31
Table 3-1 Nominal chemical composition of the alloys used in this study	68
Table 4-1 Chemical composition of the alloys from XRF analysis.....	84
Table 4-2 Structure, microstructure, average grain size of the titanium alloys.	87
Table 4-3 the results from combined DTA/TGA experiments (Fig 4-7 and 4-8) performed in this study.	92
Table 4-4 results from DSC experiments (Fig 4-10) performed in this study.	93
Table 4-5 EDX results of Ti-Mo ₈ -Nb ₄ -Zr ₂ obtained for the three spectra highlighted in figure 4-11.	94
Table 4-6 EDX results of Ti-Mo ₈ -Nb ₆ -Zr ₄ obtained for the seven spectra highlighted in Fig 4-2.	95
Table 4-7 EDX results of Ti-Mo ₈ -Nb ₄ -Zr ₅ obtained for the four spectra highlighted in Fig 4-3.	96
Table 4-8 EDX results of Ti-Ta ₃₀ obtained for the four spectra highlighted in Fig 4 -14.	97
Table 4-9 EDX results of Ti-Ta ₂₇ -Al ₅ obtained for the eight spectra highlighted in Fig 4-15. 98	
Table 4-10 Estimation of reduced elastic modulus and nano-hardness through nanoindentation technique at different loads.	102
Table 4-11 Estimation of reduced elastic modulus and nano-hardness through nanoindentation technique with the constant load.	104
Table 6-1 The average OCP values extracted from the figure 6-1	143
Table 6-2 Electrochemical parameters of titanium alloys from potentiodynamic curves.	146
Table 6-3 Electrochemical parameters of titanium alloys from Tafel plot.....	149
Table 6-4 Electrochemical parameters of titanium and titanium alloys after tribocorrosion tests under OCP rubbing conditions.	151
Table 6-5 Electrochemical parameters of titanium alloys after tribocorrosion tests under cathodic potentiostatic rubbing conditions.	152
Table 6-6 Electrochemical parameters of titanium and titanium alloys after tribocorrosion tests under anodic potentiostatic rubbing conditions.	153

List of Abbreviations and Symbols

A_f	Austenite finish transformation temperature
A_P	Austenitic peak temperature
Ar	Argon
A_s	Austenite start transformation temperature
at. %	Atomic percent
Aust	Austenite
CE	Counter Electrode
CP Ti	Commercial pure titanium
d	Dimension of the diagonal
DSC	Differential scanning calorimetry
DTA	Differential thermal analysis
E_{corr}	Corrosion potential
i_{corr}	Corrosion density
M	Martensite
M_f	Martensitic finish transformation temperature
M_P	Martensite peak temperature
M_s	Martensitic start transformation temperature
MT	Martensitic transformation
MTT	Martensitic transformation temperatures
OCP	Open Circuit Potential
P	The applied load
R.T	Room temperature

RE	Reference Electrode
RSME	Reversible shape memory effect
ST	Solution treated
TMT	Thermoelastic martensitic transformation
TT	Transformation temperatures
VAR	vacuum arc- remelting
WQ	Water quenching
Wt%	Weight percent
ΔT	Thermal hysteresis
$\Delta\sigma$	Stress hysteresis
$^{\circ}C$	Celsius degree
A^{σ}_f	Austenite finish temperatures with stress
A^{σ}_s	Austenite start temperatures with stress
CR	Cold Rolling
M^{σ}_f	Martensitic finish temperatures with stress
M^{σ}_s	Martensitic start temperatures with stress
t	Thickness
α	Alpha phase
α'	Hexagonal martensite
α''	Orthorhombic martensite
β	Beta phase
β_a	Anodic Beta
β_c	Cathodic Beta
ω	Omega phase

Chapter 1 MOTIVATION and RESEARCH AIMS

1.1 Motivation

Titanium and its alloys have been intensely researched over the last few decades because of their unique properties, such as low Young's modulus, high specific strength, low density, high biocompatibility and excellent corrosion resistance [1]. Due to these properties, Ti and Ti alloys are extensively used in biomedical applications as dental and orthopaedic implants [2, 3]. Commercial pure titanium (CP Ti), with an α phase structure, was initially used in some dental and orthopaedic applications without causing any toxicity during service [1, 4-6]. However, the mechanical properties of CP Ti are inadequate for some applications such as those that require wear resistance and high strength [7, 8]. Therefore, to overcome this issue Ti-based alloys have been developed that have high strength[9]. The Ti-6Al-4V alloy with an $\alpha+\beta$ phase structure is the main Ti-based alloy used in biomedical applications [10]. However, it was reported that the release of aluminium and vanadium ions from Ti-6Al-4V alloy during a long period of time might cause long term health issues, such as osteomalacia, neurological disorders, toxicity, peripheral neuropathy and Alzheimer's diseases. Furthermore, it was reported that these elements can delay osseointegration after implantation, in other words a delay in bone integration[7, 9, 11, 12].

Although many researchers have highlighted some positive properties of Cp-Ti and Ti-6Al-4V alloys, there are still some issues that need to be overcome. Recent studies show that the α -CP and $\alpha+\beta$ Ti-6Al-4V alloys have a high elastic modulus (above 100 GPa) compared to bone (20 GPa) that leads to a stress shielding effect and consequently to bone loss and loosening of implants [1, 13-16]. Also, it was reported that the corrosion rate of Ti- alloys with more than one phase is higher than single phase Ti-alloys [17], and the tribological and tribocorrosion properties under different loads and friction conditions are poor[18]. In order to tackle these drawbacks, many studies have been proposed to develop new Ti-based alloys with non-allergic and non-toxic elements, that are single phase, and have a low elastic modulus[19, 20]. For this purpose, lower elastic modulus and high corrosion resistance β -type Ti-based alloys containing non-toxic and non-allergic elements such as Mo, Nb, Zr and Ta have attracted attention as more competitive candidates for biomedical materials compared with the α -CP and $\alpha+\beta$ Ti-6Al-4V alloys and other conventional alloys [19, 21-23].

The literature survey shows that there has been limited work focused on the tribocorrosion behaviour of all types of Ti and Ti alloys, in contrast to the numerous works that focus on their mechanical properties and microstructure. This is surprising given that the tribocorrosion behaviour is an important factor to consider for some biomedical applications for example orthopaedic, hip-joint stems [24, 25]. All types of Ti and Ti alloy implants are normally subjected to tribocorrosion [24-27]. Indeed, analysis of retrieved implants indicates damage attributable to tribocorrosion effects is seen with all metal-containing implants. Damage through tribocorrosion can result in impaired function of the implant, through loosening, initiation of fatigue failures or adverse localised and systemic reactions to the material released from these interfaces.

The absence of investigations into tribocorrosion studies of a wide range of titanium alloys means that there is no clear understanding of what the optimum composition is. Indeed, there is no idea as to the optimum microstructure, whether it is fully stable β , near β with some α present, and what effect the presence of martensite and Ω have on the tribocorrosion behaviour. Moreover, the synergistic effect of wear and corrosion has not been considered, and the corrosion and wear are often investigated separately [10, 28]. Such alloys can have a wide range of compositions including Ti-Mo alloys, Ti-Mo-Nb-Zr alloys, Ti-Ta alloys, Ti-Ta-Al alloys all of which are candidates for biomedical applications[29, 30]. This research focuses on a number of alloys with systematic differences in microstructure and with different compositions to understand the effect of these key variables on the tribocorrosion behaviour.

1-2 Objectives of This Study

With the preceding motivation, the following objectives have been established:

1- To develop an ingot metallurgy processing method to produce a range of β -phased alloys with a systematic range of microstructures and correlate the microstructure with the process conditions and the composition of the alloys.

2- To systematically investigate the effect of the microstructures on the tribological and electrochemical response of these alloys.

3- To systematically investigate the effect of the different microstructures on the tribocorrosion behaviour of these alloys and thereby generate recommendations for the ideal implant microstructure and composition.

1-3 Thesis outline

Chapter 2, “Literature Review”, and contains a brief introduction to biomaterials.

Titanium and titanium alloys (microstructure, general properties, and motivation for design of β - titanium alloys as biomaterials) are also given in this chapter. A brief introduction to tribological, electrochemical and tribocorrosion phenomena is presented in this chapter.

Chapter 3, “Experimental Procedure”, contains the materials and methods used in this work. [This includes the detailed procedure used to prepare samples by Arc melting (materials and method, alloy fabrication, and arc melting process). Thermomechanical heat treatment and sample preparation is also explained in detail. The analysis of composition, microstructure and mechanical properties are also explained. Tribological, electrochemical and tribocorrosion tests are also presented.

Chapter 4, “Results: Structural and Properties Characterization of Titanium and Titanium Alloys Fabricated in This Work”, contains all the experimental results of composition analysis, transformation temperatures, phase analysis, microstructure analysis and mechanical properties of titanium alloys.

Chapter 5, “Results: Tribological Behaviour of Titanium and Titanium Alloys Fabricated in This Work” contains all the experimental results of the tribological behaviour of the titanium alloys, and all characterization after tribological tests.

Chapter 6, “Results: Electrochemical Behaviour of Titanium and Titanium Alloys Fabricated in This Work” contains all the experimental results of electrochemical behaviour of titanium alloys and all characterization after electrochemical tests.

Chapter 7, “Results: Tribocorrosion Behaviour of Titanium and Titanium Alloys Fabricated in This Work”, contains all experimental results of tribocorrosion behaviour, and all characterization after tribocorrosion tests.

Chapter 8, the “Discussion”, contains the discussion of experimental results for all work carried out on structural and properties characterization, tribological, electrochemical, and tribocorrosion behaviour of the alloys.

Chapter 9, “Conclusions and Recommendations for future works” contains the main conclusions and new findings from the experimental of this work. Furthermore, the suggestion and recommendation for future work are also presented.

Chapter 2 : Literature Review

2.1 Introduction

This chapter contains a review of the literature related to the present work. Firstly, biomaterials and the historical of developments of metallic biomaterials are briefly reviewed, focusing on definitions of biomaterials, biological materials and biomedical materials, and fundamental considerations in the design and selection of metallic implants. The following sections then review information related to titanium and titanium alloys, including general properties, crystal structure, titanium alloys as biomaterials, biocompatibility of alloying elements and titanium alloys. The latter two main sections include information about tribology and corrosion in general, and specifically of titanium. Finally, the last section includes a review of tribocorrosion.

2.2 Biomaterials

A common feature of biomaterials is that they can be used in intimate contact with the living body [3]. However, biomaterials have been defined in slightly different ways according to several subject experts. The National Institute of Health Consensus Development Conference, USA, states that a biomaterial is defined as “any substance (other than drugs) or combination of substances, natural or synthetic, that are used as a whole or as a part of a system to replace or assist part of an organic or tissue, which can be used for any period of time”. In Materials Science, a biomaterial is defined as “a material that has been engineered to take a form which can be used alone or as part of a complex system in intimate contact with living body, by control of interactions with components of living systems” [3]. In other words, a biomaterial is “any substance, natural in origin or man-made, which is used to replace or to assist part of an organ or tissue, while in intimate contact with it”. Hence, the prefix “bio” in biomaterials refers to “biocompatibility”, rather than “biomedical or biological” [3]. Furthermore, the term biomaterial is used with various definition boundaries in the scientific and legal communities. According to the legal field, a biomaterial is defined as a component of medical devices [3, 31]. Medical devices are defined as, “any instrument, implement, machine, apparatus, implant, in vitro reagent or calibrator, software, material or other similar or related articles, intended using manufacture to be used alone or as apart (combination) for human being to one or more specific purposes of investigation, monitoring, prevention, diagnosis, control of conception, supporting or sustaining life, and disinfection of medical devices”[3, 31]. For example, and according to the definition in the legal field, the materials used for corrective

eye-wear and artificial leg prostheses are an example of biomedical devices, while the materials used for contact lenses and total hip replacement (THR) are examples of biomaterials [3]. Figure 2.1 presents the definition boundaries of biomedical materials, biomaterials and biological materials [3], and figure 2.2 summarizes the major applications of biomaterials in the human body [32], while figure 2.3 represents the different medical devices[33].

In general, Materials Science classifies materials into four main groups: metals, polymers, ceramics and composite materials. Natural biomaterial groups can be added to previous groups in the field of biomaterials. More details about polymers, ceramics, engineered composites and natural biomaterials as biomaterials (properties and applications) can be found in references [32, 34-45]. The following section will briefly discuss metallic implant biomaterials.

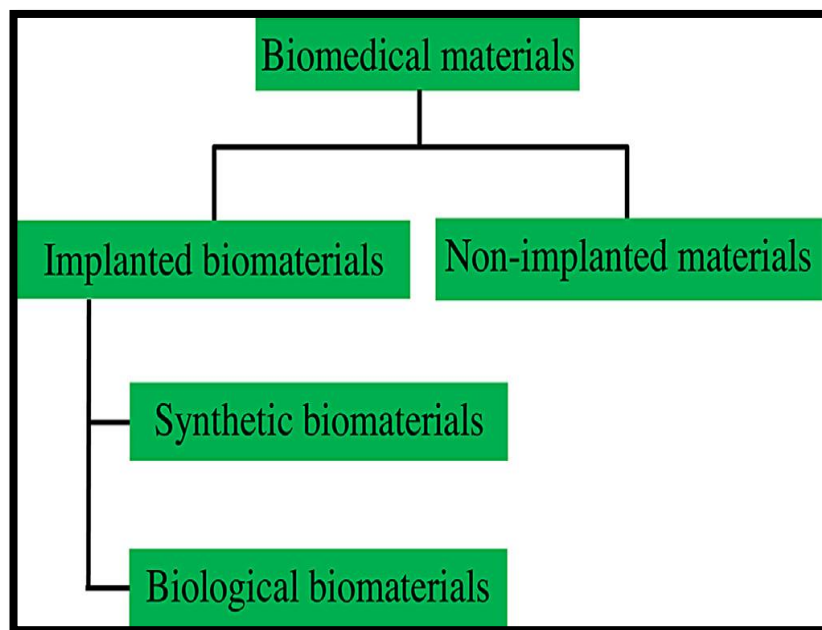


Figure 2-1 The definition boundaries of biomedical materials, biomaterials, and biological materials [3]

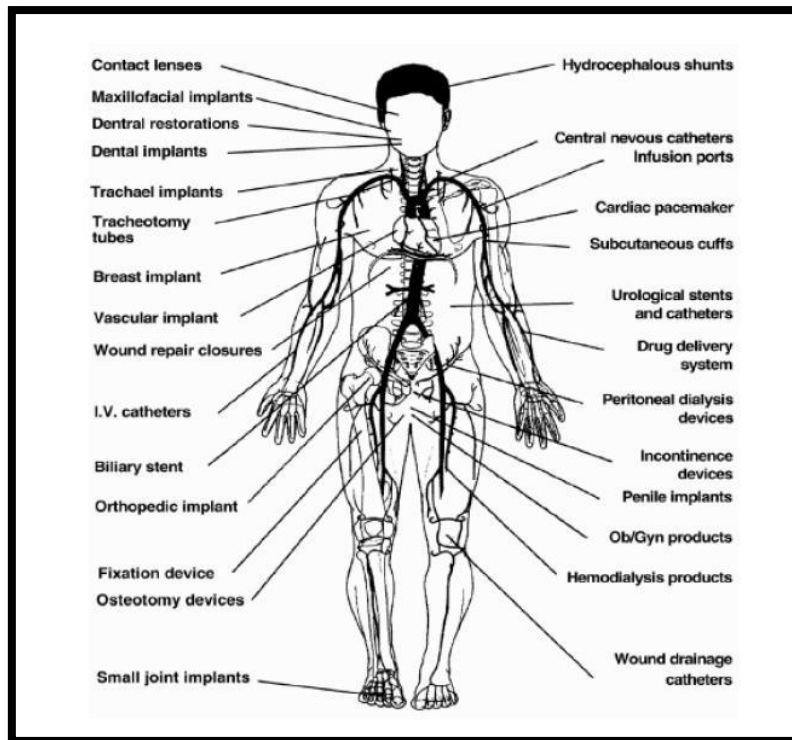


Figure 2-2 The major applications of biomaterials in the human body [32]

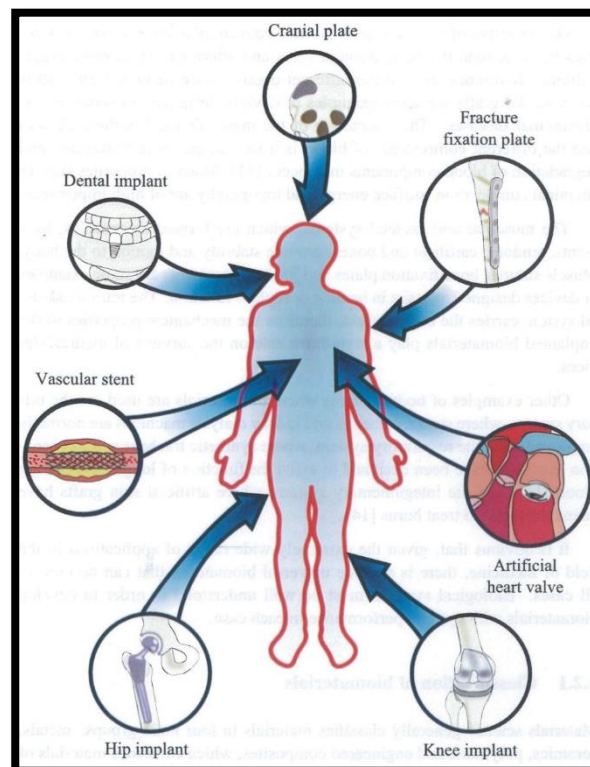


Figure 2-3 Representation of different medical devices [33]

2.2.1 Historical Developments of Metallic Biomaterials

Metals and their alloys are widely used as medical implants, and this can be traced back to the 19th century [3]. With the development of the economy and technology, a large number of metals and alloys are produced by industry. However, few metals and alloys are biocompatible and capable of long-term success as a medical implant [3]. Based on the major alloying element, these few metals and alloys can be categorized into four groups, namely: stainless steels, cobalt-based alloys, titanium – based alloys and miscellaneous others [3]. The use of stainless steel alloys for medical implants can be traced back to the 1920s (see figure 2.4)[46] and among the stainless steels, 316L is the most common biomaterial that has been used for a long time. Although this alloy has the ability to passivate and form a passive oxide film mainly composed of chromium oxide, stainless steel tends to corrode inside the body under certain circumstances in highly stressed and oxygen depleted regions. It was reported that crevice and fretting corrosion, poor osseointegration in the presence of granulated tissue between the alloys surface and the surrounding bone (see section 2.2.2.5), and a very high Young's modulus are the most common problems which limit the use of stainless steel alloys as biomaterials [3, 46, 47].

Cobalt-based alloys have been used for biomedical applications for the last fifty years, as these alloys have good corrosion resistance and wear resistance significantly higher than that of stainless steels [3, 46, 47]. Because stainless steel and cobalt-based alloys usually contain some harmful elements, including Ni, Co, and Cr, commercially pure titanium and titanium alloys were proposed as an alternative for stainless steel alloys (316L) and cobalt-based alloys. Therefore, titanium and some titanium alloys have been used for biomedical applications since the early 1970s [3, 48, 49] (see figure 2.4). Firstly, Cp-Ti was proposed for use as a biomedical material, as it has a higher corrosion resistance and has the ability to form an inert and stable oxide film spontaneously when Cp-Ti surface is exposed to oxidising environment [3, 48, 49]. According to the American Society for Testing and Materials (ASTM), Cp-Ti can be specified as unalloyed Cp-Ti grades 1 to 4. CP-Ti grade 2 titanium is the main unalloyed Ti used in dental implant applications [2, 48]. As much as Cp-Ti has many advantages, however it has some disadvantages, namely, the mechanical properties of Cp-Ti cannot satisfy the requirements of biomedical applications in some cases, such as intensive wear use (poor wear resistance) and hard tissue replacement [2, 3, 50, 51]. To overcome this restriction, titanium-6% aluminium -4% vanadium (Ti-6Al-4V) with α - β -phase structure was proposed to substitute the Cp-Ti alloy. However, there are concerns regarding

the toxicity of aluminium and vanadium, which may cause severe issues once the metal ions are released inside the living body. To tackle potential vanadium toxicity, new titanium alloy compositions with V-free α - β -type titanium based alloys have been developed [2, 3, 50, 51]. Two alloys with good mechanical properties and similar metallurgical behaviour to Ti-6Al-4V were developed to address the toxicity of vanadium, including Ti-6Al-7Nb and Ti-5Al-2.5Fe [1, 49, 52]. Although these alloys have a number of advantages, the elastic modulus of α -type and α - β -type titanium-based alloys is significantly higher than that of human bone, which leads to the stress shielding effect (see section 2. 2.2.3) [49, 51, 53-55]. Consequently, β -type titanium alloys with a low modulus were proposed to alleviate the stress shielding effect; more than one system of β -type titanium alloys can be found in [2, 55-63] (more detail about titanium and titanium alloys will be discuss in section 2.3).

Recently, NiTi shape memory alloys and new magnesium-based alloys have been introduced. Due to their unique material properties, which include the shape memory of NiTi and degradability of magnesium alloys, these materials are currently being developed [64-67]. These properties could meet more specialized requirements, such as non-conventional reconstructive surgery hard tissues/organs (NiTi shape memory alloys as vascular stents), and bone tissue engineering and regeneration (magnesium -based alloys) [64-67]. The advantages, disadvantages and principal applications of metallic implants used in the human body are listed in table 2.1 [7, 47, 68-70]. Figures 2.5 and 2.6 show a typical clinical application of metallic materials; in figure 2.5a the Harrington rod is an example of a stainless-steel surgical device, and 2.5b is the stem of a THR, which is usually made from either stainless steel, cobalt-based alloys or titanium – based alloys. Figure 2.6 shows an example of the use a NiTi shape memory alloy, (a) is a vascular stent and (b) an aneurysm clip [3].

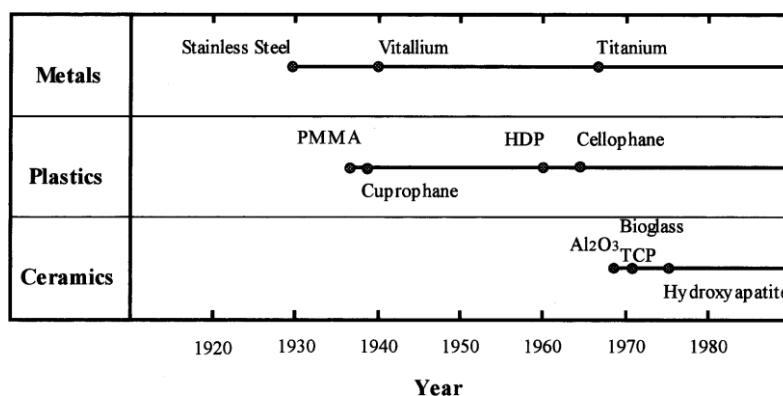


Figure 2-4 History of metals and various materials for biomedical applications[46]

Table 2-1 Comparison of metallic implants used in the human body [7, 47, 68-70]

Metals and alloys	Selected examples	Advantages	Disadvantages	Principal applications
Titanium-based Alloys	CP-Ti, Ti-Al-V, Ti-Al-Nb, Ti-13Nb-13Zr, Ti-Mo-Zr-Fe	High biocompatibility, Low Young's modulus, excellent corrosion resistance, low density	Poor tribological properties, Toxic effect of Al and V on long term	Bone and joint replacement, fracture fixation, dental implants, pacemaker encapsulation
Cobalt and Cr alloys	Co-Cr-Mo, Cr-Ni-Cr-Mo	High wear resistance	Allergy consideration with Ni, Cr and Co, much higher modulus than bone	Bone and joint replacement, dental implants, dental restorations, heart valves
Stainless steels	316L stainless steel	High wear resistance	Allergy consideration with Ni, Cr and Co, much higher modulus than bone	Fracture fixation, stents, surgical instruments
Others	Ni-Ti	Low Young's modulus	Ni cause allergy	Bone plates, stents, orthodontic wires
	Platinum and Pt-Ir	High corrosion resistant under extreme voltage potential and charge transfer conditions		Electrodes
	Hg-Ag-Sn amalgam	Easy <i>in situ</i> formability to a desired shape, susceptible to corrosion in the oral environment	Concerns related to Hg toxicity	Dental restorations

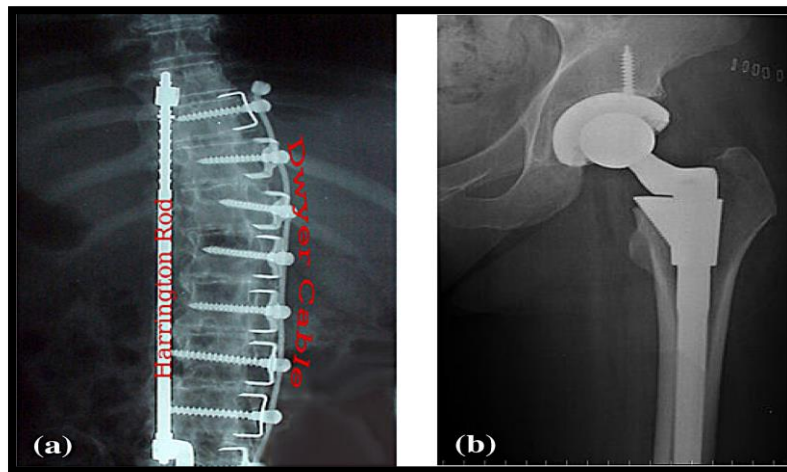


Figure 2-5(a) The Harrington rod, (b) The stem of a total hip replacement [3]

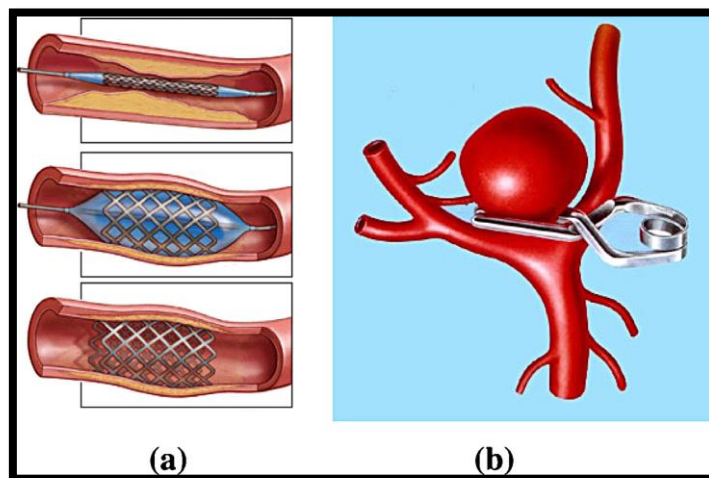


Figure 2-6(a) A vascular stent, (b) an aneurysm clip [3]

2.2.2 Fundamental Considerations in Design and selection of Metallic Implants

The design and selection of metallic biomaterials depends on their particular medical use and in order to use the metallic implants in the living body without rejection for a long time, a metallic implant should have the fundamental characteristics of: excellent biocompatibility, high corrosion resistance, suitable mechanical properties, high wear resistance, and osseointegration [3]:

2.2.2.1 Excellent biocompatibility

The design and selection of materials for biomedical implants should be compatible with the living body and not cause any negative local or systemic effects on the components of a living body [3]. No material is completely inert when used as an implant in the living system for a reasonable time, and to avoid any negative effects (local or systemic), the first thought in the design and selection of a biomaterial is the use of elements that already exist in the living system [3]. Common elements found in the human body are listed in table 2.2, most of the human body is oxygen, hydrogen, nitrogen and carbon, which are 96% of the mass of the body, and these elements are the building blocks of proteins and water. The rest of the mass of the human body (4%) exists either largely in blood, extracellular fluid majority of (Na, K, and Cl) or in the bones (Ca, Mg, and P), these elements are listed in table 2.3 [71].

Furthermore, the roles of micronutrients or trace elements in the human body are listed in table 2.4, which are all toxic at high levels, therefore these elements need to be at low levels for proper growth, physiology and development of the body[71, 72]. The known trace or micronutrients are listed in table 2.5 [3].

In summary, many metals can be used in the human body, and although many of these elements exist as micronutrients at low levels, they are toxic at higher levels [3]. Figure 2.7 shows the biocompatibility of pure metals and these alloys, which can be used as metallic biomaterials [73]. Ideally, to design and select a biomaterial, toxic elements should not be selected as alloying elements for the biomaterial alloy. However, and as mentioned above, no metals are completely inert or non-toxic, consequently the alloys used as a biomedical implants should be selected with virtually inert elements, or those that exist as micronutrients in the human body, or elements with high corrosion resistance (passive elements such as titanium) [3].

Table 2-2 Elements in the human body [3]

Element	O	C	H	N	Ca	P	K	S	Na	Cl	Mg	Trace element
Wt%	65.0	18.5	9.5	3.3	1.5	1.0	0.4	0.3	0.2	0.2	0.1	<0.01
At%	25.5	9.5	63.0	1.4	0.31	0.22	0.06	0.05	0.3	0.03	0.1	<0.01

Table 2-3 Roles of macro elements in the human body [3, 71]

Macro elements	Roles
O, C, H, N	in water and the molecular structures of proteins
Ca	Structure of bone and teeth.
P	Structure of bone and teeth. Required for ATP, the energy carrier in animals.
Mg	Important in bone structure. Deficiency results in tetany (muscle spasms) and can lead to a calcium deficiency.
Na	Major electrolyte of blood and extracellular fluid. Required for maintenance of pH and osmotic balance.
K	Major electrolyte of blood and intracellular fluid. Required for maintenance of pH and osmotic balance.
Cl	Major electrolyte of blood and extracellular and intracellular fluid. Required for maintenance of pH and osmotic balance.
S	Element of the essential amino acids methionine and cysteine. Contained in the vitamins thiamin and biotin. As part of glutathione it is required for detoxification. Poor growth due to reduced protein synthesis and lower glutathione levels potentially increasing oxidative or xenobiotic damage are consequences of low sulfur and methionine and/or cysteine intake.

Table 2-4 Roles of trace elements in the human body [3]

Trace elements	Roles
Fe	Contained in heme groups of hemoglobin and myoglobin which are required for oxygen transport in the body, as well as many other metabolic enzymes and Fe-S proteins. Part of the cytochrome p450 family of enzymes. Anemia is the primary consequence of iron deficiency. Excess iron levels can enlarge the liver, may provoke diabetes and cardiac failure. The genetic disease hemochromatosis results from excess iron absorption. Similar symptoms can be produced through excessive transfusions required for the treatment of other diseases.
Cu	Contained in enzymes of the ferroxidase system which regulates iron transport in the blood and facilitates release from storage. A structural element in the enzymes tyrosinase, cytochrome c oxidase, ascorbic acid oxidase, amine oxidases, and the antioxidant enzyme copper zinc superoxide dismutase, amongst others. A copper deficiency can result in anemia from reduced ferroxidase function. Excess copper levels cause liver malfunction and are associated with genetic disorder Wilson's Disease
Mn	Major component of the mitochondrial antioxidant enzyme manganese superoxide dismutase. A manganese deficiency can lead to improper bone formation and reproductive disorders. An excess of manganese can lead to poor iron absorption.
I	Required for production of thyroxine which plays an important role in metabolic rate. Deficient or excessive iodine intake can cause goiter (an enlarged thyroid gland).
Zn	Important for reproductive function due to its role in FSH (follicle stimulating hormone) and LH (leutinizing hormone). Required for DNA binding of zinc finger proteins which regulate a variety of activities. A component of the enzymes alcohol dehydrogenase, lactic dehydrogenase, carbonic anhydrase, ribonuclease, DNA Polymerase and the antioxidant copper zinc superoxide dismutase. An excess of zinc may cause anemia or reduced bone formation.
Se	Contained in the antioxidant enzyme glutathione peroxidase and heme oxidase. Deficiency results in oxidative membrane damage with different effects in different species. Human deficiency causes cardiomyopathy and is known as Keshan's disease.
Co	Contained in vitamin B12. An excess may cause cardiac failure.
Mo	Contained in the enzyme xanthine oxidase. Required for the excretion of nitrogen in uric acid in birds. An excess can cause diarrhea and growth reduction.
Cr	A cofactor in the regulation of sugar levels. Chromium deficiency may cause hyperglycemia (elevated blood sugar) and glucosuria (glucose in the urine). Elevated levels of some forms of chromium, such as Cr(VI), can be carcinogenic.

Table 2-5 List of trace elements in the human body [3]

Barium	Chromium	Iron	Selenium
Beryllium	Cobalt	Lithium	Strontium
Boron	Copper	Molybdenum	Tungsten
Cesium	Iodine	Nickel	Zinc

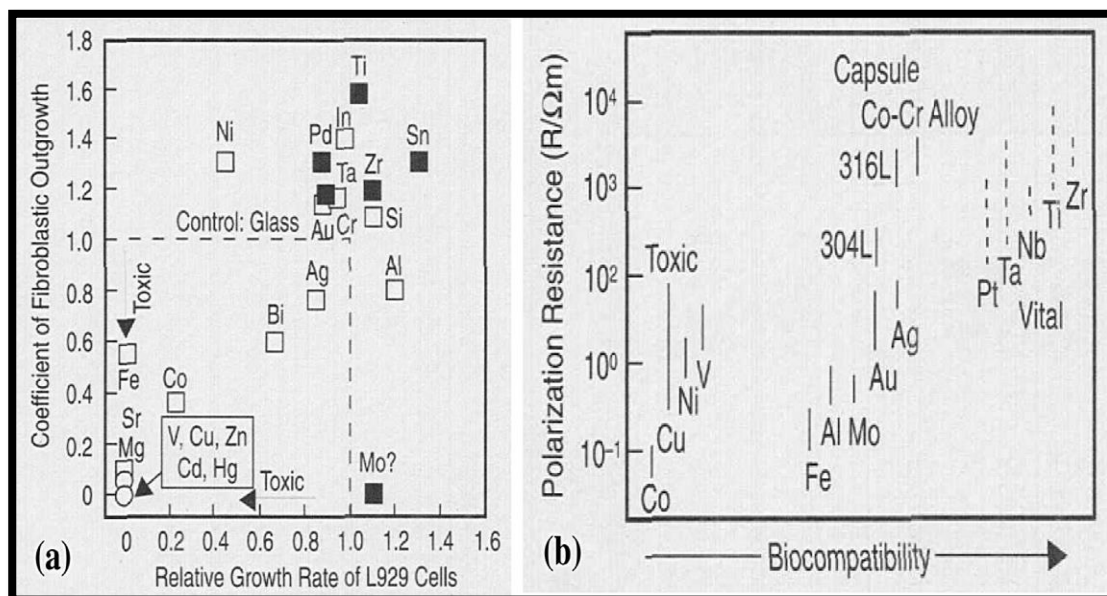


Figure 2-7(a) Cytotoxicity of some pure metals, (b) the relationship between polarization resistances and biocompatibility of pure metals, cobalt-chromium alloy and stainless steels [73]

2.2.2.2 High corrosion resistance

The environment outside the human body (ambient conditions) is different physically and chemically from the environment inside the human body [3]. Under normal conditions, the human body fluids contain a solution of mostly Na^+ , Cl^- and other trace ions, amino acids, soluble protein, and around 9% saline. The ionic concentration of human blood plasma is listed in table 2.6 [74]. The pH of these fluids is a nearly neutral pH with a value of 7.2-7.4 under 1 atm. of pressure and 37°C [75]. Furthermore, different parts of the human body exhibit different oxygen concentrations and different pH values. Consequently, an implant can have good corrosion resistance in one region of the body, but low corrosion resistance in another [75].

In reality, the pH of human body fluid can be in the range from 7.2 -7.4 to 3-4 under some conditions, for example, during surgery or injury, leading to inflammation due to inflammatory cell secretions. Furthermore, fluctuations in ionic strength can occur which are related to high blood pressure or ion deposits. Consequently, the human body's response to an implant will be as an aggressive environment. In addition, the partial pressure of oxygen in the body is about one quarter of the atmospheric oxygen pressure, leading to an increase in the corrosion rate of metallic implants by slowing down the formation of the passive layer of the protective film on the surface of an implant after it is broken or removed [3, 75]. Ideally, a metallic implant should have good corrosion resistance; consequently, the release of metal ions from a metallic biomaterial, which in turn produces toxic reactions, should be minimized and remain at satisfactorily low levels under the harshest conditions and for more than 30 years (a long-term service) under normal physiological conditions [3].

Table 2-6 The ionic concentrations (mM) of human blood plasma [74]

Ion	Human tissue fluid	Human blood plasma
Na ⁺	142.0	142.0
HCO ³⁻	4.2	27.0
K ⁺	5.0	5.0
HPO ₄ ²⁻	1.0	1.0
Mg ²⁺	1.5	1.5
Cl ⁻	147.8	103.0
Ca ²⁺	2.5	2.5
SO ₄ ²⁻	0.5	0.5

2.2.2.3 Suitable mechanical resistance

A metallic implant that is used to replace any part of the living body (bone for example), must be able to match the mechanical performance of the bone [3]. Consequently, the mechanical properties of the metallic implant which include Young's modulus, toughness, and ultimate tensile strength (UTS) all need to be considered during the design and selection of a metallic implant. The mechanical properties of the dominant metallic biomaterials (stainless steels, cobalt based alloys, and titanium based alloys) are listed in table 2.7 [76] .

The Young's modulus of stainless steel, cobalt-based alloys and titanium-based alloys (>100 GPa) are significantly higher than that of bone (10-30 GPa) [76]. Therefore, when using a metallic implant with a high Young's modulus, the metallic implant bears a greater mechanical load than that of the bone, leading to biological responses particularly around the

implant site, such as atrophy, and in this case revision surgery is needed. This is called the “stress shielding effect”. Ideally, an implant with a similar Young’s modulus to that of bone should be selected as a metallic implant that is used to replace the bone [3].

Fatigue strength is the range of cyclic stress that can be applied to a material without failure under fatigue. In reality, skeletal bone implants (e.g. knee joints, artificial hip joints, plates, spinal fixations, and wires) can suffer from fatigue because of cyclic loading. The service conditions (cycle frequency, wearing, corrosion environment and load vectors), surface quality of products and microstructure of materials are all factors that influence the fatigue strength sensitively [3].

No material is perfect, therefore, the mechanical working conditions inside a living body are complex. Fatigue can be more complicated by concurrent friction and corrosion, particularly when the material has imperfections (inhomogeneity of microstructure (particles of the second phase, impurities and the grain boundaries), manufacturing imperfections (pits, notches, filets, holes, and welds) or surface defects from machining actions), which lead to stress concentrating locally to these sites when subjected to external loading [3, 77-79].

Therefore, these sites can escalate to permanent defects that cannot be removed by unloading, and a crack can initiate at these sites, leading to fatigue fractures without any warning before rupture under normal service conditions. More details about fatigue mechanisms in metallic implants can be found in references [77, 78]. Hence, it is desirable to have a metallic implant with a high fatigue strength, excellent friction and corrosion resistance [3]. Figure 2-8 shows the fatigue strength at 10^7 cycles of biomedical, cobalt alloys, stainless steel, titanium and its alloys and the bone [80].

Table 2-7 Mechanical properties of metallic biomaterials and cortical bone [76]

Materials	Young's modulus/GPa	Ultimate tensile strength/MPa	Fracture toughness (MPa \sqrt{m})
CoCrMo alloys	240	900-1540	~100
316L stainless steel	200	540-1000	~100
Ti alloys	105-125	900	~80
Mg alloys	40-45	100-250	15-40
NiTi alloy	30-50	1355	30-60
Cortical bone	10-30	130-150	2-12

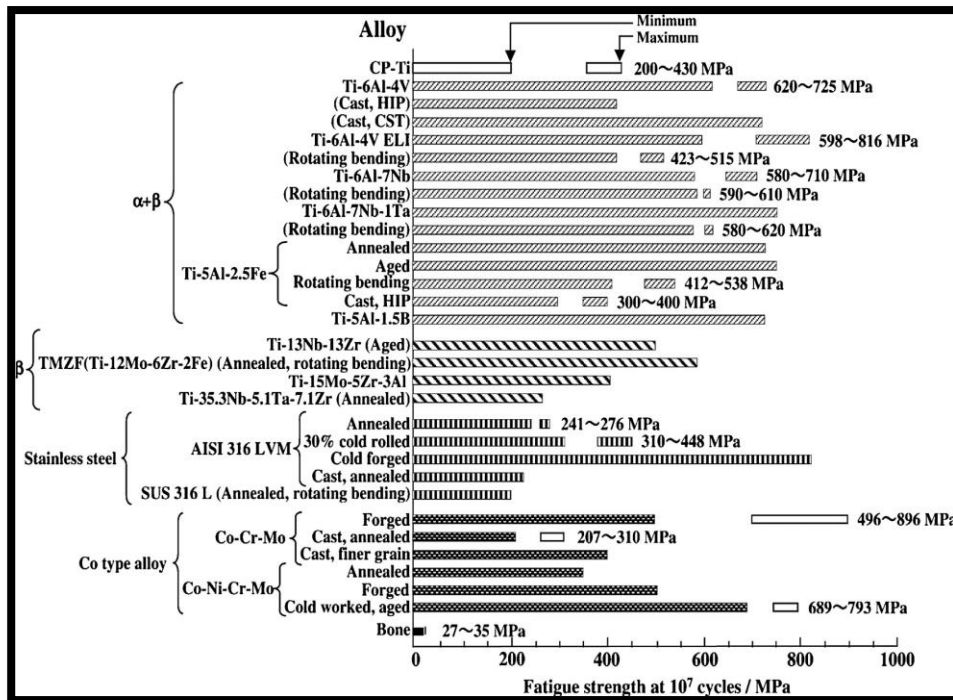


Figure 2-8 Fatigue strength at 10^7 cycles of biomedical, cobalt alloys, stainless steel, titanium and its alloys, and bone [80]

2.2.2.4 High wear resistance

In any joint replacement wear is an inevitable issue no matter what biomedical materials are used [3]. The kind of joint plays a key role for selection of biomedical material types. The hip, ankle, elbow, shoulder and knee are examples of joints between long bones, while a tooth, skull and wrist are examples of static joints [3]. Depending on how closely the opposed bones fit together, the mobile joints can be categorized as congruent and incongruent. Hip and shoulder joints are examples of congruent joints (figure 2-9), while knee and ankle joints are examples of incongruent joints (figure 2.10) [3]. As can be seen from figure 2-9, a ball-shaped head fits closely to a cup-like socket, therefore the stress is distributed equally; brittle ceramic materials can be used as articulating surfaces for ball and socket joints [3]. The ranking of articulating surfaces for joint prosthetics in terms of wear-resistance is listed in table 2-8 [3]. From figure 2-10 a contact of two incongruent hard surfaces can be seen which leads to a highly heterogeneous stress, therefore the brittle ceramic materials cannot be used to sustain this kind of the stress, so that hard polymeric and metallic are used in these cases[3].

At present, joint replacement can be categorized either as “Hard-on-Soft”, and in these cases joint replacement is made of “Ceramic-on-Ultra-high molecular weight polyethylene (UHMWPE), Metallic-on-UHMWPE; and as “Hard-on-Hard”, and in these cases the joint replacement is made of “Ceramic-on-Ceramic, Al₂O₃-on-CoCrMo, or CoCrMo-on-CoCrMo” [3]. Ideally, the wear resistance should be higher, or friction coefficient should be low for a metallic implant that is used as a joint implant of the human body. Using a metallic implant with a high friction coefficient or low wear resistance leads to implant loosening, and the wear debris formed can cause inflammation similar to the bacteria or pyrogens resulting in destruction of the bone supporting the metallic implant [3, 81-83].

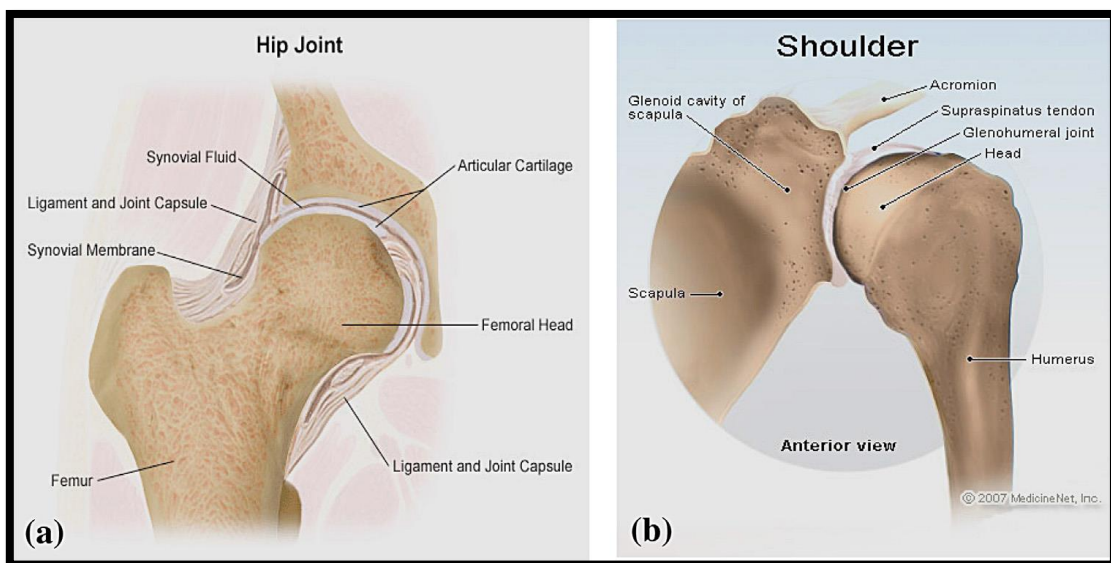


Figure 2-9 Two congruent joints in human bodies, (a) hip, and (b) shoulder [3]

Table 2-8 Ranking of articulating surfaces for joint prosthetics in terms of wear-resistance [3]

Ball and socket	Wearing resistance
Ceramic-on-Ceramic (Al ₂ O ₃ or ZrO ₂)	Superior
CoCrMo-on-CoCrMo	Excellent
Al ₂ O ₃ -on-CoCrMo	Excellent
Al ₂ O ₃ on UHMWPE ^a	Excellent
CoCrMo on UHMWPE	Good
Ti6Al4V on UHMWPE	Good
Metal on metal (stainless steels or titanium alloys)	Poor

^a UHMWPE, ultra-high molecular weight polyethylene.



Figure 2-10 Two artificial incongruent joints (knee) and (b) ankle [3]

2.2.2.5 Osseo-integration

Osseo-integration is another important term that needs to be considered in the biomedical science field. Osseo-integration can be defined as “a term that describes the process of new bone formation and bone healing” and is a fundamental requirement in orthopaedics [84]. The non-integration of an implant surface into the adjacent bone and other tissue around the implant leads to loosening of the prosthesis. Consequently, it is essential for an implant to integrate properly, which usually requires it has an appropriate surface that will promote integration with the surrounding bone and tissues. The surface roughness, surface chemistry and surface topography are all factors that play a major role and must be considered for good osseo-integration [3, 85-88].

2.3 Titanium

Compared with stainless steel and cobalt based alloys, titanium and titanium alloys have excellent properties for use as implant biomaterials, including lower elastic modulus, superior biocompatibility and higher corrosion resistance. Consequently, the use of titanium alloys as biomaterials has been increasing over the last two decades. Pure titanium Cp-Ti and the first generation titanium alloys $\alpha+\beta$ Ti-6Al-4V were introduced some time ago, but recently the second generation titanium alloys, the β -titanium alloys, have received much interest [89]. This section will briefly discuss the general properties of titanium, titanium crystal structure, titanium alloys, titanium alloys as biomaterials, and the biocompatibility of titanium alloys.

2.3.1 General Properties of Titanium

Titanium is a transition metal that belongs to Group IV of the Period 4 in the periodic table. It has a silver-like metallic appearance, is the ninth most abundant element, and is the fourth

most abundant metal on Earth after Al, Fe, and Mg [90]. Titanium has a density of approximately 0.6 of the density of iron and nearly 0.5 of the density of cobalt. Titanium and its alloys have a low modulus of elasticity which about 0.5 that of stainless steels and cobalt - molybdenum alloys [3, 90] . Titanium is superior in strength/density (specific strength), while inferior in tribological properties to stainless steels and cobalt - chromium alloys [3]. Due to the properties of titanium being inbetween those of steel and aluminium, titanium has many industrial applications. 73% of all Ti metal is used in aerospace applications, while 27% is used in the chemical, marine, electrochemical processing equipment, medical, sporting goods and power generation [91]. Titanium is widely used in medical applications due to its low density, superior corrosion resistance and high biocompatibility [92]. However, on the negative side, titanium and its alloys have some issues, including fabrication difficulties, high cost, high reactivity at elevated temperature above 480°C, high production energy content, and embrittlement due to the oxygen diffusion through the surface oxide layer at high temperatures.

2.3.2 Titanium Crystal Structure

Pure titanium has a hexagonal close packed (hcp) structure (α titanium phase) at low temperatures, while upon heating the β -transus the temperature at which the alloy transformed to β , the crystal structure transforms to the body centred cubic (BCC) β phase (figure 2-11)[93]. The β -transus for pure titanium is 882 ± 2 °C and it depends on the composition of titanium [3, 90]. The lattice parameter of the hexagonal close packed structure, the α titanium phase are $a = 2.95$ Å, and $c = 4.685$ Å. The ideal c/a ratio for hexagonal close packed is 1.633, while the α titanium phase has a c/a ratio of 1.587 Å. However, these values increase slightly when using an interstitial element (O, N, C) and substitutional elements (Al). The lattice parameter of the body centred cubic (BCC) β phase is 3.32 Å [90]. The microstructure of titanium can be controlled using thermal and thermomechanical processes, and crystallographic texture could be developed during the processes, therefore, the microstructure can be controlled for various applications [90].

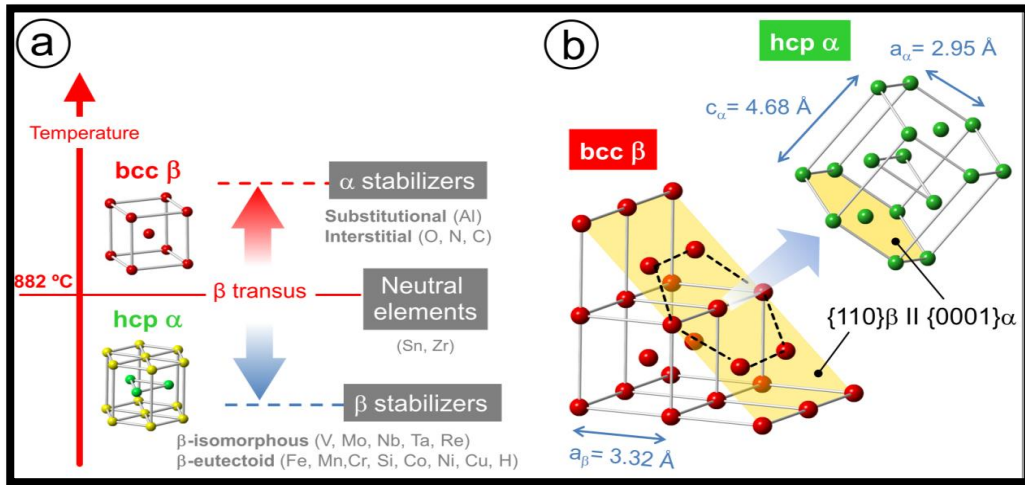


Figure 2-11 The hcp α structure titanium, β structure titanium and their lattice parameters at (RT for α and 900 °C for β)[93]

2.3.3 Titanium Alloys

In general, titanium alloys are categorized into five classes that depends on their microstructure after processing, which include α - alloys, near- α -alloys, α - β alloys, metastable β and stable β alloys. All mechanical properties of titanium alloys are influenced by the alloying elements [89]. Alpha (α) has good corrosion resistance; near- α , which also has good corrosion resistance; α + β that exhibit a higher strength; metastable β ; and stable β that exhibits a higher corrosion resistance and a low elastic modulus [94]. It is documented that the β type titanium-based alloys have two stable phases, the first one at high temperature with a BCC crystal structure the β phase, and the second one at lower temperature with the α phase HCP crystal structure. Furthermore, these alloys exhibit three metastable phases: hexagonal martensite (α'), orthorhombic martensite (α'') and an omega phase (ω) with a hexagonal structure [94, 95]. It has been shown that the α' and α'' are formed by quenching from the β phase [96]. On the other hand, the omega phase is easily created by either by quenching from high temperatures, in which case the omega phase is called athermal ω , or formed by isothermal treatment, in other words heat-treatment at intermediate temperatures and the omega phase is known as isothermal ω [95, 96]. Both phases (isothermal and athermal omega) have a hexagonal structure [95, 96]. In addition, the alloying elements that are added to the titanium can be classified into three categories, the first one is α stabilizers such as Al, O, N, and C, which raises the β -transus temperature. The second is β stabilizers and these can be isomorphous elements for example, V, Nb, Ta, Mo and eutectoid elements such as Fe, W, Cr, Ni, Si, Co, Mn, and H; these elements reduce the β -transus temperature. The third

category are elements that have a neutral effect, for instance Zr and Sn. These elements have a slight effect on the β -transus temperature [97, 98](figure 2.12)[90].

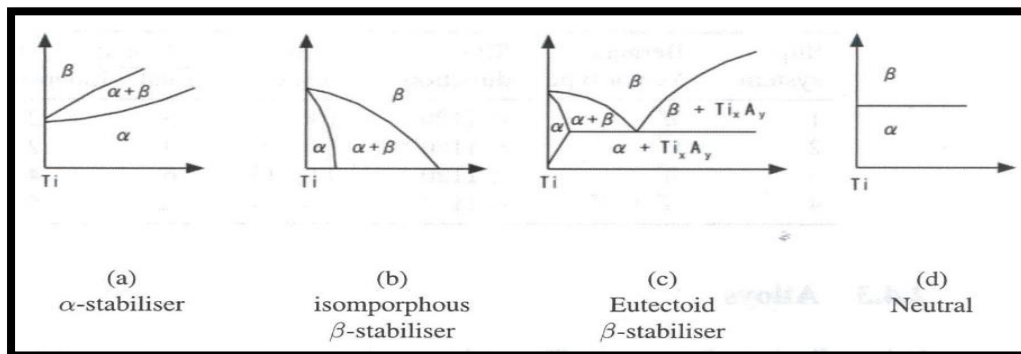


Figure 2-12 Schematic diagrams showing the effect of alloying elements on the β -transus temperature [90]

2.3.3.1 α - and near α titanium alloys

These alloys include Cp-Ti, super- α or near- α alloys. Cp-Ti (98.-99.6% Ti) which has 100% α -phase, exhibits low strength, high ductility, with a UTS in the range 240-550MPa, a yield strength in the range 170-480MPa, depending on the impurity and interstitials levels [89].

The α - alloys can be classed as super- α or near- α alloys when they contain small additions of β stabilizers. Although these alloys contain some β -phase, they still behave more like α phase Cp-Ti alloys than α - β alloys. Due to their low strength at ambient conditions, α and near- α alloys have not found an application in medical implants compared to α - β or β alloys [3, 89]. However, Cp-Ti grades are preferred for corrosion resistance and non-load bearing applications [3, 89].

2.3.3.2 α - β titanium alloys

There are four ASTM standardized α - β alloys used in medical devices, namely Ti-6Al-4V, Ti-6Al-4V ELI, Ti-6Al-7Nb and Ti-5Al-2.5Fe [3]. The first-generation titanium alloys Ti-6Al-4V and Ti-6Al-4V ELI are most widely used in the medical device. Compared with Ti-6Al-4V, Ti-6Al-7Nb and Ti-5Al-2.5Fe are vanadium free, which is documented to be toxic and to show adverse tissue effects, these alloys are similar to Ti-6Al-4V metallurgically [89].

The microstructure of α - β alloys is sensitively affected by the alloy composition, cooling rate, solution -treating temperature and section size. Solution and aging heat treatment can be used to increase the strength of these alloys. The microstructure is also affected by the subsequent

ageing treatment conditions (at 480-650 °C), used to precipitate fine α that leads to a fine mixture of $\alpha + \beta$ microstructure. However, the transformation dynamic, kinetics and microstructure in α - β alloys are generally complex; more detail and analysis can be found in references [3, 99]. It was reported that the strength of these alloys can be enhanced by 0.3-0.5 using solution treatment and aging, while their Young's modulus remains constant [99]. Compared with α -titanium alloys, the fatigue strength of these alloys can be increased using solution and aging heat treatment and the fatigue strength is comparable or higher than that of cobalt and 316L stainless steels.

2.3.3.3 Metastable and stable β -titanium alloys

The second-generation β -titanium alloys have a Young's modulus closer to that of bone [100-104]. Therefore, these alloys have attracted considerable interest as they offer the potential to address stress shielding associated with the high Young's modulus of the implant [3]. The development of these alloys for orthopaedic implants took place in the 1990s [46, 73]. β -titanium alloys are vanadium free and contain elements all of which exhibit suitable biocompatibility, for example, molybdenum, niobium, tantalum, zirconium and iron. Compared with first-generation titanium biomaterials Ti-6Al-4V and other α - β alloys, these alloys have lower elastic moduli, enhanced biocompatibility and good corrosion resistance. To date, and among all β -titanium alloys, Ti-Nb-Zr-Ta (TNZT) alloys exhibit the lowest elastic moduli of any metallic implant alloy [46, 73]. β -titanium alloys have UTS values lower than those of cobalt alloys and are comparable with that of 316L stainless steel. Moreover, the yield strength is closer to that of cobalt alloys and comparable with that of 316L stainless steels [3]. Although many researchers have highlighted some positive properties of β -titanium alloys, these alloys also have some drawbacks, for example the fatigue strength of these alloys is lower than that of cobalt alloys, and they also exhibit poor wear resistance [3, 92].

2.3.4 Titanium Alloys as Biomaterials

As noted before, due to their excellent properties including high specific strength and high resistance to corrosion, titanium and some titanium alloys are an excellent choice for biomedical applications [58, 105]. Since the 1970s, titanium and some titanium alloys have been used as biomedical implant materials, and commercially pure titanium Cp-Ti and Ti-6Al-4V (Ti-64) alloys have been used for the fabrication of titanium implants [48]. According to the American Society for Testing and Materials (ASTM) Cp-Ti and Ti-64 can

be categorized as grades 1-5. Unalloyed Cp-Ti is separated into 1-4 grades based on the residual oxygen and iron contents (see table 2-9), while grade 5 is Ti-6Al-4V [2, 48]. The mechanical properties of titanium alloys are listed in table 2-10. Grade 2 titanium exhibits a yield strength that is equivalent to that of heat treated austenitic stainless steels (275 MPa) and this value is the minimum compared with other titanium grade [2].

Although the beneficial characteristics of Cp-Ti and Ti-6Al-4V have been reported by many studies, there are still issues that need to be addressed, for example, poor tribological properties, the vanadium content (cytotoxic) and high elastic modulus compared to bone [50, 51, 54] . Therefore, new titanium alloy compositions have been developed to tackle these issues. The first-generation titanium alloys Ti-6Al-7Nb, and Ti-5Al-2.5Fe were developed to overcome the vanadium cytotoxicity issue [50]. Second-generation titanium biomaterial β -titanium alloys containing Mo, Nb, Ta, and Zr were developed to address the stress shielding associated with high Young's modulus of the implant, as well as the vanadium cytotoxicity issue (see 2.3.3.3).

Table 2-9 Impurity limits for Cp-Ti (wt%) [106]

Materials	N	C	H	Fe	O
ASTM grade 1	0.03	0.08	0.015	0.20	0.18
ASTM grade 2	0.03	0.08	0.015	0.30	0.25
ASTM grade 3	0.05	0.08	0.015	0.30	0.35
ASTM grade 4	0.05	0.08	0.015	0.50	0.40

Table 2-10 The mechanical properties of titanium alloys

Material	Specification	Tensile strength (MPa)	0.2% Proof stress (MPa)	Elongation (%)	Elastic modulus (GPa)
CP-Ti	ASTM F67 Grade 1	240	170	24	103-107
-	ASTM F67 Grade 2	345	275	20	103-107
-	ASTM F67 Grade 3	450	380	18	103-107
-	ASTM F67 Grade 4	550	483	15	103-107
Ti6Al4V	ASTM F136 Grade 5	860	795	10	114-120

MPa = megapascal, GPa = gigapascal.

2.3.4.1 Biocompatibility of Alloying Elements

Among the long list of alloying elements that are usually added to titanium alloys, V, Nb, Mo, Ta, Zr, and Al are the most important for medical biomaterials, as can be seen from table 2-11 [3, 106]. In this section biocompatibility and biological functions of titanium, vanadium, niobium, tantalum, zirconium and aluminium is briefly discussed.

Table 2-11 ASTM/UN standards for titanium and titanium alloys used for medical implants [3].

Category	ASTM	UNs no.	Materials
α microstructure	F67	R50250	CP-Ti grade 1
		R50400	CP-Ti grade 2
		R50550	CP-Ti grade 3
		R50700	CP-Ti grade 4
α - β microstructure	F136	R56401	Ti-6Al-4V ELI (currently standardized)
	F1472	R56400	Ti-6Al-4V (currently standardized)
	F1295	R56700	Ti-6Al-7Nb (not currently standardized)
	F2146	R56320	Ti-3Al-2.5V (not currently standardized)
β microstructure	F1713		Ti-13Nb-13Zr
	F1813	R58120	Ti-12Mo-6Zr-2Fe
	F2066	R58150	Ti-15Mo

- **Titanium (Ti)**

Titanium has no known biological role in the human body and titanium is a non-toxic element even in large doses [107, 108]. Titanium osseointegrates well and is not rejected by the body or by the host bone. However, *in vitro* tests showed that titanium can cause genetic alterations in the connective tissue, and inhibit osteogenic differentiation of mesenchymal stem cells [3, 109, 110]. Furthermore, titanium also has a biological influence on white blood cells in the body, when the titanium particles have a specific size in vivo [111].

- **Vanadium (V)**

Vanadium has both negative and positive cellular responses [111]. However, it plays a less known biological role in the human's body [112, 113]. Vanadium compounds such as vanadium oxides exhibit toxicity [114]. It was reported that in animal trials inhalation or oral exposures to V and V compounds lead to carcinogenicity and could cause various adverse influences on the blood parameters, respiratory system, neurological system, liver, and other organs [115, 116]. Recently, it was reported that there are links between the implant failure and vanadium release. Nonetheless, the toxicity of V when used as alloying elements in titanium alloys for biomedical applications is still entirely clear [117].

- **Niobium (Nb)**

Niobium has a little known biological role in the human body, however, some niobium compounds exhibit toxicity, for example, niobium chloride and niobates [118, 119].

Recently, one study reported that niobium is one of the more toxic metals ions, which can cause immune cell death and encourage DNA damage [119]. Therefore, niobium should be treated carefully until more information becomes available, especially when used with several alloying elements [3].

- **Molybdenum (Mo)**

Molybdenum is an essential trace element in the body and plays a key role for many enzymes, including sulphite oxidase, aldehyde oxidase and xanthine oxidase [120].

Molybdenum can be found in the human body at about 0.07 mg/kg of Mo, with lower concentrations in the vertebrae and higher concentrations in the kidneys and liver [3, 121, 122]. Molybdenum is also found in human tooth enamel, and helps prevent tooth decay[122]. Molybdenum is less toxic than Cr, Co, and Ni [120, 123, 124]. Based on published studies, the acute toxicity of Mo has not been reported in humans, also practically no chronic toxicity data for Mo in humans has been reported. However in the case of animal studies, it was reported that the chronic ingestion of more than 10 mg/day can lead to diarrhoea, infertility, low birth weight , growth retardation, gout, with further effects on the liver, lungs and kidneys [123, 125]. Furthermore, it was reported that in patients with metal-on-metal (M-O-M) THR and hip resurfacing arthroplasty the concentration of Mo in serum is generally lower than that of the Cr and Ni [126, 127]. So far, there is no study that been reported on systemic toxicity of Mo when used as a metallic implant [3].

- **Tantalum (Ta)**

Tantalum is non-toxic and has no known biological role in humans [128]. Ta is the most biocompatible among all metals used for implantable devices, having even better biocompatibility than that of titanium [92]. However, there is some evidence linking tantalum oxide to toxicity of alveolar cells and local sarcomas [3].

- **Zirconium (Zr)**

Zirconium exists in the human body with 1mg on average and does not play a natural biological role in humans. Zr compounds exhibit low toxicity. However, exposure to Zr powder for a short-time has been shown to lead to irritation, while it can also lead to skin and

lung granulomas when inhaled. It was reported that long-term exposure to Zr tetrachloride leads to increased mortality rates of guinea pigs and a decrease of red blood cells and blood haemoglobin in dogs [3, 129-131].

- **Aluminum (Al)**

Despite aluminium being an abundant element, it has a little-known biological role in the human body. However, aluminium can cause acute toxicity when it is present in a very high dose [132]. It was reported that the aluminium toxicity is a major issue in patients with kidney disease, and played a role with altered function of brain neurotoxicity and the blood-brain barrier [133-135]. Furthermore, it was suggested that excessive exposure to aluminium can increase the risk of breast cancer and Alzheimer's disease [136, 137]. Newer evidence reported that *in vitro*, aluminium can increase gene expression in human breast cancer cells due to its role in estrogen receptors [138]. Nevertheless, there is no evidence, and no scientific consensus suggesting that the use of aluminium cookware led to aluminium toxicity or could directly increase disease risk [3].

2.4 Tribology

Tribology is defined as the science and technology of friction, wear and lubrication [139-141]. Knowledge as to the contact mechanics and structural chemistry of the metallic biomedical surface are all factors that need to be considered for improving material longevity, durability and reduction in implant loosening [142]. This section will briefly discuss friction, wear and lubrication. Then it will briefly discuss the tribological behaviour of titanium, and finally will briefly discuss the tribological testing system and characterization techniques for the tribology of metallic biomaterials.

2.4.1 Friction

During the movement of two contacting bodies, a resistance force will be generated, which is known as friction [143]. Friction response of any material is influenced by material structure, surface state of the material, and whether contact is lubricated, dry or corrosive [143].

Friction has a positive and a negative side in different applications; bearing and gears are examples of the negative side when friction is unwanted. In contrast, brakes and clutches are examples of the positive side of the friction when the friction is wanted [142, 144]. Friction is often associated with mechanical wear, therefore, it is very important and relevant to control the level of the friction between the contact surfaces of the two bodies [145].

2.4.1.1 The coefficient of friction

The usual measure of friction is through the coefficient of friction (COF). COF is influenced by more than one factor which changes during the mechanical wear process including chemical changes, topological changes and structure changes during mechanical wear and at the sliding contact [143, 144]. The friction coefficient between any contacting surfaces is calculated using [143]:

$$\mu = \frac{F_t}{F_n} \quad 2 - 1$$

Where: μ = the coefficient of friction, F_t = the tangential force which is required to move two bodies when they are forced to move relative to each other, and F_n is the normal load of the desired moving body.

2.4.1.2 Components of friction

Friction can be subdivided into two components, the deformation friction force (F_d) and adhesive friction force (F_a), and both will occur during sliding [142-145]:

$$F_t = F_d + F_a \quad 2 - 2$$

Where: F_t is the total frictional force, F_d is the deformation friction force, and F_a is the adhesive friction force.

The surface roughness is factor that needs to be considered to control friction processes (figure 2-13). As can be observed from figure 2.13, at high surface roughness, deformation friction dominates, while at low surface roughness adhesive friction dominates. Furthermore, the lowest friction can be observed under an optimum surface roughness range, friction increases below the optimum roughness range, due to increased adhesion between the smooth surface, and friction also increases above the optimal roughness range due to an increase in the asperity deformation [142-146].

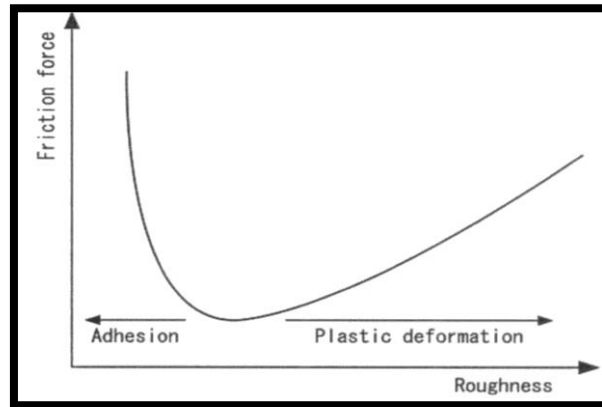


Figure 2-13 The impact of roughness on friction [146]

2.4.2 Wear

Wear can be defined as one of the main methods of material surface damage, which occurs because of relative motion between two surfaces. During wear, material degradation will occur, which can lead to failure and the rate of material degradation is mostly related to the surface of the two contact materials and environment conditions [143, 145-148]. The volume of the material loss during the wear process can be calculated from the following equation[148]:

$$\frac{V}{L} = K \frac{F_n}{H} \quad 2 - 3$$

Where: V = the volume loss during wear process, L = the total sliding distance during wear process, F_n = the normal applied load during wear process, H = the hardness of the materials, K = the coefficient of wear.

The above equation can be rearranged, and can be used to calculate the volume of material lost during the wear process per unit distance and per unit load as follows [148]:

$$k' = \frac{K}{H} \quad 2 - 4$$

$$k' = \frac{V}{LF_n} \quad 2 - 5$$

Where k' is the dimensional wear coefficient ($\text{mm}^3\text{N}^{-1}\text{m}^{-1}$).

2.4.2.1 Mechanisms of wear

Wear can either be non-lubricated (dry wear) or could be lubricant wear. Lubricants are often used to reduce the wear rate. However, wear can be classified depending on the mechanisms

of the wear response of the material. Budinski suggested the most commonly used approach, namely abrasive wear, adhesive wear, surface fatigue wear and corrosion wear [145, 147, 148]. Adhesive wear can occur because of micro-junctions (welding) between the two surfaces during rubbing, as shown in figure 2-14. Abrasive wear occurs when a hard surface rubs against a softer surface. Hence, two body abrasive wear or three body abrasive wear can occur as shown in figure 2-14. In the case of two body abrasive wear, two rubbing parts are involved in the friction process, while in the case of three body abrasive wear there is a hard particle trapped between the rubbing surfaces. Furthermore, abrasive wear can occur as ploughing, cutting and cracking (brittle fracture). Fatigue wear can occur when there is a cycling loading during wear as can be observed in figure 2-14. During corrosion wear, wear can be accelerated by the corrosion (oxidation) of the rubbing surface, rubbing taking place in a corrosive environment [145, 147, 148].

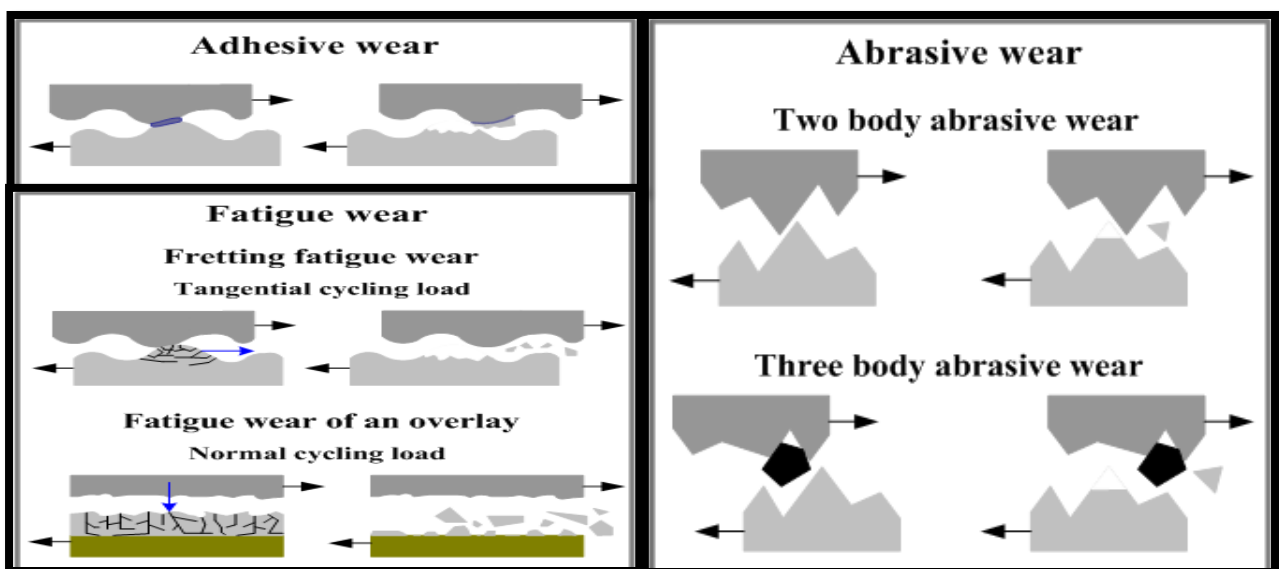


Figure 2-14 Schematic of mechanisms of wear [149]

2.4.3 Lubrication

To reduce friction between rubbing surfaces, lubrication is commonly used. Oils or greases are the most common form of lubrication used. However, lubricants can be in solid or liquid form [145, 147, 148]. It was reported that the flow properties of lubricating liquids are related directly to the reduction in friction during lubricated sliding. A measure of how likely and how severe asperity contact will during lubricated sliding is provided by λ calculated using the following equation [150]:

$$\lambda = \frac{t_{min}}{\sigma^*} \quad 2 - 6$$

Where, t_{min} is the minimum film thickness, and σ^* is the root mean square surface roughness of the rubbing surface that can be calculated using the following equation:

$$\sigma^{*2} = R_{q1}^2 + R_{q2}^2 \quad 2 - 7$$

Where, R_{q1}^2 is the mean square surface roughness value of the first surface, and R_{q2}^2 is the mean square surface roughness of the second surface.

$\lambda > 3$ indicates that a full fluid separating the rubbing surface leading to low friction and low wear, which is the hydrodynamic lubrication regime. When $1 < \lambda < 3$ suggests that a fluid film exists between the rubbing surfaces, but there is still asperity contact, which is the mixed elastrohydrodynamic lubrication regime. When $\lambda < 1$, usually associated with high loads or low sliding speeds, results in boundary lubrication which can lead to severe surface damage [145, 147, 148, 150].

The friction coefficient is directly proportional to lubricant viscosity (η), the inverse of the contact pressure (P), and the relative speed of the two surfaces (ω), and can be calculated using the following equation [150]:

$$\mu = \frac{\eta\omega}{P} \quad 2 - 8$$

The Stribeck diagram is used to plot this relationship (figure 2-15), with the term on the right-hand side of the equation known as the lubrication parameter. Three lubricating regimes are shown in the figure: boundary lubrication, mixed elastrohydrodynamic lubrication and hydrodynamic lubrication. In boundary lubrication, the friction coefficient changes little with the lubrication parameter, a result of the large amounts of surface contact during rubbing. With an increase in the lubrication parameter, a fluid film between the rubbing surfaces is generated leading to reduced surface contact, called the mixed lubrication regime. An increase in lubrication parameter in this regime ultimately leads to the lowest friction coefficient, figure 2-15. However, with a further increase in the lubrication parameter, the coefficient of the friction increases, related to fluid drag and shear within the lubricant itself.

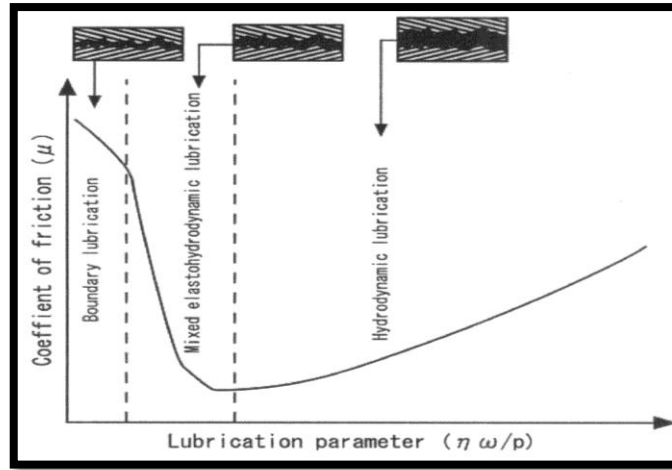


Figure 2-15 The Stribeck curve [148]

2.4.4 Tribological Testing Systems and Characterization Techniques

In general, the tribometer has the facility to measure the evolution of the friction coefficient and is used to monitor the tribological response from the test system. There are many methods used to study the tribological behaviour of metallic biomaterials, including block-on-disc, ball-on-disc, and pin-on-disc (figure 2-16). To simulate real or ambient conditions during the tribological testing system, simulated body fluid at $37 \pm 0.1^\circ\text{C}$ is used as an environment during the tribological test. However, the tribological testing is also carried out under dry sliding conditions [7, 151-158]. The advantages and disadvantages of various wear methods that are used in the tribological testing system are listed in table 2-12 [159].

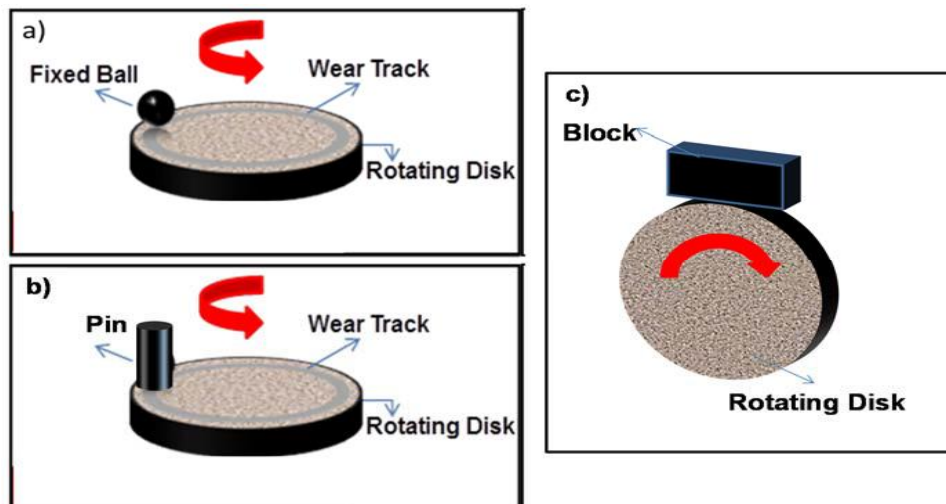


Figure 2-16 Schematic of wear test methods[7]

Table 2-12 Advantages and disadvantages of various wear test methods [159]

Test	Advantages	Disadvantages
Pin-on-Disk	After run-in, surface pressure remains constant. Easy to determine wear volume and wear rate. The model closely simulates a linear friction bearing.	Difficult to align pin. If the pin does not stand perfectly vertical on the plate, edge contact results. A very long run-in time is therefore necessary. The front edge of the pin can skim off lubricant. This makes a defined lubrication state impossible.
Ball-on-Disk	High surface pressures are possible. The ball skims off lubricant less than a pin does. The model is similar to a linear friction bearing and a radial friction bearing.	Very small contact ratio: The contact surface of the ball is small compared to the sliding track on the disk. The contact area is enlarged by wear. Difficult to determine the wear volume of the ball.
Block-on-disc	The model is capable of simulating a variety of harsh field conditions, e.g., high temperature, high speed, and high loading pressure.	

2.4.5 Tribology of Titanium

Due to the unique combination of the properties of titanium, which includes high strength, lightweight, biocompatibility and excellent corrosion resistance, titanium and titanium alloys have been intensely researched over the last few decades. However, results from published literature on the tribology response of titanium have reported that the titanium is not suitable for tribological applications [160, 161]. Dong and Bell have investigated the tribology response of titanium in 2002 [160], they claim there is more than one factor involved during the frictional response of titanium. Furthermore, they suggest that the main contribution factors that result in large wear rates and severe adhesive wear during the tribology tests is the combined influence of crystal structure, electron configuration, and lubrication ineffectiveness (figure 2-17). This compounded effect results in highly unstable friction of titanium in tribological applications [160, 162].

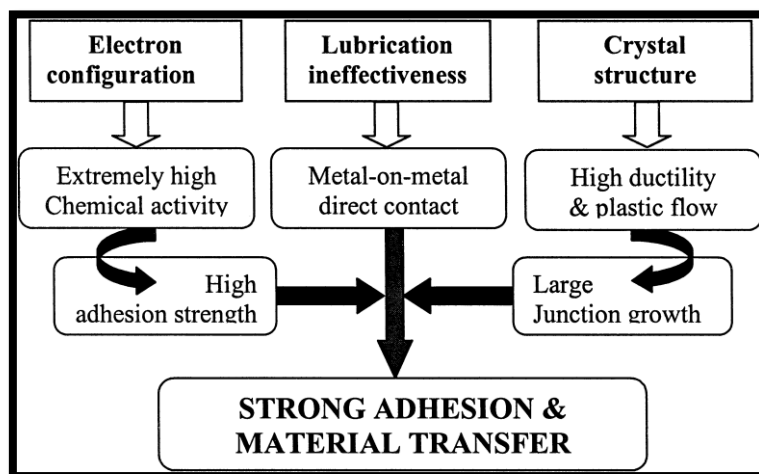


Figure 2-17 Materials factors affecting the tribological performance of titanium [160]

There are several recent studies which focus on the tribological properties of different types of titanium alloys and has shown that the wear resistance and friction coefficient has been improved under different conditions. The passivity and repassivation through the formation of an oxide film during rubbing can have a considerable effect on the tribological behaviour of titanium alloys. Among the studies that have shown the tribological behaviour of titanium alloys and influence of passive oxide layer during rubbing is a publication by Alam et al. [70]. In the study the authors reported that the $\alpha''+\beta$ microstructure Ti-24Al-11Nb has the ability to form a protective oxide layer during rubbing resulting in an improved wear resistance of the alloy. Their results reported that the $\alpha''+\beta$ microstructure alloy Ti-24Al-11Nb exhibited a wear rate about 48 times lower than that of $\alpha-\beta$ microstructure of Ti-6Al-4V under a normal load 45N. More studies on the tribological behaviour of new titanium alloys was carried out by Choubey et al. [163]. Their study presented results of tribological behaviour of Cp-Ti, Ti-6Al-4V, Ti-5Al-2.5Fe, Ti-13Nb-13Zr and Co-28Cr-6Mo. They reported that the lowest coefficient of friction was exhibited by Ti-5Al-2.5Fe. Among the studies that have shown the tribological behaviour of different types of titanium alloys (one aims of this work) is a publication by Ramos Saenz et al. [164]. In this study comparisons were carried out between oxidized and non-oxidized γ -TiAl (Ti-48Al-2Nb-2Cr at%), Ti-6Al-4V and Cp-Ti. The results showed that the higher coefficient of friction was observed for oxidized γ -TiAl alloy. Also, they found that the oxidized γ -TiAl alloy exhibited lower wear volume than that of Cp-Ti and Ti-6Al-4V.

More studies on the tribological behaviour of titanium alloys was carried out by Cvijović-Alagić et al. [152]. Their study presented results of the tribological behaviour of $\alpha'+\beta$ Ti-13Nb-13Zr and $\alpha+\beta$ Ti-6Al-4V ELI under different heat treatments. They reported that the $\alpha+\beta$ Ti-6Al-4V exhibited superior wear resistance to that of $\alpha'+\beta$ Ti-13Nb-13Zr under all heat treatment condition. More studies on the influence of heat treatment on the tribological behaviour of titanium alloys was carried out by Lee et al. [165]. Their study presented results of the tribological behaviour of warm-rolled and hot rolled Ti-13Nb-13Zr alloys in Hanks solution at 37 °C. They reported that there was no notable difference in wear resistance between the warm-rolled and hot rolled Ti-13Nb-13Zr $\alpha+\beta$ microstructure. Also, they pointed out that the friction coefficient of both alloys around 0.42-0.45.

As more titanium alloys have been suggested for orthopaedic applications, the researchers are increasingly investigating tribological behaviour of titanium alloys. The tribological behaviour of titanium alloys for total hip prosthesis was carried out by Fellah et al. [166]. In

the study the authors investigated the tribological behaviour of $\alpha+\beta$ Ti-6Al-7Nb and Ti-6Al-4V under different conditions of normal load 3, 6 and 10 N and sliding speeds 1, 15 and 25 mm.s⁻¹. They reported that the wear resistance of $\alpha+\beta$ Ti-6Al-7Nb was substantially lower than that of Ti-6Al-4V. They also found that the two alloys exhibited similar friction and wear performance. No significant variation of coefficient of friction with sliding speed was obtained in Ti-6Al-7Nb, while it increased linearly with increasing sliding speed in Ti-6Al-4V.

The above review clearly brings out observation that the wear resistance of titanium alloys has been improved under different conditions. In general, Nb addition to Ti alloys enhances the wear resistance and increases the COF of titanium alloys. Heat treatment of titanium alloys with Nb also increases the wear resistance because of the formation of Nb₂O₅ particles. Furthermore, coating and surface treatment are important to increase the wear and friction resistance of titanium alloys. It was observed that the predominant wear mechanism is abrasive wear [7, 70, 158, 167-170]. From this perspective, one aims of the current work addresses the tribological behaviour of different types of titanium alloys to understand the influence the wear on the accelerated (synergism) the corrosion rate during rubbing under tribocorrosion behaviour of tested alloys.

2.5 Corrosion

Corrosion is defined as a natural process, and according to the second law of thermodynamics, the system is moving into a thermodynamically more stable condition [171]. For metals, corrosion is defined as an irreversible chemical or an electrochemical reaction occurring at the interface of the metal and its environment[172].

Three responses of the metal can occur when it is placed in a corrosive environment, which depends on the metal, and the environment. The first one is an immune state, where the metal is not corroded. The second response is where the metal is in an active state, where it will corrode and cause metal loss and/or dissolution of one of the constituents of the corrosive environment into the metal. The third state is a passive state, where the metal has the ability to generated a protective oxide passive film on its surface which will reduce the corrosion rate [145, 173]. Figure 2-18 shows the general electrochemical reaction involved in the corrosion of an active metal and a passive metal [33].

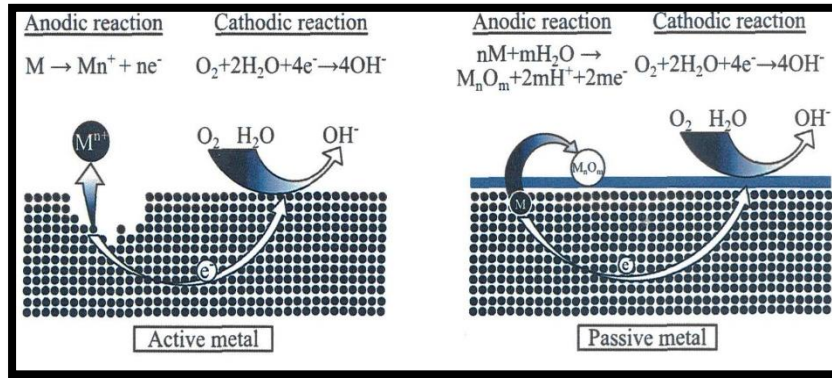


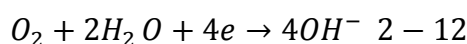
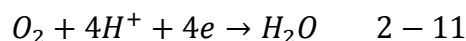
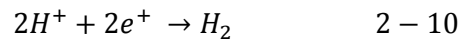
Figure 2-18 Schematic presents the electrochemical reactions involves in the corrosion of an active and a passive metal [33]

Aqueous corrosion is the most common form of corrosion in the case of metallic biomaterials. Two reactions occur on the surface of a metallic in an aqueous electrolyte. The anodic reaction, removal of electron from metal atoms (oxidation), and cathodic reaction, consumption of electron by an oxidization agent (reduction).

The anodic half – cell reaction can be represented using the following equation [174]:



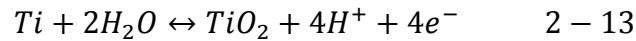
The most common cathodic half – cell reactions can be represented using the following equations:



Equation 2-10 represented the cathodic half-cell reaction for hydrogen evolution, while equations 2-11 and 2-12 represented the cathodic half – cell reaction for oxygen reduction in acidic and alkali solutions respectively [174].

The rate of reaction in equation 2-9 is used to calculate the corrosion rate of a metal, M, which depends on the electrode potential called the corrosion potential under equilibrium conditions. However, under working conditions the corrosion potential is influenced by a variety of factors. The kinetics of the reduction reaction, formation of passive surface film, temperature, mass transport conditions, galvanic contacts with other metals are factors that can influence the corrosion potential of a metallic component in practical systems. Therefore, depending on the environmental conditions a metal can experience different corrosion potentials [24, 175].

It is essential that passive materials are used in biomedical applications. Titanium and its alloys are generally passive because of spontaneous formation of a protective oxide film on the titanium surface according to the following reaction:



A hypothetical polarisation curve of a passive material is presented in Fig.2-19 [176]. Four potential domains are observed: cathodic, anodic, passive and trans-passive domains. When the potential is below the corrosion potential E_{corr} the metal is in the cathodic region and in this case the current is determined by the reduction of water and the amount of dissolved oxygen. The metal becomes anodic when the potential increasing above the E_{corr} . The metal remains active in the anodic region until the passivation region, E_{pp} , is reached. At this point the current density drops and the potential reaches the passivation value E_{pp} and the current is the passive current density i_{pp} . The drop in the current density is related to the formation of the protective passive oxide film on the surface of the metal. In the passivation region the metal can still suffer from corrosion but at lower rate. The metal will start to rapidly corrode in the trans-passive region and the potential will reach the breakdown potential E_b . If the metal exhibits more positive E_b , this metal has more stable passive oxide film. If the metal exhibits a large difference between E_b and E_{corr} , then the metal will exhibit higher stability against crevice and pitting corrosion. The metal exhibits higher resistance to localised corrosion when the difference between E_b and E_r (re-passivation potential) is small [177, 178].

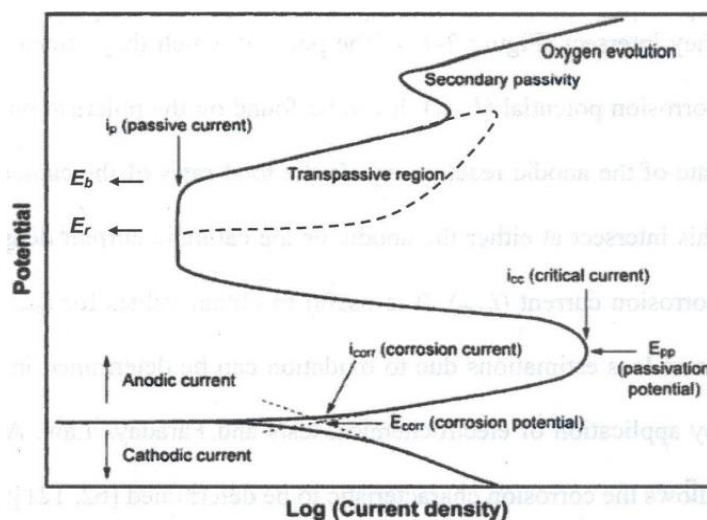


Figure 2-19 Typical polarisation plot for a passive material [176]

More than one corrosion phenomena can occur in a biosystem involving metallic biomaterial including the system being active, passivation, passive dissolution, transpassive, localized corrosion and adsorption [175]. Figure 2-20 shows a schematic of the reactions occurring at a metallic biomaterial surface in contact with an electrolyte [175]. The metal will be active when it is free from oxide film. The formation of a thin oxide layer on the surface of a metal is known as passivation. In the transpassive state a metal will start to rapidly corrode. Localized corrosion occurs when an intensive attack occurs in a small local site with rate higher than that of the rest of the surface. Adsorption is another common phenomenon in biosystems which occurs when a certain species is present in the body fluid, for example proteins, biomolecules and cells. According to these phenomena, corrosion rate can be controlled by the kinetics of a charge transfer reactions at the metal-electrolyte interface, the rate of mass transport of anodic reaction products and properties of the passive oxide layers [175].

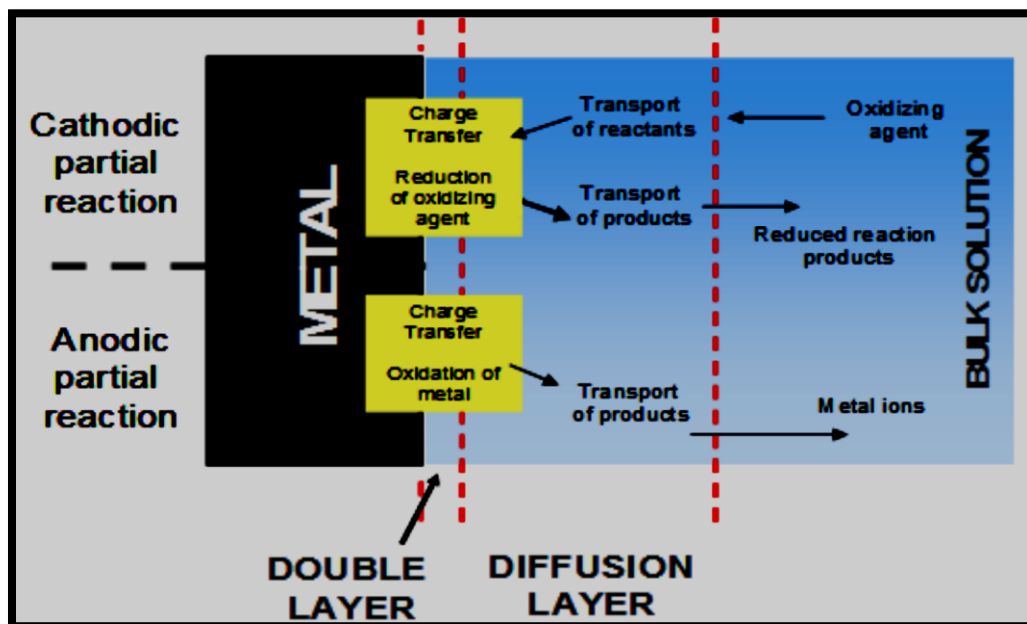


Figure 2-20 Scheme of the reactions occurring at a biomaterial metallic surface in contact with electrolyte [175]

2.5.1 Electrochemical Techniques for Corrosion Study

There are many techniques that can be used to understand the corrosion mechanisms and measure the corrosion rate of materials. To investigate the corrosion response of a specific part of a material over long periods of time, the field and simulated service techniques are

used. While in case of a particular environment and for a more general view about the corrosion mechanisms and the corrosion rate laboratory accelerated tests are used [171].

Three-electrode cell is used for the laboratory technique to investigate the electrochemical properties of materials. In the three-electrode cell, a reference electrode (RE) is needed to measure the potential of the working electrode. The counter/auxiliary electrode (CE) is made from gold, graphite or platinum, and is used to carry the current created in the circuit. The working electrode (WE) is the investigated sample. All electrodes are connected to a source of e.m.f, a voltmeter, and a galvanometer in electrolyte solution [171, 179]. The potential, current and also the change in current at set potentials can be measured to investigate the corrosion mechanisms and the influence of potential in the electrochemical responses of the materials [171, 179]. The following techniques are commonly used to study the electrochemical response of the materials.

2.5.1.1 Open Circuit Potential (OCP)

In this type of the measurement, the cathodic and anodic reaction rates are equal. During the open circuit potential technique (OCP), in other words free corrosion potential (E_{corr}), there is no external voltage or current applied, therefore, the net current flow from the electrode or to the electrode is zero. The value of E_{corr} is often measured and it will give initial information about the surface state of the material, any changes that might happen in the material surface condition, and whether the material is active or passive in the studied environment.

Furthermore, OCP can be used to give an indication of whether the protective film on the surface of the material in the studied environment has been removed or damaged with time and at what point it loses its integrity[25, 180]. The material is in an active state and corrosion is more likely to happen if it has a relatively low open circuit potential. In contrast, the material is in a passive state when it exhibits a relatively high open circuit potential. The OCP is useful for giving information about the state of the material with the time, and showing any sudden shifts in the potential, which are related to a change in the material surface during the test. Cathodic shifting could happen to the material when the open circuit potential changes from a high value to a low value, and this signals the material has an activated surface. In contrast, if the open circuit potential changes from a low value to a high value this indicates the onset of passivation.

Even though there are lots of advantages for using the open circuit potential, it is important to mention some of the drawbacks. For example, the value of the open circuit potential

generated during this technique is an average value of all of the surface of the material and it does not indicate local areas that might be cathodic and/or anodic potential. Therefore, some areas in the surface of the material might be corroding at a potential less than the value of the open circuit potential suggested. Furthermore, the open circuit potential represents only the surface condition of the material with the time during the test under a corrosive media and does not present any information about the rate of corrosion and the amount of corrosion occurring over time. The data of the open circuit potential can be compared between different materials to give an indication of the corrosion response of these materials, and the corrosion resistance of each material compared to another [180, 181].

2.5.1.2 Potentiodynamic polarization (PD)

This technique is one of the most widely used electrochemical methods used for corrosion studies. During this technique, the current density as a function of the applied potential can be established dynamically, which is known as a polarisation curve. The material is subjected to an applied potential which varies from cathodic to anodic potential during a potential sweep. The change in the current density during this technique gives an indication of the change of corrosion rate over time [25].

A hypothetical polarisation curve of a passive material is presented in Fig.2-21 [182]. The material will have good corrosion resistance if it exhibits a low current density in the passive state, a wide passive potential and a high corrosion potential. In contrast, the material is more active when it exhibits a larger current density and is oversensitive to corrosion attack[183]. Potentiodynamic polarisation can be used to calculate the corrosion current density (i_{corr}) and the free corrosion potential of the material in a particular corrosive environment using one of the simplest techniques to measure the corrosion rate under free corroding conditions which is known the Tafel plot [182, 184]. A typical Tafel plot is presented in Fig.2-22 [183].

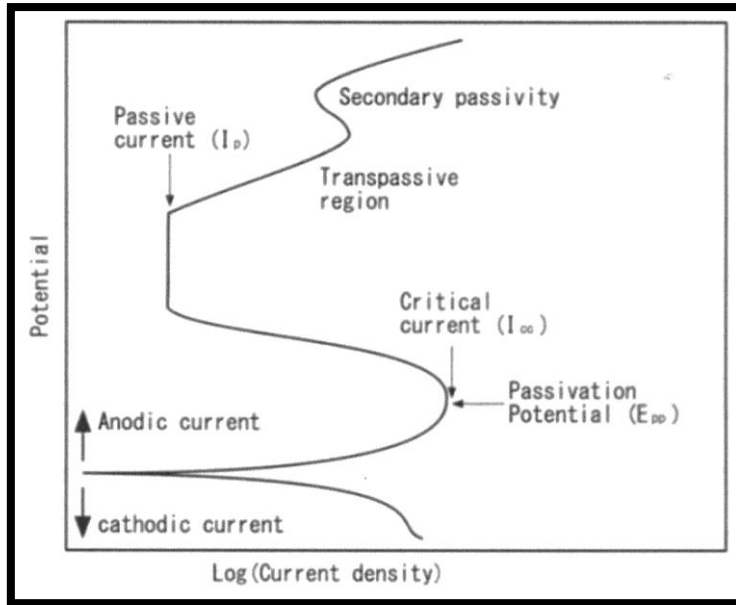


Figure 2-21 A hypothetical polarisation of a passive metal [182]

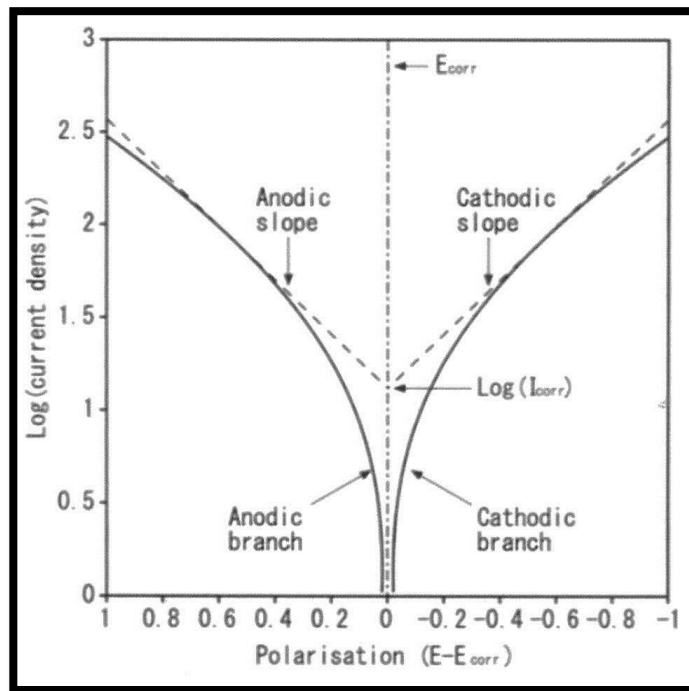


Figure 2-22 Tafel plot that can be used to calculate the corrosion parameters [183]

2.5.1.3 Potentiostatic Polarization (PS)

With this technique the material is subjected to a constant potential either cathodically or anodically, and the current is calculated with time. The relationship between the current and the time can give an indication of the electrochemical kinetics involved during the test [24].

This technique can be used to measure the growth or the decay of passive films on the surface of passive materials in a corrosive environment. The High Field Theory (HFT) and the Point Defect Model (PDM) are used to explain the variation in the ion flux at the passive material surface [185-187]. The thickness of the passive film increases with time; therefore, the ion flux will reduce, which will lead to a reduction in the conduction, and as result the current density will be lower.

The following equation can be used to calculate the decay of the current with time [186-188]:

$$I = 10^{(-A+K \log t)} \quad 2 - 14$$

Where the K value is the slope of the curve of log I against log t. It has been claimed that the value of K can give information about the structure of the passive film and the condition of the surface of the passive material in an environment. For example, if the value of K= -1, this can indicate that the oxide film is strong and protective. However, if the value of K= -0.5, this can indicate that the oxide film is not a protective film, and this might be being broken or a passive film is not present. The value of K can be used to analyse the sensitivity of the oxide film to corrosion attack, when the value of K is close to -1, the oxide film is more strong, stable and protective under a particular corrosive environment [186, 187].

2.5.1.4 Electrochemical Impedance Spectroscopy and Equivalent Circuits

In order to obtain further information on the nature of the electrochemical processes, reactions mechanisms and kinetics, an electrochemical impedance spectroscopy technique is used (EIS) [25]. It is a relatively modern technique widely extended in several scientific fields. EIS is a powerful method for studying corrosion, batteries, semiconductors, electroplating and electro-organic synthesis. This is because EIS can exhibit accurate, error – free kinetic and mechanistic information using a variety of technique and output formats[189].

During the EIS technique a perturbation sinusoidal voltage is applied at a frequency to the electrode system. The electrochemical impedance (Z), which can be defined as the relationship between the applied potential and the resulting intensity, is expressed in terms of the displacement of the vector $Z\omega$ [189-192]. Impedance is expressed using its imaginary (Z_{im}) and real (Z_{re}) parts as can be seen in the following equation [189-192]:

$$Z\omega = Z_{re} + jZ_{im} \quad 2 - 15$$

The modulus $|Z|$ and the phase angle θ of $Z\omega$ can be obtained using the following equations:

$$|Z| = \sqrt{Z_{re}^2 + Z_{im}^2} \quad 2 - 16$$

$$\theta = \arctan\left(\frac{Z_{re}}{Z_{im}}\right) \quad 2 - 17$$

The EIS data can be presented in various ways; the Nyquist plot is one of the graphical representations of impedance, figure 2-23. In this diagram impedance Z represented in the complex plane, where the imaginary part (Z_{im}) is plotted on the y-axis, and the real part (Z_{re}) is plotted on the x-axis of a chart for different frequencies ω . The Bode plot, figure 2-24 is another graphical representation of impedance, whereby the impedance modulus $|Z|$, plotted in a logarithmic scale and the phase angle both on the y-axis versus frequency are plotted on a logarithmic scale [189].

An equivalent electrical circuit (EEC) that consists of the electrical elements resistance, capacitance and inductance can be used to describe the physical properties of the system can be used to fit the experimental data. The best fitting and the corresponding values of the electrical element can be measured using the Zview software package [189-192]. The simplest (EEC) used for fitting the experimental results of the active metals and non-active metals are represented in figure 2-25 [193]. As can be observed in figure 2-25a and in the case of the non-active metals, the EEC for this impedance behaviour is simple, and the metals form a passive compact film. $R\Omega$ is the resistance of the solution between the working and reference electrodes, R_{pf} is the resistance of the passive film, the polarization resistance or charge -transfer resistance at the electrode/solution interface, C_{pf} is the capacitance of the passive film[190]. While in the case of active metals, the response is different, with an additional circuit element, C_{dl} , which is the double-layer capacitance, and R_{ct} is the charge -transfer resistance or the pore resistance[190]. More detail about this technique can be found in the references[189-192].

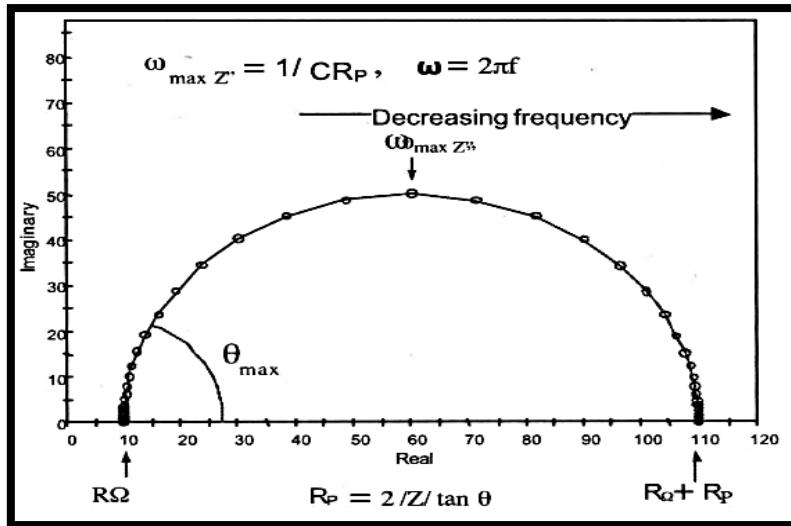


Figure 2-23 Nyquist Plot for a Simple Electrochemical System [189].

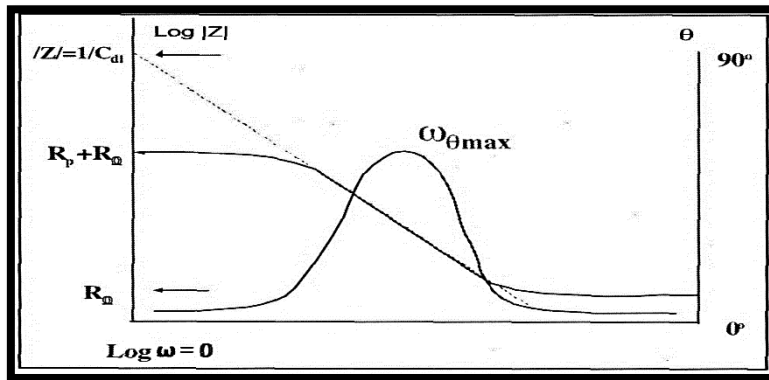


Figure 2-24 Bode Plot for a Simple Electrochemical System [189].

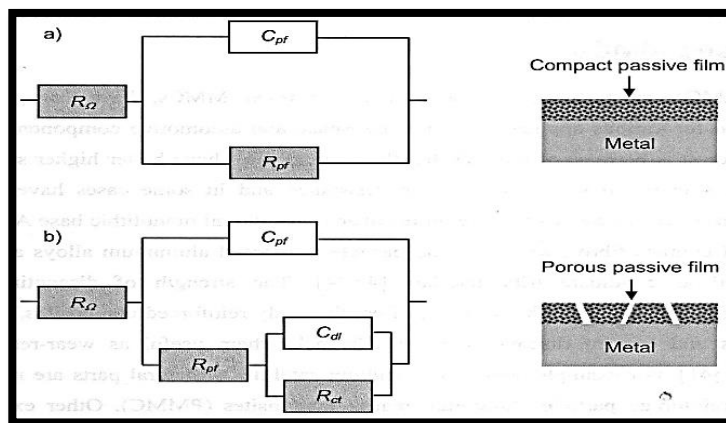


Figure 2-25 Equivalent Electrical Circuit a) Compact oxide film, b) Porous passive layer [193].

2.5.2 Corrosion Mechanisms

The nature of corrosion, appearance of the corroded material and the mechanism of corrosion are the determining factors which can be used to identify the corrosion type. Furthermore, visual identification can be used to specify the type of corrosion, and give an indication into the corrosion mechanisms taking place on the material surface in a particular environment [194]. Corrosion is not just affected by the nature of the metals or alloys, but also affected by the environmental conditions. The corrosion response of metals or alloys can be affected by the environment parameters such as temperature, presence of biological organisms, pH, motion of the electrolyte and the concentration of the electrolyte. Corrosion environments can be atmospheric, water, underground or soil, alkaline and acidic electrolyte, the combination between these environments are probable [181, 194]. Fig.2-26 presents a graphical representation of the main types of corrosion. Fontana and Greene [174] in 1978 performed a comprehensive study of the various types of corrosion, which included uniform or general corrosion, pitting corrosion, crevice corrosion, galvanic corrosion, intergranular corrosion, selective leaching, erosion corrosion and environmentally assisted corrosion. More details about these types of corrosion found in [174]. The following section will briefly discuss galvanic corrosion in general and galvanic coupling during rubbing of passive materials.

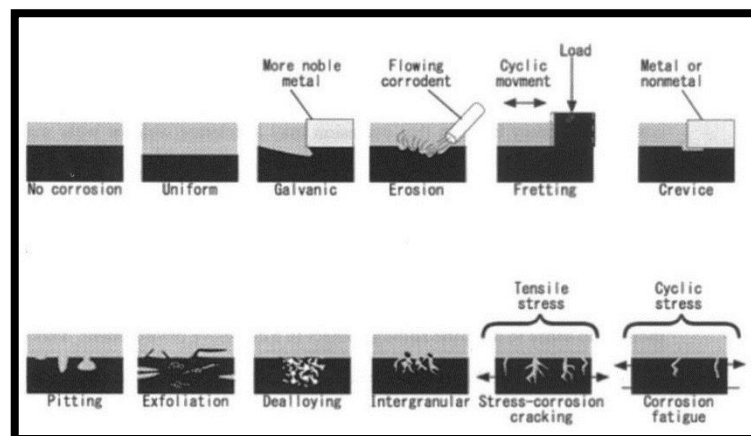


Figure 2-26 Schematic represent the types of corrosion [181].

2.5.2.4 Galvanic corrosion

During this type of corrosion, electron flow occurs between the metals or alloys when a potential difference is established between the two when immersed in a corrosive and/or conductive solution. Figure 2-27 shows a schematic of galvanic corrosion between anodic and cathodic regions, which could be from contact between dissimilar metals, or active and passive regions of the same metal. The materials response to galvanic corrosion can be

predicted from the galvanic series, figure 2-28. Galvanic corrosion is controlled by the position of the metal in the galvanic series, the distance from anode to cathode, the environment and anode to cathode area ratio are factors [174].

Galvanic couplings are also established in the case of passive materials during rubbing. When an alloy surface is subject to mechanical wear during rubbing, the protective film will be destroyed, and a galvanic couple will be established between the areas depassivated by mechanical wear, which act as an anode, and the surrounding passivated, unworn, area which acts as a cathode [195, 196]. Figure 2-29 shows a schematic of galvanic couples that can arise during tribocorrosion at the OCP. The sign + and – indicates sites with higher potential that act as cathodes and lower potential that act as anodes [196]. Galvanic couples are established between the completely depassivated wear track and the area surrounding area, as shown in figure 2-29 a. Galvanic couples are also established between depassivated regions and areas that remain passive within the wear track and on the area immediately surrounding the wear track (figure 2-29 b). However, in the case of extensive wear, this second case is expected to be negligible [196].

Besides the macroscopic galvanic coupling mentioned above, microscopic galvanic couplings are established in two-phase materials because of the potential difference between the two phases for example α -phase and β -phase [195, 197]. In this case one phase serves as the cathode and the second phase serves as the anode. Figure 2-30 shows a schematic of macroscopic galvanic coupling and microscopic galvanic coupling mechanisms arising during tribocorrosion behaviour of 304SS in artificial seawater at OCP [195]. Macroscopic galvanic couplings occurred between the passive film acting as a cathode and γ phase that acts as the anode (figure 2-30 a). Microscopic galvanic couplings occurred between the γ phase with a higher standard electrode that acts as a cathode, and α' phase with lower standard electrode potential that act as the anode.

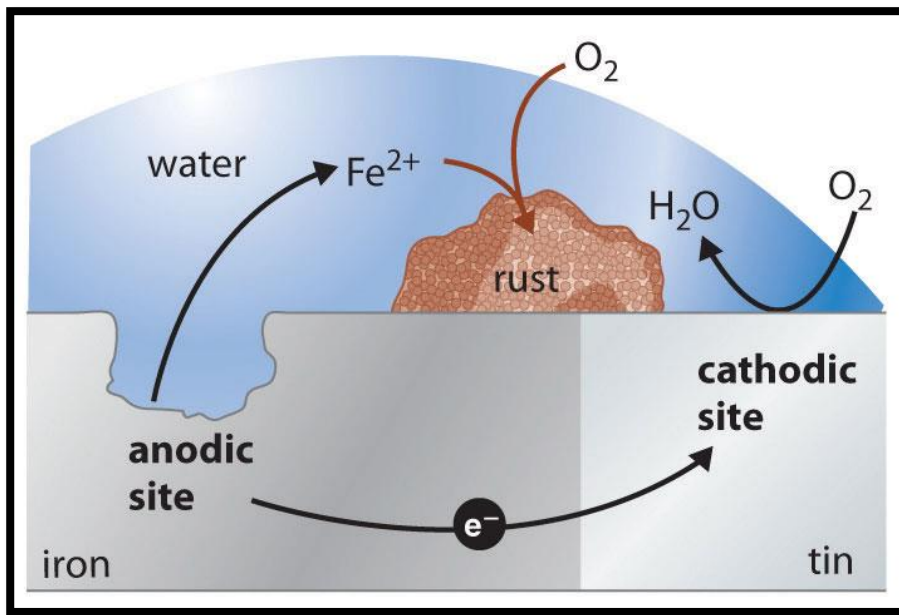


Figure 2-27 Scheme of Galvanic corrosion [198].

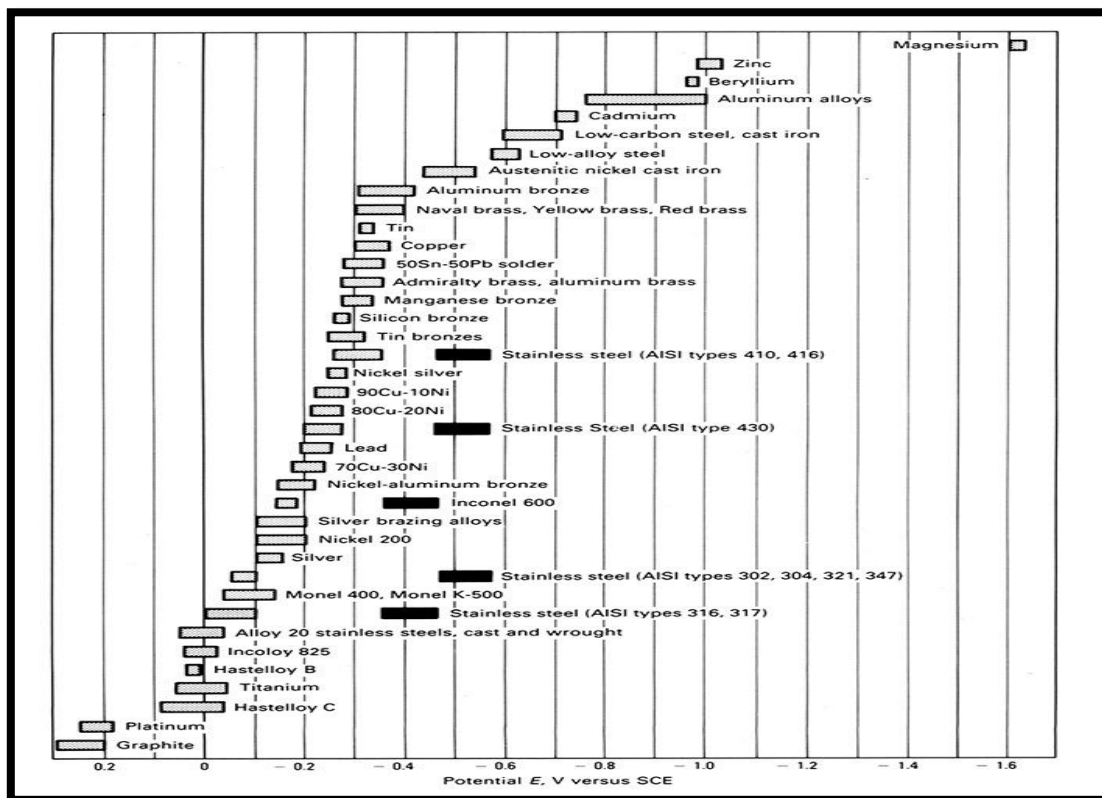


Figure 2-28 Galvanic series of various metal in salt water [198].

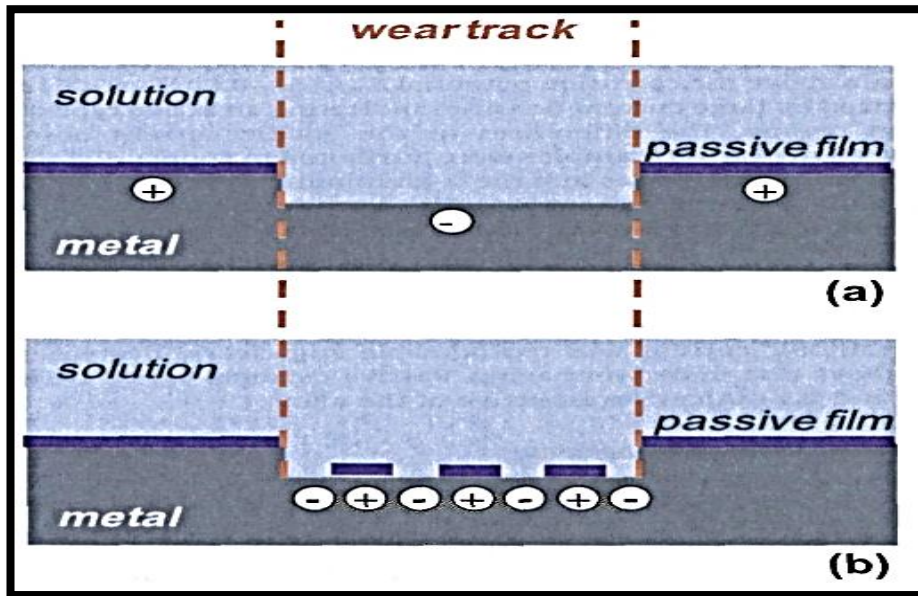


Figure 2-29 Schematic representation of two theoretically limiting galvanic coupling situations that can arise during tribocorrosion at OCP [196].

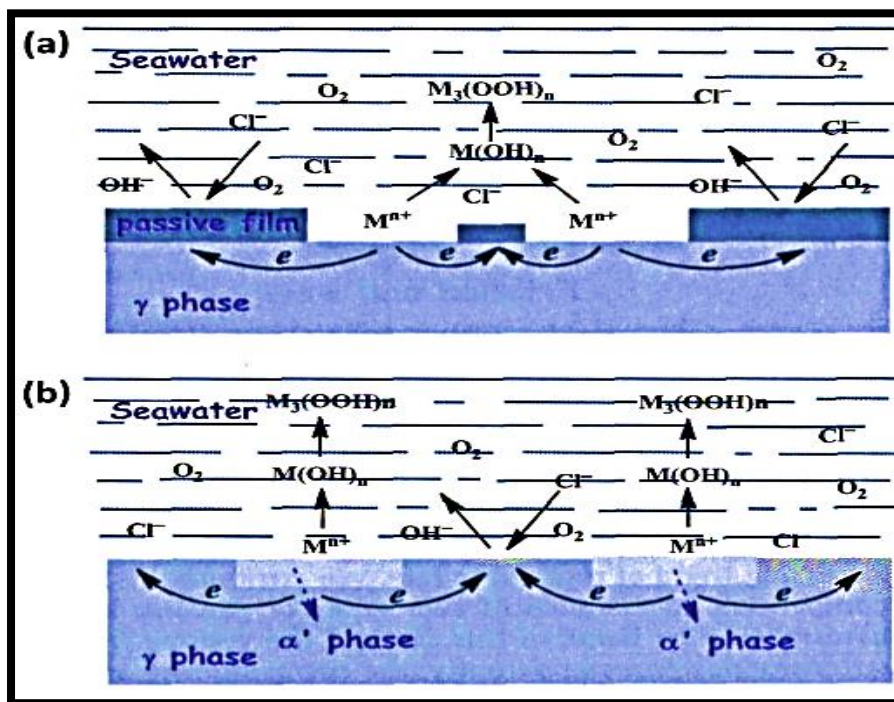


Figure 2-30 Schematic representation of two types of galvanic coupling mechanisms arising during tribocorrosion of 304SS in artificial seawater at OCP [195].

2.5.3 Corrosion of Titanium and Titanium Alloys

Titanium and titanium alloys have the natural ability to form and develop a protective passivating oxide surface film with a thickness range from 2-5nm [98, 199]. Therefore, titanium and titanium alloys exhibit excellent corrosion behaviour in a wide range of

corrosion media. The oxide layers on titanium exhibit a good adherence to the substrate surface and have the ability to rebuild itself when damaged. This allows titanium and its alloys to resist most oxidising media, for example, chlorides, sulphates, hydrochlorides, salt, sulphides and nitric acid solution [98, 199]. However, titanium and its alloys are not able to withstand in the present of fluoride ions under very powerful oxidising environments, and in reducing agents [98, 199, 200]. These corrosive environments can damage and breakdown the passivating oxide film [200]. Different types of corrosion that titanium and titanium alloys are prone to when used in some implant applications are presented in figure 2-31 [200].

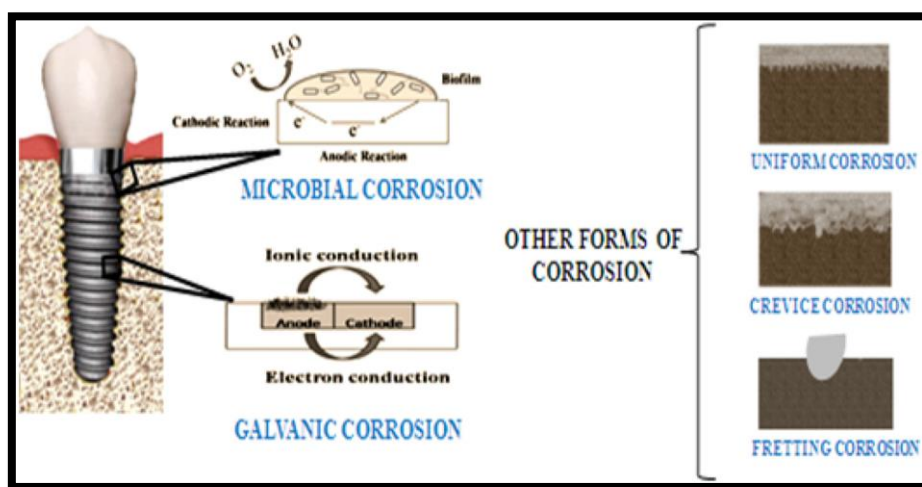


Figure 2-31 Types of corrosion taking place in implant [200].

Kelly et al. investigated the corrosion behaviour of titanium in aqueous solutions[190]. They reported that there are four kinds of response, the four states are shown in Fig. 2-32 [190]. The first state of response is an active response, in which the titanium can be oxidised forming Ti (III) ions with a high oxidation rate. The second state is a passive state, in which the titanium is covered by stable and protective oxide layers, which greatly reduces the oxidation rate. However, Ti (IV) ions can be formed by increasing the time of immersion; this ion could migrate into the oxide layer on the surface of the substrate or enter the solution. The third state is an active-passive state (also known as a translational state). During this state the oxide film incompletely covers the surface of the titanium, leading to impeding the passivation of the titanium. The fourth state is a hydrogen evolution state, during which titanium could be corroded by hydrogen evolution when the titanium is subjected to a sufficiently negative potential[190]. It has been reported that the responses depend on more than one environmental factor, and these include temperature, pH, and exposure time[190].

Results from published literature on the corrosion response of the titanium and titanium alloys for the biomedical applications suggested that the corrosion response of titanium can be improved by the addition of alloying elements, for example adding Nb, Mo, Ta, and Zr. It has been reported that these alloying elements can stabilize the oxide layers in biological media, and form a protective stable oxide, for example Nb_2O_5 , Ta_2O_5 , and ZrO_2 [201-205]. It has been claimed that the titanium and its alloys with these alloying elements exhibit a corrosion resistance better than that of the wrought CoNiCr alloy and stainless steel (AISI 316L)[201]. The influence of microstructural features on the corrosion response of titanium and its alloys for biomedical applications has been extensively investigated. The early work of Dull and Raymond in 1969 indicated that when increasing the ratio of α to β phases in Ti-6Al-4V, the passive corrosion current density increased. These increases were because of the generation of a galvanic cell between the α and β phases in the Ti-6Al-4V. It has been suggested that the type of microstructure has a key role in the corrosion response of titanium and its alloys when used as biomedical materials [197]. Previous work on the thermal and thermomechanical process show that the type of the thermal heat treatments and the type of thermomechanical process have a considerable effect on the corrosion response of titanium and its alloys for biomedical applications [206]. For example, the corrosion response after the solution heat treatment (ST) is different from the response under an aging heat treatment. Furthermore, the type of cooling media, the type of thermomechanical process, cold rolling, hot rolling, forging and heat treatment also had an important role in the corrosion response of titanium alloys [206-211].

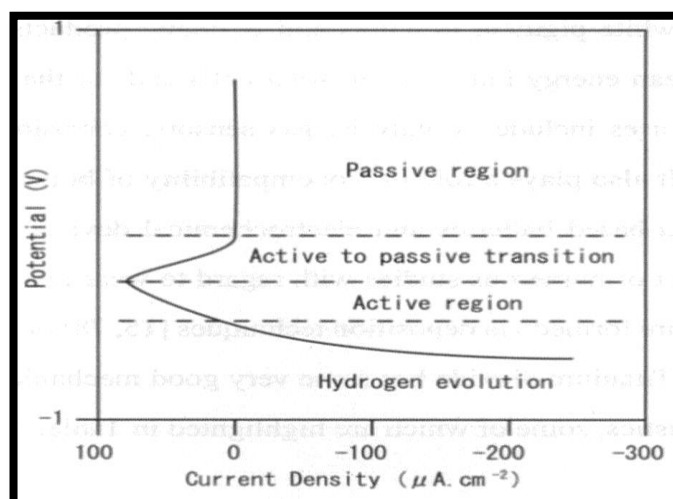


Figure 2-32 Schematic illustration of the current -potential relationship for titanium in an acidic solution [190].

Among the studies that have shown the β -microstructure single phase titanium alloys are more corrosion resistant than that $\alpha+\beta$ microstructure Ti-6Al-4V is a publication by de Almeida et al. [212]. In the study the authors investigated the electrochemical behaviour of metastable β -microstructure Ti-12Mo-13Nb and Ti-10Mo-20Nb alloys aged at 500 °C/24h and 500 °C/4h in Ringers solution. They found that the β -microstructure Ti-10Mo-20Nb alloy aged at 500 °C/24h exhibited more resistance to corrosion than that of Ti-12Mo-13Nb and the $\alpha+\beta$ microstructure Ti-6Al-4V. More studies on the electrochemical behaviour of metastable β -microstructure was carried out by Atapour et al. [197]. Their study presented results of electrochemical behaviour of β -microstructure Ti-13Mo-27Zr-3Fe, $\alpha+\beta$ -microstructure Ti-35Nb-7Zr-5Ta, and extra -low interstitial $\alpha+\beta$ - microstructure Ti-6Al-4V in 0.9 NaCl and 5M HCl solutions. The alloys exhibited spontaneous passivity in the NaCl solution. The single phase β - microstructure Ti-13Mo-7Zr-3Fe exhibited the lowest corrosion current and the most noble corrosion potential. Also, they found the β - microstructure alloy exhibited better corrosion resistance compared to $\alpha+\beta$ -microstructure Ti-35Nb-7Zr-5Ta, and extra -low interstitial $\alpha+\beta$ - microstructure Ti-6Al-4V. They reported that the composition of the microstructure and the stability of the passive film are the main factors influencing the electrochemical behaviour of the test alloys.

The electrochemical behaviour of Ti-alloys has been investigated extensively in different solutions. They reported that the corrosion rate of titanium alloys is considerably reduced by the formation of a protective passive film on the surface of the alloy. Also, they found that the repassivation behaviour after corroding also plays a vital role in the electrochemical behaviour of titanium alloys.

More results in this area were then published by Chelarice et al. [213]. Their report published results of the effect of niobium additions to Ti-Mo alloys on the electrochemical behaviour of Ti-Mo alloys. Comparisons was carried out between β -microstructure alloys Ti-12Mo, Ti-10Mo-8Nb, Ti-8Mo-16Nb, Ti-6Mo-24Nb and Ti-4Mo-32Nb in 0.9 wt.% NaCl saline solution at 25°C. Potentiodynamic polarization and electrochemical impedance spectroscopy methods were carried out to characterize the electrochemical behaviour of test alloys. The results revealed that in comparison to the Ti-12Mo, the alloys with niobium had a significant improvement of corrosion resistance. Also, they found that the improved corrosion resistance can be attributed to the hindrance of electron transfer across the passive film on the surface of alloys with niobium, which enhances passivation and reduces dissolution of the passive film.

More studies on the modification of the passive titanium oxide TiO_2 by alloying elements was carried out by Zhou et al. [204]. Their study presented results of the addition Ta with 10, 30 and 70 mass% to Ti-Ta alloys exhibited higher corrosion resistance than α + β -microstructure Ti-6Al-4V and α -microstructure Cp-Ti. They reported that the Ta addition improved passivation by the formation of a more stable oxide Ta_2O_5 that is stronger than the TiO_2 passive film, giving improved corrosion resistance compared to the α + β -microstructure Ti-6Al-4V and α -microstructure Cp-Ti. Among the studies that have shown the addition of Ta enhances passivation and corrosion resistance is a publication by Mareci et al. [205]. In the study the authors investigated the electrochemical behaviour of Ti alloys containing Ta and Mo as β -stabilizer elements for dental applications. Open circuit potential, potentiodynamic polarization curves and electrochemical impedance were used to examine β -microstructure Ti-60Ta, Ti-12Mo and α -microstructure Cp-Ti in artificial saliva and fluoridated artificial saliva. They reported that the β -microstructure Ti-60Ta alloy exhibited superior corrosion resistance than the β -microstructure Ti-12Mo and α -microstructure Cp-Ti in both solutions.

In a later study Nakagawa et al. [214] also found the electrochemical resistance of the passive film depended on the oxides film formed by the alloying elements. In the study the authors compared the electrochemical behaviour of Ti-6Al-7Nb, Ti-20Pd and Ti-6Al-4V. The results of their study revealed that the Pd alloy exhibited superior corrosion resistance than Ti-6Al-4V and Ti-6Al-7Nb alloys by the formation of a more stable oxide than when alloyed by Nb and V in Ti-6Al-7Nb and Ti-6Al-4V respectively. More studies were carried out by Namchi et al. [30]. Their study presented results of the electrochemical behaviour of Ti-8Mo-6Nb-4Zr, Ti-8Mo-6Nb-3Zr, Ti-8Mo-4Nb-2Zr, and Ti-8Mo-4Nb-5Zr in Hanks solution at 37°C. Potentiodynamic polarization curves were used to examine the alloys. The results of their study revealed that the corrosion and passive densities decrease with an increase in the niobium content and the alloys could potentially be used for biomedical applications. Some of these alloys will be investigated in this work given the systematic change in alloy microstructure that they produce.

The opposite results were later reported by Cordeiro et al. [215]. They showed that the Ti-35Nb-5Zr alloy exhibited the worst behaviour compared to that of Cp-Ti, Ti-6Al-4V, Ti-5Zr, and Ti-10Zr. Their results differ from those of previous studies of Ti-Nb-Zr. The previous studies reported that the electrochemical behaviour of Ti-Nb-Zr alloy played a similar or noble than that of α -microstructure Cp-Ti and α + β microstructure Ti-6Al-4V.

The microstructure developed and the redistribution of the alloying elements during heat treatment also plays a vital role in the electrochemical behaviour of titanium alloys. It has been reported that in $\alpha+\beta$ -microstructure Ti-6Al-4V the alloy has good corrosion resistance because the form of TiO_2 and Al_2O_3 on the surface of alloy [19]. When comparing the electrochemical behaviour of the $\alpha+\beta$ Ti-6Al-7Nb microstructure and $\alpha+\beta$ Ti-6Al-4V - microstructure, it was found that the $\alpha+\beta$ -microstructure Ti-6Al-7Nb exhibited higher corrosion resistance than the Ti-6Al-4V and thus related to the formation of Nb_2O_5 , which is chemically more stable than V_2O_5 found on Ti-6Al-4V [19]. Also, they found that where the β -phase contained elements such Ta, Nb in the $\alpha+\beta$ alloy, the electrochemical resistance of the alloy was improved. However, care should be taken to ensure a uniform distribution of elements in both phases by controlling the heat treatment, so no galvanic corrosion occurs between the two phases. Thair et al.[216] reported that Ti-6Al-7Nb heat treated at 950 °C, followed by air cooling and ageing at 550 °C showed the best electrochemical performance in Ringers solution. They reported that reason for this was related to the formation of duplex microstructure leading to uniform distribution of alloying elements. More results were then published by Geethaha et al. [217]. Their report confirmed that the $\beta+\alpha$ microstructure Ti-13Nb-13Zr with sub transus heat treatment exhibited superior corrosion resistance to that of the β -microstructure with solution heat treatment.

Among the studies that have shown the influence of different thermo-mechanical processing on the electrochemical of Ti-alloys is a publication by Mohammed et al. [210]. They investigated the influence of different thermomechanical processing parameters on the electrochemical behaviour of Ti-20Nb-13.6Zr-0.5V in Ringers solution with a pH of 7-4 at 37 °C. Open circuit potential and passive current density were used to examine the alloys. They reported that the water quenched samples exhibited better corrosion resistance than the solution treated sample because of a smaller amount of α -phase in the microstructure.

The above review clearly demonstrates that the passive film formed on the surface of titanium alloys should be highly stable in various environments. It is highly essential to select the alloying elements and heat treatment to have high corrosion resistance surface. From this perspective, one of the aims of the current work was to addresses the electrochemical behaviour of different types of titanium alloys to understand the influence of corrosion on the accelerated (synergistic) or deaccelerated (antagonistic) tribocorrosion behaviour.

2.6 Tribocorrosion

Tribocorrosion is defined as an irreversible transformation of a material resulting from the combined action of the mechanical loading (friction, erosion, abrasion) and corrosion attack caused by the environment (chemical and/or electrochemical interaction) [179]. Figure 2-33 presents the basic definition and concept of the tribocorrosion [24, 179, 183, 218, 219]; it covers the interaction of two major areas of application and significance in the mechanical system tribology and corrosion [179, 220]. During the tribocorrosion process, mechanical wear might accelerate the electrochemical or the corrosion attack, or the corrosion attack might be accelerated by the mechanical wear. By investigating the responses of the wear and corrosion and the influence of both during the tribocorrosion process, it is possible to understand whether the corrosion attack accelerates the mechanical wear, or the mechanical wear accelerate the corrosion attack. Tribocorrosion mechanism is presented by the schematic in figure 2-34 [200].

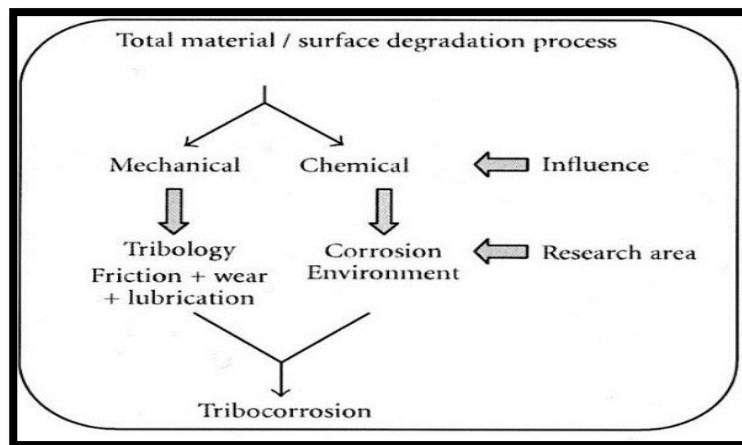


Figure 2-33 Basic concept and definition of tribocorrosion [179].

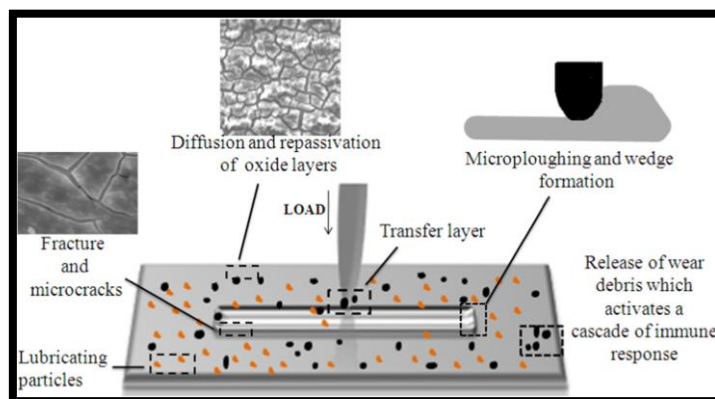


Figure 2-34 Schematic representation of tribocorrosion mechanism [200].

The early work in tribocorrosion or the tribo- electrochemistry was completed by Edison in 1875, when he investigated the variation of the friction coefficient (COF) at various applied potentials [221]. Recently, the number of studies in the field of tribocorrosion has developed and grown, and being investigated under two categories including tribocorrosion in industrial systems and tribocorrosion in living systems [139, 140, 219-221]. Despite numerous studies carried out in tribocorrosion, it is still poorly understood. The holistic understanding of the tribocorrosion phenomena is an integration of research from various disciplines including Material Science, Surface Engineering, Mechanical Engineering, Tribology, Electrochemistry/ Chemistry, Medicine, and Biology are required. Furthermore, investigating interactions starting at the microscopic level of the material surface at the micro and nano-levels could give an important indication about the tribocorrosion process and its mechanisms [222, 223].

Tribocorrosion processes are encountered in a wide range of technological and industrial applications. Tribocorrosion or the tribo-electrochemical phenomena can cause the loss of performance, durability, safety, reliability, health as well as the pollution and uneconomical material in a wide variety of applications. Some industries and living systems where the tribocorrosion phenomena can occur are shown in figure 2-35 [179]. As shown in figure 2-35, tribocorrosion is encountered in industrial systems including the process industry, mining, marine industry, automotive industry, aerospace industry, nuclear, material handling, offshore, chemical and petrochemical industry, food, and biomedical applications [25, 224]. Furthermore, tribocorrosion is also encountered in living systems as in the case of a metallic implant in the living body including orthopaedic plates and screws, artificial joints and dental implants [24, 183] .

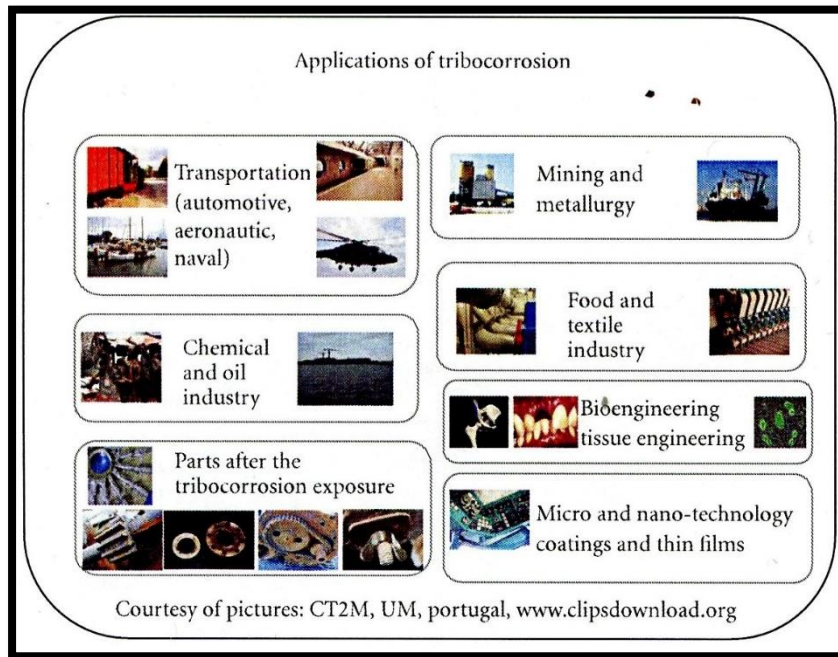


Figure 2-35A spectrum of practical importance of tribocorrosion [179].

2.6.1 Factors Affecting Tribocorrosion Rate and Mechanisms

There is more than one factor that can influence the tribocorrosion of materials as shown in figure 2-36 [179]. As can be seen from the figure, the tribocorrosion response depends on the properties of the materials, mechanical/ operational, solution/environment, and electrochemical parameters [24, 141, 224].

a). Materials

The properties of the materials have a crucial role in the tribocorrosion rate and mechanisms, and this includes the properties that influence the tribological and electrochemical response during the tribocorrosion. These parameters include, hardness, plasticity, microstructure, inclusions, surface roughness, oxide film properties, wear debris and material transfer. However, the relationship between these properties and their influence in tribocorrosion rate and the mechanisms are not very clear[25, 224].

b). Mechanical/ operational parameters

These parameters include the applied force, and the type of contact (fretting, sliding, impact, or rolling). Furthermore, it also includes the type of motion, sliding velocity, vibration, and the shape and size of contact bodies. These parameters have a significant influence on the

tribocorrosion rate and mechanisms. In general, different mechanical/operational processes exhibit different parameters influencing the tribocorrosion rate and mechanisms [179].

c). Solution/environment

The type of solution/environment and its corresponding properties have a major role that influences the tribocorrosion rate and mechanisms; more specifically, the form of the medium at the interface and its corresponding properties. For example, whether it is solid, gaseous or liquid and its corresponding properties, and these include the viscosity, corrosivity, conductivity, temperature and pH. In general, these parameters play a major role in influencing the corrosion mechanism and corrosivity, leading to an influence in the tribocorrosion rate and mechanisms [179].

d). Electrochemical parameters

The electrochemical parameters, which include the applied potential, passivation, film growth, ohmic resistance, valence and repassivation kinetics have a significant influence on the tribocorrosion rate and mechanisms. More specifically, this influence can be related to the repassivation of the metal during the sliding (electrochemistry, corrosion), and how the surface oxidation under the rubbing (tribological) influences the rate of wear (mechanical) [25, 218-221].

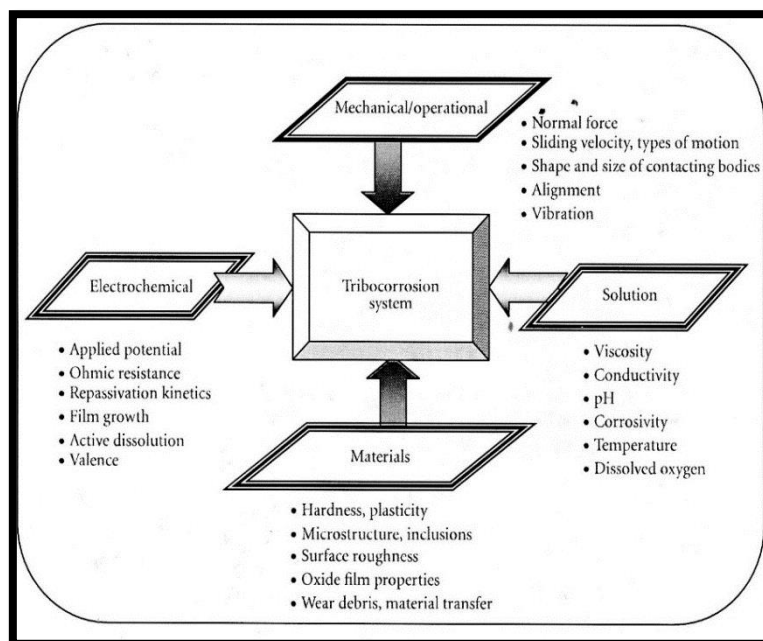


Figure 2-36 Factors influencing the tribocorrosion [179].

2.6.2 Tribocorrosion Approaches

2.6.2.1 The synergistic approach

To calculate the total volume of the material removed during the tribocorrosion test, it is important to consider the synergistic effect between the corrosion and mechanical wear. In this type of approach, it cannot be assumed that the total volume lost during the test is just equal to the summation of the volume lost due to pure corrosion and pure wear [225].

Watson in 1995 proposed the combined effect of wear and corrosion using the following equation [226]:

$$V_{total} = V_w + V_c + V_s \quad 2 - 18$$

Where: V_{total} = the total of material removed, V_w = the volume of material lost due to mechanical, V_c = the volume of material lost due to corrosion, V_s = the volume of material lost due to the combined synergistic influence between the corrosion and wear.

The above mathematical expression can be represented as the following equation

$$T = W_o + C_o + S \quad 2 - 19$$

Where: T = the total materials loss during tribocorrosion, W_o = the material loss due pure wear (mechanical), C_o = the material loss due to pure corrosion (no wear), S = the sum of wear accelerates corrosion and corrosion accelerate wear.

2.6.2.2 The mechanistic approach

In this type of approach, the total material lost during tribocorrosion is combined with the wear and corrosion conditions because of two main contributions, mechanical wear and wear accelerated by corrosion. In mechanical wear, the metal is removed, and the metal surface will have worn due to the mechanical contact influence and exposing fresh metal will be generated because of this. During wear accelerated corrosion, and due to exposure of the fresh metal which was generated by the mechanical wear, the corrosion will accelerate because these areas will be more reactive than that at the surface of the metal during the tribocorrosion test [26, 140, 225, 227, 228]. Therefore, in this approach the total material lost can be calculated from the following equation [24]:

$$V_{total} = V_{mech} + V_{chem} \quad 2 - 20$$

Where: V_{Tot} = the total volume lost during the tribocorrosion process, V_{mech} = the volume lost due to mechanical wear during the tribocorrosion process, V_{chem} = the volume lost due to chemical or electrochemical mechanisms during the tribocorrosion process.

Faraday's law can be used to calculate the volume removed by anodic oxidation in the wear track (V_{chem}):

$$V_{chem} = \frac{Q \cdot M}{nF\rho} \quad 2 - 21$$

$$Q = \int I dt \quad 2 - 22$$

$$V_{chem} = \frac{I \cdot t \cdot M}{nF\rho} \quad 2 - 23$$

Where: Q is the electric charge, I is the average current (A), t is the time (s) of sliding contact, n is the charge number for oxidation reaction, F is the Faraday constant (96500 Cmol⁻¹), ρ is density of alloy, M is the atomic mass of alloy.

In this approach, particularly with chemical or electrochemical wear, it is important to understand that the corrosion response in the unworn areas is different from that in worn areas, particularly with passive materials. For a highly passive material, the corrosion response for the unworn areas is negligible, therefore, the volume lost due to chemical or electrochemical V_{chem} is related almost entirely to the corrosion response in the worn area of the material [24]. Even though this approach has been used [10, 24, 183, 229-233], there are some issues that still need to be considered. The volume is a result of the whole process, and there is no information generated as to differing electrochemical or chemical states on the surface of the material over the time during the progress of the process [24].

2.6.2.3 The third- body approach

Figure 2-37 is a schematic of possible material flow during the formation of third bodies in a tribocorrosion system [24]. Firstly, the wear debris will have been removed from the substrate metal by the counter face material. Secondly, the wear debris might be ejected directly from the contact zone or formation of the third-bodies when they are trapped within the contact zone between the two bodies. In the next step, the wear debris can be fragmented into smaller particles or can be attached to the substrate or the counter face. After that, the wear debris will reach the critical or small enough of the size and will be ejected from the

contact zone, transfer back on the material surface by smearing or get oxidized [24, 183, 225].

Numerous parameters can influence the behaviour and properties of third bodies: chemical, mechanical and material property aspects [225]. The contact pressure, lubrication and sliding velocity are examples of the mechanical factors. Metal oxidation and dissolution, adsorption of chemical compounds generated in the corrosive environment are examples of chemical factors. Hardness, composition and microstructure are examples of material property factors. It has been reported that the amount of the wear debris generated during tribocorrosion increases with applied load; furthermore, the amount of wear debris generated in the hard material is higher than that of the high strength material, the rate and properties of the third bodies are directly influence by the electrochemical state of the material in the contact zone [225].

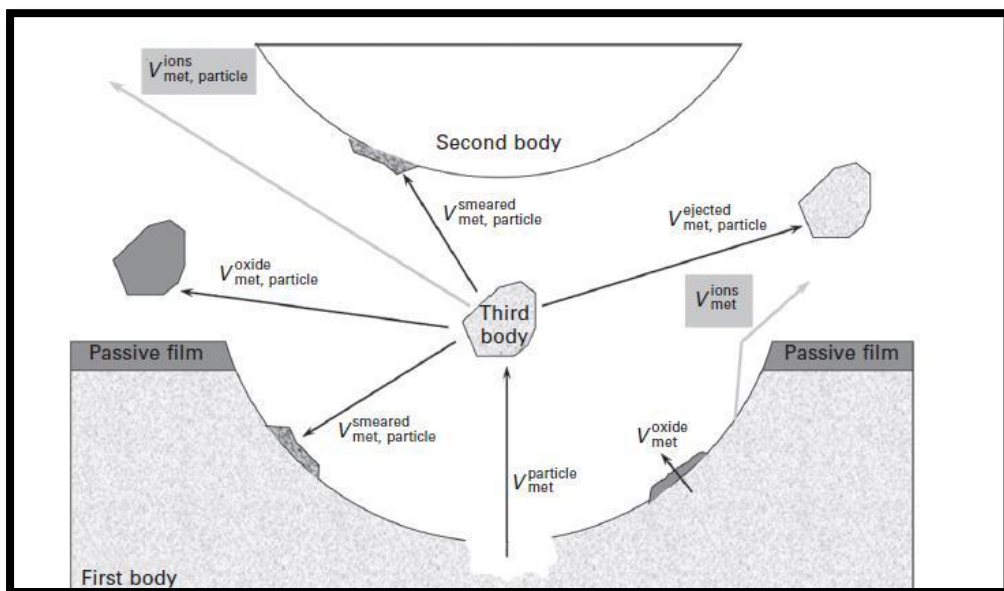


Figure 2-37 Schematic diagram of material flows occurring during the formation of third bodies in a tribocorrosion experiment of passive metal [24].

2.6.3 Electrochemical Techniques for Tribocorrosion Study

Electrochemical techniques can be used in conjunction with the tribological tests during investigating the tribocorrosion response of the alloys. Hence, the alloys will have been subjected to numerous environmental and loading conditions, which lead to both the electrochemical and the mechanical characteristic of the alloy being investigated.

Tribocorrosion is very effective at analysing the combined influence of wear and corrosion.

Tribocorrosion techniques can be carried out under open circuit potential combined with wear, the potentiodynamic technique combined with wear, and the potentiostatic technique combined with wear.

2.6.3.1 Open circuit potential technique (OCP)

During this technique, the material is subjected to open circuit potential combined with wear testing, which gives information about the electrochemical state of the material along with the wear response during the test. Due to the influence of mechanical wear, the material will change from the passive to active state and galvanic corrosion occurs. Therefore, the potential measured during the test reflects this type of the corrosion which is generated between the unworn area and the wear scar [234]. The tribocorrosion responses of the material can be investigated using a comparative study of the material in an environment under the same conditions between the response of the material without rubbing (without mechanical wear), and the response with during rubbing (with mechanical wear) under open circuit potential.

It has been reported that passive materials are more influenced by rubbing during the test compared with active materials. For a passive material, a cathodic shift can be exhibited during rubbing due to the influence of mechanical wear which leads to removal of the passive oxide and the generation of new active areas on the surface of the passive material. In contrast, no large structural or chemical differences are exhibited during the test of active materials. Therefore, there is a very little difference in the potential measured during rubbing compared to that measured without rubbing [183, 225, 234-237].

2.6.3.2 Potentiodynamic technique (PD)

During this technique, rubbing or sliding wear can be applied in conjunction with potentiodynamic sweeps, with the current measured. The shift in the current and corrosion potential can be related to the passive to active ratio in the surface of the material under rubbing [25, 183]. This technique does not just give an indication of the electrochemical change during the combination of mechanical wear and the potentiodynamic sweep, but also gives an indication about the chemical change of the material, as measured by the friction response during the test. The friction response is also influenced by the potential sweep, therefore, it might be increased or reduced related to the chemical states of the material and changing of the wear mechanisms during the test [25, 183]. Hydrogen embrittlement could be exhibited during the test, when the material under test is subjected to polarisation with a large

cathodic potential, which leads to the increasing the hardness of the surface of the material, and leads to increasing the friction of the materials [25, 183, 190].

2.6.3.3 Potentiostatic technique (PS)

During this technique, rubbing or sliding wear is applied in conjunction with a single fixed potential. The current density and friction response of the material is measured during the test. This test can give an indication of the electrochemical kinematics of the material for a particular environment and rubbing condition [183]. Depending on the fixed potential applied during the test, in combination with the mechanical wear, the passive and active areas could be investigated to better understand the mechanism of the tribocorrosion (corrosion and wear) response of each state of the material [183, 231, 232].

2.6.4 Tribocorrosion test system

Figure 2-38 shows the basic methodology of a tribocorrosion test, while figure 2-39 shows the general steps in a tribocorrosion test [179]. As can be seen from figure 2-38, the tribometer has the facility to calculate the evolution of the friction coefficient and the electrochemical technique is used to measure and monitor the current or the potential (corrosion response) during tribocorrosion tests. A potentiostat and three electrode attachments can be used to measure the electrochemical response (current or potential) during rubbing. The three electrodes used are a reference electrode (RE) (either standard calomel electrode (SCE) or standard hydrogen electrode (SHE)), a counter electrode (CE) (either platinum wire or graphite rod) and the working electrode (WE) which is the sample used for testing.

The first step in figure 2-39 is the selection of test parameters (tribological and corrosion parameters) and this depends on the area of research and the application of interest. For example, the influence of the load or number of cycles are parameters of interest in the case of orthopaedic applications. In contrast, the pH of the solution is the parameter of interest in the case of dental application. Tribocorrosion tests can be performed under open circuit potential (OCP), in which case the actual wear condition will be measured. In addition, the test can be performed under constant potential (cathodic or anodic), where the change in the current density due to the wear are measured. Rather than a constant potential, a scanned potential range can be used. To understand and characterise the passive films formed at the contact surface under rubbing during a tribocorrosion tests, electrochemical impedance spectroscopy (EIS) can be used. Usually, such techniques are applied before and after

rubbing and sometimes during rubbing. The electrochemical parameters, either the current (during constant potential technique) or the potential (during OCP technique) can be correlated with the friction coefficient and the wear rate and subsequent analysis of the worn surface structure.

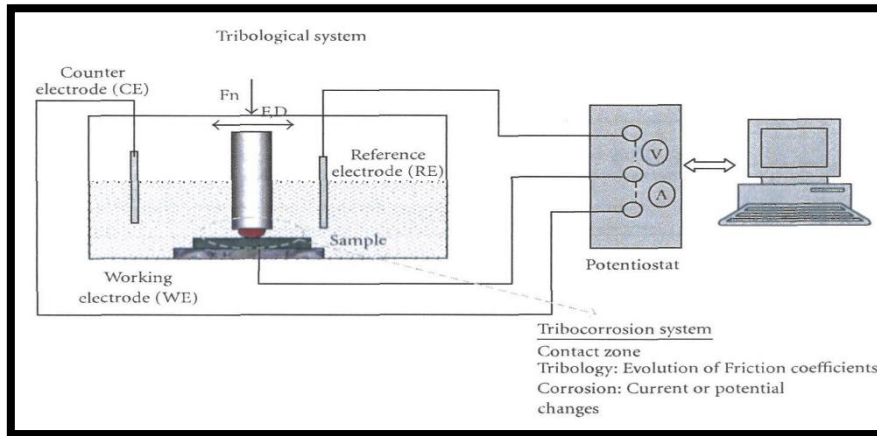


Figure 2-38 Basic methodology in a tribocorrosion study [179].

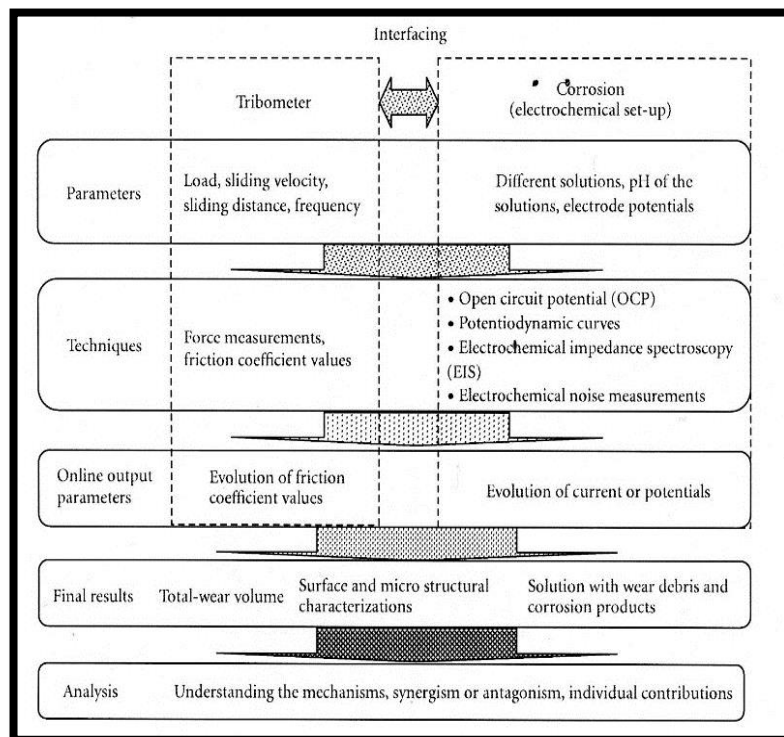


Figure 2-39 Basic steps in tribocorrosion study [179].

2.6.5 Tribocorrosion of Titanium and Titanium Alloys

Tribocorrosion studies of titanium and titanium alloys have focused on the investigation of the influence of surface treatments on improving the corrosion and wear performance of Cp-Ti and its alloys, and on examination of the influence of environmental variables including pH, temperature, fluoride content (in artificial saliva) and the tribocorrosion response of titanium and titanium alloys [238-243]. Tribocorrosion studies are carried out under different mechanical conditions, in a large variety of the electrolytes (from simple solutions to more complex formulations), in the average speed range 0.1 up to 1000 mm/s, and average contact pressure is between 23 MPa and 3.15 GPa. The tribocorrosion testing of titanium and titanium alloys has carried out under open circuit potential (OCP) and using a passive potential [10, 244-249]. It has been shown that the extent of the dissolution of the passive film depends on the surface treatment of the titanium and titanium alloys, the load, contact pressure, frequency and the type of the electrolyte [240, 243, 250].

Several recent studies focus on the tribocorrosion properties of different type of titanium alloys to understand the performance of implants and mechanisms. Many researchers have tried to understand synergistic and antagonistic mechanisms. However, tribocorrosion phenomenon are more complex because the number of influencing parameters that make it more complex. Diomedis et al. [230] investigated the fretting - corrosion behaviour of β -microstructure Ti-12Mo, Ti-13Nb-13Zr, and Ti-29Nb-13Ta-4.6Zr alloys in simulated synovial fluid, tested under OCP and passive applied potential. A Ti-6Al-4Fe $\alpha+\beta$ microstructure alloy was also investigated for comparison. They reported that the Ti-13Nb-13Zr and Ti-29Nb-13Ta -4.6Zr exhibited the ability to regain their passive state during fretting at the open circuit potential. Ti-29Nb-13Ta-4.6Zr can also regained its passive state during fretting at an applied potential in the passive region. On the contrary, $\alpha+\beta$ microstructure Ti-6Al-4Fe exhibited a widespread depassivation during fretting at a passive applied potential. All alloys except Ti-29Nb-13Ta-4.6Zr exhibited a lower wear volume at the open circuit potential than that at a passive applied potential. No material transfer could be found on the alumina ball counterbody after the fretting experiments. The results of their study revealed that no dependence of fretting response and wear volumes of the tested alloys on the mechanical properties of alloys. In a later study, More et al. [10] also found that these alloys exhibited a tendency to repassivate during sliding at open circuit potential and passive applied potential when they investigated the tribocorrosion behaviour against ultra-high molecular weight polyethylene in Hanks balanced salt solution. Also, they reported that the

predominant wear mechanism was third body wear with the transfer of polyethylene to the titanium alloy surface. They highlighted that only very weak wear accelerated corrosion can be measured and the coefficient of friction remained mainly unaffected by potential and the alloy composition. Dimach et al. [246] investigated the influence of the alloy microstructure and composition on the tribo-electrochemical behaviour of Ti-Grade2, Ti-6Al-4V and Ti-6Al-4V ELI in phosphate buffered solution (PBS) and phosphate buffered solution with bovine serum albumin (PBS+BSA) under sliding conditions. The results of their study revealed that the main effect of alloy composition and microstructure was found in the wear accelerated corrosion, which is twice in the case of the Ti-Grade 2. The results showed that Al and V in titanium alloys reduce the passive dissolution of titanium and considerably decrease the wear accelerated corrosion under tribocorrosion conditions. Also, they reported that there was no effect of mechanical properties on the tribocorrosion response and wear volume. More studies on tribocorrosion of $\alpha+\beta$ microstructure Ti-6Al-4V was carried by Runa et al. [28]. Their study presented results of the tribocorrosion behaviour of etched Ti-6Al-4V alloys under reciprocating sliding in a phosphate buffer solution (PBS) containing protein. The results revealed that the complex interactions and specific interaction pathway of portions with the Ti-6Al-4V surface need to be considered during tribocorrosion. They also found that albumin plays an important role affecting the tribocorrosion behaviour of Ti-6Al-4V depending on the stage of passive film. More results of the study tribocorrosion behaviour of Ti-6Al-4V were then published by Licausi et al. [245]. Their report published results of the influence of the fabrication process and fluoride content in the tribocorrosion behaviour of Ti-6Al-4V alloy in artificial saliva. In their study the tribocorrosion behaviour of cast Ti-6Al-4V and sintered Ti-6Al-4V in artificial human saliva solution with and without fluoride additions have been investigated at open circuit potential and passive applied potential. The results showed that at low applied passive potential, wear rates are similar for both alloys to those obtained under open circuit potential. The fluoride increases the wear accelerated corrosion. In a later study, the same authors also found the same results when they investigated the tribocorrosion behaviour of the above alloys in artificial human saliva solution with different pHs (3, 6, 9) and in an acidic saliva with fluoride. They reported that the addition of fluorides changes the degradation mechanism towards active dissolution of the Ti-6Al-4V alloy. Also, they reported independently on the pH, wear damage is mainly due to mechanical action but the main degradation mechanism changes to corrosion when added fluorides to acidified artificial saliva with pH=3.

The tribocorrosion behaviour of titanium grade 2 was also studied by Priya et al. [251]. The authors compared the tribocorrosion of titanium grade 2 with 304L stainless steel, zirconium 702 and zircaloy 4 in 1M HNO₃ using a pin on disc. The assessment showed that the Ti-grade2 exhibited trans passive behaviour under rubbing conditions in 1M HNO₃. Also, they found that Ti-grade2 and Zr-based materials had higher coefficient of friction and wear depth when compared to that of 304L stainless steel. They reported that the wear accelerated corrosion is more pronounced in Ti grads and Zr-based material than of 304L stainless steel.

Among the studies that have shown the improve the tribocorrosion resistance of Ti-6Al-4V is a publication by Oladele et al. [252]. In this study the authors showed that the tribocorrosion resistance of Ti-6Al-4V could be improved by laser surface cladding with TiNiZrO₂ composite coating in 1M H₂SO₄. Their results showed that the addition of ZrO₂ to TiNi coatings improved tribocorrosion resistance of the coating in the investigated electrolyte. They also reported that the TiNi10ZrO₂ had better tribocorrosion than TiNi5ZrO₂ coatings. More studies on the improve tribocorrosion resistance of Cp-Ti grade 2 was carried by Bailey [146]. In this study the authors investigated the tribocorrosion behaviour of thermally oxidized commercial titanium in a 0.9 NaCl solution at +1000, -500, -900, - 1500 mV_{SCE}, and open circuit potential. Their study showed that the thermally formed oxide layer offers lower friction and higher wear resistance during tribocorrosion than untreated Cp-T under the open circuit potential. The opposite when the thermally oxide titanium is polarized anodically during rubbing low friction and high volume loss than of untreated Cp-Ti. When the two materials cathodically churched to high potential -1500 mV_{SCE} during rubbing experience a reduction in total volume loss.

Among the studies that have shown the tribocorrosion behaviour of different types of titanium alloys is a publication by Hacisalihoglu et al. [253]. In the study the authors investigated the tribocorrosion properties of β -microstructure alloys β -Ti-13Nb-13Zr and β -Ti-45Nb, α -Cp Ti, and α + β -microstructure Ti-6Al-4V in simulated body fluid (SBF) at open circuit potential, cathodic and three different anodic potentials under reciprocating sliding conditions. They reported that the α + β -microstructure Ti-6Al-4V and β -microstructure Ti-13-Nb-13Zr showed lower friction coefficient and lower wear volume during tribocorrosion tests than others. They also reported that at open circuit potential during rubbing α -Cp Ti showed the noblest behaviour, while α + β Ti-6Al-4V exhibited the most active behaviour. The β alloys exhibited the lost potential values. Also, they found that the total volume loss of β -microstructure alloys decreased with increasing potential. Their study also showed that the

$\alpha+\beta$ Ti-6Al-4V exhibited superior tribocorrosion behaviour. However, they suggested that the β - Ti1313 alloy has the potential to be the best candidate with relatively low elastic modulus and less material loss, comparable mechanical and tribocorrosion behaviour and nontoxic alloying elements. More studies on the tribocorrosion behaviour of β -microstructure was carried out by Guinon Pian et al. [254]. Their study presented results of the tribocorrosion behaviour of three different β -microstructure Ti-30Nb, Ti-30Nb-2Sn and Ti-30Nb-4Sn in phosphate buffer saline solution at open circuit potential and -1 V Ag/AgCl, 0 Ag/AgCl, and 2 Ag/AgCl. They reported that all the alloys spontaneously passivate in the solution and the alloys exhibited the same tribocorrosion mechanisms passive dissolution and plastic deformation. The wear accelerated corrosion increased with increase in Sn content. They also found that the corrosion rate increases during wear under tribocorrosion tests, when Sn content above 2%. They claim the Ti-30Nb-2Sn alloy can be considered the most suitable alloy under tribocorrosion.

As more β -microstructure alloys are becoming more competitive candidates for biomedical compared with α -microstructure Cp -Ti and $\alpha+\beta$ microstructure Ti-6Al-4V, research is increasingly focused on the tribocorrosion behaviour of β -microstructure alloys. Correa et al.[255] investigated the tribocorrosion behaviour of β -microstructure alloys Ti-15Zr-7.5Mo and Ti-15Zr-15Mo at open circuit potential in SBF solution at 37 °C and compared the results with α -microstructure Cp-Ti. The β -microstructure alloys exhibited tribocorrosion superior to α -Cp Ti. Also, they reported that the tribocorrosion mechanisms was abrasion. The β -microstructure Ti-15Zr-7.5Mo had a lower wear volume than others. They suggested that the β -microstructure Ti-15Zr-7.5Mo have potential for dental applications.

The above review clearly brings out fact that the passivation and repassivation during rubbing plays a vital role in tribocorrosion behaviour of titanium alloys. Also, the microstructure (α , $\alpha+\beta$, and β) has a considerable effect on the tribocorrosion behaviour of titanium alloys. Tribological and electrochemical properties also play a vital role in wear accelerated corrosion, or corrosion accelerated wear. The authors believe that the tribocorrosion behaviour of titanium alloys for biomedical applications is the most important area to be addressed to understand synergism and antagonism mechanisms to have high tribocorrosion resistance for biomedical applications. From this perspective, one aim of the current work addresses the tribocorrosion behaviour of different type titanium alloys.

Chapter 3 : Experimental Procedure

3.1 Introduction

In this chapter, the materials, equipment and methods used in this study are presented. To achieve the objectives of this study, five different vanadium free β –titanium-based alloys, Ti-Ta₃₀, Ti-Ta₂₇-Al₅, Ti-Mo₈-Nb₄-Zr₂, Ti-Mo₈-Nb₄-Zr₅ and Ti-Mo₈-Nb₆-Zr₄, were prepared by vacuum arc- remelting (VAR) and subsequently characterised in detail. All alloy compositions are given in at%, unless otherwise stated.

The alloy selection was based around β titanium alloys, but with a range of stabilities. The Ti-Ta alloy was selected on the basis that it should provide a stable single phase β alloy, but with the Ta addition giving strong repassivation properties. The selection of the Ti-Mo_x-Nb_x-Zr_x were made on the basis of the work of Nnamchi [29] and that these alloy additions are believed to be acceptable for biomedical applications. Nnamchi used Bo (the covalent bond strength between Ti and the alloying elements) and Md (the mean d-orbital energy level) to design a range of titanium alloys [29]. In so doing, he showed that these alloys varied from a highly stable β alloy through to a metastable β alloy that would be expected to exhibit the formation of martensite. In addition, the work hardening behaviour of these alloys would be different with the potential for twinning induced plasticity (TWIP), and transformation induced plasticity (TRIP). Moreover, the alloys would exhibit a range of elastic moduli, which would be expected to be important in the wear behaviour. As noted before, it is far from clear which microstructure is ideal for biomedical applications and a principal objective of this study was to understand which microstructure is ideal.

The properties of β –titanium alloys depend strongly on processing parameters and are very sensitive to microstructural changes [256, 257]. Therefore, the processing of β – titanium alloys required special care. Conventional commercially available α -CP- Ti and α + β Ti-6Al-4V alloys were also tested for comparison. The experimental procedure used to prepare samples by arc melting (materials and method, alloy fabrication, and arc melting process) is presented in detail. Homogenization heat treatment, cold rolling and recrystallization treatment, solution heat treatment and sample preparation are also explained. Composition analysis using X-Ray fluorescence and density measurements using Archimedes' principle are explained. Transformation (β -transition and α'' transition) temperature measurements using differential scanning calorimetry (DSC) and combined DTA/TGA techniques are also explained. Microstructural investigations including optical microscopy, scanning electron

microscopy, transmission electron microscopy, electron back-scatter diffraction, energy dispersive X-ray analysis, X-ray diffraction and focused ion beam (FIB) are presented. Mechanical tests such as nanoindentation, micro-hardness and elastic modulus measurement by ultrasound techniques are also explained. Tribological, electrochemical and tribocorrosion tests are also presented in this chapter.

3.2 Arc Melting

3.2.1 Material and Methods

Ingot metallurgy processing routes and microstructural characterization procedures were used in this study. High purity starting materials were used. High purity titanium foil (Ti 99.5 % annealed) with 100 mm width, 500 mm length and 0.25 mm thick and tantalum foil (Ta 99.5 % annealed) molybdenum, niobium and zirconium foil, all with dimensions 200 x 200 x 0.127 mm, were purchased from Alfa Aesar (United States). High purity aluminium foil (Al 99.999 % as rolled) with 100 x 100 x 1.0 mm dimensions was purchased from Goodfellow Cambridge Limited (England).

3.2.2 Alloy Fabrication

Five different vanadium free β -titanium ingots were prepared by vacuum arc-remelting (VAR) in an Edmund Buhler GmbH Germany Arc Melter AM (Arc Melting System AM, 5 Generator Tetrax 1002, Pumping System HVT 150, Option Suction Casting and Sample manipulator) equipped with a water – cooled copper hearth and a tungsten electrode under an argon atmosphere. Ti, Ta, Al, Mo, Nb and Zr were used as raw materials for vacuum arc remelting (VAR), with the nominal chemical composition listed in Table 3-1. All surfaces of the raw materials were ground using 220 grit silicon carbide abrasive paper. Further cleaning was completed by ultrasonic cleaning in acetone and ethanol baths, and then dried with a hair dryer prior to melting. A Precisa XB 120 Switzerland precision balance with an accuracy of ± 0.0001 g was used to weigh the raw materials to control the alloy Ti/Ta/Al and Ti/Mo/Nb/Zr ratios.

Table 3-1 Nominal chemical composition of the alloys used in this study

Alloys	Alloying Elements wt. % (at%)					
	Mo	Nb	Zr	Ta	Al	Ti
Ti-Ta ₃₀	-	-	-	61.83(30)	-	Balance
Ti-Ta ₂₇ -Al ₅	-	-	-	59.03(27)	1.63(5)	Balance
Ti-Mo ₈ -Nb ₄ -Zr ₂	14.11(8)	6.83(4)	3.35(2)	-	-	Balance
Ti-Mo ₈ -Nb ₄ -Zr ₅	13.78(8)	6.67(4)	8.19(5)	-	-	Balance
Ti-Mo ₈ -Nb ₆ -Zr ₄	13.66(8)	9.92(6)	6.49(4)	-	-	Balance

3.2.3 The Arc Melting Process

3.2.3.1 Ti-Ta based alloys

Arc melting was completed in Ar with 99.9999 vol. % purity at a pressure of 700 mbar. Prior to melting, the chamber was evacuated three times to a pressure of 5×10^{-2} mbar and flushed back with argon. To minimize the oxidation potential of the ingots, a separate piece of Ti was melted to act as a getter and held in the liquid state for 1 min before the melting of the ingots. Then the Ti, Ta and Al raw materials were melted.

Firstly, Ta pieces were placed on top of the Ti pieces (Ti-Ta alloys) or on top of the Ti and Al pieces (Ti-Ta-Al alloys). These were selectively heated by the plasma arc, using a maximum current of 400 A. During this procedure, the Ta melt envelops the Ti (Ti-Ta alloys) and Al pieces (Ti-Ta-Al), which then dissolve into the Ta melt. When melting was complete, the ingot was held in the liquid state for 20 s and solidified into a button shaped ingot. To provide a homogeneous ingot, the button was turned over after each arc-melting step and the procedure repeated for a total of 12 times. The final button shaped ingots cooled down to room temperature within 5 min. The mass of all ingots was measured using a four-digital weight balance after arc melting to evaluate whether evaporation during melting process results in composition changes. The mass loss after melting was approximately (0.1-0.16wt. %). After that, all ingots were subjected to a homogenization heat treatment.

3.2.3.2 Ti-Mo based alloys

The arc melting procedure was similar to the procedure described for the Ti-Ta based alloy (see 2.2.3.1). Firstly, the Mo pieces that were laid on top of the Nb, Zr and Ti pieces were selectively heated by the plasma arc, using a maximum current of 400 A. The Mo melt enveloped the Nb, Zr and Ti pieces which dissolved into the Mo melt. When completely

melted, the ingot was held in a liquid state for 20 s and solidified into a button shaped ingot. To provide a homogeneous ingot, the button was turned over after each arc-melting step and the procedure was repeated 8 times. The melt was cast as a button shaped ingot that cooled down to room temperature within 5 min. The mass of all ingots was measured using four digital weight balances after arc melting to evaluate whether evaporation during melting process results in composition changes. The mass loss after melting was < 0.1. %. After that, all ingots were subjected to a homogenization heat treatment.

3.3 Thermal and Thermomechanical Treatment

3.3.1 Homogenization Heat Treatment

The purpose of the homogenization heat treatment is to remove micro-scale concentration gradients and to obtain a uniform composition throughout the ingot [258]. Ingots were wrapped in tantalum foil then homogenized at 1100 ° C for 25 h under argon in a tubular furnace [257]. The ingots were immediately quenched in cold water at the end of the annealing period to avoid omega (ω) phase precipitation, which is formed at intermediate and slow cooling rates as reported in [259].

3.3.2 Cold Rolling and Recrystallization treatments

Button shaped ingots were cut prior to cold rolling to achieve a uniform reduction. After that, the surface of the ingots was cleaned using emery papers with 400-800 mesh grit and then ultrasonically cleaned with isopropanol for 5 min. Cold rolling reduction was calculated using equation 3-1.

$$\text{Cold rolling reduction (\%)} = (T_1 - T_2 / T_1) \times 100 \quad 3-1$$

Where T_1 was the sample thickness before cold rolling, T_2 was the sample thickness after cold rolling. Cold rolling of the Ti-Ta based alloys was completed with a ~0.2 mm reduction per feed using the Hille rolling mill. Multiple passes achieved a 49.8% reduction in area. The cold rolled strip was then subjected to 10 min annealing at 800 ° C with argon in a tubular furnace and then quenched in water at room temperature. The samples were then cold rolled with a 64% reduction, again with ~0.2 mm reduction per feed. Finally, the cold rolled strip was recrystallized at 1000 ° C for 10 min in flowing argon inside a tubular furnace and then quenched in water at room temperature. No intermediate treatment was necessary for Ti-Mo based alloys fabricated in this work during cold rolling, because Ti-Mo based alloys exhibited excellent cold workability during cold rolling.

3.3.3 Solution heat treatment

After cold rolling, the strip samples were cut into the desired shape (20mm x 20mm x 3mm), after that the samples were mechanically polished using a SiC emery with 400-800 mesh grit, washed with distilled water and cleaned with isopropanol in an ultrasonic bath for 5 min. Solution heat treatment was carried out at 950 ° C under high vacuum for 2h inside a tubular furnace. The samples were immediately quenched in cold water at the end of the annealing period.

3.4 Composition Analysis and Density of Alloys

The chemical composition of the alloys was analysed by PANalytical Zetium X-Ray Fluoresce (XRF). The density of all alloys was measured by Archimedes' principle using a balance (New Classic MF MS 104S/01) with an accuracy of ± 0.0001 g.

3.5 Transformation Temperatures

It is important to determine the $\alpha \leftrightarrow \beta$ transition temperature (T_{β}) accurately to select appropriate heat treatment temperatures. Furthermore, it is important to characterise the thermal effect associated with martensitic transformation in the alloys.

Differential scanning calorimetry (DSC) and combined DTA/TGA were carried out to determine the β transition temperature and characterize the thermal effect associated with the martensitic transformation in the alloys. DSC was performed using a PERKIN-ELMER Diamond DSC Differential Scanning Calorimeter. Combined DTA/TGA was completed using TA Instruments/ SDT Q600. Specimens for measuring the transformation temperatures with masses between 20 mg and 40 mg were cut from the alloys and ground. For DSC, to determine the martensitic transformation temperatures, the samples were heated from -80 °C where they were held for 2 min to establish thermal equilibrium. Then, the DSC test was carried out by heating the specimens to 300 ° C where they were held for 2 min, and then cooled down to -80 ° C with the heating and cooling rate of 10 ° C min⁻¹, under an argon shielding atmosphere. For DTA/TGA, to determine the β - transition temperature, the samples were heated at 20 ° C where they were held for 2min to establish thermal equilibrium. Then, the DTA/TGT test was completed by heating the specimens to 1200 ° C where they were held for 2min, with the heating rate of 20 ° C min⁻¹, under an argon shielding atmosphere. For all tests, DSC and DTA/TGA were run with empty pans, to calculate the baseline curves of the samples, which are then subsequently subtracted from

the origin data curves, to obtain the more accurate curves. All baseline scans were run directly after the test.

3.6 Material Characterization

The procedures used for microstructural investigation, mechanical properties, tribological, electrochemical and tribocorrosion characterisations are described in the following section:

3.6.1 Microstructural Investigations

3.6.1.1 Sample Preparation

All specimens were cut into the desired shapes using an Isomet 5000 linear precision saw or a Struers Secotom 50 cutting machine. Prior to optical microscopy, scanning electron microscopy and micro-hardness planar samples were fabricated by cutting the samples into the desired shape, then the specimens were mounted using cold-mounting in an EpoxicureTm – Epoxy Resin 20-3430-064 mix with Epoxicure 2 Hardener 20-3430-064 to avoid any transformation which might occur during hot mounting.

Next, the exposed planar face was mechanically ground using SiC papers (P800 grit for 120 seconds, then P1200 grit for 180 seconds, force 15N, counter rotation, 150rpm and coolant water) by a Buehler AUTO Met 250 Grinder-Polisher machine capable of grinding six samples together, and then followed by polishing using diamond suspensions (9 μ m diamond suspension for 5-10 mins on a MD-Largo surface (Struers), force 15N, counter rotation, 150rpm). Finally, chemical/mechanical polishing was undertaken for 6 mins with a polishing suspension (OP-S with 20% H₂O₂ (30%)) colloidal silica suspension mixed with hydrogen peroxide on a MD-Chem polishing cloth (Struers). After washing with water for 5 min the samples were ultrasonically cleaned in ethanol for 3-5 min. Between each step, the samples were washed with water, flushed with isopropanol and dried with a hand dryer.

3.6.1.2 Optical Microscopy (OM)

The microstructures of the alloys were analysed using optical microscopy (OM). OM was performed using a Nikon Eclipse LV 150 light microscope, and good contrast was obtained using polarized light.

3.6.1.3 Scanning electron microscopy (SEM)

The samples were prepared for scanning electron microscopy (SEM) (see 3.6.1.1). For SEM, the sample was carbon coated, then silver paint was used to improve the imaging of

samples. The SEM analysis was undertaken using a FEI Inspect F and a FEI Inspect F50 (both with field emission guns), equipped with an Oxford Instruments Energy Dispersive X-ray spectrometer (hereafter EDX) with Aztec software version 3.1, which was used for chemical analysis. Secondary Electron (hereafter SE) and Back Scatter Electron (hereafter BSE) detectors were used for imaging.

3.6.1.4 X-ray diffraction (XRD)

Phase constitution at room temperature was measured by XRD analysis using a Siemens D 5000 Glancing Angle XRD (GAXRD) and Bruker D2 Phaser both with Cu K α ($\lambda = 1.5418$ Å) radiation in the range of $2\theta = 20^\circ$ to 90° at an accelerating voltage of 40 kV and an electrical current of 40 mA, with a 0.02 step size and 1s dwell time. Quantitative phase analysis was completed with the EVA software package.

3.6.1.5 Transmission electron microscopy

Transmission electron microscopy (TEM) was performed using a Philips EM420 operating at 120 kV. TEM foil of the alloys fabricated in this study was prepared using mechanical grinding and polishing to a thickness of about 120 μm . Then disks of 3mm diameter were punched out. These disks were reduced to a thickness of about 80 μm using mechanical grinding and polishing. Subsequent electro-polishing was undertaken using a standard double-jet procedure (TenuPol-5, Struers) with an electrolyte consisting of 15% perchloric acid, 35% 2-butoxyethanol and 50% methanol. Electro-polishing was completed at -35 to -40°C and a voltage of 30 V at pump flow rate (12-14).

3.6.2 Mechanical characterization

3.6.2.1 Nanoindentation Test

Hardness and reduced elastic modulus of the titanium and titanium alloys used in this work were obtained by nanoindentation. The test was carried out with a Hysitron Triboscope Nanomechanical tester (TS70) coupled to a scanning probe microscope. A Berkovich diamond tip was used and area function was calibrated using fused silica. The test was performed with different forces from 100 to 10000 μN , also the test was performed with a constant load 5000 μN . Indentation was performed in 16 different regions.

3.6.2.2 Micro-hardness testing

The specimens were prepared for micro-hardness testing (see 3.6.1.1) to identify the influence of thermo and thermomechanical processing on the mechanical properties of alloys. The

micro-hardness measurement was implemented by ten points measurements with a 0.2 kg load and 15 s holding time using the Mitutoyo model: MH-101, with a 50x objective lens Vickers hardness testing machine. The diagonals of the indent were measured, then the value of Vickers micro-hardness of each diagonal was calculated using the table and averaged to give the value of the hardness.

3.6.2.3 Elastic modulus measurement by ultrasound technique

The elastic modulus of the titanium and titanium alloys used in this study was determined the by ultrasound technique. An Olympus EPOCH 600 digital ultrasonic flaw detector with a resolution of 10 ns was used for measurement of longitudinal and shear velocities of the wave. A longitudinal transducer with 20 MHz was used to measure the longitudinal velocity, which was in contact with the sample via an Olympus Couplant Glycerin, and the range of frequency used for such measurement was 8-26.5 MHz. A shear transducer with 5MHz was used to measure the shear velocity, which was in contact with sample via shear wave Couplant Olympus / shear Gel 54-T04, normal incidence 12154 shear gel, and the range of frequency used for such measurements was 1.5-8 MHz.

The density of the alloys was determined by the Archimedes method (see 3.3), as well as the transit time of the wave using longitudinal and shear transducer and the thickness of samples (20mm x 20mm x 3mm), which was used to calculate the longitudinal and shear ultrasonic wave velocity using the following equations [260]:

$$V_L = 2l/t_L \quad 3-2$$

$$V_S = 2l/t_S \quad 3-3$$

Where: V_L = longitudinal ultrasonic wave velocity, V_S = shear ultrasonic wave velocity, t_L = longitudinal ultrasonic wave transit time, t_S = shear ultrasonic wave transit time.

The elastic modulus of alloys used in this study was calculated using the following equation[260]:

$$E = \frac{\rho V_S^2 (3V_L^2 - 4V_S^2)}{V_L^2 - V_S^2} \quad 3 - 4$$

Where:

E = Youngs modulus of alloy, ρ = density of alloys (see 3.3).

The modulus value reported was the average of ten measurements.

3.6.3 Tribology, Electrochemical, and Tribocorrosion Tests

3.6.3.1 Samples Preparation

Specimens for tribology, electrochemical, and tribocorrosion testing were cut into size of 20mm x 20mm x 3mm and metallographically polished using the method described in section 3.6.1.1. The last step used a chemical/mechanical polishing with a polishing suspension (OP-S with 20% H₂O₂ (30%)) colloidal silica suspension mixed with hydrogen peroxide for 5min on a MD-Chem polishing cloth (Struers). Finally, after washing in water, the samples were degreased with acetone followed by ultrasonic cleaning in ethanol for 3-5 min; between each step, the samples were washed with water, flushed with isopropanol and dried with hand dryer.

3.6.3.2 Lubricant and electrochemical media

Bovine calf serum was selected as the lubricant used in the tribology and tribocorrosion tests, as well as electrochemical electrolyte for electrochemical tests. Due to its protein content, bovine calf serum is the most widely used as a lubricant in joint simulation. Because the protein concentration is not always constant, and the viscosity of the lubricant plays an important role for judging the joint lubricant system, significant research efforts have been reported on the using new-born calf serum with variable concentrations [261-264]. The ultra-pure water used in this work is HPLC Gradient grade water from Fisher Scientific, UK with a viscosity of 0.001 Pa.s. The ultra-pure water was used in order to avoid the chemomechanical influence of the thin layer between the water and the two counter surfaces, and to inhibit the electric potential role on the wear and friction response [265, 266].

In the present work, 25 vol% bovine calf serum solution was used supplied by First Link Ltd UK. The total protein composition of sterile bovine calf serum is 63.3 g/l, and it is composed of 28.7g/l albumin, 0.1092 g/l haemoglobin, 12.5 g/l alpha globulins, 7g/l beta globulins, and 15.1 gamma globulins. The bovine calf serum with a viscosity of 0.0012 Pa. s was made by dilution with phosphate buffered saline, which contains sodium phosphate, potassium phosphate and sodium chloride (25% v/v bovine calf serum with 75%v/v phosphate buffered saline). The phosphate buffer saline was made by dissolving tablets of phosphate buffer saline (Sigma-Aldrich, UK) with ultra-pure water (HPLG Grade liquid H₂O, Fisher Scientific UK), as 1 tablet with 200 ml of ultra-pure water. Furthermore, and in order to avoid the

bacteria influence and degradation issue of bovine calf serum at R.T, 0.1 wt.% of sodium azide (Fisher Scientific , UK) was added as an anti-bacterial agent [267, 268]. Magnetic stirring was used to dissolve tablets of phosphate buffer saline and the powder of sodium azide with new-born serum and ultra - pure water.

3.6.3.3 Tribology test

The reciprocating wear tests were conducted using a reciprocating ball-on-flat (UMT-2, centre for tribology Inc. Bruker Nano Inc. (CETR) Campbell, CA, USA). All tribological tests were conducted using a 4mm diameter high purity alumina balls manufactured by Okawade Ltd. UK. The lubricants used in the lubricant tribological tests was 25 vol% bovine calf serum solution. The normal loads in the tribology tests were 0.25, 0.5, 1 and 2N, and the reciprocating motion was set as 300 rpm. The frequency was 5Hz for all the sliding tests, with an identical stroke length of 2mm. To avoid any interaction between the sliding contacts and contaminates, all samples were carefully cleaned prior to testing using ultrasonic cleaning with alcohol 20 min before and after the sliding tests and then dried with compressed air. Before all tribological tests, a square sample was mounted in the lubricant chamber, and fresh lubricant 25vol% bovine calf serum was transferred into the lubricant chamber before each test. During the tribological tests the friction coefficient (COF) and the sliding time were automatically recorded by the machine, which allowed COF vs time plots to be made directly. All tribological tests were carried out at room temperature and open to the air, a sliding velocity of 300 rpm sliding during 3 h and applying a normal load of 0.25, 0.5, 1 and 2 N was applied on the counterpart. All tests were repeated at least twice to check for reproducibility of the measurements.

3.6.3.4 Electrochemical test

To analyse the electrochemical behaviour of titanium alloys various techniques were used. Free corrosion potential and potential dynamic tests were performed. The electrochemical measurement was carried out using a potentiostat Versa Stat 3F Ametek Princeton Applied Research. All the tests were carried out using a three-electrode corrosion cell setup: a silver-silver chloride (Ag/AgCl) reference electrode (RE) was used. A platinum coiled wire was used as the counter electrode (CE). The samples were used as the working electrode (WE). The electrolyte used for the test was 100 ml of 25vol% bovine calf serum, with all the experiments conducted at 37 ± 1 ° C and open to the air.

3.6.3.4.1 Open circuit potential (OCP) measurements

During this experiment, free corrosion potential (E_{corr}) was measured. To calculate the E_{corr} of the titanium and titanium alloys fabricated in this work, the open - circuit potential of all alloys was recorded for 1800s (30 mins) immersion in the electrolyte. This period appeared to create a steady state condition with the electrolyte.

3.6.3.4.2 Potentiodynamic measurements

The potentiodynamic polarization measurement was carried out at a sweep rate of 1mVs^{-1} in the range starting from a cathodic potential of $-0.6V_{\text{Ref}}$ versus the reference electrode, to an anodic potential of $2V_{\text{Ref}}$ versus the reference electrode. The corrosion parameters were determined using the Tafel extrapolation method.

3.6.3.4.3 Electrochemical parameters measurements

During OCP and potentiodynamic tests several electrochemical parameters were measured from OCP and potentiodynamic curves using the Tafel extrapolation method. Tafel extrapolation was completed using CorrView software, during this method, the density ($\text{g}\cdot\text{cm}^{-3}$ see 3.3), area (1.54cm^2), equivalent weight (M , see equation 3-5) of alloys, and the reference electrode (Ag/AgCl) were used. The value of M for the alloys was calculated using [269]:

$$M = \frac{1}{\sum \frac{n_i f_i}{W_i}} \quad 3 - 5$$

Where: M = equivalent weight of the i^{th} element of alloy, n_i = valence of the i^{th} element in the alloy, f_i = mass fraction i^{th} element in the alloy, W_i = atomic weight of the i^{th} element in the alloy.

Corrosion current density (I_{corr}), corrosion potential (E_{corr}), corrosion rate (mpy), cathodic slope (cathodic beta), and anodic slope (anodic beta), were calculated from the OCP and potentiodynamic curves using the Tafel extrapolation method. All the electrochemical parameters were calculated for the starting surface of the alloys used in this work, as well as after OCP-wear, cathodic potentiostatic-wear, and anodic potentiostatic-wear tests.

3.6.3.5 Tribocorrosion test

Tribocorrosion experiments were completed on a ball-on-flat tribometer (UMT-2, centre for tribology Inc. Bruker Nano Inc. (CETR) Campbell, CA, USA) with an integrated

potentiostat (Versa Stat 3F Ametek Princeton Applied Research). Alumina balls were used as the counterface. Tribocorrosion test were carried out at 37 ± 1 ° C in air, a sliding velocity at 300 rpm sliding for 3 h and a normal load of 1 N was applied. Potentiodynamic measurements were conducted on the samples under sliding at a sweep rate of 1mVs^{-1} . The lower part of the sample was insulated from the electrolyte but electrically connected to the potentiostat, while only the upper surface with 1.54cm^2 exposed to the electrolyte served as a working electrode (WE). The reference electrode (RE) was a silver-silver chloride electrode (Ag/AgCl). A platinum coiled wire was used as the counter electrode (CE).

Specimens for tribocorrosion testing were cut into a size of 20mm x 20mm x 3mm and prepared. The samples were metallographically polished using the same procedure outlined before in section 3.6.1.1, finishing with chemical/mechanical polishing with a polishing suspension OP-S with 20% H_2O_2 (30%) colloidal silica suspension mixed with hydrogen peroxide for 5mins on a MD-Chem polishing cloth (Struers). Finally, the samples were washed and then degreased with acetone followed by ultrasonic cleaning in ethanol for 3-5 min. Between each step, the samples were washed with water, flushed with isopropanol and dried with a hand dryer. The electrolyte used in this test was 100 ml of 25vol% bovine calf serum, all experiments were carried out at 37 ± 2 ° C under aerated conditions. The tribocorrosion tests were performed in three stages:

- 1- Open Circuit Potential (OCP) wear tests: in this stage, the actual wear condition was measured.
- 2- Cathodic potentiostatic wear tests. In this stage, the change in current density due to the wear and volume loss at constant cathodic potential was measured.
3. Anodic potentiostatic wear tests. In this stage, the change in current density due to the wear and volume loss at constant anodic potential was measured.

3.6.3.5.1 Open circuit potential (OCP) wear test

To obtain a constant potential, all samples were immersed in the test solution for 1800 s before and after the tribocorrosion test under OCP conditions. During this period, no force was applied to the titanium alloys, with the alumina ball and the ball holder lifted outside the cell. All sliding tests were carried out after obtaining a stable starting potential (after 1800 s) for a duration of 10800 s (3 hr).

3.6.3.5.2 Potentiostatic wear tests

Tribocorrosion tests were undertaken at constant cathodic and anodic potential. All the samples were immersed in the test solution for 1800 s, and then the selected cathodic or anodic potential was applied. The potentiostatic wear test under cathodic potential was carried out at a scan rate of 1mVs^{-1} with potential initiated at -0.5 V vs OCP. The potentiostatic wear test under anodic potential was completed at 0.3 V vs OCP with scan rate of 1mVs^{-1} . All the sliding tests under the potentiostatic sliding test were undertaken for 10800s (3 hr).

3.6.3.5.3 Electrochemical test of alloys during and after tribocorrosion test

To understand the electrochemical behaviour of titanium alloys during and after tribocorrosion tests, the electrochemical test was carried out using a Tafel fit technique $\pm 0.25\text{ V}$ vs OCP. All the electrochemical tests were carried out without rubbing, during rubbing at OCP and directly after finishing the tribocorrosion tests at OCP, cathodic and anodic wear conditions. During this experiment the corrosion current density, corrosion potential, corrosion rate, cathodic slope and anodic slope were measured using the Tafel plot method.

3.6.3.6 Wear track analysis

At the end of the tribological and tribocorrosion tests, the wear track was examined using 3D optical microscopy, scanning electron microscopy (SEM), Energy Dispersive X-ray (EDX) spectroscopy, focused ion beam (FIB) and Raman spectroscopy.

3.6.3.6.1 Wear track profiles

To measure the wear track profiles, parameters (length, depth, width and volume) as well as 3D profilometry, and wear scar roughness a Veeco / Bruker Contour GT Optical Microscope in conjunction with specialized Vision64 software was used. Vertical scanning interferometry (VSI), with 5, 10, and 50X objective lenses with 0.55, 1, 2X optical multiplier was used to measure the wear track profiles. During all tests, the scanning speed was 1X with 20% overlapping. The length, width, depth and volume loss of the wear track were measured using Vision64 software (see 3.6.5.2). Roughness properties of the wear scar of all alloys was assessed via 2D profilometry using Vision64 software. All tests were repeated 8 times at different locations around the wear track to check for reproducibility of the measurements and to obtain the most reliable and representative set of data.

3.6.3.6.2 Total materials loss rate

The total materials loss rate was measured using the Contour GT. Mid ordinate integration was used to calculate the total material loss, and numerical integration was used to calculate the cross sectional area of the wear track profile (Fig.3-1), using the following equations [146]:

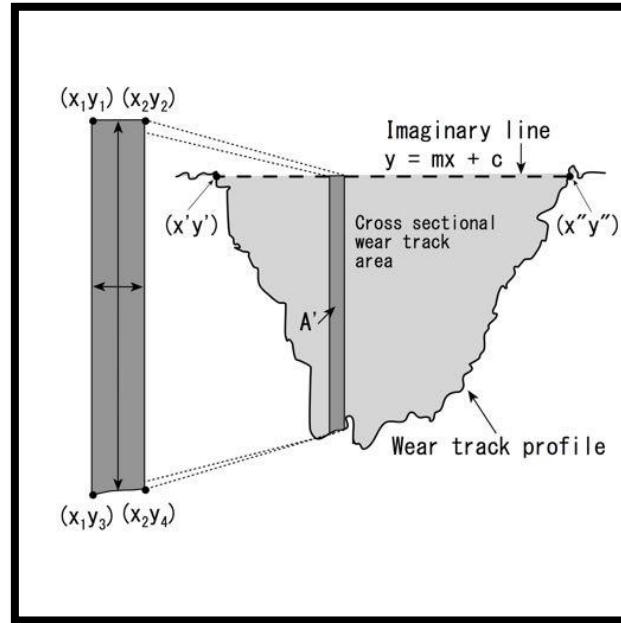


Figure 3-1 Schematic of cross sectional area of the wear track calculation via numerical integration [146]

$$A^* = (x_2 - x_1) \left(\frac{(y_1 - y_3) + (y_3 - y_4)}{2} \right) \quad 3 - 6$$

$$A = \sum A^* \quad 3 - 7$$

$$V = AXD_W \quad 3 - 8$$

$$TMLR = \frac{V}{D_S X P} \quad 3 - 9$$

Where: A = cross sectional area, V = volume loss materials, D_W = length of the wear track, D_S = the sliding distance, P = the applied load, $TMLR$ = total materials loss rate.

For reproducibility of the measurements and to obtain the most reliable and representative set of data, the wear track profiles were measured 8 times at different locations around the wear track.

3.6.3.6.3 Surface characterization

Surface morphology of the wear track was analysed by scanning electron microscopy (SEM) using the secondary and backscattered electron signals, using the microscopes detailed before in section 3.6.1.3 (FEI Inspect F and FEI Inspect F50 FEI, both equipped with Oxford instruments EDX detectors).

3.6.3.6.4 Focused ion beam (FIB)

To characterise the deformation in the surface region, close to the worn surface, focused ion beam (FIB) was carried out using a Quanta 200 (FEI, the Netherlands) system incorporating a tungsten SEM and focused ion beam column. To prepare ion contrast image using the FIB, the following procedure was used. First, to get the sample perpendicular to the ion beam column the sample stage was tilted to 52° from the horizontal. Then, a carbon film of about $2\mu\text{m}$ thickness was deposited on the top of the area of interest to protect the worn surface layer before Ga^+ milling using the ion beam with a beam current of 0.3 nA on an area of $15 \times 2\mu\text{m}^2$ on the worn surface. The second step consisted of cutting trenches in front of the deposited area, on one side of the area to be investigated using ion beam current of 5nA and dimensions of the selected area were $20 \times 8\mu\text{m}^2$ and a depth of $4\mu\text{m}$. The current was then reduced to 3nA and the dimensions of the selected area to $20 \times 4\mu\text{m}^2$ and a depth of $4\mu\text{m}$. This was followed by further reductions in the current step by step (1, 0.5 and 0.1 nA) and the dimensions of the selected area to $20 \times 4\mu\text{m}^2$ and a depth of $4\mu\text{m}$. Finally, the current was reduced to 50 pA and the dimensions of the selected area to $20 \times 4\mu\text{m}^2$ and a depth of $4\mu\text{m}$. Then a low ion current of 10 pA was used to find the trenches, then the ion current was increased to 50 pA. Finally, the orientation contrast imaging was taken using 50 pA ion current with a 1ms scan rate.

3.6.3.6.5 Raman Spectroscopy

Raman spectra were measured inside the wear scar to obtain and analyse the surface reaction. A Renishaw inVia Raman microscope with 20mW laser power, 514.5 nm wave length laser light and WiRE 3.4 software was used to measure the Raman spectra.

The Raman instrument was calibrated before all tests using a silicon wafer. The Raman scattered light was collected in backscattering geometry using 50X objective lenses, the range of scan $100\text{-}2000\text{ cm}^{-1}$, exposure time 15 seconds for each one, laser power 10%, number of accumulations 2, and number of acquisitions was 1.

3.6.3.6.6 Wear-corrosion synergism

In a tribocorrosion system several mechanisms contribute to overall materials loss, and the total degradation taking place under tribocorrosion can be described by [270]:

$$V_{total} = V_{mech} + V_{chem} \quad 3 - 10$$

Where, V_{total} the total material loss, V_{mech} the mechanical wear, and V_{chem} the chemical wear. Faraday's law can be used to calculate the volume removed by anodic oxidation in the wear track (V_{chem}):

$$V_{chem} = \frac{Q.M}{nF\rho} \quad 3 - 11$$

$$Q = \int Idt \quad 3 - 12$$

$$V_{chem} = \frac{I.t.M}{nF\rho} \quad 3 - 13$$

Where: Q is the electric charge, I is the average current (A), t is the time (s) of sliding contact, n is the charge number for oxidation reaction, F is the Faraday constant (96500 Cmol^{-1}), ρ is density of alloy, M is the atomic mass of alloy.

In this study the total material removed from the wear tracks (V_{total}) during tribocorrosion is the result of mechanical wear (V_{mech}) and chemical wear (V_{chem}). At the OCP, the total volume V_{total} was determined by measuring the cross section of the wear track equation 3-9. The chemical component (V_{chem}) can be roughly estimated by the excess current measured during sliding according to Faraday's law using equation 3-13. The mechanical wear volume V_{mech} was calculated by the difference between the total volume V_{total} and the chemical volume V_{chem} using equation 3-14. At OCP the corrosion currents estimated from Tafel plots were used to estimate the chemical wear component at OCP. To measure the corrosion current during rubbing from only inside the wear track, the remainder of the sample surface was covered with an inert coating using Lacomit Varnish. The measurement of the current during rubbing at cathodic conditions allows the quantification of the wear- accelerated corrosion. Therefore, applying Faraday's law and the mechanistic approach for tribocorrosion can quantitatively determine the chemical and mechanical contribution to material loss during tribocorrosion at cathodic rubbing conditions. Therefore, at anodic and cathodic potentiostatic conditions, the chemical volume V_{chem} removed by anodic oxidation in the wear track was calculated from equation 3-11, where Q is the electric charge flowing in the wear track. The

total volume V_{total} was determined by measuring the cross section of the wear track equation 3-9. The mechanical wear volume, V_{mech} , was calculated by the difference between the total volume V_{total} and the chemical volume V_{chem} .

$$V_{mech} = V_{total} - V_{chem} \quad 3 - 14$$

Chapter 4 Results: Structure and Property Characterization of Titanium Alloys

4.1 Introduction

In this chapter, experimental results for work carried out on alloy fabrication, microstructure and property characterization are presented. All alloys in this work were arc melted, homogenized, cold rolled, and subjected to a solution heat treatment and then quenched in water. The composition, density, transformation temperatures, materials characterization (X-ray diffraction, optical microscopy, scanning electron microscopy (SEM/BSE), EDX spectroscopy, and transmission electron microscopy (TEM)), mechanical testing (reduced elastic modulus, nano-hardness, elastic modulus, and micro-hardness) were investigated. Commercially pure Ti (Cp-Ti, grad 2) and Ti-6Al-4V alloys were also investigated for comparison (more details are described in chapter 3).

4-2 Composition Analysis and Density

Table 4-1 presents the chemical composition of the titanium alloys obtained by XRF analysis. The concentrations of tantalum, aluminium, molybdenum, niobium and zirconium in the alloys were close to the nominal value, with insignificant quantities of impurities.

The average density of the alloys compared with the theoretical value obtained from the composition of the alloy is shown in Fig. 4-1. It can be seen from the figure that the density of all alloys fabricated in this study is higher than the density of Cp-Ti ($4.45 \pm 0.06 \text{ g/cm}^3$) and Ti-6Al-4V ($4.56 \pm 0.03 \text{ g/cm}^3$). Ti-Ta₃₀ had the highest density ($8.25 \pm 0.04 \text{ g/cm}^3$), while the Ti-Mo₈-Nb₄-Zr₂ had the lowest density value ($5.12 \pm 0.045 \text{ g/cm}^3$). Ti-Mo₈-Nb₆-Zr₄, Ti-Mo₈-Nb₄-Zr₅, and Ti-Ta₂₇-Al₅ showed average density values of 5.28 ± 0.048 , 5.22 ± 0.045 , $7.9 \pm 0.05 \text{ g/cm}^3$ respectively. The chemical distribution of the titanium alloys fabricated in this study is shown in Fig 4-2 and was homogeneous.

Table 4-1 Chemical composition of the alloys from XRF analysis

Alloys	Alloying Elements wt. % (at)								Absolute Error %
	Mo	Nb	Zr	Ta	Al	V	Ti	Other	
CP Ti	-	-	-	-	0.01	-	99.86	0.12	0.003
Ti-6Al-4V	-	-	-	-	6.29	4.04	Balance	0.23	0.003
Ti-Ta ₃₀				61.38 (30)	-	-	Balance	0.15	0.017
Ti-Ta ₂₇ -Al ₅	-	-	-	59.99 (27)	1.41 (5)		Balance	-	0.004
Ti-Mo ₈ -Nb ₄ -Zr ₂	14.64 (8)	6.49 (4)	2.8 (2)	-	-	-	Balance	0.34	0.007
Ti-Mo ₈ -Nb ₄ -Zr ₅	14.64 (8)	6.33 (4)	7.2 (5)	-	-	-	Balance	0.37	0.003
Ti-Mo ₈ -Nb ₆ -Zr ₄	14.79 (8)	9.41 (6)	5.28 (4)	-	-	-	Balance	0.35	0.004

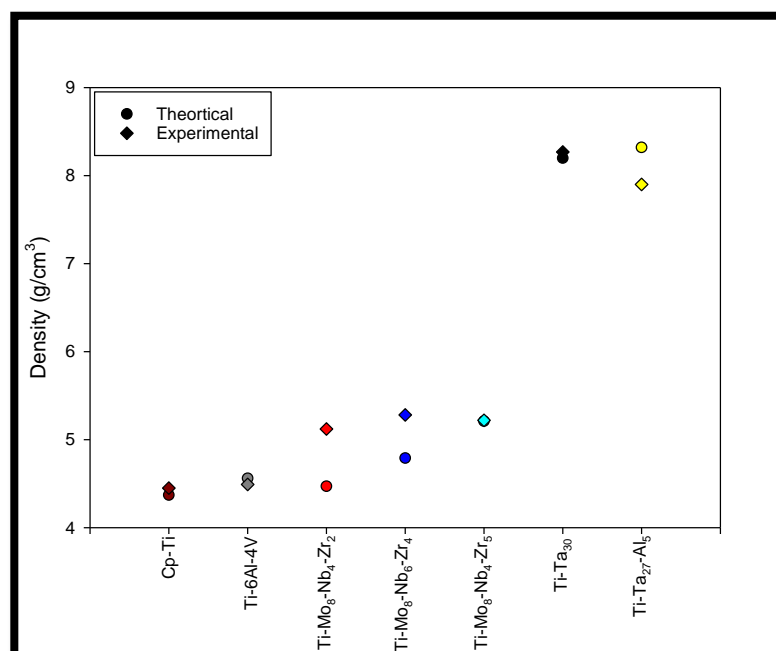


Figure 4-1 Density for titanium and titanium alloys used in this study.

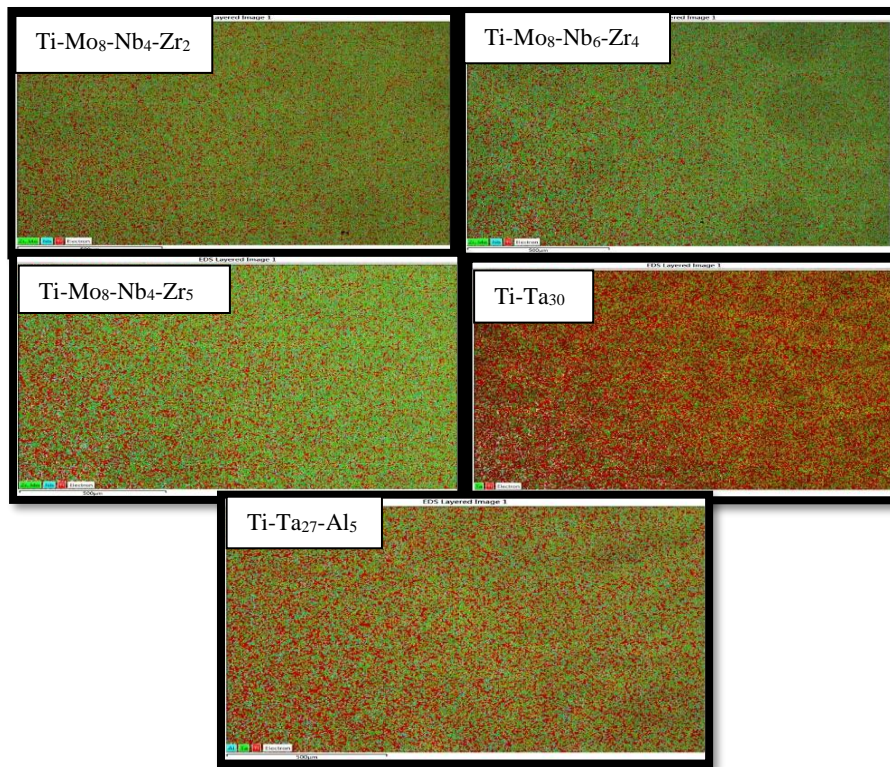


Figure 4-2 Chemical distribution of the titanium alloys fabricated in this study, where for Ti-Mo alloys (red=Ti, green=Mo, Cyan=Nb, and green=Zr), for Ti-Ta alloys (red=Ti, green=Ta, and cyan Al).

4-3 Microstructure and Phase Constitution of Titanium Alloys

Optical images of typical microstructures of the titanium alloys are shown in Fig 4-3. The microstructure of the as quenched quaternary alloys after solution heat treatment comprised equiaxed single phase β grains. The average grain size of Ti-Mo₈-Nb₄-Zr₂ was $219 \pm 2 \mu\text{m}$ (Table 4-2). The grain size became slightly larger with an increase in the zirconium content, the average grain size of Ti-Mo₈-Nb₄-Zr₅ was about $221 \pm 1 \mu\text{m}$ (Table 4-2). Increasing the niobium and zirconium together also led to a small increase in grain size of Ti-Mo₈-Nb₆-Zr₄ of about $229 \pm 2 \mu\text{m}$ (Table 4-2). The microstructure of Ti-Ta₃₀ consisted of single phase equiaxed β grains with an average grain size $42 \pm 2 \mu\text{m}$ (Table 4-2). The microstructure of Cp-Ti shown in figure 4.3 a, was the single phase α , as expected, while the microstructure of Ti-6Al-4V consisted of α and β . The microstructure of Ti-Ta₂₇-Al₅ consisted of thin needles of α'' orthorhombic martensitic inside an equiaxed β phase microstructure, the average grain size of the β phase was $45 \pm 1 \mu\text{m}$ (Table 4-2).

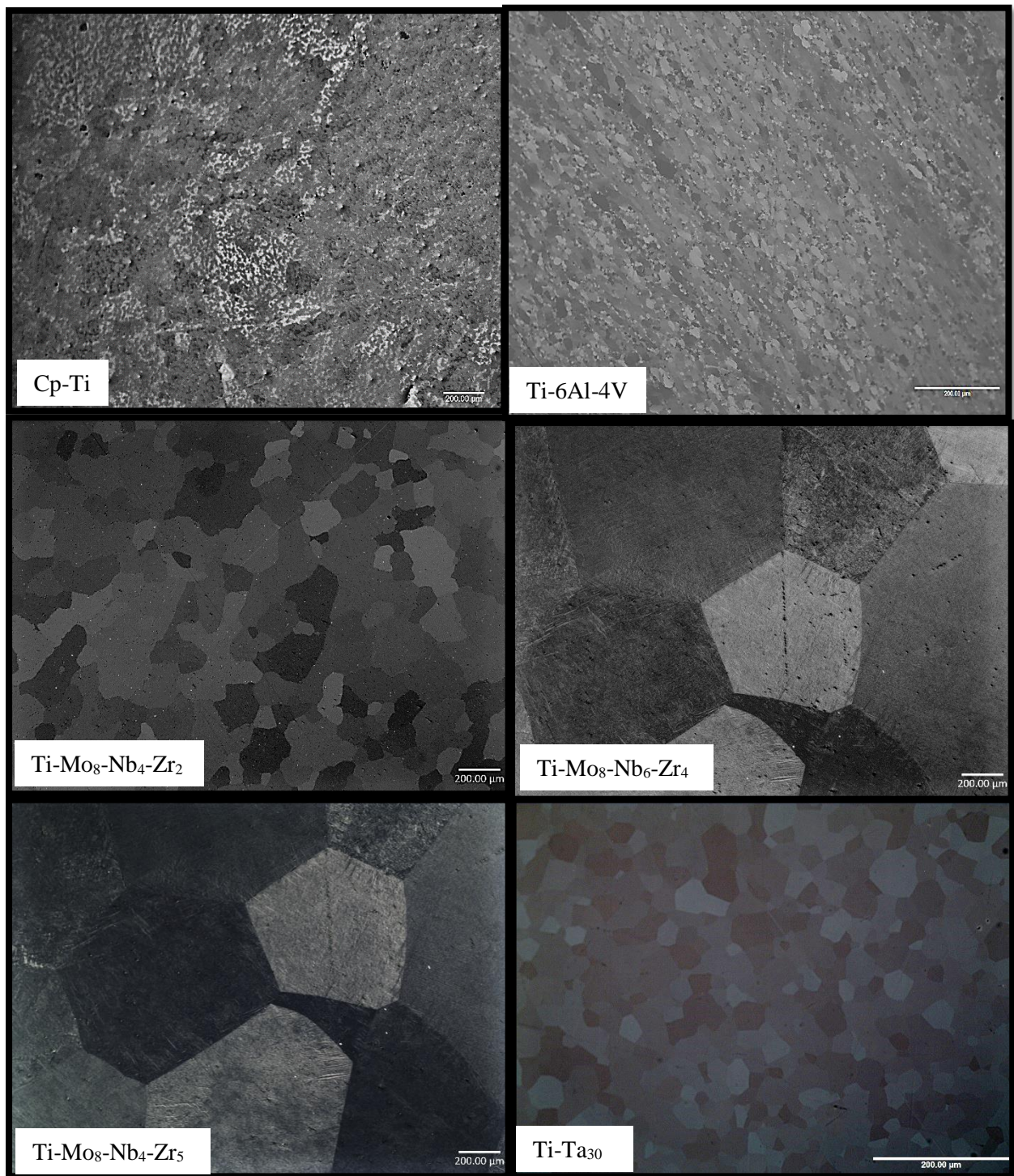


Figure 4-3 Light micrographs showing microstructure of the titanium alloys.

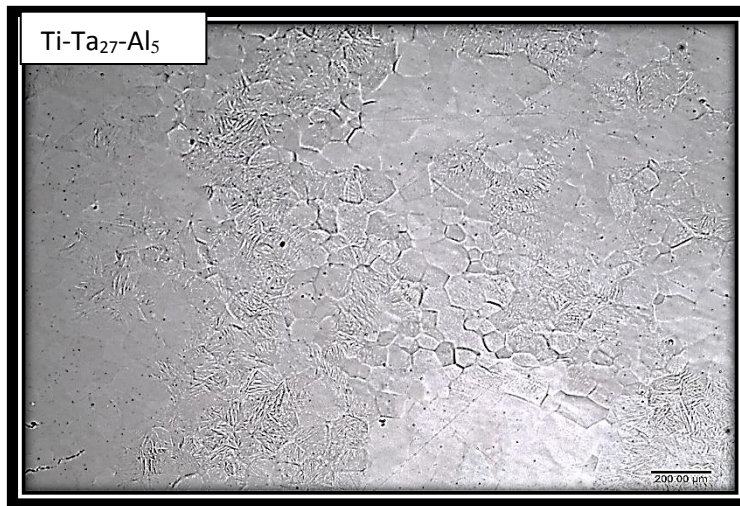


Figure 4-3 Continued.

Table 4-2 Structure, microstructure, average grain size of the titanium alloys.

Alloys	Structure	Microstructure	Average Grain Size (μm)
Ti-Ta ₃₀	β	Equiaxed grain	42 \pm 2
Ti-Ta ₂₇ -Al ₅	$\beta + \alpha''$	Equiaxed grain+ thin α'' needles	45 \pm 1
Ti-Mo ₈ -Nb ₄ -Zr ₂	β	Equiaxed grain	219 \pm 2
Ti-Mo ₈ -Nb ₄ -Zr ₅	β	Equiaxed grain	221 \pm 1
Ti-Mo ₈ -Nb ₆ -Zr ₄	β	Equiaxed grain	229 \pm 2

Backscattered electron (BSE) images, showing orientation and composition contrast of titanium alloys are shown in Fig 4-4. The microstructure of the Cp-Ti is single phase α grains, confirmed by XRD (Fig 4-5). The microstructure of Ti-6Al-4V is a fine-grained microstructure of the α phase, with a small amount of the β phase, as confirmed by XRD (Fig 4-5). The Ti-Mo₈-Nb₄-Zr₂, Ti-Mo₈-Nb₆-Zr₄, Ti-Mo₈-Nb₄-Zr₅, and Ti-Ta₃₀ alloys were equiaxed grained β phase. These results agree with the XRD analysis (Fig 4-5), which indicated the single phase β , with no evidence of α , α' , α'' or ω . The Ti-Ta₂₇-Al₅ alloy was predominantly the β phase with an equiaxed grain structure, however, α'' orthorhombic martensitic with thin needles/ plates was observed in some regions. The presence of α'' was confirmed by XRD (Fig 4 - 6).

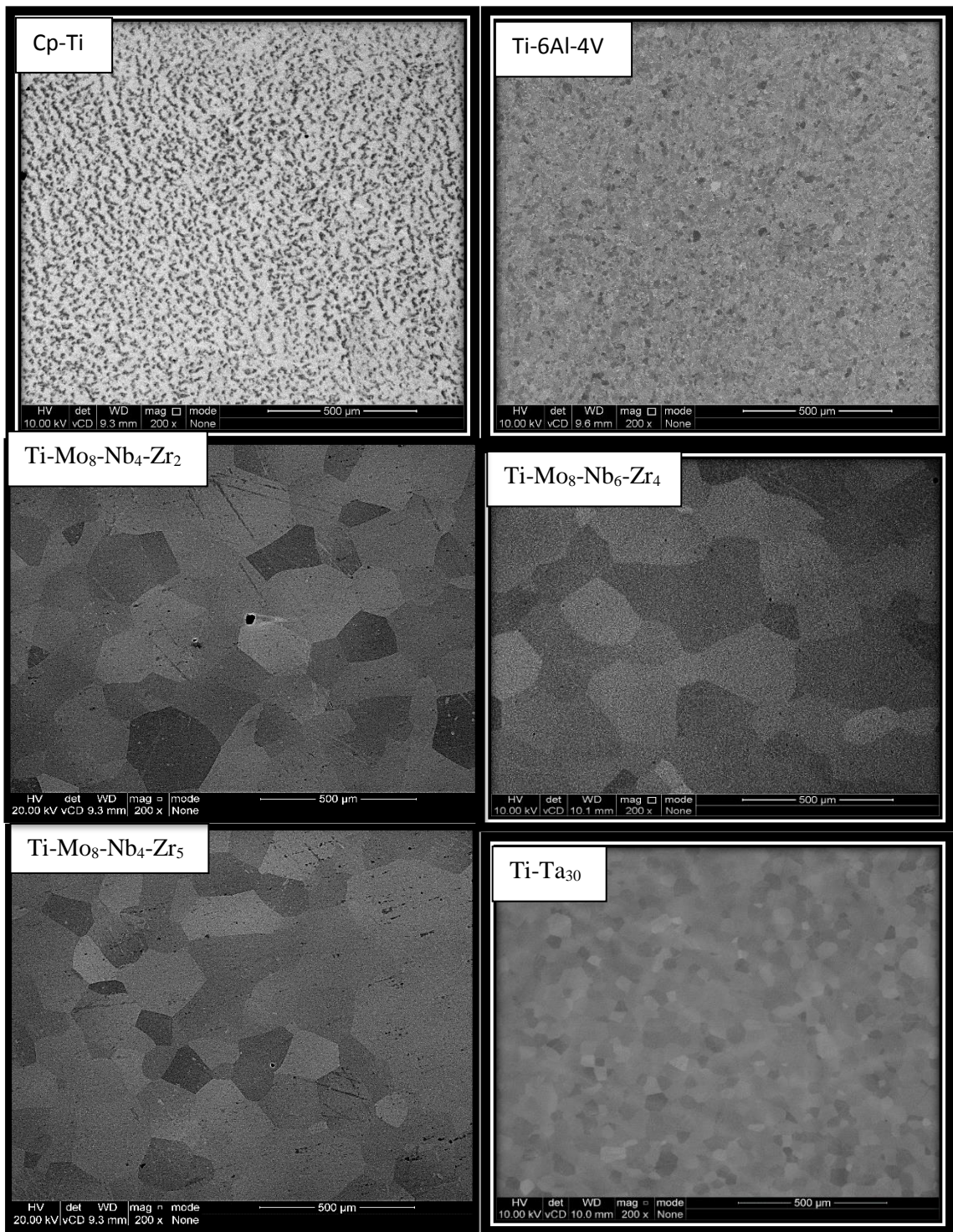


Figure 4-4 SEM micrographs (BSE, orientation and composition contrast) of the microstructure of titanium alloys.

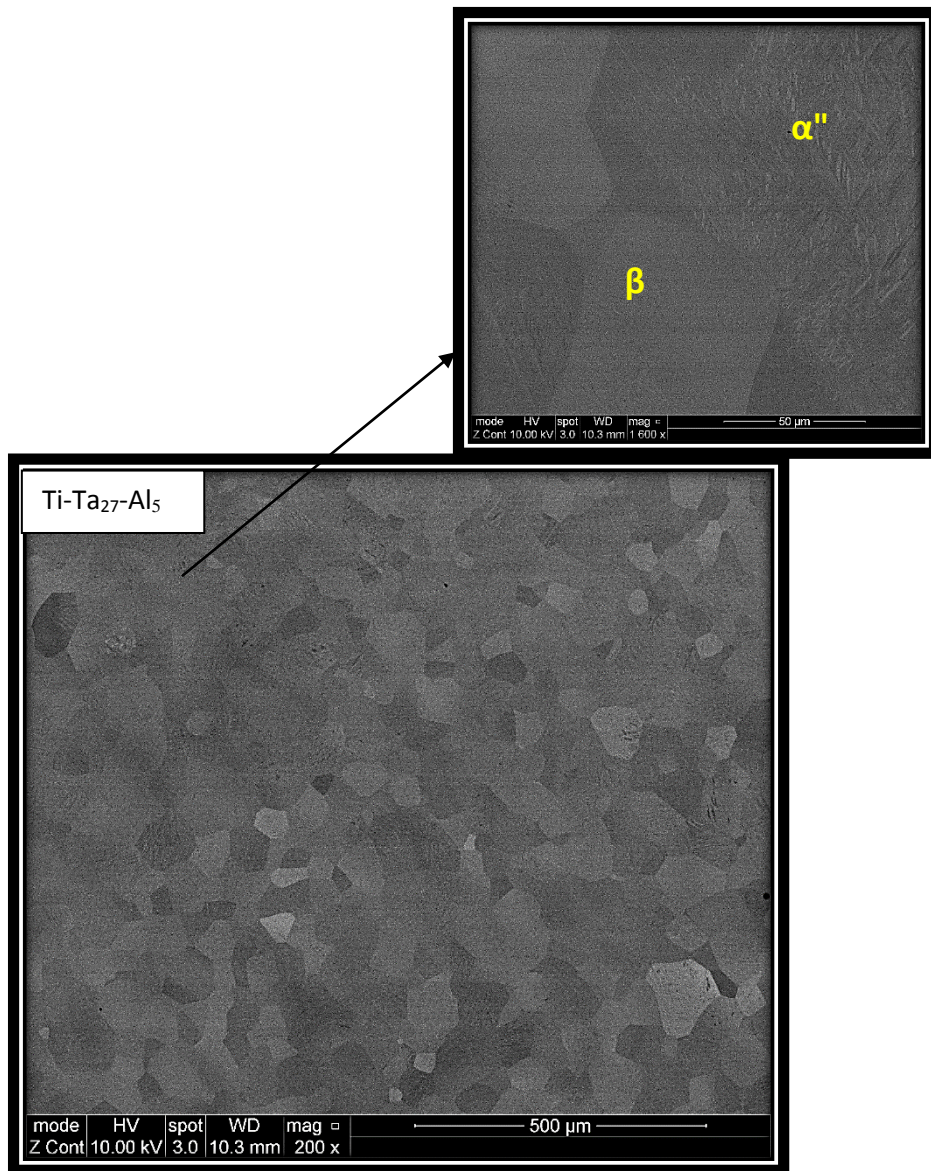


Figure 4-4 continued

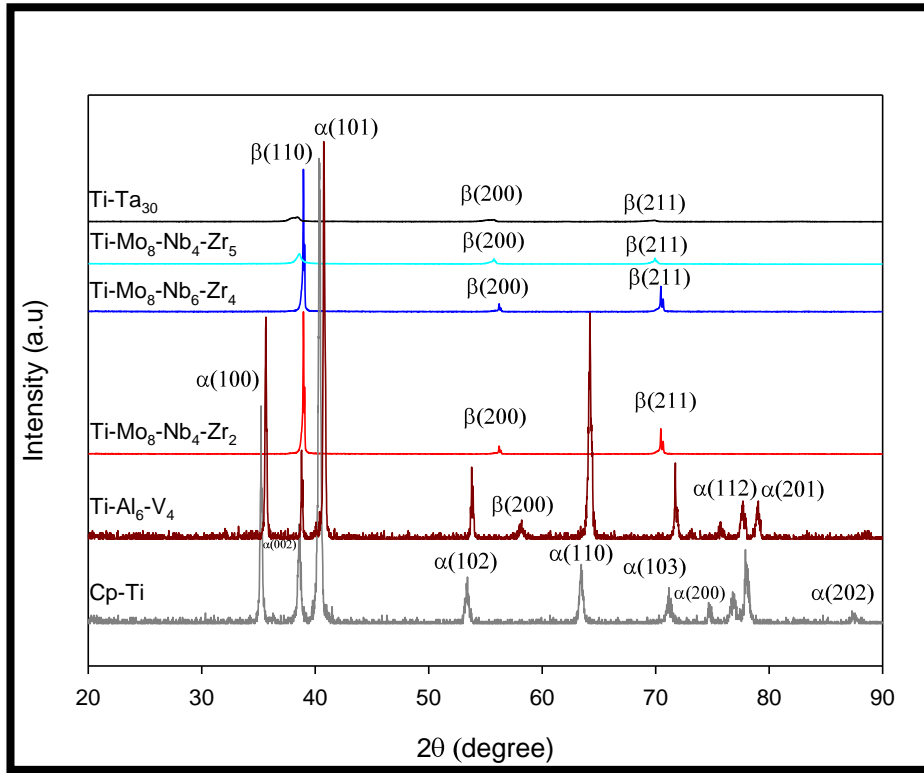


Figure 4-5 X-ray diffraction pattern of titanium alloys.

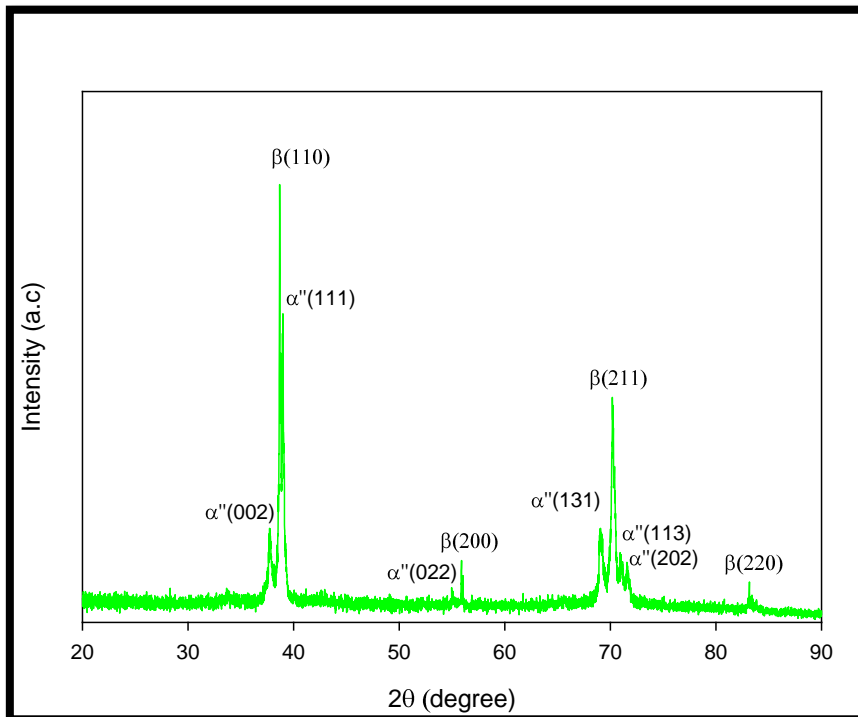


Figure 4-6 X-ray diffraction pattern of the Ti-Ta₂₇-Al₅ alloy.

Figure 4-7 shows DSC heating and cooling cycles for the Ti-Mo₈-Nb₄-Zr₂, Ti-Mo₈-Nb₄-Zr₅, Ti-Mo₈-Nb₆-Zr₄, and Ti-Ta₃₀ alloys. The alloys did not exhibit any peaks during either heating or cooling cycles and transformation temperature was not observed. Furthermore, Fig 4-8 shows the combined DTA/TGA results for the Ti-Mo₈-Nb₄-Zr₂, Ti-Mo₈-Nb₄-Zr₅, and Ti-Mo₈-Nb₆-Zr₄ alloys. It can be seen that the β transus- temperatures T_{β} of Ti-Mo₈-Nb₄-Zr₂, Ti-Mo₈-Nb₄-Zr₅, and Ti-Mo₈-Nb₆-Zr₄ are 768, 764 and 761 °C, which are lower than the transus-temperature of the common metastable β (Ti-Mo₈) alloy \approx 820 °C [271].

Figure 4-9 shows the combined DTA/TGA results for Ti-Ta₃₀ and Ti-Ta₂₇-Al₅ alloys. The β transus- temperature T_{β} of the Ti-Ta₃₀ was 598 °C (Table 4-3), which is close to the reported T_{β} temperature for this alloy (600 °C) [257]. On the other hand, the transus temperature T_{β} of Ti-Ta₂₇-Al₅ was 668 °C (Table 4-3), which is higher than that for Ti-Ta₃₀. The results of the differential scanning calorimetry for the Ti-Ta₂₇-Al₅ also confirmed that the transformation to martensite α'' orthorhombic phase occurs in this alloy (Fig 4-10). It clearly indicates the DSC peaks during both heating and cooling, with the peak on cooling representing the forward martensite transformation from β to orthorhombic martensite. The results obtained from the DSC charts are compiled in Table 4-4.

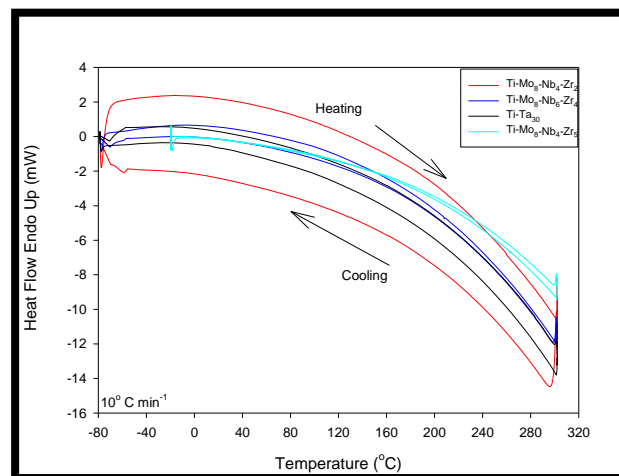


Figure 4-7 DSC heating and cooling curves of the titanium alloys.

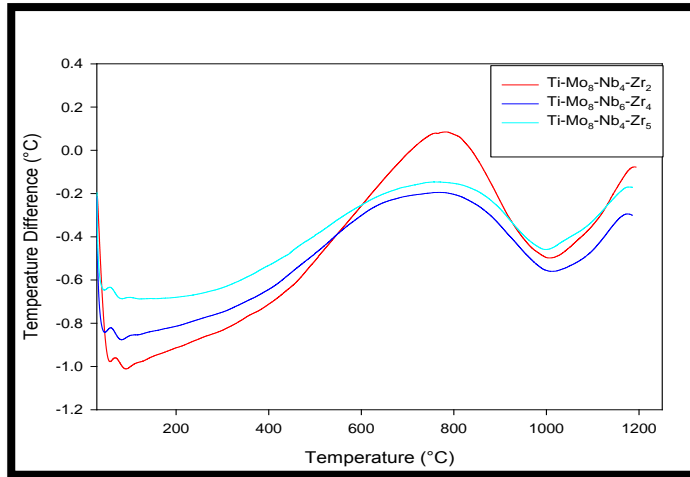


Figure 4-8 Combined DTA/TGA heating curves of the titanium alloys.

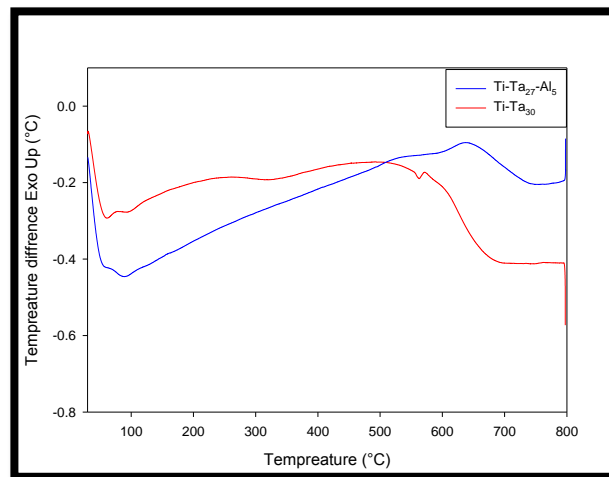


Figure 4-9 Combined DTA/TGA heating curves of Ti-Ta₃₀ and Ti-Ta₂₇-Al₅ alloys.

Table 4-3 the results from combined DTA/TGA experiments (Fig 4-7 and 4-8) performed in this study.

Alloys	Combined DTA/TGA			β transus- temperature T_{β} (°C)
	Cooling /heating rate (°C min ⁻¹)	Tmin(°C)	T max (°C)	
Ti-Ta ₃₀	10	25	800	598
Ti-Ta ₂₇ -Al ₅	10	25	800	668
Ti-Mo ₈ -Nb ₄ -Zr ₂	10	25	1200	768
Ti-Mo ₈ -Nb ₄ -Zr ₅	10	25	1200	764
Ti-Mo ₈ -Nb ₆ -Zr ₄	10	25	1200	761

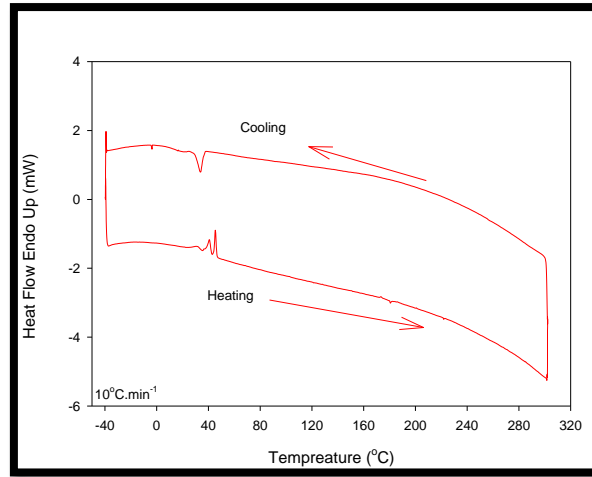


Figure 4-10 DSC heating and cooling curves of the Ti-Ta₂₇-Al₅ alloy.

Table 4-4 results from DSC experiments (Fig 4-10) performed in this study.

Ti-Ta ₂₇ -Al ₅ ingot metallurgy parameters	DSC conditions			Transformation characteristics					
	Cooling /heating rate (Kmin ⁻¹)	T min (K)	Tmax (K)	A _f (K)	LH _{α→β} (mw)	M _s (K)	LH _{β→α} (mw)	T ₀ (K)	Hysteresis (K)
1273 K-9h → cold rolling→ 1073 K for 25 h → WQ→SH	10	-40	573	323	-1.69	311	1.44	317	12

Figures 4-11 through to 4-15 show the EDX results for Ti-Mo₈-Nb₄-Zr₂, Ti-Mo₈-Nb₆-Zr₄, Ti-Mo₈-Nb₄-Zr₅, Ti-Ta₃₀ and Ti-Ta₂₇-Al₅, with the results tabulated in tables 4-5 through 4-9. These show that the contrast in back scattered images (Fig 4-10, 4-11, 4-12, and 4-13) is from crystal orientation and not composition, with the alloys having homogeneous compositions.

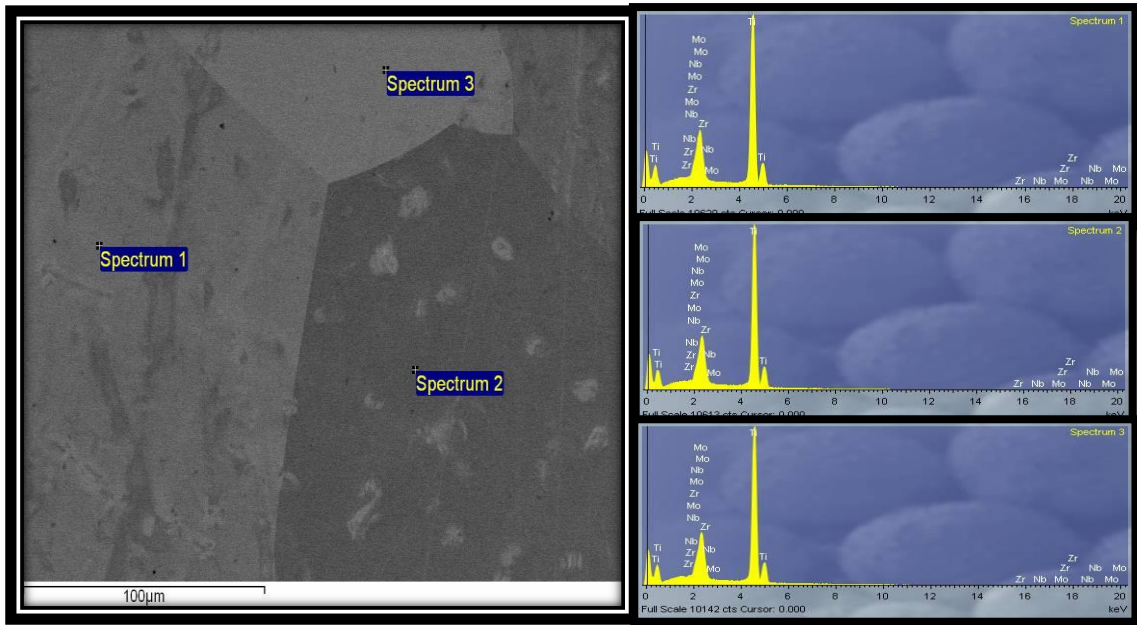


Figure 4-11 SEM (BSE) and Energy Dispersive X-ray (EDX) spectroscopy results of Ti-Mo₈-Nb₄-Zr₂ obtained from the three spectra highlighted in SEM (BSE).

Table 4-5 EDX results of Ti-Mo₈-Nb₄-Zr₂ obtained for the three spectra highlighted in figure 4-11.

Spectrum	Ti (at %)	Mo (at %)	Nb (at %)	Zr (at %)
1	84.16	9.16	4.50	2.19
2	84.26	9.11	4.51	2.13
3	83.91	9.26	4.54	2.29
Mean	84.11	9.18	4.51	2.20
Std.deviation	0.18	0.08	0.02	0.08
Max.	84.26	9.26	4.54	2.29
Min.	83.91	8.1	4.50	2.13

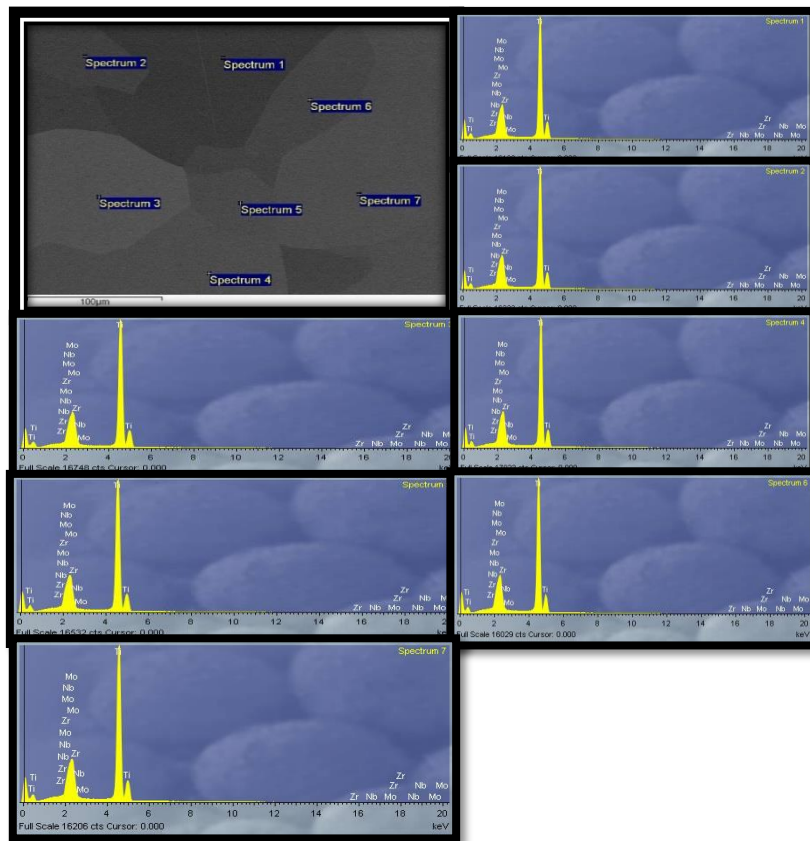


Figure 4-12 SEM (BSE) and Energy Dispersive X-ray (EDX) spectroscopy results of Ti-Mo₈-Nb₆-Zr₄ obtained from the seven spectra highlighted in SEM (BSE).

Table 4-6 EDX results of Ti-Mo₈-Nb₆-Zr₄ obtained for the seven spectra highlighted in Fig 4-2.

Spectrum	Ti (at %)	Mo (at %)	Nb (at %)	Zr (at %)
1	80.40	8.74	6.53	4.33
2	80.32	8.68	6.62	4.38
3	80.42	8.70	6.60	4.28
4	80.33	8.68	6.64	4.35
5	80.47	8.59	6.59	4.35
6	80.46	8.74	6.62	4.18
7	80.46	8.63	6.63	4.29
Mean	80.41	8.68	6.60	4.31
Std.deviation	0.06	0.05	0.04	0.07
Max.	80.47	8.74	6.64	4.38
Min.	80.32	8.59	6.53	4.18

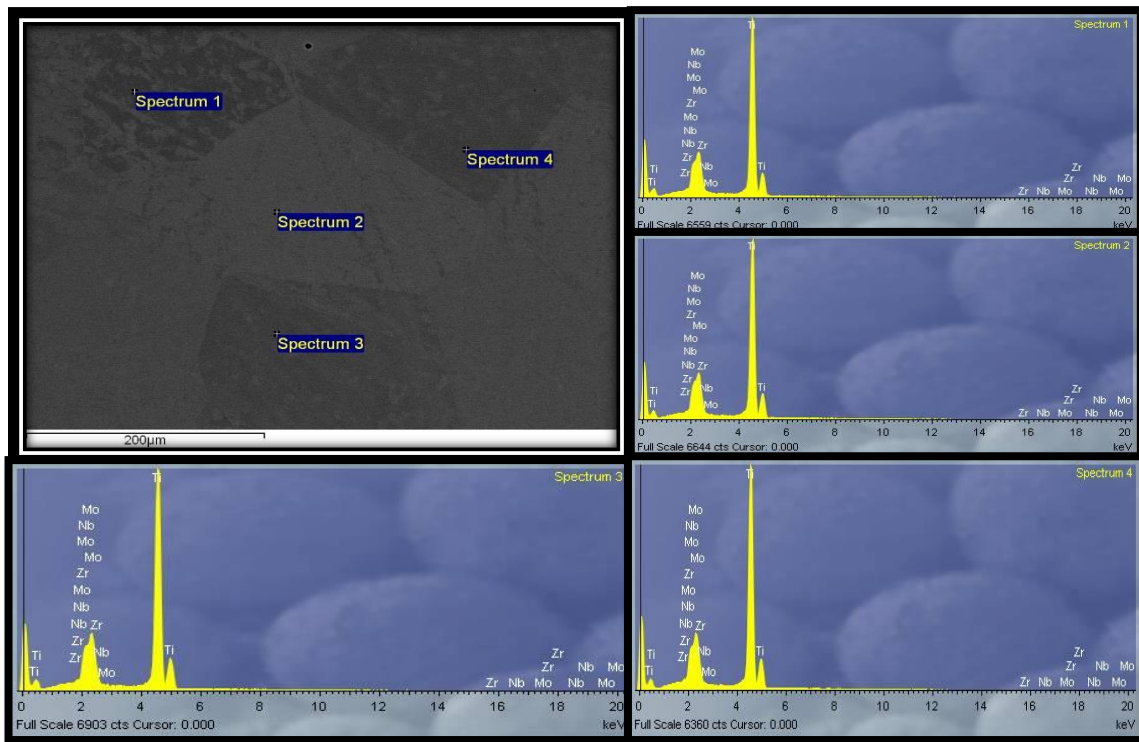


Figure 4-13 SEM (BSE) and Energy Dispersive X-ray (EDX) spectroscopy results of Ti-Mo₈-Nb₄-Zr₅ obtained from the four spectra highlighted in SEM (BSE).

Table 4-7 EDX results of Ti-Mo₈-Nb₄-Zr₅ obtained for the four spectra highlighted in Fig 4-3.

Spectrum	Ti (at %)	Mo (at %)	Nb (at %)	Zr (at %)
1	81.04	8.85	4.52	5.59
2	81.07	8.74	4.71	5.48
3	81.13	8.66	4.62	5.59
4	81.06	8.91	4.46	5.57
Mean	81.07	8.79	4.58	5.56
Std.deviation	0.04	0.11	0.11	0.05
Max.	81.13	8.91	4.71	5.59
Min.	81.04	8.66	4.46	5.48

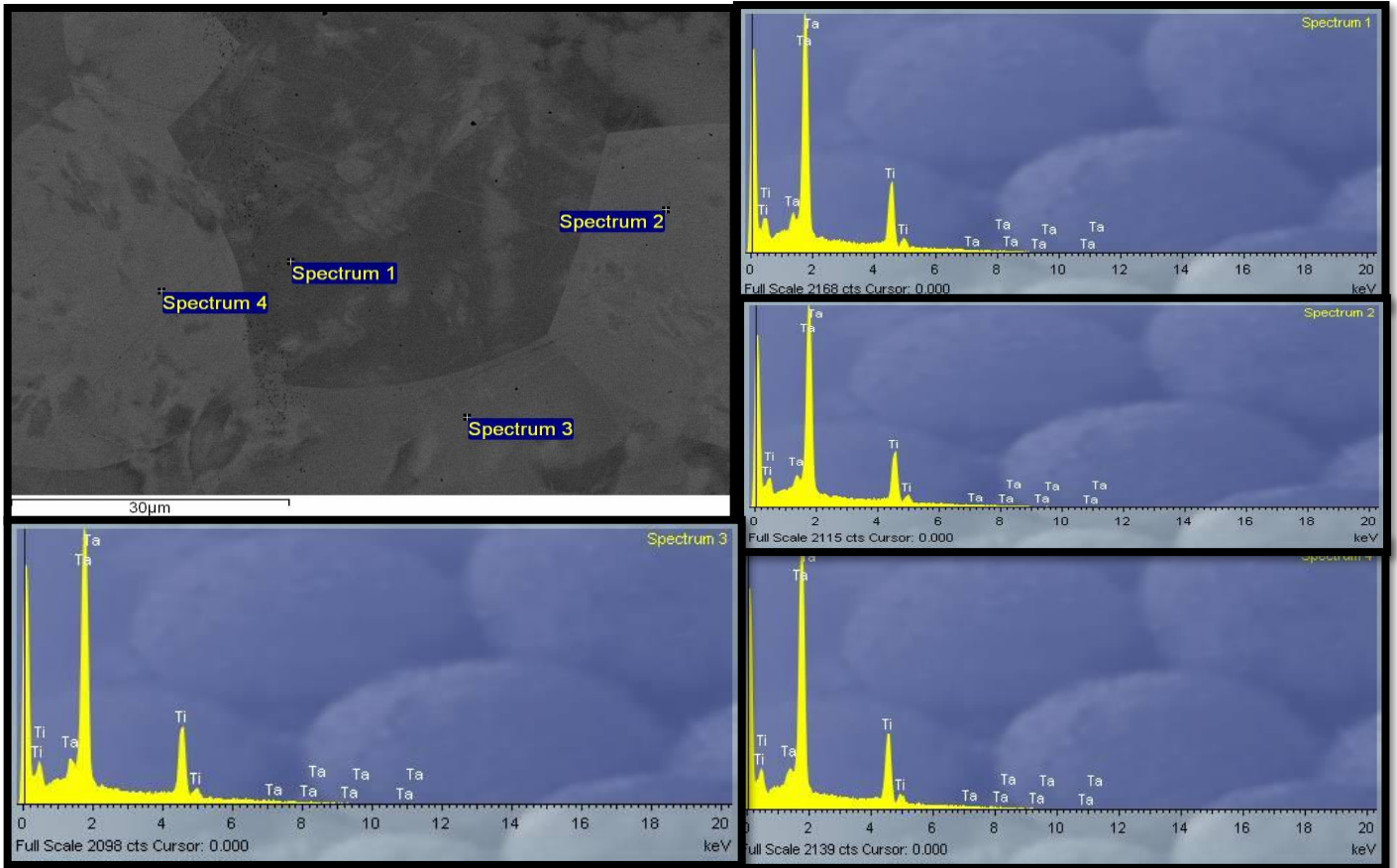


Figure 4-14 SEM (BSE) and Energy Dispersive X-ray (EDX) spectroscopy results of Ti-Ta₃₀ obtained from the four spectra highlighted in SEM (BSE).

Table 4-8 EDX results of Ti-Ta₃₀ obtained for the four spectra highlighted in Fig 4 -14.

Spectrum	Ti (at %)	Ta (at %)
1	66.23	33.7
2	65.51	34.49
3	65.85	34.15
4	66.65	33.35
Mean	66.06	33.35
Std.deviation	0.49	0.49
Max.	66.65	34.49
Min.	65.51	33.35

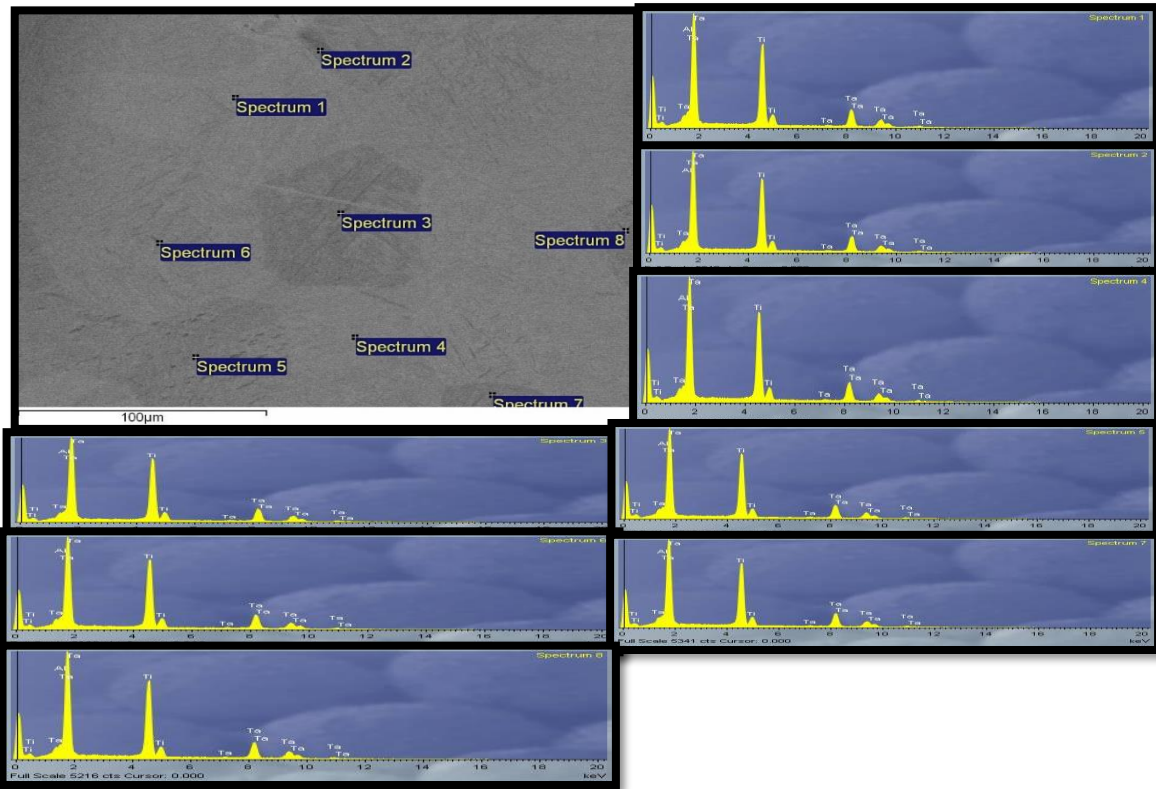


Figure 4-15 SEM (BSE) and Energy Dispersive X-ray (EDX) spectroscopy results of Ti-Ta₂₇-Al₅ obtained from the eight spectra highlighted in SEM (BSE).

Table 4-9EDX results of Ti-Ta₂₇-Al₅ obtained for the eight spectra highlighted in Fig 4-15.

Spectrum	Ti (at %)	Ta (at %)	Al (at %)
1	66.00	29.53	4.48
2	66.57	29.64	3.79
3	66.38	29.59	4.02
4	66.20	29.80	4.00
5	65.79	30.01	4.20
6	66.37	29.56	4.07
7	66.03	29.82	4.15
8	66.26	29.78	3.79
Mean	66.20	29.72	4.08
Std.deviation	0.25	0.16	0.20
Max.	66.57	30.01	4.48
Min.	65.79	29.53	3.79

To confirm the results of the OM, SEM and XRD, transmission electron microscopy (TEM) was performed. Figure 4-16 shows typical bright field TEM images and corresponding selected area electron diffraction (SAED) patterns for the Ti-Mo₈-Nb₄-Zr₂, Ti-Mo₈-Nb₆-Zr₄, Ti-Mo₈-Nb₄-Zr₅, Ti-Ta₃₀ and Ti-Ta₂₇-Al₅. The diffraction patterns could be indexed as β -phase with bcc structure for the Ti-Mo₈-Nb₄-Zr₂, Ti-Mo₈-Nb₆-Zr₄, Ti-Mo₈-Nb₄-Zr₅ and Ti-Ta₃₀ alloys. For the Ti-Ta₂₇-Al₅ alloy, the typical martensite structure α'' was observed within the β -phase matrix, as confirmed by indexing the diffraction pattern.

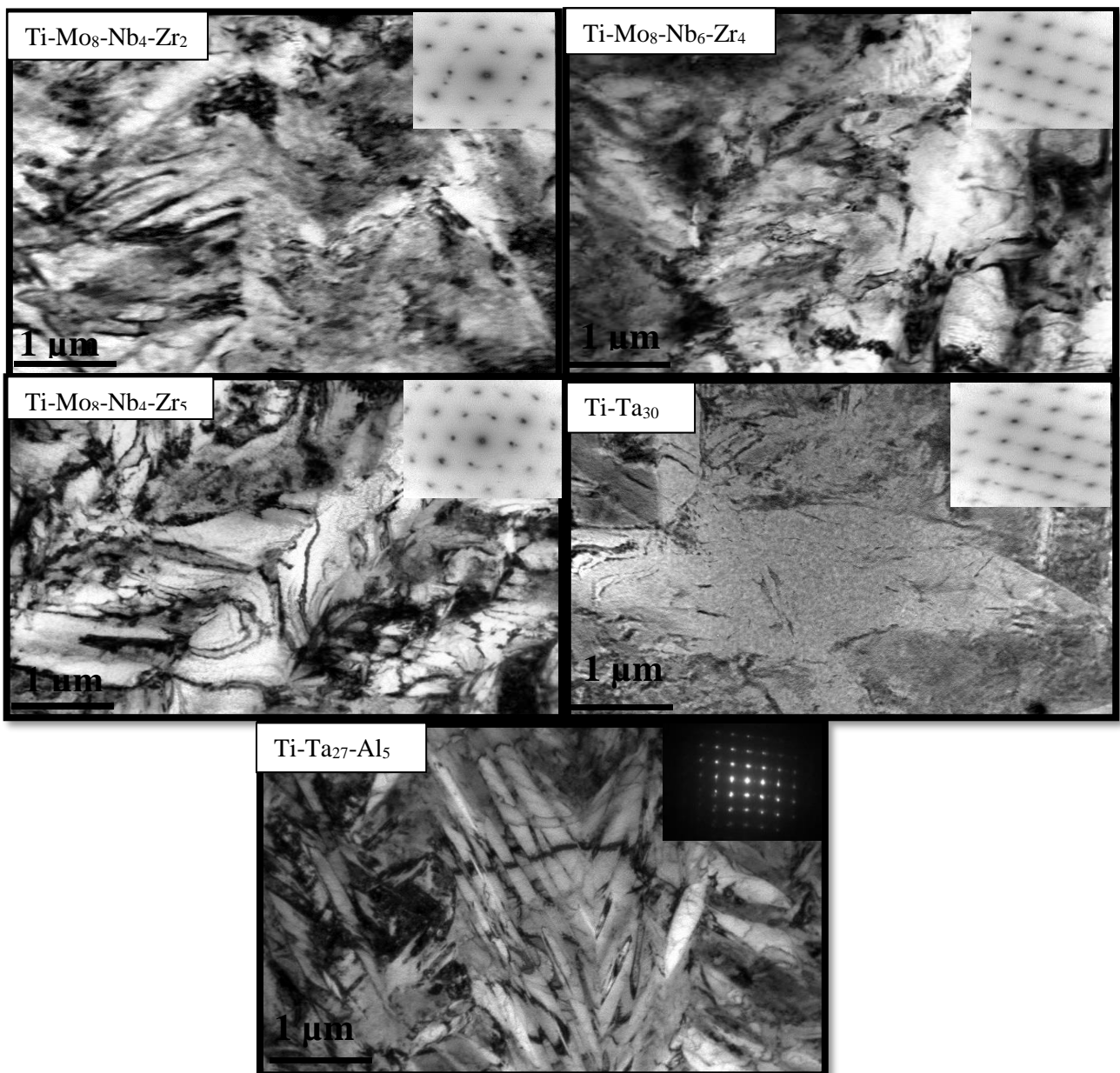


Figure 4-16 Bright field TEM image and the corresponding electron diffraction of solution treated titanium alloys.

4-4 Mechanical Characterization

4-4-1 Reduced Modulus and Nanoindentation Hardness

The reduced elastic modulus of titanium alloys measured by nano-indentation as a function of load are shown in Fig 4-17 and contact depth in Fig 4-18. The average value of the reduced elastic modulus of Cp-Ti and Ti-6Al-4V was 136.7 ± 3 GPa and 148.6 ± 2 GPa respectively, while for Ti-Mo₈-Nb₄-Zr₂, Ti-Mo₈-Nb₄-Zr₅, Ti-Mo₈-Nb₆-Zr₄, Ti-Ta₃₀ and Ti-Ta₂₇-Al₅ was 102.3 ± 1 , 101.2 ± 1.4 , 103.8 ± 1.2 , 88.7 ± 1 , and 86.8 ± 0.89 GPa respectively. Fig 4-19 presents nanoindentation hardness values as a function of load for the titanium alloys, while Fig 4-20 gives the corresponding nanoindentation hardness as a function of the contact depth. The measure of nanoindentation hardness values were 3.94 ± 0.4 , 4.9 ± 0.5 GPa for the Cp-Ti and Ti-6Al-4V respectively. For the Ti-Mo₈-Nb₄-Zr₂, Ti-Mo₈-Nb₄-Zr₅, Ti-Mo₈-Nb₆-Zr₄, Ti-Ta₃₀, and Ti-Ta₂₇-Al₅ the nanoindentation hardness values were 3.79 ± 0.3 , 3.75 ± 0.3 , 4.06 ± 0.4 , 4.46 ± 0.3 , and 3.37 ± 0.6 GPa respectively. Table 4-10 shows the average values of the reduced elastic modulus and nanoindentation hardness for the titanium alloys as a function of load.

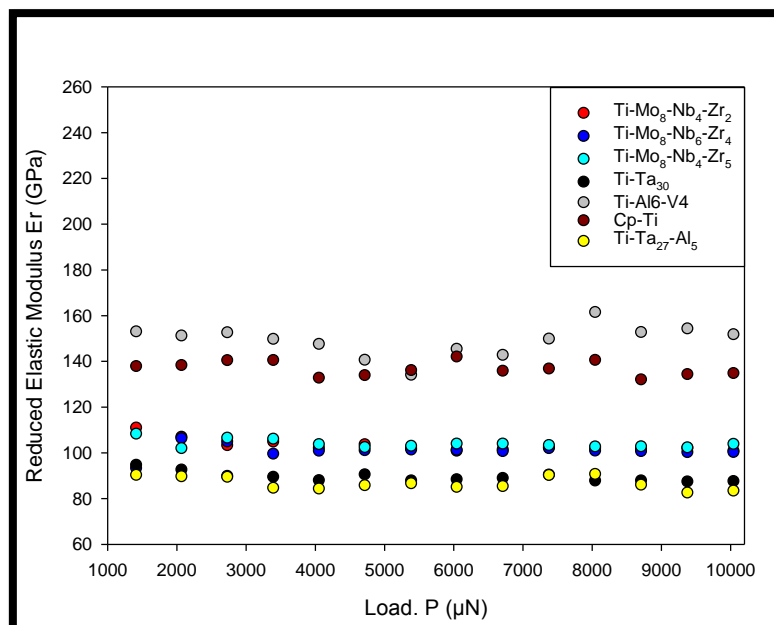


Figure 4-17 Reduced elastic modulus of titanium and its alloys measured by nano-indentation at different loads.

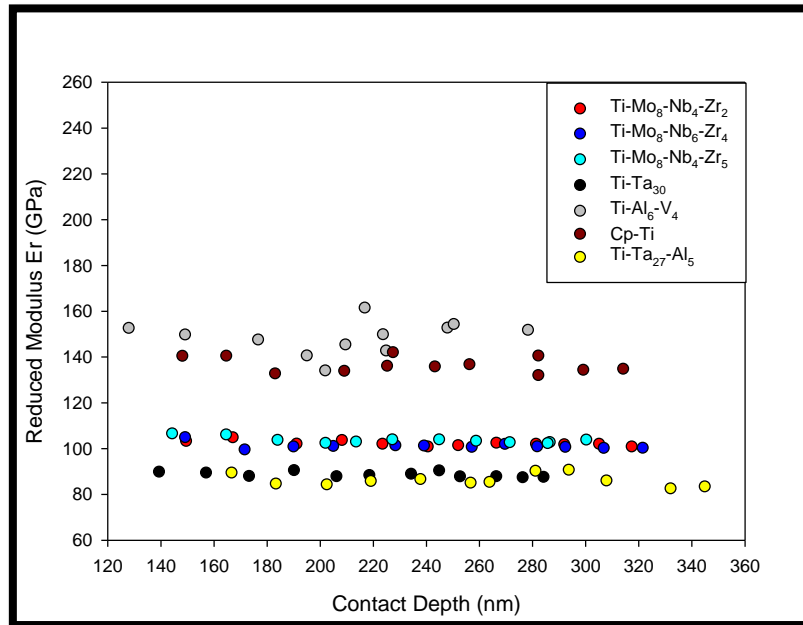


Figure 4-18 Reduced modulus of titanium and its alloys measured by nano-indentation technique as a function of the contact depth with different loads.

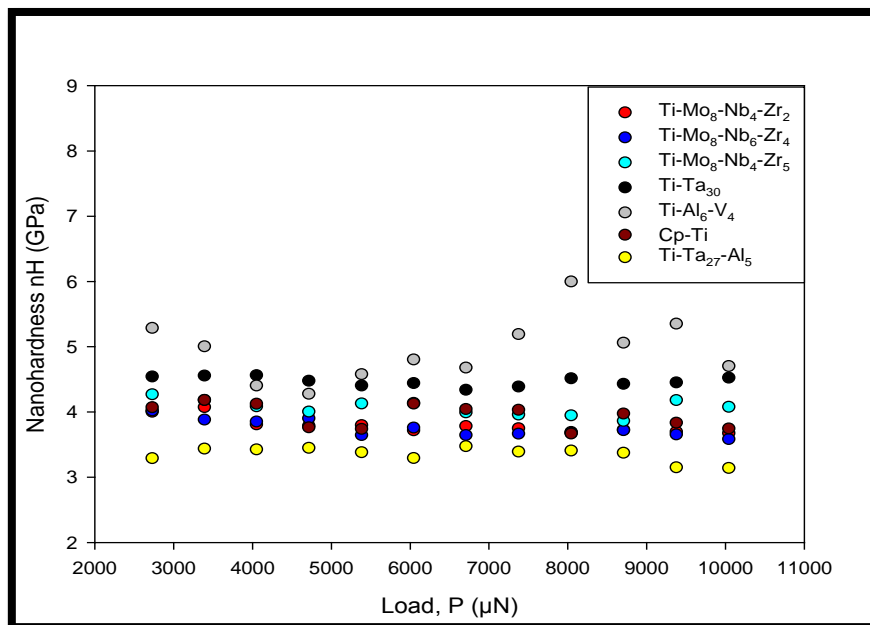


Figure 4-19 Nanoindentation hardness of titanium and its alloys used in this study measured by nano-indentation at different loads.

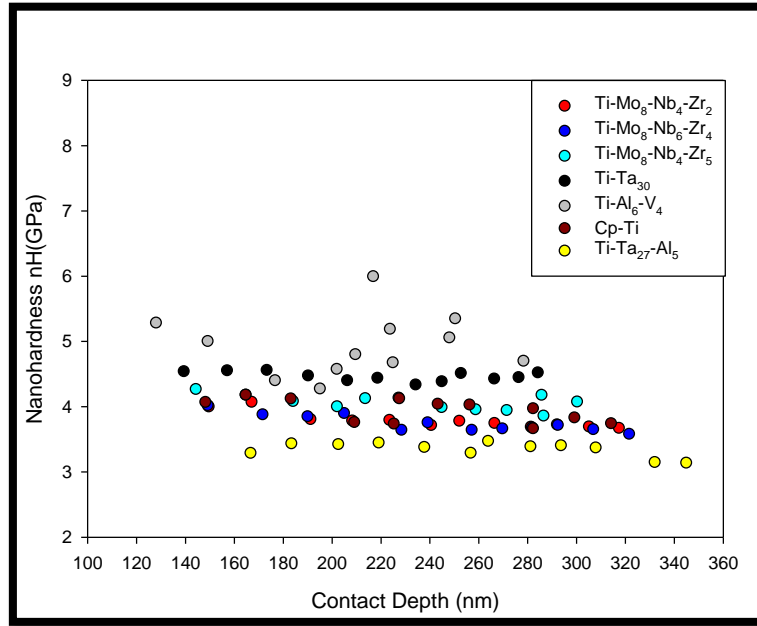


Figure 4-20 Nanoindentation of titanium and its alloys used in this study measured by nano-indentation as a function of the contact depth with different loads.

Table 4-10 Estimation of reduced elastic modulus and nano-hardness through nanoindentation technique at different loads.

Alloy	Contact Depth (nm)	Reduce Elastic Modulus Er(GPa)	Nanoindentation hardness (GPa)
Cp-Ti	236.2	136.7	3.9
Ti-6Al-4V	208.5	148.6	4.9
Ti-Mo ₈ -Nb ₄ -Zr ₂	241.1	102.3	3.8
Ti-Mo ₈ -Nb ₆ -Zr ₄	242.6	101.2	3.8
Ti-Mo ₈ -Nb ₄ -Zr ₅	231.9	103.8	4.1
Ti-Ta ₃₀	220.2	88.7	4.5
Ti-Ta ₂₇ -Al ₅	238.4	86.8	3.4

The reduced elastic modulus and nano-hardness of alloys was also measured using a nanoindentation, but with a constant load of 5000 μ N. Fig 4-21 gives the reduced elastic modulus and figure 4-22 gives corresponding nano-hardness of all alloys, with values summarized in Table 4-10. The CP-Ti (141 ± 3 GPa) and Ti-6Al-4V(151 ± 2 GPa) had the highest modulus values. Among all β Ti- alloys, Ti-Mo₈-Nb₄-Zr₂ had the the highest reduced elastic modulus (99.7 ± 2 GPa), while Ti-Ta₃₀ has the lowest value of reduced elastic modulus

(85 ± 1 GPa). The reduced elastic modulus of Ti-Mo₈-Nb₆-Zr₄, Ti-Mo₈-Nb₄-Zr₅ and Ti-Ta₂₇-Al₅ was 94.3 ± 0.7 , 96.8 ± 0.6 , and 88.7 ± 0.66 GPa respectively.

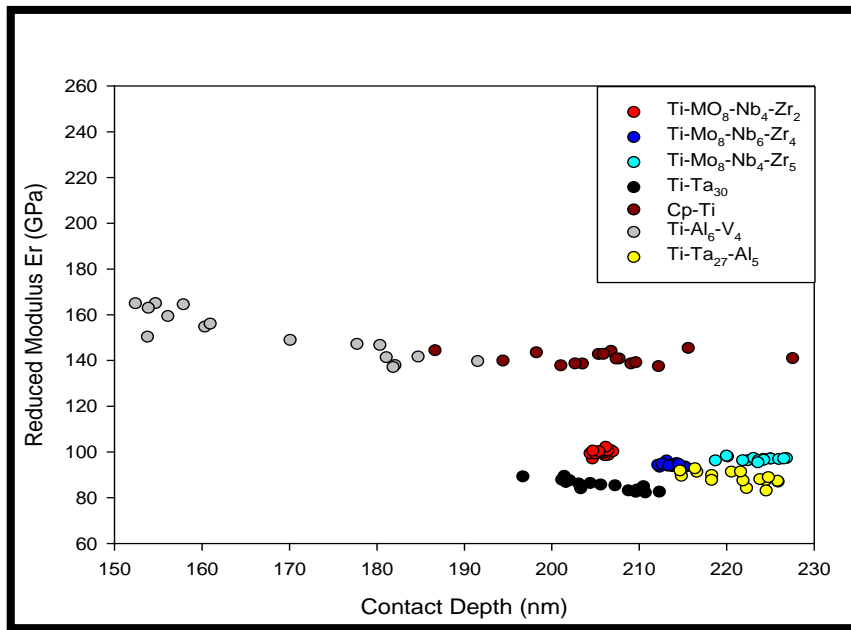


Figure 4-21 Reduced modulus of titanium and its alloys measured by nano-indentation at constant load.

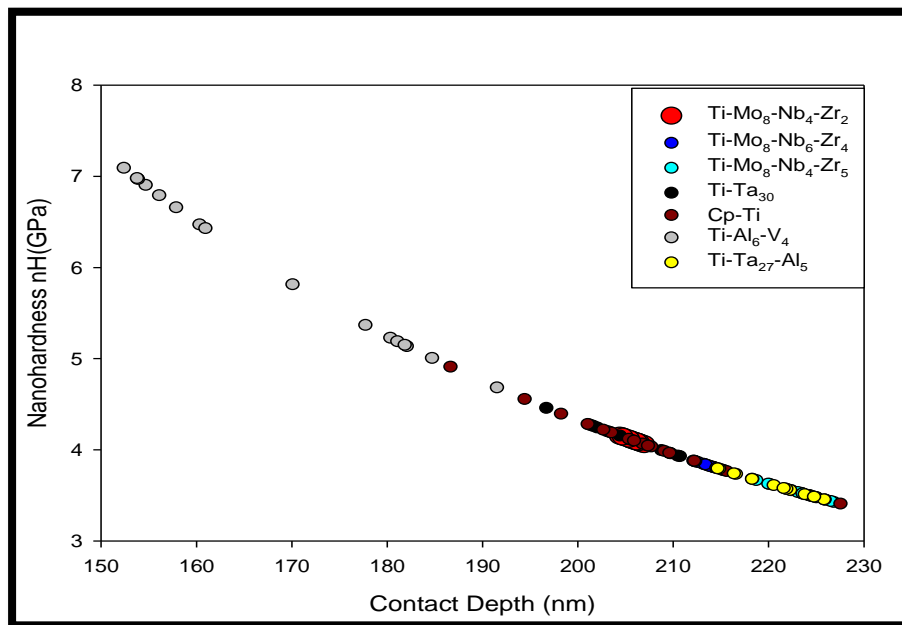


Figure 4-22 Nanoindentation hardness of titanium and its alloys measured by nano-indentation at constant load.

Table 4-11 Estimation of reduced elastic modulus and nano-hardness through nanoindentation technique with constant load.

Alloy	Contact Depth CD(nm)	Reduce Elastic Modulus Er(GPa)	Nanohardness (GPa)
Cp-Ti	205.8	141±3	4.12±0.5
Ti-6Al-4V	168.6	151.1±2	5.9±0.3
Ti-Mo ₈ -Nb ₄ -Zr ₂	205.7	99.7±2	4.1±0.2
Ti-Mo ₈ -Nb ₆ -Zr ₄	213.7	94.3±0.7	3.8±0.4
Ti-Mo ₈ -Nb ₄ -Zr ₅	223.4	96.8±0.6	3.5±0.6
Ti-Ta ₃₀	205.5	85.4±1	4.1±0.4
Ti-Ta ₂₇ -Al ₅	220.9	88.7±0.66	3.6±0.2

4.4.2 Elastic Modulus

The elastic modulus of titanium alloys is presented in Fig.4-23. The average value of the elastic modulus of Cp-Ti and Ti-6Al-4V was 120.6±3 and 115.9 ±2. On the other hand, the Ti-Ta₃₀ alloy showed the lowest elastic modulus (52.2±3). All alloys exhibited an elastic modulus lower than Cp-Ti and Ti-6Al-4V. The average elastic modulus of Ti-Mo₈-Nb₄-Zr₂, Ti-Mo₈-Nb₆-Zr₄, Ti-Mo₈-Nb₄-Zr₅, and Ti-Ta₂₇-Al₅ was 78.9±2, 76.3 ±2.5, 60.1 ±2, and 55.8 ±3 GPa respectively. In contrast, Cp-Ti exhibited the highest elastic modulus, as expected.

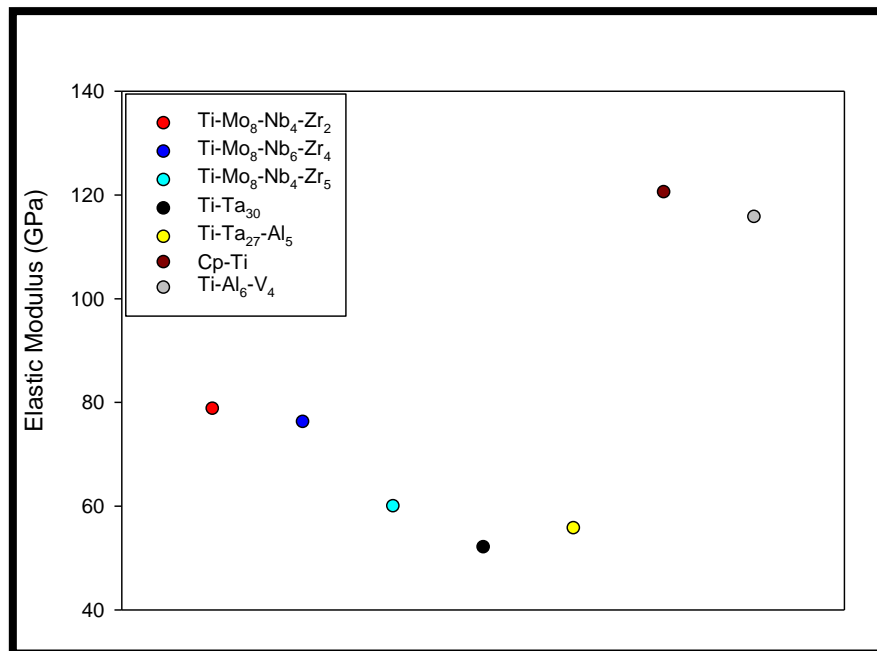


Figure 4-23 The average elastic modulus of titanium alloys.

4.4.3 Micro-Hardness

The average Vickers micro-hardness values ($HV_{0.2}$) of titanium alloys are presented in Fig 4-24. The hardness of Ti-Mo₈-Nb₄-Zr₂, Ti-Mo₈-Nb₆-Zr₄, Ti-Mo₈-Nb₄-Zr₅, Ti-Ta₃₀, and Ti-Ta₂₇-Al₅ alloys were above the value of the grade 2 Cp-Ti (199 $HV_{0.2}$). However, the hardness of alloys was less than the value of Ti-6Al-4V (358 $HV_{0.2}$). It can be seen from Figure 4-24 the average Vickers micro-hardness of β -Ti alloys fabricated in this study were all higher than 200 $HV_{0.2}$. The average Vickers micro-hardness of Ti-Ta₃₀ alloy was the highest (321 $HV_{0.2}$) and that of the Ti-Ta₂₇-Al₅ was the lowest (230 $HV_{0.2}$). The average Vickers micro hardness of Ti-Mo₈-Nb₄-Zr₂, Ti-Mo₈-Nb₆-Zr₄, Ti-Mo₈-Nb₄-Zr₅ and was 264, 268, and 282 $HV_{0.2}$ respectively.

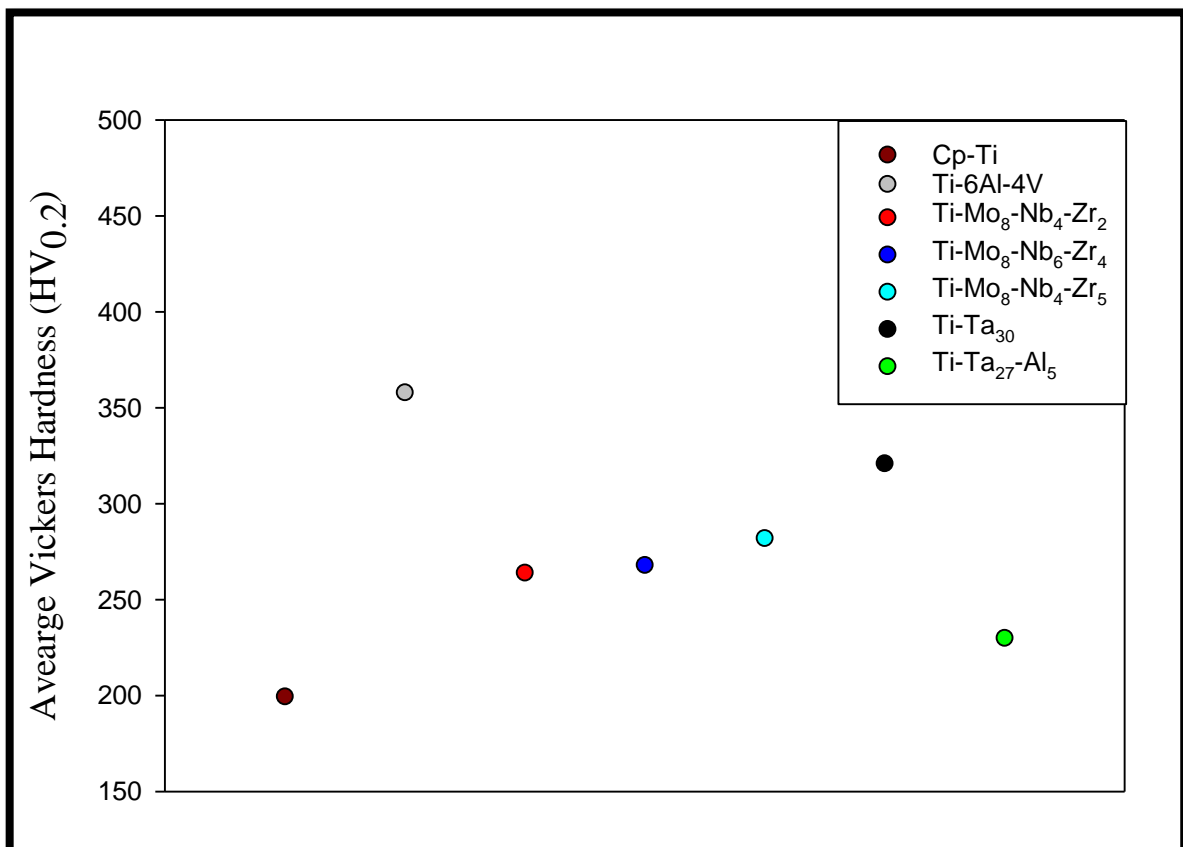


Figure 4-24 Microhardness of titanium alloys.

4.5 Summary

The investigation of structure and properties of titanium alloys can be summarised as follows:

- The arc-melted titanium alloys comprised equiaxed single phase β phase grain with no evidence of any intermediate phase. The exception to this was the Ti-Ta₂₇-Al₅, which was predominantly the β -phase with an equiaxed grain structure, but also contained orthorhombic martensitic.
- All titanium alloys had lower elastic modulus than that of Cp-Ti and Ti-6Al-4V alloys.
- All titanium alloys showed excellent cold workability except the Ti-Ta₃₀, which require an intermediate annealing treatment to increase the cold workability.
- All titanium alloys had average Vickers micro-hardness values higher than that of Cp-Ti and lower than that of Ti-6Al-4V

These results show that the produced titanium alloys exhibited both good quality and homogeneity that make them a great candidate for analysis to understand the tribological, electrochemical and tribocorrosion behaviour for biomedical applications.

Chapter 5 Results: Tribological Behaviour of Titanium Alloys

5.1 Introduction

In this chapter, the results of the investigation into all work completed on the tribological behaviour all titanium-based alloys (β , and $\beta+\alpha''$) fabricated in this work against an alumina ball are presented and the friction and wear characteristics and mechanisms involved are explored. A comparison was also made between these alloys and the α -phase Cp-Ti and the $\alpha+\beta$ Ti-6Al-4V alloys, which are used as implant materials. Tribological tests were carried out in a 25vol% bovine calf serum at room temperature under a contact load of 0.25, 0.5, 1 and 2N. The wear scar characteristics were investigated using SEM, 3D optical microscopy, focused ion beam and Raman spectrometry.

5.2 Lubricated Sliding Friction

The friction coefficient of titanium alloys as a function of test time in 25% vol bovine calf serum at a normal load of 0.25, 0.5, 1 and 2 N under lubricated rubbing conditions are shown in Fig.5-1 through to 5-4. The coefficient of friction as a function of time for the $\alpha+\beta$ microstructure Ti-6Al-4V and α -microstructure Cp-Ti at normal load of 1 and 2N respectively are an indication of the stability of the tests. All alloys exhibited an initial run-in period followed by a maximum before reaching a steady state friction coefficient. Friction was clearly dependent on the alloy composition and structure. Some alloys reached a steady state after a few seconds, other alloys showed a gradual increase in the coefficient of friction after the first increase, before a steady state was reached, although some peaks in friction occurred during sliding. The curves of the $\alpha+\beta$ microstructure Ti-6Al-4V and α -microstructure Cp-Ti were smoother than those of β microstructure alloys and the $\beta+\alpha''$ microstructure. The coefficient of friction for the β microstructure alloys was observed to fluctuate more after the run-in period, which could be related to the interaction of wear debris during rubbing, which was produced from removal of oxide. Regarding the friction coefficient, the results indicated that the average coefficient of friction increased with a normal load, as can be observed in Figure 5-5. The $\beta+\alpha''$ microstructure Ti-Ta₂₇-Al₅ alloy exhibited the highest coefficient of friction at all normal loads, while the $\alpha+\beta$ microstructure Ti-6Al-4V alloy had the lowest coefficient of friction. The β microstructure Ti-Ta₃₀ had a similar COF of Ti-Mo₈-Nb₄-Zr₂ at 0.25 and 2N, while it had a similar COF of Ti-Mo₈-Nb₆-

Zr₄ at 1N. The α + β microstructure Ti-6Al-4V and α -microstructure Cp-Ti had a similar COF at 2N.

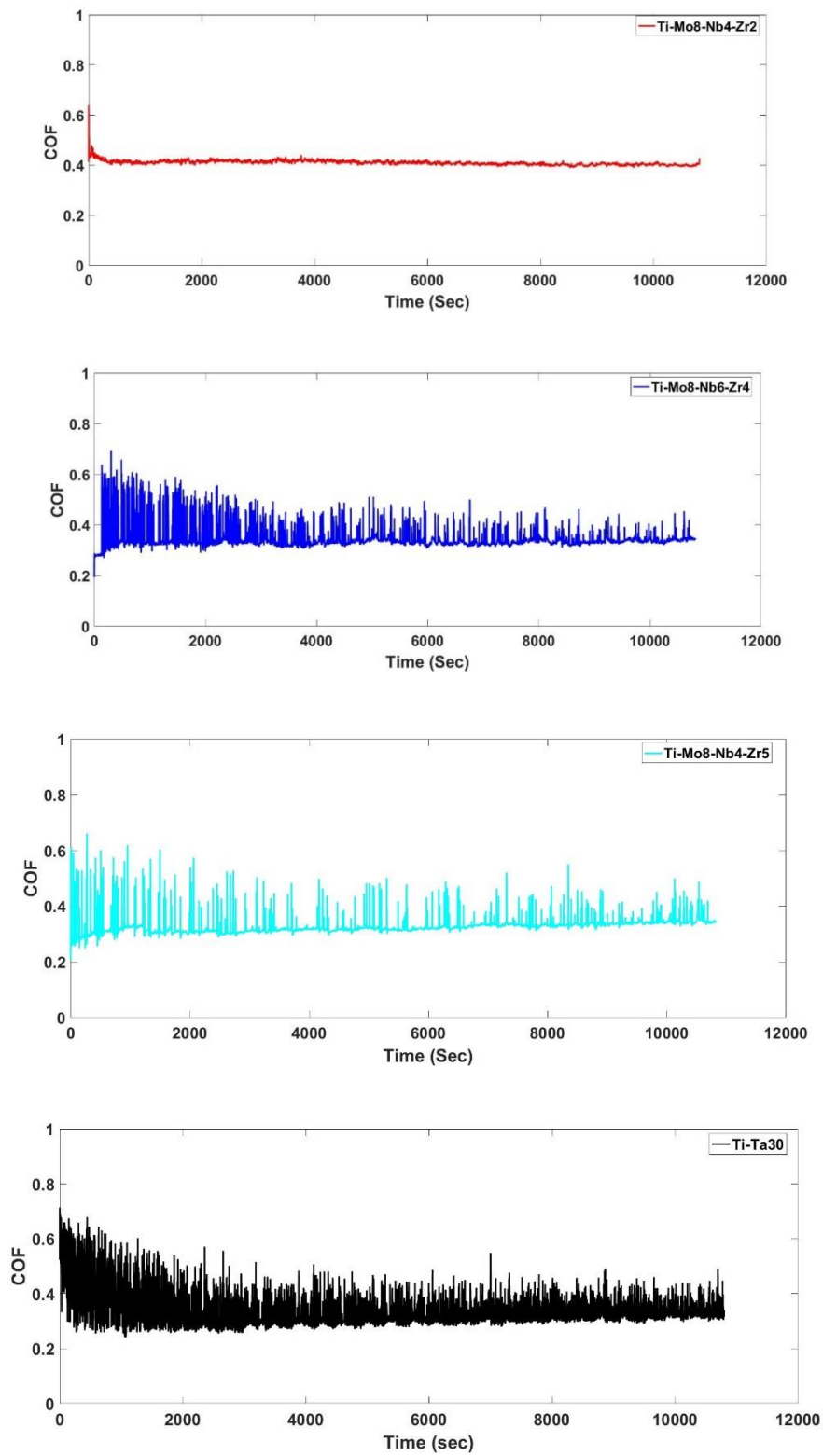


Figure 5-1: The evolution of the coefficient of friction of titanium alloys at a normal load of 0.25 N under lubricated conditions.

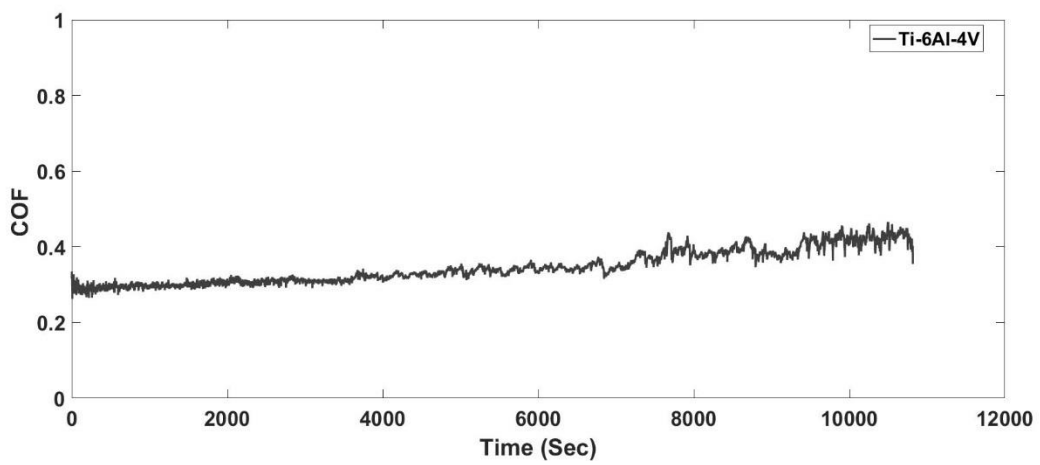
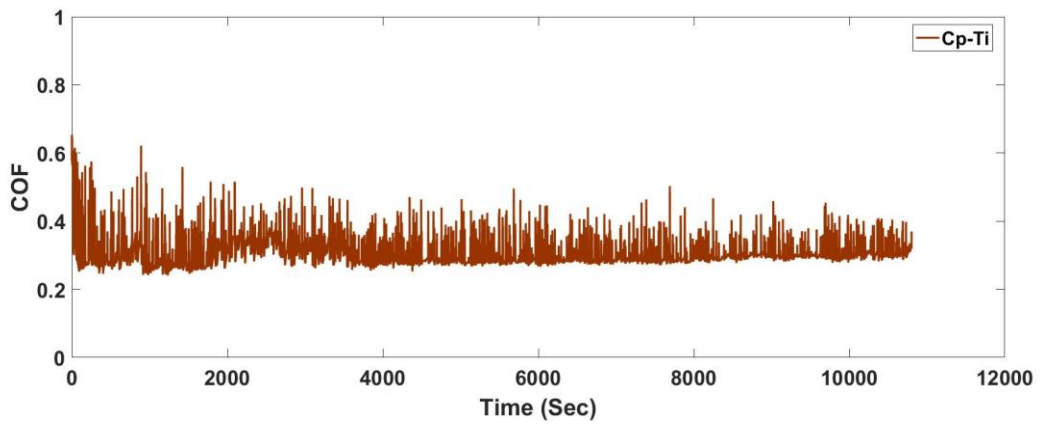
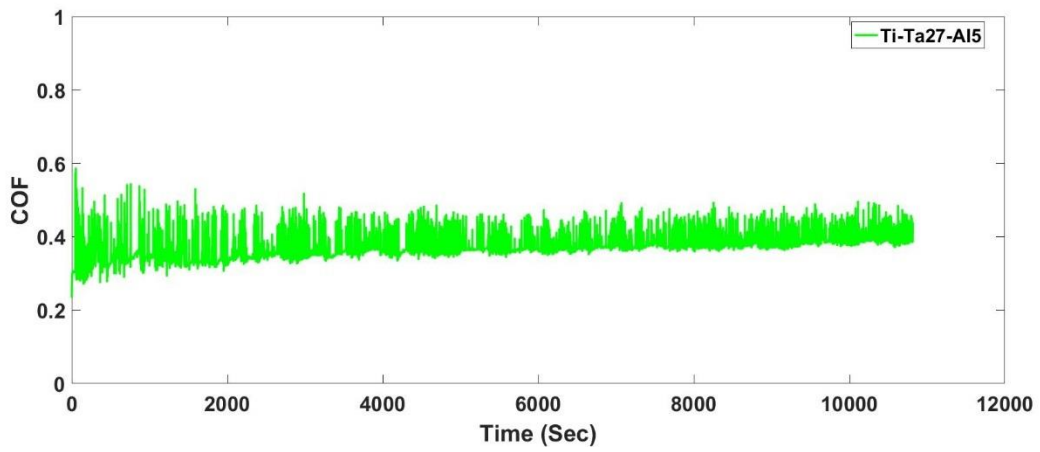


Figure 5-1: Continued

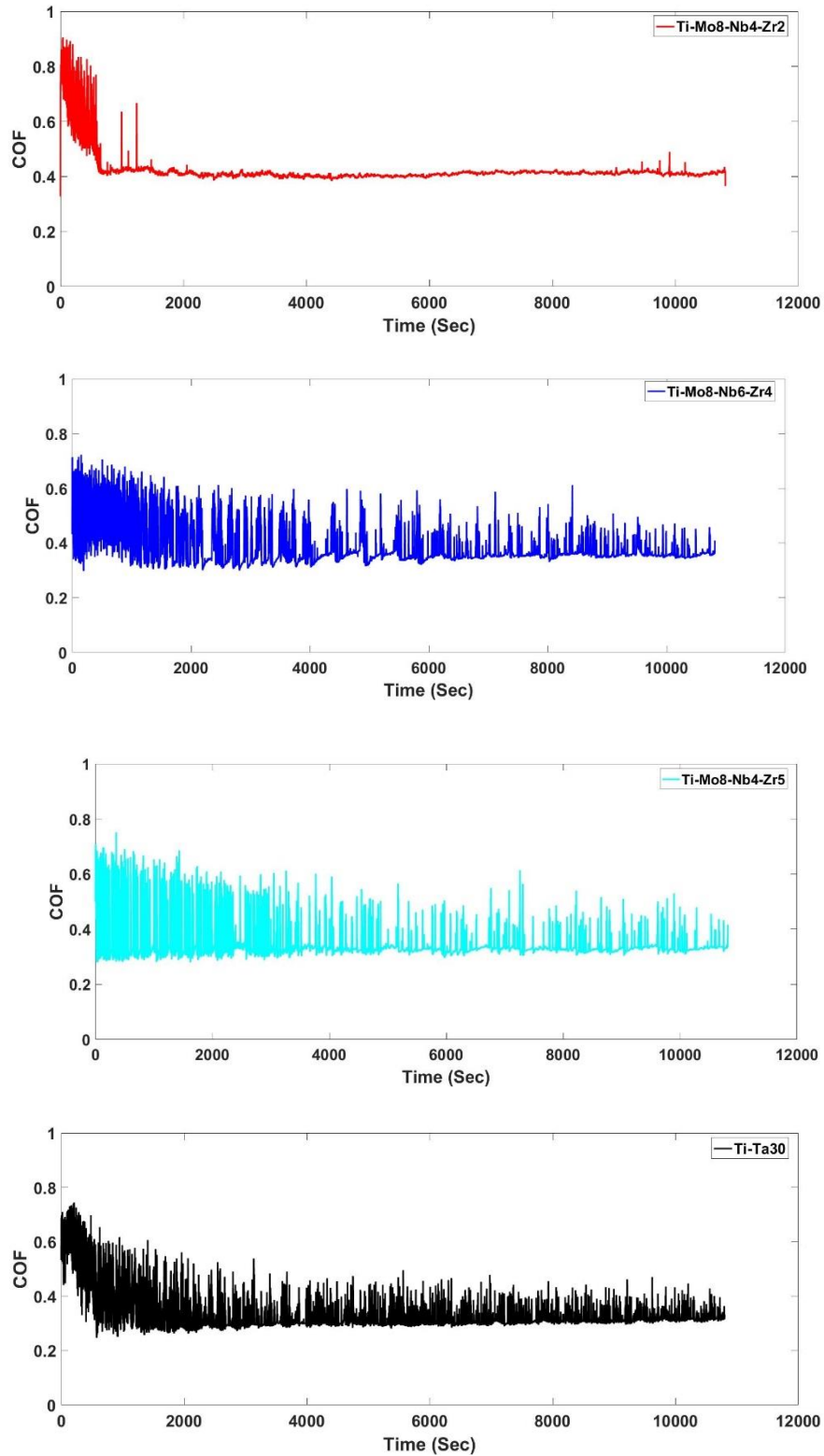


Figure 5-2: The evolution of the coefficient of friction titanium alloys at a normal load of 0.5 N under lubricated conditions.

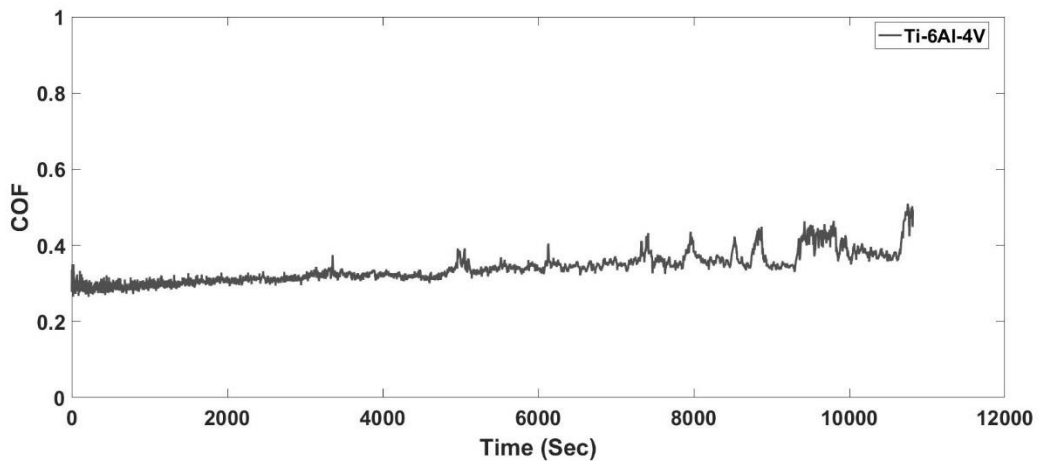
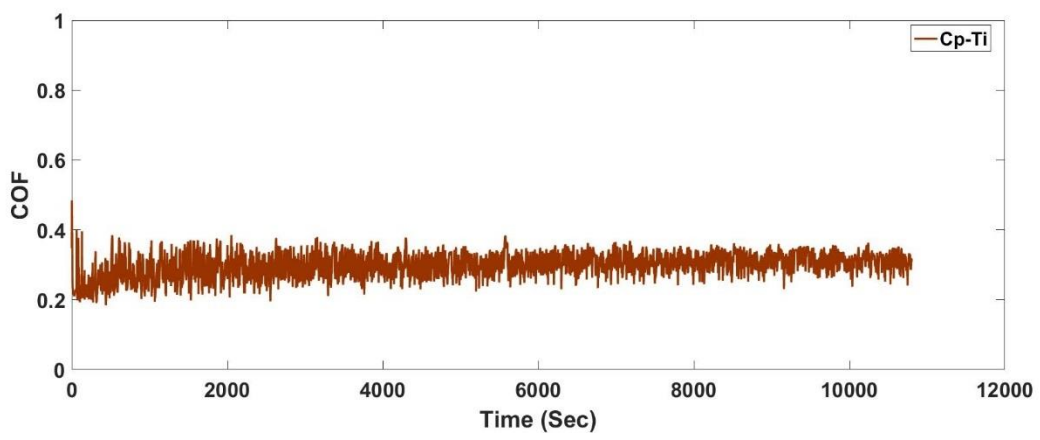
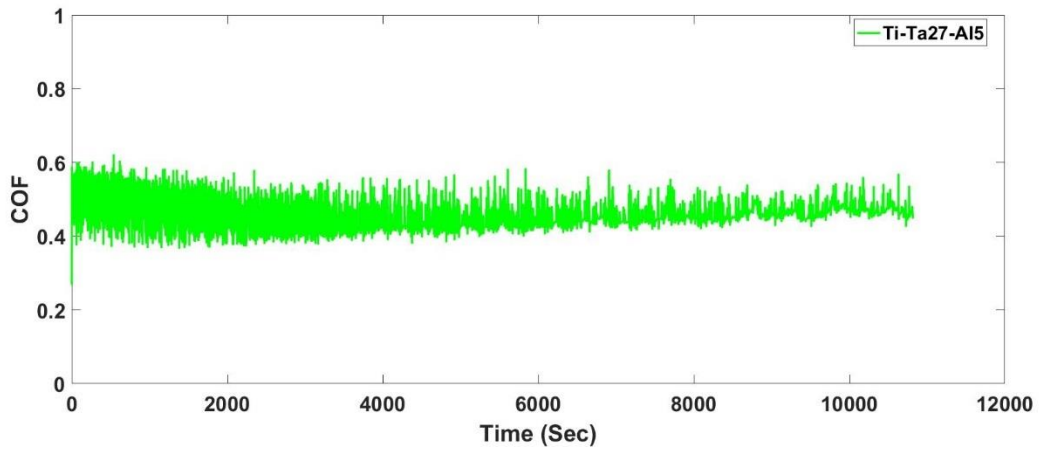


Figure 5-2: Continued

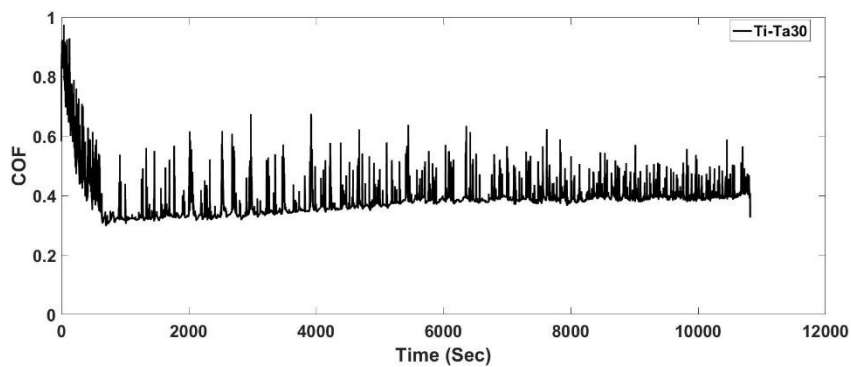
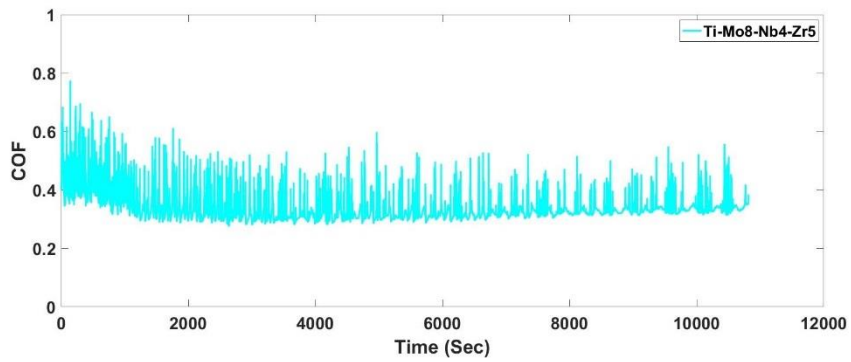
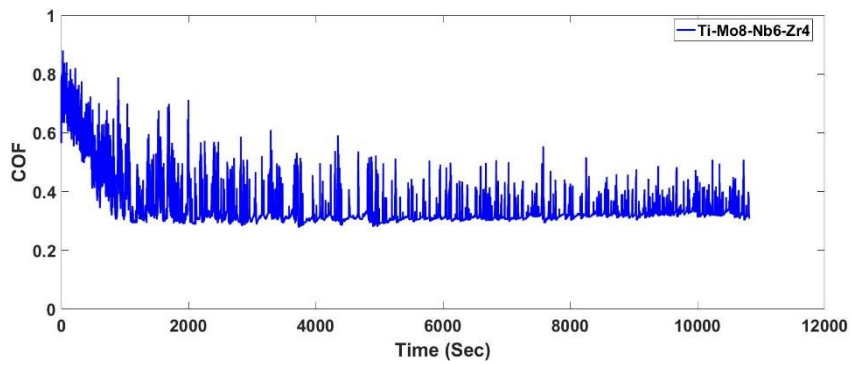
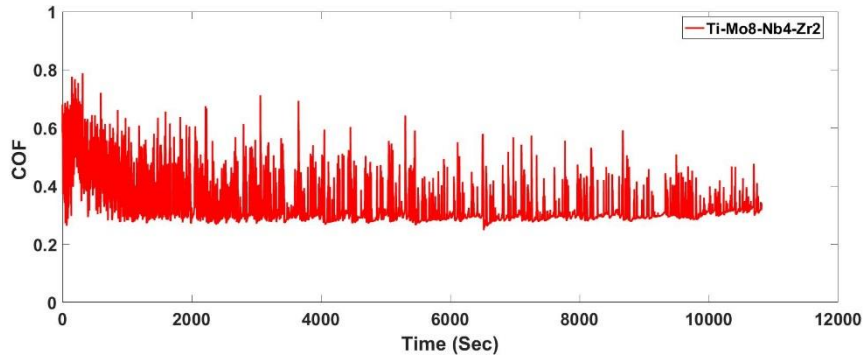


Figure 5-3: The evolution of the coefficient of friction of titanium alloys at a normal load of 1 N under lubricated conditions.

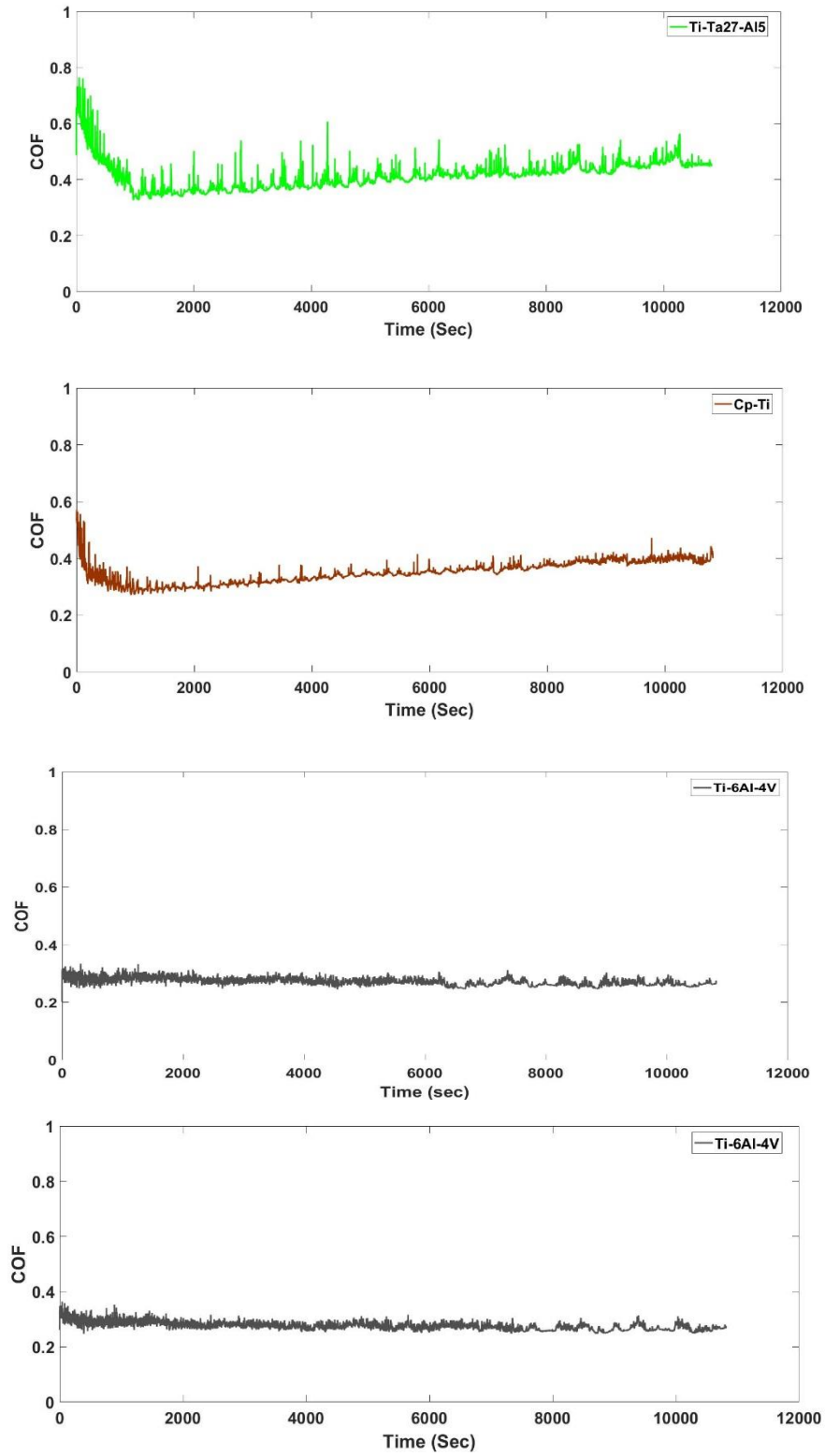


Figure 5-3: Continued

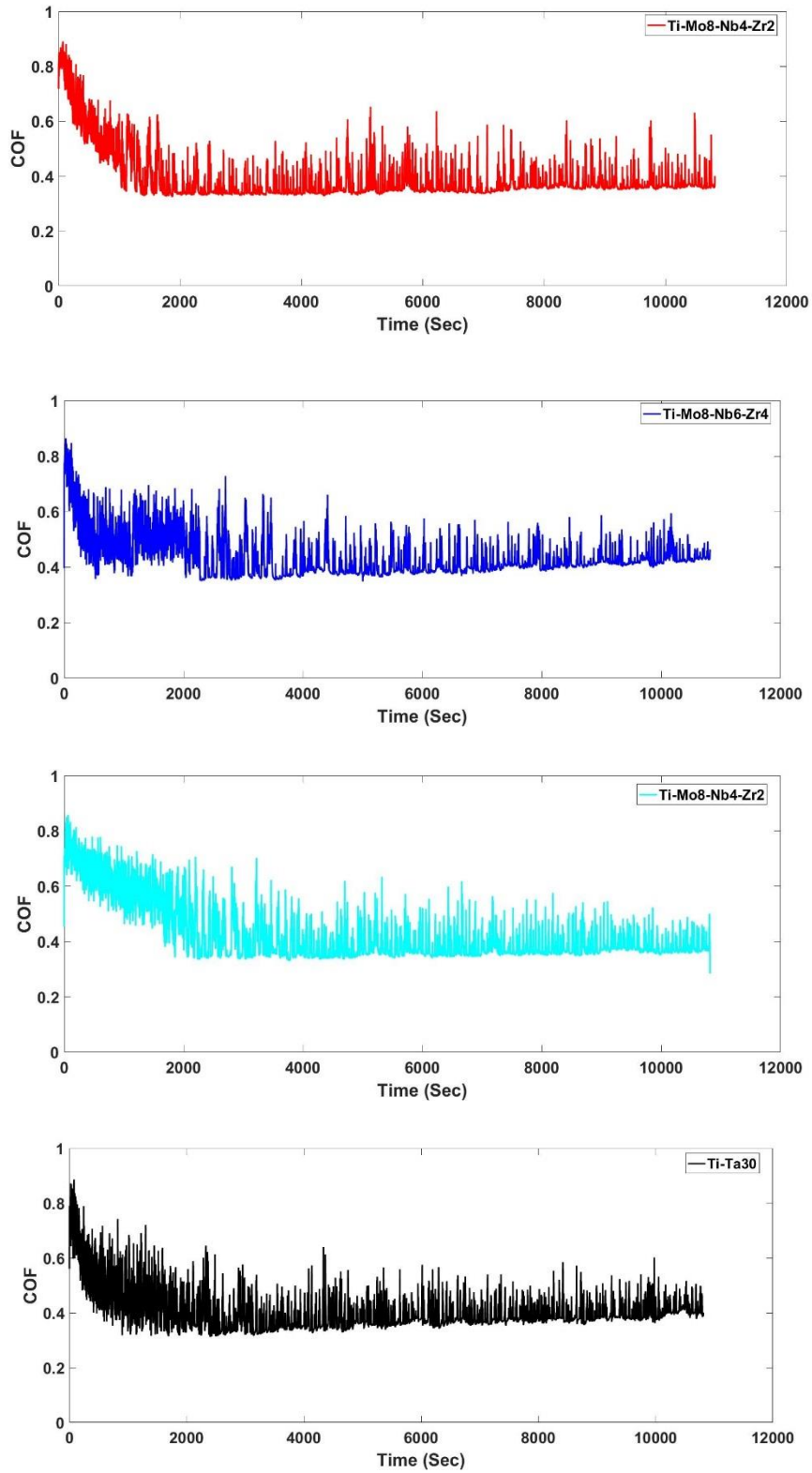


Figure 5-4: The evolution of the coefficient of friction of titanium alloys at a normal load of 2 N under lubricated conditions.

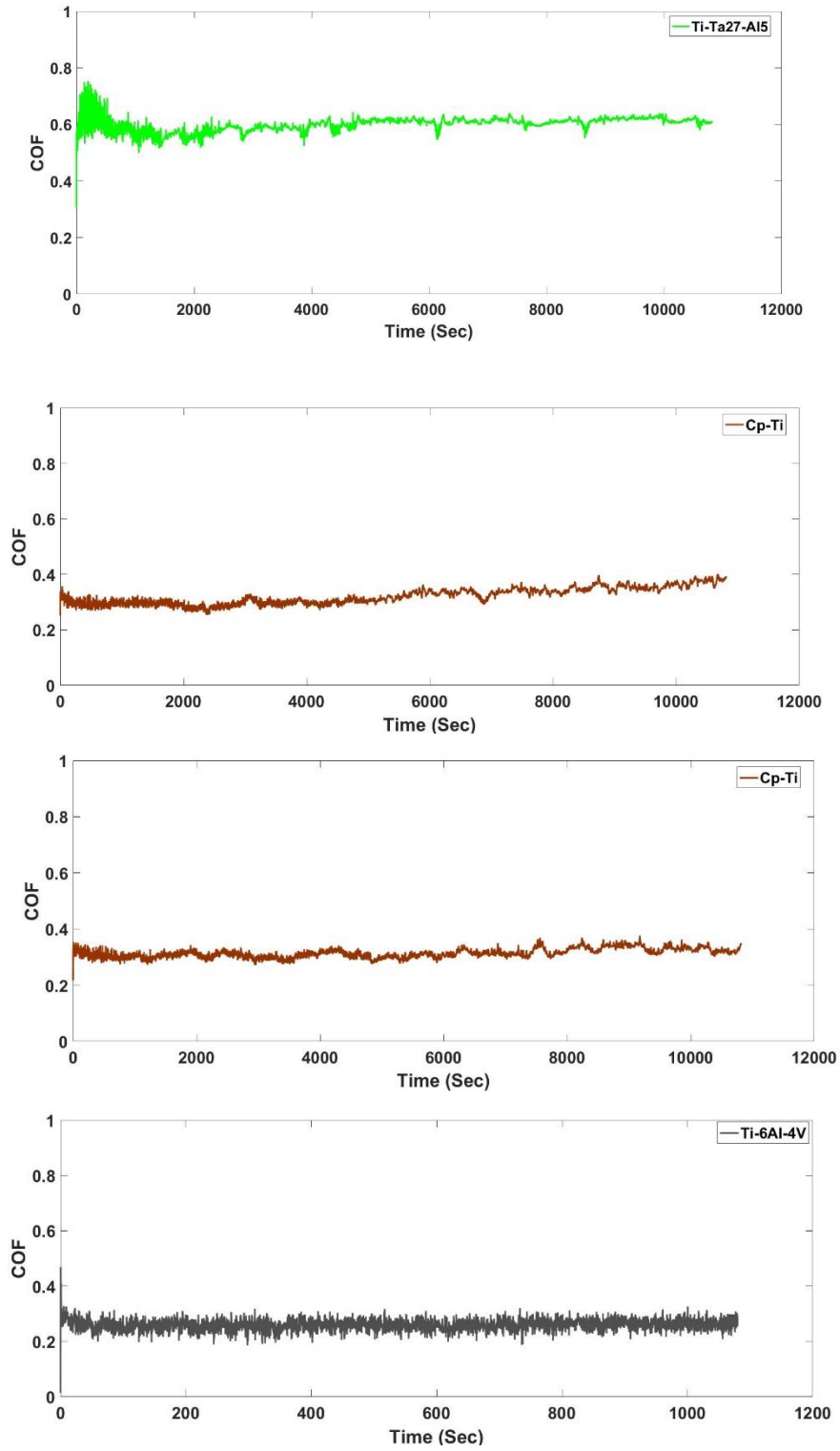


Figure 5-4: Continued

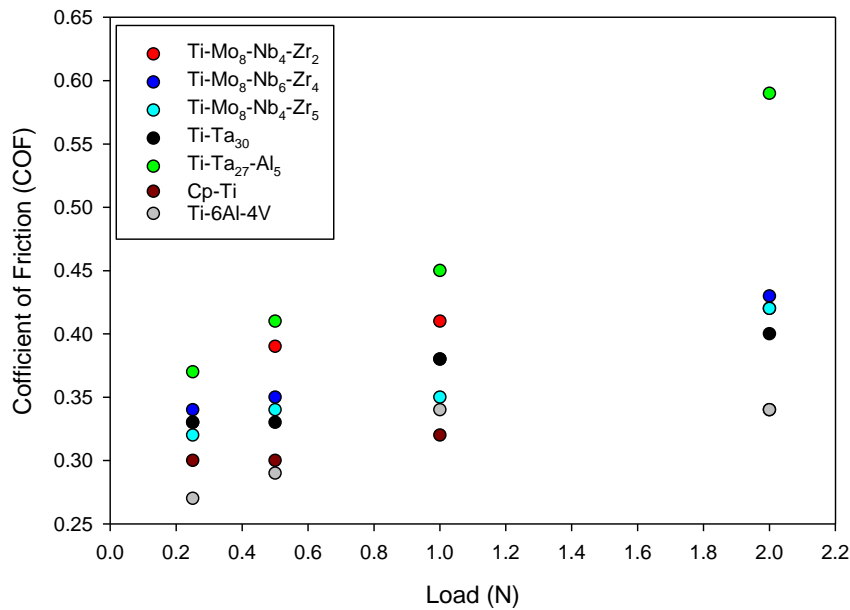


Figure 5-5 The mean friction coefficient values of titanium alloys under different loads in lubricated conditions

5.3 Wear Track Morphology, Chemistry and Roughness

SEM images of the centre of the wear track at a normal load of 0.25N are shown in figure 5-6. Figures 5-7, 5-8 and 5-9 give a detailed morphology of the worn surface at normal loads of 0.5N, 1N and 2N respectively. Wear occurred predominantly by ductile and plastic deformation ploughing, with some signs of delamination. A small number of isolated debris particles, and flake-like debris were observed inside the worn surface. Wear debris fragments were observed on the worn surface (see Figure 5-8). No cracking was observed within the worn surface in any of the tests. The surface of the alloys also appears to be covered by a light grey layer, as well as small dark spots, which indicated the formation of carbonaceous layer on the surface of alloys. EDX and Raman analyses confirmed the formation of this carbonaceous layer.

The EDX elemental mapping results of the centre of the wear tracks at a contact load of 0.25 N are presented in Figure 5-10, corresponding to the boxed area covering the surface shown in the image top right of all Figure 5-10. The corresponding maps for loads of 0.5, 1 and 2 N are Figures 4, 5, 6 of Appendix A. The EDX analysis revealed the presence of the elements present in the substrate as well as carbon and oxygen. The EDX results indicated that the carbon is present at the surface of the wear track (tribofilm), which is in agreement with the results of Raman spectra of the centre of the wear track. Figure 5-11 shows typical Raman

spectra taken at the centre of the wear track at normal loads of 0.25, 0.5, 1 and 2N respectively. The spectra show disordered graphite (D band) and the single crystalline graphite (G band) centred on 1383 and 1567 cm^{-1} related to sp^2 -carbon and sp^3 -band carbon respectively. The α -microstructure Cp-Ti alloy had the highest Raman spectrum intensity among all alloys at normal loads of 0.25, 0.5 and 2N, while the $\beta+\alpha''$ microstructure had the highest Raman D and G band intensity at 1N. However, at 0.5 N the β microstructure Ti-Mo₈-Nb₆-Zr₄ had the highest Raman spectrum intensity among all alloys, but the Raman peaks from the surface of this alloy, but the small peaks did not correspond to D and G bands. It is far from clear why the β -phase Ti-Mo₈-Nb₆-Zr₄ exhibited such different behaviour to the other β alloys at 0.5 and 1N. Thin films are known to be generated in biomedical materials during sliding motion, known as tribological films [272]; however, the structure and formation of the tribological film is not fully understood and knowledge about them is limited. According to XPS analysis of the tribological film, it has been suggested in the literature that the tribological films originated from the pseudo-synovial fluid and composed of something similar to denatured protein [273-278]. More particularly, and in the case of lubricant tests in bovine calf serum, a recent study suggested that the tribological film is inorganic graphitic carbon, and most materials decomposed to disordered graphite D-band sp^2 -carbon [279-281].

There was no evidence of transfer from the alumina ball to the titanium alloy surface during rubbing at all normal loads under lubricated rubbing conditions. The morphology of the wear tracks on the alumina balls were evaluated using optical microscopy, scanning electron microscopy and EDX analysis. Figures 5-12, 5-13 and 5-14 show typical optical images, scanning electron microscopy and the EDX elemental mapping results of the wear tracks on the alumina ball after the wear tests. No significant material transfer could be observed by optical microscopy, scanning electron microscopy and EDX analysis on the alumina ball counterbody after the wear experiments. However, scanning electron microscopy and EDX analysis show marginal amounts of transferred titanium at a normal load of 1N, and loss of material on the alumina ball at a normal load of 2N. The titanium transfer was much less at 2N. Fig 5-15 shows the average surface roughness of titanium alloys at different loads after tribological experiments in 25% vol bovine calf serum. Fig 5-16 shows a surface roughness 3D image and 2D top view of the centre of the wear track for the tests at 0.25 N. The surface roughness 3D image and 2D top view of the centre of the wear track for all alloys tested at 0.5, 1, and 2 N in 25% vol bovine calf serum are presented in Figs 1, 2 and 3 appendix A. By

comparing the results in Figure 5-15, it can be observed that all alloys exhibited a smooth appearance at lower contact loads, with Ra values of 0.22-0.5 μm . The wear track surface became rougher when the contact load was increased to the 2N with Ra values of 0.74-1.4 μm . Not surprisingly, the worn surface roughness increased with load, with a marked increase from 0.5N to 1N. The increase in roughness was associated with more extensive plastic ploughing of the surface.

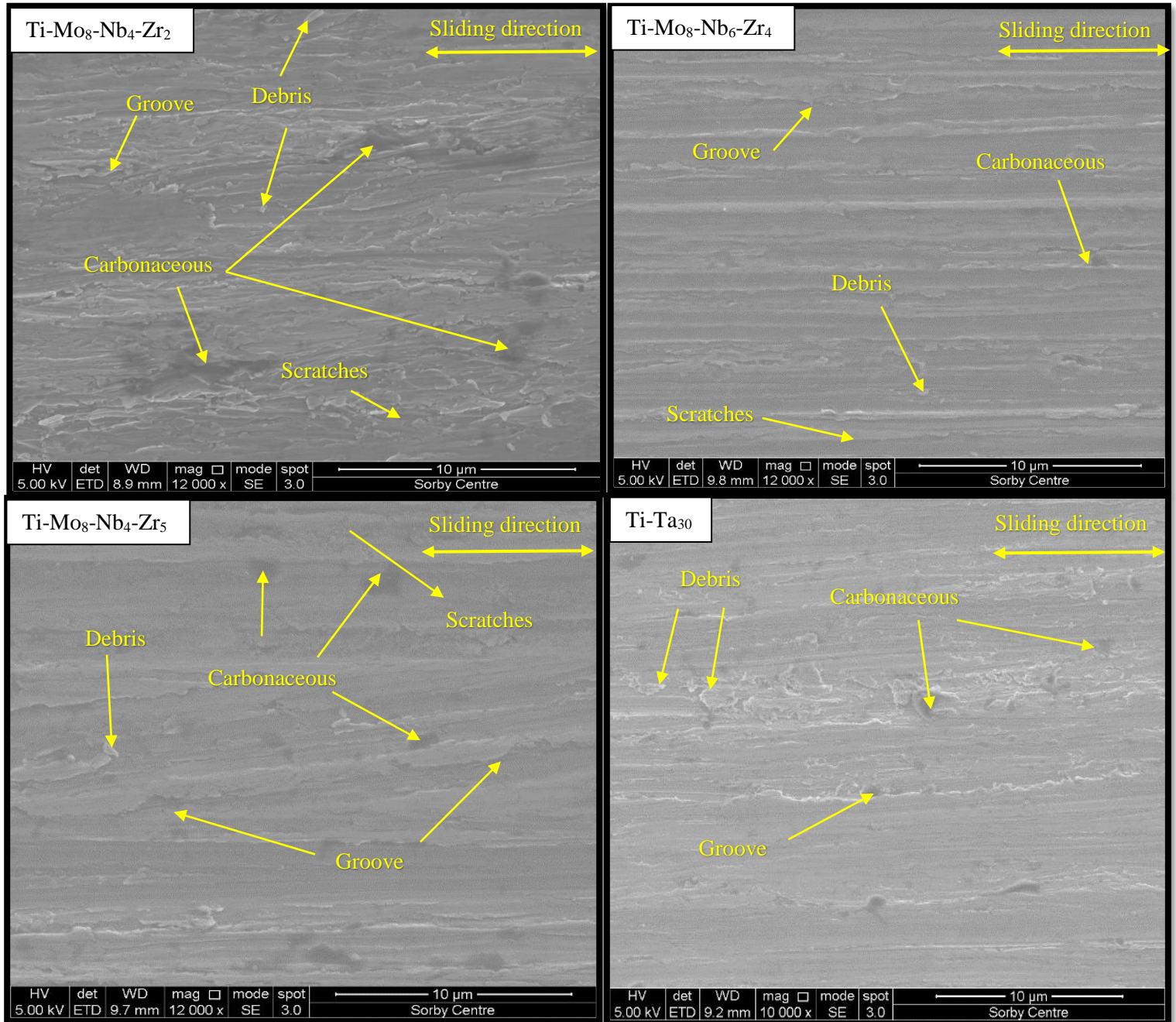


Figure 5-6: SEM micrographs of wear track of titanium alloys at a normal load of 0.25 N under lubricated conditions.

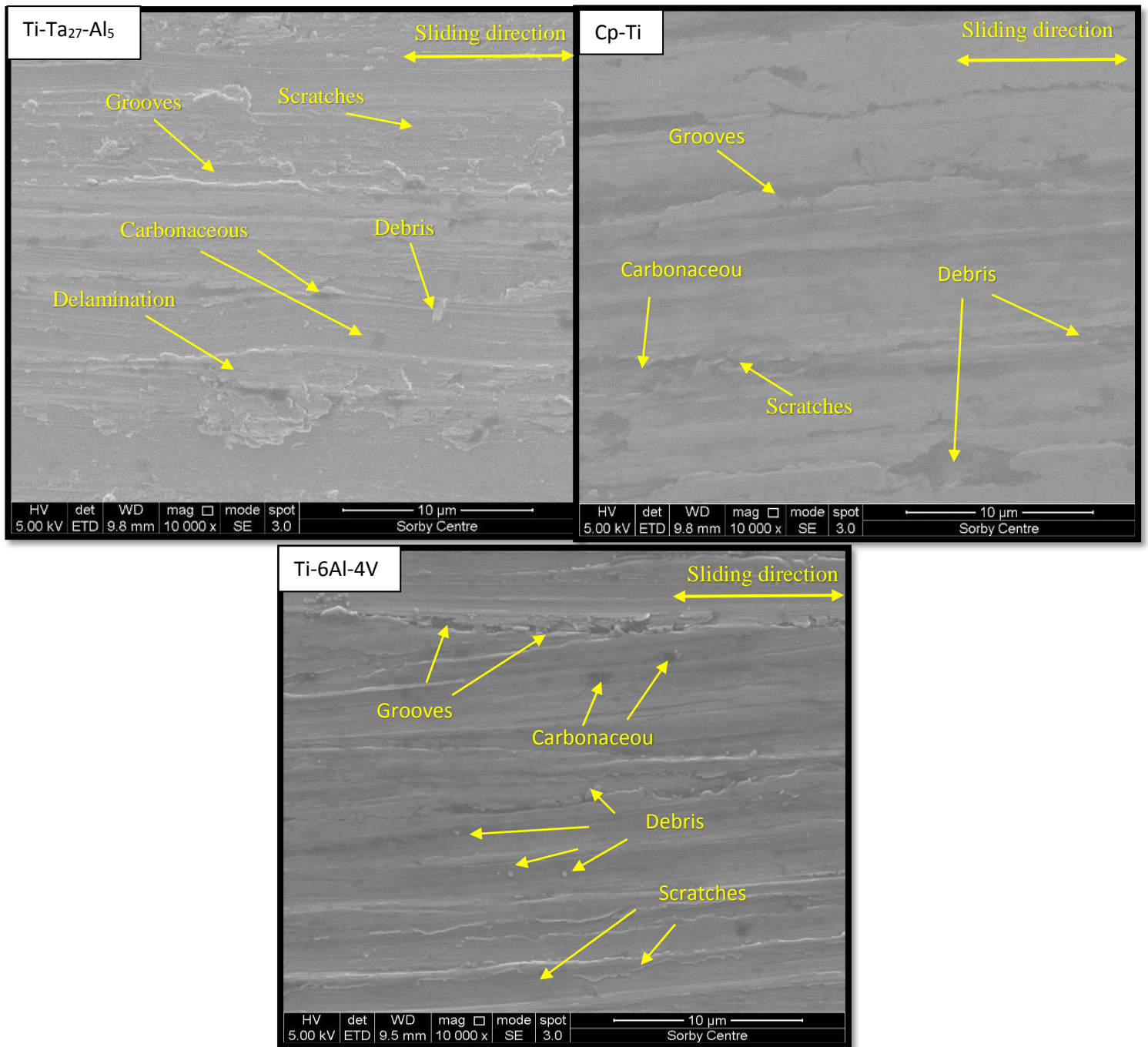


Figure 5-6: Continued.

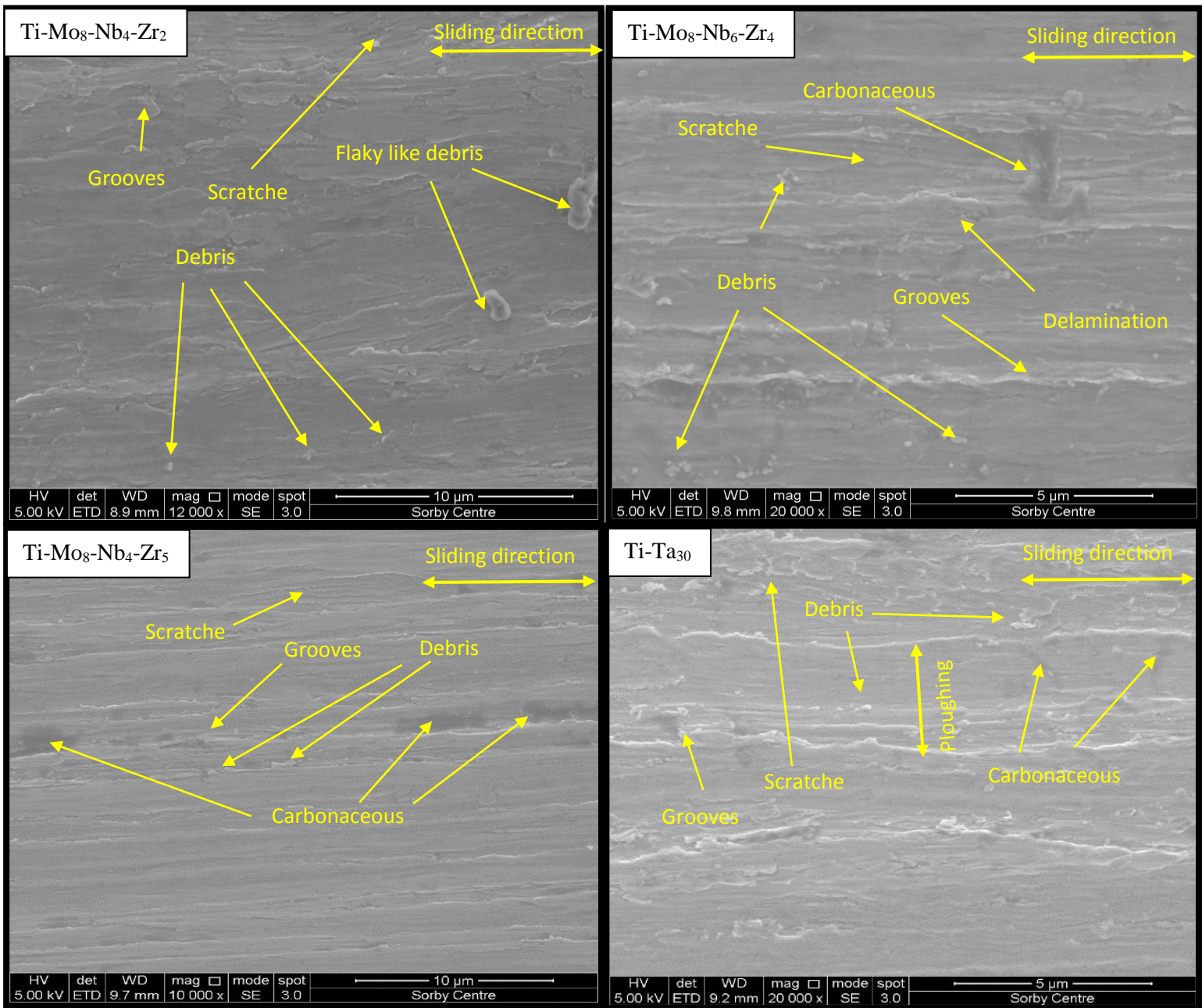


Figure 5-7: SEM micrographs of wear track of titanium alloys at a normal load of 0.5 N under lubricated conditions.

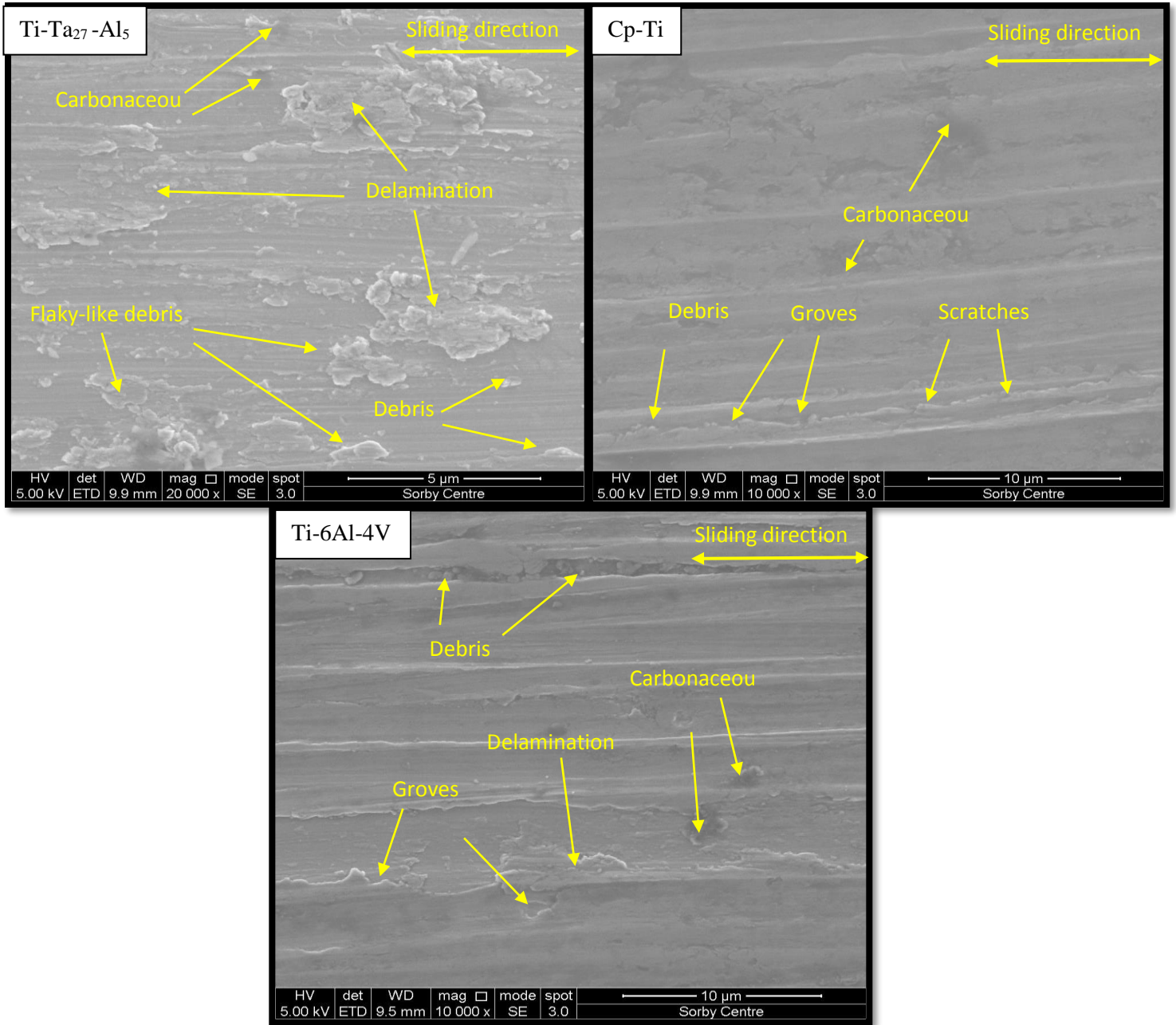


Figure 5-7: Continued.

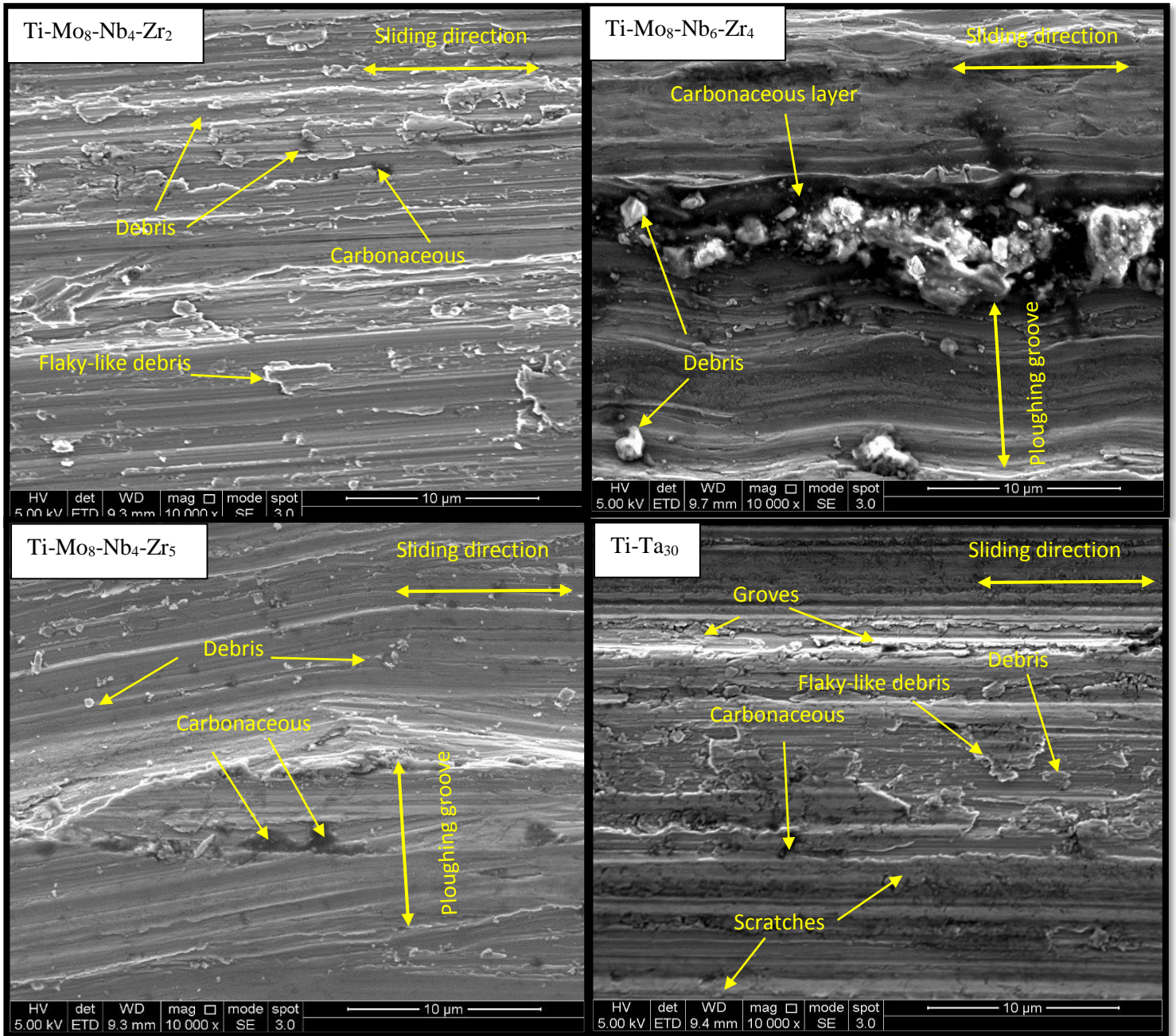


Figure 5-8: SEM micrographs of wear track of titanium alloys at a normal load of 1 N under lubricated conditions.

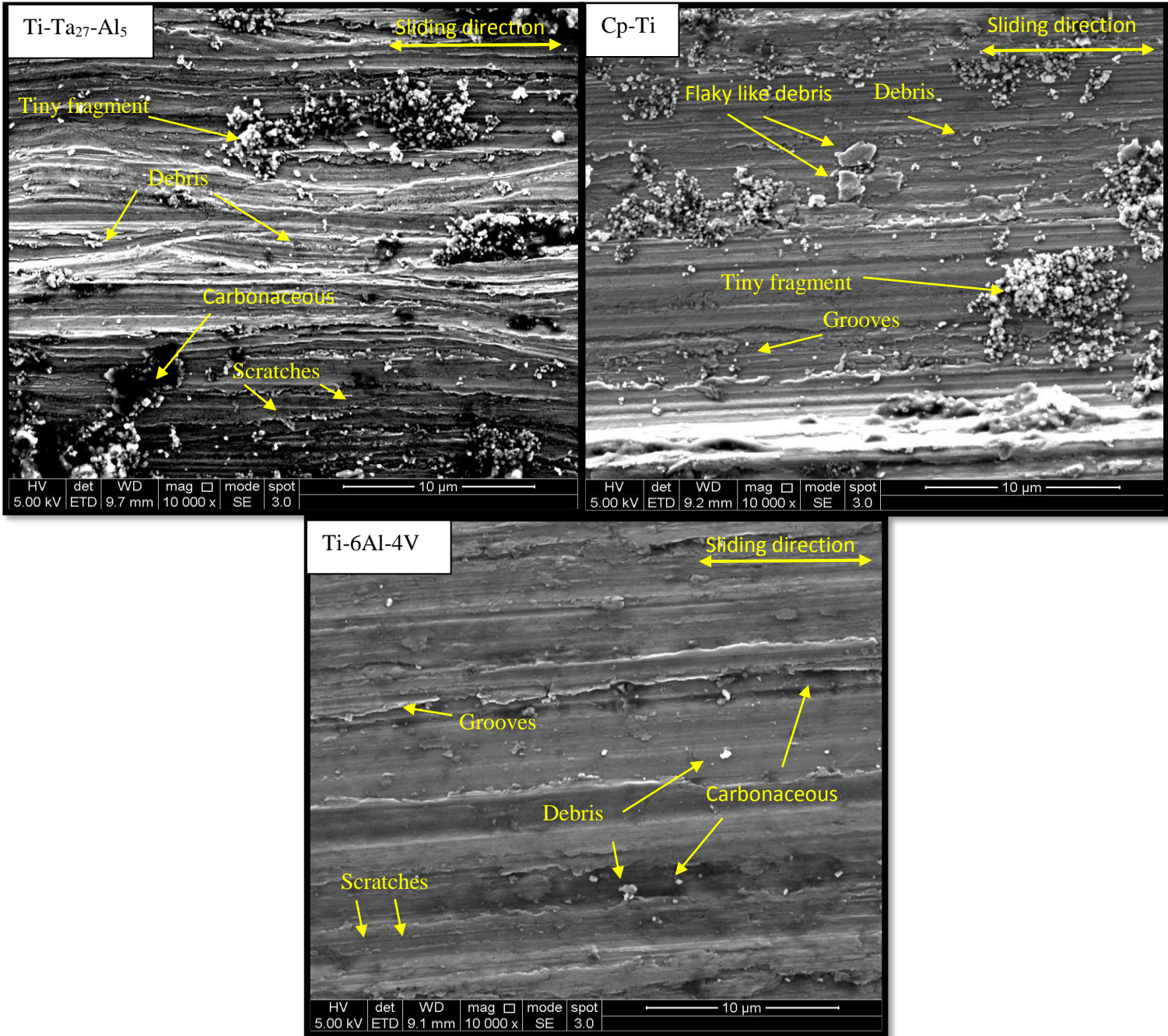


Figure 5-8: Continued.

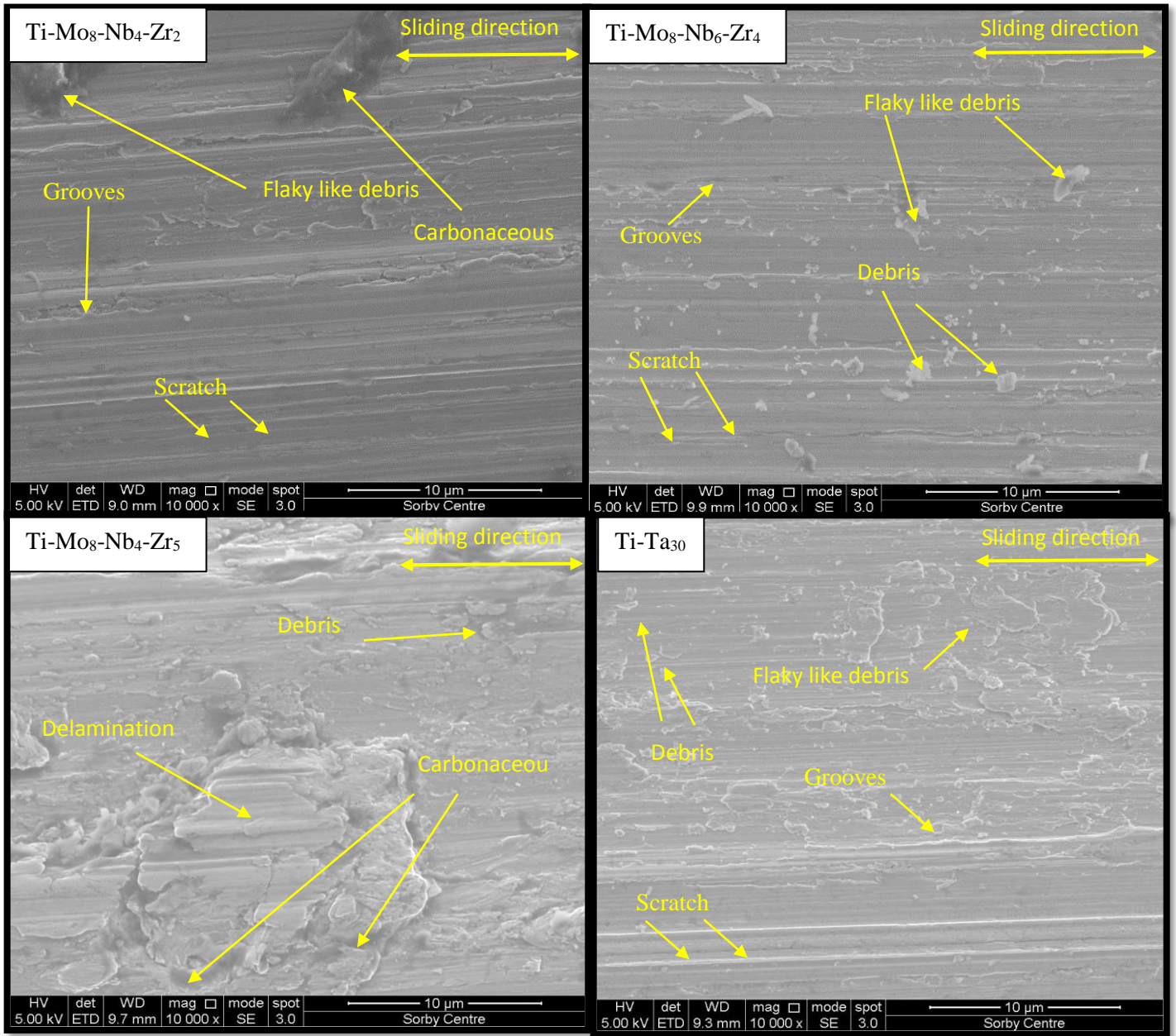


Figure 5-9: SEM micrographs of wear track of titanium alloys at a normal load of 2 N under lubricated conditions.

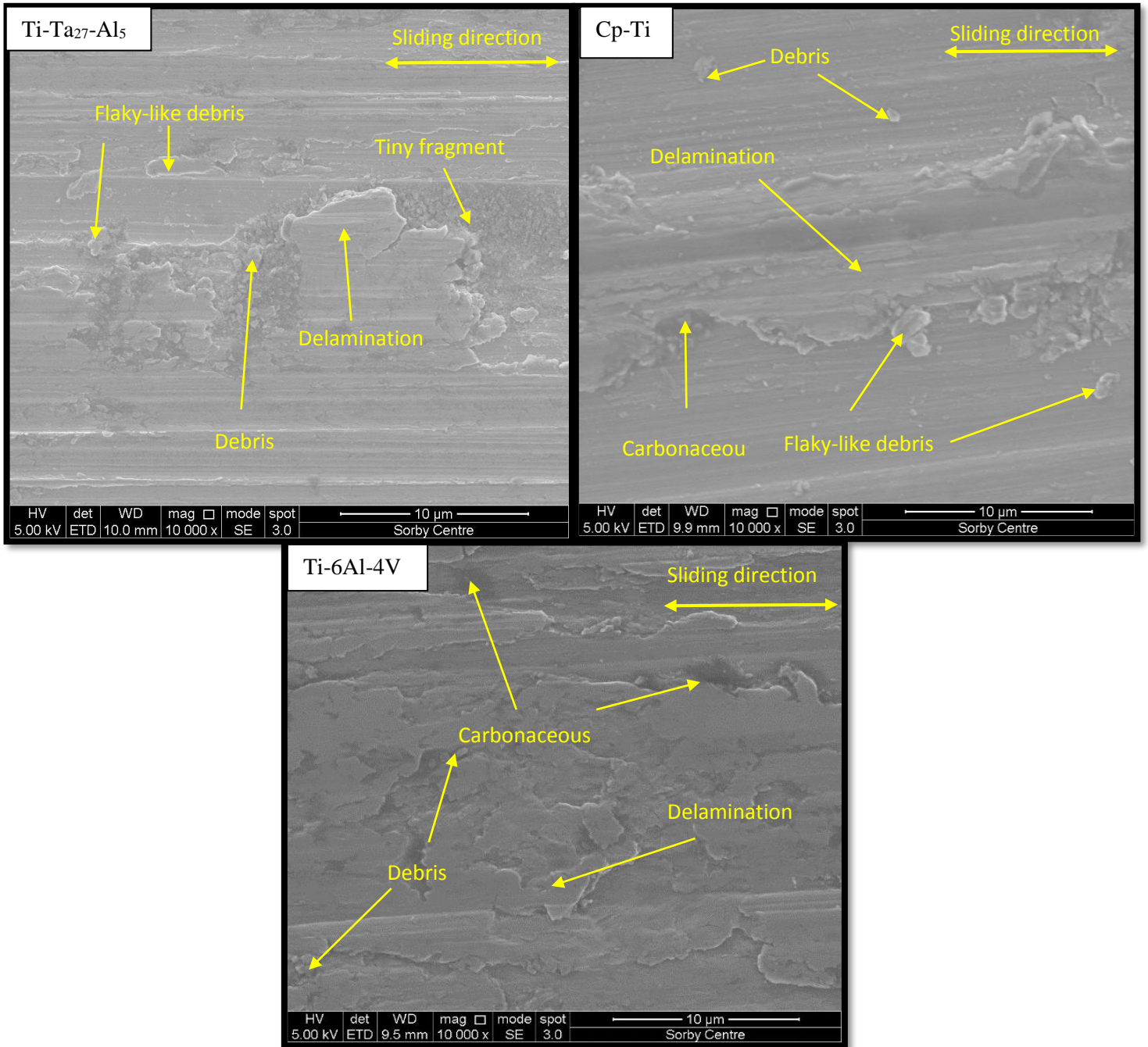


Figure 5-9: Continued

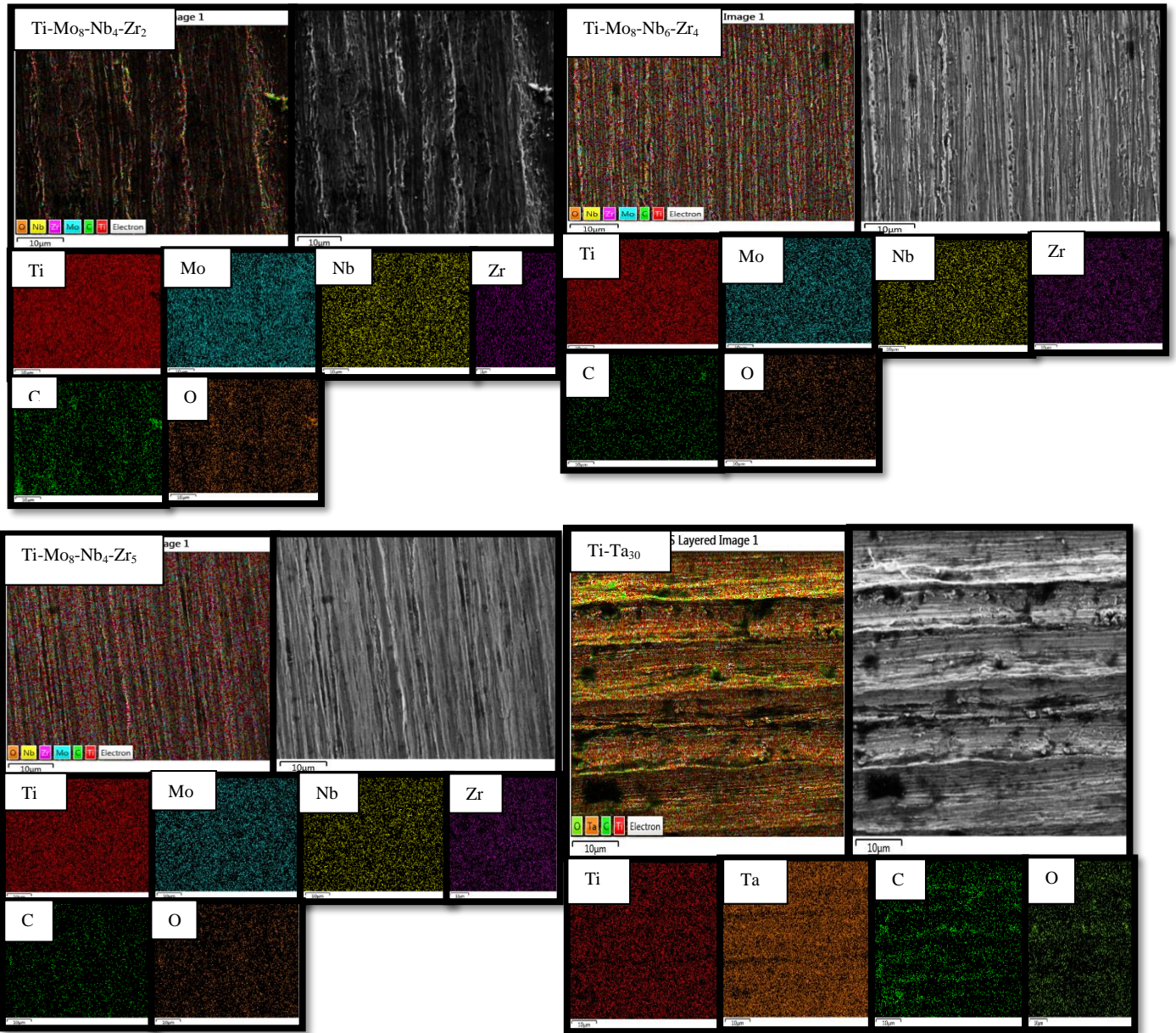


Figure 5-10: EDX element mapping of the wear track of titanium alloys at a normal load 0.25N under lubricated rubbing conditions.

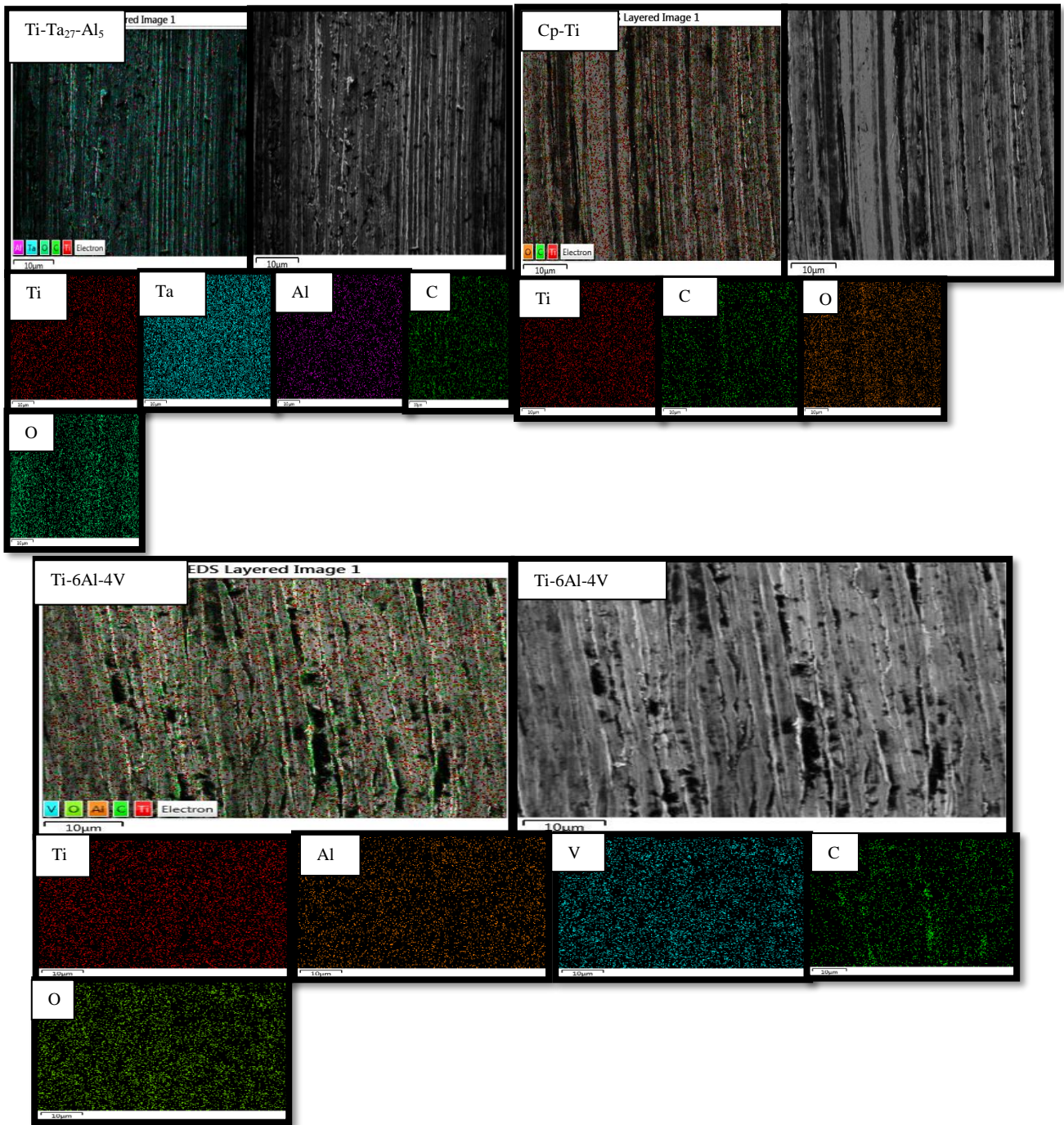


Figure 5-10: Continued.

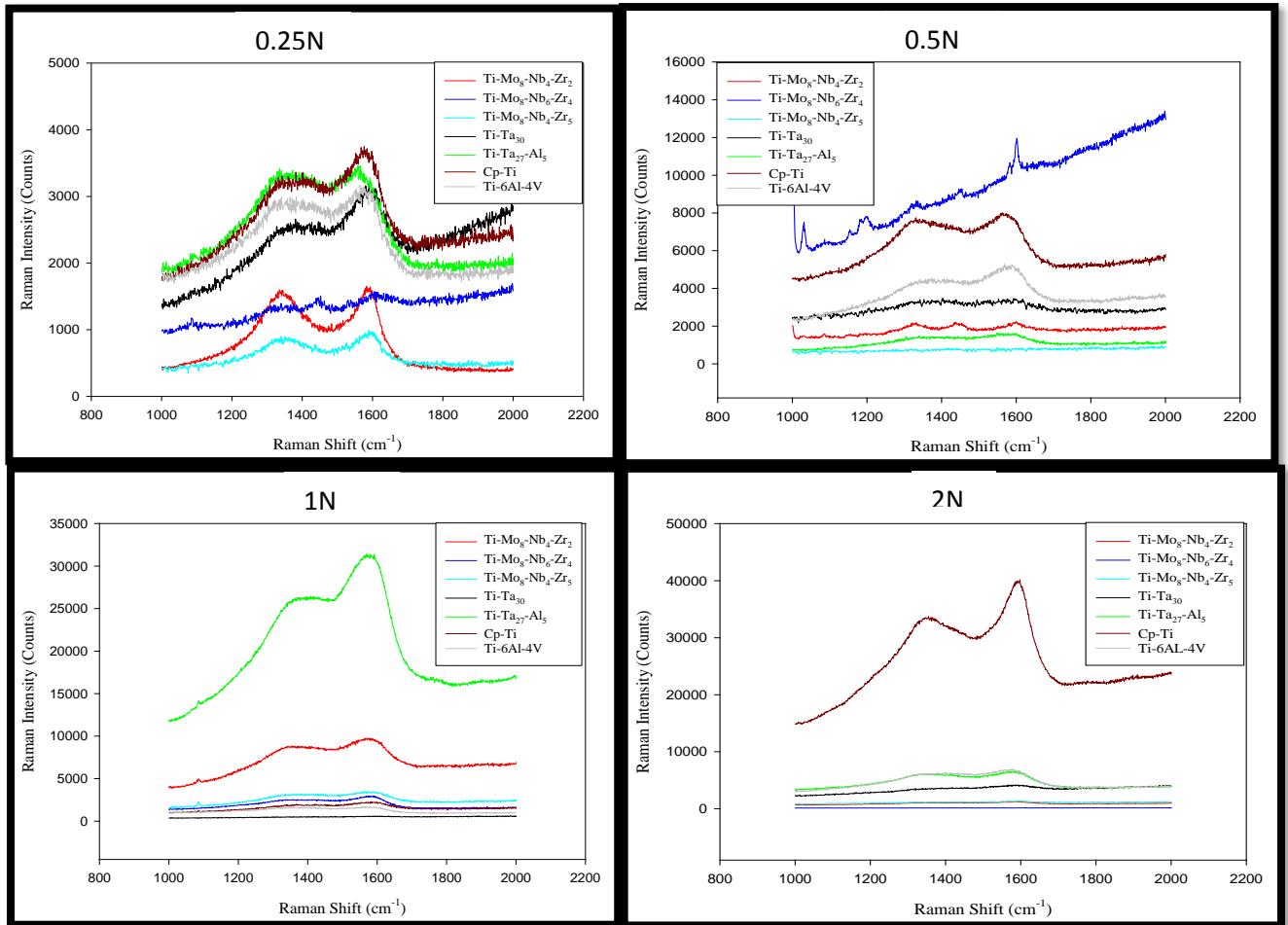


Figure 5-11: Raman spectra of the wear track of titanium alloys under lubricated conditions.

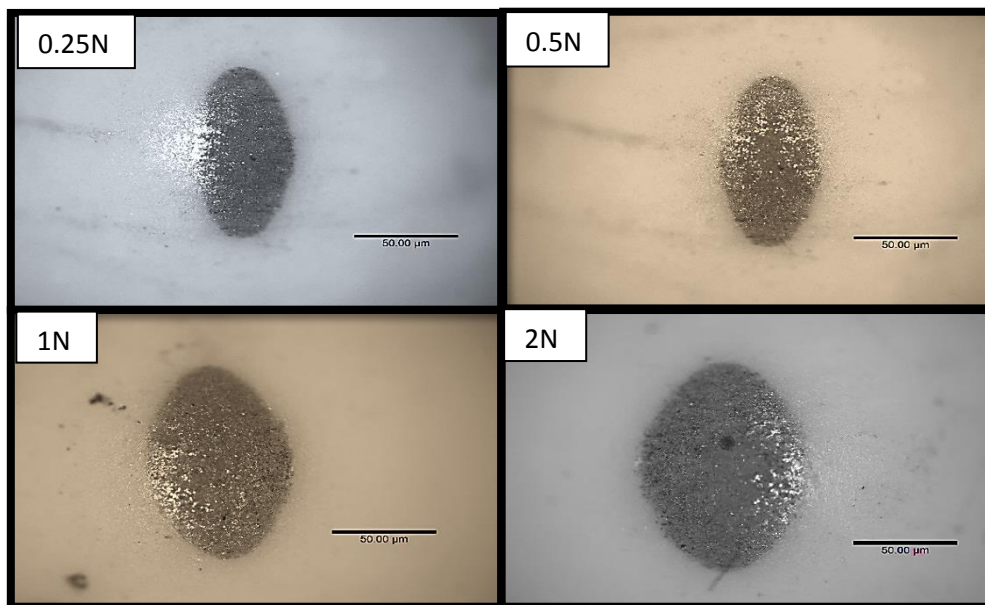


Figure 5-12 Optical images of the alumina ball after wear tests.

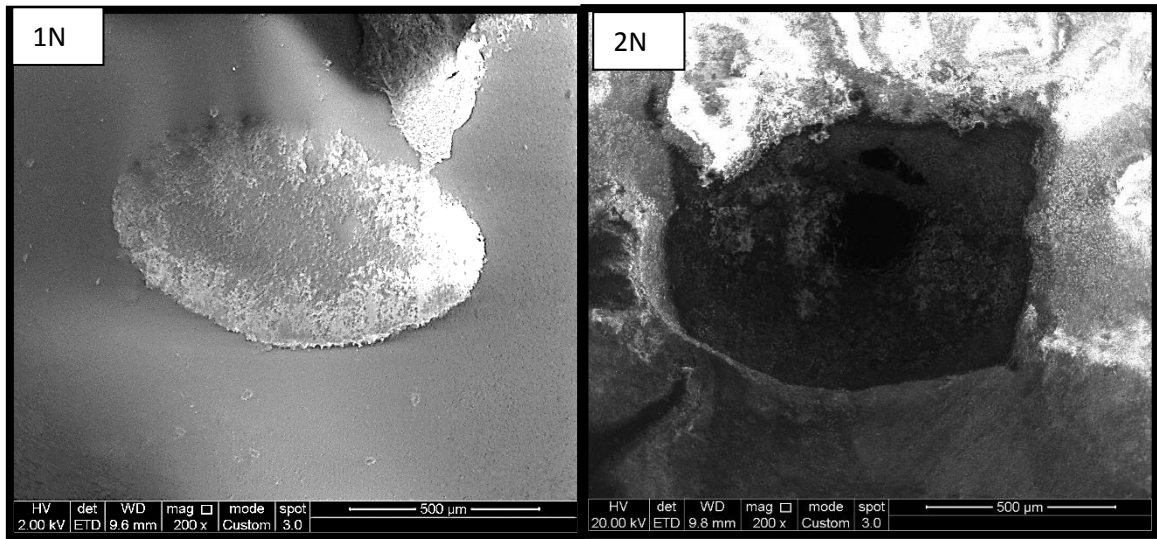


Figure 5-13 SEM images of the alumina ball after wear tests.

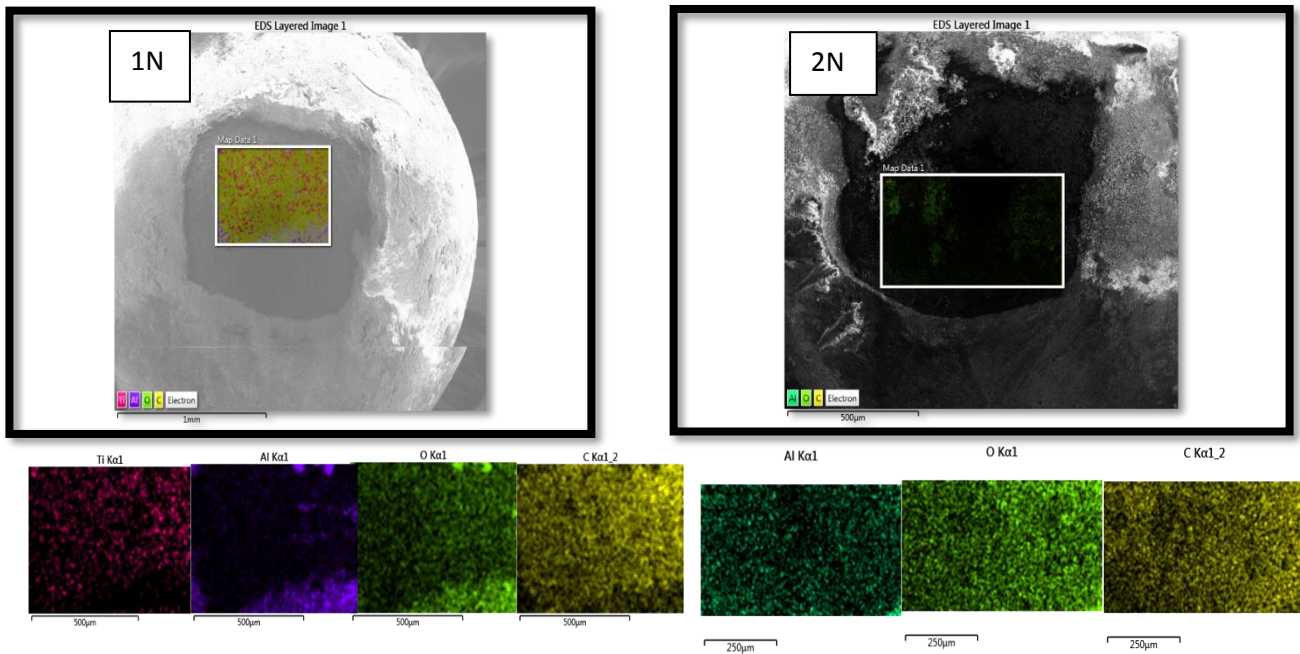


Figure 5-14 EDX element mapping of the alumina ball after wear tests.

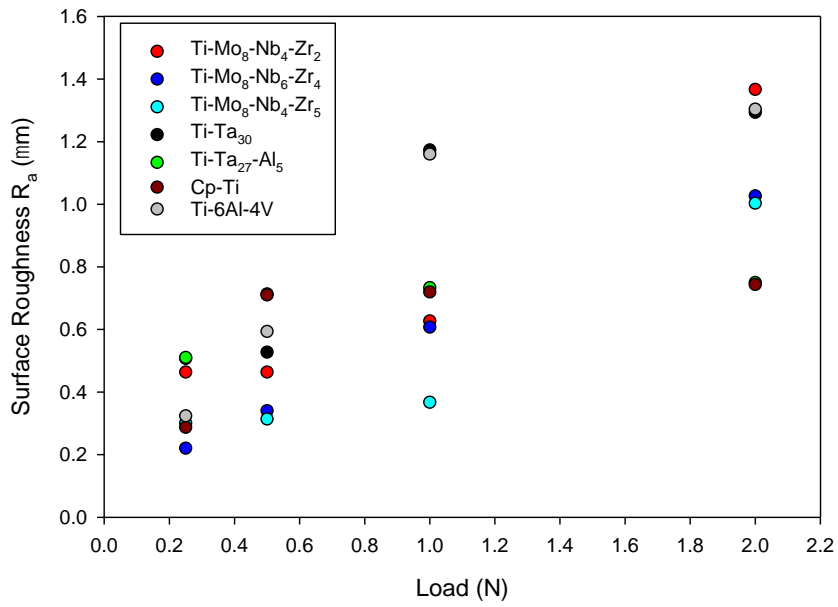


Figure 5-15 The average surface roughness titanium alloys at different loads under lubricated conditions.

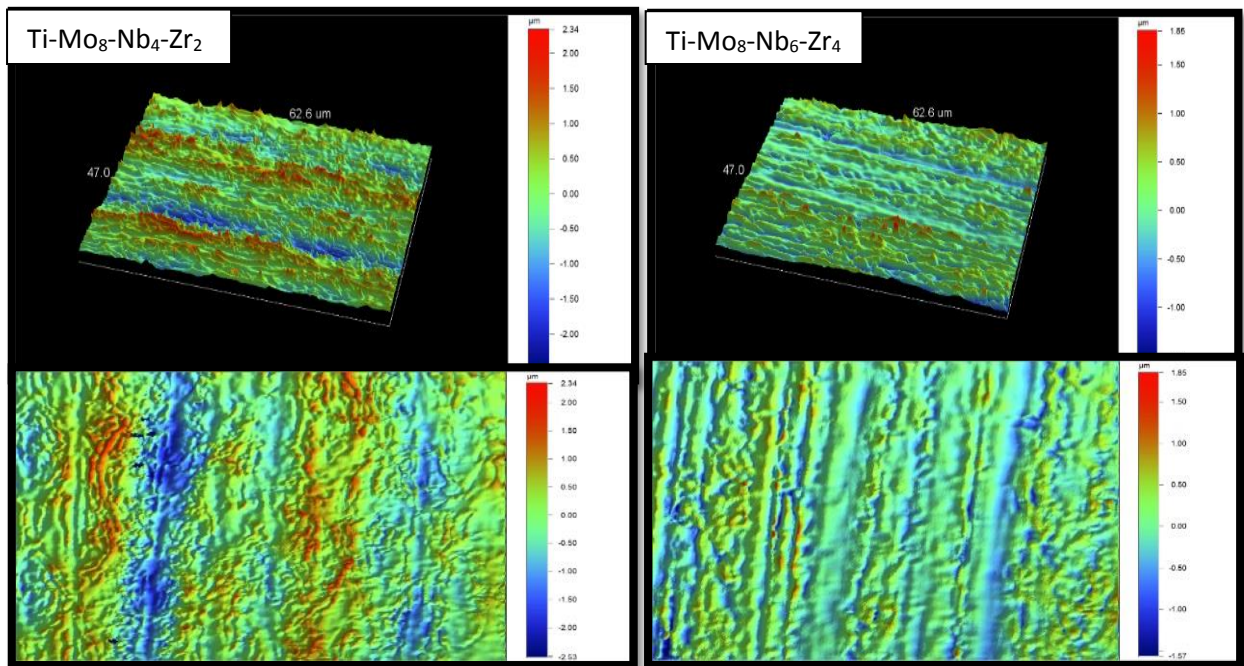


Figure 5-16: Surface roughness, 3D, X, Y profile, and 2D top view of the wear track at a normal load of 0.25N under lubricated conditions.

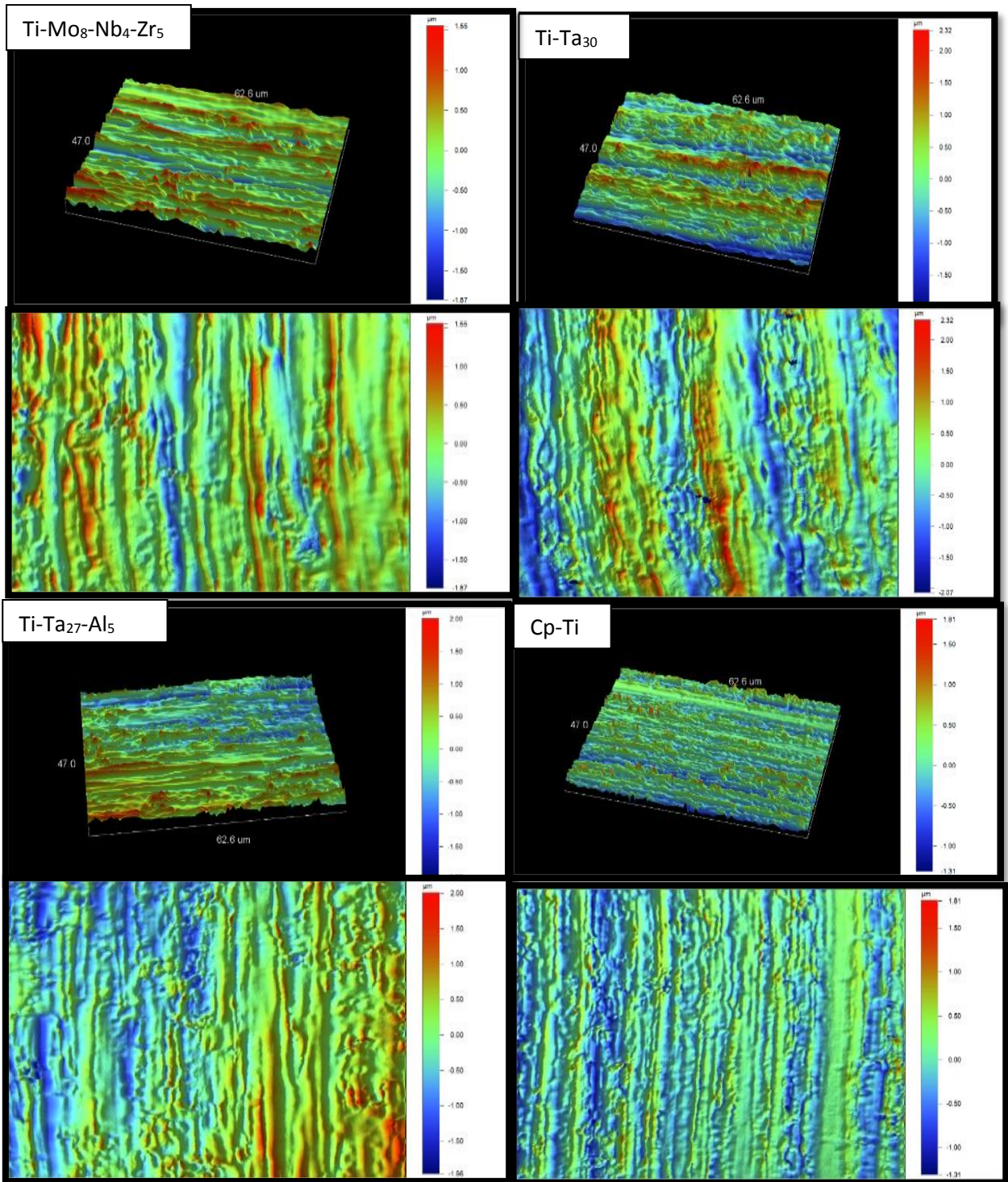


Figure 5-16: Continued

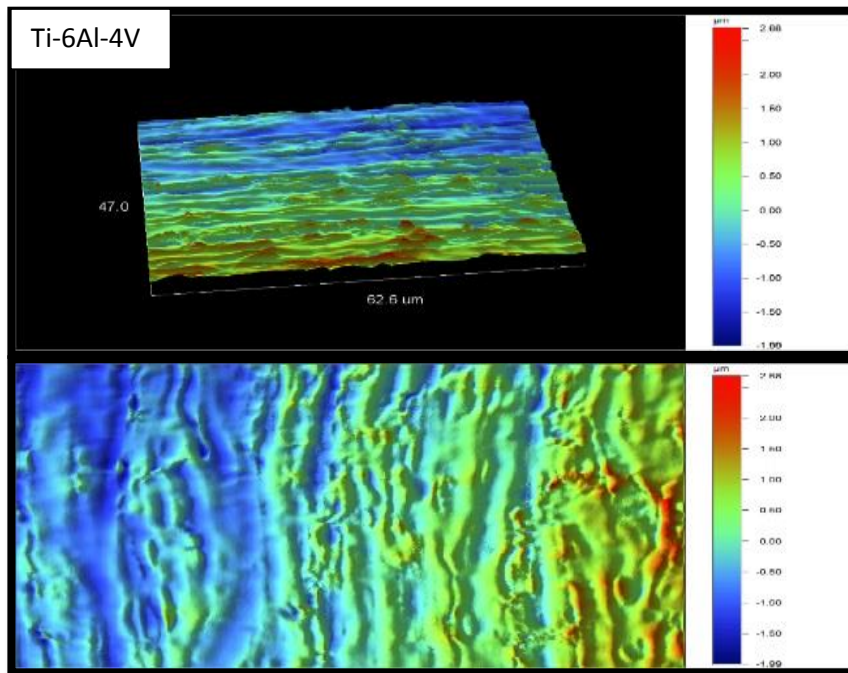


Figure 5-16: Continued.

5.4 Wear Rate

3D images of the wear track of the titanium and titanium alloys after tribological tests in bovine calf serum at normal loads of 0.25, 0.5, 1, and 2 N are presented in Figures 5-17 through to 5-20. The smallest wear track was obtained from the α - β phase Ti-6Al-4V and the α -phase Cp-Ti alloy. The wear tracks of the β -phase titanium alloys (Ti-Mo-Nb-Zr, Ti-Ta) and the β + α' -phase Ti-Ta₂₇-Al₅ alloy were relatively large and distinct with high wear rates. The average wear volume at normal loads of 0.25, 0.5, 1 and 2 N are shown in Figure 5-21, with the corresponding specific wear rates in figure 5-22. The total wear volume increased with load. The specific wear rate increased slightly with the normal load for all alloys, but there was no significant change. In all cases, the specific wear rates were very high. The α - β phase Ti-6Al-4V and the α -phase Cp-Ti alloy had a lower specific wear rate than that of the β -phase titanium alloys, and the β - α' -phase Ti-Ta₂₇-Al₅ alloy.

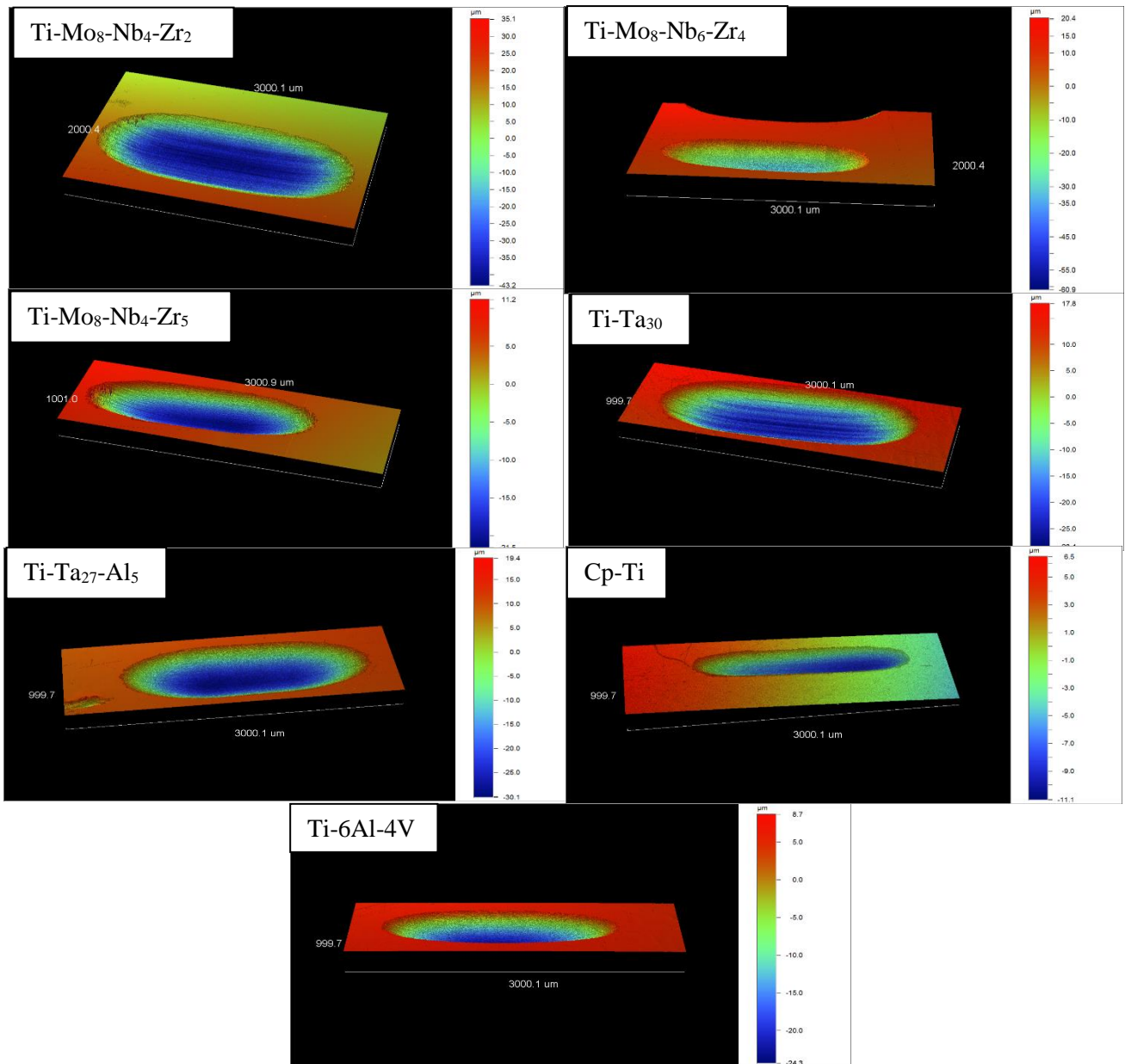


Figure 5-17: 3D images of wear track of titanium and titanium alloys fabricated in this study at a normal load of 0.25N under lubricated rubbing conditions.

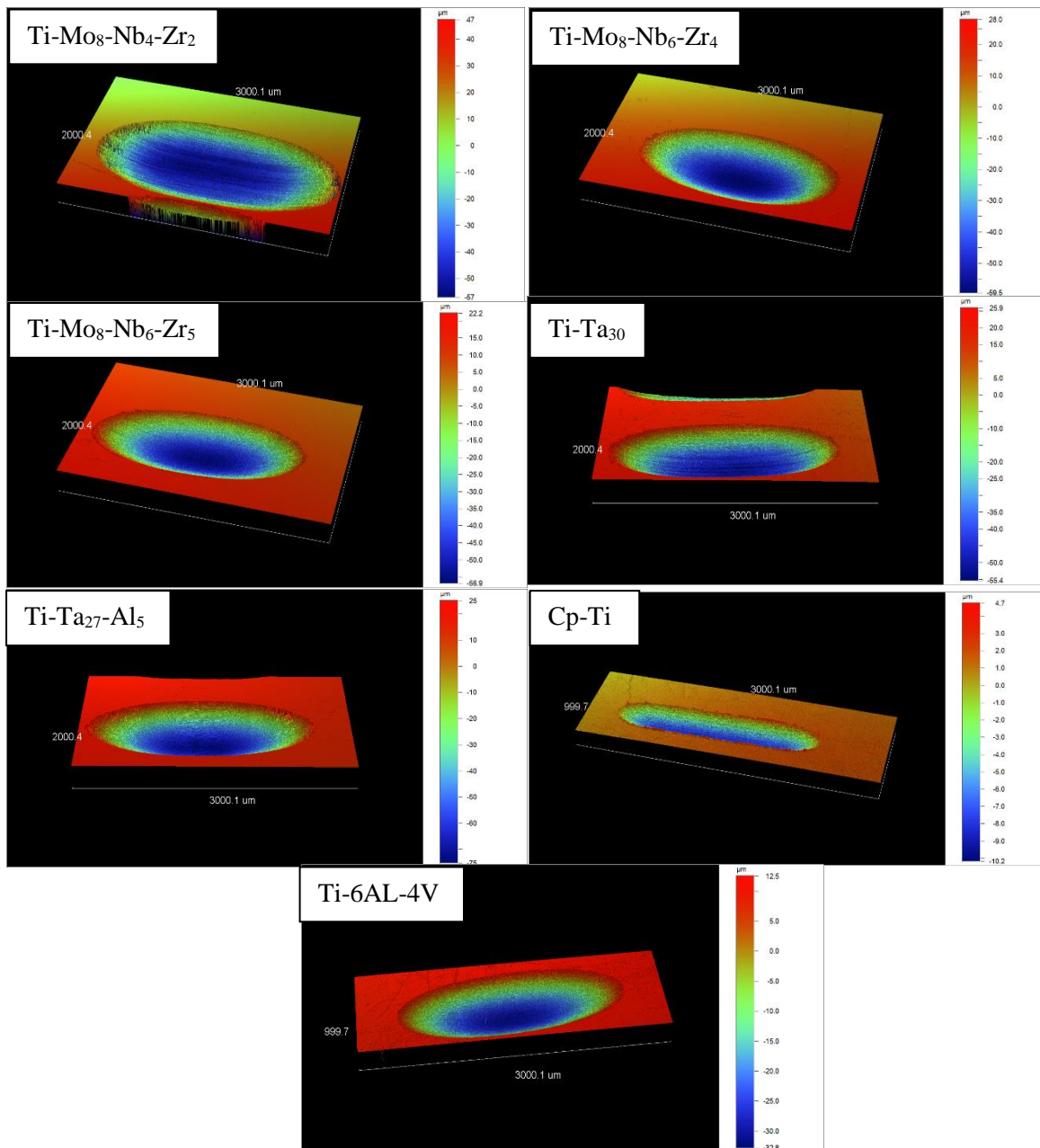


Figure 5-18: 3D images of wear track of titanium and titanium alloys fabricated in this study at a normal load of 0.5N under lubricated rubbing conditions.

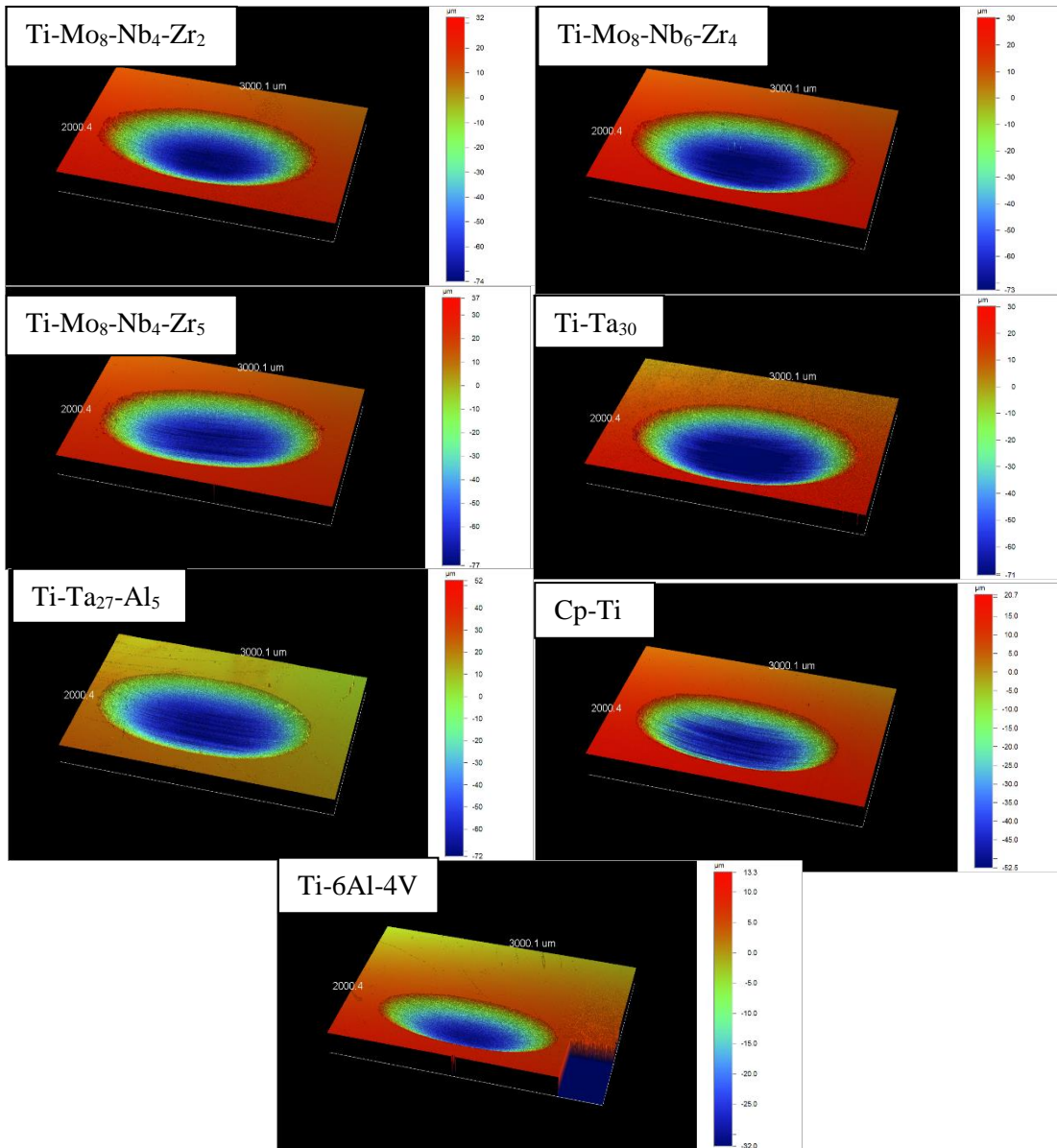


Figure 5-19: 3D images of wear track of titanium and titanium alloys fabricated in this study at a normal load of 1N under lubricated rubbing conditions.

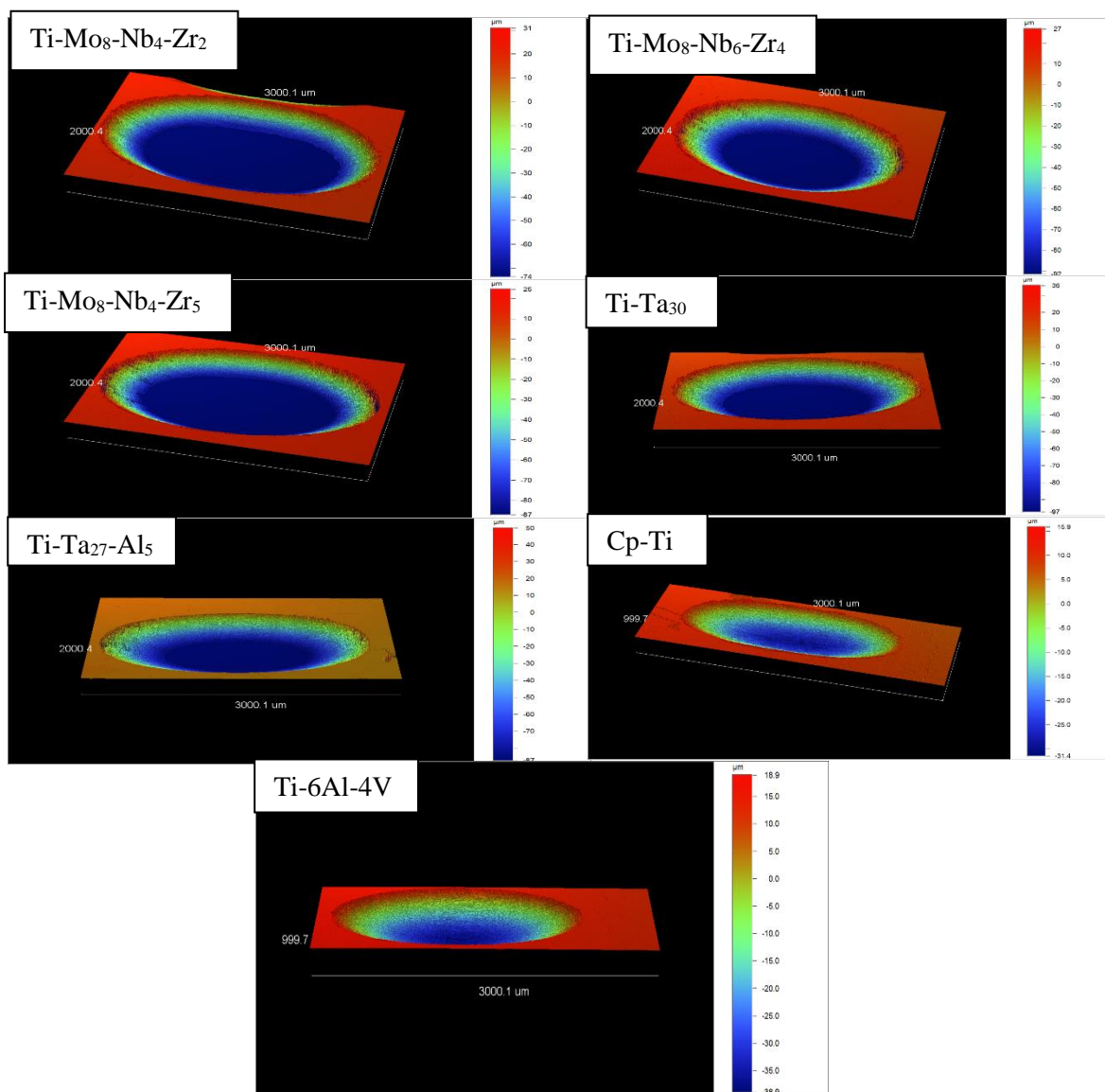


Figure 5-20: 3D images of wear track of titanium and titanium alloys fabricated in this study at a normal load of 2N under lubricated rubbing conditions.

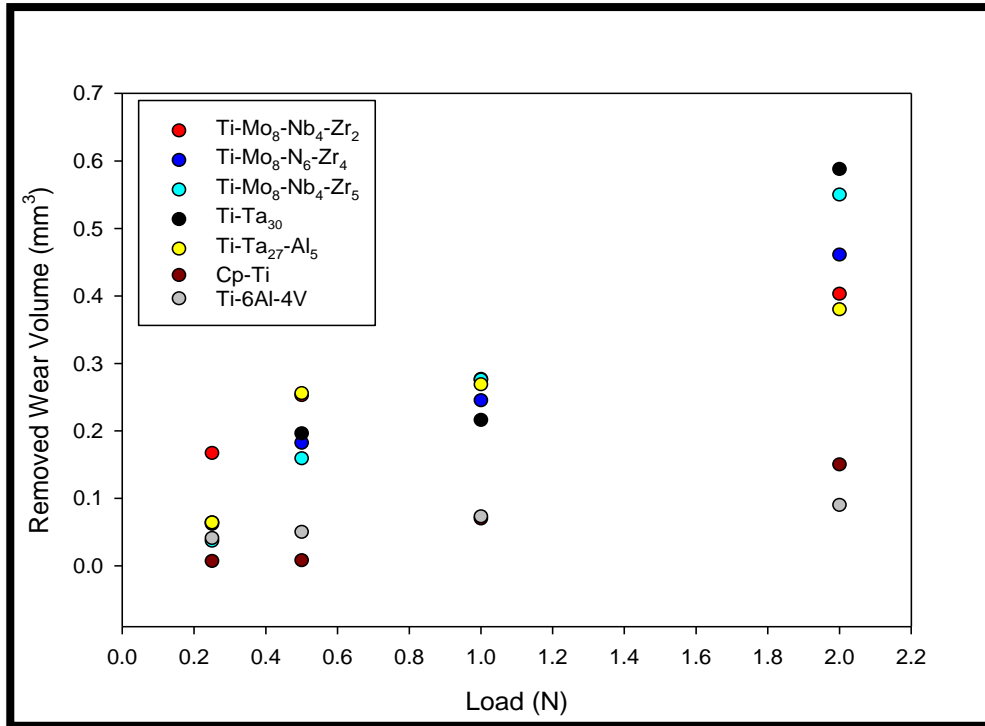


Figure 5-21: Wear volumes for titanium alloys at different loads.

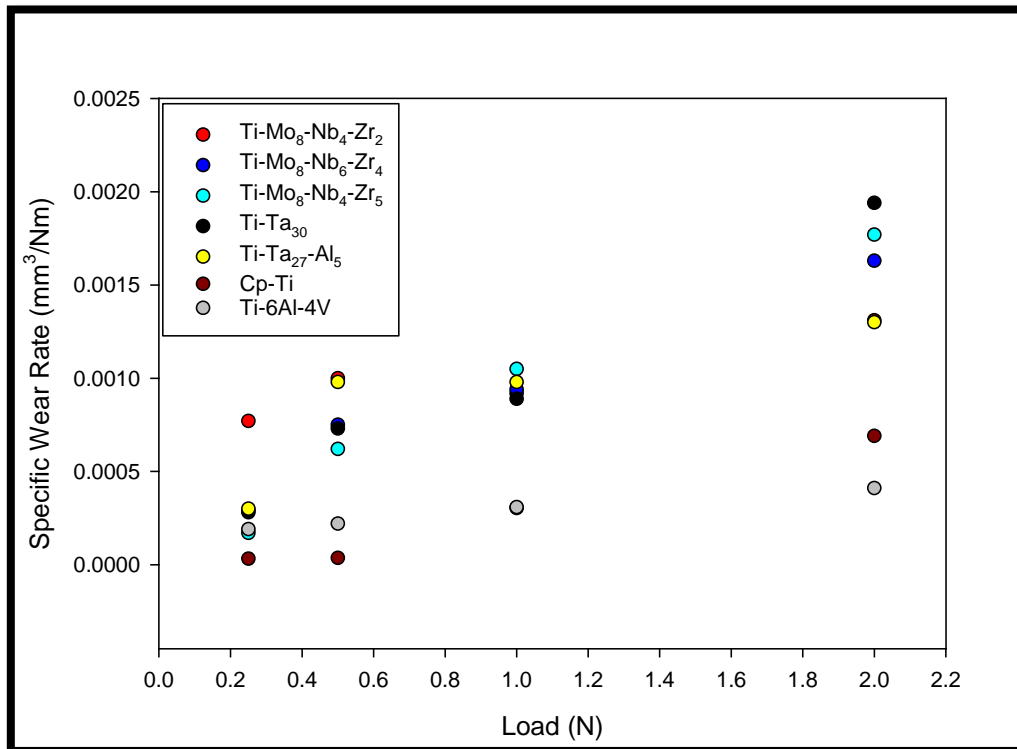


Figure 5-22: Specific wear rates of titanium alloys at different loads.

5.5 Wear Tracks Subsurface Morphology

To obtain more details about the wear mechanisms, a cross-section of the wear track was prepared by FIB with ion channelling contrast used for imaging and this was compared to a FIB section of the unworn surface. The investigated areas were in the centre of the wear track. Figure 5-23 shows an ion channelling contrast image of the bulk alloy of Ti-Ta₂₇-Al₅, while Figures 5-24 and 5-25 show ion channelling contrast images of the wear tracks formed at the β -microstructure Ti-Mo₈-Nb₄-Zr₂ under lubricated rubbing conditions at normal loads of 0.5 and 2 N respectively. Figures 5-26 and 5-27 show an ion channelling contrast image of the wear tracks formed at the $\beta+\alpha''$ -microstructure Ti-Ta₂₇-Al₅ under lubricated rubbing conditions at normal loads of 0.5 and 2N respectively. Grain refinement was observed, with the thickness of the grain refinement dependent on applied load. After increasing the load to 2N an increase in the extent of grain refinement was observed. The thickness of grain refinement at 0.5N load for the β -microstructure Ti-Mo₈-Nb₄-Zr₂ and $\beta+\alpha''$ -microstructure Ti-Ta₂₇-Al₅ was considerably less than that when the load was 2N for the β -microstructure Ti-Mo₈-Nb₄-Zr₂ and $\beta+\alpha''$ -microstructure Ti-Ta₂₇-Al₅.

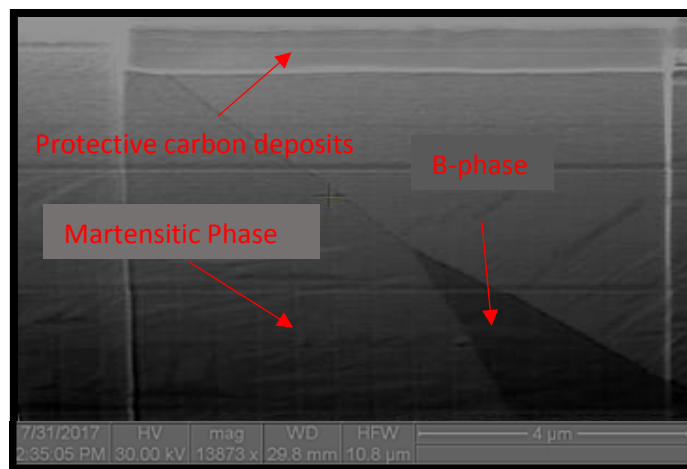


Figure 5-23 Ion channelling contrast image of bulk Ti-Ta₂₇-Al₅ alloy.

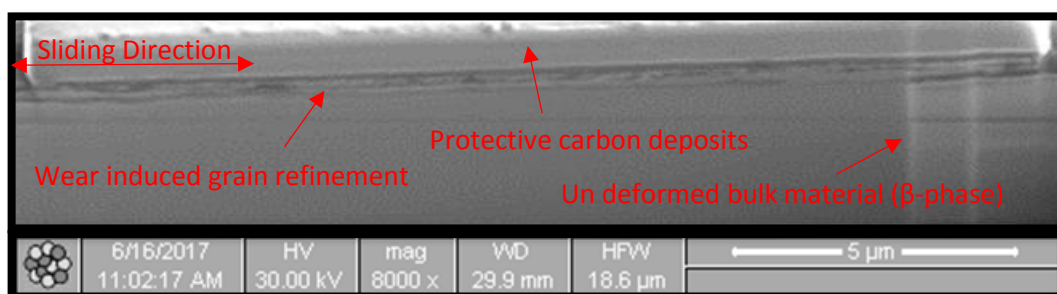


Figure 5-24 Ion channelling contrast image of a transverse cross-section of wear track formed at Ti-Mo₈-Nb₄-Zr₂ under a normal load of 0.5N.

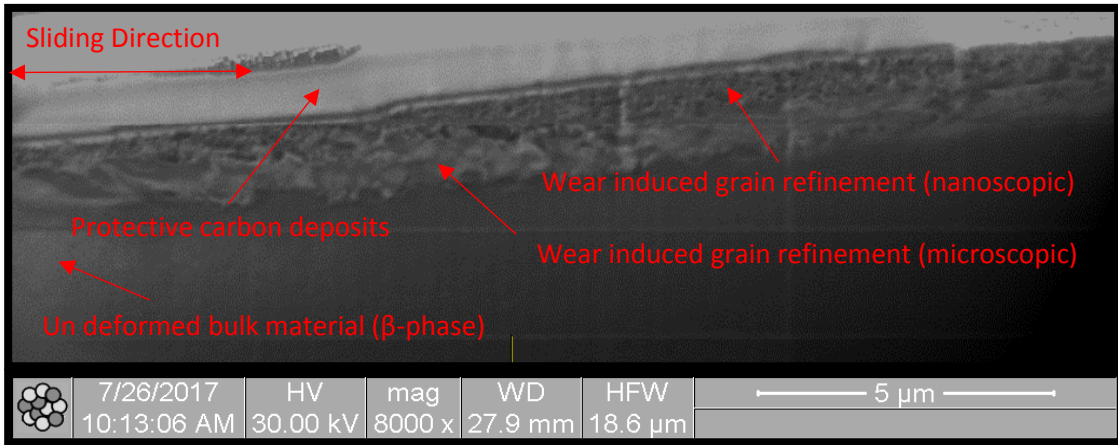


Figure 5-25 Ion channelling contrast image of a transverse cross-section of wear track formed at Ti-Mo₈-Nb₄-Zr₂ under a normal load of 2N.

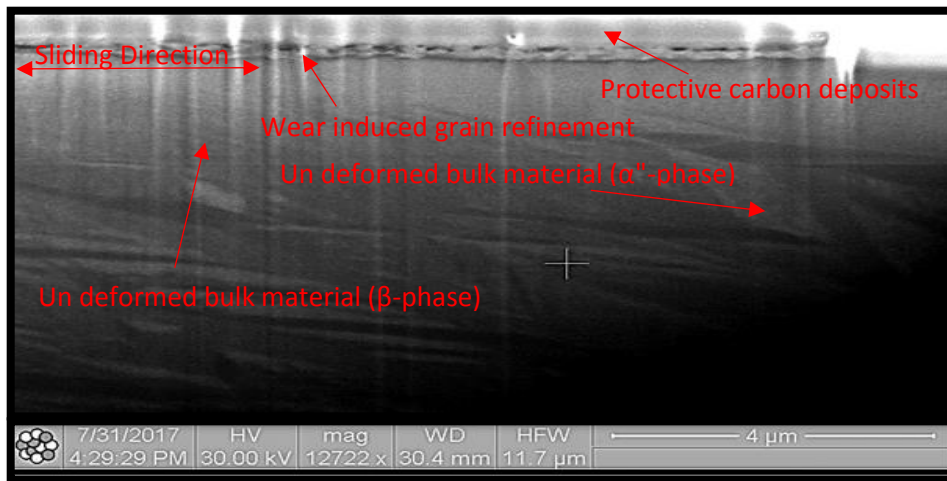


Figure 5-26 Ion channelling contrast image of a transverse cross-section of wear track formed at Ti-Ta₂₇-Al₅ under a normal load of 0.5N.

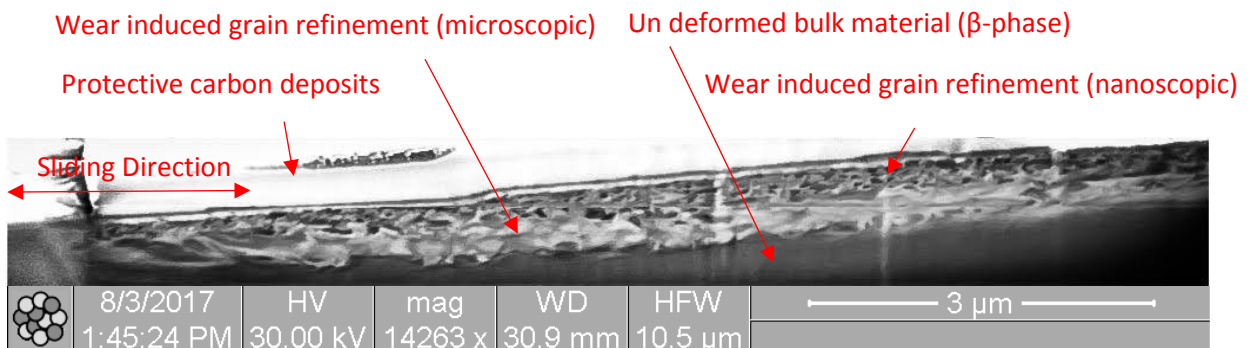


Figure 5-27 Ion channelling contrast image of a transverse cross-section of wear track formed at Ti-Ta₂₇-Al₅ under a normal load of 2N.

5.6 Summary

The investigation of tribological behavior of titanium alloys in bovine calf serum can be summarised as follows:

- The coefficient of friction and wear volume increased with load, the specific wear rate increased slightly with load, although there was no significant change.
- All alloys except the α -microstructure Cp-Ti and $\alpha+\beta$ -microstructure Ti-6Al-4V exhibited a large wear volume.
- The dominant wear mechanism was abrasive ploughing.
- The β -microstructure alloys were more susceptible to wear compared to α -microstructure Cp-Ti and $\alpha+\beta$ -microstructure Ti-6Al-4V alloys.
- No evidence of transfer from the alumina ball to the titanium alloy surface during rubbing. Also, no significant materials transfer from the titanium alloys to the alumina ball was observed.
- A carbonaceous film formed on the surface of the wear track which was believed to limit friction and wear. However, the formation of this carbonaceous layer did not appear to correlate with the alloy structure, it appeared to be more dependent on the load than the alloy composition.
- Tribological grain refinement (TGR) did occur adjacent to rubbing surface, and no evidence of twinning was observed.

The above results show that the wear and coefficient of friction correlates with alloy structure, and β -microstructure alloys are more susceptible to wear compared to α -microstructure and $\alpha+\beta$ -microstructure alloys. The surface chemistry in the wear track also plays an important role in the tribological behavior of titanium alloys.

Chapter 6 Results: Electrochemical Behaviour of Titanium Alloys

6.1 Introduction

This chapter reports the investigation into the electrochemical behaviour of the titanium-based alloys fabricated in this work, to establish which alloy has the best corrosion resistance. A comparison was made between the new alloys and Cp-Ti and Ti-6Al-4V alloys, which are used as implant materials under the same electrochemical measurements. Electrochemical tests were completed in a 25vol% bovine calf serum at $37\pm 1^\circ\text{C}$. The electrochemical tests were carried out using the open circuit potential and potentiodynamic polarisation tests. Electrochemical tests were conducted for the starting surface of the alloys, during the wear tests and after the tribocorrosion tests.

6.2 Electrochemical Behaviour of Starting Surface of Alloys

The time profiles of the open-circuit potential are presented in Fig 6-1. It should be noted that these curves are quite similar in nature for all alloys. The OCP curves of each alloy exhibit a rapid increase in potential from negative values up to steady state level after 600 seconds of immersion in bovine calf serum. This indicates that all the alloys formed a passive film and the passive film became more stable and covered the titanium alloys surface. A drop in the potential of β -microstructure Ti-Mo₈-Nb₆-Zr₄ and $\beta+\alpha''$ -microstructure Ti-Ta₂₇-Al₅ was observed at the beginning of the experiment, which then reached a stable potential value. The drop of potential in these alloys could be a result of rapid release of titanium from the alloys upon the immersion of the alloys into bovine calf serum. Average values of the OCP are given in table 6-1. By comparing the OCP values of the titanium alloys, it can be observed that the β -microstructure Ti-Ta₃₀ alloy had the most positive values, while the $\alpha+\beta$ -microstructure Ti-6Al-4V exhibited the most negative values. These results indicate the positive contribution of the alloying elements Mo, Nb, Zr and Ta in the formation of passive film on the surface of the titanium alloys.

To obtain further information on the influence of the phase composition and alloy additions on the electrochemical responses and the characteristics of the passive films of the titanium-based alloys, potentiodynamic polarization experiments were completed. The potentiodynamic curves are presented in Figure 6-2. The corresponding corrosion parameters such as corrosion potential (E_{corr}), corrosion current density (i_{corr}) and corrosion rate were obtained by the Tafel extrapolation method, while passive current density (i_{pass}) was

determined from the potentiodynamic polarization curves. The corresponding corrosion parameters are presented in Table 6-2.

As can be seen in Figure 6-2, the polarization curves for all alloys show similar corrosion characteristics, and essentially show a response that is characteristic of titanium alloys. This is related to the natural passive film of titanium oxide which formed on the surface after immersion in the bovine calf serum at $37\pm 1^\circ\text{C}$. The polarization curves of all the alloys, except the $\alpha+\beta$ microstructure Ti-6Al-4V, show four potential domains. The first one is cathodic and in this case all potentials were below the E_{corr} . The second domain is the transition from a cathodic to an anodic current, and the potential ranged around E_{corr} (-0.15 to -0.40 V). The third domain is the passive region, in which the passive film forms on the surface of the alloys. The fourth domain is the transpassive region. No evidence of an active-passive transition was observed in the $\alpha+\beta$ microstructure Ti-6Al-4V polarization curve, a large passive zone was found and continued up to 2V. The $\alpha+\beta$ Ti-6Al-4V passivated first, and the passivation potential of these alloys was ~ 0.01 V vs. Ref. Among the other alloys, the β - microstructure Ti-Ta₃₀ passivated last and the passivation potential was ~ 1.1 V versus Ref.

The β -microstructure Ti-Mo₈-Nb₆-Zr₄ had the highest current density in the passive region (0.257 V to 0.348 V), while the lowest current density was obtained from α -microstructure Ti-6Al-4V in the passive region (0.019 V to 1.929 V). There was no evidence of a breakdown of the passive films related to the initiation of localized corrosion in all the alloys. This result was confirmed by optical microscopy and secondary electron microscopy of the surface after potentiodynamic tests. Optical microscopy investigations showed that there were no crevice and pit damage on the surface of any of the alloys after scanning to 2V vs Ref. Secondary electron images of the surface of the alloys after potentiodynamic tests is shown in Figure 6-3. No pits or any evidence of corrosion could be detected in the secondary electron images in any of the alloys. Small dark spots were observed that are probably dislocation etch pits induced during sample preparation, which are often observed on the titanium alloys during preparation.

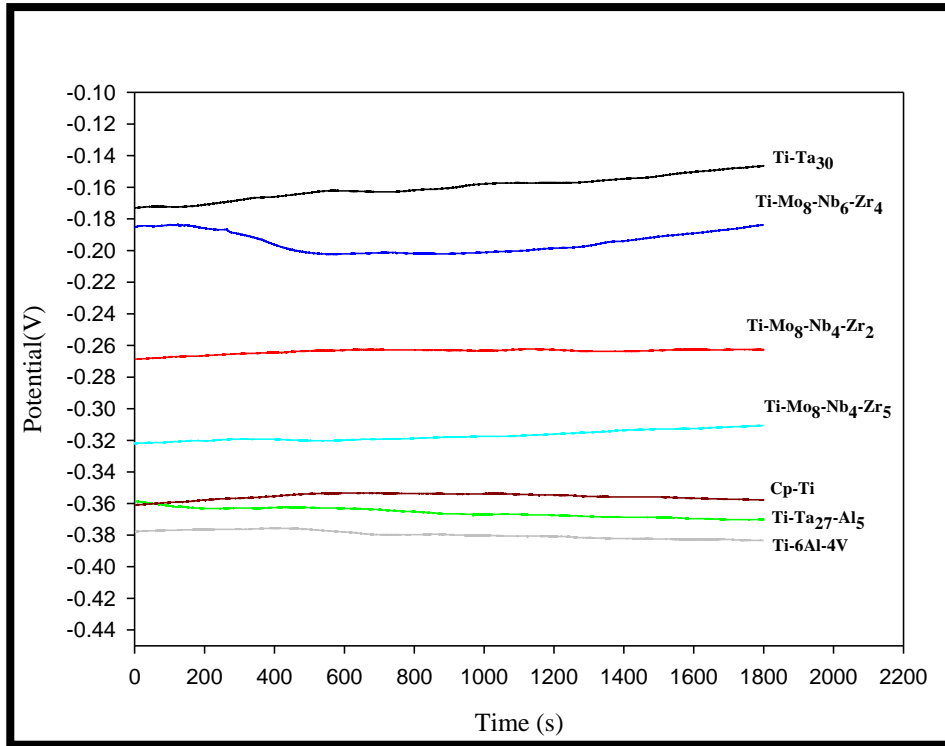


Figure 6-1 Variation of OCP with time for titanium alloys in bovine calf serum solution.

Table 6-1 The average OCP values extracted from the figure 6-1

ALLOYS		OCP V
Ti-Mo ₈ -Nb ₄ -Zr ₂	β	-0.26
Ti-Mo ₈ -Nb ₆ -Zr ₄	β	-0.19
Ti-Mo ₈ -Nb ₄ -Zr ₅	β	-0.31
Ti-Ta ₃₀	β	-0.16
Ti-Ta ₂₇ -Al ₅	$\beta + \alpha''$	-0.36
Cp-Ti	α	-0.35
Ti-6Al-4V	$\alpha + \beta$	-0.37

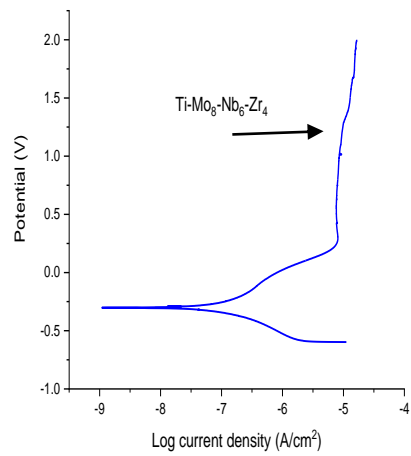
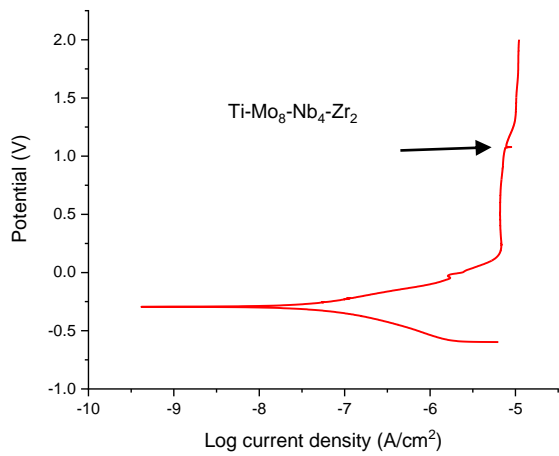
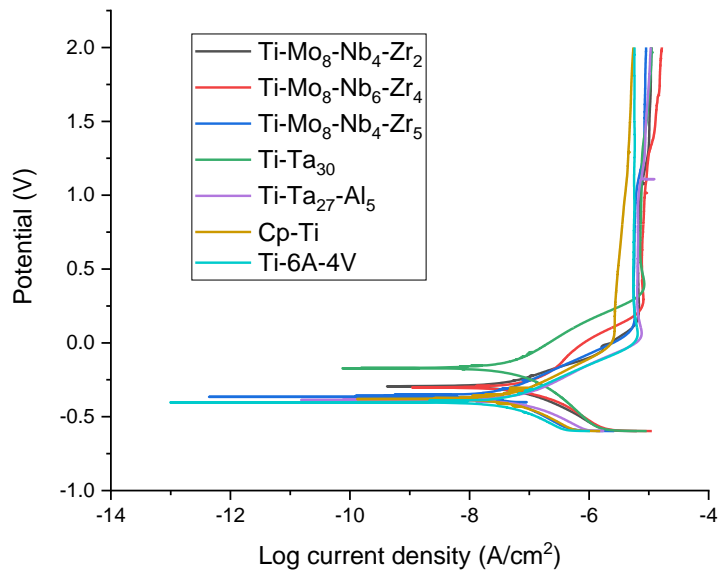


Figure 6-2 Potentiodynamic polarization curves of titanium alloys in new-born caff serum solution, the arrows indicates the formation of new passive region.

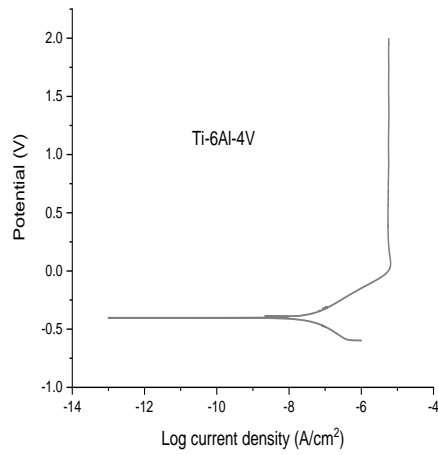
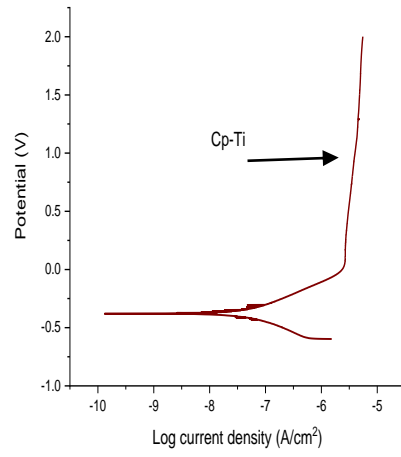
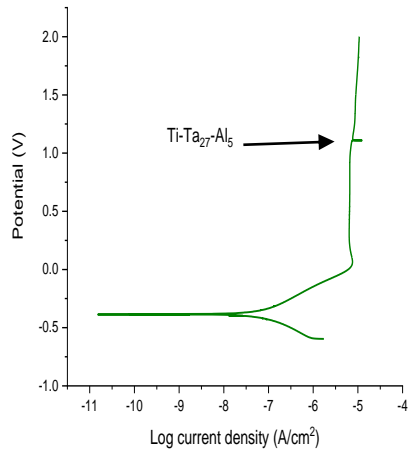
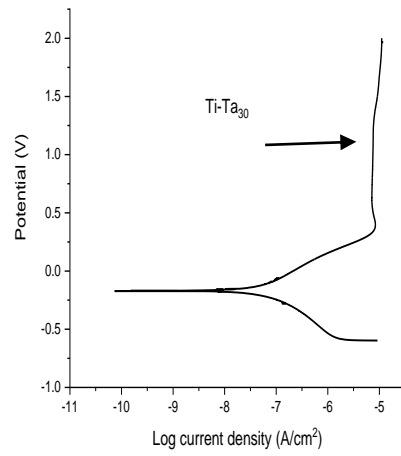
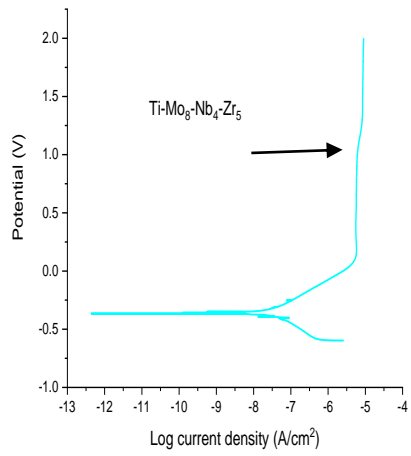


Figure 6-2: continued

Table 6-2 Electrochemical parameters of titanium alloys from potentiodynamic curves.

ALLOYS		E_{Corr} (V)	i_{Corr} ($A \cdot cm^{-2}$) $\cdot 10^{-8}$	$E_{pass.}$ V	$i_{pass.}$ A	Corrosion Rate (mmPY)	Anodic Beta (mV)	Cathodic Beta (mV)
Ti-Mo ₈ -Nb ₄ -Zr ₂	β	-0.29	4.42	0.16	$1 \cdot 10^{-5}$	0.00037	139.52	125.33
Ti-Mo ₈ -Nb ₆ -Zr ₄	β	-0.29	9.80	0.25	$1.2 \cdot 10^{-5}$	0.00082	263.33	194.8
Ti-Mo ₈ -Nb ₄ -Zr ₅	β	-0.35	3.31	0.11	$8.39 \cdot 10^{-6}$	0.00028	163.47	159.53
Ti-Ta ₃₀	β	-0.16	2.58	0.5	$1.17 \cdot 10^{-5}$	0.00021	133.38	112.12
Ti-Ta ₂₇ -Al ₅	$\beta + \alpha''$	-0.38	6.87	0.14	$1.06 \cdot 10^{-5}$	0.00059	169.76	146.85
Cp-Ti	α	-0.37	6.23	0.03	$4.03 \cdot 10^{-6}$	0.00054	236.94	215.73
Ti-6Al-4V	$\alpha + \beta$	-0.40	5.90	0.01	$9.3 \cdot 10^{-6}$	0.00049	225.34	228.18

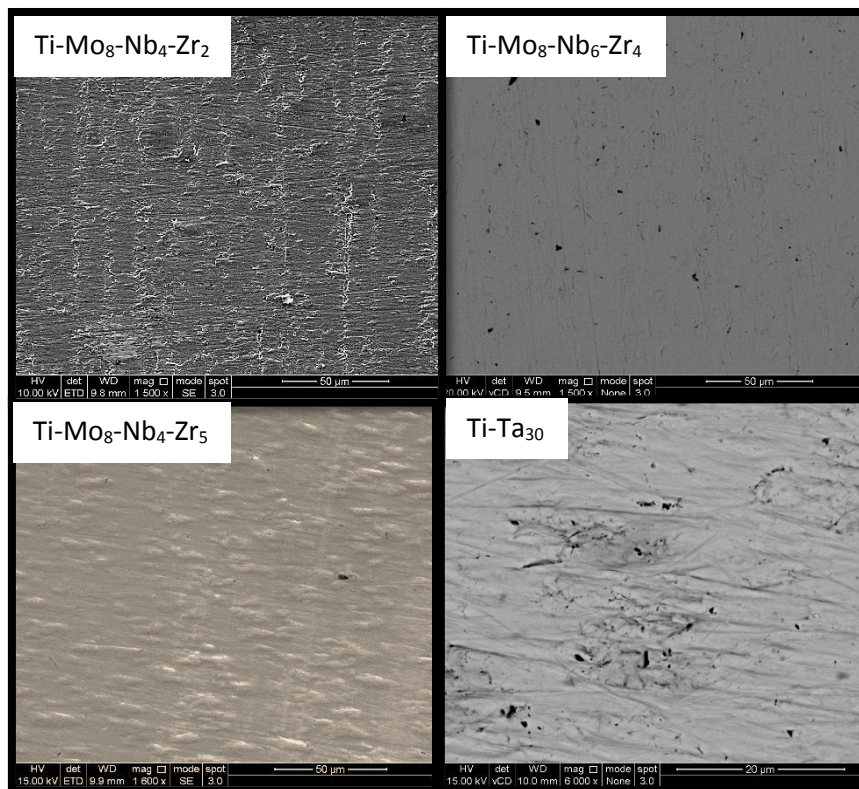


Figure 6-3 The surface morphology of titanium alloys after potentiodynamic polarization.

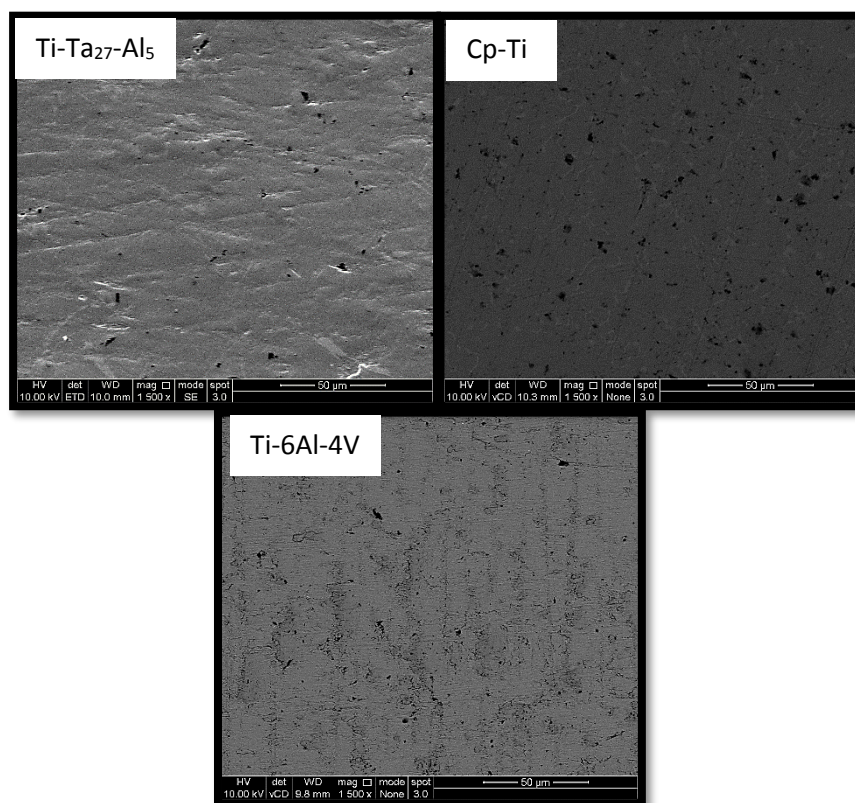


Figure 6-3 Continued

6.3 Electrochemical Behaviour during and after Rubbing

To characterize the electrochemical behaviour of the alloys in a solution that simulated the physiological media during and after rubbing, the Tafel extrapolation analysis method using both anodic and cathodic branches of the polarization curves was carried out over potential ranges relative to the OCP of -0.25mV vs OCP to 0.25mV vs OCP . All tests were completed during rubbing under OCP conditions and after rubbing under OCP, cathodic and anodic potentiostatic tests. The starting surface without rubbing of all alloys was analysed using the same conditions for comparison.

Figure 6-4 shows the Tafel extrapolation analysis curves of the titanium alloys without rubbing. The corresponding electrochemical parameters were measured using the Tafel extrapolation analysis method are listed in Table 6-3. The lowest i_{CORR} is shown by the β -microstructure Ti-Ta₃₀, while the β -microstructure Ti-Mo₈-Nb₄-Zr₂ shows the highest. This can be related to the formation of Ta₂O₅ which resulted in improved corrosion resistance of the Ti-Ta₃₀ alloy due to the modification of the passive TiO₂ oxide by the more stable passive oxide Ti₂O₅ [204].

Figure 6-5 shows the Tafel extrapolation analysis curves of titanium alloys during rubbing under OCP conditions. No distinct cathodic region was observed in the Tafel curves obtained from any of the alloys during rubbing under OCP conditions. Compared with static corrosion, the Tafel curves during rubbing had distinct and major fluctuations. These results indicate that the wear accelerated the corrosion due to depassivation of worn areas, and friction was not stable (distinct and major fluctuations compared with static corrosion are seen in Figures 6-4 and 6-5).

Figures 6-6 through to 6-8 show the Tafel extrapolation analysis curves of titanium alloys after rubbing under OCP, cathodic and anodic potentiostatic conditions respectively, with corresponding electrochemical parameters listed in Tables 6-4 through to 6-6. The i_{corr} increased after rubbing and E_{corr} shifted towards lower or higher values depending on the alloy and electrochemical condition. The lowest i_{corr} is shown by β -microstructure Ti-Mo₈-Nb₄-Zr₂, while β -microstructure Ti-Mo₈-Nb₄-Zr₅ shows the highest i_{corr} after rubbing under OCP conditions. The opposite was observed after rubbing under cathodic conditions. The lowest i_{corr} was shown by the β -microstructure Ti-Mo₈-Nb₄-Zr₂, while the α -microstructure Cp-Ti showed the highest i_{corr} after rubbing under anodic conditions. Rubbing under anodic conditions shifts the E_{corr} towards lower values. The opposite was observed after rubbing under cathodic conditions. After rubbing under OCP, the E_{corr} shifts toward lower or higher values depending on the alloy. During rubbing the titanium alloy's surface suffered the same wear mechanism. Consequently, the electrochemical behaviour of titanium alloys was attributed to the ability of the alloys to recover their passive film, the amount of damage on the surface caused by the wear mechanism (wear track depth, length, and total materials loss), and the properties of the newly formed passive film compared with a naturally formed passive film present on titanium alloys before the rubbing. However, repassivation was not instantaneous and the alloy needed a longer rest time to completely recover the passive film. Therefore, when the rubbing stopped, the alloys cannot completely recover their passive film, and some uncovered bare areas will exist on the worn surface wear track. This leads to the formation of galvanic coupling between re-passivated areas, which acts as an anode, and de-passivated areas (not completely covered with passive film) leading to a decrease in the corrosion resistance of titanium alloys.

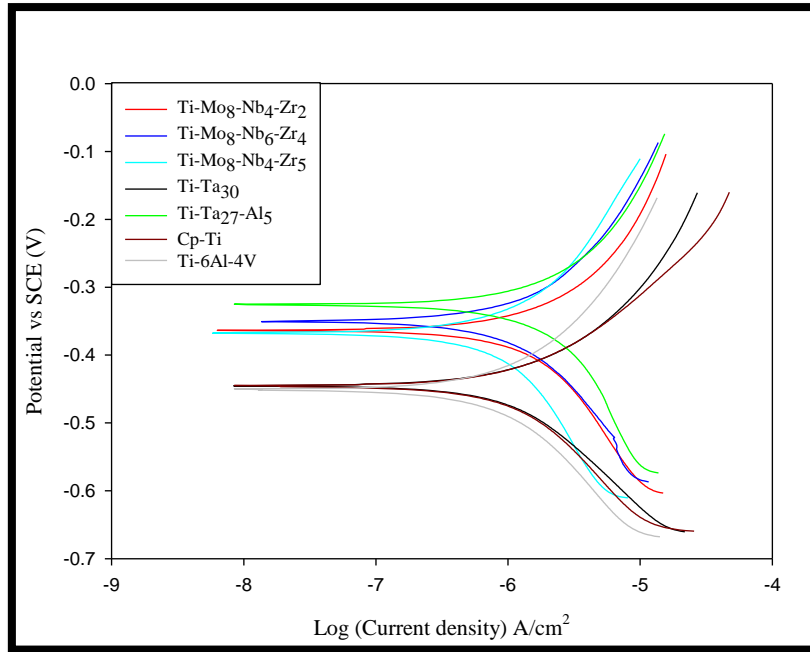


Figure 6-4 Tafel curves of titanium alloys

Table 6-3 Electrochemical parameters of titanium alloys from Tafel plot

ALLOYS		E_{Corr} (V)	i_{corr} ($\text{A}\cdot\text{cm}^{-2}$) $\cdot 10^{-6}$	Corrosion Rate (mmPY)	Anodic Beta (mV)	Cathodic Beta (mV)
Ti-Mo ₈ -Nb ₄ -Zr ₂	β	-0.12	6.25	0.05	320.23	730.19
Ti-Mo ₈ -Nb ₆ -Zr ₄	β	-0.11	4.28	0.03	322.65	425.63
Ti-Mo ₈ -Nb ₄ -Zr ₅	β	-0.13	4.70	0.03	395.28	113.80
Ti-Ta ₃₀	β	-0.21	2.06	0.01	151.71	205.80
Ti-Ta ₂₇ -Al ₅	$\beta + \alpha''$	-0.09	4.05	0.033	244.18	356.52
Cp-Ti	α	-0.21	2.66	0.02	170.00	285.07
Ti-6Al-4V	$\alpha + \beta$	-0.21	2.63	0.02	273.96	327.83

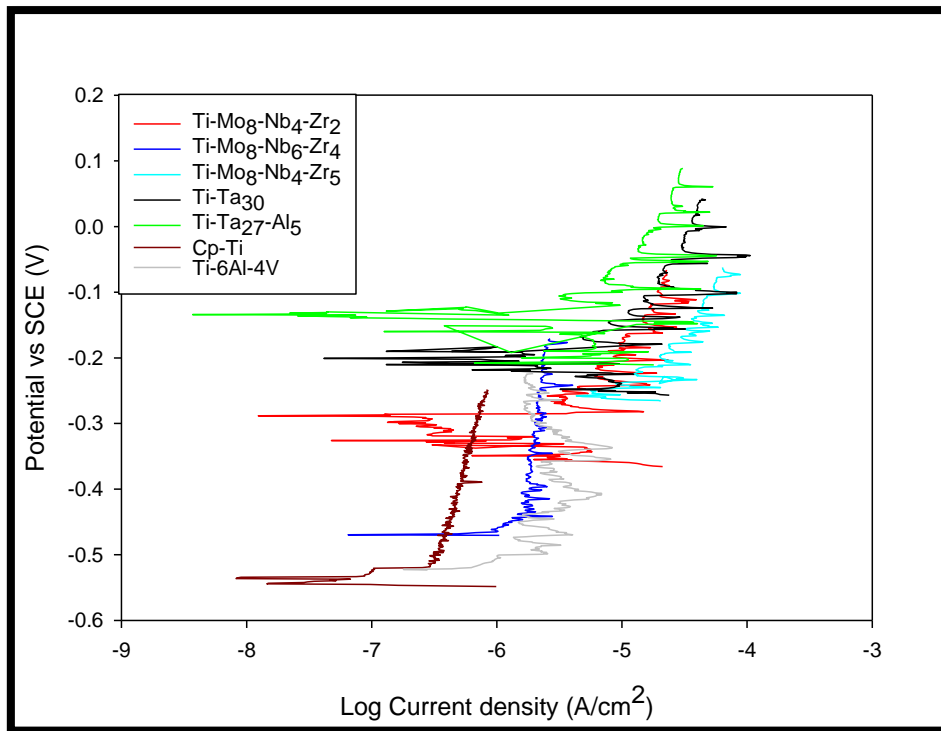


Figure 6-5 Tafel curves of titanium alloys during rubbing under OCP conditions.

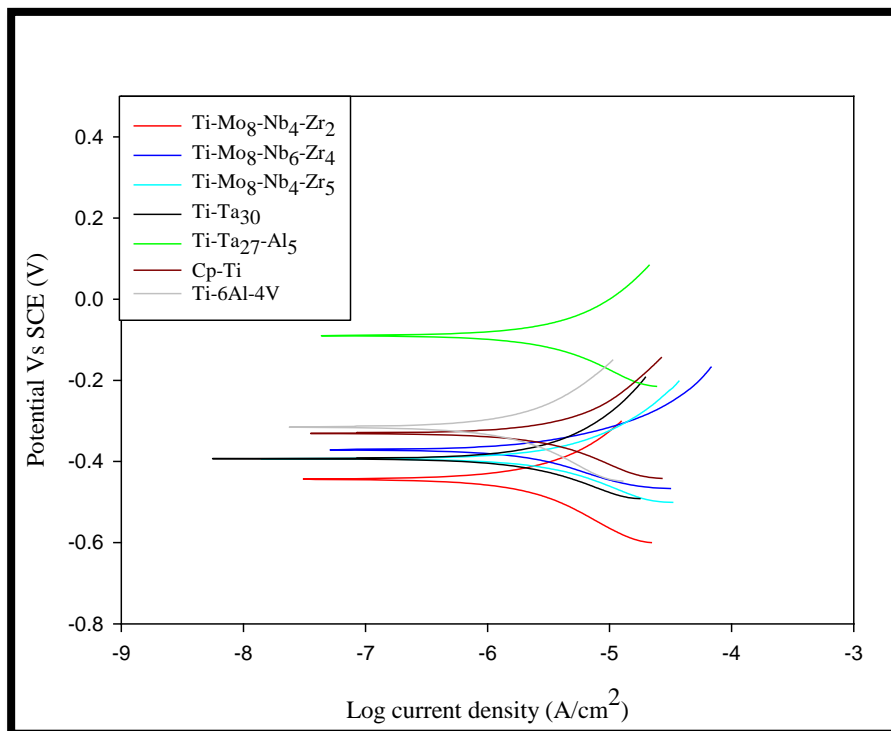


Figure 6-6 Tafel curves of titanium alloys after tribocorrosion tests under OCP rubbing conditions.

Table 6-4 Electrochemical parameters of titanium and titanium alloys after tribocorrosion tests under OCP rubbing conditions.

ALLOYS		E_{Corr} (V)	i_{corr} ($A \cdot cm^{-2}$) $\cdot 10^{-6}$	Corrosion Rate (mmPY)	Anodic Beta (mV)	Cathodic Beta (mV)
Ti-Mo ₈ -Nb ₄ -Zr ₂	β	-0.20	3.53	0.03	171.31	183.84
Ti-Mo ₈ -Nb ₆ -Zr ₄	β	-0.13	6.19	0.05	130.98	177.29
Ti-Mo ₈ -Nb ₄ -Zr ₅	β	-0.15	7.72	0.06	195.76	169.08
Ti-Ta ₃₀	β	-0.15	6.37	0.05	267.30	182.49
Ti-Ta ₂₇ -Al ₅	$\beta + \alpha''$	-0.09	5.14	0.04	240.84	209.7
Cp-Ti	α	-0.09	4.51	0.04	174.06	143.11
Ti-6Al-4V	$\alpha + \beta$	-0.08	5.00	0.04	297.36	266.62

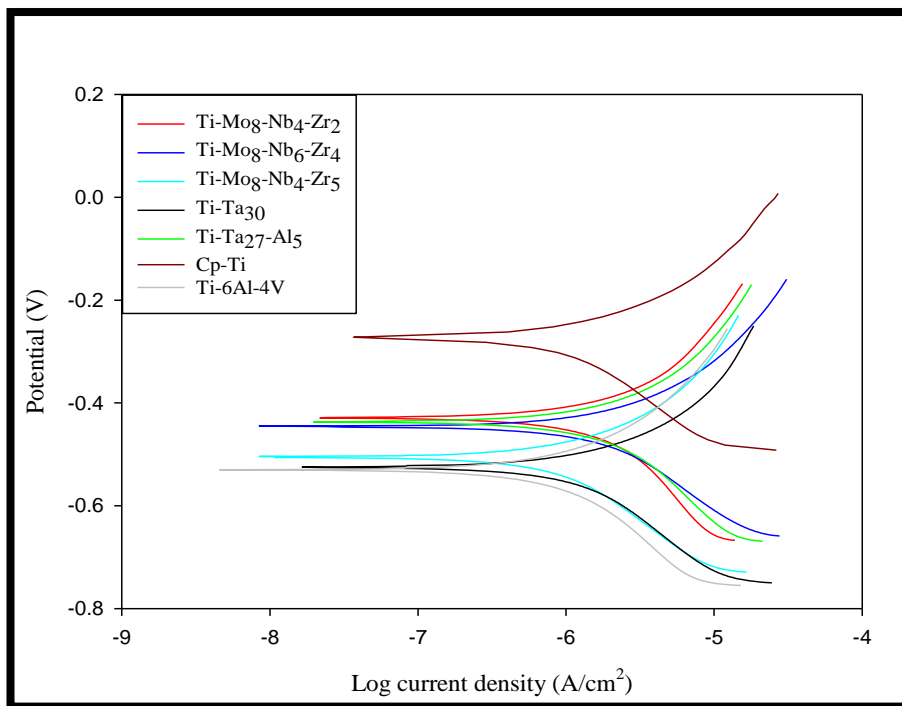


Figure 6-7 Tafel curves of titanium alloys after tribocorrosion tests under cathodic potentiostatic rubbing conditions.

Table 6-5 Electrochemical parameters of titanium alloys after tribocorrosion tests under cathodic potentiostatic rubbing conditions.

ALLOYS		E_{Corr} (V)	i_{corr} ($A \cdot cm^{-2}$) $\cdot 10^{-6}$	Corrosion Rate (mmPY)	Anodic Beta (mV)	Cathodic Beta (mV)
Ti-Mo ₈ -Nb ₄ -Zr ₂	β	-0.19	8.63	0.07	417	10101
Ti-Mo ₈ -Nb ₆ -Zr ₄	β	-0.21	5.90	0.04	234.88	351.29
Ti-Mo ₈ -Nb ₄ -Zr ₅	β	-0.26	1.00	0.008	130.63	176.96
Ti-Ta ₃₀	β	-0.29	3.77	0.03	221.03	429.84
Ti-Ta ₂₇ -Al ₅	$\beta + \alpha''$	-0.20	7.44	0.06	373.28	596.81
Cp-Ti	α	-0.30	2.75	0.03	272.06	244.05
Ti-6Al-4V	$\alpha + \beta$	-0.29	2.71	0.02	265.42	393.81

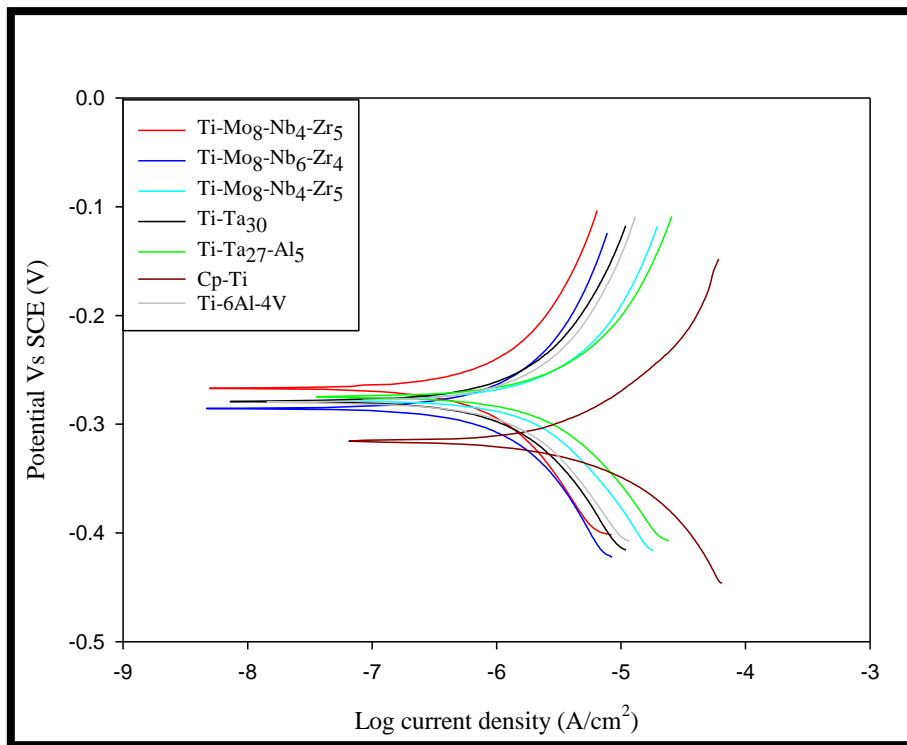


Figure 6-8 Tafel curves of titanium alloys after tribocorrosion tests under anodic potentiostatic rubbing conditions.

Table 6-6 Electrochemical parameters of titanium and titanium alloys after tribocorrosion tests under anodic potentiostatic rubbing conditions.

ALLOYS		E_{Corr} (V)	i_{corr} ($A.cm^{-2}$) $*10^{-6}$	Corrosion Rate (mmPY)	Anodic Beta (mV)	Cathodic Beta (mV)
Ti-Mo ₈ -Nb ₄ -Zr ₂	β	-0.03	4.64	0.03	396.27	358.76
Ti-Mo ₈ -Nb ₆ -Zr ₄	β	-0.05	5.63	0.04	394.08	358.75
Ti-Mo ₈ -Nb ₄ -Zr ₅	β	-0.04	6.18	0.05	199.49	218.56
Ti-Ta ₃₀	β	-0.04	5.02	0.04	277.49	274.45
Ti-Ta ₂₇ -Al ₅	$\beta + \alpha''$	-0.03	5.42	0.04	164.49	160.87
Cp-Ti	α	-0.08	9.94	0.08	150.37	119.96
Ti-6Al-4V	$\alpha + \beta$	-0.04	6.73	0.05	312.13	312.71

6.4 Summary

In this chapter the electrochemical behaviour of titanium alloys before, during rubbing and after rubbing was investigated. The results are summarised as follows:

- A stabilization of the oxide layer was achieved within 30mins.
- The alloying elements and microstructure hardly influenced the OCP values of titanium alloys in bovine calf serum.
- All β -microstructure alloys exhibited spontaneous passivity and very low corrosion current density in the bovine calf serum, which is attributed to the passive film formation of a mixture of a mixture of MO_2 , Nb_2O_5 , ZrO_2 , Ta_2O_5 and TiO_2 on the Ti-Mo-Nb-Zr and Ti-Ta alloys.
- No breakdown potential was identified in potentiodynamic polarization curves for the tested potential range, and no pits or any evidence of corrosion could be detected on the surface of alloys after potentiodynamic tests.
- No distinct cathodic region was observed in the Tafel curves obtained from any of the alloys during rubbing at OCP conditions.
- The wear accelerated the corrosion due to depassivation of worn areas.

The above results indicate a stable passive behaviour and alloys exhibit a passive oxide in the bovine calf serum. The oxide spontaneously developed at the surface of titanium alloys upon immersion in the bovine calf serum exhibits passivation characteristics. The

role of a stable passive layer during rubbing in increasing or decreasing the wear or corrosion resistance will be investigated in the next chapter.

Chapter 7 Results: Tribocorrosion Behaviour of Titanium Alloys

7.1 Introduction

This chapter reports the investigation into the tribocorrosion behaviour of the titanium-based alloys in a 25% vol% bovine calf serum solution. All the tests were completed at $37\pm 1^\circ\text{C}$ under aerated conditions. The friction coefficient, open circuit potential, cathodic and anodic current changes were measured in situ as a function of time. A comparison was also made between these alloys with the α -microstructure Cp-Ti and $\alpha+\beta$ - microstructure Ti-6Al-4V alloys, which are used as implant materials. The wear scar characteristics were investigated using SEM, EDX, 3D optical microscope, focused ion beam (FIB) and Raman spectrometry.

7.2 Tribocorrosion at Open Circuit Potential

7.2.1 Sliding Friction Response

The evaluation of the friction coefficient and open circuit potential as a function of testing time in 25% vol bovine calf serum at $37\pm 1^\circ\text{C}$ are shown in Figures 7-1 through to 7-7. The perturbation in all figures half way through sliding is a result of an undertaking a Tafel test (presented later). The behaviour shown by Figures 7-1 and 7-7 are an indication of the reproducibility of the tests. After an initial running period, the corrosion potential of all titanium alloys decreased, and this is related to depassivation. The lowest OCP value was obtained from the α -microstructure Cp-Ti followed by the $\alpha+\beta$ microstructure Ti-6Al-4V, β -microstructure Ti-Ta₃₀, β -microstructure Ti-Mo₈-Nb₄-Zr₂, β -microstructure Ti-Mo₈-Nb₆-Zr₄, $\beta+\alpha''$ -microstructure Ti-Ta₂₇-Al₅, and β -microstructure Ti-Mo₈-Nb₄-Zr₅. After a short time, the corrosion potential of all the alloys became steady. In general, the noblest OCP was recorded for the β -phase Ti-Mo₈-Nb₄-Zr₅ followed by β -phase Ti-Mo₈-Nb₆-Zr₄, β -phase Ti-Mo₈-Nb₄-Zr₂, β -phase Ti-Ta₃₀, Ti-Ta₂₇-Al₅, α -phase Cp-Ti, and $\beta+\alpha$ phase Ti-6Al-4V. At the end of the rubbing, the open circuit potential OCP rises again, which is related to the spontaneous regrowth of the superficial passive layer.

Figure 7-8 shows the average values of friction coefficient of each alloy with average potential values during rubbing. Typically, steady state was established after a run-in period. The average value of friction coefficients varies considerably between 0.25 and 0.36, and there is no strong evidence that an alloy microstructure/composition effect can be observed. Additionally, the potential during rubbing showed large fluctuations, therefore, no clear alloy

microstructure effect can be extracted. The α -microstructure Cp-Ti and $\alpha+\beta$ microstructure Ti-6Al-4V alloys exhibited the lowest mean friction coefficient values among the others. In contrast the $\alpha''+\beta$ microstructure Ti-Ta₂₇-Al₅ alloy had the highest mean friction coefficient values.

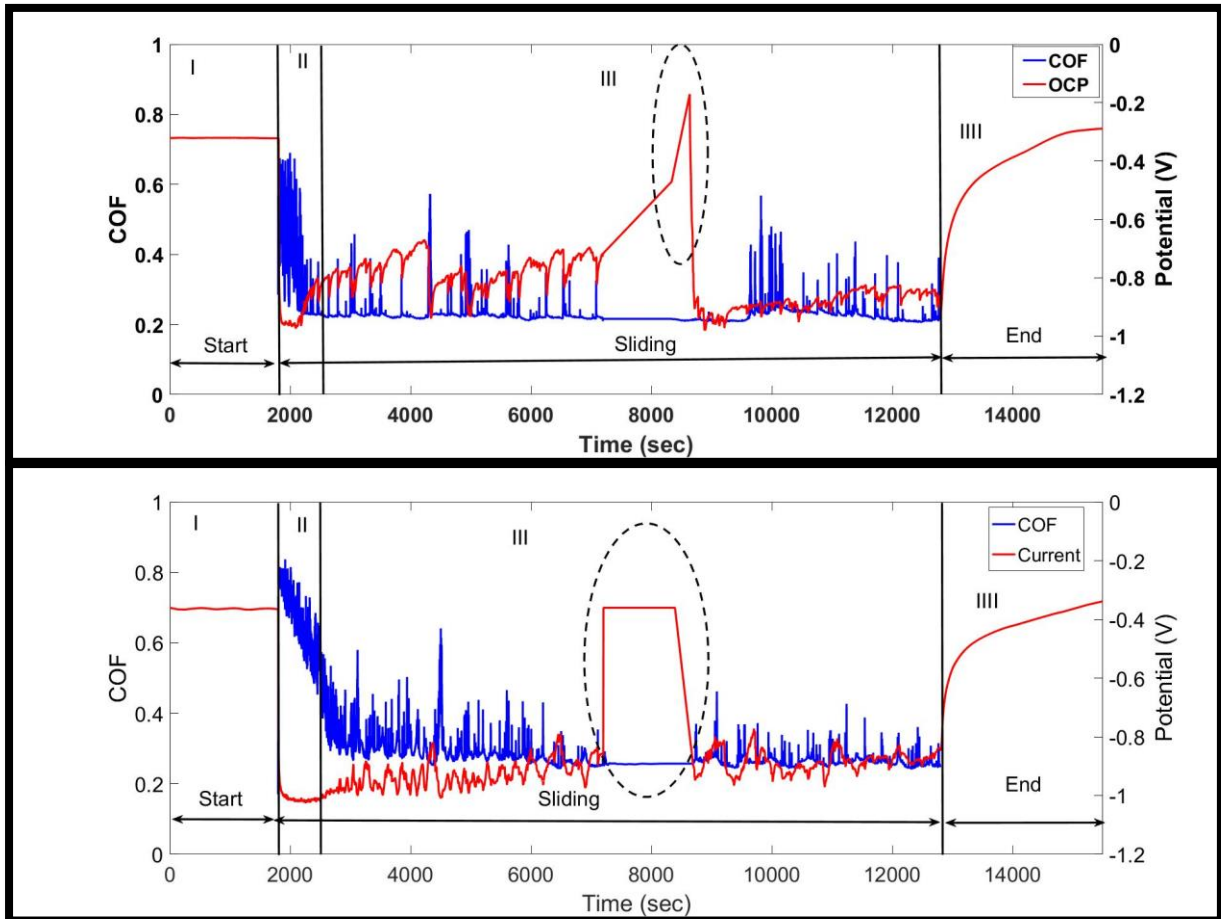


Figure 7-1: The evolution of the coefficient of friction and the open circuit potential of Ti-Mo₈-Nb₆-Zr₄ under OCP-rubbing conditions. The two graphs show the repeatability of the same test.

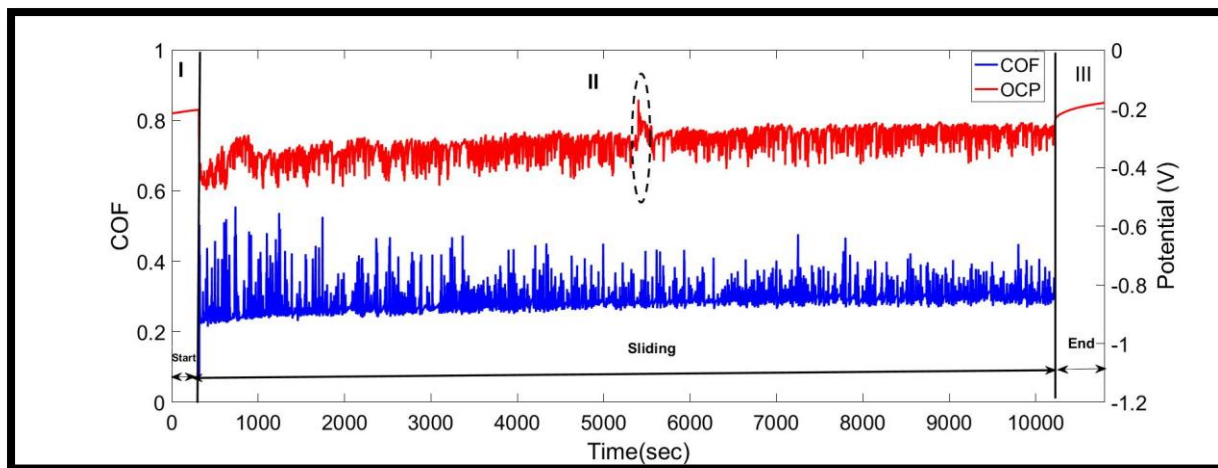


Figure 7-2: The evolution of the coefficient of friction and the open circuit potential of Ti-Mo₈-Nb₄-Zr₂ under OCP-rubbing conditions.

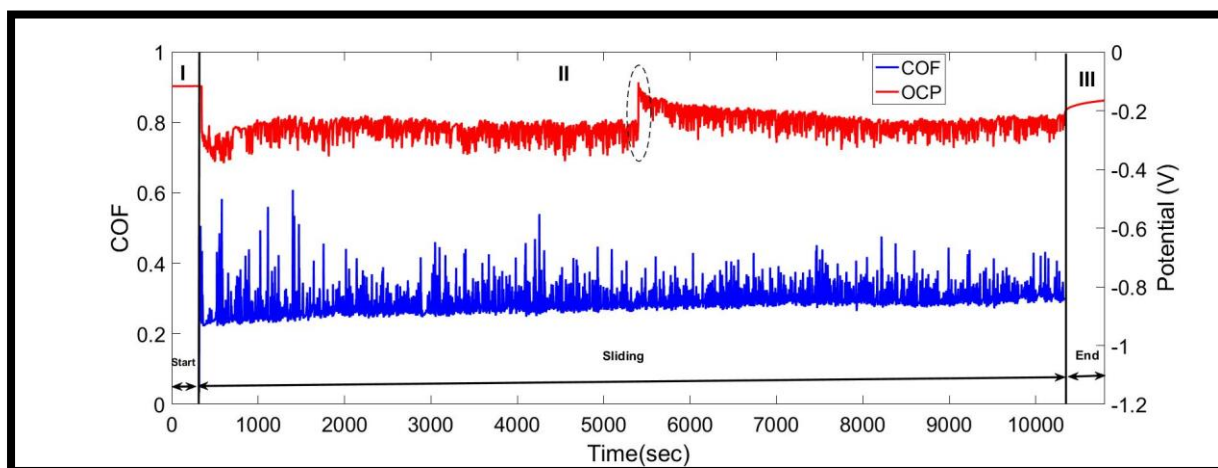


Figure 7-3: The evolution of the coefficient of friction and the open circuit potential of Ti-Mo₈-Nb₄-Zr₅ under OCP-rubbing conditions.

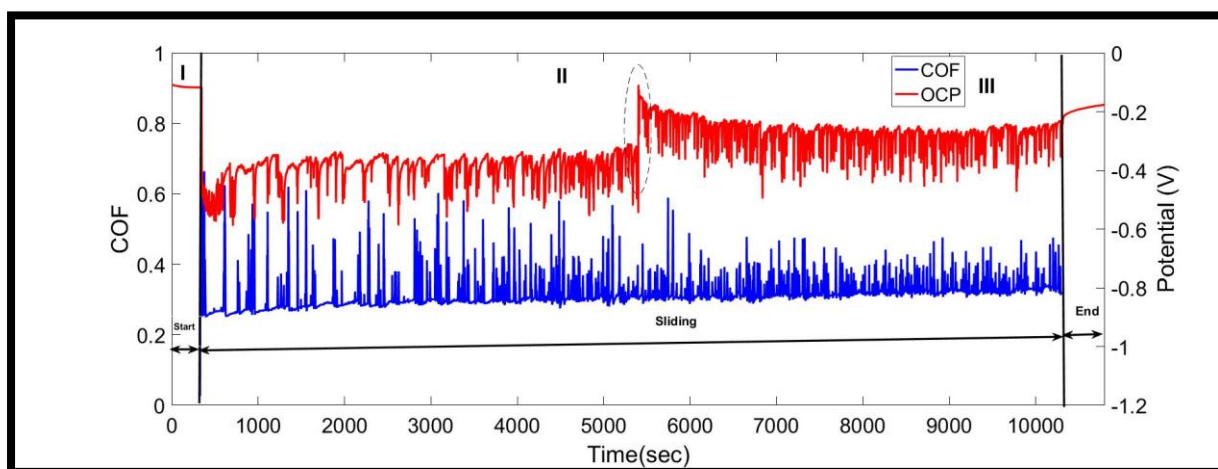


Figure 7-4: The evolution of the coefficient of friction and the open circuit potential of Ti-Ta₃₀ under OCP-rubbing conditions.

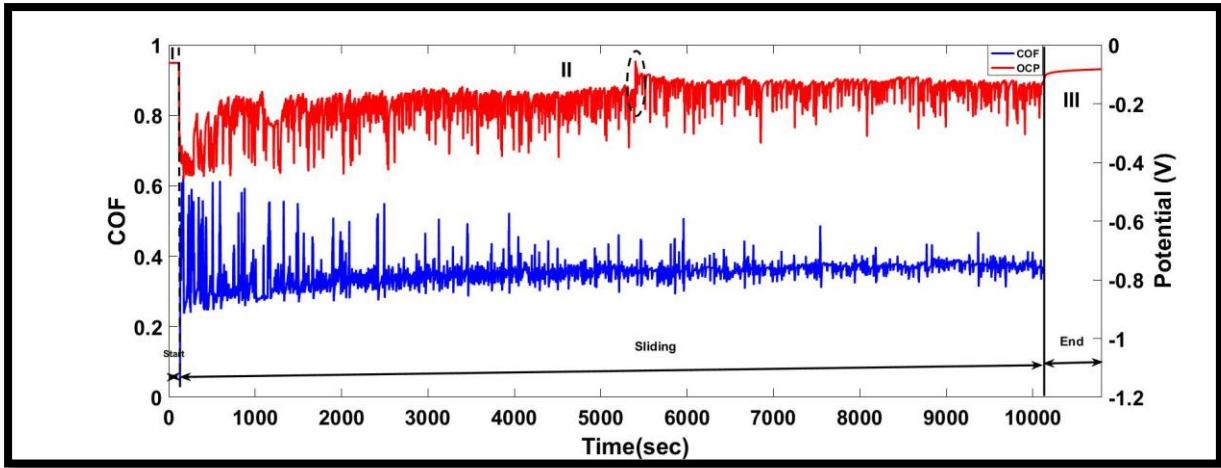


Figure 7-5: The evolution of the coefficient of friction and the open circuit potential of Ti-Ta₂₇-Al₅ under OCP-rubbing conditions.

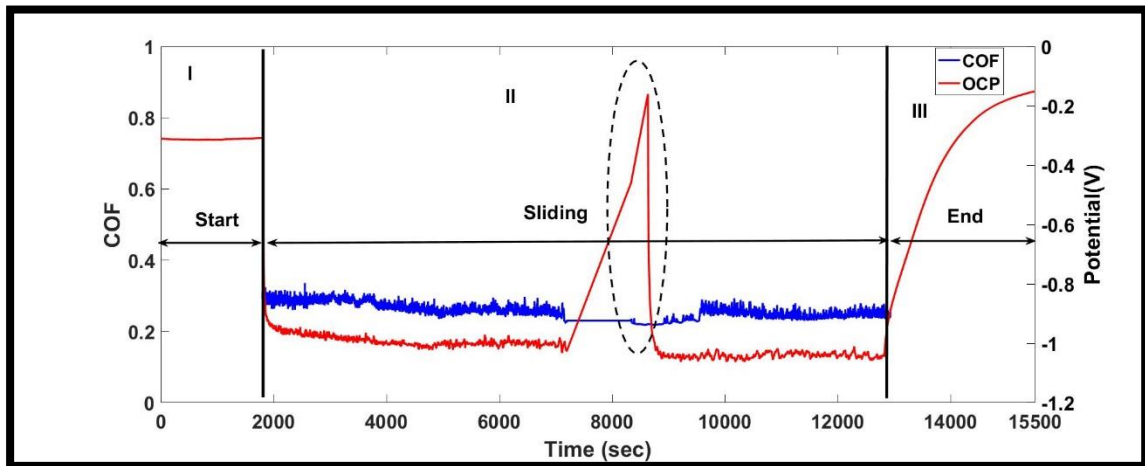


Figure 7-6: The evolution of the coefficient of friction and the open circuit potential of Cp-Ti under OCP-rubbing conditions.

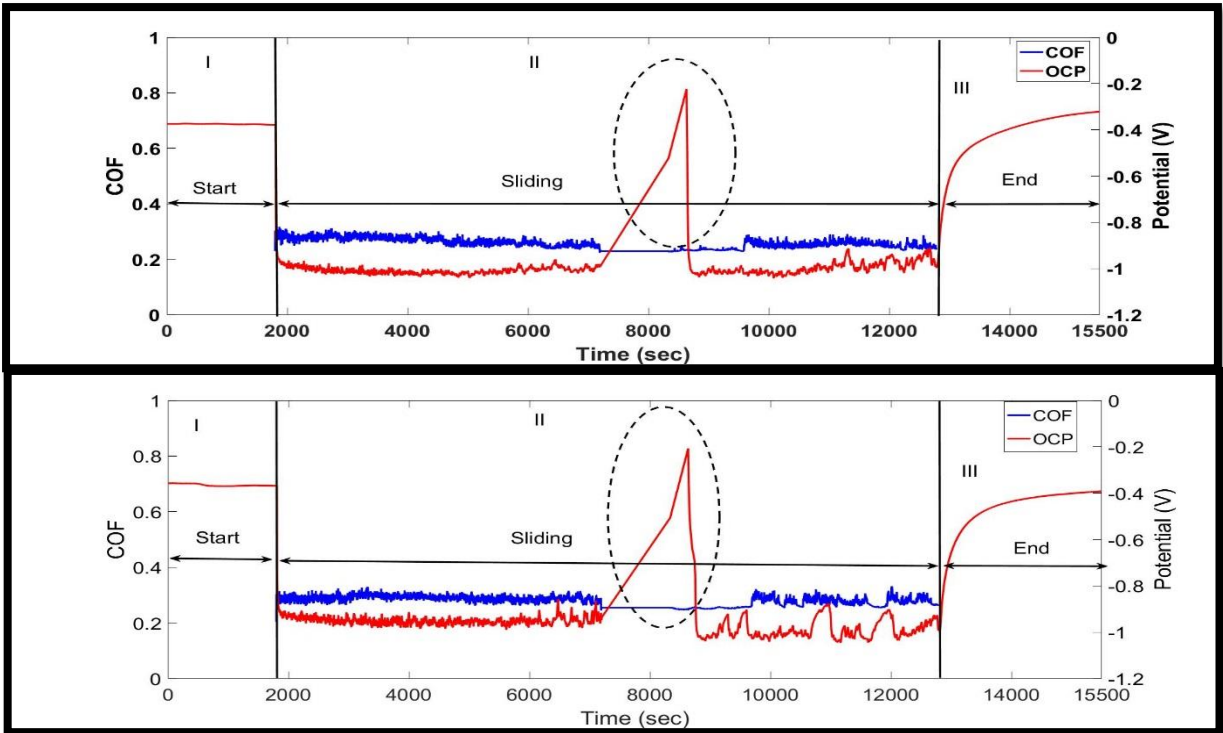


Figure 7-7: The evolution of the coefficient of friction and the open circuit potential of Ti-6Al-4V under OCP-rubbing conditions. The two graphs show the repeatability of the same test.

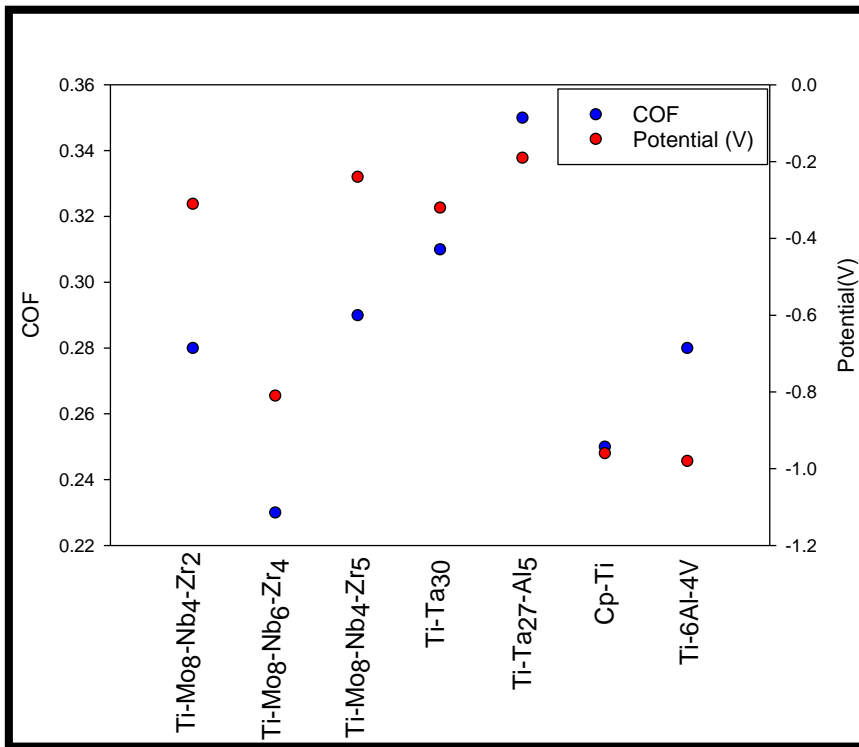


Figure 7-8 The mean friction coefficient and potential values of titanium alloys under OCP rubbing conditions.

7.2.2 Wear Morphology, Chemistry and Roughness under OCP conditions

SEM was used to evaluate the morphology of the wear tracks. The topographical features of the alloys after tribocorrosion experiments under OCP rubbing conditions are displayed in Figure 7-9. All alloys exhibited similar features showing scratches, grooves and plastic deformation on the wear surface. However, the depth of the grooves was greater in the α -microstructure Cp-Ti, $\alpha+\beta$ -microstructure Ti-6Al-4V and $\beta+\alpha''$ -microstructure Ti-Ta₂₇-Al₅. In addition, the wear tracks from these alloys showed a greater presence of wear debris and delamination. The surface of alloys also appears to be covered by a light grey layer as well as small dark spots can be observed at various places in the surface of the wear scar. This indicated a carbonaceous film formed on the surface of the wear tracks.

EDX and Raman analyses confirmed the formation of this carbonaceous layer on the surface of the wear tracks. The EDX elemental maps under OCP rubbing conditions are presented in Figure 7-10, corresponding to the boxed area in the image top right of Figure 7-10. The substrate elements were present as well as carbon and oxygen, which is consistent with the Raman spectra findings of the centre of the wear track. Figure 7-11 shows typical Raman spectra taken at the centre of the wear track after tribocorrosion under OCP rubbing conditions. The spectra show disordered graphite (D band) and the single crystal graphite (G band) centred on 1383 and 1567 cm^{-1} related to sp^2 -carbon and sp^3 -band carbon respectively. There was no evidence of transfer from the alumina ball to the titanium alloy surface. The morphology of the wear tracks on the alumina balls were evaluated using optical and scanning electron microscopy. Figures 7-12 and 7-13 show typical optical and SEM images of the wear tracks on the alumina ball after the tribocorrosion tests under OCP conditions. No significant material transfer and no significant damage was observed on the alumina ball counterbody after tribocorrosion tests under OCP. These results are consistent with the results of EDX on the alumina ball counterbody after tribocorrosion tests under OCP, Figure 7-14. The average surface roughness (Ra) of the alloys after tribocorrosion experiments under OCP rubbing conditions are presented in Figure 7-15. Figure 7-16 shows the surface roughness 3D image and the top view 2D image of the centre of the wear track for all alloys tested. The $\alpha+\beta$ microstructure Ti-6Al-4V had the highest surface roughness, while the β microstructure Ti-Mo₈-Nb₆-Zr₄ had the lowest.

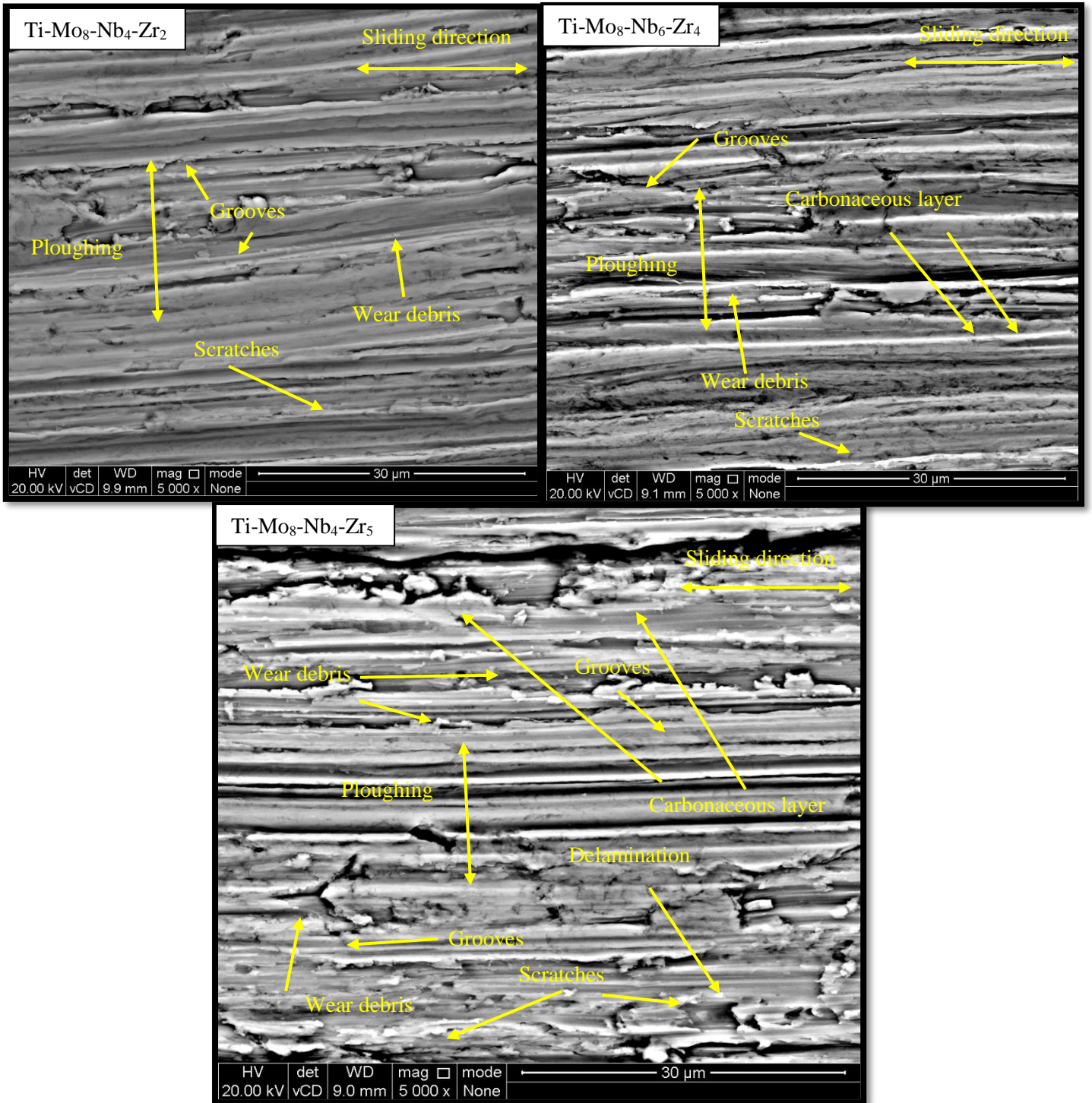


Figure 7-9: SEM micrographs of wear tracks of the titanium alloys under OCP rubbing conditions.

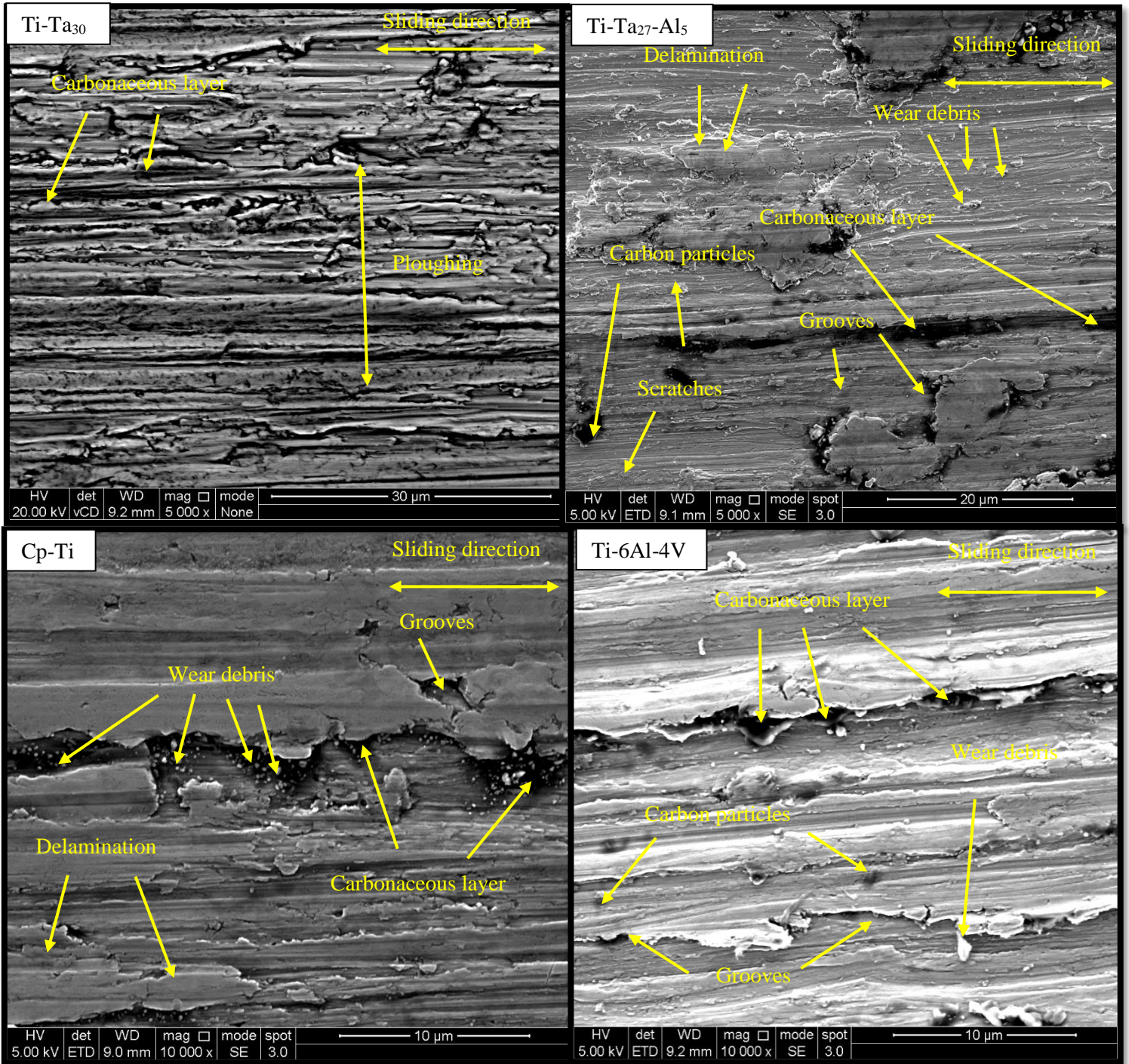


Figure 7-9: Continued

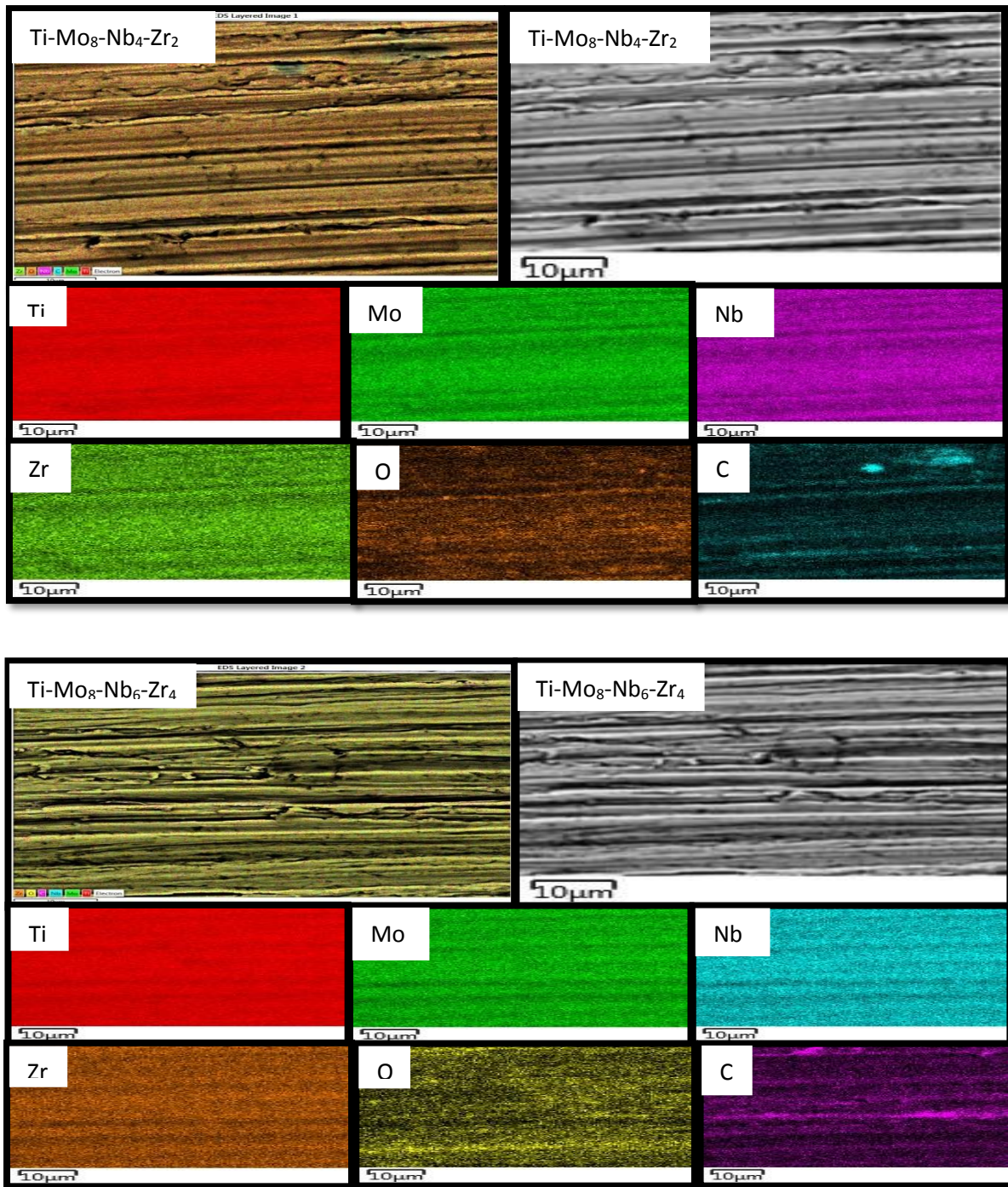


Figure 7-10: EDX element mapping of the wear track of titanium alloys under OCP rubbing conditions.

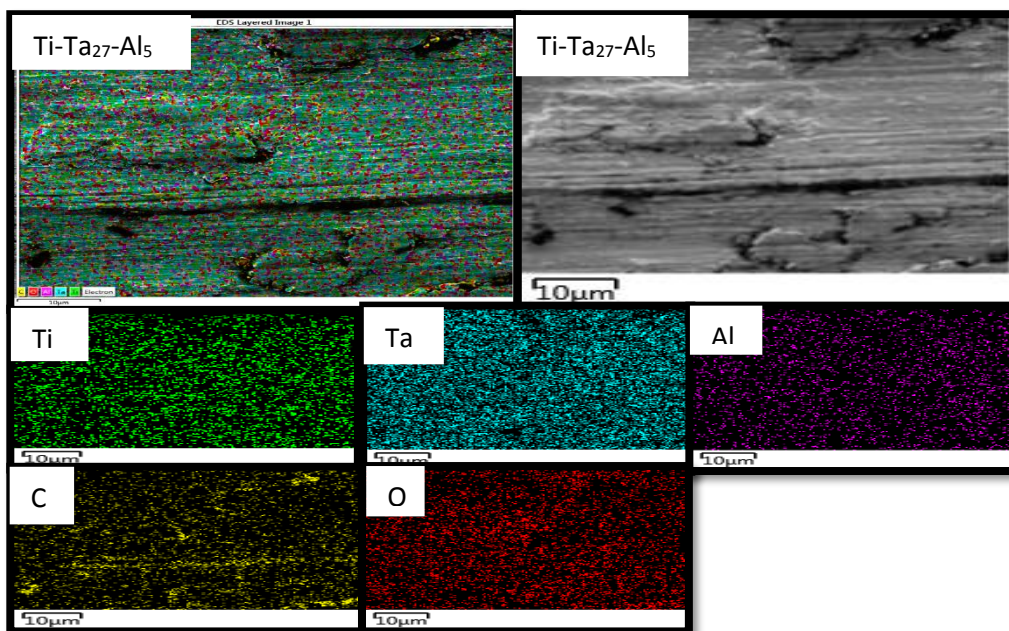
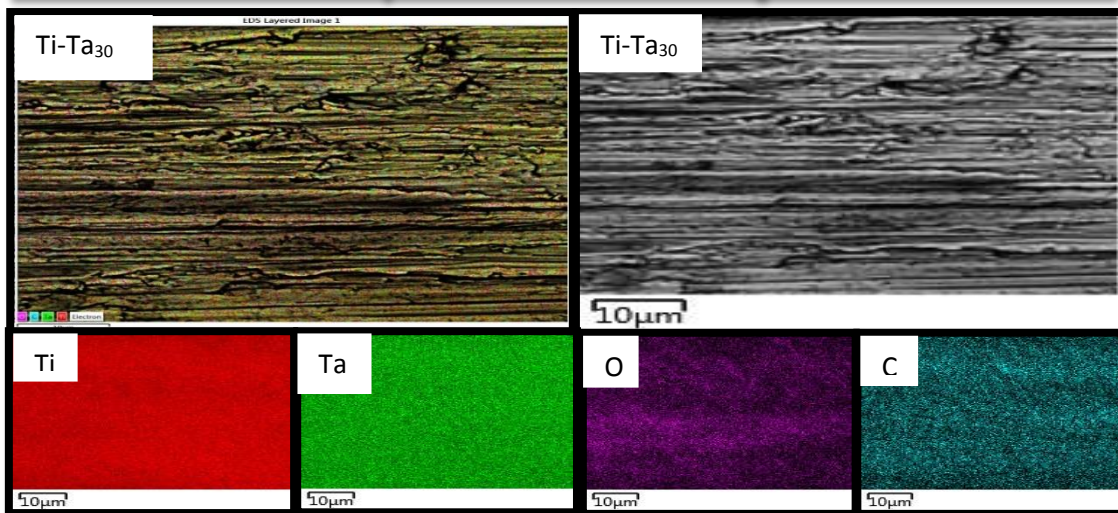
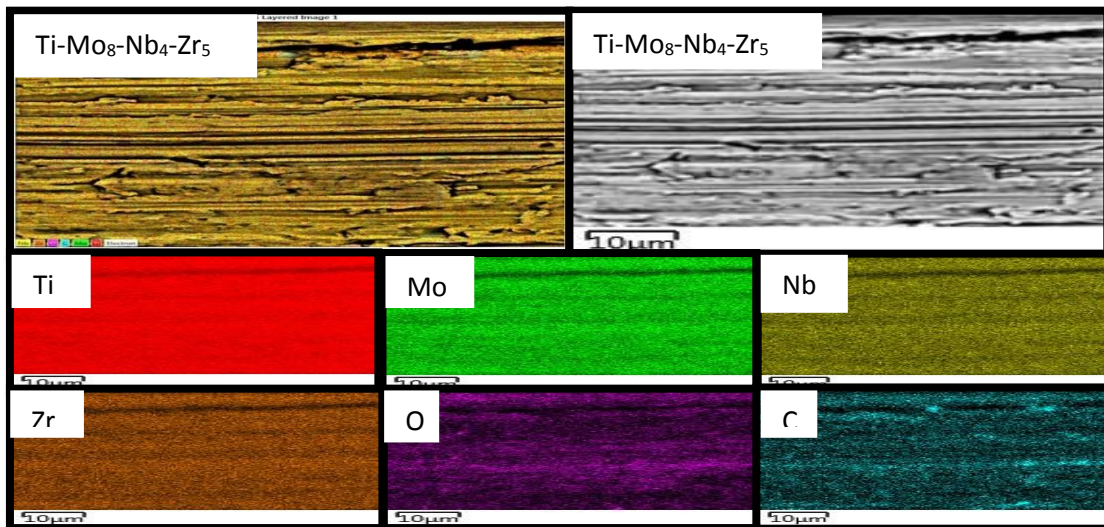


Figure 7-10: Continued

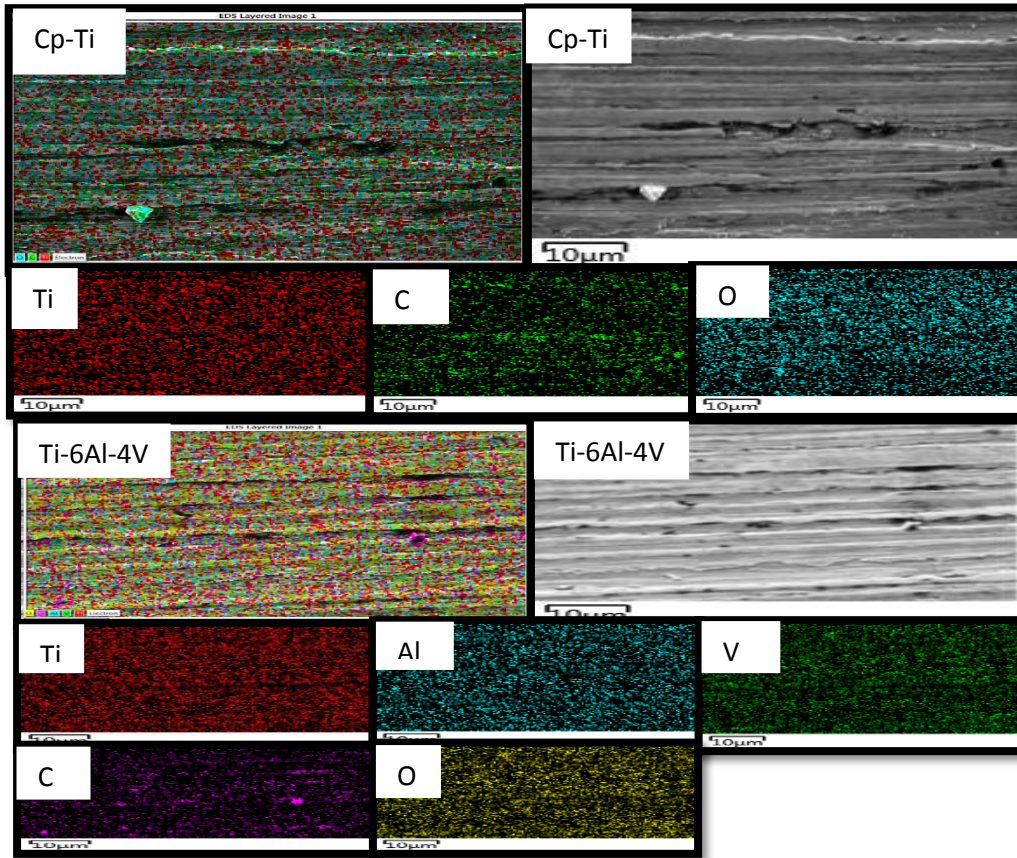


Figure 7-10: Continued

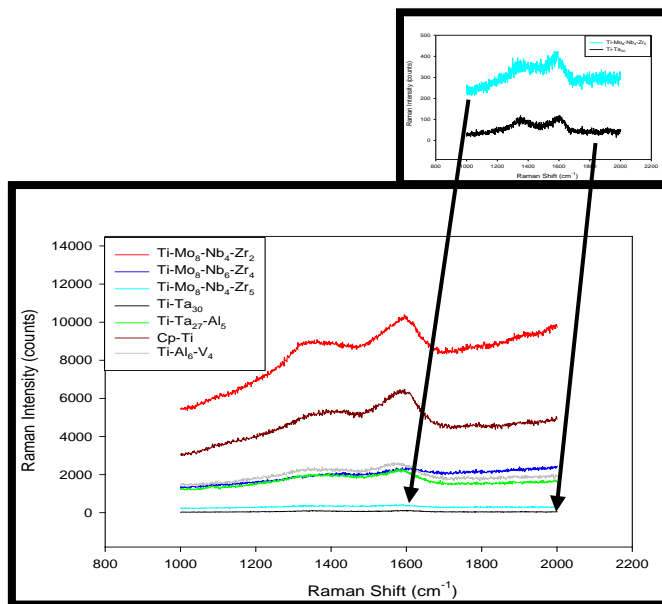


Figure 7-11: Raman spectra of the wear track of titanium alloys under OCP rubbing conditions.

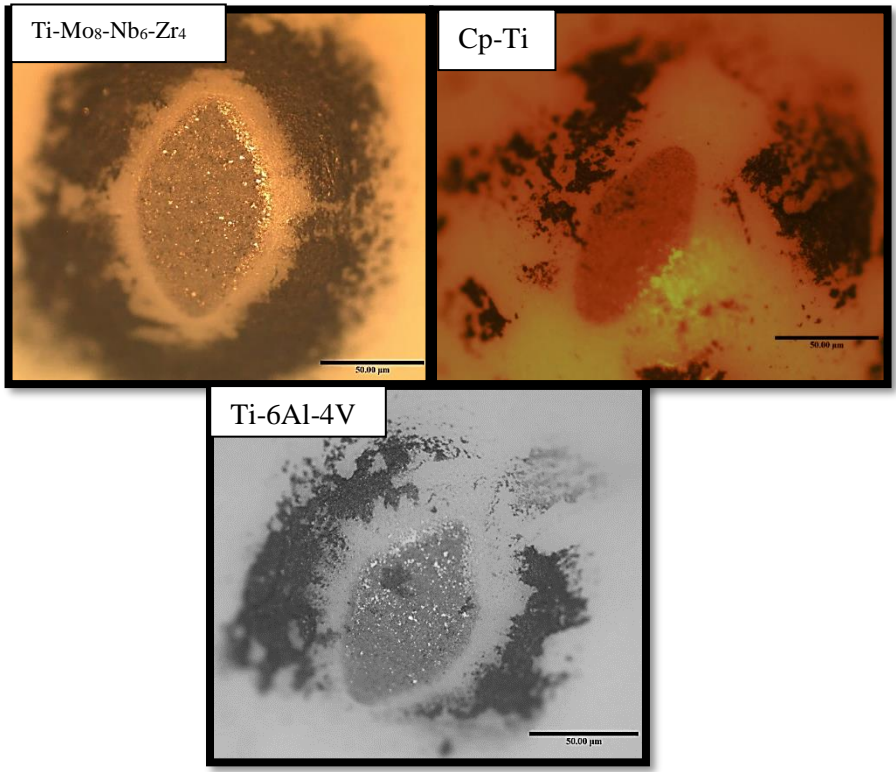


Figure 7-12 Optical images of the alumina balls rubbing against the titanium alloys under OCP rubbing conditions.

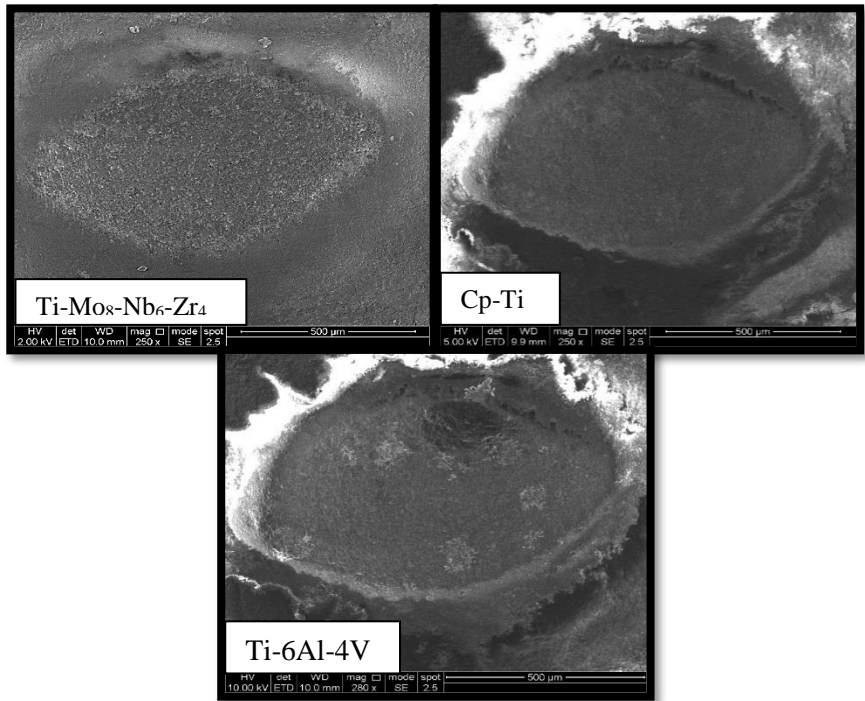


Figure 7-13 SEM images of the alumina balls rubbing against the titanium alloys under OCP rubbing conditions.

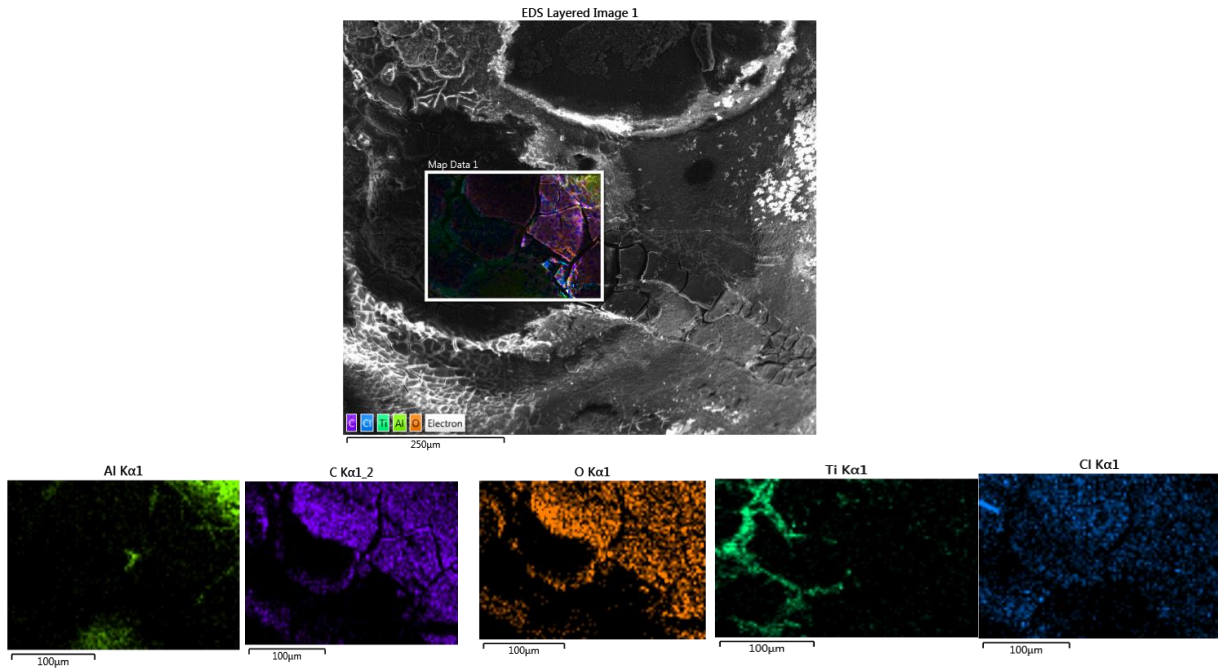


Figure 7-14 EDX element mapping of the alumina ball after rubbing against Cp-Ti under OCP rubbing conditions.

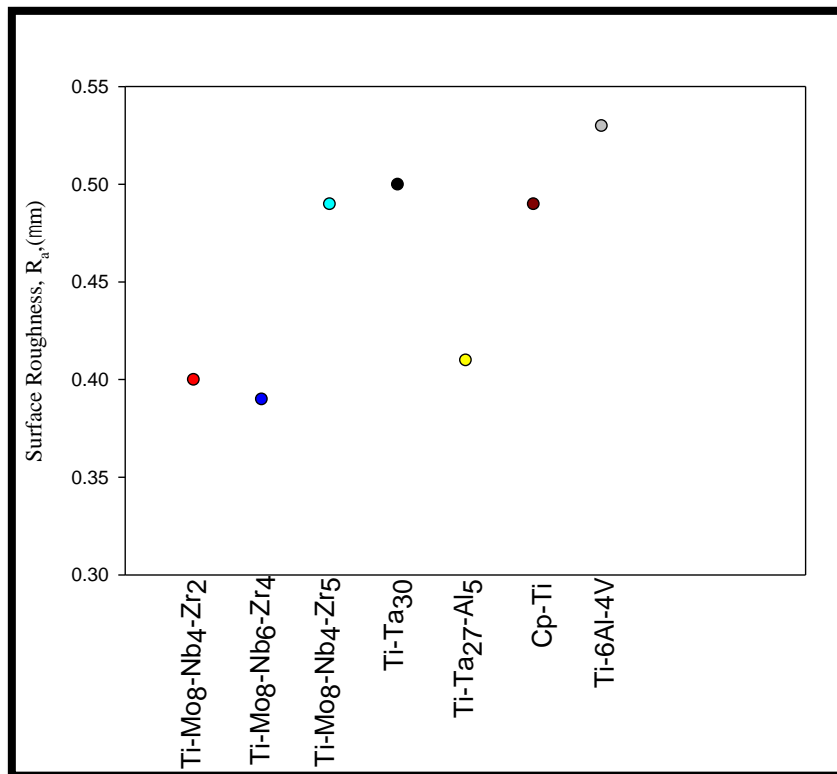


Figure 7-15 The average surface roughness of titanium alloys under OCP rubbing conditions.

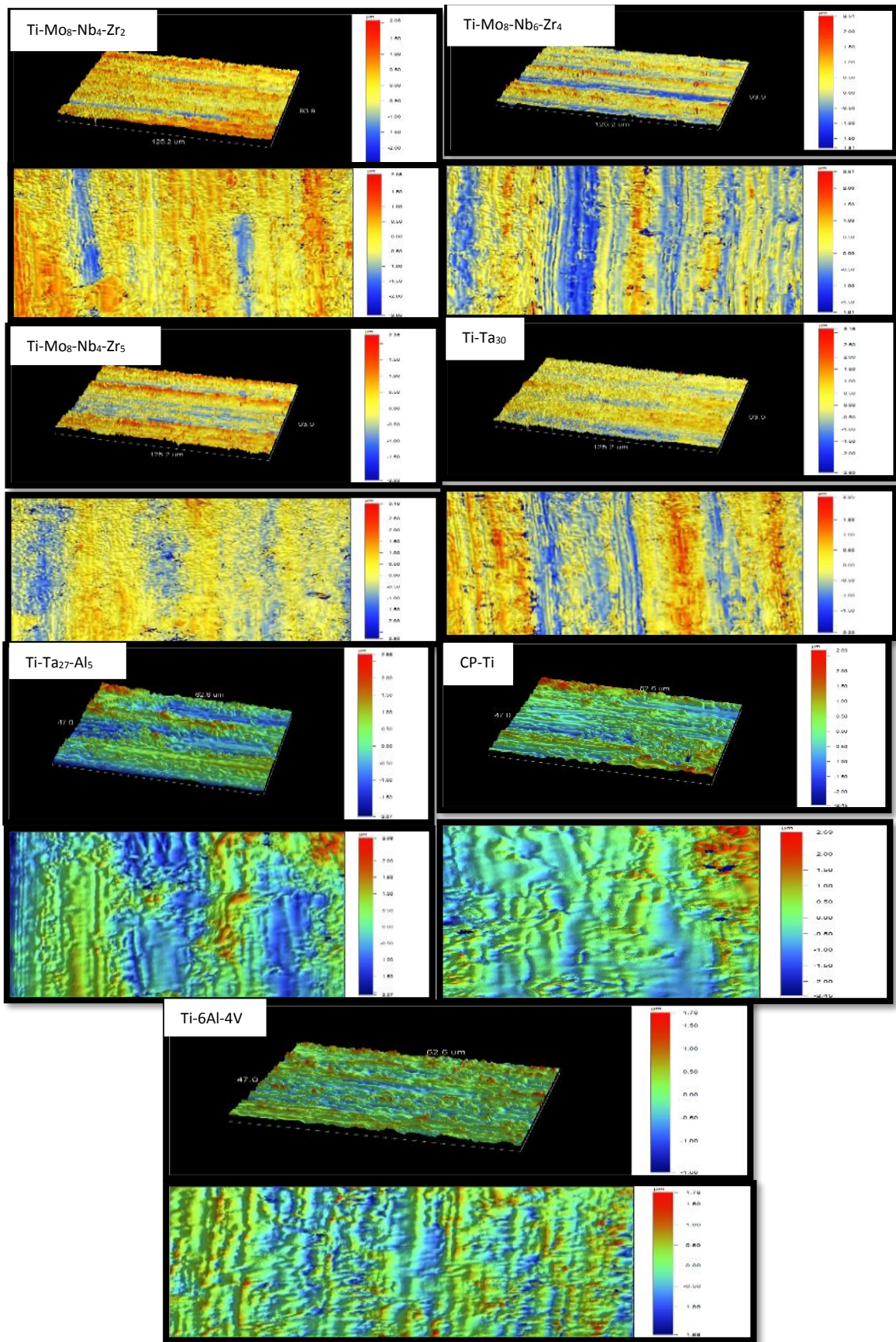


Figure 7-16: Surface roughness 3D and 2D top view of the wear track under OCP rubbing conditions.

7.2.3 Total Material Loss Rate

3D images of the wear track under OCP rubbing conditions in bovine calf serum are presented in Figure 7-17. All alloys tested had a regular wear track and the depth of the wear track in the β microstructure Ti-Mo₈-Nb₄-Zr₂, Ti-Mo₈-Nb₆-Zr₄, Ti-Mo₈-Nb₄-Zr₅ and Ti-Ta₃₀ of 52, 58, 55, 57 μm respectively was larger than that of $\beta + \alpha''$ microstructure Ti-Ta₂₇-Al₅ (49 μm), $\alpha + \beta$ microstructure Ti-6Al-4V (36 μm), and the α microstructure Cp-Ti (11 μm). The average of the total removed volume of wear tracks under OCP rubbing conditions is shown in Figure 7.18 a. The Cp-Ti and the Ti-6Al-4V had the lowest average total volume of 0.008 and 0.04 mm^3 respectively. All β - microstructure titanium alloys had a similar average total volume of 0.09 mm^3 , while $\alpha'' + \beta$ microstructure Ti-Ta₂₇-Al₅ had an average total volume of 0.08 mm^3 . The average specific wear rate after tribocorrosion experiments under OCP rubbing conditions is presented in figure 7-18 b. Among all titanium alloys used in this study Cp-Ti and the Ti-6Al-4V had the lowest specific wear rate of 0.00003 and 0.0001 mm^3/Nm respectively. The average specific wear rate of $\alpha'' + \beta$ microstructure Ti-Ta₂₇-Al₅ was 0.003 mm^3/Nm , while the β microstructure titanium alloys had the similar specific wear rate of 0.0004 mm^3/Nm .

The total material removed from the wear tracks (V_{total}) during tribocorrosion is a result of the mechanical wear (V_{mech}) and chemical wear (V_{chem}). The total volume V_{total} was determined by measuring the cross section of the wear track and using equation 3-9. The chemical component (V_{chem}) can be roughly estimated by the excess current measured during sliding according to Faraday's law using equation 3-13. The mechanical wear volume V_{mech} was derived from difference between the total volume V_{total} and the chemical volume V_{chem} using equation 3-14. At OCP, the corrosion currents estimated from Tafel plots in Figure 7-19 were used to estimate the chemical wear component at OCP. The samples were covered in Lacomit varnish in order to ensure the corrosion current during rubbing at OCP was only from inside the wear track. Figure 7-20 presents the contribution of mechanical wear (V_{mech}) and electrochemical wear (V_{chem}) to calculate the total material loss (V_{total}) after tribocorrosion tests under open circuit potential rubbing conditions.

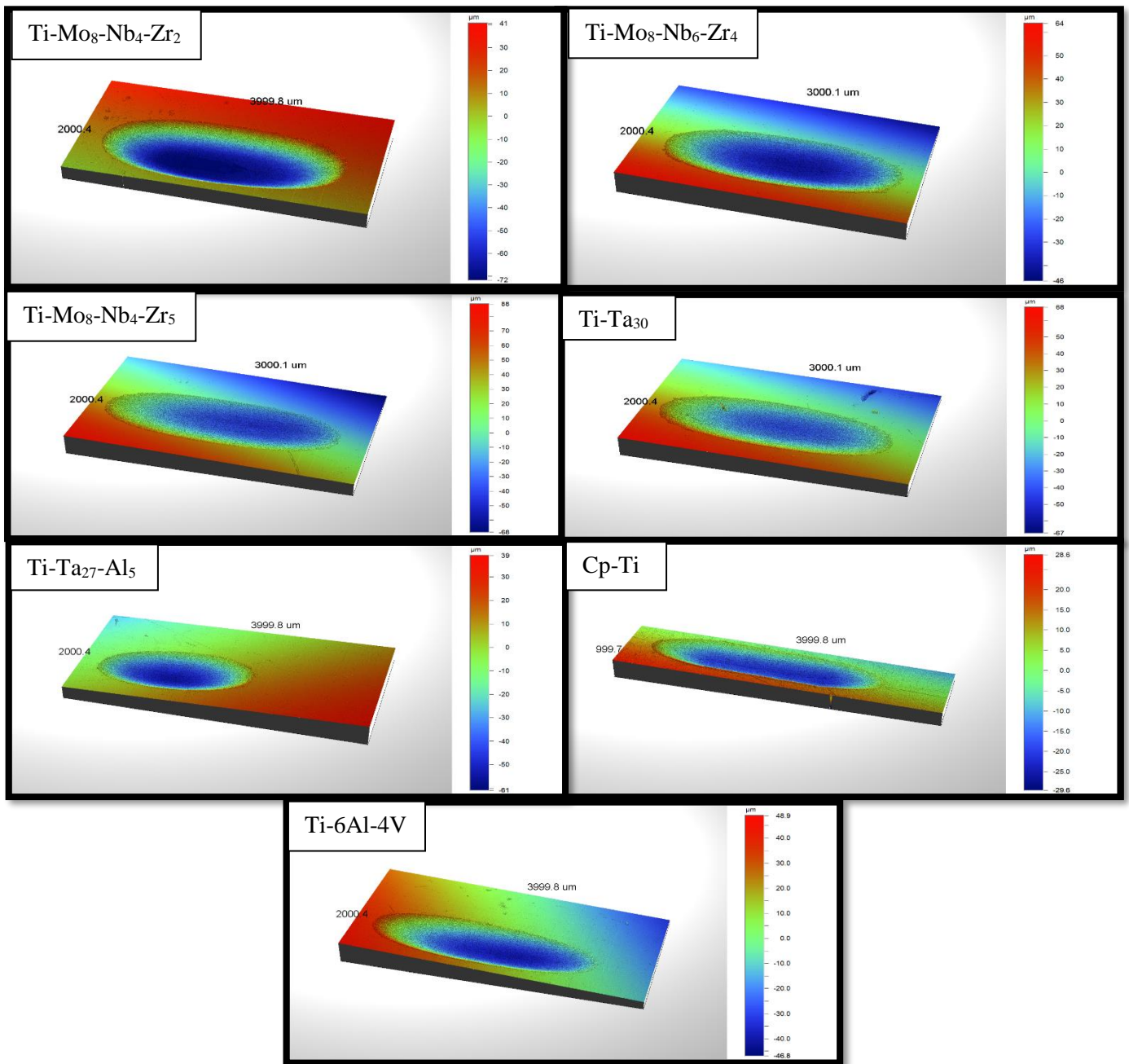


Figure 7-17: 3D images of wear track of titanium alloys under OCP rubbing conditions.

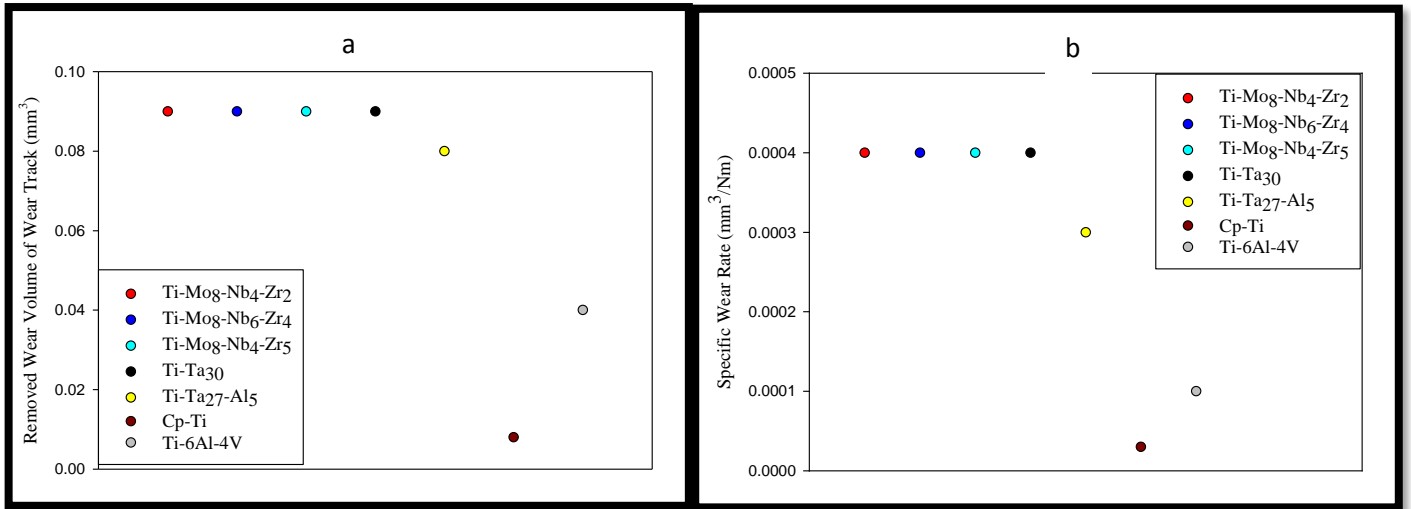


Figure 7-18: (a) Wear volumes (b) Specific wear rate of wear track for titanium alloys under OCP rubbing conditions.

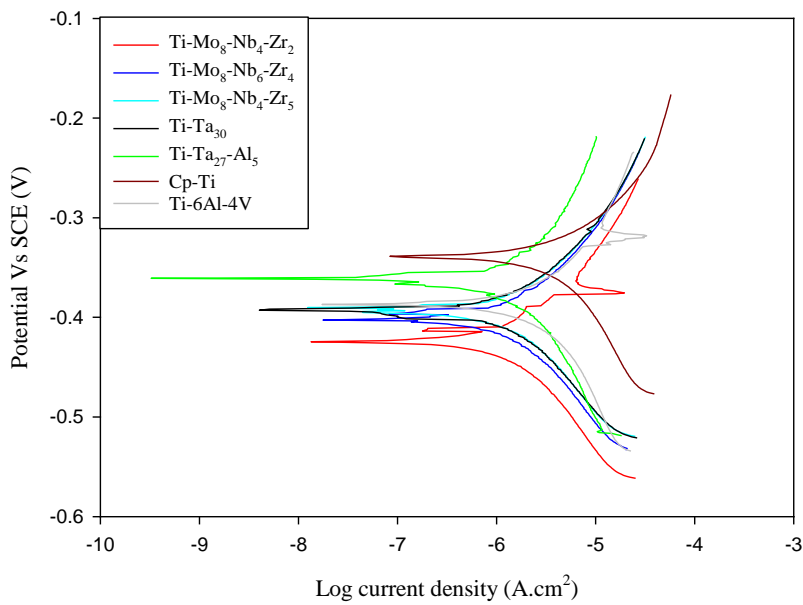


Figure 7-19 Tafel plots during rubbing at OCP.

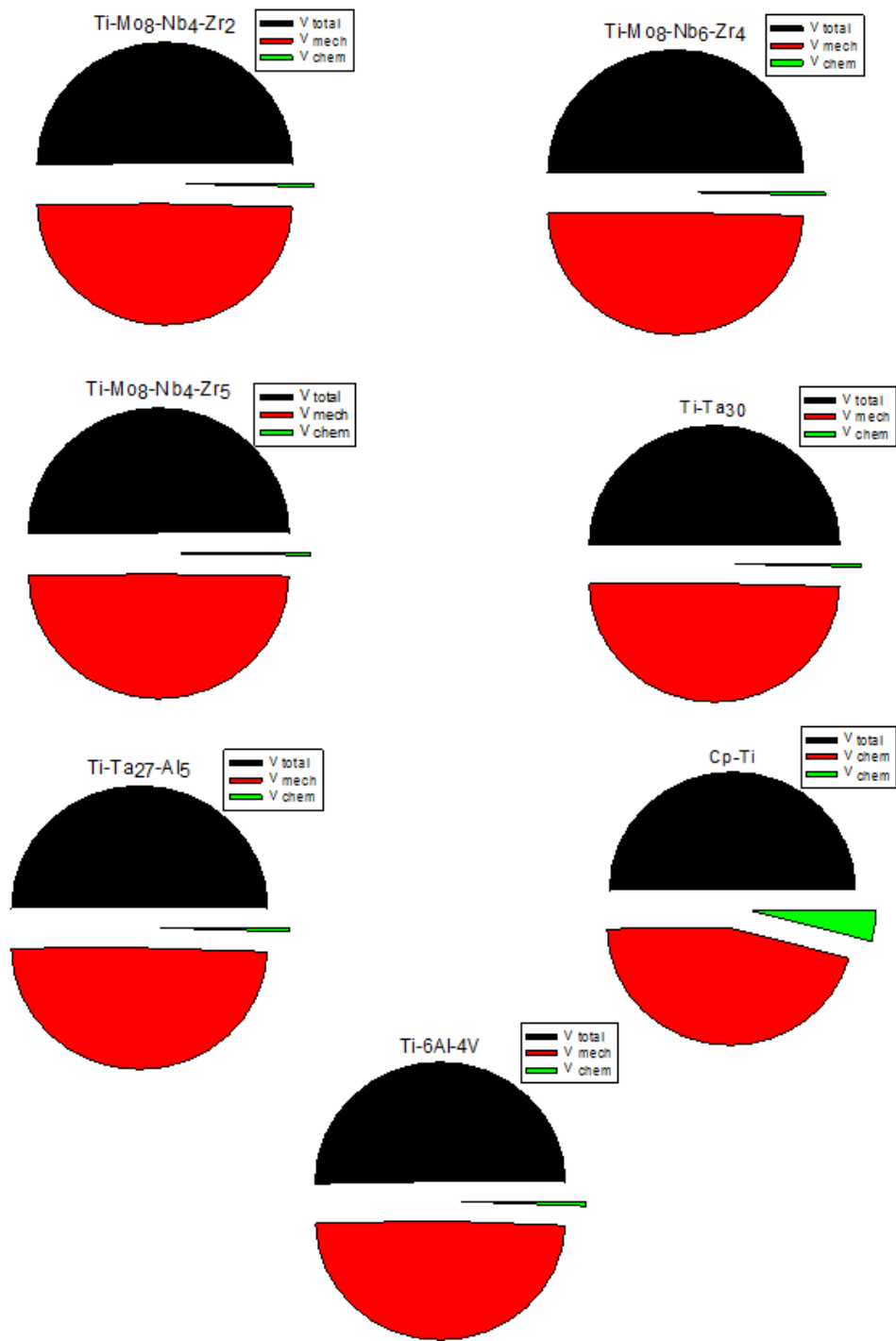


Figure 7-20 Contribution of mechanical wear and electrochemical to total material loss rate volume of titanium alloys after tribocorrosion tests under OCP rubbing conditions.

7.2.4 Subsurface Morphology

Subsurface morphology provides more detail about the tribocorrosion mechanisms. To start with, a cross-section was prepared through FIB of wear track. The areas investigated were in the centre of the wear track. Figure 7-21 shows an ion channelling contrast image of the wear track formed at the β -phase Ti-Mo₈-Nb₄-Zr₅, while Figure 7-22 shows an ion channelling contrast image of the wear tracks formed at the $\beta + \alpha''$ - phase Ti-Ta₂₇-Al₅. Characterization of subsurface microstructures indicate a continuous nanocrystalline layer was formed after tribocorrosion tests at OCP. The grain size increase with depth, and there was a clear boundary between the nanocrystalline and microcrystalline grains.

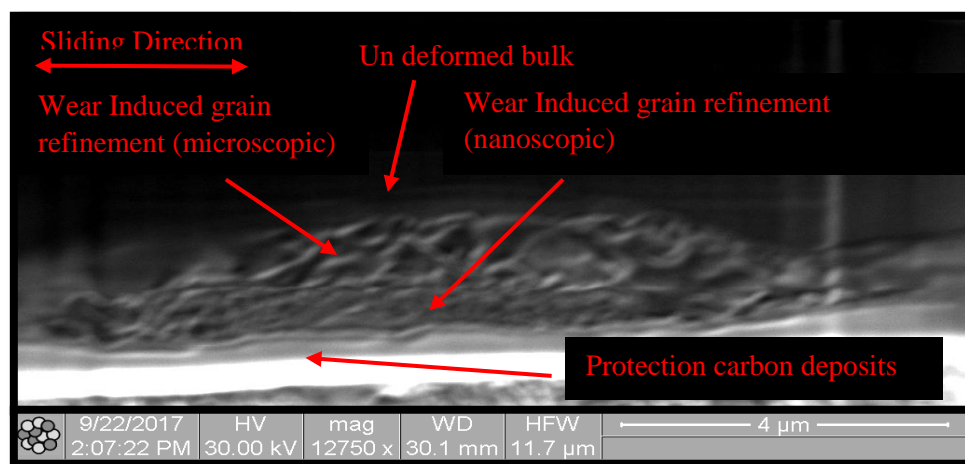


Figure 7-21 Ion channelling contrast image of a transverse cross-section of wear track formed at Ti-Mo₈-Nb₄-Zr₅ under OCP rubbing conditions.

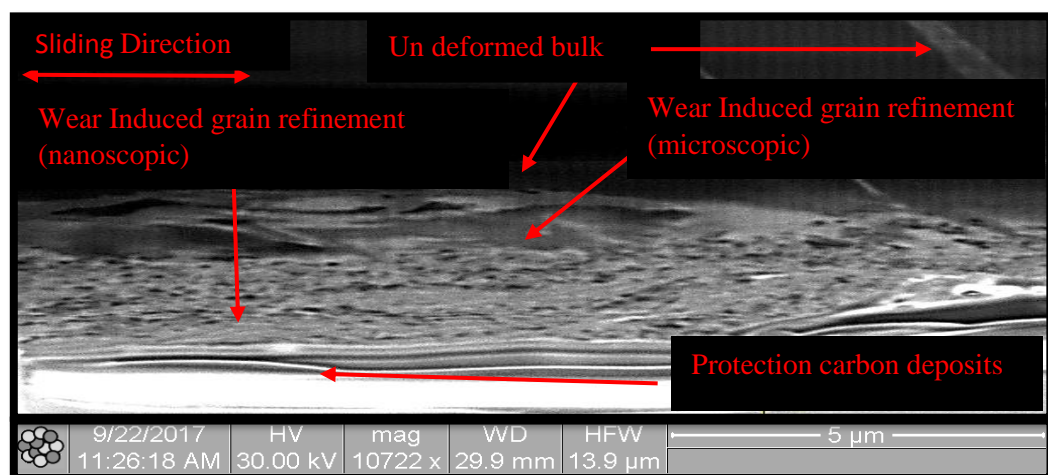


Figure 7-22 Ion channelling contrast image of a transverse cross-section of wear track formed at Ti-Ta₂₇-Al₅ under OCP rubbing conditions.

7.3 Tribocorrosion at Cathodic Potentiostatic (-0.5V vs OCP)

7.3.1 Sliding Friction Response

Figures 7-23 through to 7-29 show the evolution of the cathodic current and friction coefficient over time in 25% vol bovine calf serum at $37\pm 1^\circ\text{C}$ under cathodic potentiostatic rubbing conditions (-0.5V vs OCP). The behaviour shown in Figures 7-23 and 7-29 indicates the excellent reproducibility of the tests. The graphs could be subdivided into three main zones. The first region is the waiting time under cathodic potential, with the expected negative current. The second zone corresponds to when rubbing was started. A significant anodic increase in the current was observed, but the current still had a positive value. Finally, rubbing was stopped in the third region, and the current decreased to the value observed at beginning of the test. The average friction coefficients and average current during rubbing are shown in Figure 7-30. The Ti-6Al-4V with $\alpha+\beta$ -microstructure and α - microstructure Cp-Ti alloys showed the lowest mean friction coefficient values. The $\alpha''+\beta$ microstructure Ti-Ta₂₇-Al₅ alloy had the highest mean friction coefficient values. The $\alpha''+\beta$ microstructure Ti-Ta₂₇-Al₅ alloy had the highest current during rubbing, while the β microstructure Ti-Ta₃₀ had the lowest current.

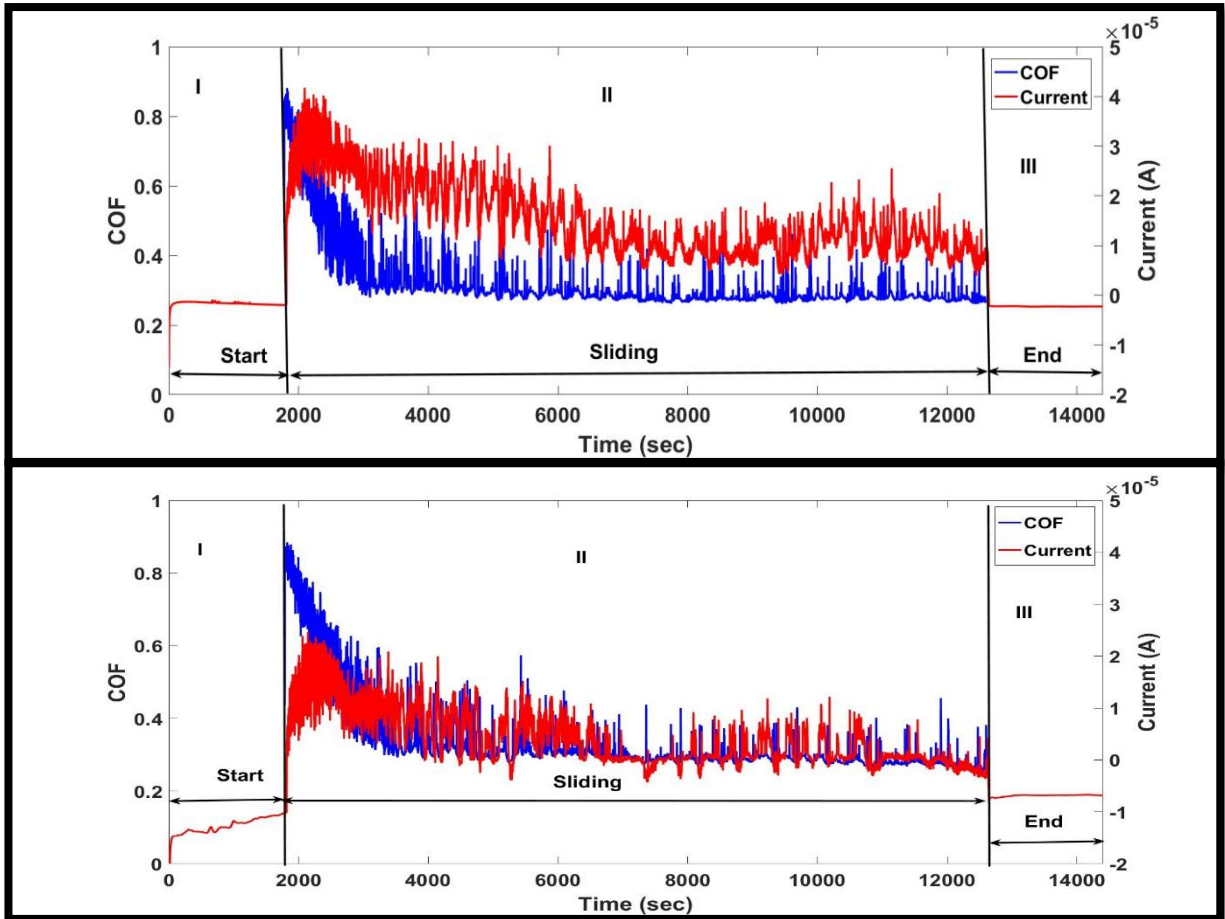


Figure 7-23: The evolution of the coefficient of friction and the current of Ti-Mo₈-Nb₆-Zr₄ alloy under cathodic potentiostatic rubbing conditions. The two graphs are repeat of the same test.

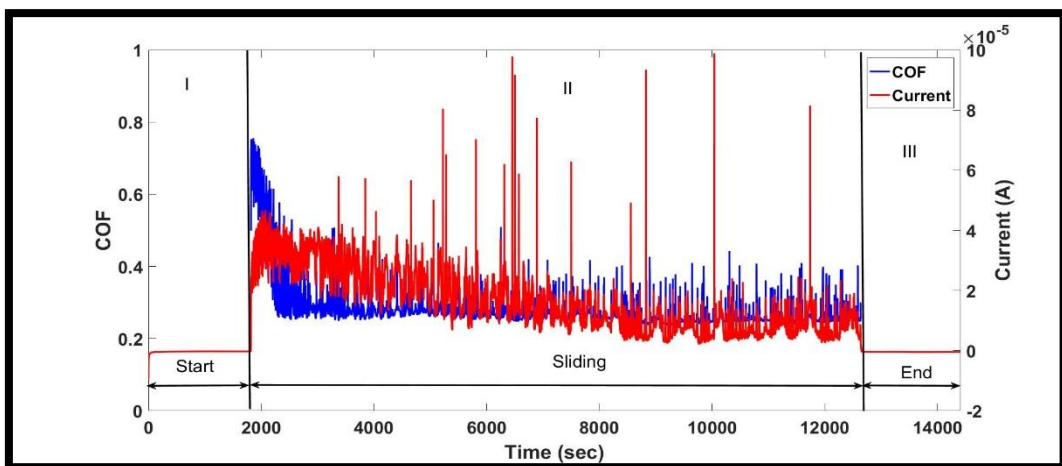


Figure 7-24: The evolution of the coefficient of friction and the current of Ti-Mo₈-Nb₄-Zr₂ alloy under cathodic potentiostatic rubbing conditions.

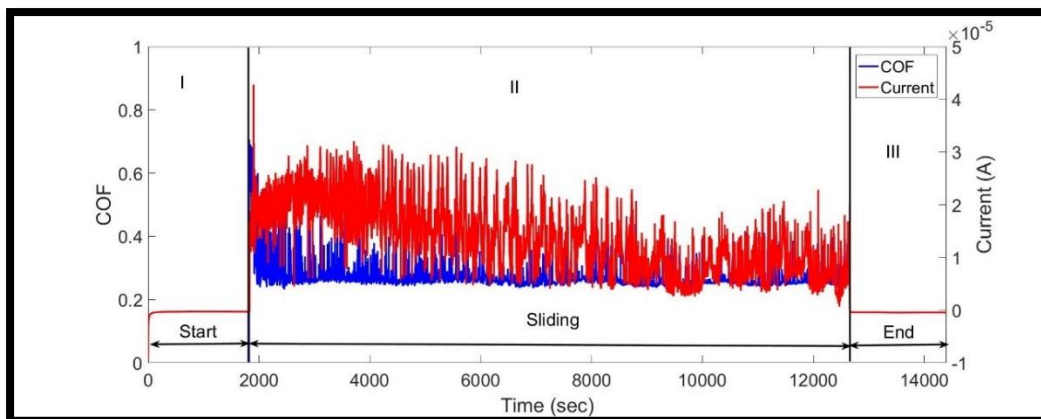


Figure 7-25: The evolution of the coefficient of friction and the current of Ti-Mo₈-Nb₄-Zr₅ alloy under cathodic potentiostatic rubbing conditions.

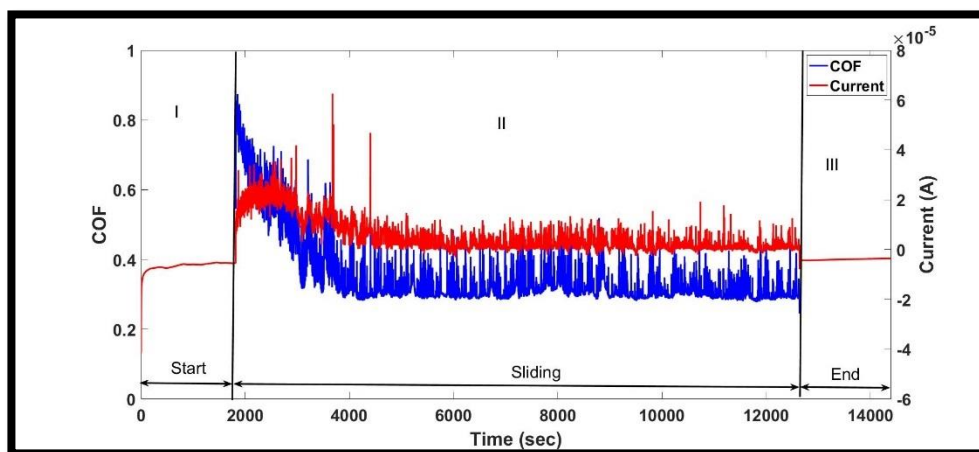


Figure 7-26: The evolution of the coefficient of friction and the current of Ti-Ta₃₀ alloy under cathodic potentiostatic rubbing conditions.

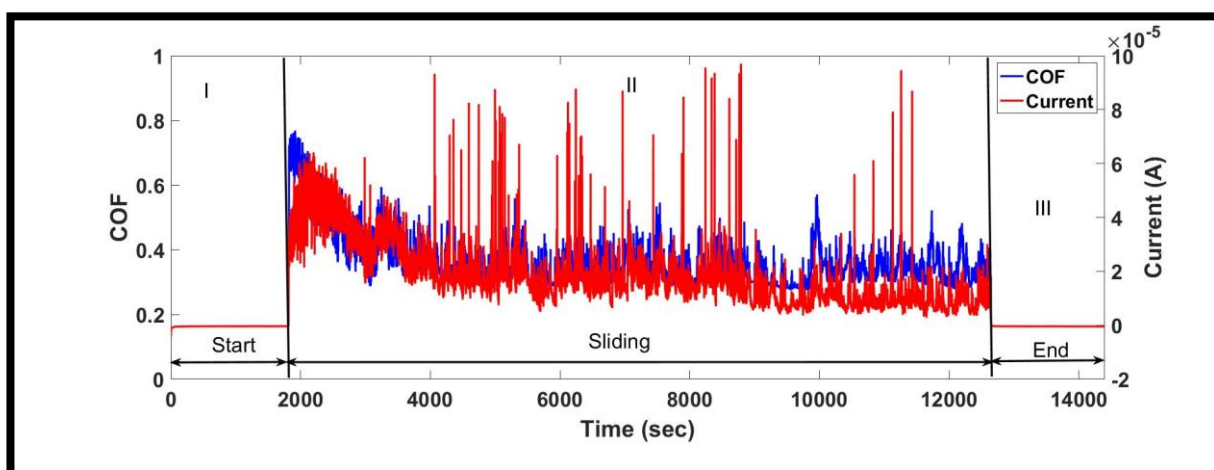


Figure 7-27: The evolution of the coefficient of friction and the current of Ti-Ta₂₇-Al₅ alloy under cathodic potentiostatic rubbing conditions.

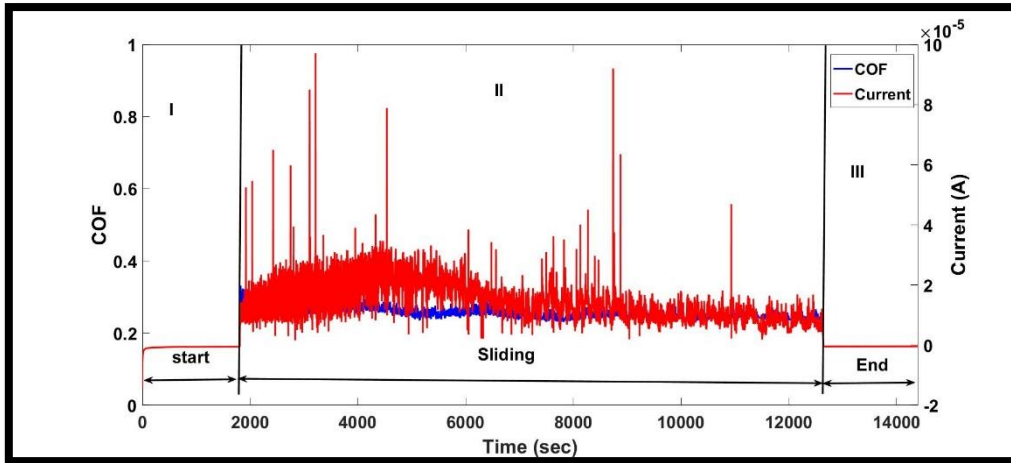


Figure 7-28: The evolution of the coefficient of friction and the current of Cp-Ti under cathodic potentiostatic rubbing conditions.

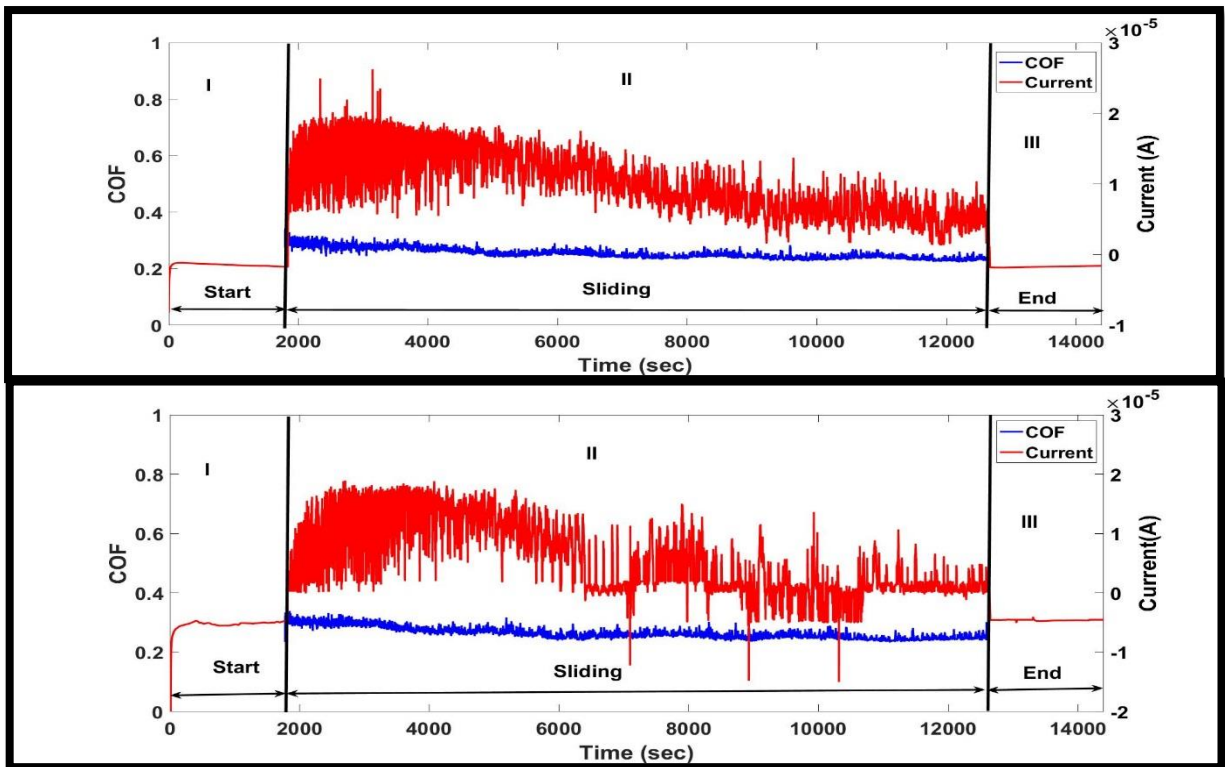


Figure 7-29: The evolution of the coefficient of friction and the current of Ti-6Al-4V under cathodic potentiostatic rubbing conditions. The two graphs are repeat of the same test.

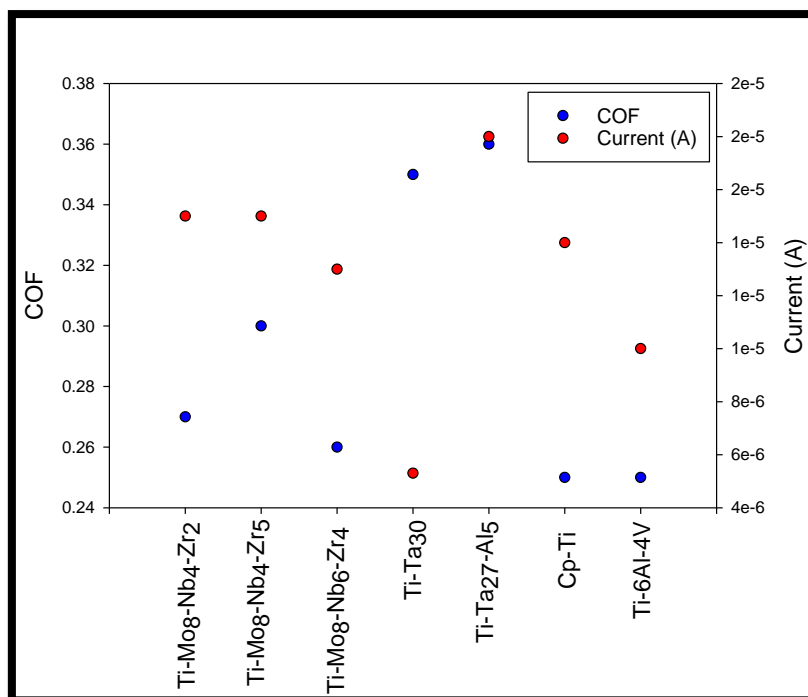


Figure 7-30 The average friction coefficient and current values of titanium alloys under cathodic potentiostatic rubbing conditions.

7.3.2 Wear Morphology, Chemistry and Roughness under cathodic conditions

SEM was used to evaluate the morphology of the wear tracks for alloys tested under cathodic conditions (-0.5V vs OCP). There were no significant differences in the wear morphology and all titanium alloys showed the presence of ductile and plastic deformation, scratches, grooves, wear debris in the form of both fine particles as well as plate like and delamination on the worn surface (Figure 7-31). The worn surface of all alloys appeared to be partially covered by a light grey layer, as well as small dark spots that were observed at various places. This indicated a carbonaceous film formed on the surface of the wear tracks, which was confirmed by EDX and Raman analyses. The EDX elemental maps at cathodic rubbing conditions are shown in Figure 7-32, which corresponds to the boxed area covering the surface shown in the top right of all figures. The EDX analysis revealed the presence of the elements in the substrate as well as carbon and oxygen. Accordingly, Raman spectra were obtained from the centre of the wear track (Figure 7-33). The spectra show disordered graphite (D band) and the single crystal graphite (G band) centred on 1383 and 1567 cm^{-1} related to sp^2 -carbon and sp^3 -band carbon respectively. There was no transfer from the alumina ball to the titanium alloys surface. The morphology of the wear tracks on the alumina balls were evaluated using optical and scanning electron microscopy. Figures 7-34 and 7-35 shows the typical optical and SEM images of the

wear tracks on the alumina ball after the tribocorrosion tests under (-0.5V vs OCP) conditions. No significant material transfer could be observed by optical and scanning electron microscopy on the alumina ball counterbody after tribocorrosion tests under (-0.5V vs OCP). These results are in agreement with the results of EDX on the alumina ball counterbody after tribocorrosion tests under (-0.5V vs OCP) as can be observed from Figure 7-36. However, significant damage and loss of material on the alumina surface was observed by SEM images after tribocorrosion tests under (-0.5V vs OCP). The average surface roughness (Ra) of the worn surfaces is shown in Figure 7-37; Figure 7-38 shows surface roughness 3D image and 2D top view of the centre of the wear track. Among all titanium alloys, the $\alpha+\beta$ microstructure Ti-6Al-4V had the lowest surface roughness, while the β microstructure Ti-Mo₈-Nb₄-Zr₅ had the highest.

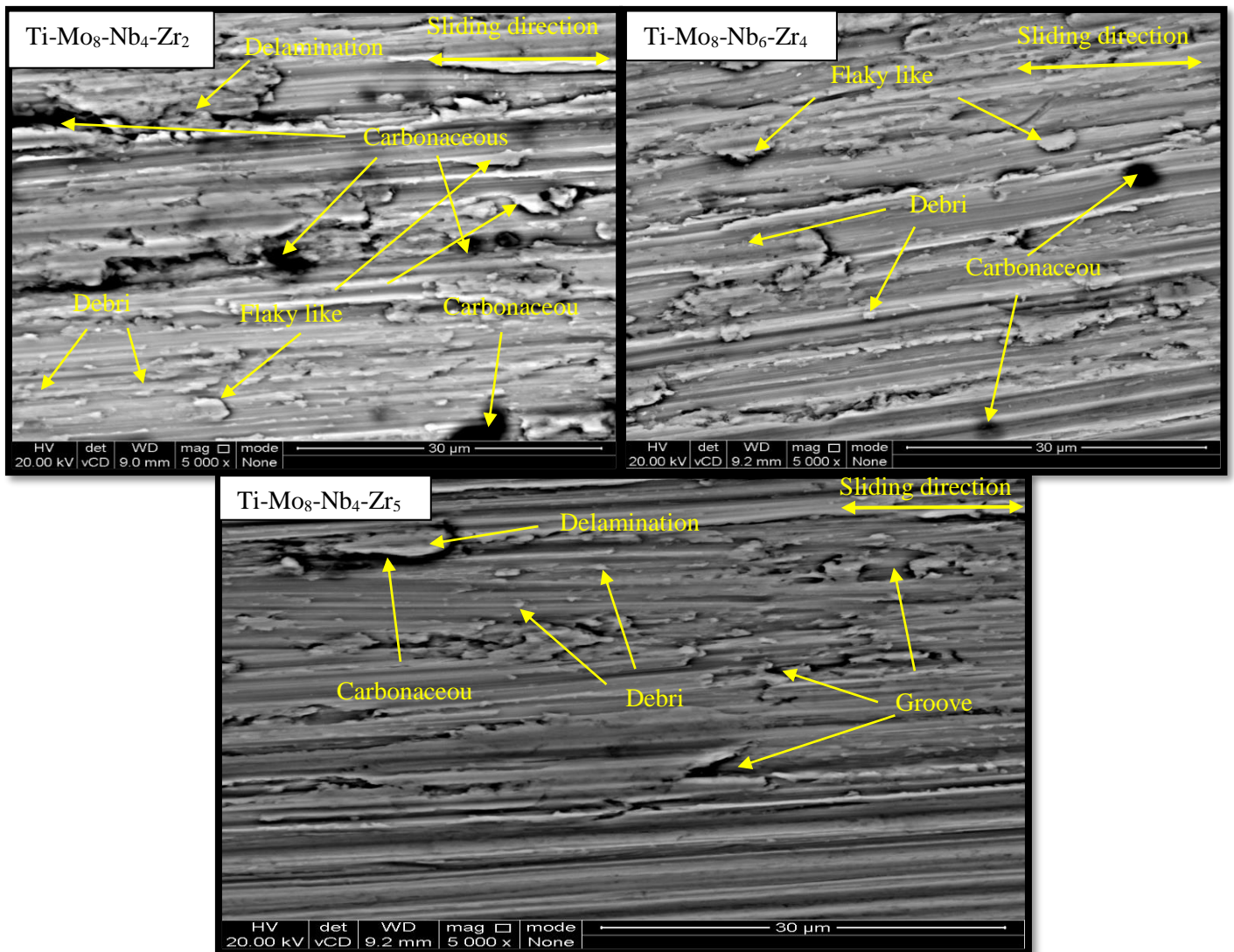


Figure 7-31: SEM micrographs of wear tracks of titanium alloys under cathodic potentiostatic rubbing conditions.

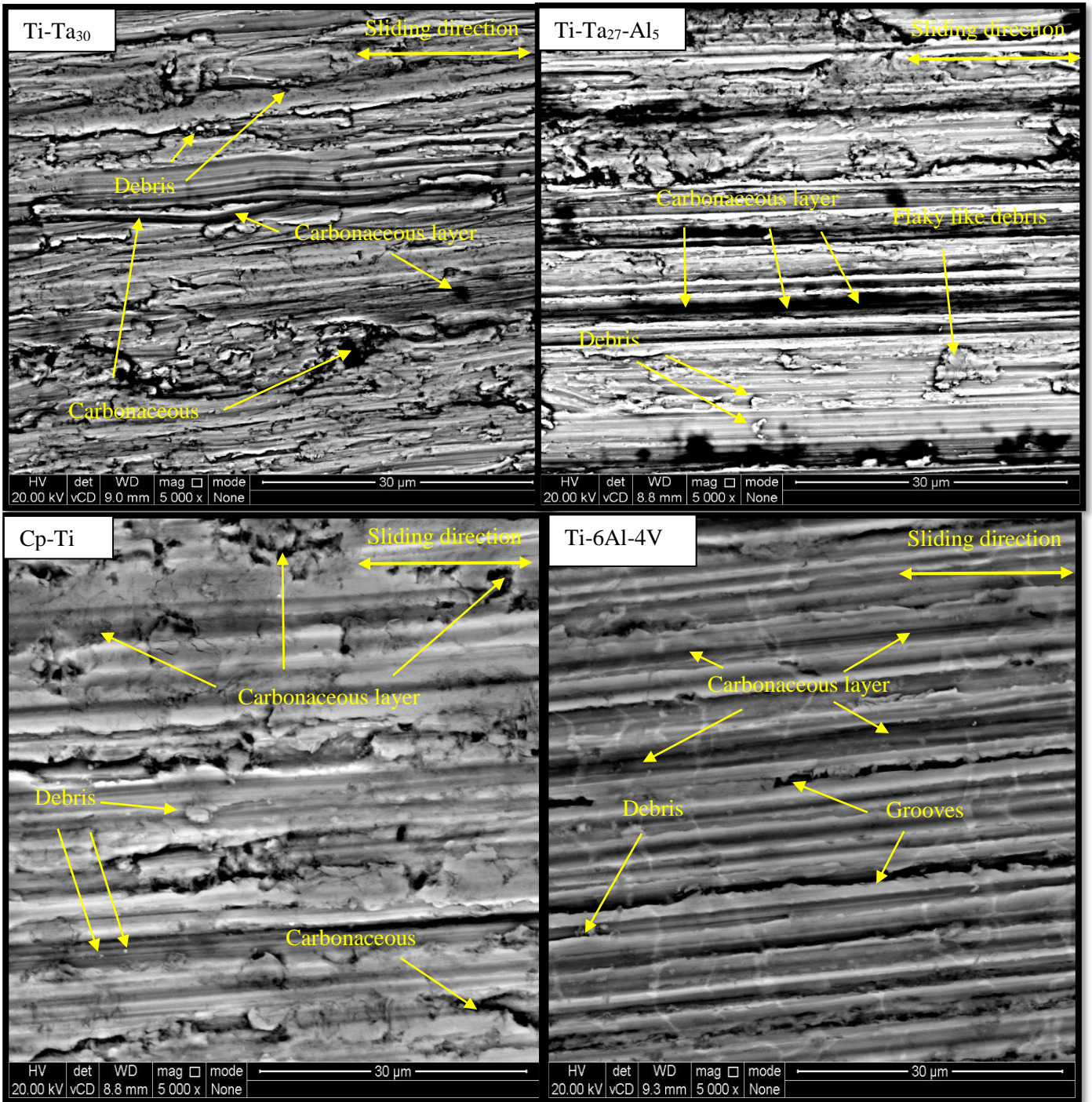


Figure 7-31: Continued

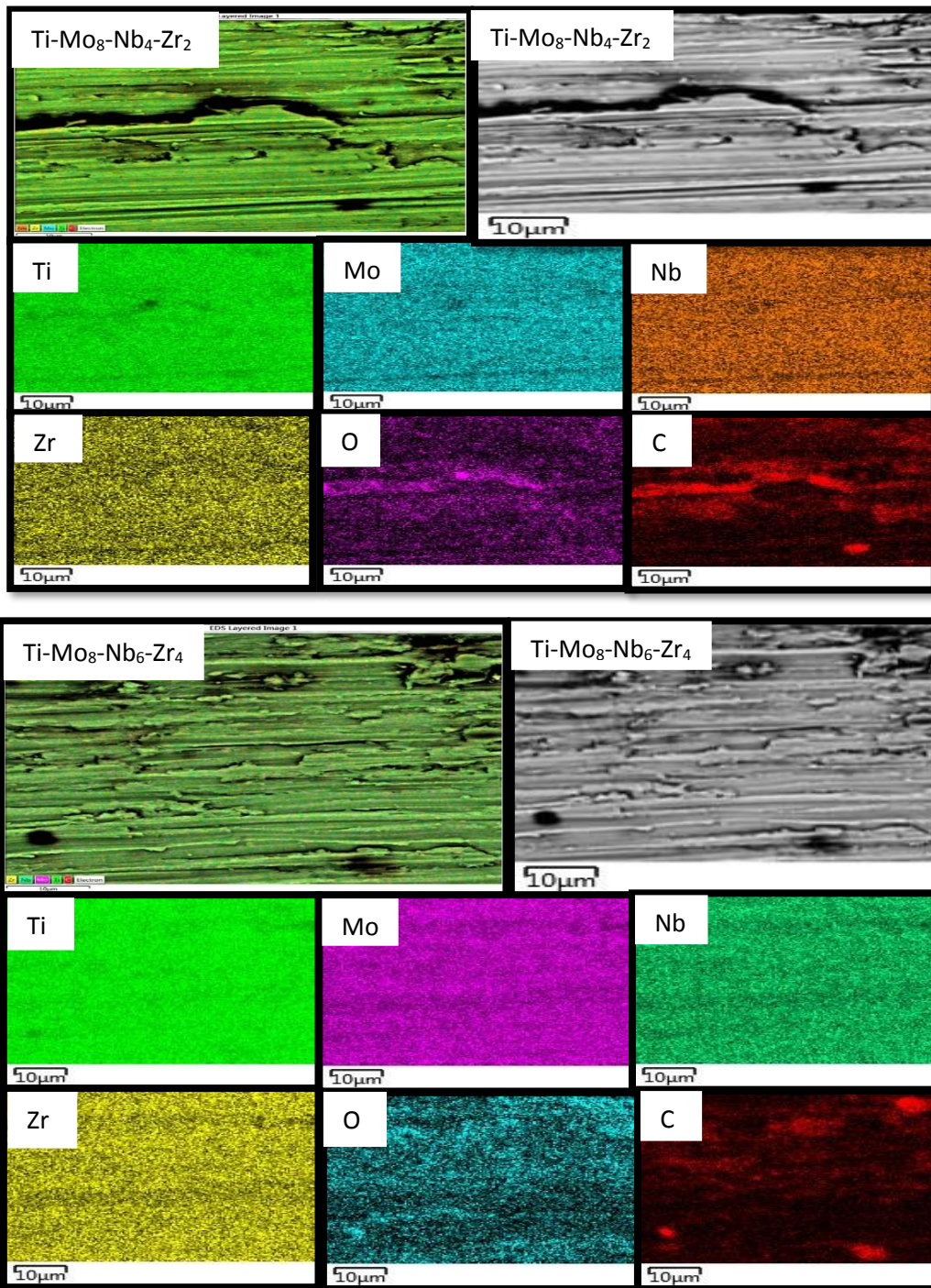


Figure 7-32: EDX element mapping of titanium alloys under cathodic potentiostatic rubbing conditions.

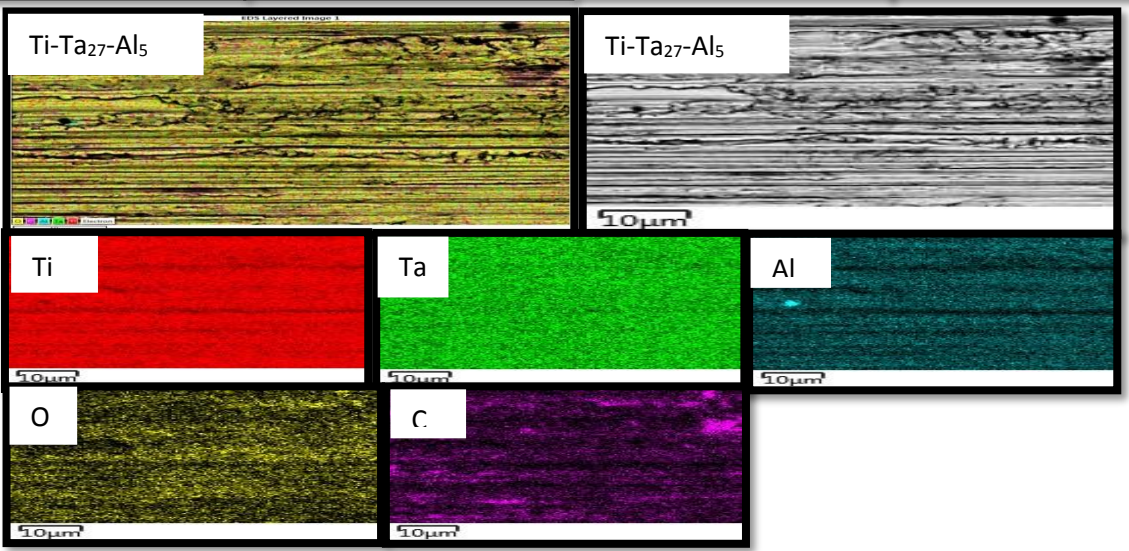
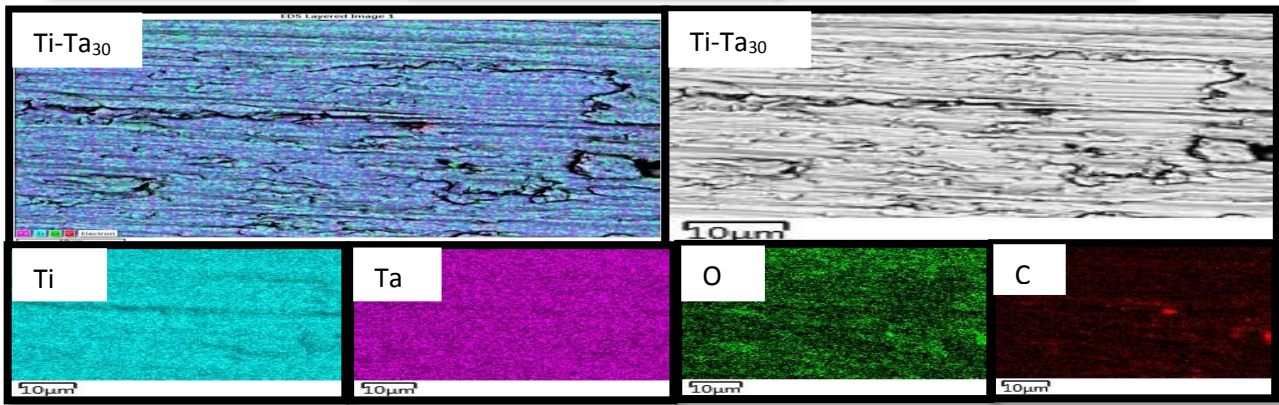
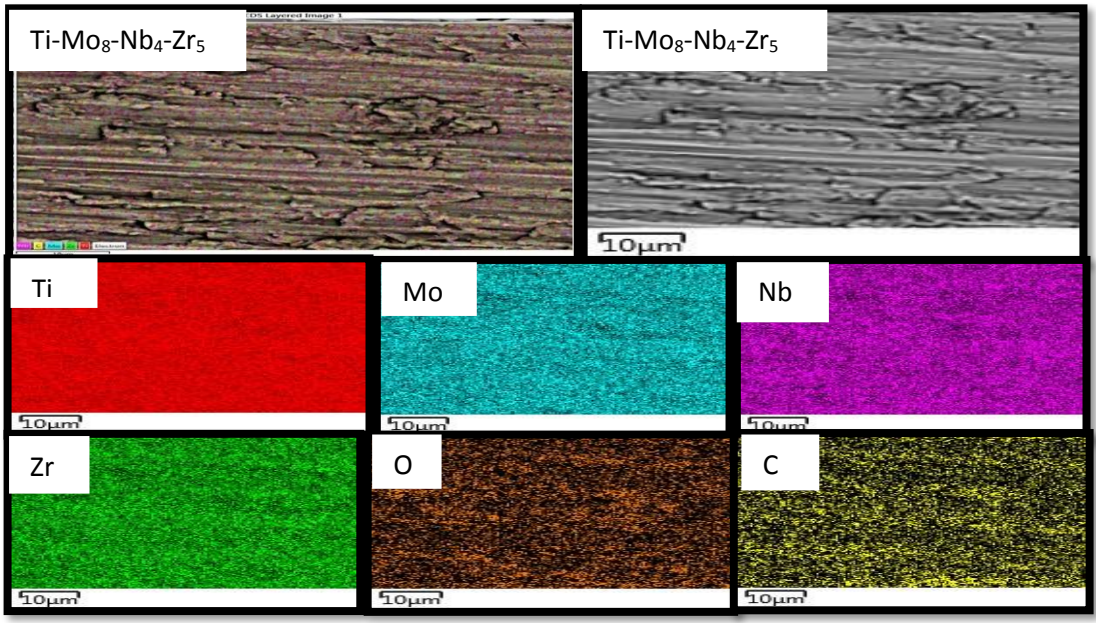


Figure 7-32: Continued

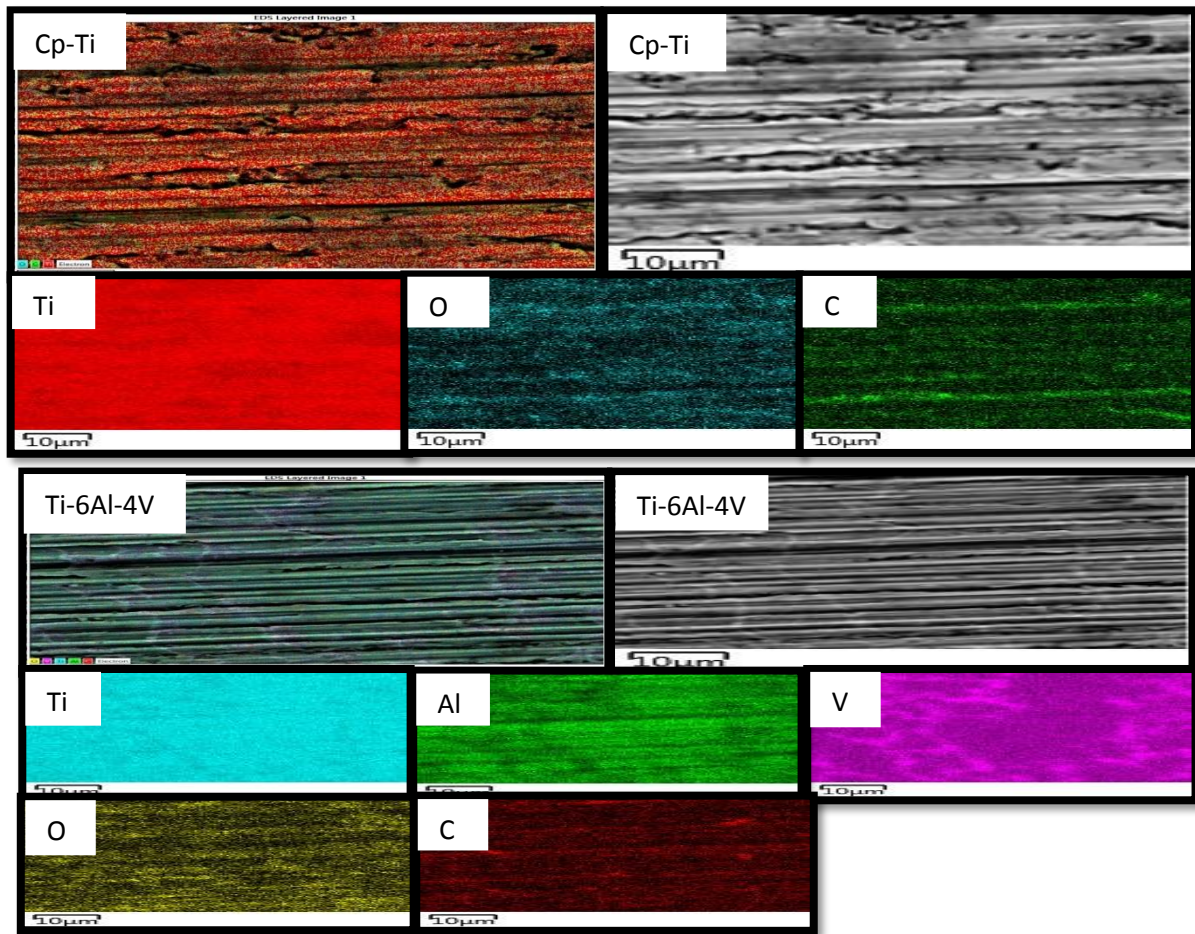


Figure 7-32: Continued

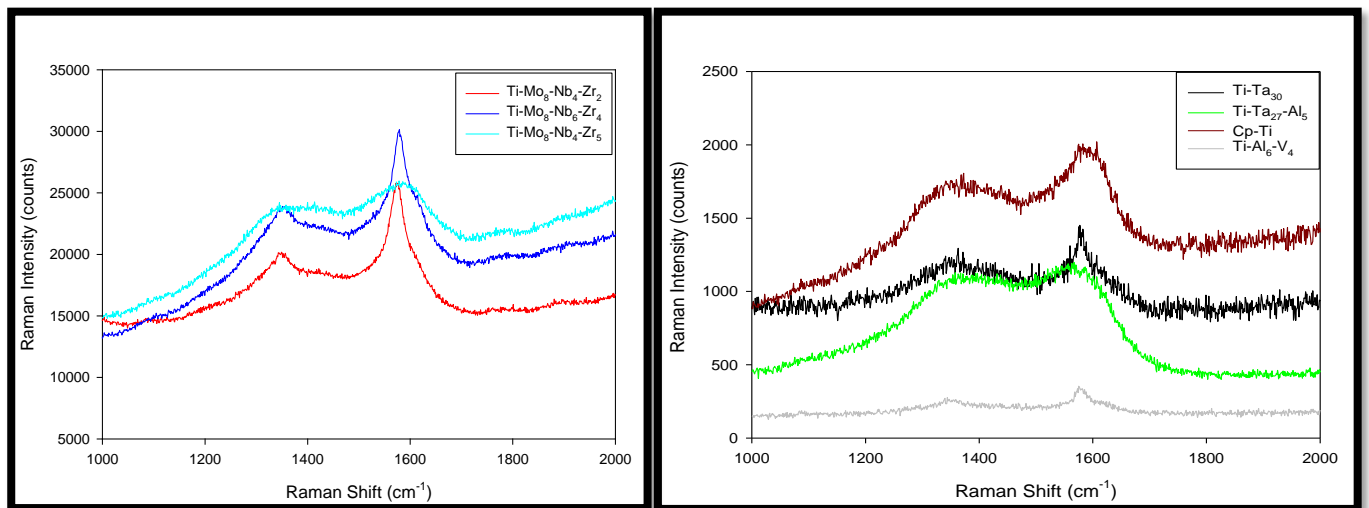


Figure 7-33: Raman spectra of the wear track of titanium alloys under cathodic potentiostatic rubbing conditions.

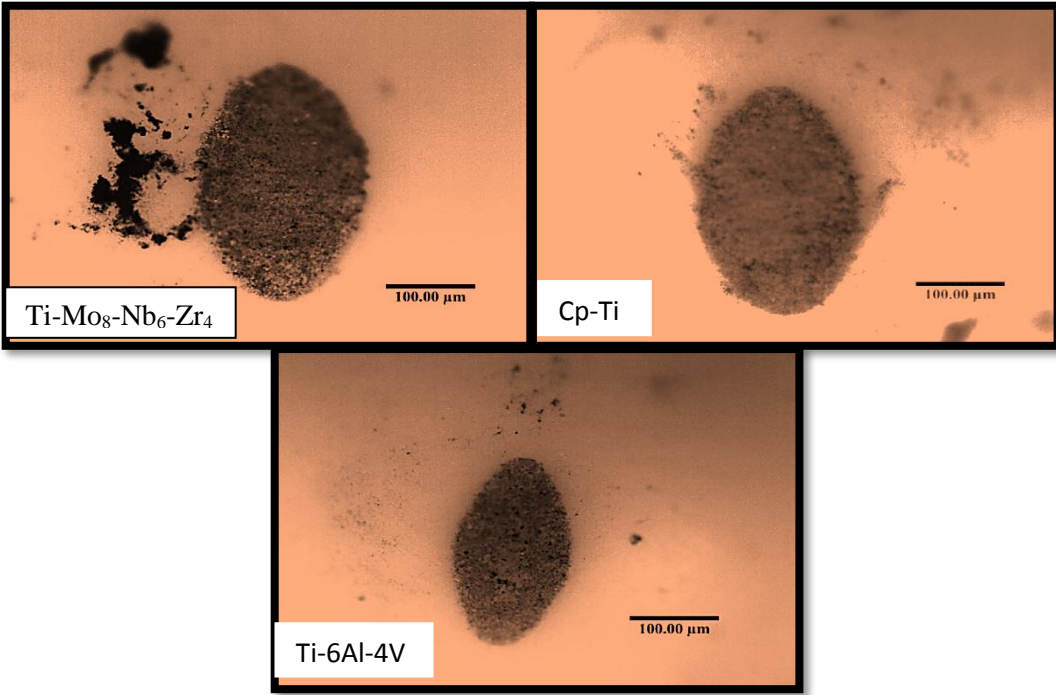


Figure 7-34 Optical images of the alumina balls rubbing against the titanium alloys under cathodic rubbing conditions.

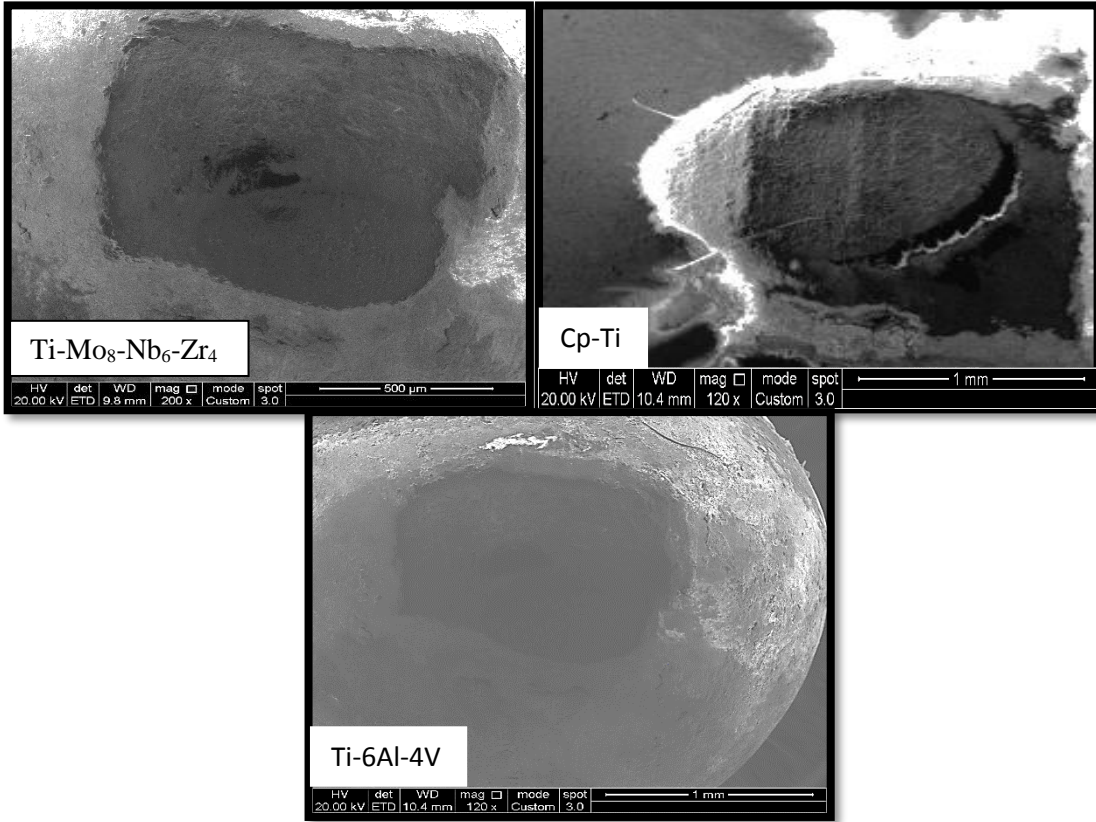


Figure 7-35 SEM images of the alumina balls rubbing against the titanium alloys under cathodic rubbing conditions.

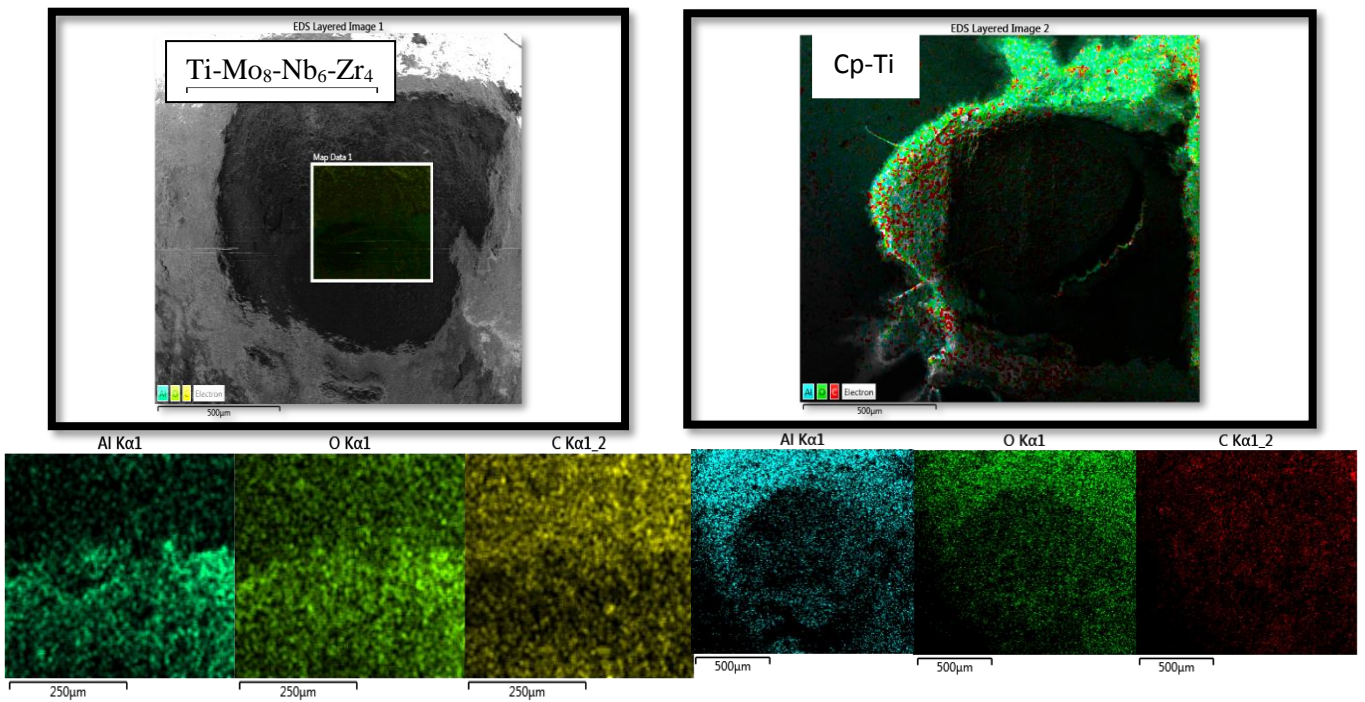


Figure 7-36 EDX element mapping of the alumina ball after rubbing against Ti-Mo₈-Nb₆-Zr₄ and Cp-Ti alloys under cathodic rubbing conditions.

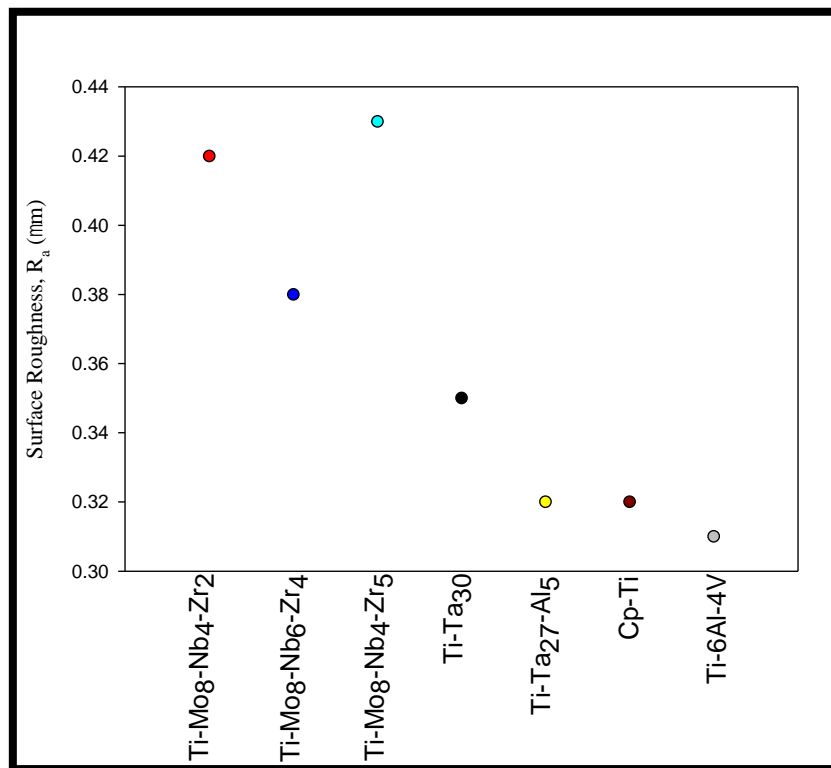


Figure 7-37 The average surface roughness titanium alloys under cathodic potentiostatic rubbing conditions.

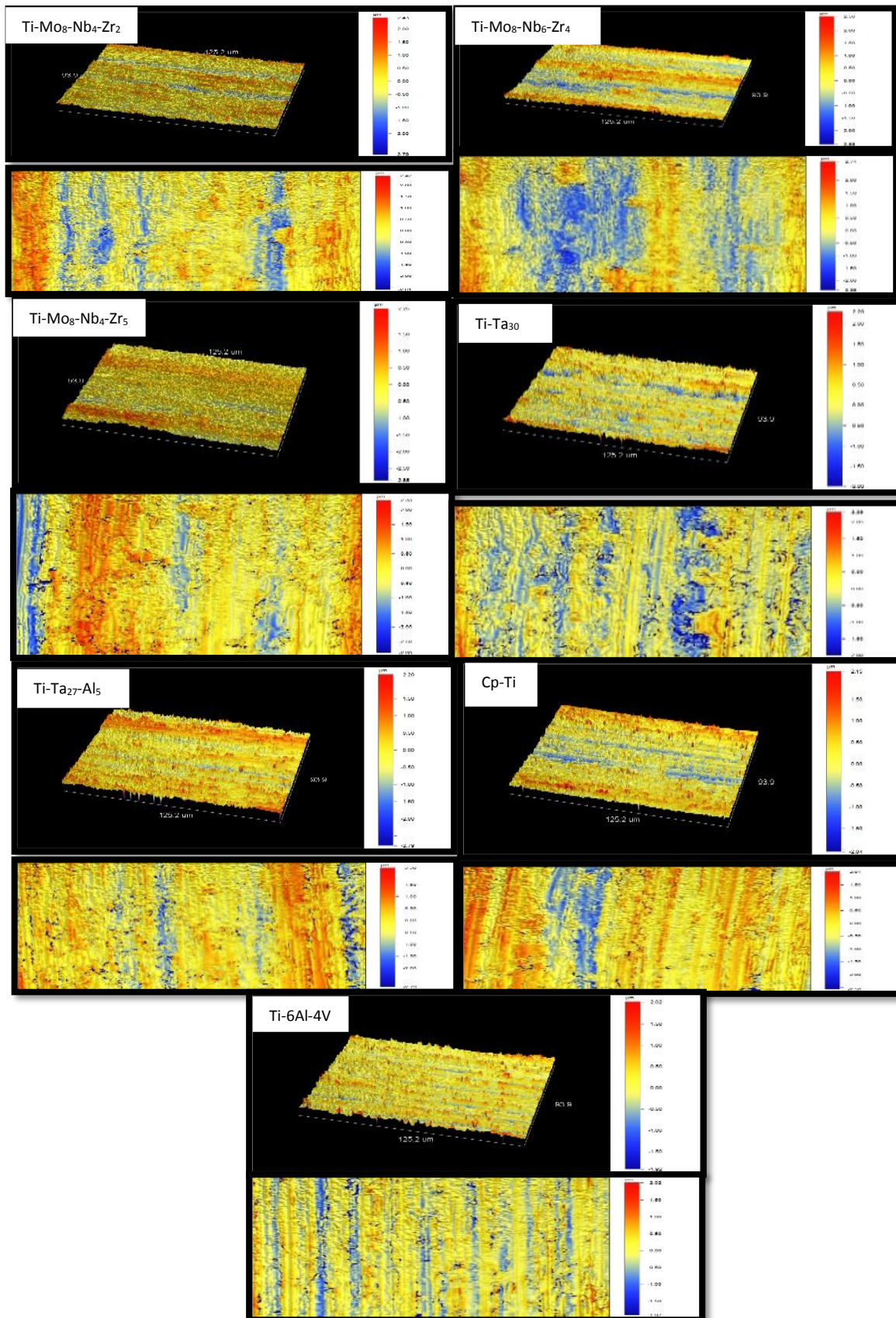


Figure 7-38: Surface roughness, 3D and 2D top view of the wear track under cathodic potentiostatic rubbing conditions.

7.3.3 Total Material Loss Rate

3D images of the wear track after testing under cathodic potentiostatic rubbing conditions in bovine calf serum are presented in Figure 7-39. All alloys exhibited a regular wear track. The wear track depth of the β microstructure Ti-Ti-Mo₈-Nb₆-Zr₄, Ti-Mo₈-Nb₄-Zr₅, and Ti-Ta₃₀ of 89, 92, 91 μm respectively was larger than that of $\beta + \alpha''$ microstructure Ti-Ta₂₇-Al₅ (56 μm), $\alpha + \beta$ microstructure Ti-6Al-4V (53 μm), the β microstructure Ti-Mo₈-Nb₄-Zr₂ of (44) and the α microstructure Cp-Ti (30 μm).

The average wear volume is shown in Figure 7-40 a. The α microstructure Cp-Ti and the β microstructure Ti-Mo₈-Nb₄-Zr₂ had the lowest average total volume of 0.04 and 0.06 mm^3 respectively, while the β microstructure Ti-Mo₈-Nb₄-Zr₅ and Ti-Ta₃₀ had the highest total volume of 0.18 mm^3 . The average total volume of the $\alpha'' + \beta$ microstructure Ti-Ta₂₇-Al₅ alloy was similar to that of the $\alpha + \beta$ microstructure Ti-6Al-4V of 0.09 mm^3 . In contrast the β microstructure Ti-Mo₈-Nb₆-Zr₄ had an average total volume of 0.16 mm^3 . The average specific wear rate is presented in Figure 7-40 b. Amongst the titanium alloys used in this study Cp-Ti and Ti-Mo₈-Nb₄-Zr₂ alloys had the lowest specific wear rate of 0.0001 and 0.0002 mm^3/Nm respectively. The average specific wear rate of the $\alpha'' + \beta$ microstructure Ti-Ta₂₇-Al₅ alloy was similar to that of $\alpha + \beta$ microstructure Ti-6Al-4V of 0.0004 mm^3/Nm . The β microstructure Ti-Mo₈-Nb₄-Zr₅ and Ti-Ta₃₀ had the highest average specific wear rate of 0.0008 mm^3/Nm . The β microstructure Ti-Mo₈-Nb₆-Zr₄ had an average specific wear rate of 0.0007 mm^3/Nm .

The measurement of the anodic current during rubbing at cathodic conditions (-0.5V vs OCP) allowed for quantification of the wear-accelerated corrosion. Therefore, applying Faraday's law and the mechanistic approach for tribocorrosion the chemical and mechanical contribution to material loss during tribocorrosion at (-0.5V vs OCP) can be quantitatively determined. Figure 7-41 presents the contribution of mechanical wear (V_{mech}) and electrochemical (V_{chem}) to total material loss rate volume (V_{total}) of titanium and titanium alloys after tribocorrosion tests under cathodic conditions (-0.5V vs OCP).

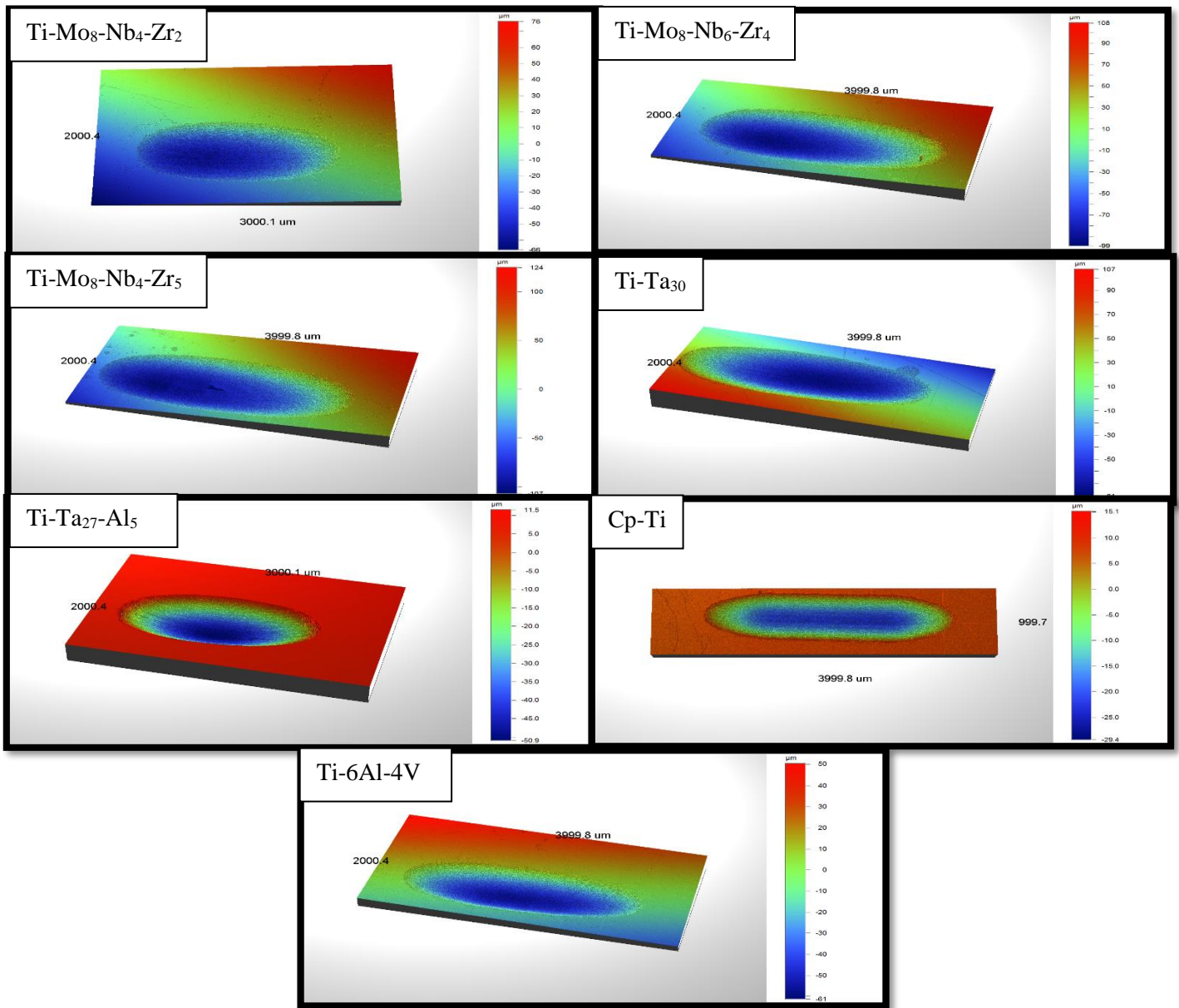


Figure 7-39: 3D images of the wear track of titanium and titanium alloys fabricated in this study under cathodic potentiostatic rubbing conditions.

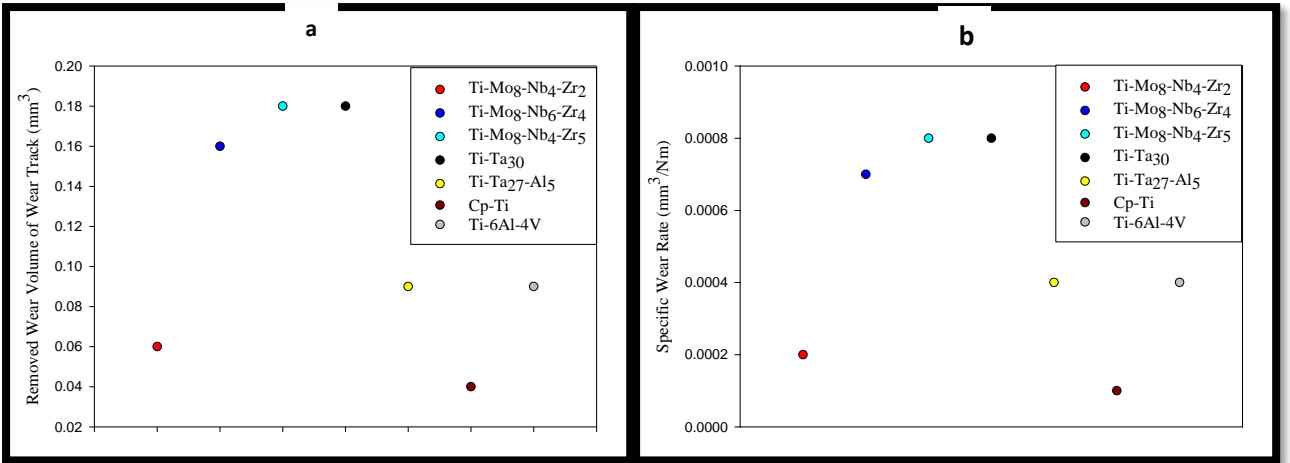


Figure 7-40: (a) Removed wear volumes (b) Specific wear rates of wear track for titanium alloys under cathodic potentiostatic rubbing conditions.

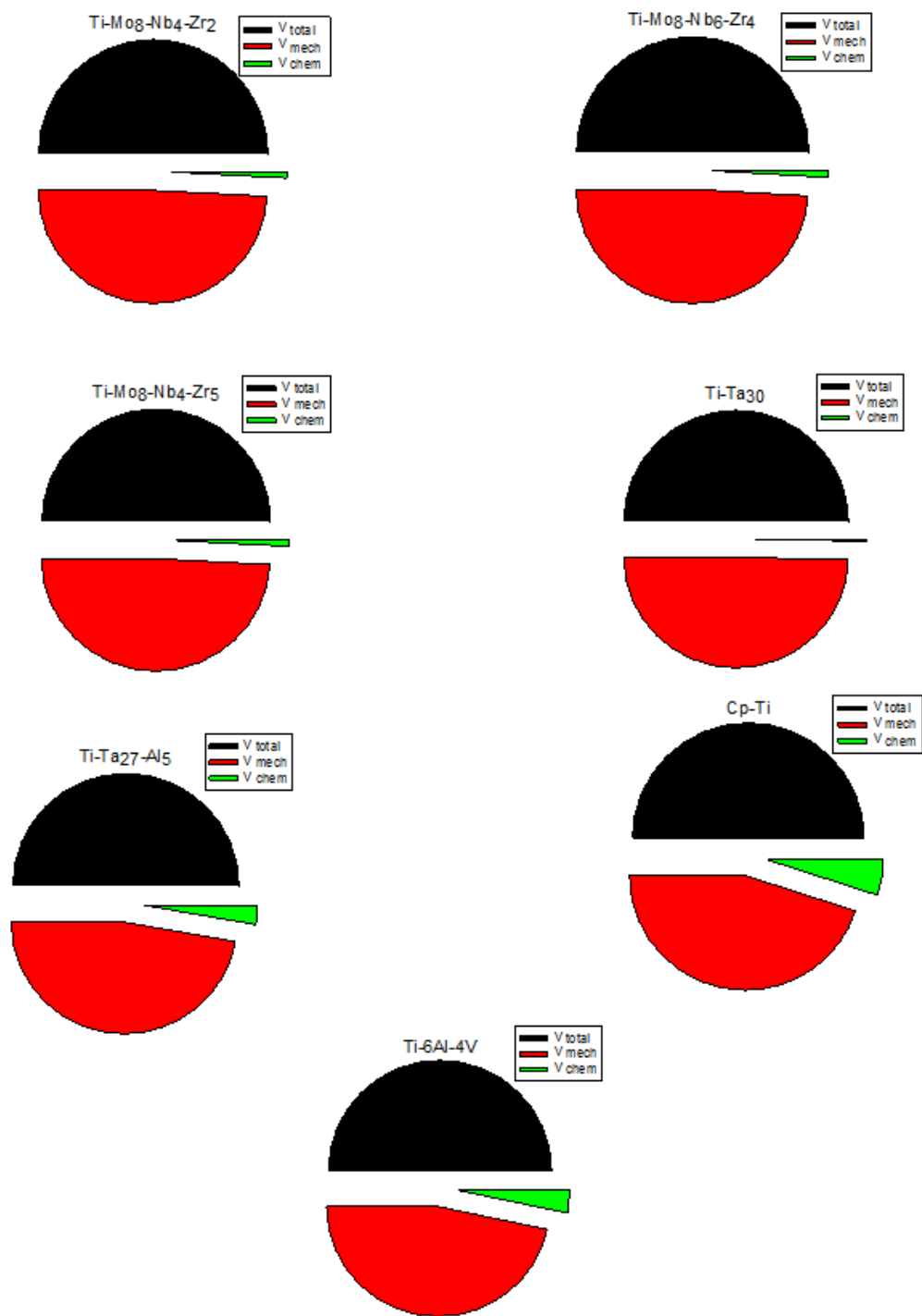


Figure 7-41 Contribution of mechanical wear and electrochemical to total material loss rate volume of titanium alloys after tribocorrosion tests under cathodic potentiostatic rubbing conditions.

7.3.4 Subsurface Morphology

To better understand the tribocorrosion mechanism, a cross-section was prepared by FIB at the centre of the wear track. Figure 7-42 shows an ion channelling contrast image of the wear tracks formed at the $\beta + \alpha''$ - microstructure Ti-Ta₂₇-Al₅, while Figure 7-43 shows an ion channelling contrast image of the wear tracks formed at the β - microstructure Ti-Mo₈-Nb₄-Zr₅. A continuous nanocrystalline layer was observed after cathodic rubbing conditions, with a large variation in grain size with both lateral and depth position. There was a clear boundary between the nanocrystalline and microcrystalline regions in the case of the $\beta + \alpha''$ microstructure Ti-Ta₂₇-Al₅ alloy, while there was no clear nanocrystalline region in the case of the β - microstructure Ti-Mo₈-Nb₄-Zr₅ alloy.

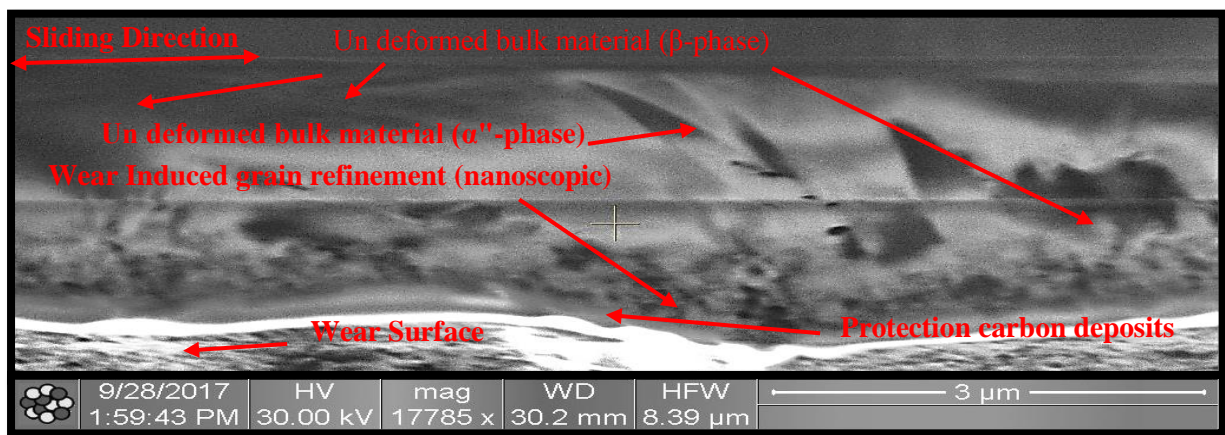


Figure 7-42 Ion channelling contrast image of a transverse cross-section of wear track formed at Ti-Ta₂₇-Al₅ under cathodic rubbing conditions.

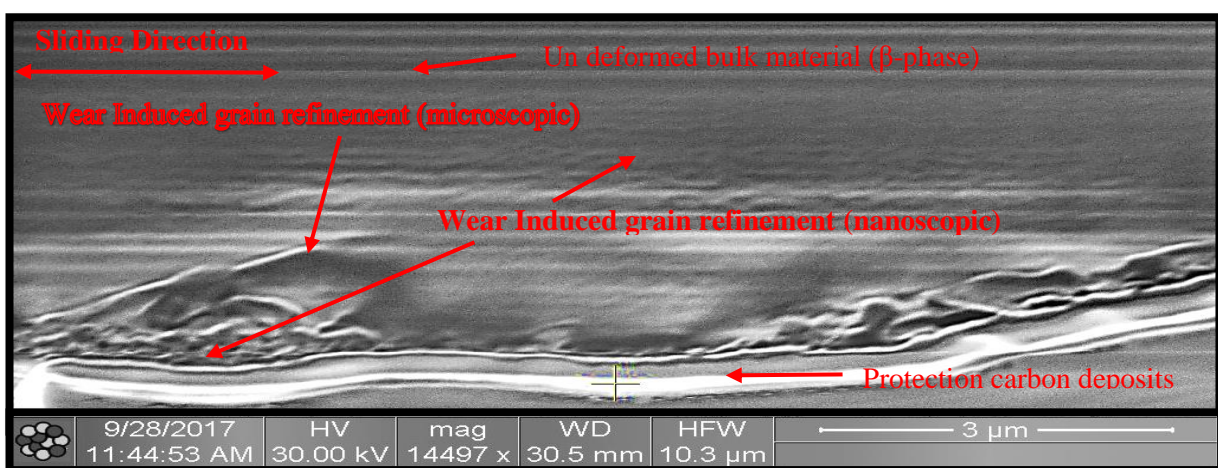


Figure 7-43 Ion channelling contrast image of a transverse cross-section of wear track formed at Ti-Mo₈-Nb₄-Zr₅ under cathodic rubbing conditions.

7.4 Tribocorrosion Under Anodic Potentiostatic Conditions

7.4.1 Sliding Friction Response

The evolution of the coefficient of friction and the anodic current with time during tribocorrosion experiments under anodic conditions (+0.3V vs OCP) is shown in Figures 7-44 through 7-50. The behaviour shown by Figures 7-44 and 7-50 is an indication of the reproducibility of the tests. The initial sliding created a significant increase in the anodic current that was observed for all alloys. This response was related to the depassivation mechanism by the counter-body sliding on the surface of alloys, thus leading to removal of the passive film in the contact region when sliding starts and exposing the surface of fresh active titanium to the electrolyte. Consequently, a rapid reaction between the active titanium surface and electrolyte leads to accelerated electrochemical corrosion and anodic metal oxidation. The higher anodic current was recorded for Ti-Ta₂₇-Al₅ followed by Cp-Ti, Ti-Ta₃₀, Ti-Mo₈-Nb₆-Zr₄, Ti-Mo₈-Nb₄-Zr₂, Ti-Mo₈-Nb₄-Zr₅, and Ti-6Al-4V respectively. During the sliding period, the anodic current reached the steady state value after a few seconds. There was no significant variation in the anodic current observed during sliding, except several isolated peaks indicating that the titanium alloys surface undergoes a local depassivation mechanism in small spots that is followed by rapid repassivation. The anodic current shows large fluctuations during rubbing, therefore the alloy composition effect on anodic current could not be extracted. However, the lowest anodic current during rubbing was recorded for Ti-6Al-4V followed by Ti-Mo₈-Nb₄-Zr₅, Ti-Mo₈-Nb₆-Zr₄, Ti-Mo₈-Nb₄-Zr₂, Ti-Ta₃₀, and Ti-Ta₂₇-Al₅ respectively. Finally, at the end of sliding, the anodic current decreased again to the initial value observed at the beginning of the tests before rubbing. This indicates repassivation of the worn area. After some time of repassivation, the anodic current of the alloys reached the value initially recorded before the start of rubbing test. The mean friction coefficient and average current during rubbing are shown in Figure 7-51. The lowest coefficient of friction was recorded for Ti-6Al-4V, while the highest was for Ti-Ta₃₀.

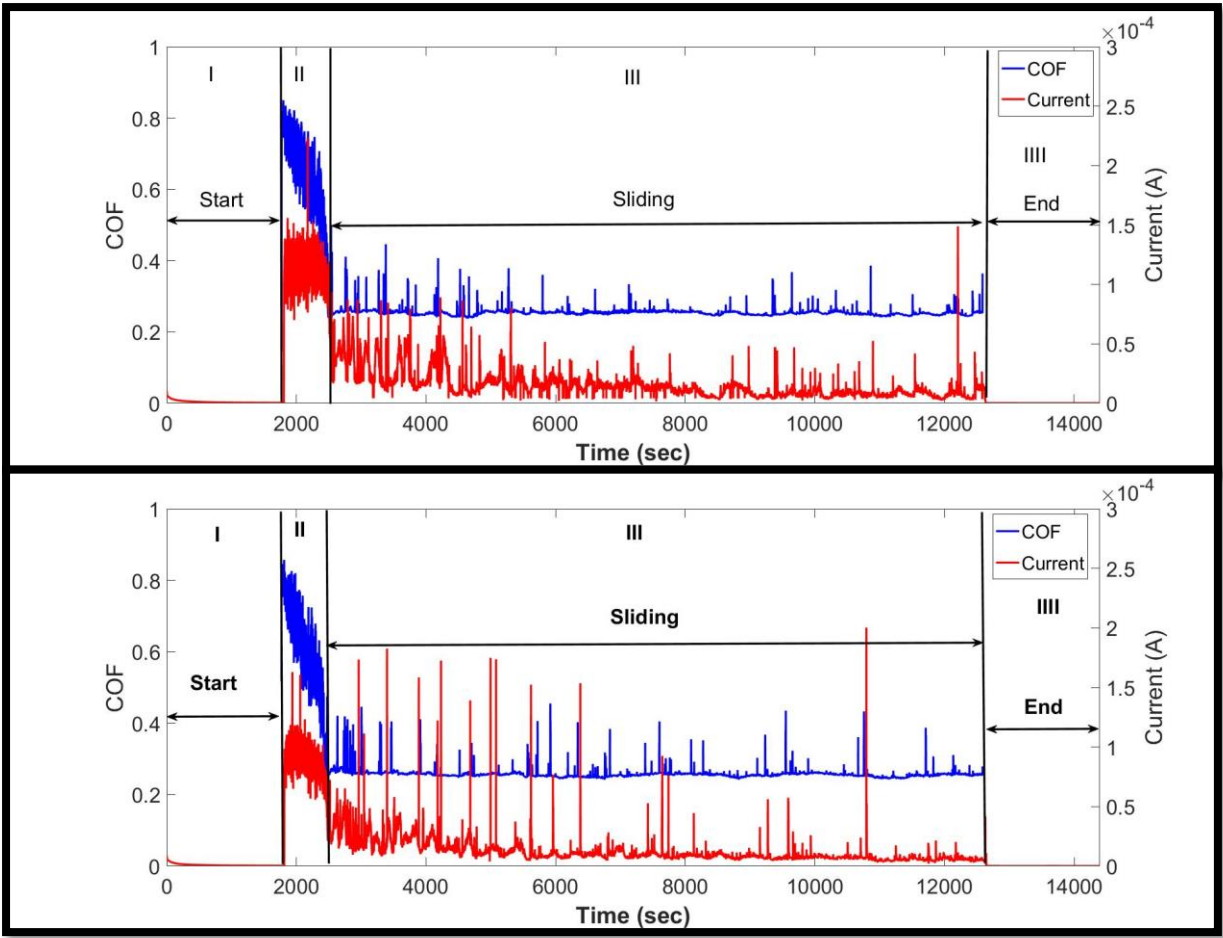


Figure 7-44: The evolution of the coefficient of friction (COF) and the current of Ti-Mo₈-Nb₆-Zr₄ alloy under anodic potentiostatic rubbing conditions. The two graphs show the repetition of the same test, which gives very consistent results.

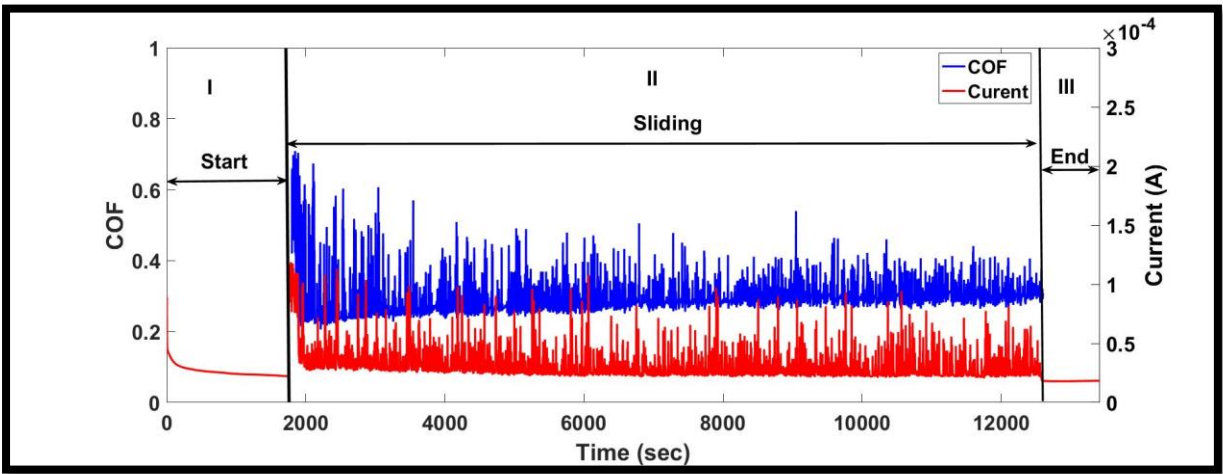


Figure 7-45: The evolution of the coefficient of friction (COF) and the current of Ti-Mo₈-Nb₄-Zr₂ alloy under anodic potentiostatic rubbing conditions.

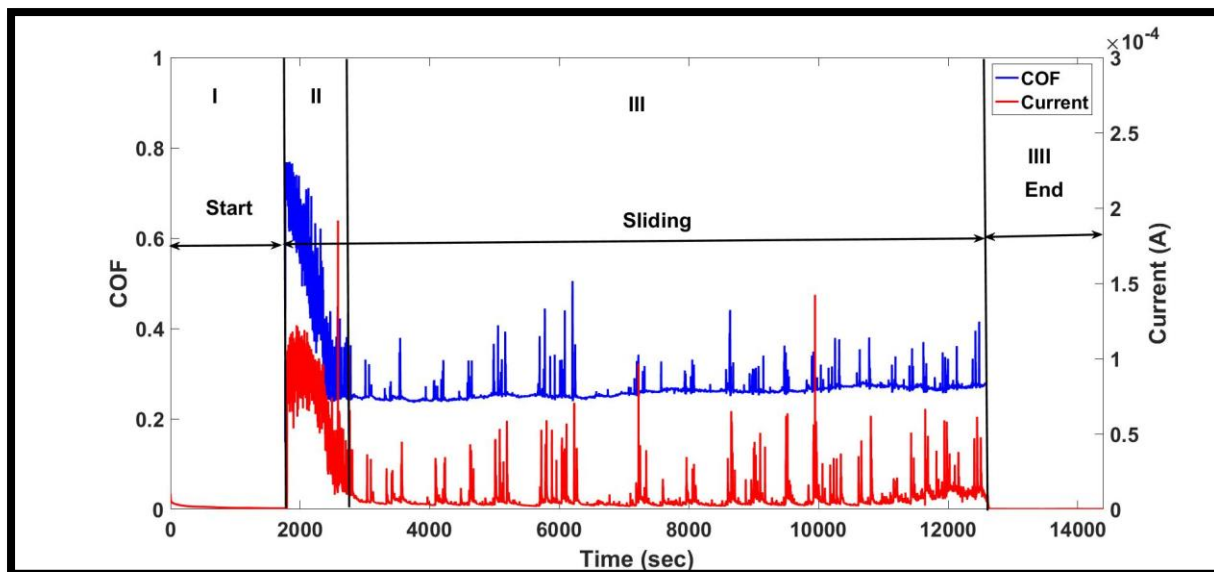


Figure 7-46: The evolution of the coefficient of friction (COF) and the current of Ti-Mo₈-Nb₄-Zr₅ alloy under anodic potentiostatic rubbing conditions.

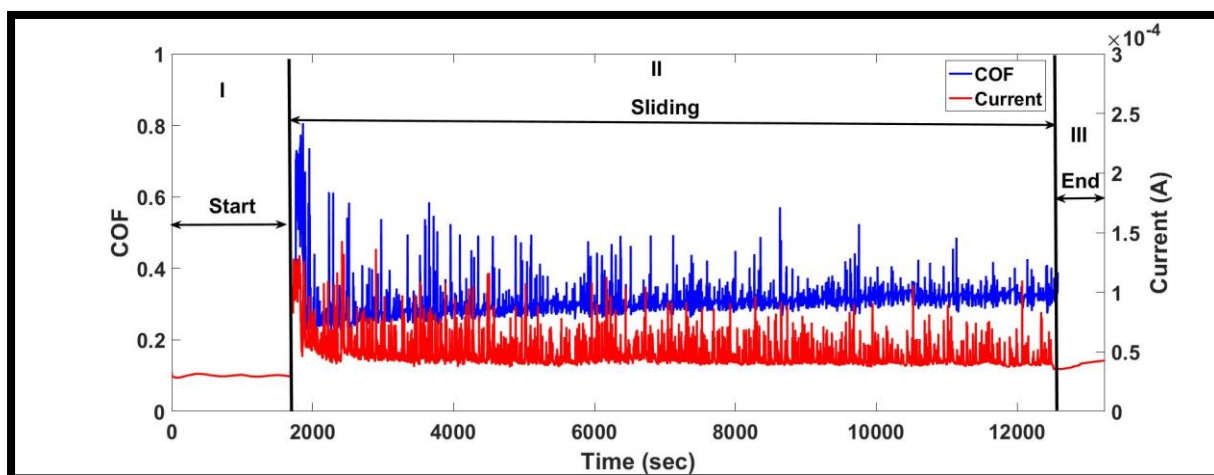


Figure 7-47: The evolution of the coefficient of friction (COF) and the current of Ti-Ta₃₀ alloy under anodic potentiostatic rubbing conditions.

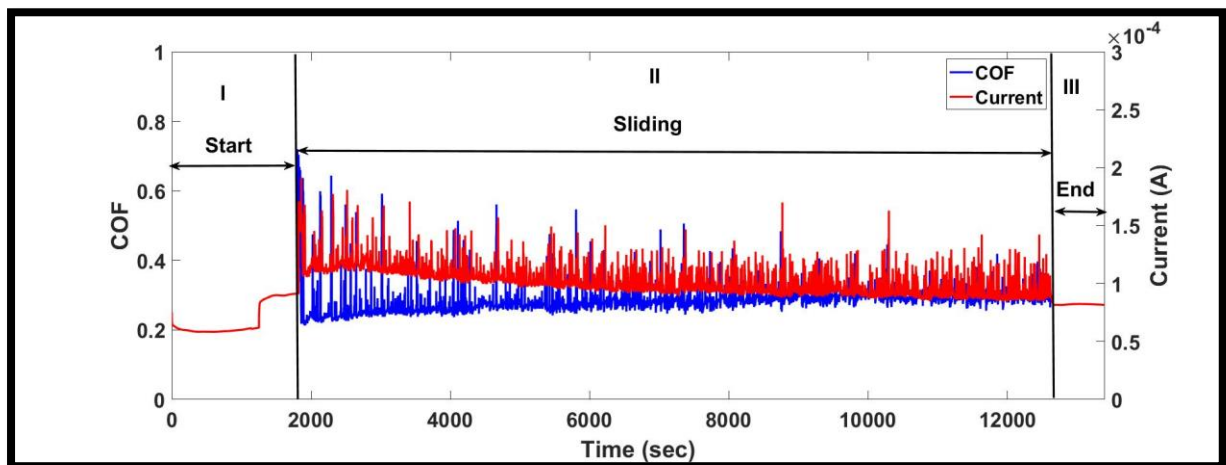


Figure 7-48: The evolution of the coefficient of friction (COF) and the current of Ti-Ta₂₇-Al₅ alloy under anodic potentiostatic rubbing conditions.

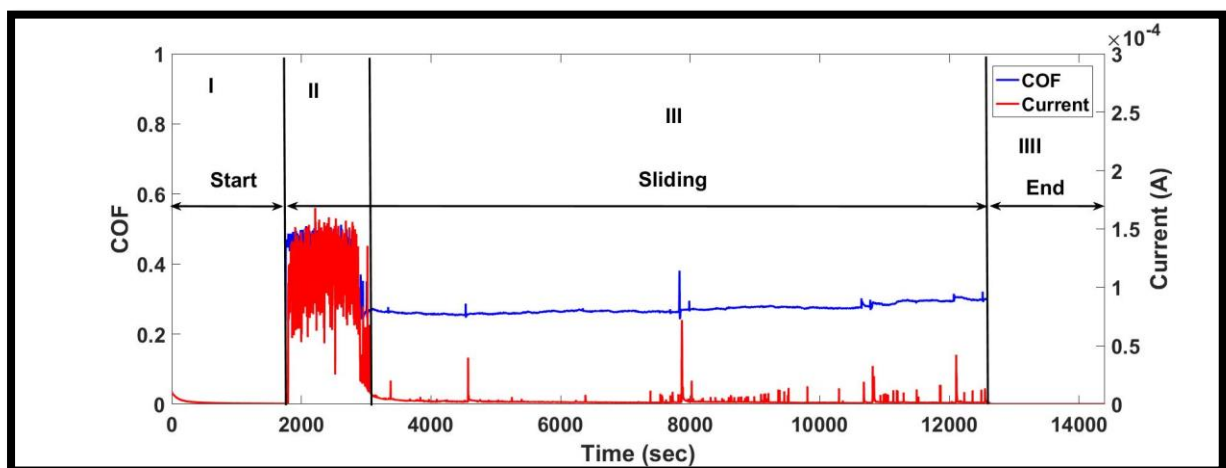


Figure 7-49: The evolution of the coefficient of friction (COF) and the current of Cp-Ti alloy under anodic potentiostatic rubbing conditions.

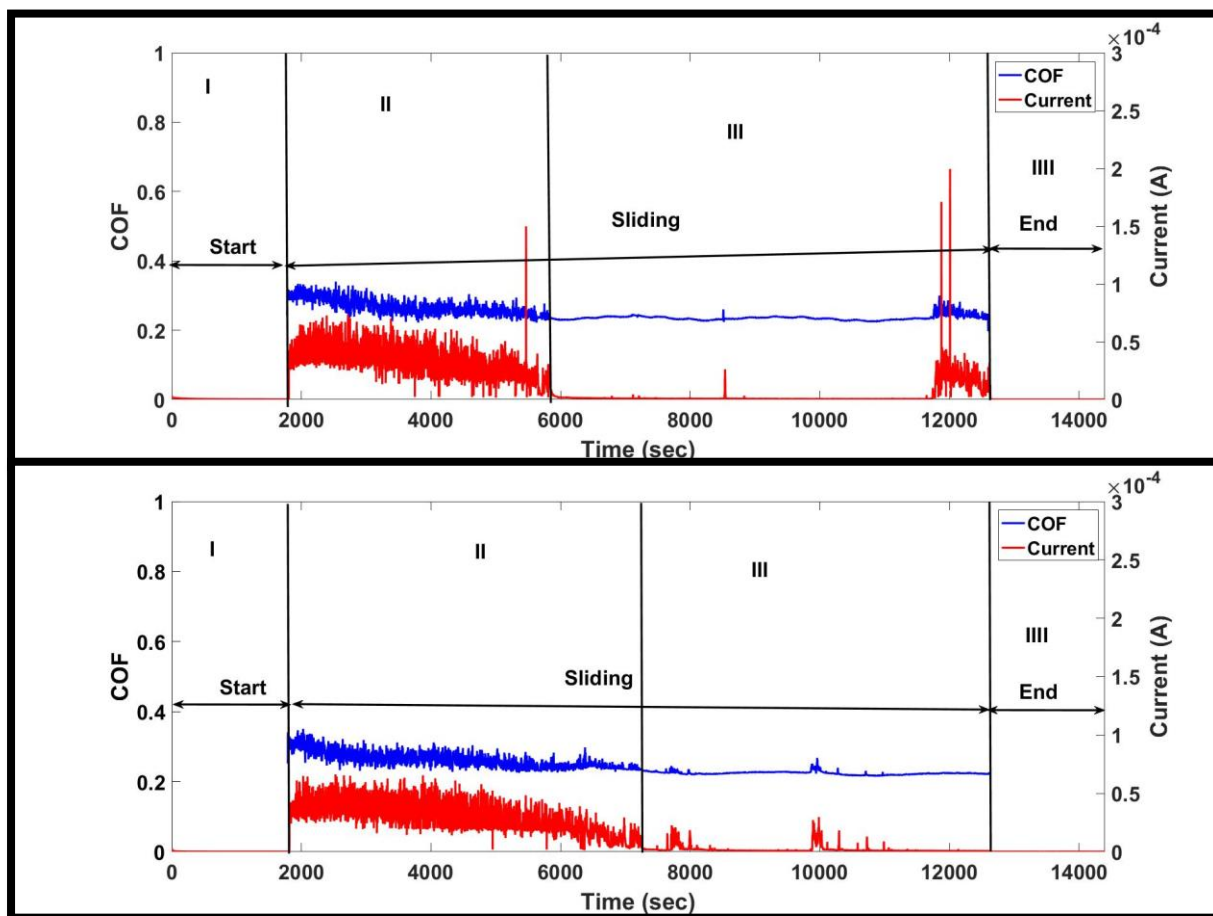


Figure 7-50: The evolution of the coefficient of friction (COF) and the current of Ti-6Al-4V alloy under anodic potentiostatic rubbing conditions. The two graphs show the repetition of the same test, which gives very consistent results.

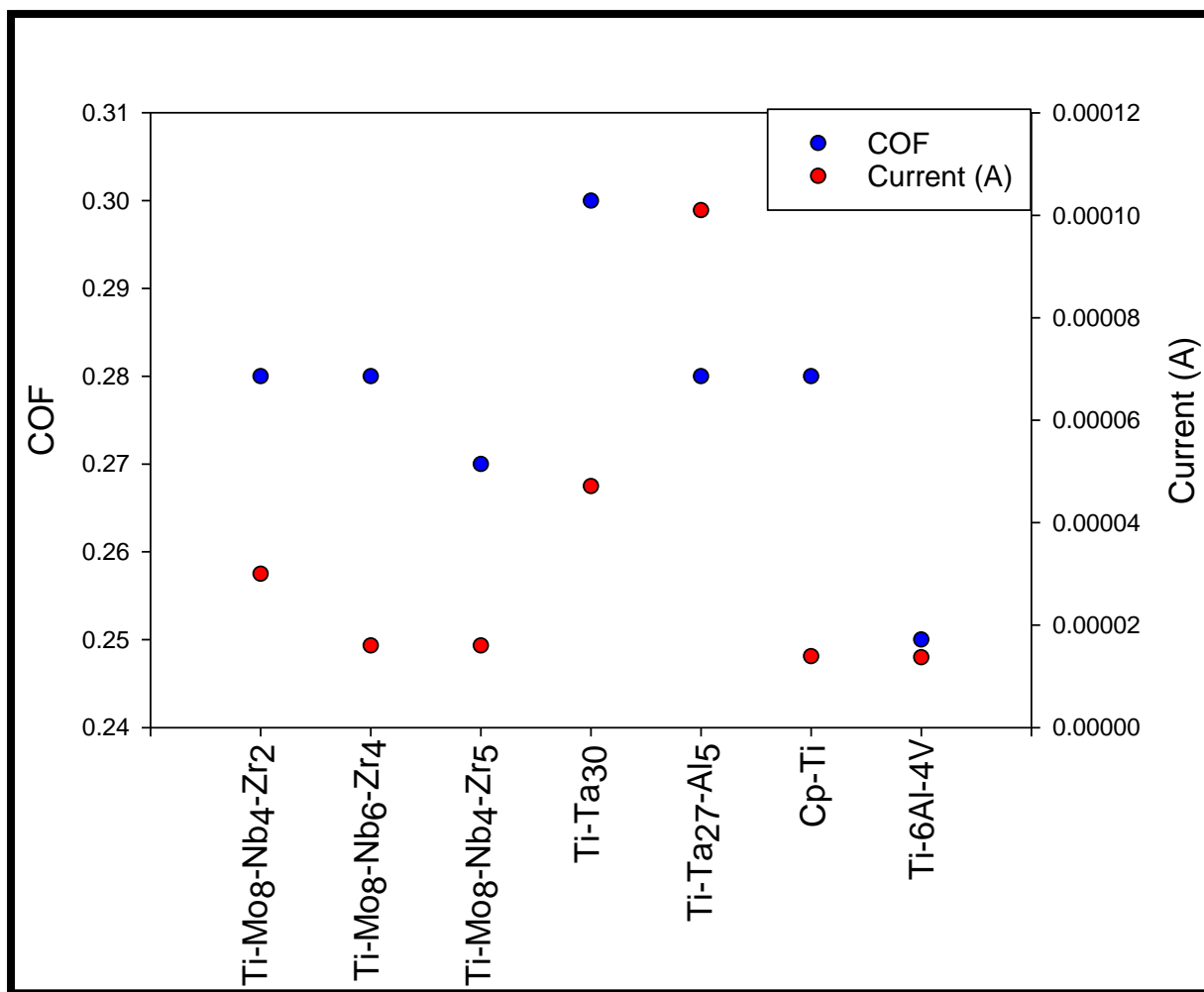


Figure 7-51 The mean friction coefficient and current values of titanium alloys under anodic potentiostatic rubbing conditions.

7.4.2 Wear Morphology, Chemistry and Roughness under anodic conditions

Typical secondary electron SEM images of worn surfaces after tribocorrosion experiments at anodic potentiostatic rubbing conditions are shown in Figure 7-52. The plastic deformation grooves and the relatively smooth appearance of the worn surface was observed in all cases. The worn surface of all alloys appears to be covered by a light grey layer at various places in the surface of the worn tracks. This indicated a carbonaceous film formed on the surface of the wear tracks. EDX and Raman analyses confirmed the formation of this carbonaceous layer.

The EDX elemental maps for the anodic potentiostatic rubbing are presented in Figure 7-53, corresponding to the boxed area covering the surface shown in the image top right of all figures. As well as the substrate elements, carbon and oxygen were observed. Given that

carbon and oxygen were present on the surface of the wear track Raman spectroscopy was undertaken. Figures 7-54 show typical Raman spectra taken at the centre of the wear track. The spectra show disordered graphite (D band) and the single crystal graphite (G band) centred on 1383 and 1567 cm^{-1} related to sp^2 -carbon and sp^3 -band carbon respectively. There was no transfer from the alumina ball to the titanium alloys surface. The morphology of the wear tracks on the alumina balls were evaluated using optical and scanning electron microscopy. Figures 7-55 and 7-56 show typical optical and SEM images of the wear tracks on the alumina ball after the tribocorrosion tests under OCP conditions. No significant material transfer and no significant damage could be observed by optical and scanning electron microscopy on the alumina ball counterbody after tribocorrosion tests under OCP. These results are in agreement with the results of EDX on the alumina ball counterbody after tribocorrosion tests under OCP as can be observed from Figure 7-57.

The average surface roughness (Ra) of the wear tracks after tribocorrosion experiments under anodic potentiostatic conditions are presented in Figure 7.58. Figure 7-59 shows surface roughness 3D image and 2D top view of the centre of the wear track after tribocorrosion test under anodic potentiostatic rubbing conditions. Among all titanium alloys, the β -microstructure Ti-Ta₃₀ had the lowest surface roughness, while the α -microstructure Cp-Ti had the highest.

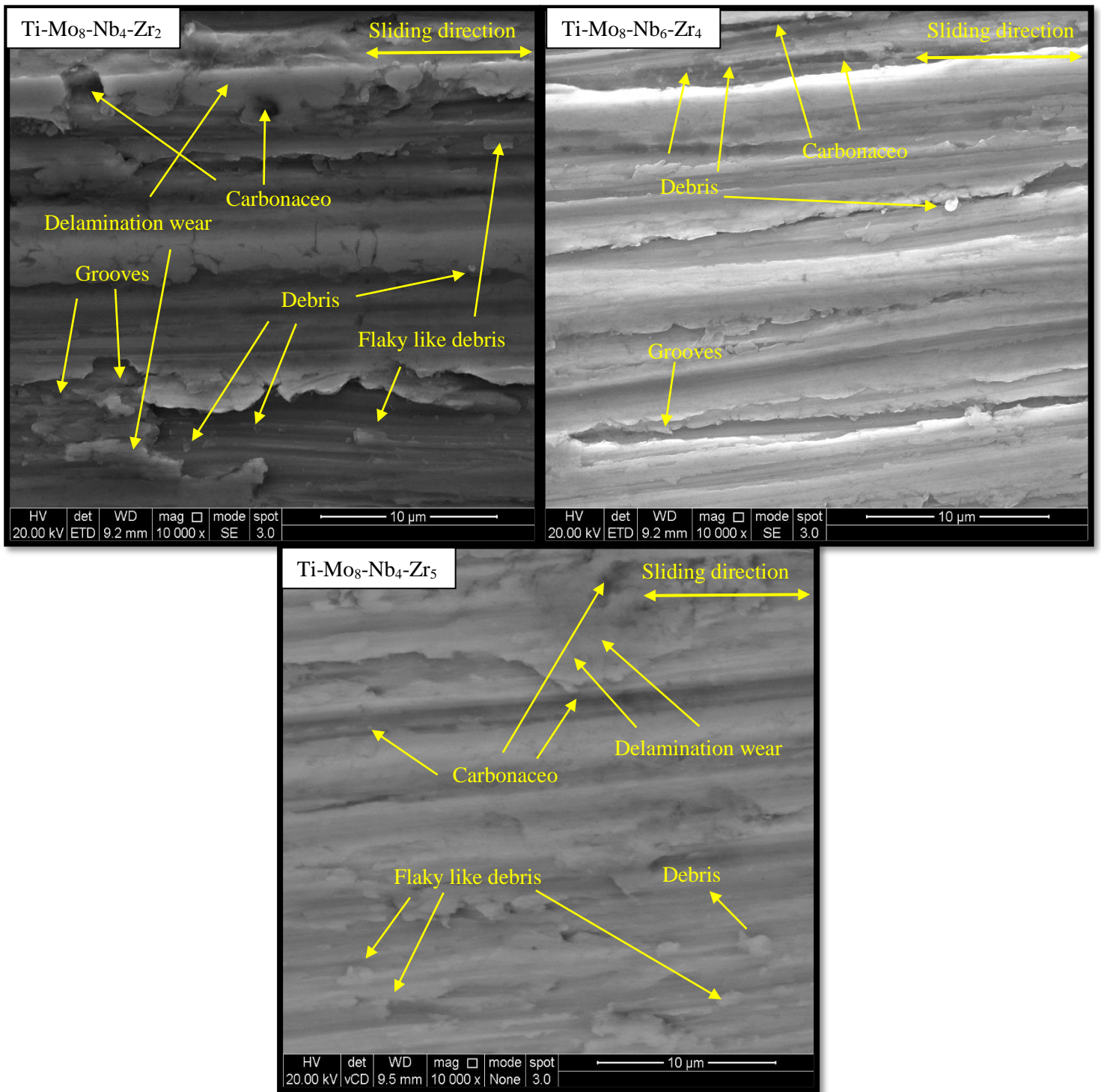


Figure 7-52: SEM micrographs of wear tracks of titanium alloys under anodic potentiostatic rubbing conditions.

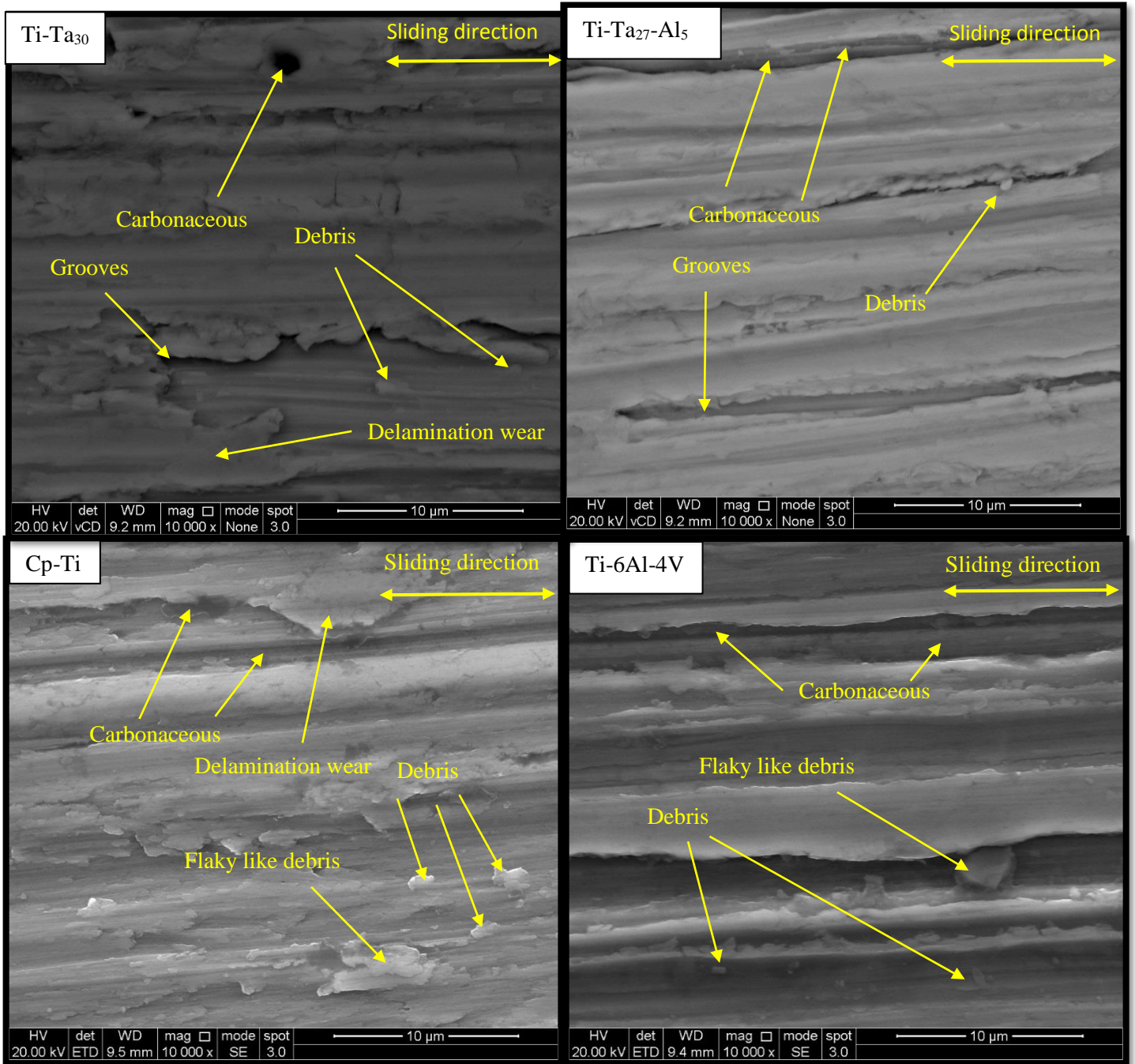


Figure 7-52: Continued

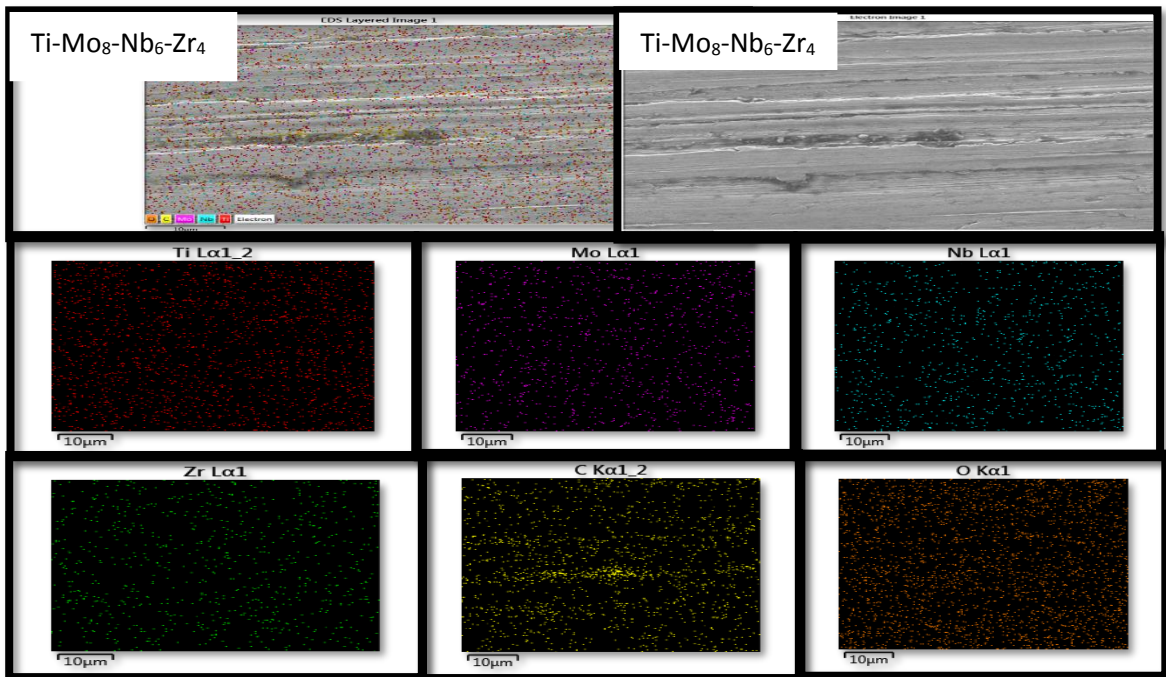
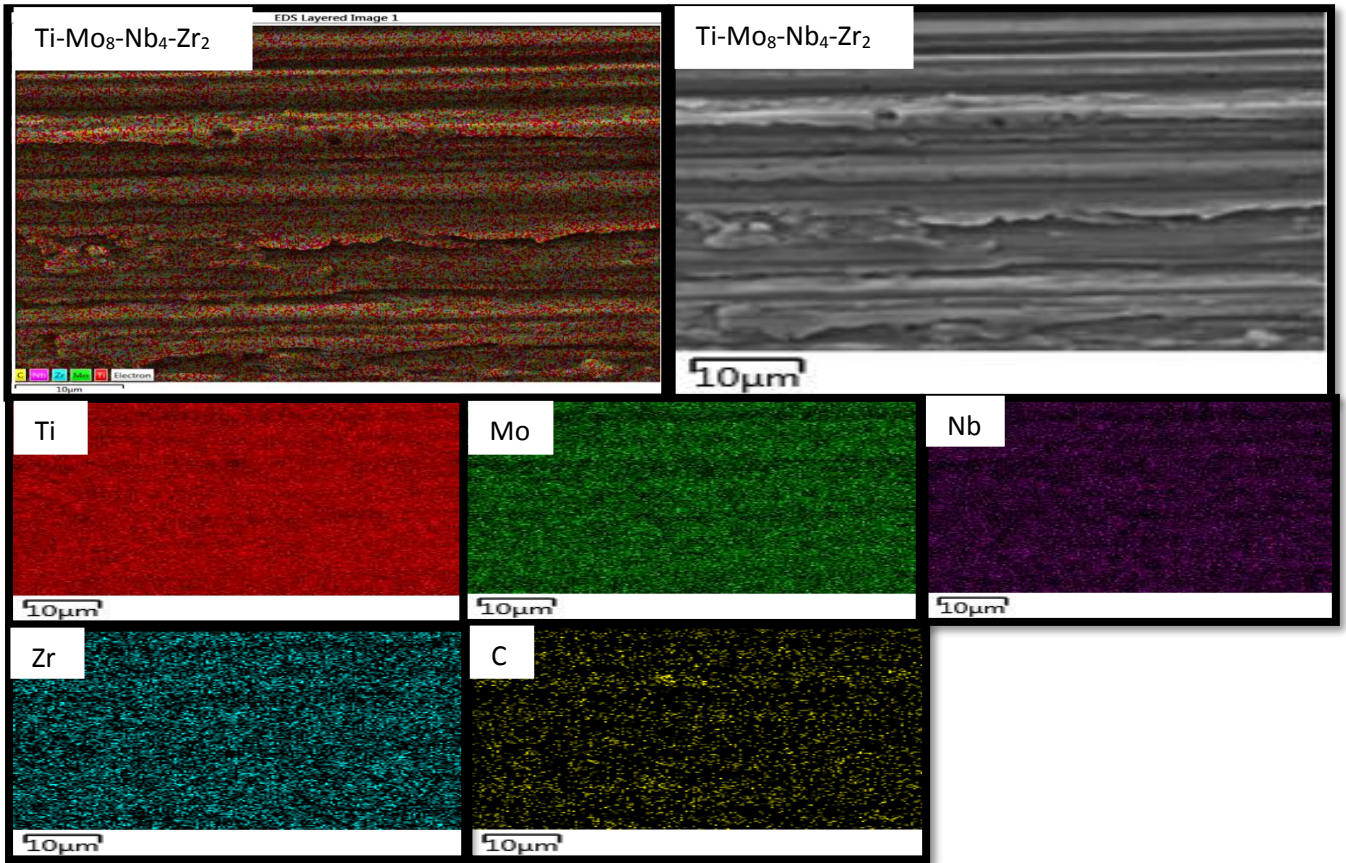


Figure 7-53: EDX element mapping of the wear track of titanium alloys under anodic potentiostatic conditions.

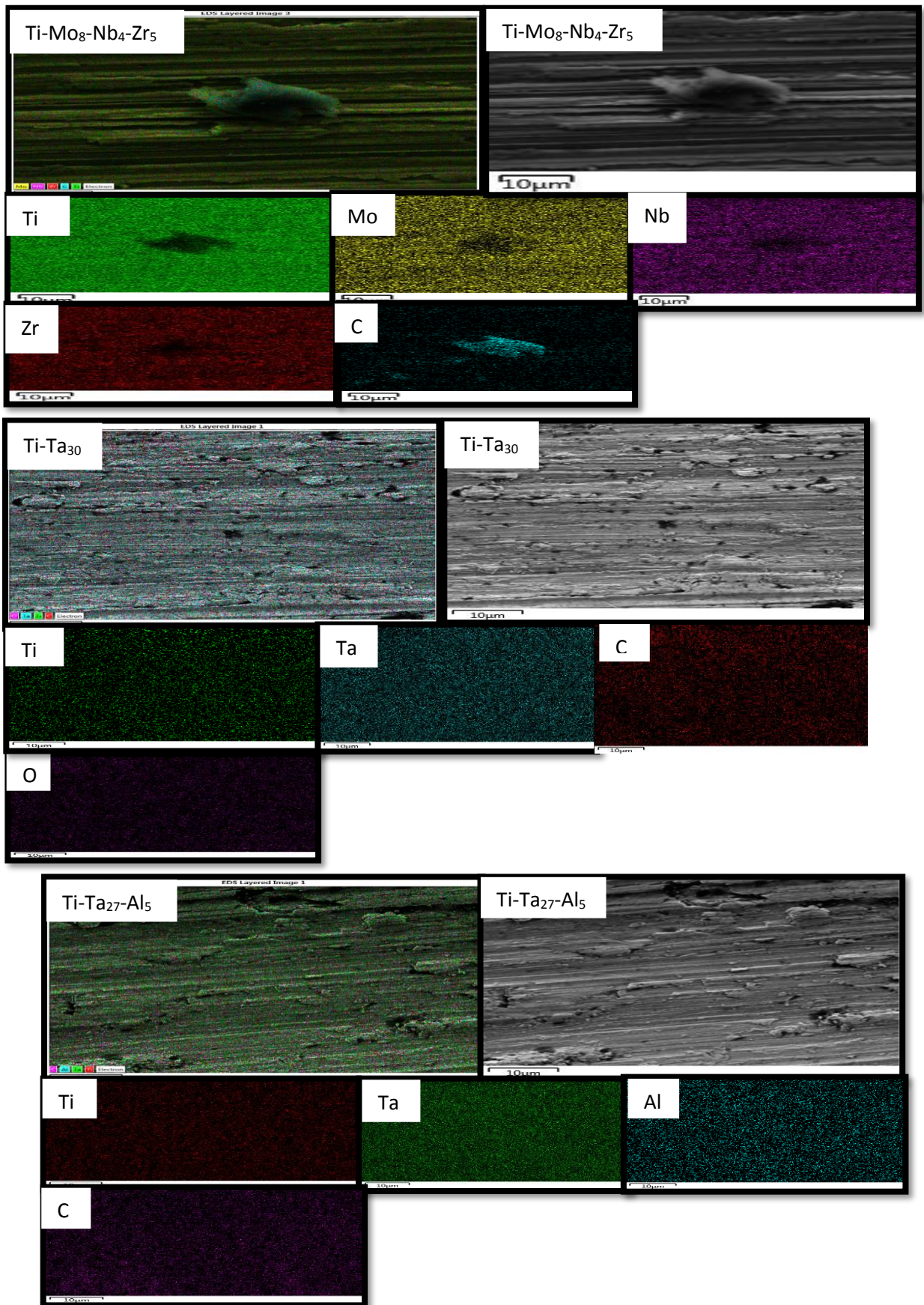


Figure 7-53: Continued

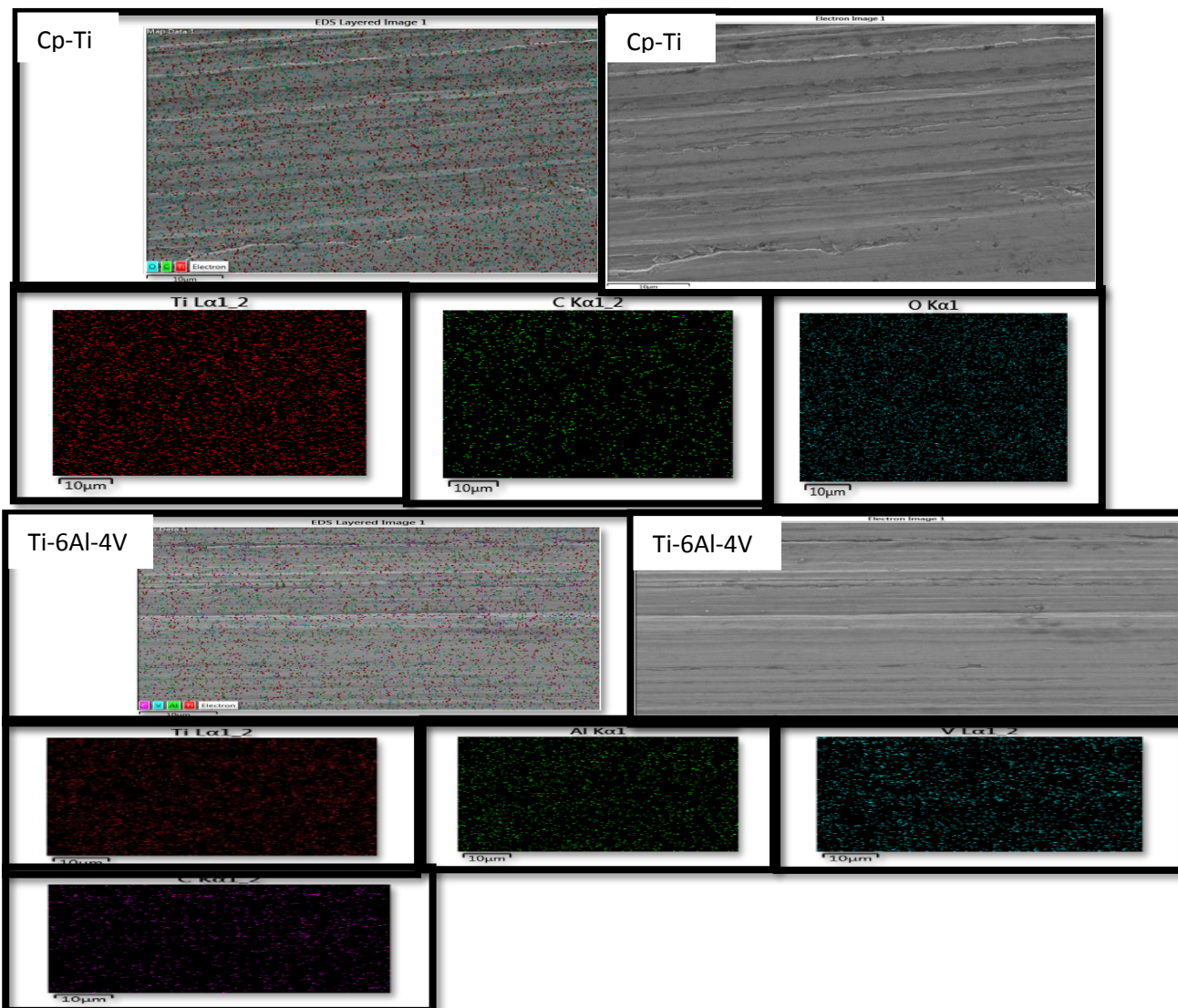


Figure 7-53: Continued

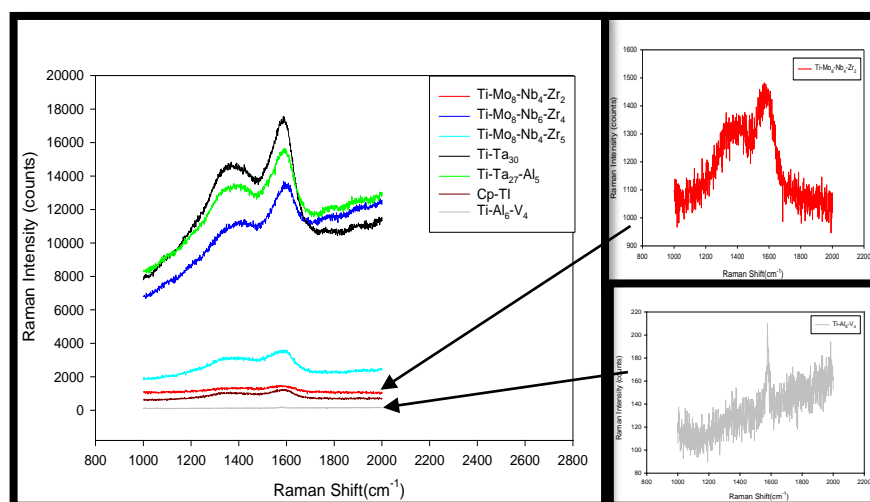


Figure 7-54: Raman spectra of the wear track of titanium alloys under anodic potentiostatic conditions.

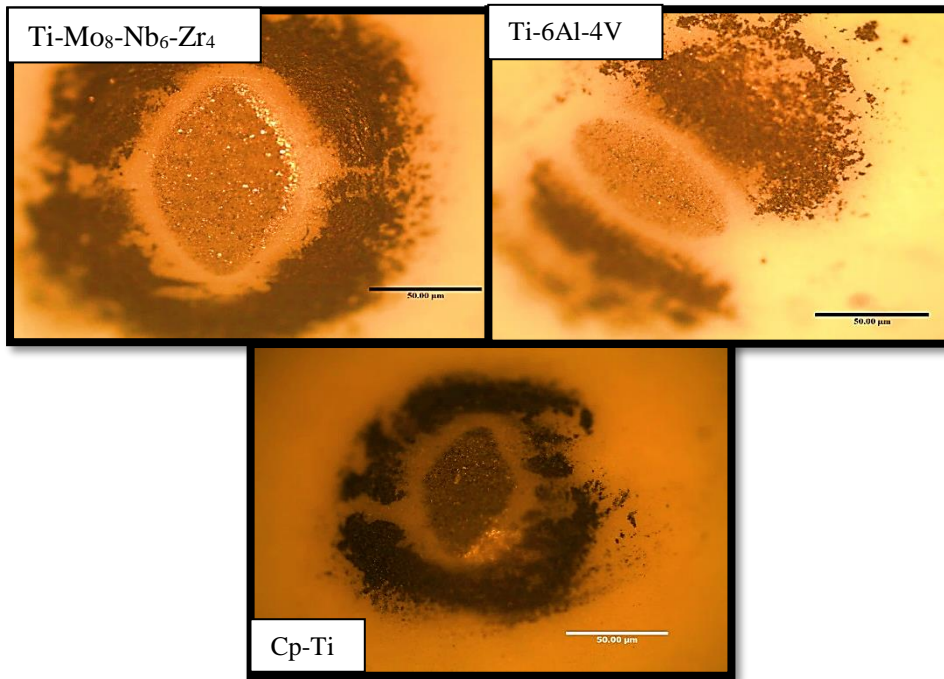


Figure 7-55 Optical images of the alumina balls rubbing against the titanium alloys under anodic rubbing conditions.

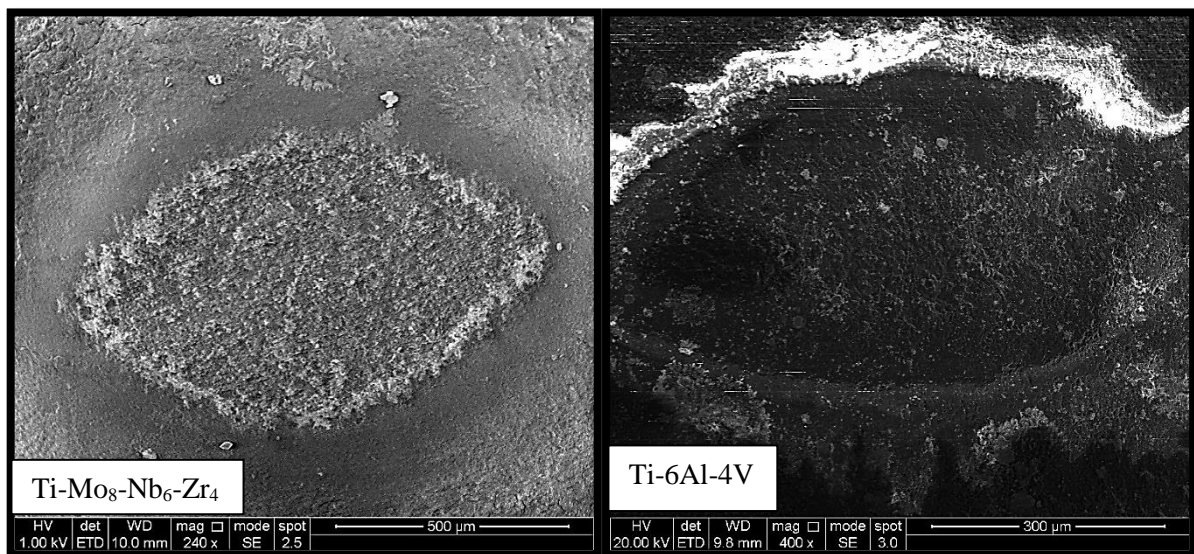


Figure 7-56 SEM images of the alumina balls rubbing against the titanium alloys under anodic rubbing conditions.

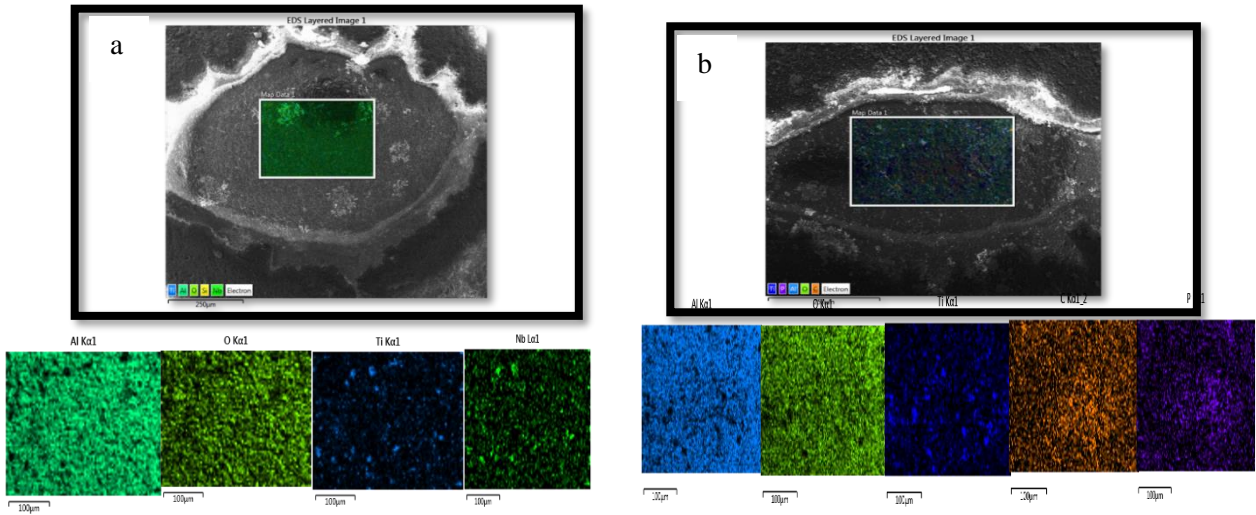


Figure 7-57 EDX element mapping of alumina ball rubbing against (a) Ti-Mo8-Nb6-Zr4 and (b) Ti-6Al-4V under anodic rubbing.

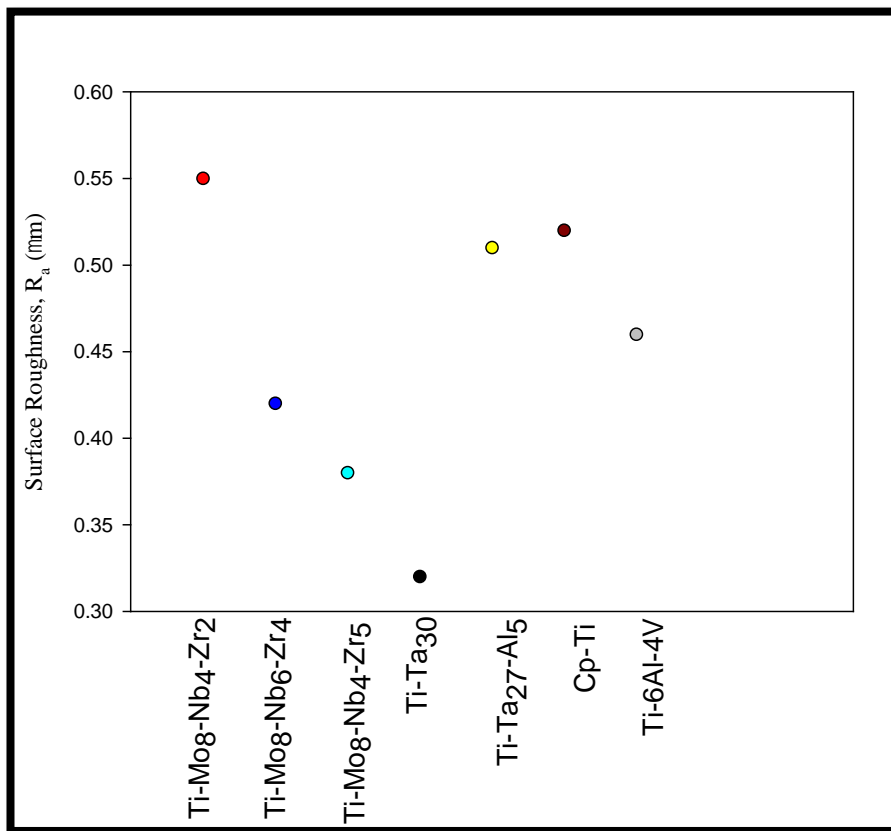


Figure 7-58 The average surface roughness of titanium alloys under anodic potentiostatic conditions.

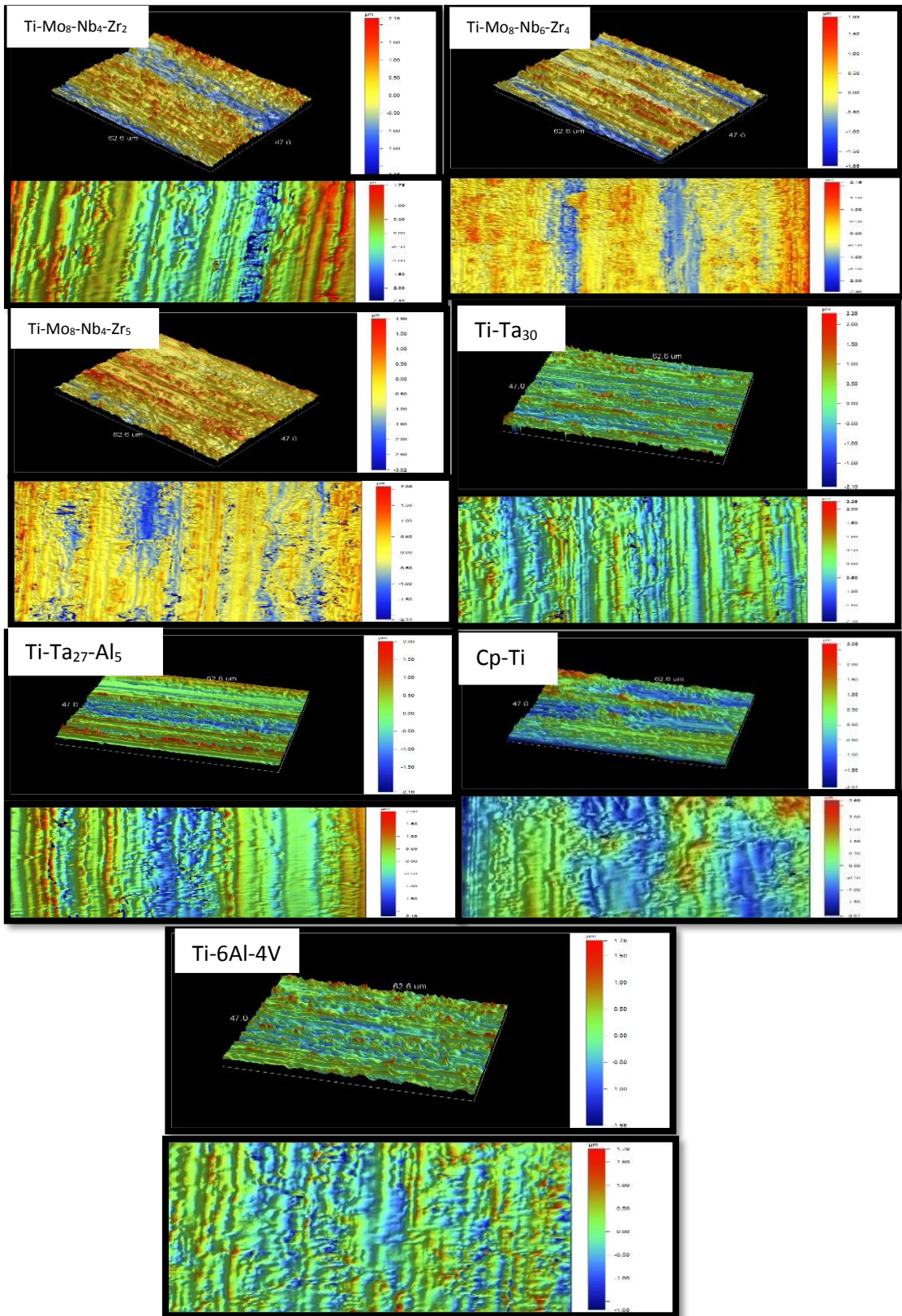


Figure 7-59: Surface roughness, 3D and 2D top view of titanium alloys under anodic potentiostatic conditions.

7.4.3 Total Material Loss Rate for anodic conditions

3D images of the wear track after anodic potentiostatic rubbing conditions in bovine calf serum are presented in Figure 7-60. All alloys tested had a regular wear track. The wear track depth of the β microstructure Ti-Mo₈-Nb₄-Zr₂, Ti-Mo₈-Nb₄-Zr₅, and Ti-Ta₃₀ was 43, 45, 44 μm respectively. This was larger than that of $\alpha+\beta$ phase Ti-6Al-4V (24 μm) and α microstructure Cp-Ti (17 μm). The wear track depth of the β microstructure of the Ti-Mo₈-Nb₆-Zr₄ and the $\beta+\alpha''$ microstructure Ti-Ta₂₇-Al₅ were 23 and 41 μm respectively.

The average wear volume under anodic potentiostatic rubbing conditions is shown in Figure 7-61 a. The α - microstructure Cp-Ti had the lowest average total volume of 0.01 mm^3 . The average total volume of Ti-Mo₈-Nb₄-Zr₂ alloy was similar to that of the Ti-Mo₈-Nb₄-Zr₅, Ti-Ta₃₀, and Ti-Ta₂₇-Al₅ of 0.06 mm^3 (the highest), while Ti-Mo₈-Nb₆-Zr₄ had an average total volume similar to that of Ti-6Al-4V of 0.02 mm^3 . The average specific wear rate after tribocorrosion experiments under anodic potentiostatic rubbing conditions is presented in Figure 7-61 b. Amongst the titanium alloys used in this study, Cp-Ti had the lowest specific wear rate of 0.00004 mm^3/Nm . The β phase Ti-Mo₈-Nb₄-Zr₂, Ti-Mo₈-Nb₄-Zr₅, and Ti-Ta₃₀ had the similar specific wear rate of the $\beta+\alpha''$ -phase Ti-Ta₂₇-Al₅ of 0.0002 mm^3/Nm . The Ti-Mo₈-Nb₆-Zr₄ had the same average specific wear rate of the Ti-6Al-4V of 0.0009 mm^3/Nm . Figure 7-62 presents the contribution of mechanical (V_{mech}) and electrochemical (V_{chem}) wear to total material loss rate volume of titanium and titanium alloys after tribocorrosion tests under anodic potentiostatic rubbing conditions.

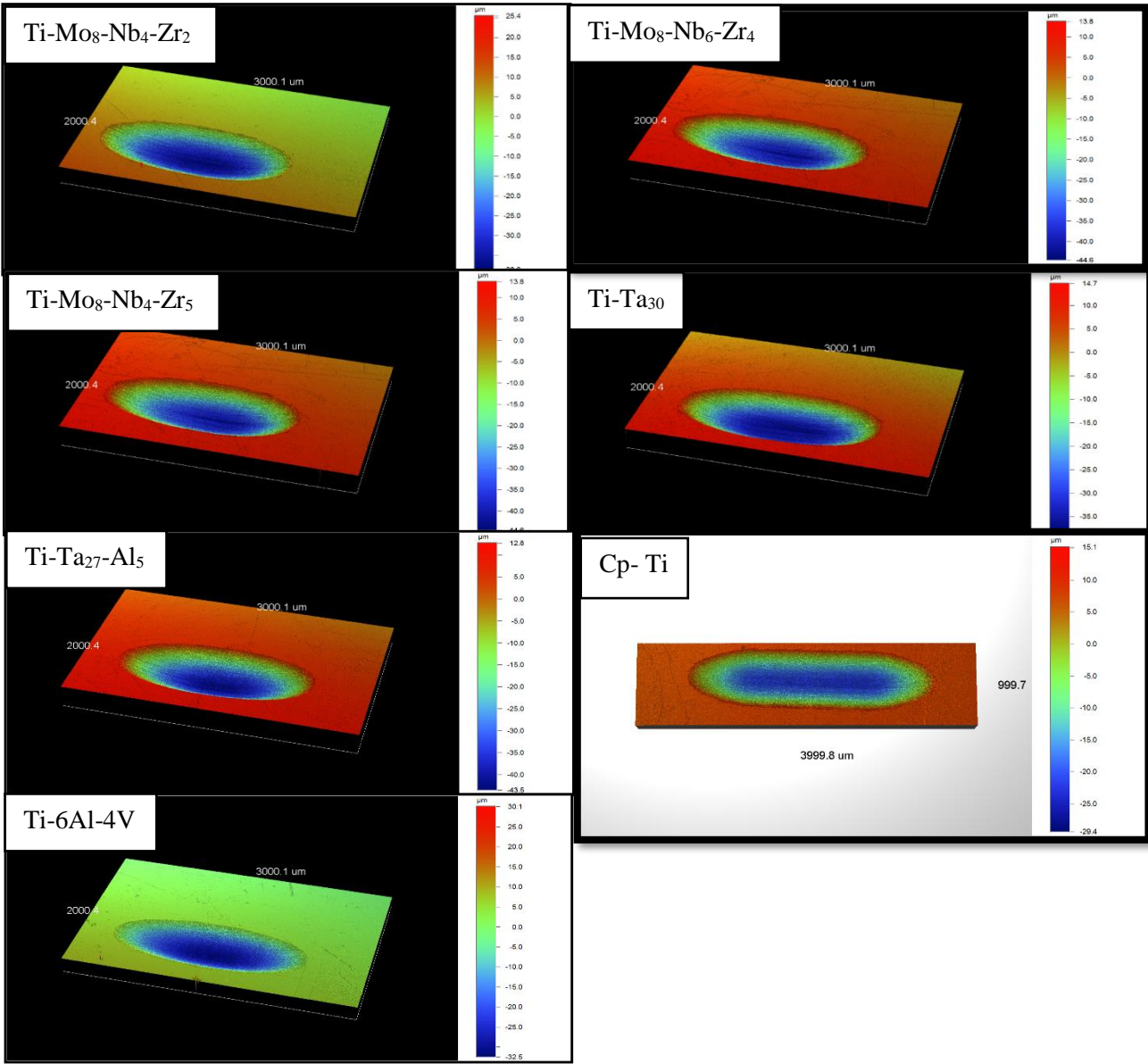


Figure 7-60: 3D images of wear track of titanium alloys under anodic potentiostatic conditions.

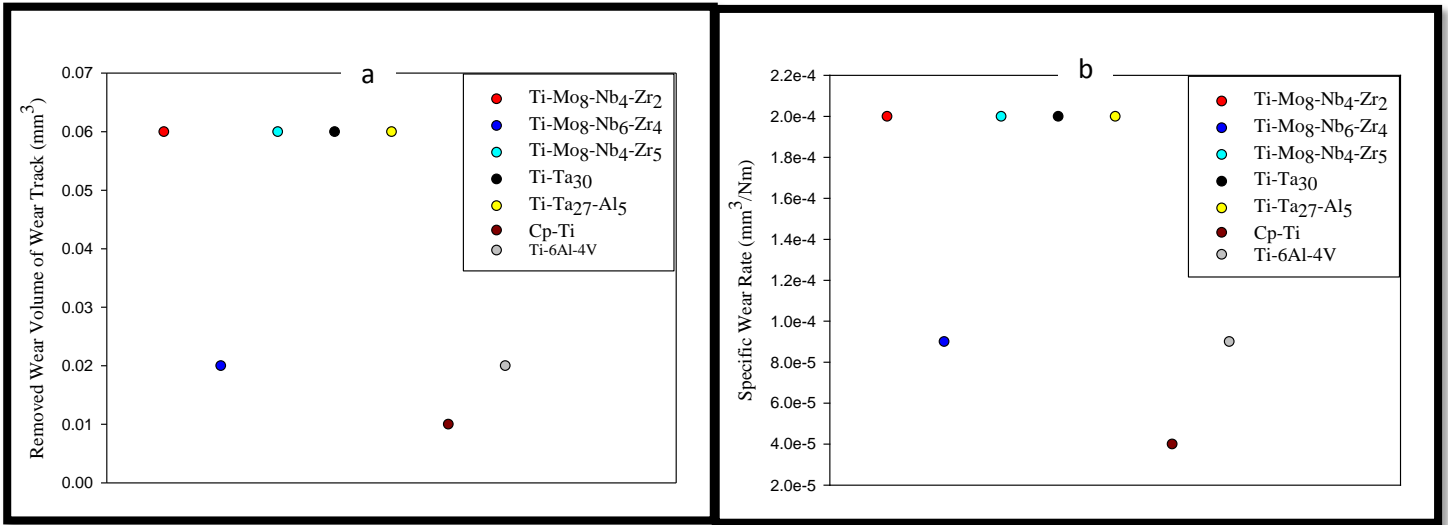


Figure 7-61: (a) Removed wear volumes (b) Specific wear rates of wear track for titanium alloys under anodic potentiostatic conditions.

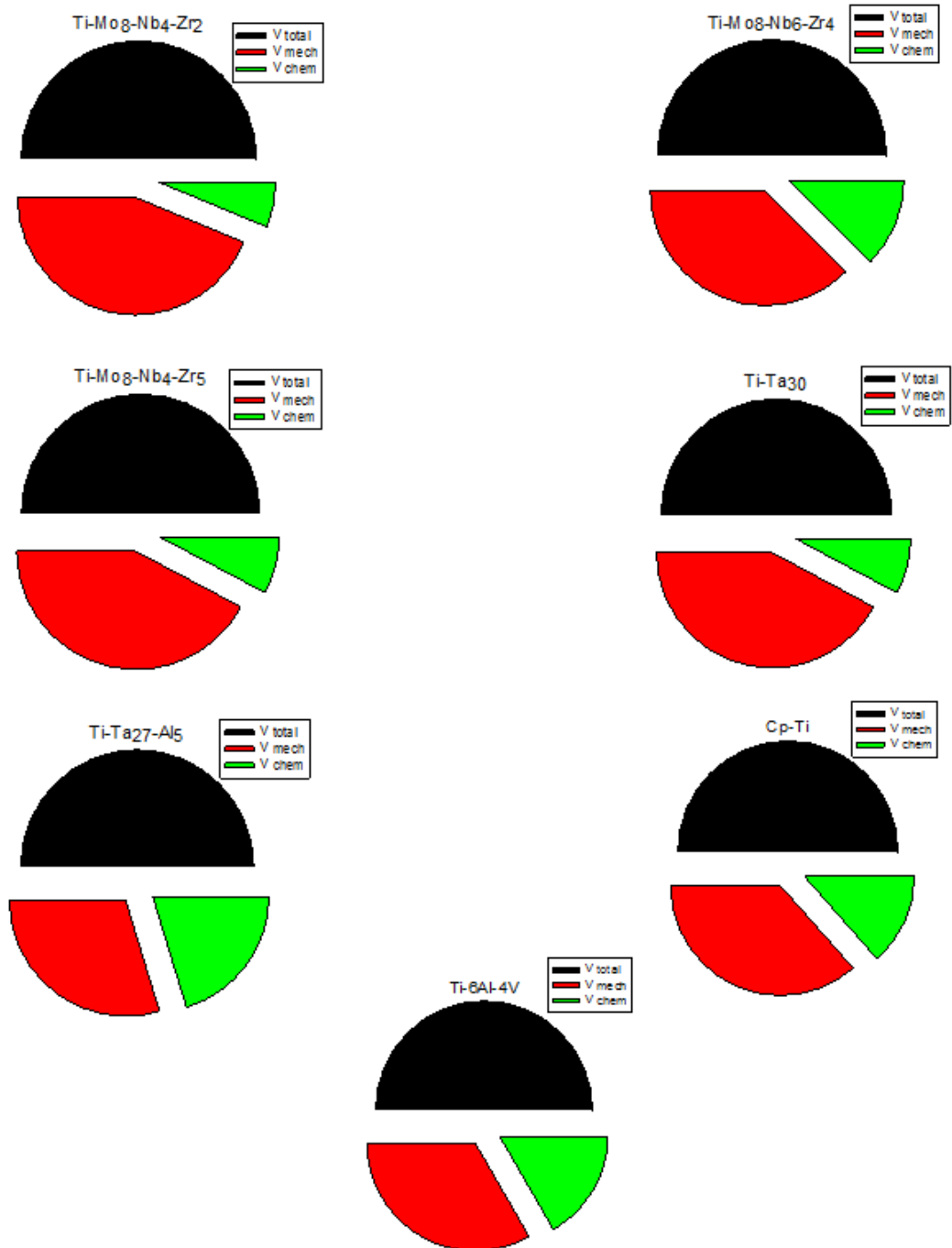


Figure 7-62 Contribution of mechanical wear and electrochemical to total material loss rate volume of titanium alloys after tribocorrosion tests under anodic potentiostatic rubbing conditions.

7.3.4 Subsurface Morphology

To get more details about the tribocorrosion mechanisms, a cross-section prepared through FIB of wear track was carried out. The investigated areas were in the centre of the wear track. Figures 7-63 and 7-64 show ion channelling contrast images of the wear tracks formed at Ti-Mo₈-Nb₆-Zr₄ and Ti-Ta₂₇-Al₅ respectively. A thin nanocrystalline layer was observed after anodic rubbing conditions adjacent to the rubbing surface, and well-defined microcrystalline grains were observed below the thin nanocrystalline layer.

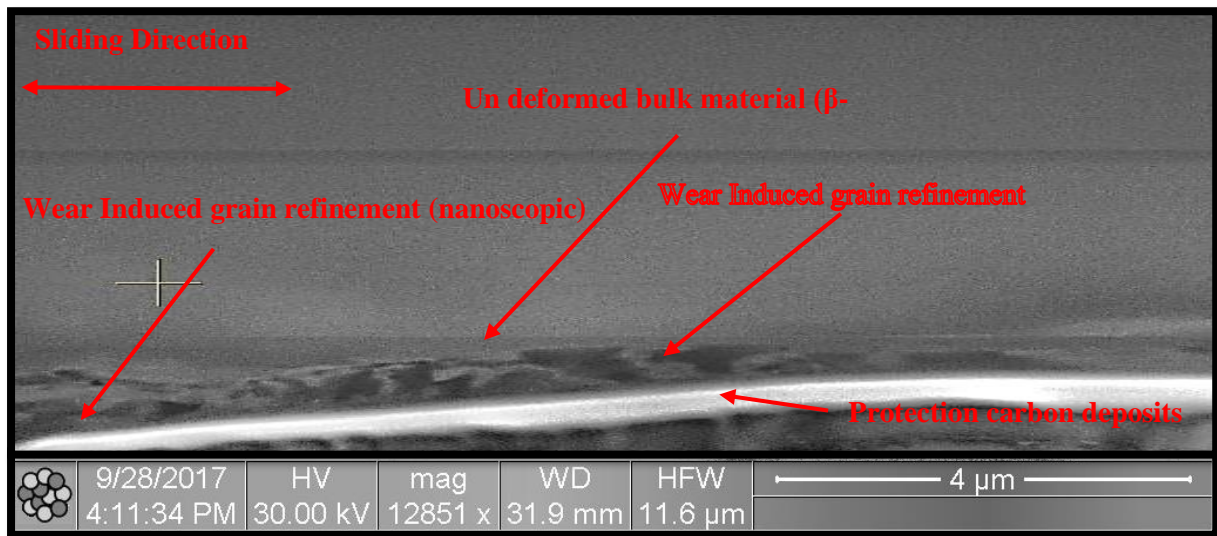


Figure 7-63 Ion channelling contrast image of a transverse cross-section of wear track formed at Ti-Mo₈-Nb₆-Zr₄ under anodic rubbing conditions.

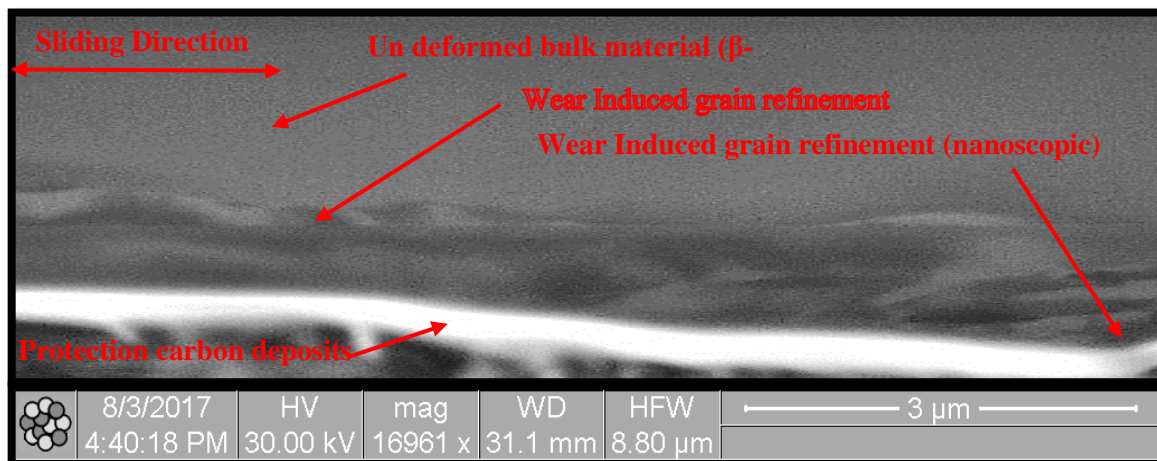


Figure 7-64 Ion channelling contrast image of a transverse cross-section of wear track formed at Ti-Ta₂₇-Al₅ under anodic rubbing conditions.

7.4 Summary

The investigation of tribocorrosion of titanium alloys can be summarised as follows:

- For OCP conditions, as rubbing started, the lowest OCP value was obtained from the α -microstructure Cp-Ti followed the other alloys in the order of $\alpha+\beta$ microstructure Ti-6Al-4V, β -microstructure Ti-Ta₃₀, β -microstructure Ti-Mo₈-Nb₄-Zr₂, β -microstructure Ti-Mo₈-Nb₆-Zr₄, $\beta+\alpha''$ -microstructure Ti-Ta₂₇-Al₅, and β -microstructure Ti-Mo₈-Nb₄-Zr₅. The noblest OCP during rubbing regime was recorded for the β -phase Ti-Mo₈-Nb₄-Zr₅ followed by β -phase Ti-Mo₈-Nb₆-Zr₄, β -phase Ti-Mo₈-Nb₄-Zr₂, β -phase Ti-Ta₃₀, Ti-Ta₂₇-Al₅, α -phase Cp-Ti, and $\beta+\alpha$ phase Ti-6Al-4V.
- For OCP conditions, the α -microstructure Cp-Ti and $\alpha+\beta$ microstructure Ti-6Al-4V alloys exhibited the lowest mean friction coefficient values among the others. The $\alpha''+\beta$ microstructure Ti-Ta₂₇-Al₅ alloy had the highest mean friction coefficient values.
- Under OCP conditions, chemical wear contributed to about 0.5% of total material removed from β microstructure alloys, while about 1%, 1.2% and 8.2% from $\beta + \alpha''$ microstructure, $\alpha+\beta$ microstructure and α -microstructure respectively.
- Under cathodic potentiostatic conditions (-0.5 V vs OCP) a significant increase in the current density was observed with the current showing an anodic shift to a positive current. The highest current was recorded for the $\alpha''+\beta$ microstructure Ti-Ta₂₇-Al₅ alloy.
- Under cathodic potentiostatic conditions, the α -microstructure Cp-Ti and $\alpha+\beta$ microstructure Ti-6Al-4V alloys exhibited the lowest mean friction coefficient values among all alloys. The $\beta + \alpha''$ microstructure Ti-Ta₂₇-Al₅ alloy had the highest mean friction coefficient values.
- Under cathodic potentiostatic conditions (-0.5 V vs OCP), chemical wear contributed to about 1% of total material removed from β microstructure alloys, while about 5% from $\beta + \alpha''$ microstructure, 6% from $\alpha+\beta$ microstructure and 10% from the α -microstructure.
- Under anodic potentiostatic conditions (0.3 V vs OCP), as rubbing started a higher anodic current was recorded for Ti-Ta₂₇-Al₅ followed by Cp-Ti, Ti-Ta₃₀, Ti-Mo₈-Nb₆-Zr₄, Ti-Mo₈-Nb₄-Zr₂, Ti-Mo₈-Nb₄-Zr₅, and Ti-6Al-4V respectively.

- Under anodic potentiostatic conditions, the $\alpha+\beta$ microstructure Ti-6Al-4V alloys exhibited the lowest mean friction coefficient values among all alloys. The β microstructure Ti-Ta₃₀ alloy had the highest mean friction coefficient values.
- Under anodic potentiostatic conditions, chemical wear contributed to about 15% of total material removed from β microstructure alloys, while about 40% from the $\beta + \alpha''$ microstructure Ti-Ta₂₇-Al₅, 33% from the $\alpha+\beta$ microstructure Ti-6Al-4V and 27% from the α -microstructure Cp-Ti.
- In general, all the wear surfaces formed under OCP, anodic and cathodic conditions were free from corrosion products. Under OCP and cathodic potentiostatic rubbing conditions, the wear tracks were extremely rough large grooves and scratches. In contrast, under anodic conditions, the wear tracks were very smooth. Thus, the tribocorrosion mechanisms depended on the corrosion conditions.
- There was no evidence of transfer from the alumina ball to the titanium alloy surface. Equally, there was no significant material transfer from the titanium alloy to the alumina ball. There was minimal wear of the alumina ball, but the wear resulted in a rough surface that would have been responsible for the 2-body abrasion seen on the titanium surface.
- The friction coefficient values obtained in all potentiostatic conditions was similar.
- The principal tribocorrosion mechanism of titanium alloys is composed mechanical and chemical wear. However, the mechanical wear was totally dominant under all conditions.
- All alloys exhibited a greater total removed wear volume under cathodic conditions than at OCP and anodic potentiostatic rubbing conditions.
- The results of the FIB cross sections (ion channelling contrast images), the nature and extent of deformation underneath the worn surface of alloys depended on the electrochemical conditions (OCP, cathodic or anodic potential) applied during tribocorrosion tests. More deformation was accumulated when a cathodic potential was applied during rubbing.

Chapter 8: Discussion

8.1 Structural and Properties Characterization of Titanium Alloys

8.1.1 Introduction

This chapter will discuss the experiment results on alloys fabrication, microstructure and property characterization. All alloys were arc melted, homogenized, cold rolled and finally subjected to solution heat treatment and quenched in water. The composition, density, transformation temperatures, materials characterization (X-ray diffraction, optical microscopy, scanning electron microscopy, energy dispersive analysis of X-rays (EDX), and transmission electron microscopy (TEM)), mechanical testing (reduced elastic modulus, nano-hardness, and micro-hardness) results will be discussed. Commercially pure Ti (Cp-Ti, grad 2) and Ti-6Al-4V alloys results also will be discussed for comparison.

8.1.2 Composition Analysis and Density

Table 4-1 presents the chemical composition of the alloys obtained by XRF analysis. The concentrations of tantalum, aluminium, molybdenum, niobium, and zirconium were close to the nominal value, with no significant quantities of metallic impurities. The average density of the alloys compared with the theoretical value are shown in figure 4-1. It can be seen from the figure that the density of all alloys was higher than the density of Cp-Ti ($4.45 \pm 0.06 \text{ g/cm}^3$) and Ti-6Al-4V ($4.56 \pm 0.03 \text{ g/cm}^3$). The Ti-Ta₃₀ had the highest density ($8.25 \pm 0.04 \text{ g/cm}^3$), while Ti-Mo₈-Nb₄-Zr₂ had the lowest density value ($5.12 \pm 0.045 \text{ g/cm}^3$). Ti-Mo₈-Nb₆-Zr₄, Ti-Mo₈-Nb₄-Zr₅, and Ti-Ta₂₇-Al₅ showed average density values of 5.28 ± 0.048 , 5.22 ± 0.045 , $7.9 \pm 0.05 \text{ g/cm}^3$ respectively. The increase in the density of the alloys compared with Cp-Ti and Ti-6Al-4V occurs due to the higher density of the alloy elements used, with tantalum (16.6 g/cm^3), molybdenum (10.22 g/cm^3), niobium (8.57 g/cm^3), and zirconium (6.51 g/cm^3) compared to titanium (4.51 g/cm^3) [282]. Furthermore, the theoretical density was close to the experimental values, which confirmed that the stoichiometry of alloys fabricated in this study were correct. Moreover, the microstructure showed a homogeneous distribution shown in figure 4-2. The analysis of chemical composition and density show that the alloys achieved both good quality and homogeneity.

8.1.3 Microstructure and Phase Constitution

Optical images of typical microstructures are shown in Figure 4-3. The microstructure of the as quenched quaternary alloys after solution heat treatment comprised equiaxed single phase β

grains. The average grain size of Ti-Mo₈-Nb₄-Zr₂ was 219±2 μm (Table 4-2). The grain size became slightly larger with an increase in the zirconium content; the average grain size of Ti-Mo₈-Nb₄-Zr₅ was 221± 1μm (Table 4-2). Increasing the niobium and zirconium together also led to an increase in the grain size of Ti-Mo₈-Nb₆-Zr₄ to 229± 2 μm (Table 4-2). The microstructure of the Ti-Ta₃₀ consisted of single phase equiaxed β grains with an average grain size of 42±2 μm (Table 4-2), which was much smaller than the Ti-Mo_x-Nb_x-Zr_x alloys. The microstructure of the Cp-Ti, Figures 4-3 and 4-4, was single phase α, while the microstructure of Ti -6Al-4V consisted of α and β (Figure 4-3), as expected. The Ti-Ta₂₇-Al₅ consisted of thin needles of α'' orthorhombic martensitic inside an equiaxed β phase microstructure (Figures 4-3, 4-4); the average grain size of the β phase was 45± 1μm (Table 4-2). Small dark spots were observed which are probably dislocation etch pits resulting from sample preparation which are often observed on the β-phase titanium alloys during preparation [102].

The metallographic observations agree with the XRD analysis (Figure 4-5), which indicated the single phase β with no evidence of α, α', α'', or ω. The Ti-Ta₂₇-Al₅ alloy was predominantly the β phase with an equiaxed grain structure; however, α'' orthorhombic martensite with thin needles/plates was observed in some regions (Figure 4-4). The presence of α'' was confirmed by XRD (Fig 4-6).

The metallographic examination also agrees with the differential scanning calorimetry (DSC) and combined DTA/TGA results. Figure 4-7 shows DSC heating and cooling cycles for the Ti-Mo₈-Nb₄-Zr₂, Ti-Mo₈-Nb₄-Zr₅, Ti-Mo₈-Nb₆-Zr₄, and Ti-Ta₃₀ alloys. The alloys did not exhibit any peaks during either heating or cooling such that no transformation was observed. Furthermore, Figure 4-8 shows the combined DTA/TGA results for the Ti-Mo₈-Nb₄-Zr₂, Ti-Mo₈-Nb₄-Zr₅, and Ti-Mo₈-Nb₆-Zr₄ alloys. It can be seen that the β transus- temperatures T_β of Ti-Mo₈-Nb₄-Zr₂, Ti-Mo₈-Nb₄-Zr₅, and Ti-Mo₈-Nb₆-Zr₄ was 768 , 764 and 761°C, which are lower than the transus-temperature of the common metastable β (Ti-Mo₈) alloy ≈ 820°C [271]. The lower T_β temperature is due to the presence of the stabilizing elements (Mo, Nb, Zr) which decrease the transus temperature of the alloys [283, 284]. Figure 4-9 shows the combined DTA/TGA results for Ti-Ta₃₀ and Ti-Ta₂₇-Al₅ alloys. The β transus- temperature T_β of the Ti-Ta₃₀ was 598 °C (Table 4-3), which is close to the reported T_β temperature for this alloy at 600 °C [257]. On the other hand, the transus temperature T_β of Ti-Ta₂₇-Al₅ was 668 °C (Table 4- 3), which is higher than that for Ti-Ta₃₀. The higher T_β temperature of Ti-Ta₂₇-Al₅ is a result of adding the α stabilizing element Al [283, 284]. The DSC for the Ti-Ta₂₇-Al₅ also confirmed that the transformation to martensite α'' orthorhombic phase occurs

in this alloy (figure 4-10), with a peak present during both heating and cooling; with the peak on cooling representing the forward martensite transformation from β to orthorhombic martensite.

EDX was performed to obtain information on the chemical nature of different regions in the titanium alloys fabricated in this study. Figs. 4-11 through to 4-15 show the EDX results for Ti-Mo₈-Nb₄-Zr₂, Ti-Mo₈-Nb₆-Zr₄, Ti-Mo₈-Nb₄-Zr₅, Ti-Ta₃₀ and Ti-Ta₂₇-Al₅, with the results tabulated in Tables 4-5 through 4-9. The results show that there was no significant difference in concentrations of Ti, Mo, Nb and Zr at % of the Ti-Mo-Nb-Zr alloys and Ti and Ta of Ti-Ta alloy. Therefore, the contrast in the backscattered images is associated with different crystallographic orientations of the β grains and not associated with chemical segregation within the β phase grains.

TEM was performed for higher resolution studies of microstructure and phase information. Typical bright-field images and the corresponding selected area electron diffraction patterns for Ti-Mo₈-Nb₄-Zr₂, Ti-Mo₈-Nb₆-Zr₄, Ti-Mo₈-Nb₄-Zr₅, Ti-Ta₃₀ and Ti-Ta₂₇-Al₅ are presented in Figure 4-16. The diffraction patterns could be indexed as β -phase with bcc structure for the Ti-Mo₈-Nb₄-Zr₂, Ti-Mo₈-Nb₆-Zr₄, Ti-Mo₈-Nb₄-Zr₅, and Ti-Ta₃₀. For the Ti-Ta₂₇-Al₅ alloy, the orthorhombic martensite α'' phase was observed within the β -phase matrix (Figure 4-16), confirmed by indexing the diffraction pattern. These results are consistent with recent works of [285-287]. The TEM results are consistent with XRD analysis, also with OM and SEM characterization, and all of them confirm that two phases, α'' orthorhombic phase martensite and the β -phase, are present in the Ti-Ta₂₇-Al₅ alloy.

Based on the discussion presented earlier, obtaining a fully β phase structure in the Ti-Mo₈-Nb_x-Zr_x, is related to the concentration of Mo and Nb the stabilizing elements. These elements decrease the transus temperature to below room temperature [288, 289]. They are easily dissolved in Ti at high temperature because they have the same bcc structure, space group and similar crystal lattice constant to β titanium [290], [291]. Pure β phase can be obtained in Ti-Mo alloys provided intermediate phases α'' and ω are suppressed. This requires a sufficient concentration of β stabilizing elements, such as Mo and Nb, which was achieved in this work. Furthermore, it has been reported that Zr additions can effectively suppress the formation of the intermediate phases [292, 293]. These results are in accordance with recent works of [288, 289, 294-301].

8.1.4 Mechanical Characterization

8.1.4.1 Reduced Modulus, Nanoindentation Hardness and Elastic Modulus

The reduced elastic modulus of titanium alloys measured by nano-indentation as a function of load are shown in Figure 4-17. Figure 4-18 shows the reduced elastic modulus as a function of the contact depth at different loads. The average value of the reduced elastic modulus of Cp-Ti and Ti-6Al-4V was 136.7 ± 3 GPa and 148.6 ± 2 GPa respectively, while for Ti-Mo₈-Nb₄-Zr₂, Ti-Mo₈-Nb₄-Zr₅, Ti-Mo₈-Nb₆-Zr₄, Ti-Ta₃₀, and Ti-Ta₂₇-Al₅ it was 102.3 ± 1 , 101.2 ± 1.4 , 103.8 ± 1.2 , 88.7 ± 1 and 86.8 ± 0.9 GPa respectively. Figure 4-19 presents nano-hardness values as a function of load for titanium alloys and figure 4-20 gives the corresponding nano-hardness as a function of the contact depth. The measured nano-hardness values were 3.94 ± 0.4 and 4.94 ± 0.53 for the Cp-Ti and Ti-6Al-4V. For Ti-Mo₈-Nb₄-Zr₂, Ti-Mo₈-Nb₄-Zr₅, Ti-Mo₈-Nb₆-Zr₄, Ti-Ta₃₀ and Ti-Ta₂₇-Al₅ the nano-hardness values were 3.79 ± 0.3 , 3.75 ± 0.3 , 4.06 ± 0.4 , 4.46 ± 0.3 , and 3.37 ± 0.6 GPa respectively (Table 4-10). The elastic modulus and nanohardness of alloys were also measured using nanoindentation, but with a constant load of 5000 μ N. Figure 4-21 gives the reduced elastic modulus and figure 4-22 gives the corresponding nano-hardness of all alloys, with values summarized in table 4-11. The CP-Ti (141 ± 3 GPa) and Ti-6Al-4V (151 ± 2 GPa) had the highest modulus values. Among all β Ti-alloys, Ti-Mo₈-Nb₄-Zr₂ had the highest reduced elastic modulus (99.7 ± 2 GPa), while Ti-Ta₃₀ had the lowest value (85 ± 1 GPa). The reduced elastic modulus of Ti-Mo₈-Nb₆-Zr₄, Ti-Mo₈-Nb₄-Zr₅ and Ti-Ta₂₇-Al₅ was 94.3 ± 0.7 , 96.8 ± 0.6 , and 88.7 ± 0.66 GPa respectively. The values for Ti-Mo₈-Nb₄-Zr₂, Ti-Mo₈-Nb₆-Zr₄, Ti-Mo₈-Nb₄-Zr₅, Ti-Ta₃₀, and Ti-Ta₂₇-Al₅ were lower than that of Cp-Ti by 29, 33, 31, 39, and 37 % respectively. Furthermore, they were lower than that of Ti-6Al-4V by 34, 37, 35, 43, and 41 % respectively.

The elastic modulus of titanium alloys was measured by the ultrasonic technique and results are presented in Figure 4-23. The average value of the elastic modulus of Cp-Ti and Ti-6Al-4V was 120.6 ± 3 GPa and 115.9 ± 2 GPa. On the other hand, the Ti-Ta₃₀ alloy showed the lowest elastic modulus (52.2 ± 3 GPa). All alloys exhibited an elastic modulus lower than Cp-Ti and Ti-6Al-4V. The average elastic modulus of Ti-Mo₈-Nb₄-Zr₂, Ti-Mo₈-Nb₆-Zr₄, Ti-Mo₈-Nb₄-Zr₅, and Ti-Ta₂₇-Al₅ was 78.9 ± 2 , 76.3 ± 2 , 60.1 ± 2 , and 55.8 ± 3 GPa respectively. In contrast, Cp-Ti exhibited the highest elastic modulus, as expected.

The elastic modulus of titanium alloys is sensitive to alloy composition and phase constitution [302]. Each phase (α , β , α' , α'' , and ω) has a different elastic modulus, with the

elastic modulus of a body centre cubic structure lower than that of the orthorhombic and hexagonal structures; the elastic modulus of orthorhombic structures is lower than that of the hexagonal structure [294, 303-305]. The elastic modulus increases in the sequence $\omega > \alpha > \alpha'' > \beta$ [303-305], that means a fully β phase alloy exhibits a much lower elastic modulus when compared with the ω , α'' and α phases, or a β phase alloy containing these phases.

Furthermore, it has been shown that the elastic modulus of the different phases (ω , α and β) can be related by $E_\alpha = 1.5 E_\beta$ and $E_\omega = 2 E_\beta$ [305]. In a multiphase alloy, the elastic modulus is calculated using the specific modulus of phases and their volume fractions in the alloy [302, 303]. Alloys with a $\beta + \alpha''$ mixture exhibit elastic modulus lower than that of α , and alloys with $\alpha + \beta$ mixture offers elastic modulus higher than that of β phase [302, 303, 306].

Based on the discussion presented above, the difference in elastic modulus measured in this work is directly correlated with the microstructure of alloys. The Cp-Ti showed the highest elastic modulus, as expected from its single α phase structure. All β phase alloys fabricated in this study, exhibited the low elastic modulus, but although they were all single-phase equiaxed β , the elastic modulus depended on composition. Ti-Ta₂₇-Al₅ gives the elastic modulus close to Ti-Ta₃₀, consistent with the β phase and α'' structure. The alloy had a higher volume fraction of β compared with α'' phase, and because of the large amount of β in the microstructure, the alloy had an elastic modulus close to Ti-Ta₃₀.

8.1.4.2 Micro-Hardness

The average Vickers micro-hardness values ($HV_{0.2}$) of the alloys are presented in Figure 4-24. The hardness of all titanium alloys fabricated in this work were above the value of the grade 2 Cp-Ti (199 $HV_{0.2}$). However, the hardness of the β phase alloys was less than the value of Ti-6Al-4V (358 $HV_{0.2}$), but higher than 200 $HV_{0.2}$, Figure 4-24. The average Vickers micro-hardness of the Ti-Ta₃₀ alloy was the highest (321 $HV_{0.2}$) and that of the Ti-Ta₂₇-Al₅ alloy was the lowest (230 $HV_{0.2}$). The average Vickers micro hardness of Ti-Mo₈-Nb₄-Zr₂, Ti-Mo₈-Nb₆-Zr₄, Ti-Mo₈-Nb₄-Zr₅ was 264, 268, and 282 $HV_{0.2}$ respectively.

It is known that the micro hardness values could be effected by more than one factor; for example, precipitation hardening, solid solution strengthening, grain size, crystal structure/phase (α , α'' , β), and casting defects, such as voids and porosity[298]. All Ti-Mo based alloys fabricated in this work had much higher microhardness values than that of Cp-Ti, and these results are in accordance with previous work [298, 299, 301, 307]. The increase in the micro-hardness values compared to Cp-Ti occurs due to the mechanisms of solid solution

strengthening of Ti with the addition of β - stabilizer elements (Mo, Ta, and Nb) [308, 309]. Additionally, it has been documented in the literature that Mo and Zr both stabilize the β -phase which lead to an increased hardness due to solid solution strengthening [307]. The orthorhombic α'' is believed to be an intermediate phase between bcc and hcp structures. Furthermore, it was reported in previous study that the β phase alloys exhibited a higher hardness level than α'' phase alloys. Therefore, the Ti-Ta₂₇-Al₅ alloy had the lowest micro-hardness value, and this can be related to the formed α'' orthorhombic martensitic phase with less hardness [310, 311].

8.2 Tribological Behaviour of Titanium Alloys

8.2.1 Introduction

The tribological behaviour of alumina sliding against all alloys fabricated in this work is explored and mechanisms involved discussed. A comparison is made between the alloys fabricated in this work with Cp-Ti and Ti-6Al-4V alloys which are used as implant materials. Tribological tests were carried out in a 25vol% bovine calf serum at room temperature, under 0.25, 0.5, 1, and 2N. The wear scar characteristics results SEM, EDX, 3D optical microscopy, focused ion beam and Raman spectrometry will be discussed.

8.2.2 Lubricated Sliding Friction

During lubricated wear without an applied potential, the friction coefficient increased slightly with the normal load and decreased gradually with time before reaching steady state (Figures 5-1 through to 5-4). However, the time required to reach steady state depended on the alloy. Some alloys reached the steady state after a few seconds, while other alloys showed a gradual increase in friction after the initial increase before the steady state was reached. The friction curves for the α -microstructure Cp-Ti and $\alpha+\beta$ - microstructure Ti-6Al-4V were smoother than those for the β - microstructure and $\beta+\alpha''$ - microstructure. This might be associated with the repeated removal of metal followed by rapid repassivation.

Before the start of a wear test, it would be expected that the titanium alloys would have a passive titanium oxide layer on the surface, of a composition that depended on the alloy composition. At an initial running-in period, the passive film breaks up under the mechanical contact and a fresh titanium surface comes in to contact with the ceramic counterbody face. This will have led to an increase in the coefficient of friction between the surface of the titanium alloys and the alumina counterbody [167, 251, 312]. The subsequent steady state

friction indicates that the passive state has been regained. After the first ~100 seconds of rubbing, there was no significant variation in the coefficient of friction.

It can be seen from Figures 5.1 through to 5.5 that β -microstructure and $\beta+\alpha''$ -microstructure alloys had higher friction coefficients with greater fluctuations than the α - microstructure Cp-Ti and $\alpha+\beta$ - microstructure Ti-6Al-4V. The lowest friction coefficient was obtained from the $\alpha+\beta$ - microstructure Ti-6Al-4V. The higher friction coefficient of the β -microstructure and $\beta+\alpha''$ -microstructure alloys may be a result of their bcc structure, which is believed to give inherently higher friction than a hexagonal crystal structure [160]. The higher friction may also be attributed to the different chemical composition of the oxide film. It is well known that the wear resistance of the alloys depends on the contact pressure and the mechanical properties of the oxide film[246], while contact pressure can be considered the same for each alloy at normal load, the mechanical properties of oxide film depended mainly on the composition of the alloy. For example, TiO_2 , Nb_2O_5 , Ta_2O_5 , MO_3 and ZrO_2 oxides may have been present on the surface of β -microstructure alloys [197], while TiO_2 , Al_2O_3 , and V_2O_5 may have been present on the surface of α - microstructure Cp-Ti and $\alpha+\beta$ - microstructure Ti-6Al-4V [246]. The considerable fluctuation of coefficient of friction of the β -microstructure and $\beta+\alpha''$ -microstructure at higher normal load could be related to the interaction of wear debris during rubbing, which was produced from removal of oxide. Any entrapment of removed oxide would be expected to increase the friction force due to the increase of ploughing effect [251].

Furthermore, the results show that the coefficient of friction is affected by the formation of the carbonaceous film, which builds up during rubbing and leads to a decrease in the coefficient of friction. The low friction coefficient of the α -microstructure Cp-Ti alloy compared with that of β -microstructure titanium alloys and $\alpha+\beta$ - microstructure Ti-6Al-4V alloys, particularly at high load, can be also explained by the formation of the carbonaceous film. The α -microstructure Cp-Ti alloy shows the same friction coefficient as the $\alpha+\beta$ - microstructure Ti-6Al-4V, particularly at a normal load of 2N; the alloy has higher peak intensity of the carbonaceous layer, which indicated a greater film thickness. This carbonaceous layer can be protective by reducing the friction and wear on the α - microstructure Cp-Ti alloy surface.

8.2.3 Wear Track Morphology, Chemistry, and subsurface Morphology

SEM was used to evaluate the morphology of the wear tracks. EDX analysis was used to identify material transfer from the counter-body Al_2O_3 to the titanium alloys or from the titanium alloys to the counter-body. Surface chemistry of the wear tracks was analysed using Raman spectroscopy to identify possible chemical changes induced by rubbing at different normal loads under lubricated conditions.

The typical worn surface morphology of the alloys is presented in Figures 5-6 through to 5-9. Wear occurred predominantly by ductile and plastic deformation ploughing, with delamination at the edge of the grooves. A small number of isolated debris particles and flake like debris were observed inside the worn surface. Not surprisingly, the worn surface roughness increased with load, with a marked increase from 0.5N to 1N. The increase in roughness was associated with more extensive plastic ploughing of the surface. No cracking was observed within the worn surface in any of the tests.

The wear track at lower normal load was characterised by a relatively smooth appearance and low average roughness (Figure 5-15). However, the worn surface exhibited an extensive ploughed appearance, indicating the poor resistance of the titanium alloys to surface plastic deformation. The extent of scratching and grooving increased with load, such that at higher loads the wear track exhibited deep scratching, extensive deformation in the form of grooves and generally a very rough worn surface (R_a of 0.5-1.2 μm when the load was increased from 1 to 2N (Figures 5-15 and 5-16). The above results are in agreement with the literature [28, 168].

There was no evidence of transfer from the alumina ball to the titanium alloy surface during rubbing at all normal loads under lubricated rubbing conditions (Figures 5-10). Equally, there was no significant transfer from the titanium alloys to the alumina surface and the wear of the alumina was minimal. (Figures 5-12 through to 5-14).

A carbonaceous film formed on the surface of the wear track under certain conditions (Figures 5-10 and 5-11). Two Raman peaks were observed centred around 1383 and 1567 cm^{-1} , which can be attributed to the disordered graphite and a single crystal graphite, D-band and G-band respectively[273]. The α -microstructure Cp-Ti alloy had the highest Raman spectrum intensity among all alloys at normal loads of 0.25, 0.5 and 2N, while the $\beta+\alpha''$ Ti-Ta₂₇-Al₅ had the highest Raman spectrum intensity among all alloys at a normal load 1N.

When the contact load was increased to 1N, D and G Raman bands were only obtained from the Ti-Ta₂₇-Al₅ alloy and the Ti-Mo₈-Nb₄-Zr₂ alloys. Thus, the formation of this carbonaceous layer did not appear to correlate with the alloy structure (β , α or α''). Rather, its formation appeared to be more dependent on the load than the alloy composition.

Thin films are known to be generated *in vivo* during sliding motion, known as tribological films [272]; however, the structure and formation of the tribological film is not fully understood and knowledge about it is limited. According to XPS analysis of the tribological film, it has been suggested in the literature that the tribological films originated from the pseudo-synovial fluid and composed of something similar to denatured protein [273-278]. More particularly, and in the case of lubricant tests in bovine calf serum, a recent study suggested that the tribological film is inorganic graphitic carbon, and most materials decomposed to disordered graphite D-band sp²-carbon [279-281].

The α + β -microstructure Ti-6Al-4V alloy had the lowest friction coefficient, which was attributed to crystal structure and the mechanical properties of the alloys (elastic modulus and hardness). However, at a normal load of 2N the α -microstructure Cp-Ti had the same coefficient of friction as the α + β -microstructure Ti-6Al-4V. This friction coefficient was attributed to the carbonaceous layer, or tribofilm, which is believed to reduce friction. The Cp-Ti alloy had a higher Raman D-G band intensity from the carbonaceous layer, which may be indicative of a thicker carbonaceous layer. It was reported that the tribological film thickness in the case of tests in bovine calf serum is 40-50 nm for the low pressure, while it is 5-50 nm under high contact pressure [313, 314].

To further investigate the wear mechanisms, the subsurface deformation structure in the wear track was characterised using a cross-section prepared by FIB. It has been reported that there are three subsurface zones typically observed after a tribological test: zone 1: the bulk material, zone 2: the plastically deformed layer, and zone 3: the mixed nano-crystalline surface layer [315]. Characterization of subsurface microstructures after tribology tests at different normal loads showed that tribological grain refinement (TGR) did occur adjacent to the rubbing surface. The samples rubbed at 2N normal load clearly exhibited higher deformation than those rubbed at 0.5N (figures 5-24 through to 5-27). After increasing the normal load an increase in the extent of grain refinement was observed. There was no evidence of twinning observed, and the different contrasts shown by the ion beam channelling images was associated with plastic deformation during rubbing rather than the

formation of a new phase. TGR formed during tribological process due to plastic deformation and the thickness of the nanocrystalline layer increased with an increase in the normal load.

8.2.4 Wear Rate

The wear volume increased with normal load (figure 5-21) for tests undertaken without potentiostatic conditions. The specific wear rate increased slightly with normal load for all alloys (figure 5-22), although there was no significant change. All alloys, except the α -microstructure Cp-Ti alloy and $\alpha+\beta$ - microstructure Ti-6Al-4V alloy, exhibited a very large specific wear rate. The specific wear rate was relatively insensitive to load for the α -microstructure Cp-Ti alloy and $\alpha+\beta$ - microstructure Ti-6Al-4V alloy. In contrast, the β -microstructure Ti-Ta₃₀ alloy exhibited an approximately linear increase in specific wear rate with load, indicating that the wear was becoming more severe.

The smallest volume loss was obtained with the α - microstructure Cp-Ti at normal loads 0.25 and 0.5 N, despite this alloy having the lowest hardness. The $\alpha+\beta$ - microstructure Ti-6Al-4V alloy showed the smallest volume loss at a normal load of 2N. Both alloys Cp-Ti and Ti-6Al-4V had the same volume loss at a normal load of 1N. The β - microstructure alloys showed the highest volume loss. The reduction in wear rate of the α - microstructure Cp-Ti at lower loads may be attributed to the presence of carbonaceous layer on the surface of α -microstructure Cp-Ti, which may aid lubrication and reduction of wear. It has been reported that a tribological film can reduce the wear rate and coefficient of friction [316-318]. The carbonaceous film can act as a lubricant by acting as a barrier which inhibits the contact between the counterbody and the fresh surface of the titanium alloy to reduce the wear [319, 320]. At higher loads, the reduction in wear rate of the $\alpha+\beta$ microstructure Ti-6Al-4V could be attributed to higher hardness. It has been reported in the literature that hardness is usually regarded to be important mechanical property for assessing the tribological resistance [152, 166, 321], therefore the variation in wear resistance can be explained by hardness variation. However, a previous study showed that the wear resistance can be better estimated from H/E or H^3/E^2 ratio rather than the hardness alone [321]. An increase in the value of H/E or H^3/E^2 results in a higher resistance to wear [152, 322]. In this study, the maximum value of H/E ratio was about 0.04 GPa for the Ti-Mo₈-Nb₄-Zr₂, Ti-Ta₃₀ and Ti-Ta₂₇-Al₅ alloys followed by Ti-6Al-4V, Ti-Mo₈-Nb₆-Zr₄, Ti-Mo₈-Nb₄-Zr₅ with H/E ratio of about 0.03 GPa and Cp-Ti with value of about 0.02 GPa. Also, the maximum value of H^3/E^2 ratio of about 0.008 GPa for Ti-Mo₈-Nb₄-Zr₂ and Ti-Ta₃₀ followed by Ti-6Al-4V with value of about 0.005 GPa and Cp-Ti, Ti-Mo₈-Nb₆-Zr₄ and Ti-Ta₂₇-Al₅ with the same value of about 0.003 GPa. The lowest

value of H^3/E^2 ratio of about 0.002 GPa for Ti-Mo₈-Nb₄-Zr₅. These results confirm that no direct relationship could be established between the wear volume and the mechanical properties of the alloys (elastic modulus and hardness). The same was also reported previously for β and $\alpha+\beta$ titanium alloys by [230, 246].

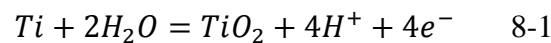
8.3 Electrochemical Behavior of Titanium Alloys

8.3.1 Introduction

In this part, the results of the investigation into all work carried out on the electrochemical behaviour of the titanium alloys fabricated in this work, to establish which alloy has the best corrosion resistance will be discussed. A comparison was made between the alloys fabricated in this work and Cp-Ti and Ti-6Al-4V alloys, under the same electrochemical measurements, the results of these alloys will also be discussed. Electrochemical tests were completed in 25vol% bovine calf serum at $37^\circ\text{C}\pm 1$, in open circuit potential and potentiodynamic conditions. Electrochemical tests were carried out for the starting surface, during the wear tests and after the tribocorrosion tests.

8.3.2 Electrochemical Characterization: Corrosion Resistance

Titanium and its alloys are generally passive in most lubricants due to the spontaneous production of a protective oxide film when titanium reacts with water according to the following reaction:



In simulated body fluid, such as bovine calf serum, titanium alloys passivate, and the open circuit potential lies within the passive domain (figure 6-1). In bovine calf serum, the protecting passive oxide forms rapidly and acts as a barrier to titanium dissolution, which results in a reduction in the corrosion rate. The shift in the open circuit potential to more passive values are indicative of an increase in corrosion resistance of titanium alloys in the bovine calf serum. The open circuit potential curves of all titanium alloys indicated a stabilization of oxide layer was achieved within 30 min, which is typical for titanium and titanium alloys [323].

The β -microstructure Ti-Ta₃₀ had the most positive values, while the $\alpha+\beta$ -microstructure Ti-6Al-4V exhibited the most negative values (Table 6-1). In general, the open circuit potential value for the all β -microstructure was more positive than that of $\alpha+\beta$ -microstructure Ti-6Al-4V, α -microstructure Cp-Ti, and $\beta+\alpha''$ -microstructure Ti-Ta₂₇-Al₅. Also, this indicated the

positive contribution of the alloying elements Mo, Nb, Zr, Ta in the formation of passive film on the surface of titanium alloys.

The results of open circuit potential are agreement with the results of electrochemical parameters E_{corr} and i_{corr} extracted from the potentiodynamic polarization curves of titanium alloys (figure 6-2) from Tafel curves (Table 6-2). The electrical parameters showed that the β -microstructure Ti-Ta₃₀ exhibited statistically significant higher resistance than the other alloys. The β -microstructure Ti-Ta₃₀ had a much lower value of corrosion current density when compared to other alloys. Also, all β -microstructure alloys had the most positive values, while the $\alpha+\beta$ -microstructure Ti-6Al-4V, α -microstructure Cp-Ti and $\beta+\alpha''$ -microstructure Ti-Ta₂₇-Al₅ exhibited the most negative value. The β -microstructure titanium alloys showed nobler electrochemical behaviour than the $\alpha+\beta$ -microstructure Ti-6Al-4V, α -microstructure Cp-Ti and $\beta+\alpha''$ -microstructure Ti-Ta₂₇-Al₅ in bovine calf serum.

The main reason for the superiority of the β -microstructure Ti-Ta and Ti-Mo-Nb-Zr alloys is believed to be the modification of the passive oxide film TiO₂ by the alloying elements Ta, Mo, Nb and Zr. The TiO₂ passive films were strengthened by the more stable Ta₂O₃, MO₃, Nb₂O₅ and ZrO₂ passive oxide films in thickening and improved structural integrity of the alloys native passive film that resulted in improved corrosion resistance of Ti-Ta and Ti-Mo-Nb-Zr alloys [197, 204]. It has been reported that the Nb₂O₅ improves the thermodynamic stability of the titanium oxide[197]. The resistance of the TiO₂ oxide to chemical dissolution can be increased by ZrO₂ [197]. The formation of Ta₂O₅ in the passive layer can improve the corrosion resistance of titanium [204]. Therefore, the presence of MO₂, Nb₂O₅, ZrO₂ and Ta₂O₅ in the titanium oxide may be responsible for the excellent behaviour of Ti-Mo-Nb-Zr and Ti-Ta₃₀ compared to the other alloys [204, 205, 208, 213, 324, 325].

Additionally, the difference observed between the β -microstructure, and the $\beta+\alpha''$ - and $\alpha+\beta$ -microstructure can be attributed to the different microstructure, in which the two-phase structure resulted in a galvanic cell formation. The galvanic effect is not present in the β -microstructure Ti-Ta and Ti-Mo-Nb-Zr alloys in this study because these alloys are essentially homogeneous solid solutions with only the single β -microstructure present and no α'' or α phase [197].

All titanium alloys showed similar corrosion, characteristic of materials exhibiting a passive behaviour in the test environment. The polarization curves of all alloys can be divided into three potential domains cathodic, anodic and passive. The first potential domain is the

cathodic region in which all potentials are below the corrosion potential, and the current is determined by the reduction of water and oxygen in cases where the experiment is carried out under aerated conditions. The corrosion potential is the potential where the current changes from cathodic (negative) to anodic (positive). The second potential domain is the anodic region where all the potentials are above the corrosion potential, resulting in the dissolution of the metal into the solution. An increase in the anodic current density is observed with increase potential, related to the reaction kinetics of active metal dissolution. The third potential domain is the passive region where the surface is covered by a thin protective passive film, where the anodic current density considerably decreases with increase potential. This is because passivation films slow down and impede metal dissolution and reduce the corrosion rate. More than one passive region was observed in the polarization curves of all alloys except Ti-6Al-4V.

No evidence of an active- passive transition was observed from the potentiodynamic polarization curves in this work. However, different passivation regions indicated by the arrows in figure 6-2 formed depending on the microstructure of titanium alloys because of the formation one or more protective films during corrosion processes. Additionally, no breakdown of the passive films was observed in any of the alloys for the tested potential range (-0.6 V vs Ref. to +2V vs Ref.). These results are in agreement with the surface morphologies of the titanium alloys after potentiodynamic polarization tests in the bovine calf serum (Fig 6-3). The oxide films formed on the surface of all titanium alloys are basically compact and uniform characterization by ridge and grooves (Fig 6-3). No pits or any evidence of corrosion could be detected in the secondary electron images and back scatter electron images.

The passivation regions were investigated. The α - β -microstructure Ti-6Al-4V was passivated first and the passivation potential of this alloy is ~ 0.01 V vs Ref. Among the other alloys, β -microstructure Ti-Ta₃₀ was passivated last with a potential of ~ 0.5 V vs Ref. At the beginning of the formation passive region, indicated by arrow in Figure 6-2, protective oxide films formed effectively in all titanium alloys. With increasing potential, the protective oxides were broken in all titanium alloys, except the α + β -microstructure Ti-6Al-4V and lost their passivity. However, the second passivation like behaviour started directly indicating repeated rupture and repassivation of micro size pores. The Ti-6Al-4V continued its passive behaviour up to 2V. The α -microstructure Cp-Ti had the lowest current density in the passive region.

The values of the corrosion current densities determined by the Tafel method were smaller than the passivation current densities determined from passive regions for all alloys Table (6-2). All titanium alloys are passive at E_{corr} and the values given in Table 6-2 correspond to a mixed potential. Therefore, values of i_{corr} do not correspond to the actual corrosion rate of titanium alloys in bovine calf serum because of the presence of the passive film on the surface of all titanium alloys after immersion in bovine calf serum. However, the values of i_{corr} and E_{corr} in Table 6-2 may be used to provide a relative ranking of corrosion resistance of titanium alloys used in this study in bovine calf serum. This data is consistent with the observation that the β -microstructure titanium alloys showed better corrosion resistance than the α -microstructure Cp-Ti, $\alpha+\beta$ -microstructure, and $\beta+\alpha''$, while in the passive region α -microstructure Cp Ti had the lowest current density. The same observed was found by [213].

8.3.3 Electrochemical Behavior During and After Rubbing

Under pure corrosion conditions, the β -microstructure Ti-Ta₃₀ showed the highest corrosion resistance (lower i_{corr}) when compared to the current densities obtained in the other alloys (Figure 6-4 and Table 6-3) and all β -microstructure alloys showed better corrosion behavior than that of α , $\alpha+\beta$ and $\beta+\alpha''$ microstructure. The results are consistent with the results of the open circuit potential and potentiodynamic Tafel regions (Figures 6-1 and 6-2). The reasons behind such behavior are associated with a difference in the oxide film as a function of alloy composition, and the difference between the single phase and dual phase microstructures. [102, 197, 204, 205, 208, 213, 324, 325]. The microstructure of titanium alloys had a major influence on the electrochemical behavior, as the single phase β -microstructure performed better than the two phase $\alpha+\beta$ -microstructure and $\beta+\alpha''$ -microstructure in bovine calf serum. It has been reported that the corrosion attack in $\alpha+\beta$ -microstructure titanium alloys often initiates at the α/β interface [197]. Also, the different rate of film formation on the α and β or β and α'' phases can cause oxide film fracture at α/β interface thereby initiating corrosion attack [197]. Additionally, there is a potential difference between the two phases α and β or β and α'' phases that creates a galvanic coupling between the α and β or β and α'' in Ti-6Al-4V and Ti-Ta₂₇-Al₅ alloys in this study after immersion in bovine calf serum [195].

Under rubbing, which gives a combination of mechanical and chemical actions, no significant cathodic region was observed in the Tafel plots curves (Figure 6-5). These results are in agreement with those of other studies that have found no cathodic region during rubbing of titanium alloys [253]. By comparing the polarization curves of the all titanium alloys under tribocorrosion rubbing with that of pure corrosion, the potential dynamic polarization curves

had distinct and major fluctuations in anodic region, attributed to a transition from depassivation (passive film removed)/repassivation (passive film recovery) on the worn surface. This indicates that the wear had an important role in decreasing the corrosion resistance of titanium alloys, as expected [326]. Indeed, wear accelerated the corrosion due to depassivation of worn areas leading to an unstable friction [183, 327, 328]. The depassivation rate is influenced by more than one factor including the counterbody, contact pressure, sliding velocity, and the mechanical properties of the passive film. For this condition, the counterbody, contact pressure, and sliding velocity were the same, and therefore the increase in corrosion due to wear could be related to mechanical properties of the passive film. The mechanical properties of the passive film depend on the chemical composition of the oxide film which determines its structure and adhesion to the substrate. Therefore, alloy composition plays a critical role in corrosion behaviour under rubbing. However, titanium alloys corrode easily under the synergy of corrosion and wear, and the passive film is easily damaged which removes the protection for the alloy and accelerates the corrosion rate [246].

When rubbing was stopped, the i_{corr} of all titanium alloys was still higher than that recorded for pure corrosion. The lowest i_{corr} was shown by the β -microstructure Ti-Mo₈-Nb₄-Zr₂ in both cases after testing at open circuit potential and after anodic potentiostatic conditions, while the β -microstructure Ti-Mo₈-Nb₄-Zr₅ showed the lowest i_{corr} under cathodic potentiostatic conditions. After rubbing, the current densities decreased again in all alloys due to repassivation.

At all investigated potentials and electrochemical conditions (OCP, cathodic or anodic), the titanium alloy surface suffered the same wear mechanism. In addition, all titanium alloys recovered their passive film at the end of rubbing (more detail is discussed in 8.4).

Consequently, the electrochemical behaviour of titanium alloys after rubbing depended on the ability of alloys to recover their passive film, the mechanical damage on the surface and the properties of the newly formed passive film. However, repassivation was not instantaneous and the rest time to completely recover the passive film depended on the alloy composition. Therefore, immediately after rubbing stopped, the alloys did not completely recover their passive film, and some uncovered bare metallic areas existed on the worn surface. This led to the formation of a galvanic coupling between the re-passivated areas that acted as an anode, and de-passivated areas (not completely covered with passive film), which acted as a cathode [240, 250, 329].

Because the Tafel tests were carried out directly after rubbing, the values of the corrosion current density listed in Tables 6-4 through to 6-6 do not correspond to the actual corrosion rate of the alloys. This is due to repassivation that was not instantaneous and is only reached after a longer rest time. The values given in Tables 6-4 through to 6-6 can be used to provide a relative ranking of repassivation. This shows that the β -microstructure Ti-Mo₈-Nb₄-Zr₂ repassivated the quickest of all alloys for both open circuit potential and anodic potentiostatic rubbing conditions, while the β -microstructure Ti-Mo₈-Nb₄-Zr₅ repassivated first after cathodic potentiostatic rubbing conditions. The superior corrosion behaviour of the β -microstructure can be attributed to the presence of Mo, Nb, Zr, and Ta in alloys that improves passivity and inhibited the dissolution of the titanium. However, the order of alloys in terms of noble behaviour changed after rubbing as compared to pure corrosion.

8.4 Tribocorrosion Behaviour of Titanium Alloys

8.4.1 Introduction

In this part, the results of the investigation into all work carried out on the tribocorrosion behaviour of the alloys in a 25% vol% bovine calf serum solution are discussed. All the tests were conducted at $37\pm 1^\circ\text{C}$ under aerated conditions. The results of friction coefficient, open circuit potential, cathodic current, and anodic current changes were measured in situ as a function of time and will be discussed in this chapter. A comparison was also made between these alloys with the α -phase Cp-Ti and $\alpha+\beta$ -phase Ti-6Al-4V alloys.

8.4.2 Sliding Friction Response of Titanium Alloys

Tribocorrosion tests were initially carried out under open circuit potential conditions. Figures 7-1 through to 7-7 show the friction coefficient and open circuit potential as a function of testing time in 25% vol bovine calf serum at $37\pm 1^\circ\text{C}$. The graphs are composed of three main zones. The frictional zones related to: (I) passivation (oxide film); (II) depassivation (removal of oxide film) and dynamic equilibrium between depassivation and repassivation (removal of oxide film/recoverable of oxide film); and (III) repassivation (bulk titanium alloy). The perturbation in all the figures half way through sliding is a result of undertaking a Tafel test.

The first zone shows the waiting time under open circuit potential. The alloys were in contact with the bovine calf serum; therefore, the OCP measured during this period is related to the presence of a passive film on the alloy's surface. The β -phase Ti-Ta₃₀ showed the noblest behaviour and the $\alpha+\beta$ phase Ti-6Al-4V showed the most active behaviour.

In the second zone, rubbing was started, and the potential dropped. The OCP exhibits a cathodic shift, suggesting the occurrence of depassivation of the surface induced by the removal of the layer of the passive film by the sliding contact with the counter face, thereby leading to the exposure of fresh active titanium to the bovine calf serum solution [228, 330]. The lowest OCP value was obtained from the α -microstructure Cp-Ti followed by the $\alpha+\beta$ microstructure Ti-6Al-4V, β -microstructure Ti-Ta₃₀, β -microstructure Ti-Mo₈-Nb₄-Zr₂, β -microstructure Ti-Mo₈-Nb₆-Zr₄, $\beta+\alpha''$ -microstructure Ti-Ta₂₇-Al₅, and β -microstructure Ti-Mo₈-Nb₄-Zr₅. As rubbing continued, the OCP increased for all alloys indicating the occurrence of repassivation, and the exact response can be attributed to the different chemical composition of the oxide film formed with respect to the exposure time. Subsequently, the OCP remained constant around the same value. Fluctuations in OCP during sliding were induced by the depassivation /repassivation mechanism and a dynamic equilibrium between passive film removed/passive film recovery mechanisms occurred [251, 315, 331]. Along with this dynamic equilibrium, the COF reaches a steady state value. The OCP curves of the α -microstructure Cp-Ti and the $\alpha+\beta$ - microstructure Ti-6Al-4V alloys are smoother than those of the β - microstructure and $\beta+\alpha''$ - microstructure alloys. Generally, the noblest OCP during the rubbing regime was recorded for the β - microstructure Ti-Mo₈-Nb₄-Zr₅ followed by β - microstructure Ti-Mo₈-Nb₄-Zr₂, β - microstructure Ti-Ta₃₀, $\beta+\alpha''$ - microstructure Ti-Ta₂₇-Al₅, β - microstructure Ti-Mo₈-Nb₆-Zr₄, α - microstructure Cp-Ti, and $\beta+\alpha$ microstructure Ti-6Al-4V.

Finally, at the end of the rubbing zone (III), the OCP increased again and exhibited an anodic shift, indicating repassivation as a result of spontaneous regrowth of the passive layer, following a parabolic increase in the potential with time, Figures 7-1 through to 7-7. This shows that repassivation was not instantaneous, and the OCP recovered its original value after longer rest time [245].

The order of the nobility behaviour in zone (III) was different to that observed in zone (I). Generally, all β -microstructure titanium alloys showed a similar response. Nevertheless, different repassivation responses were observed during and after rubbing, depending on the alloy composition. However, all β -microstructure titanium alloys tended to regain their original OCP value observed before rubbing. Ti-Mo₈-Nb₄-Zr₂ alloys recovered its passive state faster than that of the other β - microstructure alloys. These results are consistent with the results shown in figure 7-62 (see 8.4.6), which show the lowest percentage of chemical

wear was recorded for Ti-Mo₈-Nb₄-Zr₂ followed by Ti-Mo₈-Nb₄-Zr₅, Ti-Ta₃₀ and Ti-Mo₈-Nb₆-Zr₄.

The α -microstructure Cp-Ti and $\alpha+\beta$ - microstructure Ti-6Al-4V showed a different behaviour to the β based alloys. The OCP of the α -microstructure Cp-Ti and $\alpha+\beta$ - microstructure Ti-6Al-4V decreased at the start of rubbing and stabilized at a low value, indicating that no recovery of passivity took place during rubbing. This is in contrast to the wear tracks on the β -microstructure, where passivity was recovered during rubbing, which indicated that the wear accelerated corrosion was low for the β -microstructure compared to the α -microstructure Cp-Ti and $\alpha+\beta$ - microstructure Ti-6Al-4V even though the total wear volume loss was higher. This is most probably due to the modification of the passive TiO₂ layer by the alloying elements Mo, Nb, Zr, and Ta that may have introduced oxides Nb₂O₂, Ti₂O₅, MO₃ and ZrO₂ and improve the structural integrity of the alloys native passive film [215]. The ability of the β -microstructure alloy to regain its passive state during rubbing has also been reported under tribocorrosion conditions [10].

The higher friction coefficient was obtained from the $\beta+\alpha''$ - microstructure Ti-Ta₂₇-Al₅, while the α - microstructure Cp-Ti alloy had the lowest friction coefficient. This could be related to the crystal structure of the α -microstructure alloy. The low friction coefficient also can be attributed to the formation of a carbonaceous layer which builds up during rubbing and reaches the maximum effectiveness in decreasing the friction coefficient (figure 7-11). It is interesting to note that the β -microstructure Ti-Mo₈-Nb₄-Zr₂ had a higher peak intensity of the carbonaceous layer (figure 7-11) than the Ti-6Al-4V but had the same friction coefficient. Given that the friction was generally lower for the hcp alloys compared to the bcc alloys, this result suggests that the carbonaceous layer or tribofilm was protective and helped with reducing and limiting friction. The higher friction coefficient can be attributed to the interaction of wear debris produced by the removal of metal, oxide and the tribofilm during rubbing leading to an increase in the friction force due to an increase in the ploughing effect [251]. As can be observed from figure 7-8, the friction coefficient of all titanium alloys under OCP rubbing is higher than 0.1 indicating no hydrodynamic lubrication is expected to occur [10].

Tribocorrosion tests were performed under potentiostatic conditions to study the properties of the surface film under rubbing at potentiostatic potentials of -0.5V vs OCP and 0.3V vs OCP. Figures 7-23 through to 7-29 display the evolution of the friction coefficient and current with

time at an applied potential of -0.5V vs OCP for all titanium alloys in bovine calf serum. The graphs in these figures are composed of three main zones. The first region shows the waiting time under cathodic potential; therefore, the current in all alloys is negative corresponding to the measurement of the cathodic reaction, which is called the cathodic dominated region. In the second zone, rubbing was started by applying a load and motion on the cathodic layer. A significant increase in the current density was observed after a few seconds to a steady state value, although the current fluctuated with a constant interval, related related to the alloy composition and structure, with the current showing an anodic shift, but the current was positive. This result showed that a corrosion effect occurs in the cathodic region for tested potential range -0.5V vs OCP in all alloys, and the corrosive effect cannot be completely prevented. Therefore, the material loss originates from both the mechanical wear and the corrosive effect.

This result differs to previous studies of tribocorrosion for different types of titanium alloys in simulated body fluid in which the negative current values were found for titanium alloys from wear tests conducted in the cathodic region -1450mV vs Ref [253]. However, the same group found positive current values from the wear tests conducted in the cathodic region -250mV vs Ref. for the same tested titanium alloys [253]. These results indicate that electrochemical corrosion occurs, and the material loss from the wear track originates not only from the mechanical effect (pure mechanical wear). According to ASTM G133, no corrosive effect can be observed under cathodic rubbing conditions; however, this phenomenon is still not fully understood and knowledge about it is limited. There is therefore a requirement to gain further insight into the mechanisms, and also the effect of electrochemical corrosion, because the corrosive effect cannot be completely prevented[329].

In the third region of the curves (Figures 7-23 through to 7-29), rubbing was stopped and the current decreased again to the value observed at beginning of the rubbing. At the onset of sliding, the cathodic layer had been removed and there was a sharp increase in the current, resulting in a positive current.

The average friction coefficient values and average current values were calculated by averaging over the entire rubbing duration and these are shown in figure 7-30. It can be seen from the figure that the $\beta+\alpha''$ -microstructure had the highest friction coefficient, while the $\alpha+\beta$ microstructure Ti-6Al-4V alloy and the α -microstructure Cp-Ti had the lowest friction coefficient. This is probably related to their higher hardness and the hcp structure. All β -

microstructure alloys, except Ti-Ta₃₀, had an average friction coefficient close to that of the $\alpha+\beta$ microstructure Ti-6Al-4V. Thus, this can be explained by the formation of a carbonaceous layer or tribofilm, which has been reported to help with limiting friction [332]. The β -microstructure alloys exhibited a higher peak intensity from the carbonaceous layer than that of the $\alpha+\beta$ microstructure Ti-6Al-4V, $\beta+\alpha''$ -microstructure and β -microstructure, with the exception of the Ti-Ta₃₀ (figure 7-33). Also, it can be seen from figure 7-30 that the β -microstructure Ti-Ta₃₀ had the lowest current during rubbing, while the $\beta+\alpha''$ -microstructure had a higher current during rubbing. Thus, the β -microstructure alloys only suffer from wear-accelerated corrosion but benefitted from corrosion-decelerated wear. It is interesting to note that the corrosion current for β -microstructure alloys increase to high values immediately at the start of sliding, and then it decreases and stabilizes after ~3000sec, while the corrosion current of $\alpha+\beta$ microstructure Ti-6Al-4V and α -microstructure Cp-Ti increases to high values immediately at the start of sliding and then it decreases and stabilizes after ~9000sec. This shows that the wear tracks of β -microstructure alloys have the ability to recover their passivity during rubbing.

The evolution of the coefficient of friction and the anodic current with time at an applied anodic potential of 0.3V vs OCP is shown in figures 7-44 through to 7-50. At the onset of sliding, a significant increase in the anodic current was observed for all alloys. This response was related to the depassivation mechanism by the counter-body sliding on the surface of alloys, thus leading to removal of the passive film in the contact region when sliding starts and exposing the surface of fresh active titanium to the electrolyte. Consequently, a rapid reaction between the active titanium surface and electrolyte leads to accelerated electrochemical corrosion and anodic metal oxidation [183, 330]. The higher anodic current was recorded for the $\beta+\alpha''$ - microstructure Ti-Ta₂₇-Al₅ followed by the α - microstructure Cp-Ti, β - microstructure Ti-Ta₃₀, β - microstructure Ti-Mo₈-Nb₆-Zr₄, β - microstructure Ti-Mo₈-Nb₄-Zr₂, β - microstructure Ti-Mo₈-Nb₄-Zr₅, and $\alpha+\beta$ - microstructure Ti-6Al-4V respectively. During the sliding period, the anodic current reached steady state after a few seconds, and no significant variation in the anodic current was observed during sliding, except several isolated peaks. These events indicated that the titanium alloy surface locally underwent a local depassivation mechanism that was followed by rapid repassivation. The anodic current showed large fluctuations during rubbing, therefore there was no strong evidence of an alloy composition effect. However, the lowest anodic current during rubbing was recorded for the α - microstructure Cp-Ti and $\alpha+\beta$ - microstructure Ti-6Al-4V followed by β - microstructure

Ti-Mo₈-Nb₄-Zr₅, β - microstructure Ti-Mo₈-Nb₆-Zr₄, β - microstructure Ti-Mo₈-Nb₄-Zr₂ and β + α microstructure Ti-Ta₂₇-Al₅ respectively.

Finally, at the end of sliding, the anodic current decreased again to the initial value observed at the beginning of the tests before rubbing. This indicates repassivation of the worn area. These results are in agreement with the behaviour in different passive alloys, as reported in the literature [231, 251, 333]. However, the anodic current before sliding was still larger than the current measured after rubbing. This indicates a repassivation (passive film recovery) of the wear track at the active areas, while the passive films in the areas not subject to sliding continued to grow during the course of the experiment [24]. The same was not true for the Ti-Ta₃₀, where the anodic current after sliding was still higher than that observed before sliding. This indicates that the passive layers suffered significant damage during rubbing tests; therefore, the passive film layers were not completely formed on the surface of the alloys after rubbing tests, leaving an active area on the surface behind leading to anodic metal oxidation.

The average friction coefficient values and average current values were calculated by averaging over the entire rubbing duration the instantaneous value measured during the test are shown in figure 7-51. The lowest friction coefficient was obtained from the α + β -microstructure Ti-6Al-4V, while the β -microstructure Ti-Ta₃₀ had the highest friction coefficient. This is probably related to higher hardness of the α + β -microstructure Ti-6Al-4V compared to the others. However, the β -microstructure Ti-Mo₈-Nb₄-Zr₂, Ti-Mo₈-Nb₆-Zr₄, Ti-Mo₈-Nb₄-Zr₅ and β + α ' Ti-Ta₂₇-Al₅ had the same friction coefficient of α -microstructure Cp-Ti. This could be related to the formation of a carbonaceous layer or tribofilm, which has been reported to help with limiting friction [332]. The alloys have a higher peak intensity of the carbonaceous layer (figure 7-54) indicating a more extensive tribofilm on the surface. On the contrary, though the β -microstructure Ti-Ta₃₀ had a higher peak intensity from the carbonaceous layer, it exhibited a higher friction coefficient, which could be attributed to the depassivation products produced during rubbing. Also, it can be seen from figure 7-51 that the α + β -microstructure Ti-6Al-4V, α -microstructure Cp-Ti, β -microstructure Ti-Mo₈-Nb₆-Zr₄ and Ti-Mo₈-Nb₄-Zr₅ had the lowest corrosion currents during rubbing. The highest current was obtained from the β + α ' Ti-Ta₂₇-Al₅. The corrosion current of all alloys increased to a high value immediately with the start of rubbing and then progressively reduced to a steady state value. Interestingly, the corrosion current stabilized at a low value for β -microstructure Ti-Mo₈-Nb₆-Zr₄ and Ti-Mo₈-Nb₄-Zr₅, α -microstructure Cp-Ti and α + β -microstructure Ti-

6Al-4V alloys after approximately 2400 s, 2300 s, 3700 s, and 7250 s respectively. This indicated that the wear tracks on β -microstructure alloys can recover their passivity during rubbing.

In general, alloys suffer from wear-accelerated corrosion due to wear damage to the protective passive film. At OCP, depassivation took place immediately at the beginning of rubbing, such that a thin passive film was expected. At cathodic potential (-0.5 V vs OCP), before rubbing the current was negative, i.e. cathodic. During rubbing, the current was anodic with positive values, and after rubbing becomes cathodic again. This indicated that the corrosion only occurs in the wear tracks (anodic current), but not at the unworn area outside the wear tracks (cathodic current). At an anodic potential (0.3 V vs OCP), the anodic current did not increase significantly until a few hundred cycles (Figures 7-44 through to 7-50) because a thicker passive layer on the surface of alloys was expected at this anodic potential. It was reported that the corrosion in passive alloys is always accelerated by wear because of depassivation of the wear track area. However, mechanical wear is not always accelerated by corrosion. The passive film and corrosion products could modify friction and contact stress fields [334]. In this study, during rubbing at the OCP the corrosion potential of β -microstructure alloys progressively rises, and at cathodic potential (-0.5 V vs OCP) and anodic potential (0.3 V vs OCP) the anodic current decreases during rubbing. This indicates that the β -microstructure alloy tends to regain its passive state, and alloys can recover their passive during rubbing at tribocorrosion despite mechanical perturbations. The ability of an alloy to recover its passive film during rubbing at tribocorrosion tests is a critical property and depended mainly on the chemical composition of the oxide film, the thickness of the passive layer and critical pressure for depassivation [247]. The phenomenon of passivity recovery during rubbing in tribocorrosion tests is beneficial to implant applications since decreased material loss and release of metal ions and particles increases biocompatibility. Other β -microstructure have showed the ability to recover a passive state under rubbing [10, 230, 247].

The friction coefficient of all alloys showed an initial run-in period followed by a maximum before reaching a steady state friction coefficient. The present results show that the friction coefficient values obtained at the OCP and -0.5V vs OCP and 0.3V vs OCP potentiostatic conditions were similar indicating the friction coefficient of alloys remains largely unaffected by the alloy composition and the prevailing electrochemical conditions during the

tribocorrosion test. Compared with pure wear without corrosion at 1N under lubricated rubbing condition, the friction coefficient remains mainly unaffected by the potential.

8.4.3 Corrosive Wear Tracks, Surface and subsurface Morphology and Surface Chemistry

To study the wear track morphology and to unravel the wear mechanisms, scanning electron microscopy tests were carried out to examine the surface of the corrosive worn track of the titanium alloys after tribocorrosion tests under OCP and potentiostatic applied potential. The SEM micrographs of the morphological features of the worn track surface after tribocorrosion tests under OCP rubbing conditions are presented in Figure 7-9. The morphological features of the worn track surface wear after tribocorrosion tests under -0.5V vs OCP potentiostatic rubbing conditions are shown in Figure 7-31. Figure 7-52 shows the detailed morphological features of the worn track surface after tribocorrosion tests under anodic potentiostatic conditions 0.3V vs OCP. The overview of the corrosive worn track surface indicates that rubbing induced surface roughening under all rubbing conditions. These results agree with surface roughness 3D, 2D profile measurements and the average surface roughness of titanium alloys. The wear tracks produced on the surface of all the alloys, except the α -microstructure Cp Ti, β + α' -microstructure Ti-Ta₂₇-Al₅ and β -microstructure Ti-Mo₈-Nb₄-Zr₂, after OCP rubbing conditions are slightly rougher than after potentiostatic rubbing conditions. The α -microstructure Cp Ti, β + α' -microstructure Ti-Ta₂₇-Al₅ and β -microstructure Ti-Mo₈-Nb₄-Zr₂ wear tracks were rougher under anodic potentiostatic rubbing conditions than that of wear tracks under OCP and cathodic potentiostatic rubbing conditions. The smallest wear track was obtained from the α -microstructure Cp-Ti and α + β -microstructure Ti-6Al-4V after tribocorrosion under all rubbing conditions. A relatively large and distinct wear tracks were formed on the surface of the all β -microstructure alloys and the β + α' -microstructure Ti-Ta₂₇-Al₅ alloy.

At the OCP, all alloys exhibited similar features showing scratches, grooves and plastic deformation on the wear surface. However, the depth of the grooves was greater in the α -microstructure Cp-Ti, α + β -microstructure Ti-6Al-4V, and β + α' -microstructure Ti-Ta₂₇-Al₅. In addition, the wear tracks from these alloys showed a greater presence of wear debris and delamination. There were no significant differences in the wear morphologies after tribocorrosion tests under -0.5V vs OCP potentiostatic rubbing conditions, with all alloys showing the presence of ductile and plastic deformation, depth scratches and grooves, wear

debris in both case fine particles, as well as flaky-like and delamination at the worn surface. For anodic rubbing conditions 0.3V vs OCP, plastic grooves, deformation and the relatively smooth appearance of the worn surface was observed in all cases. In general, all the corrosive wear surface was free from corrosion products after tribocorrosion under all rubbing conditions. The corrosive wear tracks were extremely rough with deep and wide grooves and scratches after tribocorrosion tests under OCP and -0.5V vs OCP potentiostatic rubbing condition, while the corrosive wear tracks were very smooth after tribocorrosion tests under anodic potentiostatic rubbing conditions. Thus, the tribocorrosion mechanisms can be attributed to abrasive wear and delamination wear mechanisms.

The worn surface of all alloys under all rubbing conditions appeared to be covered by an intermittent light grey layer, as well as small spots with dark contrast. This could be attributed to the formation of carbonaceous layer, which was confirmed by the results of EDX and Raman spectrum results (Figures 7-10, 7-11, 7-32, 7-33, 7-53 and 7-54). The substrate elements were present as well as carbon and oxygen. The Raman spectra show two defined peaks: disordered graphite (D band) and the single crystal graphite (G band) centred on 1383 and 1567 cm^{-1} related to sp^2 -carbon and sp^3 -band carbon respectively. At the OCP, the β -microstructure Ti-Mo₈-Nb₄-Zr₂ alloy and the α - microstructure Cp-Ti had the highest Raman spectra intensity, while the β - microstructure Ti-Ta₃₀ alloy had the lowest Raman spectra intensity. At -0.5V vs OCP, all the β -microstructure alloys, except Ti-Ta₃₀ had the highest Raman spectra intensity, while the α - β -microstructure Ti-6Al-4V alloy had the lowest Raman spectra intensity. At 0.3V vs OCP the β -microstructure Ti-Ta₃₀ alloy and the β - α'' -microstructure Ti-Ta₂₇-Al₅ alloy had the highest Raman spectra intensity, while the α -phase Ti-6Al-4V had the lowest Raman spectra intensity. It has been reported that the tribofilm could be beneficially during tribocorrosion experiments [25, 317]. The formation of the tribofilm, as well as the details of its influence to the tribocorrosion process are not fully understood, and needs to be further investigated [335-340]. However, it has been reported that there is an interaction between the released ions during rubbing and the proteins in the electrolyte, leading to formation carbonaceous film. This leads to degradation of the proteins which then deposit on the surface of the alloy, which together with ions and salt will form the carbonaceous layer [341]. A small amount of oxygen existed after tribocorrosion experiments, see the EDX results (Figures 7-10, 7-32 and 7-53). These results are in agreement with the observation that some oxygen with a ratio of C/O 1/0.07 is present in the

carbonaceous film, and the significant oxygen peaks in a control sample of dried bovine calf serum[335].

There was no evidence of transfer from the alumina ball to the titanium alloy surface. However, the optical, SEM and EDX element mapping on the alumina balls at the end of the tribocorrosion tests showed a small amount of matter transferred from titanium alloys and a loss of material on the alumina surface (Figures 7-12 through to 7-14, Figures 7-34 through to 7-36 and Figures 7-55 through to 7-57).

When an alloy surface is subject to mechanical wear during tribocorrosion, the subsurface of the worn area can suffer deformation, compaction of debris and recrystallization. This can result in the modification of the mechanical wear performance and induce hardening of the surface of the alloy. It was reported that there are three subsurface zones are typically observed after a tribological test: zone 1 the bulk material, zone 2 the plastic deformed layer, and zone 3 the mixed nano-crystalline surface layer [315]. The samples rubbed at anodic potential 0.3V vs OCP potentiostatic clearly exhibited less deformation than that the samples rubbed at OCP and -0.5 OCP potentiostatic under the same number of cycles (Figures 7-21, 7-22, 7-42, 7-43, 7-63 and 7-64).

In the case of samples rubbed at OCP, three zones in the subsurface regions below the worn surface were observed after tribocorrosion tests. A continuous nanocrystalline layer was clearly identified by the grain refinement at the surface. Microcrystalline scale grains were observed below the nanocrystalline layer. A mixed nanocrystalline and microcrystalline zone was observed and no a clear boundary between nanocrystalline and microcrystalline could be seen in the case of the $\beta+\alpha''$ - microstructure Ti-Ta₂₇-Al₅ alloy. In contrast, in the case of the β -microstructure Ti-Mo₈-Nb₄-Zr₅, no mixed zone was observed and there was a clear boundary between the nanocrystalline and microcrystalline grain. In the case of samples rubbed at -0.5V vs the OCP, a continuous nanocrystalline layer was clearly identified and the thickness of the nanocrystalline layer was thinner than that of the samples rubbed at OCP potential, but thicker than that of samples rubbed at anodic potentialiostatic 0.3V vs OCP. The grain size decreased continuously as the worn surface approached, and the change in grain size with depth was quite different compared with the OCP and anodic potential. There was a clear boundary between the nanocrystalline and microcrystalline grains for the β -microstructure Mo₈-Nb₄-Zr₅. For the $\beta+\alpha''$ - microstructure Ti-Ta₂₇-Al₅ there was no clear boundary between the nanocrystalline grains and the microcrystalline grains close to bulk

material. In the case of samples rubbed at an anodic potential, the thickness of the deformation layer was less than that of samples rubbed at OCP and cathodic potential. A thin, but continuous, nanocrystalline layer was observed after tribocorrosion tests, which can be attributed to the passive film layer which formed when the anodic potential was applied during rubbing. There was no evidence of twinning observed, and the different contrast shown by the ion beam channelling images was associated with plastic deformation during rubbing rather than the formation of a new phase. In accordance with above analysis, the results of the FIB cross sections (ion channelling contrast image), the nature and extent of deformation underneath the rubbed surface of alloys depends on the electrochemical conditions OCP and potentiostatic applied during tribocorrosion tests. More deformation is accumulated when the cathodic potential is applied during rubbing.

8.4.4 Total Material Loss Rate

The total material loss rate (total removed wear volume) after tribocorrosion experiments under OCP and potentiostatic rubbing conditions includes the material loss due to mechanical wear events, and the material loss due to electrochemical oxidation the corrosion mechanism was measured from the wear track profiles. The results of total material loss and specific wear rate under OCP rubbing conditions are shown in Figure 7-18. Figures 7-40 and 7-61 show the results of total material loss and the results of specific wear rate under -0.5V vs OCP and 0.3V vs OCP potentiostatic rubbing conditions respectively.

Titanium and titanium alloys are passive and show a very low passive dissolution rate. Therefore, in the present work, the amount of material loss due corrosion outside the wear track unworn area was not quantified and can be neglected and the focus has only been given to the wear accelerated corrosion in the wear track. In this study, the total material removed from the wear tracks (V_{total}) during tribocorrosion is the result of mechanical wear (V_{mech}) and chemical wear (V_{chem}). At OCP, the total wear volume was calculated from the wear track profiles at the end of tribocorrosion tests (V_{total} equation 3-9). The chemical component (V_{chem}) can be roughly estimated by the excess current measured during sliding according to Faraday's law using equation 3-13. The mechanical wear volume V_{mech} was calculated by the difference between the total volume V_{total} and the chemical volume V_{chem} using equation 3-14. At OCP, the corrosion currents estimated from Tafel plots (Figures 7-19) were used to estimate the chemical wear component at OCP. The measurement of the anodic current during rubbing at cathodic potential (-0.5V vs OCP) allows for the quantification of the wear-accelerated corrosion. Therefore, applying Faraday's law and the mechanistic approach for

tribocorrosion can quantitatively determine the chemical and mechanical contribution to material loss during tribocorrosion at cathodic rubbing conditions. Therefore, at passive applied potential (0.3V vs OCP) and cathodic potentiostatic (-0.5V vs OCP), the chemical volume V_{chem} removed by anodic oxidation in the wear track was calculated from equation 3-11, where Q is the electric charge flowing in the wear track. The total wear volume was calculated by measuring the cross section of the wear tracks by profilometry at the end of tribocorrosion tests (V_{total} equation 3-9). The difference between the V_{total} and V_{chem} gives one the V_{mech} (equation 3-14).

The smallest volume loss was obtained from α -microstructure Cp-Ti, while the β -microstructure alloys showed the highest volume loss under all conditions (Figures 7-18, 7-40 and 7-61). The highest volume loss of β -microstructure alloys could be due to the easy removal of the passive layer from the surface during rubbing leading oxidative wear. It is interesting to note that, although the $\alpha+\beta$ -microstructure Ti-6Al-4V alloy and β -microstructure alloys had higher mechanical behaviour (higher hardness), the alloys exhibited relatively higher volume loss than that of α -microstructure Cp-Ti. This could be attributed to the rate of depassivation and repassivation of β -microstructure alloys during rubbing. This indicated that the total volume loss of the tested alloys did not appear to correlate with the mechanical properties of the alloy (hardness and elastic modulus).

The results show that the total volume loss depended on alloy microstructure and on the prevailing electrochemical conditions. The fluctuation in the potential and current with time indicated that the mechanical damage with wear is pronounced. The mechanical properties of the passive film and contact pressure for the passive film removal are all factors that influence the mechanical wear resistance of an alloy. In all tribocorrosion conditions considered, the contact pressure was same for each alloy, while the mechanical properties of passive film depended mainly on the alloy's microstructure and composition. However, during rubbing, the mechanical properties of the passive film will change with mechanical action and electrochemical reactions take place on the active surface alloy. The electrochemical conditions prevailing for the OCP or potentiostatic potential in the contact during rubbing affect the mechanical properties of the passive film.

The results of total volume loss at the OCP and -0.5V vs OCP show that the wear accelerated corrosion correlated with the mechanical damage. Thus, the passive behaviour of β -microstructure did not have a positive influence on tribocorrosion performance at the OCP

and -0.5V vs the OCP leading to the β -microstructure alloys suffering from wear accelerated corrosion. At passive applied potential, the total volume loss was lower than that at the OCP and -0.5V vs OCP potentiostatic. The opposite occurs at passive applied potential. The wear accelerate corrosion of the $\beta+\alpha''$ -microstructure, $\alpha+\beta$ -microstructure Ti-6Al-4V and α -microstructure Cp-Ti was much higher than the values obtained in the β -microstructure alloys. Wear accelerated corrosion of the $\beta+\alpha''$ -microstructure, $\alpha+\beta$ -microstructure Ti-6Al-4V and α -microstructure Cp-Ti represents ~ 40, 33, 27 % of the total volume loss respectively, while in the β -microstructure alloys it only represented ~15% of the total volume loss. The percentage of chemical wear V_{chem} of the β - microstructure alloys were considerably smaller than that of the $\alpha+\beta$ -microstructure Ti-6Al-4V and α -microstructure Cp-Ti even though the total material loss volume V_{total} was higher. The lowest percentage of V_{chem} was reported for β - microstructure Ti-Mo₈-Nb₄-Zr₂ followed by β - microstructure Ti-Mo₈-Nb₄-Zr₅, β -microstructure Ti-Ta₃₀, β - microstructure Ti-Mo₈-Nb₆-Zr₄, α - microstructure Cp-Ti, $\alpha+\beta$ -microstructure Ti-6Al-4V, and $\beta+\alpha$ - microstructure Ti-Ta₂₇-Al₅. The increase in corrosion due wear in the $\beta+\alpha''$ -microstructure, $\alpha+\beta$ -microstructure Ti-6Al-4V and α -microstructure Cp-Ti could be related to the different chemical composition of microstructure and oxide film. The lower percentage of V_{chem} for β -microstructure alloys may be attributed to the passive behaviour of β -microstructure alloys. This indicates that the passivation behaviour of β -microstructure alloys has a positive influence on the tribocorrosion performance at passive applied potential due to suppression of the wear accelerated corrosion process. These results indicate that the β -phase alloys produced in this study can recover their passivity in the wear track under tribocorrosion despite the mechanical perturbation, and these alloys are more resistant to wear-accelerated corrosion. However, the β -phase alloys produced in this study are more susceptible to mechanical wear.

Interestingly, the β -microstructure Ti-Mo₈-Nb₄-Zr₂ alloy had a volume loss less than that of $\alpha+\beta$ -microstructure under -0.5V vs OCP and the β -microstructure Ti-Mo₈-Nb₆-Zr₄ had the same volume loss as the $\alpha+\beta$ -microstructure under 0.3 V vs OCP. This behaviour may be attributed to the formation of a carbonaceous layer or tribofilm which builds up during rubbing and reaches maximum effectiveness in decreasing the friction and wear on the alloy surface. The alloys have higher peak intensity of the carbonaceous layer, which indicated more carbon content was found within the tribofilm.

The total volume loss was found to be higher for pure mechanical wear than that for tribocorrosion. This is attributed to the inferior wear resistance of titanium alloys. The poor

wear resistance of titanium alloys results in more material degradation than tribocorrosion. It appears that the electrochemical conditions prevailing in the contact affect the mechanical properties of the passive film. It was reported that, on the one hand, a passive alloy's corrosion is usually accelerated by mechanical wear because of depassivation of the wear track area by the wearing action. On the other hand, corrosion does not necessarily always accelerate mechanical wear. It was reported that the factor V_{chem} electrochemical corrosion has two possible actions, and thus is dependent on the tribo-system [342]; firstly, formation of a mechanically weak layer on the surface of the alloys leading to accelerated mechanical wear. Therefore, the total wear volume will increase compared to that of pure mechanical wear. Secondly, formation of a lubricating surface layer on the surface of alloys, leading to reduction of the mechanical wear [342]. Consequently, the total wear volume will decrease compared to that of pure mechanical wear. In accordance with the above results, the total removed wear volume at pure mechanical wear was higher than that of after OCP and potentiostatic rubbing conditions (mechanical wear with corrosion). These results indicate that the titanium alloys produced in this study can recover their passivity in the wear track under tribocorrosion despite mechanical perturbation, and these alloys are more resistant to wear-accelerated corrosion. Thus, the titanium alloys in bovine calf serum are more susceptible to mechanical wear but benefit from corrosion decelerated wear.

The experimental results clearly show that the recovery of the passive state is effective in reducing material removal of β -microstructure alloys. The total materials removal from the wear track during rubbing at tribocorrosion is the results of mechanical wear (V_{mech}), which is from the underlying substrate, and chemical wear (V_{chem}), which is metal dissolution and wearing or removal of oxide film formed at contact intervals by rubbing action (materials associated with anodic current). At OCP rubbing conditions, chemical wear (V_{chem}) contributed to about 0.5% of total material removal from the β -microstructure alloys, while it was about 1%, 1.2%, 8.2% of total materials removal from $\beta+\alpha''$ -microstructure, $\beta+\alpha$ -microstructure and α -microstructure respectively (Figure 7-20). At cathodic (-0.5 V vs OCP) rubbing conditions, chemical wear (V_{chem}) contributed to about 1% of total materials removal from β -microstructure alloys, while it is about 5%, 6%, 10% of total materials removal from $\beta+\alpha''$ -microstructure, $\beta+\alpha$ -microstructure and α -microstructure respectively (Figure 7-41). The contribution of chemical wear increased significantly to ~ 40,33,27 % of total materials removal from $\beta+\alpha''$ -microstructure, $\beta+\alpha$ -microstructure and α -microstructure respectively,

while it is about ~15% of total materials removal from β -microstructure alloys at anodic potential 0.3V vs OCP (Figure 7-62).

The principle tribocorrosion mechanisms of the alloys at -0.5 V vs OCP and OCP was a mixed mechanical and chemical wear with mechanical dominance. Clearly the amount of chemical wear (V_{chem}) becomes more at anodic potential (0.3 V vs OCP), which could be attributed to increases in the thickness of oxide film build up at contact intervals [334]. However, it was small compared to the total wear (V_{total}) (Figure 7-62) indicating that the mechanisms are also a mixed chemical and mechanical wear with mechanical dominance. The percentage of chemical wear (V_{chem}) of β -microstructure alloys was considerably smaller than the one reported for α -microstructure Cp-Ti, $\beta+\alpha$ -microstructure Ti-6Al-4V and $\beta+\alpha''$ -microstructure Ti-Ta₂₇-Al₅ (Figures 7-20, 7-41 and 7-62). This indicates that the β -microstructure alloys can recover their passivity during rubbing during tribocorrosion tests but were more susceptible to mechanical wear compared to microstructure Cp-Ti and $\beta+\alpha$ -microstructure Ti-6Al-4V. The recovery of the passive state during rubbing at tribocorrosion is a characteristic of the β -microstructure alloys developed in this study, which if considered in alloy development and implant design, could be beneficial to implant applications by reducing friction and wear, limiting the release of metal ions, and increasing biocompatibility.

Chapter 9: Conclusions and Recommendations for Future Work

9-1 Conclusions

The following conclusions have been made from the experiments carried out in this work and the results and discussion presented in chapters four, five, six, seven, and eight.

9.1.1 Structure and Property Characterization of Titanium Alloys

The main conclusions from the structure and properties of alloys are as follows:

- The number of remelting cycles during melting and the combination with thermo and thermo-mechanical treatments need to be carefully controlled to produce a uniform microstructure, especially with the Ti-Ta₃₀ alloy.
- All alloys developed in this work exhibited excellent cold workability except the Ti-Ta₃₀ alloy that needed an intermediate annealing treatment during the thermo-mechanical treatment to increase its cold workability.
- All titanium alloys except Ti-Ta₂₇-Al₅ were comprised of equiaxed single-phase β phase grains with no evidence of any intermediate phase. The Ti-Ta₂₇-Al₅ alloy was predominantly β phase with an equiaxed grain structure, but also contained orthorhombic martensitic with thin needle-like structure in some regions of the sample.
- All the titanium alloys had a lower elastic modulus than that of Cp-Ti and Ti-6Al-4V.
- All alloys had an average Vickers micro-hardness values higher than that of Cp-Ti, and lower than that of Ti-6Al-4V.

9.1.2 Tribological Behavior of Titanium Alloys

The main conclusions from tribological tests are as follows:

- The friction coefficient and wear volume of alloys increased with load.
- The α -microstructure Cp-Ti and α + β -microstructure Ti-6Al-4V show relatively lower volume loss, as well as a lower friction coefficient compared to the other alloys.
- A carbonaceous layer was generated on the worn surface of the alloys, and this appeared to be beneficial by reducing the friction and wear. However, the carbonaceous layer did not appear to correlate with the alloy structure (β , α or α''). Thus, the formation of the graphitic film appeared to be more dependent on the load than the alloy composition.

- No evidence of transfer from the alumina ball to the titanium alloy surface was found, and no significant damage or material transfer could be observed on the alumina ball counterbody after wear tests.
- The wear mechanisms were attributed to abrasive ploughing wear mechanisms.
- The exact tribological response was controlled by the crystal structure, the mechanical properties of the alloy (hardness and elastic modulus), the carbonaceous layer (tribolayer) and load. However, no direct relationship could be established between the wear volume and the mechanical properties of the alloys (hardness and elastic modulus).
- No evidence for subsurface cracking could be found. Grain refinement did occur at the rubbing surface. After an increase in the normal load, an increase in the extent of grain refinement was observed.

9.1.3 Electrochemical Behaviour of Titanium Alloys

The main conclusions from electrochemical tests are as follows:

- The alloy structure and alloy composition hardly influence the OCP values of alloys, and alloys tend to form a passive film. The results indicate the positive contribution of the alloying elements Mo, Nb, Zr, and Ta that lead to a denser, thicker and more pitting resistant MO_2 , Nb_2O_5 , ZrO_2 , Ta_2O_5 passive film on the surface of the titanium alloys.
- β - microstructure Ti-Ta₃₀ had the most positive OCP value, which could be attributed to the presence of a mixture of Ta_2O_5 and TiO_2 on the Ti-Ta alloy surface, while $\alpha+\beta$ - microstructure Ti-6Al-4V exhibited the most negative value.
- Under pure corrosion, all β -microstructure alloys exhibited spontaneous passivity and very low corrosion current density, which is attributed to the passive film formation of a mixture of MO_2 , Nb_2O_5 , ZrO_2 , Ta_2O_5 and TiO_2 on the Ti-Mo-Nb-Zr and Ti-Ta alloys.
- The corrosion potential under rubbing shifted cathodically and the current density increased compared with static corrosion. In addition, the potential dynamic polarization curves had distinct and major fluctuations.
- The polarization curves obtained after tribocorrosion tests show that the corrosion potential, current densities and corrosion rate shifted compared with that of the starting surface, and that shifting is dependent on the alloy composition and the

electrochemical condition of the alloy under tribocorrosion tests (OCP, cathodic, or anodic potentiostatic).

- β -microstructure Ti-Mo₈-Nb₄-Zr₂ had lowest current density after OCP and anodic rubbing, while β - microstructure Ti-Mo₈-Nb₄-Zr₅ had the lowest after cathodic rubbing.
- The electrochemical behaviour of alloys after rubbing is attributed to the ability of alloys to recover their passive film, the amount of damage on the surface caused by the wear mechanism and the properties of the newly formed passive film compared with naturally formed passive film present on titanium alloys before rubbing.

9.1.4 Tribocorrosion Behavior of Titanium Alloys

The main conclusions from tribocorrosion characterisation are as follows:

- In OCP rubbing conditions the lowest potential value was obtained from the α -microstructure Cp Ti, while the noblest OCP during rubbing regime was recorded for the β -microstructure Ti-Mo₈-Nb₄-Zr₅.
- The α -microstructure Cp-Ti and $\alpha+\beta$ -microstructure Ti-6Al-4V show a relatively lower friction coefficient during tribocorrosion tests compared to other alloys.
- Friction coefficient values remain mainly unaffected by the prevailing electrochemical conditions (OCP, cathodic, or anodic potentiostatic) during tribocorrosion tests.
- The α -microstructure Cp-Ti shows relatively lower volume loss during tribocorrosion tests compared to others.
- All corroded wear surfaces were free from corrosion products after tribocorrosion tests; and corrosive wear tracks were extremely rough with deep and wide grooves and scratches after tribocorrosion tests at OCP and cathodic potentiostatic potential. In contrast, the corrosive wear tracks were very smooth after tribocorrosion tests at anodic potentiostatic potential.
- The tribocorrosion mechanisms were attributed to abrasive ploughing wear mechanisms. At OCP, cathodic and anodic rubbing conditions, the principal tribocorrosion mechanism of the titanium alloys is mixed mechanical and chemical wear with mechanical dominance.
- No important influence of mechanical properties (hardness and elastic modulus) of the alloys could be found on the wear volume and tribocorrosion response.

- The carbonaceous layers were generated on alloys during tribocorrosion experiments, which appear to be beneficial in limiting friction and reducing the wear rate.
- No transfer from the alumina ball to the alloy surface, and no significant damage or material transfer could be observed on the alumina ball counterbody after tribocorrosion tests. However, significant damage was observed on the alumina ball at cathodic conditions.
- All titanium alloys exhibited a large total volume loss after tribocorrosion tests at cathodic potentiostatic potential than that at OCP and anodic potentiostatic potential.
- All β -phase alloys can recover their passivity in the wear track under tribocorrosion despite mechanical perturbation, and these alloys are more resistance to wear-accelerated corrosion. However, alloys are more susceptible to mechanical wear.
- No evidence for subsurface cracking could be found. The samples rubbed under anodic potential clearly exhibited less deformation than that of the samples rubbed at OCP and cathodic potential.
- The passive behaviour of the β -microstructure alloys did not have a positive influence on its tribocorrosion performance, but it was beneficial for tribocorrosion behaviour due to the suppression the wear-accelerated corrosion process.
- Increasing potential increases the chemical volume (V_{chem}) part of total volume. However, the total volume decreases.
- $\beta+\alpha''$ microstructure, $\alpha+\beta$ microstructure and α microstructure show a higher percentage of chemical wear contribution. However, $\alpha+\beta$ microstructure and α microstructure show the lowest wear rate as compared to other types of titanium alloys.
- The enhanced tribocorrosion resistance of alloys at passive potential is derived from high hardness and good corrosion resistance leading to the both mechanical wear and chemical wear being reduced.
- The passive film formed on the surface of alloys at passive potential has a lubricating ability to reduce friction and wear.
- Only a small wear accelerated corrosion can be measured in the β -microstructure. The synergistic effect of wear accelerated corrosion is more pronounced in α -microstructure, $\alpha+\beta$ -microstructure and $\beta+\alpha''$ -microstructure than β -microstructure. Though α -microstructure and $\alpha+\beta$ -microstructure have minimum wear loss compared to β -microstructure, β -microstructure alloys are suitable alloys for plant conditions due to their

excellent corrosion resistance. Considering implant applications, the β -microstructure Ti-Mo₈-Nb₄-Zr₂ and Ti-Mo₈-Nb₄-Zr₅ may be good candidates with relatively low elastic modulus and without toxic alloying elements.

9.2 Recommendations for Future Work

During this work, the tribological, corrosion and tribocorrosion of titanium alloys were reported in this thesis. Thus, for a better understanding of all these phenomena, it would be interesting to do the following:

1- Tribological Behaviour

- The influence of sliding speed and sliding distance on friction, wear volume and wear mechanism important to consider in future stages of this research.
- TEM tests of near surface structure are necessary to be carried out to show the precise deformation mechanisms, for example, if there is any twinning occurring within tribological grain refinement.
- The effect of protein concentration on the friction coefficient, wear volume and mechanism should also be considered in future stage of this research.

2- Electrochemical Behaviour of Titanium Alloys

- An investigation should be completed using electrochemical impedance spectroscopy (EIS) to obtain further information on the characteristic of passive films formed and to investigate the film/electrolyte interface on the surface of alloys.
- The effect of protein concentration on the corrosion rate of titanium alloys should also be considered in any future stage of this research.

3- Tribocorrosion Behaviour of Titanium Alloys

- A scientific investigation should look at the tribocorrosion response using a wide range of anodic and cathodic potentiostatic to better understanding of the passivation of alloys.
- Tribocorrosion response of alloys under potentiodynamic conditions is important to consider in future stages of this research.
- Electrochemical impedance spectroscopy (EIS) is required during and after tribocorrosion tests to obtain further information on the characteristic of passive films formed and to investigate the film/electrolyte interface on the surface of alloys during and after rubbing.

- The influence of load, sliding speed and sliding distance on tribocorrosion of alloys should be completed.
- The effect of additives such as fluoride content in solution on the friction coefficient, wear volume and mechanism should also be considered in future stages of this research.
- TEM tests of subsurface structure after tribocorrosion at OCP, cathodic and anodic potentiostatic potential are necessary to confirm if there is twinning within tribological grain refinement.
- The adsorption of bovine calf serum on the alloys surface and its influence on the repassivation kinetics is important to consider in future stages of this research.
- The effect of protein concentration on the friction coefficient, wear volume and mechanism at tribocorrosion tests should also be considered in future stages of this research.

References

- [1] Y. Li, C. Yang, H. Zhao, S. Qu, X. Li, and Y. Li, "New developments of Ti-based alloys for biomedical applications," *Materials*, vol. 7, pp. 1709-1800, 2014.
- [2] A. T. Sidambe, "Biocompatibility of advanced manufactured titanium implants—A review," *Materials*, vol. 7, pp. 8168-8188, 2014.
- [3] Q. Chen and G. A. Thouas, "Metallic implant biomaterials," *Materials Science and Engineering: R: Reports*, vol. 87, pp. 1-57, 2015.
- [4] M. Long and H. J. Rack, "Titanium alloys in total joint replacement—a materials science perspective," *Biomaterials*, vol. 19, pp. 1621-1639, 1998.
- [5] G. Lütjering and J. C. Williams, *Titanium* vol. 2: Springer, 2003.
- [6] T. Hanawa, "Recent development of new alloys for biomedical use," in *Materials science forum*, 2006, pp. 243-248.
- [7] M. A. Hussein, A. S. Mohammed, and N. Al-Aqeeli, "Wear characteristics of metallic biomaterials: a review," *Materials*, vol. 8, pp. 2749-2768, 2015.
- [8] V. Oliveira, R. Chaves, R. Bertazzoli, and R. Caram, "Preparation and characterization of Ti-Al-Nb alloys for orthopedic implants," *Brazilian Journal of Chemical Engineering*, vol. 15, pp. 326-333, 1998.
- [9] Y. T. Zhu, T. C. Lowe, R. Z. Valiev, V. V. Stolyarov, V. V. Latysh, and G. J. Raab, "Ultrafine-grained titanium for medical implants," ed: Google Patents, 2002.
- [10] N. More, N. Diomidis, S. Paul, M. Roy, and S. Mischler, "Tribocorrosion behavior of β titanium alloys in physiological solutions containing synovial components," *Materials Science and Engineering: C*, vol. 31, pp. 400-408, 2011.
- [11] D. Kuroda, M. Niinomi, M. Morinaga, Y. Kato, and T. Yashiro, "Design and mechanical properties of new β type titanium alloys for implant materials," *Materials Science and Engineering: A*, vol. 243, pp. 244-249, 1998.
- [12] Y. Okazaki and E. Gotoh, "Comparison of metal release from various metallic biomaterials in vitro," *Biomaterials*, vol. 26, pp. 11-21, 2005.
- [13] R. Banerjee, S. Das, K. Mukhopadhyay, S. Nag, A. Chakraborty, and K. Chaudhuri, "Involvement of in vivo induced cheY-4 gene of *Vibrio cholerae* in motility, early adherence to intestinal epithelial cells and regulation of virulence factors," *FEBS letters*, vol. 532, pp. 221-226, 2002.
- [14] Y. Song, D. Xu, R. Yang, D. Li, and Z. Hu, "Theoretical investigation of ductilizing effects of alloying elements on TiAl," *Intermetallics*, vol. 6, pp. 157-165, 1998.
- [15] M. G. Joshi, S. G. Advani, F. Miller, and M. H. Santare, "Analysis of a femoral hip prosthesis designed to reduce stress shielding," *Journal of biomechanics*, vol. 33, pp. 1655-1662, 2000.
- [16] S. Gross and E. Abel, "A finite element analysis of hollow stemmed hip prostheses as a means of reducing stress shielding of the femur," *Journal of Biomechanics*, vol. 34, pp. 995-1003, 2001.
- [17] S. Sahu, M. Palaniappa, S. Paul, and M. Roy, "Potentiodynamic behaviour of Ti alloys in physiological solution containing lubricant," *Materials Letters*, vol. 64, pp. 12-14, 2010.
- [18] B. Obadele, A. Andrews, P. Olubambi, M. Mathew, and S. Pityana, "Tribocorrosion behaviour of laser clad biomedical grade titanium alloy," *Materials and Corrosion*, vol. 66, pp. 1133-1139, 2015.
- [19] M. Geetha, A. Singh, R. Asokamani, and A. Gogia, "Ti based biomaterials, the ultimate choice for orthopaedic implants—a review," *Progress in Materials science*, vol. 54, pp. 397-425, 2009.
- [20] M. Niinomi, M. Nakai, and J. Hieda, "Development of new metallic alloys for biomedical applications," *Acta Biomaterialia*, vol. 8, pp. 3888-3903, 2012.

- [21] D. Banerjee and J. Williams, "Perspectives on titanium science and technology," *Acta Materialia*, vol. 61, pp. 844-879, 2013.
- [22] G. Colombo, "The Effect of Equal Channel Angular Extrusion (ECAE) and Boron Additions on the Mechanical Properties of a Biomedical Ti-Nb-Zr-Ta (TNZT) Alloy," 2010.
- [23] S. Kumar and T. S. Narayanan, "Corrosion behaviour of Ti-15Mo alloy for dental implant applications," *Journal of Dentistry*, vol. 36, pp. 500-507, 2008.
- [24] S. Mischler, "Triboelectrochemical techniques and interpretation methods in tribocorrosion: a comparative evaluation," *Tribology International*, vol. 41, pp. 573-583, 2008.
- [25] P. Ponthiaux, F. Wenger, D. Drees, and J.-P. Celis, "Electrochemical techniques for studying tribocorrosion processes," *Wear*, vol. 256, pp. 459-468, 2004.
- [26] P. Jemmely, S. Mischler, and D. Landolt, "Tribocorrosion behaviour of Fe-17Cr stainless steel in acid and alkaline solutions," *Tribology International*, vol. 32, pp. 295-303, 1999.
- [27] D. Landolt, S. Mischler, M. Stemp, and S. Barril, "Third body effects and material fluxes in tribocorrosion systems involving a sliding contact," *Wear*, vol. 256, pp. 517-524, 2004.
- [28] M. Runa, M. Mathew, and L. Rocha, "Tribocorrosion response of the Ti6Al4V alloys commonly used in femoral stems," *Tribology International*, vol. 68, pp. 85-93, 2013.
- [29] P. S. U. Nnamchi, "A novel approach to Property driven design of Titanium alloys for Biomedical applications," University of Sheffield, 2014.
- [30] P. S. Nnamchi, C. Obayi, I. Todd, and M. Rainforth, "Mechanical and electrochemical characterisation of new Ti-Mo-Nb-Zr alloys for biomedical applications," *Journal of the mechanical behavior of biomedical materials*, vol. 60, pp. 68-77, 2016.
- [31] A. F. von Recum, *Handbook of biomaterials evaluation: scientific, technical and clinical testing of implant materials*: CRC Press, 1998.
- [32] J. Park and R. S. Lakes, *Biomaterials: an introduction*: Springer Science & Business Media, 2007.
- [33] J. R. Sin, "Investigation of the corrosion and tribocorrosion behaviour of metallic biomaterials," Luleå tekniska universitet, 2015.
- [34] W. D. Callister and D. G. Rethwisch, *Fundamentals of materials science and engineering: an integrated approach*: John Wiley & Sons, 2012.
- [35] Y. S. Hedberg, B. Qian, Z. Shen, S. Virtanen, and I. O. Wallinder, "In vitro biocompatibility of CoCrMo dental alloys fabricated by selective laser melting," *Dental materials*, vol. 30, pp. 525-534, 2014.
- [36] C. A. Sweeney, B. O'Brien, P. E. McHugh, and S. B. Leen, "Experimental characterisation for micromechanical modelling of CoCr stent fatigue," *Biomaterials*, vol. 35, pp. 36-48, 2014.
- [37] A. Sáenz, E. Rivera, W. Brostow, and V. M. Castaño, "Ceramic biomaterials: an introductory overview," *Journal of Materials Education*, vol. 21, pp. 267-276, 1999.
- [38] W. R. Lacefield, "Current status of ceramic coatings for dental implants," *Implant dentistry*, vol. 7, pp. 315-322, 1998.
- [39] C. E. Carraher Jr, *Carraher's polymer chemistry*: CRC Press, 2010.
- [40] R. J. Zdrahala and I. J. Zdrahala, "Biomedical applications of polyurethanes: a review of past promises, present realities, and a vibrant future," *Journal of biomaterials applications*, vol. 14, pp. 67-90, 1999.
- [41] C. Wolf-Brandstetter, S. Roessler, S. Storch, U. Hempel, U. Gbureck, B. Nies, *et al.*, "Physicochemical and cell biological characterization of PMMA bone cements

- modified with additives to increase bioactivity," *Journal of Biomedical Materials Research Part B: Applied Biomaterials*, vol. 101, pp. 599-609, 2013.
- [42] A. Gomaa, R. Lee, and C. Liu, "Polypseudophakia for cataract surgery: 10-year follow-up on safety and stability of two poly-methyl-methacrylate (PMMA) intraocular lenses within the capsular bag," *Eye*, vol. 25, pp. 1090-1093, 2011.
- [43] V. Prasad, M. Pumberger, A. Disch, I. Melcher, K.-D. Schaser, and W. Brenner, "Quantitative in-vivo fusion assessment by ¹⁸F-natriumfluorid PET/CT following en-bloc spondylectomy and carbon-composite cage reconstruction," *Journal of Nuclear Medicine*, vol. 55, pp. 1979-1979, 2014.
- [44] C. E. Schmidt and J. M. Baier, "Acellular vascular tissues: natural biomaterials for tissue repair and tissue engineering," *Biomaterials*, vol. 21, pp. 2215-2231, 2000.
- [45] R. Nagaoka, T. Izumi, K. Kubo, K. Kobayashi, and Y. Saijo, "Elasticity of artificial skin by measuring displacement induced by acoustic radiation force," in *Ultrasonics Symposium (IUS), 2012 IEEE International*, 2012, pp. 1378-1381.
- [46] M. Niinomi, "Recent metallic materials for biomedical applications," *Metallurgical and materials transactions A*, vol. 33, pp. 477-486, 2002.
- [47] M. Niinomi, "Metallic biomaterials," *Journal of Artificial Organs*, vol. 11, pp. 105-110, 2008.
- [48] C. Elias, J. Lima, R. Valiev, and M. Meyers, "Biomedical applications of titanium and its alloys," *Jom*, vol. 60, pp. 46-49, 2008.
- [49] R. Adell, U. Lekholm, B. Rockler, and P.-I. Brånemark, "A 15-year study of osseointegrated implants in the treatment of the edentulous jaw," *International journal of oral surgery*, vol. 10, pp. 387-416, 1981.
- [50] D. BomBač, M. Brojan, P. Fajfar, F. Kosel, and R. Turk, "Review of materials in medical applications Pregled materialov v medicinskih aplikacijah," *RMZ–Materials and Geoenvironment*, vol. 54, pp. 471-499, 2007.
- [51] J.-E. Bidaux, C. Closuit, M. Rodriguez-Arbaizar, D. Zufferey, and E. Carreño-Morelli, "Metal injection moulding of low modulus Ti–Nb alloys for biomedical applications," *Powder Metallurgy*, vol. 56, pp. 263-266, 2013.
- [52] G. Shibo, Q. Xuanhui, H. Xinbo, Z. Ting, and D. Bohua, "Powder injection molding of Ti–6Al–4V alloy," *Journal of Materials Processing Technology*, vol. 173, pp. 310-314, 2006.
- [53] A. Sidambe, W. Choong, H. Hamilton, and I. Todd, "Correlation of metal injection moulded Ti6Al4V yield strength with resonance frequency (PCRT) measurements," *Materials Science and Engineering: A*, vol. 568, pp. 220-227, 2013.
- [54] X. Zhao, J. Chen, X. Lin, and W. Huang, "Study on microstructure and mechanical properties of laser rapid forming Inconel 718," *Materials Science and Engineering: A*, vol. 478, pp. 119-124, 2008.
- [55] S. Ponader, C. Von Wilmowsky, M. Widenmayer, R. Lutz, P. Heinl, C. Körner, *et al.*, "In vivo performance of selective electron beam-melted Ti-6Al-4V structures," *Journal of biomedical materials research Part A*, vol. 92, pp. 56-62, 2010.
- [56] J. Parthasarathy, B. Starly, S. Raman, and A. Christensen, "Mechanical evaluation of porous titanium (Ti6Al4V) structures with electron beam melting (EBM)," *Journal of the mechanical behavior of biomedical materials*, vol. 3, pp. 249-259, 2010.
- [57] L. Murr, K. Amato, S. Li, Y. Tian, X. Cheng, S. Gaytan, *et al.*, "Microstructure and mechanical properties of open-cellular biomaterials prototypes for total knee replacement implants fabricated by electron beam melting," *Journal of the mechanical behavior of biomedical materials*, vol. 4, pp. 1396-1411, 2011.

- [58] A. Sidambe, I. Figueroa, H. Hamilton, and I. Todd, "Metal injection moulding of CP-Ti components for biomedical applications," *Journal of Materials Processing Technology*, vol. 212, pp. 1591-1597, 2012.
- [59] W. E. Frazier, "Metal additive manufacturing: a review," *Journal of Materials Engineering and Performance*, vol. 23, pp. 1917-1928, 2014.
- [60] A. T. Sidambe, I. A. Figueroa, H. G. Hamilton, and I. Todd, "Taguchi optimization of MIM titanium sintering," *International journal of powder metallurgy*, vol. 47, pp. 21-28, 2011.
- [61] R. Van Noort, "The future of dental devices is digital," *Dental materials*, vol. 28, pp. 3-12, 2012.
- [62] O. Ferri, T. Ebel, and R. Bormann, "High cycle fatigue behaviour of Ti-6Al-4V fabricated by metal injection moulding technology," *Materials Science and Engineering: A*, vol. 504, pp. 107-113, 2009.
- [63] T. Ebel, C. Blawert, R. Willumeit, B. J. Luthringer, O. M. Ferri, and F. Feyerabend, "Ti-6Al-4V-0.5 B—A Modified Alloy for Implants Produced by Metal Injection Molding," *Advanced Engineering Materials*, vol. 13, 2011.
- [64] V. Biehl, T. Wack, S. Winter, U. Seyfert, and J. Breme, "Evaluation of the haemocompatibility of titanium based biomaterials," *Biomolecular engineering*, vol. 19, pp. 97-101, 2002.
- [65] B. Zberg, P. J. Uggowitzer, and J. F. Löffler, "MgZnCa glasses without clinically observable hydrogen evolution for biodegradable implants," *Nature materials*, vol. 8, p. 887, 2009.
- [66] D. Blackwood, "Biomaterials: past successes and future problems," *Corrosion reviews*, vol. 21, pp. 97-124, 2003.
- [67] Y. Okazaki and E. Gotoh, "Metal release from stainless steel, Co-Cr-Mo-Ni-Fe and Ni-Ti alloys in vascular implants," *Corrosion Science*, vol. 50, pp. 3429-3438, 2008.
- [68] A. L. R. Ribeiro, R. C. Junior, F. F. Cardoso, R. B. Fernandes Filho, and L. G. Vaz, "Mechanical, physical, and chemical characterization of Ti-35Nb-5Zr and Ti-35Nb-10Zr casting alloys," *Journal of Materials Science: Materials in Medicine*, vol. 20, pp. 1629-1636, 2009.
- [69] V. Henriques, E. Galvani, S. Petroni, M. Paula, and T. Lemos, "Production of Ti-13Nb-13Zr alloy for surgical implants by powder metallurgy," *Journal of materials science*, vol. 45, pp. 5844-5850, 2010.
- [70] M. O. Alam and A. Haseeb, "Response of Ti-6Al-4V and Ti-24Al-11Nb alloys to dry sliding wear against hardened steel," *Tribology International*, vol. 35, pp. 357-362, 2002.
- [71] E. Whitney and S. R. Rolfes, *Understanding nutrition*: Cengage Learning, 2007.
- [72] J. Cruickshank, J. Thorp, and F. J. Zacharias, "Benefits and potential harm of lowering high blood pressure," *The Lancet*, vol. 329, pp. 581-584, 1987.
- [73] M. Niinomi, "Recent titanium R&D for biomedical applications in Japan," *Jom*, vol. 51, p. 32, 1999.
- [74] S. K. Misra, D. Mohn, T. J. Brunner, W. J. Stark, S. E. Philip, I. Roy, *et al.*, "Comparison of nanoscale and microscale bioactive glass on the properties of P (3HB)/Bioglass® composites," *Biomaterials*, vol. 29, pp. 1750-1761, 2008.
- [75] M. Sumita, T. Hanawa, I. Ohnishi, and T. Yoneyama, "Failure Processes in biometallic materials," *Compr Struct Integr*, vol. 9, pp. 131-67, 2003.
- [76] M. Long and H. Rack, "Titanium alloys in total joint replacement—a materials science perspective," *Biomaterials*, vol. 19, pp. 1621-1639, 1998.
- [77] S. Suresh, "Fatigue of Materials, Cambridge University Press," *Cambridge, England*, 1998.

- [78] R. A. Antunes and M. C. L. de Oliveira, "Corrosion fatigue of biomedical metallic alloys: mechanisms and mitigation," *Acta biomaterialia*, vol. 8, pp. 937-962, 2012.
- [79] A. Yamamoto, T. Kobayashi, N. Maruyama, K. Nakazawa, and M. Sumita, "Fretting fatigue properties of Ti-6 Al-4 V alloy in pseudo-body fluid and evaluation of biocompatibility by cell culture method," *J. Jpn. Inst. Met.(Japan)*, vol. 59, pp. 463-470, 1995.
- [80] M. Niinomi, "Fatigue characteristics of metallic biomaterials," *International Journal of Fatigue*, vol. 29, pp. 992-1000, 2007.
- [81] D. W. Lennox, B. H. Schofield, D. F. McDonald, and L. H. Riley Jr, "A histologic comparison of aseptic loosening of cemented, press-fit, and biologic ingrowth prostheses," *Clinical orthopaedics and related research*, vol. 225, pp. 171-191, 1987.
- [82] A. Schweizer, U. Riede, T. Maurer, and P. Ochsner, "Ten-year follow-up of primary straight-stem prosthesis (MEM) made of titanium or cobalt chromium alloy," *Archives of orthopaedic and trauma surgery*, vol. 123, pp. 353-356, 2003.
- [83] I. Papageorgiou, V. Shadrick, S. Davis, L. Hails, R. Schins, R. Newson, *et al.*, "Macrophages detoxify the genotoxic and cytotoxic effects of surgical cobalt chrome alloy particles but not quartz particles on human cells in vitro," *Mutation Research/Fundamental and Molecular Mechanisms of Mutagenesis*, vol. 643, pp. 11-19, 2008.
- [84] M. B. Nasab, M. R. Hassan, and B. B. Sahari, "Metallic biomaterials of knee and hip-A review," *Trends Biomater. Artif. Organs*, vol. 24, pp. 69-82, 2010.
- [85] B. Subramanian, R. Ananthakumar, A. Kobayashi, and M. Jayachandran, "Surface modification of 316L stainless steel with magnetron sputtered TiN/VN nanoscale multilayers for bio implant applications," *Journal of Materials Science: Materials in Medicine*, vol. 23, pp. 329-338, 2012.
- [86] A. Parsapour, S. N. Khorasani, and M. H. Fathi, "Effect of surface treatment and metallic coating on corrosion behavior and biocompatibility of surgical 316L stainless steel implant," *Journal of Materials Science & Technology*, vol. 28, pp. 125-131, 2012.
- [87] R. S. ONS, "Modifying biomaterial surfaces to optimise interactions with bone," *Surface Modification of Biomaterials: Methods Analysis and Applications*, p. 365, 2010.
- [88] G. Mani, M. D. Feldman, S. Oh, and C. M. Agrawal, "Surface modification of cobalt–chromium–tungsten–nickel alloy using octadecyltrichlorosilanes," *Applied Surface Science*, vol. 255, pp. 5961-5970, 2009.
- [89] A. Verstryngge, J. Van Humbeeck, and G. Willems, "In-vitro evaluation of the material characteristics of stainless steel and beta-titanium orthodontic wires," *American journal of orthodontics and dentofacial orthopedics*, vol. 130, pp. 460-470, 2006.
- [90] C. Leyens and M. Peters, *Titanium and titanium alloys: fundamentals and applications*: John Wiley & Sons, 2003.
- [91] G. Bedinger, "Mineral Commodity Summaries: Titanium and Titanium Dioxide," *US Geological Survey, Washington DC, USA*, pp. 170-171, 2014.
- [92] A. International, *Handbook of materials for medical devices*: ASM international, 2003.
- [93] P. B. Vila, "Phase transformation kinetics during continuous heating of $\alpha + \beta$ and metastable β titanium alloys."
- [94] M. T. Mohammed, Z. A. Khan, and A. N. Siddiquee, "Beta Titanium Alloys: The Lowest Elastic Modulus for Biomedical Applications: A Review."

- [95] S. Miyazaki, H. Kim, and H. Hosoda, "Development and characterization of Ni-free Ti-base shape memory and superelastic alloys," *Materials Science and Engineering: A*, vol. 438, pp. 18-24, 2006.
- [96] J. Kim, H. Kim, T. Inamura, H. Hosoda, and S. Miyazaki, "Shape memory characteristics of Ti–22Nb–(2–8) Zr (at.%) biomedical alloys," *Materials Science and Engineering: A*, vol. 403, pp. 334-339, 2005.
- [97] I. Weiss and S. Semiatin, "Thermomechanical processing of beta titanium alloys—an overview," *Materials Science and Engineering: A*, vol. 243, pp. 46-65, 1998.
- [98] M. J. Donachie, *Titanium: a technical guide*: ASM international, 2000.
- [99] G. Lütjering and J. C. Williams, "Alpha+ beta alloys," *Titanium*, pp. 203-258, 2007.
- [100] V. D. Cojocaru, D. Raducanu, T. Gloriant, E. Bertrand, and I. Cinca, "Structural observation of twinning deformation mechanism in a Ti-Ta-Nb alloy," in *Solid State Phenomena*, 2012, pp. 46-51.
- [101] D. Raducanu, E. Vasilescu, V. Cojocaru, I. Cinca, P. Drob, C. Vasilescu, *et al.*, "Mechanical and corrosion resistance of a new nanostructured Ti–Zr–Ta–Nb alloy," *Journal of the mechanical behavior of biomedical materials*, vol. 4, pp. 1421-1430, 2011.
- [102] Y. Tong, B. Guo, Y. Zheng, C. Y. Chung, and L. W. Ma, "Effects of Sn and Zr on the microstructure and mechanical properties of Ti-Ta-based shape memory alloys," *Journal of materials engineering and performance*, vol. 20, pp. 762-766, 2011.
- [103] M. Niinomi, "Mechanical properties of biomedical titanium alloys," *Materials Science and Engineering: A*, vol. 243, pp. 231-236, 1998.
- [104] M. Niinomi, "Mechanical biocompatibilities of titanium alloys for biomedical applications," *Journal of the mechanical behavior of biomedical materials*, vol. 1, pp. 30-42, 2008.
- [105] R. K. Quinn and N. R. Armstrong, "Electrochemical and surface analytical characterization of titanium and titanium hydride thin film electrode oxidation," *Journal of the Electrochemical Society*, vol. 125, pp. 1790-1796, 1978.
- [106] A. Muñoz and M. Costa, "Elucidating the mechanisms of nickel compound uptake: a review of particulate and nano-nickel endocytosis and toxicity," *Toxicology and applied pharmacology*, vol. 260, pp. 1-16, 2012.
- [107] I. Pais, M. Feher, E. Farkas, Z. Szabo, and I. Cornides, "Titanium as a new trace element," *Communications in Soil Science & Plant Analysis*, vol. 8, pp. 407-410, 1977.
- [108] S. Yaghoubi, C. W. Schwieter, and J. P. McCue, "Biological roles of titanium," *Biological trace element research*, vol. 78, p. 205, 2000.
- [109] M. L. Wang, R. Tuli, P. A. Manner, P. F. Sharkey, D. J. Hall, and R. S. Tuan, "Direct and indirect induction of apoptosis in human mesenchymal stem cells in response to titanium particles," *Journal of Orthopaedic Research*, vol. 21, pp. 697-707, 2003.
- [110] N. Coen, M. Kadhim, E. Wright, C. Case, and C. Mothersill, "Particulate debris from a titanium metal prosthesis induces genomic instability in primary human fibroblast cells," *British Journal of Cancer*, vol. 88, p. 548, 2003.
- [111] R. Kumazawa, F. Watari, N. Takashi, Y. Tanimura, M. Uo, and Y. Totsuka, "Effects of Ti ions and particles on neutrophil function and morphology," *Biomaterials*, vol. 23, pp. 3757-3764, 2002.
- [112] V. Koval'skiĭ and L. Rezaeva, "The biological role of vanadium in ascidia," *Uspekhi sovremennoi biologii*, vol. 60, pp. 45-61, 1964.
- [113] E. P. Daniel and E. M. Hewston, "VANADIUM-A CONSIDERATION OF ITS POSSIBLE BIOLOGICAL RÔLE," *American Journal of Physiology--Legacy Content*, vol. 136, pp. 772-775, 1942.

- [114] J. J. Rodríguez-Mercado, R. A. Mateos-Nava, and M. A. Altamirano-Lozano, "DNA damage induction in human cells exposed to vanadium oxides in vitro," *Toxicology in Vitro*, vol. 25, pp. 1996-2002, 2011.
- [115] L. S. Rhoads, W. T. Silkworth, M. L. Roppolo, and M. S. Whittingham, "Cytotoxicity of nanostructured vanadium oxide on human cells in vitro," *Toxicology in Vitro*, vol. 24, pp. 292-296, 2010.
- [116] N. Röss, B. Chou, R. Renne, J. Dill, R. Miller, J. Roycroft, *et al.*, "Carcinogenicity of inhaled vanadium pentoxide in F344/N rats and B6C3F1 mice," *Toxicological Sciences*, vol. 74, pp. 287-296, 2003.
- [117] B. Moretti, V. Pesce, G. Maccagnano, G. Vicenti, P. Lovreglio, L. Soleo, *et al.*, "Peripheral neuropathy after hip replacement failure: is vanadium the culprit?," *The Lancet*, vol. 379, p. 1676, 2012.
- [118] W. L. Downs, J. K. Scott, C. L. Yuile, F. S. Caruso, and L. C. Wong, "The toxicity of niobium salts," *American Industrial Hygiene Association Journal*, vol. 26, pp. 337-346, 1965.
- [119] M. Caicedo, J. J. Jacobs, A. Reddy, and N. J. Hallab, "Analysis of metal ion-induced DNA damage, apoptosis, and necrosis in human (Jurkat) T-cells demonstrates Ni²⁺ and V³⁺ are more toxic than other metals: Al³⁺, Be²⁺, Co²⁺, Cr³⁺, Cu²⁺, Fe³⁺, Mo⁵⁺, Nb⁵⁺, Zr²⁺," *Journal of Biomedical Materials Research Part A*, vol. 86, pp. 905-913, 2008.
- [120] M. Nordberg and G. F. Nordberg, "Toxicology and biological monitoring of metals," *General, Applied and Systems Toxicology*, 2009.
- [121] U. Pazzaglia, P. Apostoli, T. Congiu, S. Catalani, M. Marchese, and G. Zarattini, "Cobalt, chromium and molybdenum ions kinetics in the human body: data gained from a total hip replacement with massive third body wear of the head and neuropathy by cobalt intoxication," *Archives of orthopaedic and trauma surgery*, vol. 131, pp. 1299-1308, 2011.
- [122] M. Curzon, J. Kubota, and B. Bibby, "Environmental effects of molybdenum on caries," *Journal of Dental Research*, vol. 50, pp. 74-77, 1971.
- [123] D. G. Barceloux and D. Barceloux, "Molybdenum," *Journal of Toxicology: Clinical Toxicology*, vol. 37, pp. 231-237, 1999.
- [124] M. Coughlan, "The role of molybdenum in human biology," *Journal of inherited metabolic disease*, vol. 6, pp. 70-77, 1983.
- [125] M. Anke, M. Seifert, W. Arnhold, S. Anke, and U. Schäfer, "The biological and toxicological importance of molybdenum in the environment and in the nutrition of plants, animals and man: Part V: Essentiality and toxicity of molybdenum," *Acta alimentaria*, vol. 39, pp. 12-26, 2010.
- [126] W.-C. Witzleb, J. Ziegler, F. Krummenauer, V. Neumeister, and K.-P. Guenther, "Exposure to chromium, cobalt and molybdenum from metal-on-metal total hip replacement and hip resurfacing arthroplasty," *Acta orthopaedica*, vol. 77, pp. 697-705, 2006.
- [127] J. Antoniou, D. J. Zukor, F. Mwale, W. Minarik, A. Petit, and O. L. Huk, "Metal ion levels in the blood of patients after hip resurfacing: a comparison between twenty-eight and thirty-six-millimeter-head metal-on-metal prostheses," *JBJS*, vol. 90, pp. 142-148, 2008.
- [128] J. Black, "Biologic performance of tantalum," *Clinical materials*, vol. 16, pp. 167-173, 1994.
- [129] A. S. Martins, P. M. Fresco, and M. J. Pereira, "Toxicity of Zirconium on Growth of Two Green Algae," *Fresenius Environmental Bulletin*, vol. 16, pp. 869-874, 2007.

- [130] J. Delongéas, D. Burnel, P. Netter, M. Grignon, J. Mur, R. Royer, *et al.*, "Toxicity and pharmacokinetics of zirconium oxychloride in mice and rats," *Journal de pharmacologie*, vol. 14, pp. 437-447, 1983.
- [131] L. McClinton and J. Schubert, "The toxicity of some zirconium and thorium salts in rats," *Journal of Pharmacology and Experimental Therapeutics*, vol. 94, pp. 1-6, 1948.
- [132] S. V. Verstraeten, L. Aimo, and P. I. Oteiza, "Aluminium and lead: molecular mechanisms of brain toxicity," *Archives of toxicology*, vol. 82, pp. 789-802, 2008.
- [133] W. A. Banks and A. J. Kastin, "Aluminum-induced neurotoxicity: alterations in membrane function at the blood-brain barrier," *Neuroscience & Biobehavioral Reviews*, vol. 13, pp. 47-53, 1989.
- [134] R. A. Yokel, "The toxicology of aluminum," *Neurotoxicology*, vol. 21, pp. 813-828, 2000.
- [135] D. N. Kerr, M. K. Ward, H. A. Ellis, W. Simpson, and I. Parkinson, "Aluminium intoxication in renal disease," *Aluminium in biology and medicine*, pp. 123-141, 1992.
- [136] P. Darbre, "Environmental oestrogens, cosmetics and breast cancer," *Best practice & research clinical endocrinology & metabolism*, vol. 20, pp. 121-143, 2006.
- [137] P. C. Ferreira, K. d. A. Piai, A. M. M. Takayanagui, and S. I. Segura-Muñoz, "Aluminum as a risk factor for Alzheimer's disease," *Revista latino-americana de enfermagem*, vol. 16, pp. 151-157, 2008.
- [138] P. Darbre, "Metalloestrogens: an emerging class of inorganic xenoestrogens with potential to add to the oestrogenic burden of the human breast," *Journal of Applied Toxicology*, vol. 26, pp. 191-197, 2006.
- [139] D. Drees, J.-P. Celis, E. Dekempeneer, and J. Meneve, "The electrochemical and wear behaviour of amorphous diamond-like carbon coatings and multilayered coatings in aqueous environments," *Surface and Coatings Technology*, vol. 86, pp. 575-580, 1996.
- [140] S. Mischler, S. Debaud, and D. Landolt, "Wear-accelerated corrosion of passive metals in tribocorrosion systems," *Journal of the Electrochemical Society*, vol. 145, pp. 750-758, 1998.
- [141] J.-P. Celis, P. Ponthiaux, and F. Wenger, "Tribo-corrosion of materials: interplay between chemical, electrochemical, and mechanical reactivity of surfaces," *Wear*, vol. 261, pp. 939-946, 2006.
- [142] J. Takadoum, "Materials for Tribology," *Materials and Surface Engineering in Tribology*, pp. 109-204, 2008.
- [143] J. Williams, *Engineering tribology*: Cambridge University Press, 2005.
- [144] P. D. Jakobsen, A. Bruland, and F. Dahl, "Review and assessment of the NTNU/SINTEF Soil Abrasion Test (SAT™) for determination of abrasiveness of soil and soft ground," *Tunnelling and underground space technology*, vol. 37, pp. 107-114, 2013.
- [145] J. R. Davis, *Surface engineering for corrosion and wear resistance*: ASM international, 2001.
- [146] R. Bailey, "Surface Engineered Titanium for Improved Tribological, Electrochemical and Tribo-electrochemical Performance," 2015.
- [147] J. F. Shackelford and M. K. Muralidhara, "Introduction to materials science for engineers," 2005.
- [148] I. Hutchings and P. Shipway, *Tribology: friction and wear of engineering materials*: Butterworth-Heinemann, 2017.

- [149] D. D. Kopeliovich, "Mechanisms of wear," *Substances and Technologies*. www.substech.com, mechanisms_of_wear.txt · Last modified: 2017/07/01 by dmitri_kopeliovich.
- [150] T. Joyce, "Theoretical Calculation of Lubrication Regimes in a Metal-on-Metal First Metatarsophalangeal Prosthesis Evaluated against an Ex Vivo Sample," in *World Congress on Medical Physics and Biomedical Engineering 2006*, 2007, pp. 3315-3318.
- [151] A. Choubey, B. Basu, and R. Balasubramaniam, "Tribological behaviour of Ti-based alloys in simulated body fluid solution at fretting contacts," *Materials Science and Engineering: A*, vol. 379, pp. 234-239, 2004.
- [152] I. Cvijović-Alagić, Z. Cvijović, S. Mitrović, M. Rakin, Đ. Veljović, and M. Babić, "Tribological behaviour of orthopaedic Ti-13Nb-13Zr and Ti-6Al-4V alloys," *Tribology letters*, vol. 40, pp. 59-70, 2010.
- [153] L. Mohan and C. Anandan, "Wear and corrosion behavior of oxygen implanted biomedical titanium alloy Ti-13Nb-13Zr," *Applied Surface Science*, vol. 282, pp. 281-290, 2013.
- [154] H. Attar, K. Prashanth, A. Chaubey, M. Calin, L. C. Zhang, S. Scudino, *et al.*, "Comparison of wear properties of commercially pure titanium prepared by selective laser melting and casting processes," *Materials Letters*, vol. 142, pp. 38-41, 2015.
- [155] K. Suresh, M. Geetha, C. Richard, J. Landoulsi, H. Ramasawmy, S. Suwas, *et al.*, "Effect of equal channel angular extrusion on wear and corrosion behavior of the orthopedic Ti-13Nb-13Zr alloy in simulated body fluid," *Materials Science and Engineering: C*, vol. 32, pp. 763-771, 2012.
- [156] L.-j. Xu, S.-l. Xiao, T. Jing, and Y.-Y. Chen, "Microstructure, mechanical properties and dry wear resistance of β -type Ti-15Mo-xNb alloys for biomedical applications," *Transactions of Nonferrous Metals Society of China*, vol. 23, pp. 692-698, 2013.
- [157] F. Mamoun, A. Omar, L. Mohamed, D. Leila, and A. Iost, "Comparative Study on Tribological Behavior of Ti-6Al-7Nb and SS AISI 316L Alloys, for Total Hip Prosthesis," in *TMS 2014: 143rd Annual Meeting & Exhibition*, 2014, pp. 237-246.
- [158] S. Li, R. Yang, S. Li, Y. Hao, Y. Cui, M. Niinomi, *et al.*, "Wear characteristics of Ti-Nb-Ta-Zr and Ti-6Al-4V alloys for biomedical applications," *Wear*, vol. 257, pp. 869-876, 2004.
- [159] B. Bhushan, *Introduction to tribology*: John Wiley & Sons, 2013.
- [160] H. Dong and T. Bell, "Enhanced wear resistance of titanium surfaces by a new thermal oxidation treatment," *Wear*, vol. 238, pp. 131-137, 2000.
- [161] A. Bloyce, P.-Y. Qi, H. Dong, and T. Bell, "Surface modification of titanium alloys for combined improvements in corrosion and wear resistance," *Surface and Coatings Technology*, vol. 107, pp. 125-132, 1998.
- [162] A. Bloyce, "Surface engineering of titanium alloys for wear protection," *Proceedings of the Institution of Mechanical Engineers, Part J: Journal of Engineering Tribology*, vol. 212, pp. 467-476, 1998.
- [163] A. Choubey, B. Basu, and R. Balasubramaniam, "Tribological behaviour of Ti-based alloys in simulated body fluid solution at fretting contacts," *Materials Science and Engineering: A*, vol. 379, pp. 234-239, 2004.
- [164] C. Ramos-Saenz, P. Sundaram, and N. Difffoot-Carlo, "Tribological properties of Ti-based alloys in a simulated bone-implant interface with Ringer's solution at fretting contacts," *Journal of the mechanical behavior of biomedical materials*, vol. 3, pp. 549-558, 2010.
- [165] T. Lee, E. Mathew, S. Rajaraman, G. Manivasagam, A. K. Singh, and C. S. Lee, "Tribological and corrosion behaviors of warm-and hot-rolled Ti-13Nb-13Zr alloys in

- simulated body fluid conditions," *International journal of nanomedicine*, vol. 10, p. 207, 2015.
- [166] M. Fellah, M. Labaiz, O. Assala, and A. Iost, "Comparative Tribological study of biomaterials AISI 316L and Ti-6Al-7Nb," *TMS*, vol. 237, pp. 237-246, 2014.
- [167] S. Wang, F. Wang, Z. Liao, Q. Wang, R. Tyagi, and W. Liu, "Tribological behaviour of titanium alloy modified by carbon-DLC composite film," *Surface Engineering*, vol. 31, pp. 934-941, 2015.
- [168] M. Abad and J. Sánchez-López, "Tribological properties of surface-modified Pd nanoparticles for electrical contacts," *Wear*, vol. 297, pp. 943-951, 2013.
- [169] P. Majumdar, S. Singh, and M. Chakraborty, "Wear response of heat-treated Ti-13Zr-13Nb alloy in dry condition and simulated body fluid," *Wear*, vol. 264, pp. 1015-1025, 2008.
- [170] M. A. Wimmer, A. Fischer, R. Büscher, R. Pourzal, C. Sprecher, R. Hauert, *et al.*, "Wear mechanisms in metal-on-metal bearings: The importance of tribochemical reaction layers," *Journal of Orthopaedic Research*, vol. 28, pp. 436-443, 2010.
- [171] J. Chamberlain and K. R. Trethewey, *Corrosion for Science and Engineering*: Longman Scientific & Technical, 1995.
- [172] V. CORROSION, "Y 2, LL Shreir, RA Jarman, GT Burnstein," ed: Butterworth Heinemann, Oxford, 1994.
- [173] C. Kajdas, E. Wilusz, and S. Harvey, *Encyclopedia of tribology* vol. 15: Elsevier, 1990.
- [174] N. G. M. Fontanna, "Corrosion Engineering," *New York: Mc Graw Hill*, 1978.
- [175] D. Landolt, *Corrosion and surface chemistry of metals*: EPFL press, 2007.
- [176] R. Revie and H. H. Uhlig, "Thermodynamics: corrosion tendency and electrode potentials," *Corrosion and corrosion control*, vol. 1, pp. 22-66, 2000.
- [177] P. Süry and M. Semlitsch, "Corrosion behavior of cast and forged cobalt-based alloys for double-alloy joint endoprostheses," *Journal of biomedical materials research*, vol. 12, pp. 723-741, 1978.
- [178] D. C. Silverman, "Tutorial on cyclic potentiodynamic polarization technique," in *CORROSION 98*, 1998.
- [179] M. Mathew, P. Srinivasa Pai, R. Pourzal, A. Fischer, and M. Wimmer, "Significance of tribocorrosion in biomedical applications: overview and current status," *Advances in tribology*, vol. 2009, 2010.
- [180] C. Valero Vidal, "Study of the degradation mechanisms of the CoCrMo biomedical alloy in physiological media by electrochemical techniques and surface analysis," 2012.
- [181] J. R. Davis, *Corrosion: understanding the basics*: ASM International, 2000.
- [182] P. R. Roberge, "Handbook of corrosion engineering," *McGraw-Hill*, 2000.
- [183] D. Landolt, S. Mischler, and M. Stemp, "Electrochemical methods in tribocorrosion: a critical appraisal," *Electrochimica Acta*, vol. 46, pp. 3913-3929, 2001.
- [184] K. R. T. a. J. Chamberlain, "Corrosion for science and engineering," *Longman*, vol. ISBN 9780582238695., 1995.
- [185] Y. Zhang, D. D. Macdonald, M. Urquidi-Macdonald, G. R. Engelhardt, and R. B. Dooley, "Passivity breakdown on AISI Type 403 stainless steel in chloride-containing borate buffer solution," *Corrosion science*, vol. 48, pp. 3812-3823, 2006.
- [186] K. Raja and D. Jones, "Effects of dissolved oxygen on passive behavior of stainless alloys," *Corrosion science*, vol. 48, pp. 1623-1638, 2006.
- [187] Y. Sun, "Depth-profiling electrochemical measurements of low temperature plasma carburised 316L stainless steel in 1M H₂SO₄ solution," *Surface and Coatings Technology*, vol. 204, pp. 2789-2796, 2010.

- [188] Y. Qiao, Y. Zheng, W. Ke, and P. Okafor, "Electrochemical behaviour of high nitrogen stainless steel in acidic solutions," *Corrosion Science*, vol. 51, pp. 979-986, 2009.
- [189] "Basics of Electrochemical Impedance Spectroscopy," *Princeton Applied Research* vol. Application Note AC-1.
- [190] R. G. Kelly, J. R. Scully, D. Shoesmith, and R. G. Buchheit, *Electrochemical techniques in corrosion science and engineering*: CRC Press, 2002.
- [191] C. Zeng, W. Wang, and W. Wu, "Electrochemical impedance models for molten salt corrosion," *Corrosion science*, vol. 43, pp. 787-801, 2001.
- [192] C. Liu, Q. Bi, A. Leyland, and A. Matthews, "An electrochemical impedance spectroscopy study of the corrosion behaviour of PVD coated steels in 0.5 N NaCl aqueous solution: Part II.: EIS interpretation of corrosion behaviour," *Corrosion Science*, vol. 45, pp. 1257-1273, 2003.
- [193] S. Ferreira, "Wear, corrosion and tribocorrosion behavior of al-based composites reinforced with al-rich intermetallic compounds," 2006.
- [194] R. A. J. L. L. Shreir, and G. T. Burstein, "Corrosion (3rd Edition) Volumes 1-2. Elsevier,," 1994.
- [195] Y. Zhang, X. Yin, J. Wang, and F. Yan, "Influence of microstructure evolution on tribocorrosion of 304SS in artificial seawater," *Corrosion Science*, vol. 88, pp. 423-433, 2014.
- [196] A. Vieira, L. Rocha, N. Papageorgiou, and S. Mischler, "Mechanical and electrochemical deterioration mechanisms in the tribocorrosion of Al alloys in NaCl and in NaNO₃ solutions," *Corrosion Science*, vol. 54, pp. 26-35, 2012.
- [197] M. Atapour, A. Pilchak, G. Frankel, and J. Williams, "Corrosion behavior of β titanium alloys for biomedical applications," *Materials Science and Engineering: C*, vol. 31, pp. 885-891, 2011.
- [198] S. F. Services, "A Guide To Galvanic Corrosion and How to Treat it " *Insteel* June 26, 2017.
- [199] M. J. Donachie, "Titanium," *A Technical Guide, ASM International, Materials Park, OH*, 2000.
- [200] A. Revathi, A. D. Borrás, A. I. Muñoz, C. Richard, and G. Manivasagam, "Degradation mechanisms and future challenges of titanium and its alloys for dental implant applications in oral environment," *Materials Science and Engineering: C*, 2017.
- [201] I. Polmear, *Light alloys: from traditional alloys to nanocrystals*: Butterworth-Heinemann, 2005.
- [202] W.-F. Ho, "A comparison of tensile properties and corrosion behavior of cast Ti-7.5 Mo with cp Ti, Ti-15Mo and Ti-6Al-4V alloys," *Journal of Alloys and Compounds*, vol. 464, pp. 580-583, 2008.
- [203] Y. Wang and Y. Zheng, "Corrosion behaviour and biocompatibility evaluation of low modulus Ti-16Nb shape memory alloy as potential biomaterial," *Materials Letters*, vol. 63, pp. 1293-1295, 2009.
- [204] Y. L. Zhou, M. Niinomi, T. Akahori, H. Fukui, and H. Toda, "Corrosion resistance and biocompatibility of Ti-Ta alloys for biomedical applications," *Materials Science and Engineering: A*, vol. 398, pp. 28-36, 2005.
- [205] D. Mareci, R. Chelariu, G. Bolat, A. Cailean, V. Grancea, and D. Sutiman, "Electrochemical behaviour of Ti alloys containing Mo and Ta as β -stabilizer elements for dental application," *Transactions of Nonferrous Metals Society of China*, vol. 23, pp. 3829-3836, 2013.

- [206] M. T. Mohammed and M. GEETHA, "Effect of thermo-mechanical processing on microstructure and electrochemical behavior of Ti–Nb–Zr–V new metastable β titanium biomedical alloy," *Transactions of Nonferrous Metals Society of China*, vol. 25, pp. 759-769, 2015.
- [207] E. Vasilescu, P. Drob, D. Raducanu, V. Cojocaru, I. Cinca, D. Iordachescu, *et al.*, "In vitro biocompatibility and corrosion resistance of a new implant titanium base alloy," *Journal of Materials Science: Materials in Medicine*, vol. 21, pp. 1959-1968, 2010.
- [208] I. Cvijović-Alagić, Z. Cvijović, S. Mitrović, V. Panić, and M. Rakin, "Wear and corrosion behaviour of Ti–13Nb–13Zr and Ti–6Al–4V alloys in simulated physiological solution," *Corrosion Science*, vol. 53, pp. 796-808, 2011.
- [209] A. Alves, F. Santana, L. Rosa, S. Cursino, and E. Codaro, "A study on corrosion resistance of the Ti–10Mo experimental alloy after different processing methods," *Materials Science and Engineering: C*, vol. 24, pp. 693-696, 2004.
- [210] M. T. Mohammed, Z. A. Khan, G. Manivasagam, and A. N. Siddiquee, "Influence of thermomechanical processing on biomechanical compatibility and electrochemical behavior of new near beta alloy, Ti-20.6 Nb-13.6 Zr-0.5 V," *International journal of nanomedicine*, vol. 10, p. 223, 2015.
- [211] M. T. Mohammed, Z. A. Khan, M. Geetha, and A. N. Siddiquee, "Microstructure, mechanical properties and electrochemical behavior of a novel biomedical titanium alloy subjected to thermo-mechanical processing including aging," *Journal of Alloys and Compounds*, vol. 634, pp. 272-280, 2015.
- [212] L. De Almeida, I. Bastos, I. Santos, A. Dutra, C. Nunes, and S. Gabriel, "Corrosion resistance of aged Ti–Mo–Nb alloys for biomedical applications," *Journal of Alloys and Compounds*, vol. 615, pp. S666-S669, 2014.
- [213] R. Chelariu, G. Bolat, J. Izquierdo, D. Mareci, D. Gordin, T. Gloriant, *et al.*, "Metastable beta Ti-Nb-Mo alloys with improved corrosion resistance in saline solution," *Electrochimica Acta*, vol. 137, pp. 280-289, 2014.
- [214] M. Nakagawa, S. Matsuya, and K. Udoh, "Corrosion behavior of pure titanium and titanium alloys in fluoride-containing solutions," *Dental materials journal*, vol. 20, pp. 305-314, 2001.
- [215] J. M. Cordeiro, T. Beline, A. L. R. Ribeiro, E. C. Rangel, N. C. da Cruz, R. Landers, *et al.*, "Development of binary and ternary titanium alloys for dental implants," *Dental Materials*, vol. 33, pp. 1244-1257, 2017.
- [216] L. Thair, U. Kamachi Mudali, R. Asokamani, and B. Raj, "Influence of microstructural changes on corrosion behaviour of thermally aged Ti-6Al-7Nb alloy," *Materials and Corrosion*, vol. 55, pp. 358-366, 2004.
- [217] M. Geetha, A. Singh, K. Muraleedharan, A. Gogia, and R. Asokamani, "Effect of thermomechanical processing on microstructure of a Ti–13Nb–13Zr alloy," *Journal of Alloys and Compounds*, vol. 329, pp. 264-271, 2001.
- [218] S. Mischler, P. Ponthiaux, and C. T. du CEFACOR, "A round robin on combined electrochemical and friction tests on alumina/stainless steel contacts in sulphuric acid," *Wear*, vol. 248, pp. 211-225, 2001.
- [219] A. Basak, P. Matteazzi, M. Vardavoulias, and J.-P. Celis, "Corrosion–wear behaviour of thermal sprayed nanostructured FeCu/WC–Co coatings," *Wear*, vol. 261, pp. 1042-1050, 2006.
- [220] D. Landolt, "Electrochemical and materials aspects of tribocorrosion systems," *Journal of Physics D: applied physics*, vol. 39, p. 3121, 2006.
- [221] Y. Zhu, G. Kelsall, and H. Spikes, "The influence of electrochemical potentials on the friction and wear of iron and iron oxides in aqueous systems," *Tribology transactions*, vol. 37, pp. 811-819, 1994.

- [222] T. Yamamoto, K. Fushimi, M. Seo, S. Tsuru, T. Adachi, and H. Habazaki, "Current transients during repeated micro-indentation test of passive iron surface in pH 8.4 borate buffer solution," *Electrochemistry communications*, vol. 9, pp. 1672-1676, 2007.
- [223] L. Benea, V. Iordache, F. Wenger, and P. Ponthiaux, "NANOSTRUCTURED SiC-Ni COMPOSITE COATINGS OBTAINED BY ELECTRODEPOSITION- A TRIBOCORROSION STUDY," *Annals of "Dunarea de Jos" University Galati. Fascicle IX, Metallurgy and Material Science*, pp. 10-14, 2005.
- [224] R. J. Wood, "Tribocorrosion of coatings: a review," *Journal of Physics D: Applied Physics*, vol. 40, p. 5502, 2007.
- [225] D. Landolt and S. Mischler, *Tribocorrosion of passive metals and coatings*: Elsevier, 2011.
- [226] S. Watson, F. Friedersdorf, B. Madsen, and S. Cramer, "Methods of measuring wear-corrosion synergism," *Wear*, vol. 181, pp. 476-484, 1995.
- [227] S. Mischler, E. Rosset, and D. Landolt, "Effect of Corrosion on the Wear Behavior of Passivating Metals in Aqueous," *Thin Films in Tribology*, vol. 25, p. 245, 1993.
- [228] S. Mischler, A. Spiegel, and D. Landolt, "The role of passive oxide films on the degradation of steel in tribocorrosion systems," *Wear*, vol. 225, pp. 1078-1087, 1999.
- [229] S. Barril, S. Mischler, and D. Landolt, "Triboelectrochemical investigation of the friction and wear behaviour of TiN coatings in a neutral solution," *Tribology international*, vol. 34, pp. 599-608, 2001.
- [230] N. Diomidis, S. Mischler, N. More, M. Roy, and S. Paul, "Fretting-corrosion behavior of β titanium alloys in simulated synovial fluid," *Wear*, vol. 271, pp. 1093-1102, 2011.
- [231] Y. Sun and E. Haruman, "Effect of electrochemical potential on tribocorrosion behavior of low temperature plasma carburized 316L stainless steel in 1M H₂SO₄ solution," *Surface and Coatings Technology*, vol. 205, pp. 4280-4290, 2011.
- [232] Y. Sun and E. Haruman, "Tribocorrosion behaviour of low temperature plasma carburised 316L stainless steel in 0.5 M NaCl solution," *Corrosion Science*, vol. 53, pp. 4131-4140, 2011.
- [233] S. Mischler, A. Spiegel, M. Stemp, and D. Landolt, "Influence of passivity on the tribocorrosion of carbon steel in aqueous solutions," *Wear*, vol. 251, pp. 1295-1307, 2001.
- [234] A. A. Sagues and E. I. Meletis, *Wear-corrosion Interactions in Liquid Media: Proceedings of a Symposium Sponsored by the Corrosion and Environmental Effects Committee, Held at the Fall Meeting of the Minerals, Metals, & Materials Society in Indianapolis, Indiana, October 1-5, 1989*: Minerals, Metals, & Materials Society, 1991.
- [235] Y. Sun, "Sliding wear behaviour of surface mechanical attrition treated AISI 304 stainless steel," *Tribology International*, vol. 57, pp. 67-75, 2013.
- [236] A. Vieira, A. Ribeiro, L. Rocha, and J.-P. Celis, "Influence of pH and corrosion inhibitors on the tribocorrosion of titanium in artificial saliva," *Wear*, vol. 261, pp. 994-1001, 2006.
- [237] Ç. Albayrak, İ. Hacısalıhoğlu, and A. Alsaran, "Tribocorrosion behavior of duplex treated pure titanium in simulated body fluid," *Wear*, vol. 302, pp. 1642-1648, 2013.
- [238] H. Yu, Z. Cai, Z. Zhou, and M. Zhu, "Fretting behavior of cortical bone against titanium and its alloy," *Wear*, vol. 259, pp. 910-918, 2005.
- [239] D. Iijima, T. Yoneyama, H. Doi, H. Hamanaka, and N. Kurosaki, "Wear properties of Ti and Ti-6Al-7Nb castings for dental prostheses," *Biomaterials*, vol. 24, pp. 1519-1524, 2003.

- [240] C. Ohkubo, I. Shimura, T. Aoki, S. Hanatani, T. Hosoi, M. Hattori, *et al.*, "Wear resistance of experimental Ti–Cu alloys," *Biomaterials*, vol. 24, pp. 3377-3381, 2003.
- [241] M. Sampaio, M. Buciumeanu, B. Henriques, F. S. Silva, J. C. Souza, and J. R. Gomes, "Tribocorrosion behavior of veneering biomedical PEEK to Ti6Al4V structures," *Journal of the mechanical behavior of biomedical materials*, vol. 54, pp. 123-130, 2016.
- [242] F. Yildiz, A. Yetim, A. Alsaran, and I. Efeoglu, "Wear and corrosion behaviour of various surface treated medical grade titanium alloy in bio-simulated environment," *Wear*, vol. 267, pp. 695-701, 2009.
- [243] P. Majumdar, S. Singh, and M. Chakraborty, "The influence of heat treatment and role of boron on sliding wear behaviour of β -type Ti–35Nb–7.2 Zr–5.7 Ta alloy in dry condition and in simulated body fluids," *Journal of the mechanical behavior of biomedical materials*, vol. 4, pp. 284-297, 2011.
- [244] Z. Doni, A. Alves, F. Toptan, J. Gomes, A. Ramalho, M. Buciumeanu, *et al.*, "Dry sliding and tribocorrosion behaviour of hot pressed CoCrMo biomedical alloy as compared with the cast CoCrMo and Ti6Al4V alloys," *Materials & Design*, vol. 52, pp. 47-57, 2013.
- [245] M.-P. Licausi, A. I. Muñoz, and V. A. Borrás, "Influence of the fabrication process and fluoride content on the tribocorrosion behaviour of Ti6Al4V biomedical alloy in artificial saliva," *Journal of the mechanical behavior of biomedical materials*, vol. 20, pp. 137-148, 2013.
- [246] M. K. Dimah, F. D. Albeza, V. A. Borrás, and A. I. Muñoz, "Study of the biotribocorrosion behaviour of titanium biomedical alloys in simulated body fluids by electrochemical techniques," *Wear*, vol. 294, pp. 409-418, 2012.
- [247] N. Diomidis, S. Mischler, N. More, and M. Roy, "Tribo-electrochemical characterization of metallic biomaterials for total joint replacement," *Acta biomaterialia*, vol. 8, pp. 852-859, 2012.
- [248] M. T. Mathew, V. A. Barão, J. C.-C. Yuan, W. G. Assunção, C. Sukotjo, and M. A. Wimmer, "What is the role of lipopolysaccharide on the tribocorrosive behavior of titanium?," *Journal of the mechanical behavior of biomedical materials*, vol. 8, pp. 71-85, 2012.
- [249] J. Komotori, N. Hisamori, and Y. Ohmori, "The corrosion/wear mechanisms of Ti–6Al–4V alloy for different scratching rates," *Wear*, vol. 263, pp. 412-418, 2007.
- [250] J. Souza, S. Barbosa, E. Ariza, J.-P. Celis, and L. Rocha, "Simultaneous degradation by corrosion and wear of titanium in artificial saliva containing fluorides," *Wear*, vol. 292, pp. 82-88, 2012.
- [251] R. Priya, C. Mallika, and U. K. Mudali, "Wear and tribocorrosion behaviour of 304L SS, Zr-702, Zircaloy-4 and Ti-grade2," *Wear*, vol. 310, pp. 90-100, 2014.
- [252] B. A. Obadele, A. Andrews, M. T. Mathew, P. A. Olubambi, and S. Pityana, "Improving the tribocorrosion resistance of Ti6Al4V surface by laser surface cladding with TiNiZrO₂ composite coating," *Applied Surface Science*, vol. 345, pp. 99-108, 2015.
- [253] I. Hacisalihoglu, A. Samancioglu, F. Yildiz, G. Purcek, and A. Alsaran, "Tribocorrosion properties of different type titanium alloys in simulated body fluid," *Wear*, vol. 332, pp. 679-686, 2015.
- [254] V. G. Pina, A. Dalmau, F. Devesa, V. Amigó, and A. I. Muñoz, "Tribocorrosion behavior of beta titanium biomedical alloys in phosphate buffer saline solution," *Journal of the mechanical behavior of biomedical materials*, vol. 46, pp. 59-68, 2015.
- [255]

D.R.N.CorreaabP.A.B.KurodaabC.R.GrandiniabL.A.RochaabcF.G.M.Oliveira

- bcA.C.AlvescF.Toptanbd, "Tribocorrosion behavior of β -type Ti-15Zr-based alloys," *Materials Letters*, vol. 179, pp. 118-121, September 2016 2016.
- [256] J. Frenzel, E. P. George, A. Dlouhy, C. Somsen, M.-X. Wagner, and G. Eggeler, "Influence of Ni on martensitic phase transformations in NiTi shape memory alloys," *Acta Materialia*, vol. 58, pp. 3444-3458, 2010.
- [257] J. Zhang, R. Rynko, J. Frenzel, C. Somsen, and G. Eggeler, "Ingot metallurgy and microstructural characterization of Ti-Ta alloys," *International Journal of Materials Research*, vol. 105, pp. 156-167, 2014.
- [258] J. Frenzel, Z. Zhang, C. Somsen, K. Neuking, and G. Eggeler, "Influence of carbon on martensitic phase transformations in NiTi shape memory alloys," *Acta materialia*, vol. 55, pp. 1331-1341, 2007.
- [259] P. J. S. Buenconsejo, H. Y. Kim, H. Hosoda, and S. Miyazaki, "Shape memory behavior of Ti-Ta and its potential as a high-temperature shape memory alloy," *Acta Materialia*, vol. 57, pp. 1068-1077, 2009.
- [260] P. Majumdar, S. Singh, and M. Chakraborty, "Elastic modulus of biomedical titanium alloys by nano-indentation and ultrasonic techniques—A comparative study," *Materials Science and Engineering: A*, vol. 489, pp. 419-425, 2008.
- [261] L. Ma and W. Rainforth, "The effect of lubrication on the friction and wear of BioloX® delta," *Acta biomaterialia*, vol. 8, pp. 2348-2359, 2012.
- [262] S. Smith, D. Dowson, A. Goldsmith, R. Valizadeh, and J. Colligon, "Direct evidence of lubrication in ceramic-on-ceramic total hip replacements," *Proceedings of the Institution of Mechanical Engineers, Part C: Journal of Mechanical Engineering Science*, vol. 215, pp. 265-268, 2001.
- [263] S. Scholes, A. Unsworth, and A. Goldsmith, "A frictional study of total hip joint replacements," *Physics in medicine and biology*, vol. 45, p. 3721, 2000.
- [264] J. H. Dumbleton, *Tribology of natural and artificial joints* vol. 3: Elsevier, 1981.
- [265] G. Willmann, "Ceramics for total hip replacement-what a surgeon should know," *Orthopedics*, vol. 21, pp. 173-177, 1998.
- [266] S. Hainsworth and T. Page, "Nanoindentation studies of the chemomechanical effect in sapphire," *Journal of materials science*, vol. 29, pp. 5529-5540, 1994.
- [267] J. Tipper, A. Hatton, J. Nevelos, E. Ingham, C. Doyle, R. Streicher, *et al.*, "Alumina-alumina artificial hip joints. Part II: characterisation of the wear debris from in vitro hip joint simulations," *Biomaterials*, vol. 23, pp. 3441-3448, 2002.
- [268] L. Ma, "Wear Behaviour of BioloX delta ceramic Composite for Joint Replacements," The University of Sheffield, 2010.
- [269] BRUKER, "Tribocorrosion Module, Electro-chemical Cell for CETR-UMT & CETR-APEX Testers, User Manual Supplement " *Tribology and Mechanical Testing* November 28,2012.
- [270] M.-P. Licausi, A. I. Muñoz, and V. A. Borrás, "Tribocorrosion mechanisms of Ti6Al4V biomedical alloys in artificial saliva with different pHs," *Journal of Physics D: Applied Physics*, vol. 46, p. 404003, 2013.
- [271] R. Bhagat, M. Jackson, D. Inman, and R. Dashwood, "The production of Ti-Mo alloys from mixed oxide precursors via the FFC Cambridge process," *Journal of The Electrochemical Society*, vol. 155, pp. E63-E69, 2008.
- [272] M. Wimmer, C. Sprecher, R. Hauert, G. Täger, and A. Fischer, "Tribochemical reaction on metal-on-metal hip joint bearings: a comparison between in-vitro and in-vivo results," *Wear*, vol. 255, pp. 1007-1014, 2003.
- [273] A. C. Ferrari and J. Robertson, "Interpretation of Raman spectra of disordered and amorphous carbon," *Physical review B*, vol. 61, p. 14095, 2000.

- [274] M. Wimmer, J. Loos, R. Nassutt, M. Heitkemper, and A. Fischer, "The acting wear mechanisms on metal-on-metal hip joint bearings: in vitro results," *Wear*, vol. 250, pp. 129-139, 2001.
- [275] F. W. Chan, J. D. Boby, J. B. Medley, J. J. Krygier, S. Yue, and M. Tanzer, "Engineering issues and wear performance of metal on metal hip implants," *Clinical orthopaedics and related research*, vol. 333, pp. 96-107, 1996.
- [276] H. McKellop, S.-H. Park, R. Chiesa, P. Doorn, B. Lu, P. Normand, *et al.*, "In Vivo Wear of 3 Types of Metal on Metal Hip Prostheses During 2 Decades of Use," *Clinical orthopaedics and related research*, vol. 329, pp. S128-S140, 1996.
- [277] V. K. Maskiewicz, P. A. Williams, S. J. Prates, J. G. Bowsher, and I. C. Clarke, "Characterization of protein degradation in serum-based lubricants during simulation wear testing of metal-on-metal hip prostheses," *Journal of Biomedical Materials Research Part B: Applied Biomaterials*, vol. 94, pp. 429-440, 2010.
- [278] H. Mishina and M. Kojima, "Changes in human serum albumin on arthroplasty frictional surfaces," *Wear*, vol. 265, pp. 655-663, 2008.
- [279] Y. Liao, R. Pourzal, M. Wimmer, J. Jacobs, A. Fischer, and L. Marks, "Graphitic tribological layers in metal-on-metal hip replacements," *Science*, vol. 334, pp. 1687-1690, 2011.
- [280] J. Fink, T. Müller-Heinzerling, J. Pflüger, A. Bubenzer, P. Koidl, and G. Crecelius, "Structure and bonding of hydrocarbon plasma generated carbon films: An electron energy loss study," *Solid state communications*, vol. 47, pp. 687-691, 1983.
- [281] S. Berger, D. McKenzie, and P. Martin, "EELS analysis of vacuum arc-deposited diamond-like films," *Philosophical Magazine Letters*, vol. 57, pp. 285-290, 1988.
- [282] D. R. Lide, *CRC handbook of chemistry and physics* vol. 85: CRC press, 2004.
- [283] C. Leyens and M. Peters, *Titanium and titanium alloys*: Wiley Online Library, 2003.
- [284] G. Lütjering, J. Williams, and A. Gysler, "Microstructure and mechanical properties of titanium alloys," *Microstructure and Properties of Materials*, vol. 2, pp. 1-74, 2000.
- [285] P. J. S. Buenconsejo, H. Y. Kim, and S. Miyazaki, "Effect of ternary alloying elements on the shape memory behavior of Ti-Ta alloys," *Acta Materialia*, vol. 57, pp. 2509-2515, 2009.
- [286] T. Niendorf, P. Krooß, C. Somsen, R. Rynko, A. Paulsen, E. Batyrshina, *et al.*, "Cyclic degradation of titanium-tantalum high-temperature shape memory alloys—the role of dislocation activity and chemical decomposition," *Functional Materials Letters*, vol. 8, p. 1550062, 2015.
- [287] P. J. S. B. H. YoungKimShuichiMiyazaki, "Novel β -TiTaAl alloys with excellent cold workability and a stable high-temperature shape memory effect," *Scripta Materialia*, vol. 64, pp. 1114-1117, June 2011 2011.
- [288] M. Júnior, J. R. Severino, R. A. Nogueira, R. O. d. Araújo, T. A. G. Donato, V. E. Arana-Chavez, *et al.*, "Preparation and characterization of Ti-15Mo alloy used as biomaterial," *Materials Research*, vol. 14, pp. 107-112, 2011.
- [289] J. R. S. Martins Jr and C. R. Grandini, "Structural characterization of Ti-15Mo alloy used as biomaterial by Rietveld method," *Journal of Applied Physics*, vol. 111, p. 083535, 2012.
- [290] C. Li, Y. Zhan, and W. Jiang, " β -Type Ti-Mo-Si ternary alloys designed for biomedical applications," *Materials & Design*, vol. 34, pp. 479-482, 2012.
- [291] S. Gabriel, J. Panaino, I. Santos, L. Araujo, P. Mei, L. de Almeida, *et al.*, "Characterization of a new beta titanium alloy, Ti-12Mo-3Nb, for biomedical applications," *Journal of Alloys and Compounds*, vol. 536, pp. S208-S210, 2012.

- [292] X. Min, S. Emura, L. Zhang, and K. Tsuzaki, "Effect of Fe and Zr additions on ω phase formation in β -type Ti–Mo alloys," *Materials Science and Engineering: A*, vol. 497, pp. 74-78, 2008.
- [293] Y. Hao, S. Li, S. Sun, and R. Yang, "Effect of Zr and Sn on Young's modulus and superelasticity of Ti–Nb-based alloys," *Materials Science and Engineering: A*, vol. 441, pp. 112-118, 2006.
- [294] W.-d. Zhang, Y. Liu, H. Wu, M. Song, T.-y. Zhang, X.-d. Lan, *et al.*, "Elastic modulus of phases in Ti–Mo alloys," *Materials Characterization*, vol. 106, pp. 302-307, 2015.
- [295] F. F. Cardoso, P. L. Ferrandini, E. S. Lopes, A. Cremasco, and R. Caram, "Ti–Mo alloys employed as biomaterials: effects of composition and aging heat treatment on microstructure and mechanical behavior," *Journal of the mechanical behavior of biomedical materials*, vol. 32, pp. 31-38, 2014.
- [296] N. T. Oliveira, G. Aleixo, R. Caram, and A. C. Guastaldi, "Development of Ti–Mo alloys for biomedical applications: microstructure and electrochemical characterization," *Materials Science and Engineering: A*, vol. 452, pp. 727-731, 2007.
- [297] P. Nnamchi, R. Njoku, and O. Fasuba, "ALLOY DESIGN AND PROPERTY EVALUATION OF TI-MO-NB-SN ALLOY FOR BIOMEDICAL APPLICATIONS," *Nigerian Journal of Technology*, vol. 32, pp. 410-416, 2013.
- [298] W. Ho, C. Ju, and J. C. Lin, "Structure and properties of cast binary Ti–Mo alloys," *Biomaterials*, vol. 20, pp. 2115-2122, 1999.
- [299] A. Almeida, D. Gupta, C. Loable, and R. Vilar, "Laser-assisted synthesis of Ti–Mo alloys for biomedical applications," *Materials Science and Engineering: C*, vol. 32, pp. 1190-1195, 2012.
- [300] L.-b. Zhang, K.-z. Wang, L.-j. Xu, S.-l. Xiao, and Y.-y. Chen, "Effect of Nb addition on microstructure, mechanical properties and castability of β -type Ti–Mo alloys," *Transactions of Nonferrous Metals Society of China*, vol. 25, pp. 2214-2220, 2015.
- [301] D. R. N. Correa, F. B. Vicente, R. O. Araújo, M. L. Lourenço, P. A. B. Kuroda, M. A. R. Buzalaf, *et al.*, "Effect of the substitutional elements on the microstructure of the Ti-15Mo-Zr and Ti-15Zr-Mo systems alloys," *Journal of Materials Research and Technology*, vol. 4, pp. 180-185, 2015.
- [302] Z. Wang, H. Cai, and S. Hui, "Microstructure and mechanical properties of a novel Ti–Al–Cr–Fe titanium alloy after solution treatment," *Journal of Alloys and Compounds*, vol. 640, pp. 253-259, 2015.
- [303] Y. Hao, R. Yang, M. Niinomi, D. Kuroda, Y. Zhou, K. Fukunaga, *et al.*, "Young's modulus and mechanical properties of Ti-29Nb-13Ta-4.6 Zr in relation to α "martensite," *Metallurgical and Materials Transactions A*, vol. 33, pp. 3137-3144, 2002.
- [304] R. Banerjee, S. Nag, and H. Fraser, "A novel combinatorial approach to the development of beta titanium alloys for orthopaedic implants," *Materials Science and Engineering: C*, vol. 25, pp. 282-289, 2005.
- [305] Y.-H. Hon, J.-Y. Wang, and Y.-N. Pan, "Composition/phase structure and properties of titanium-niobium alloys," *Materials transactions*, vol. 44, pp. 2384-2390, 2003.
- [306] G. He and M. Hagiwara, "Ti alloy design strategy for biomedical applications," *Materials Science and Engineering: C*, vol. 26, pp. 14-19, 2006.
- [307] D. R. N. Correa, P. A. B. Kuroda, and C. R. Grandini, "Structure, microstructure, and selected mechanical properties of Ti-Zr-Mo alloys for biomedical applications," in *Advanced Materials Research*, 2014, pp. 75-80.
- [308] E. Collings and H. Gegel, "A physical basis for solid-solution strengthening and phase stability in alloys of titanium," *Scripta Metallurgica*, vol. 7, pp. 437-443, 1973.

- [309] W.-F. Ho, S.-C. Wu, S.-K. Hsu, Y.-C. Li, and H.-C. Hsu, "Effects of molybdenum content on the structure and mechanical properties of as-cast Ti–10Zr-based alloys for biomedical applications," *Materials Science and Engineering: C*, vol. 32, pp. 517-522, 2012.
- [310] R. Davis, H. Flower, and D. West, "Martensitic transformations in Ti-Mo alloys," *Journal of Materials Science*, vol. 14, pp. 712-722, 1979.
- [311] T. Duerig, J. Albrecht, D. Richter, and P. Fischer, "Formation and reversion of stress induced martensite in Ti-10V-2Fe-3Al," *Acta Metallurgica*, vol. 30, pp. 2161-2172, 1982.
- [312] H. Dong and T. Bell, "Tribological behaviour of alumina sliding against Ti6Al4V in unlubricated contact," *Wear*, vol. 225, pp. 874-884, 1999.
- [313] A. Mavraki and P. Cann, "Lubricating film thickness measurements with bovine serum," *Tribology International*, vol. 44, pp. 550-556, 2011.
- [314] C. Myant, R. Underwood, J. Fan, and P. Cann, "Lubrication of metal-on-metal hip joints: the effect of protein content and load on film formation and wear," *Journal of the mechanical behavior of biomedical materials*, vol. 6, pp. 30-40, 2012.
- [315] J. Perret, E. Boehm-Courjault, M. Cantoni, S. Mischler, A. Beaudouin, W. Chitty, *et al.*, "EBSD, SEM and FIB characterisation of subsurface deformation during tribocorrosion of stainless steel in sulphuric acid," *Wear*, vol. 269, pp. 383-393, 2010.
- [316] I. Duff-Barclay and D. Spillman, "Paper 10: Total Human Hip Joint Prostheses—A Laboratory Study of Friction and Wear," in *Proceedings of the Institution of Mechanical Engineers, Conference Proceedings*, 1966, pp. 90-103.
- [317] Y. Yan, A. Neville, and D. Dowson, "Biotribocorrosion of CoCrMo orthopaedic implant materials—assessing the formation and effect of the biofilm," *Tribology International*, vol. 40, pp. 1492-1499, 2007.
- [318] Y. Yan, A. Neville, and D. Dowson, "Biotribocorrosion—an appraisal of the time dependence of wear and corrosion interactions: I. The role of corrosion," *Journal of Physics D: applied physics*, vol. 39, p. 3200, 2006.
- [319] S. Field, M. Jarratt, and D. Teer, "Tribological properties of graphite-like and diamond-like carbon coatings," *Tribology International*, vol. 37, pp. 949-956, 2004.
- [320] B. Yen, "Influence of water vapor and oxygen on the tribology of carbon materials with sp² valence configuration," *Wear*, vol. 192, pp. 208-215, 1996.
- [321] A. Amanov and S. Sasaki, "A study on the tribological characteristics of duplex-treated Ti–6Al–4V alloy under oil-lubricated sliding conditions," *Tribology International*, vol. 64, pp. 155-163, 2013.
- [322] M. Fellah, Laba, #xef, M. z, O. Assala, L. Dekhil, *et al.*, "Tribological behavior of Ti-6Al-4V and Ti-6Al-7Nb Alloys for Total Hip Prosthesis," *Advances in Tribology*, vol. 2014, p. 13, 2014.
- [323] P. F. Santos, M. Niinomi, H. Liu, K. Cho, M. Nakai, A. Trenggono, *et al.*, "Improvement of microstructure, mechanical and corrosion properties of biomedical Ti-Mn alloys by Mo addition," *Materials & Design*, vol. 110, pp. 414-424, 2016.
- [324] D. Mareci, R. Chelariu, D.-M. Gordin, G. Ungureanu, and T. Gloriant, "Comparative corrosion study of Ti–Ta alloys for dental applications," *Acta Biomaterialia*, vol. 5, pp. 3625-3639, 2009.
- [325] Y.-L. Zhou and D.-M. Luo, "Corrosion behavior of Ti–Mo alloys cold rolled and heat treated," *Journal of Alloys and Compounds*, vol. 509, pp. 6267-6272, 2011.
- [326] W. Huang, Z. Wang, C. Liu, and Y. Yu, "Wear and Electrochemical Corrosion Behavior of Biomedical Ti–25Nb–3Mo–3Zr–2Sn Alloy in Simulated Physiological Solutions," *Journal of Bio-and Tribo-Corrosion*, vol. 1, p. 1, 2015.

- [327] S. Mischler and A. I. Munoz, "Wear of CoCrMo alloys used in metal-on-metal hip joints: a tribocorrosion appraisal," *Wear*, vol. 297, pp. 1081-1094, 2013.
- [328] S. Virtanen, I. Milošev, E. Gomez-Barrena, R. Trebše, J. Salo, and Y. Kontinen, "Special modes of corrosion under physiological and simulated physiological conditions," *Acta Biomaterialia*, vol. 4, pp. 468-476, 2008.
- [329] A. Vieira, L. Rocha, N. Papageorgiou, and S. Mischler, "Mechanical and electrochemical deterioration mechanisms in the tribocorrosion of Al alloys in NaCl and in NaNO₃ solutions," *Corrosion Science*, vol. 54, pp. 26-35, 2012.
- [330] É. Martin, M. Azzi, G. Salishchev, and J. Szpunar, "Influence of microstructure and texture on the corrosion and tribocorrosion behavior of Ti-6Al-4V," *Tribology International*, vol. 43, pp. 918-924, 2010.
- [331] M. Azzi, M. Paquette, J. Szpunar, J. Klemberg-Sapieha, and L. Martinu, "Tribocorrosion behaviour of DLC-coated 316L stainless steel," *Wear*, vol. 267, pp. 860-866, 2009.
- [332] S. Kerwell, D. Baer, E. Martin, Y. Liao, M. Wimmer, K. Shull, *et al.*, "Electrochemically Induced Film Formation on CoCrMo Alloy for Hip Implant Application," *Journal of Bio-and Tribo-Corrosion*, vol. 3, p. 4, 2017.
- [333] M. Stemp, S. Mischler, and D. Landolt, "The effect of mechanical and electrochemical parameters on the tribocorrosion rate of stainless steel in sulphuric acid," *Wear*, vol. 255, pp. 466-475, 2003.
- [334] Y. Sun and R. Bailey, "Improvement in tribocorrosion behavior of 304 stainless steel by surface mechanical attrition treatment," *Surface and Coatings Technology*, vol. 253, pp. 284-291, 2014.
- [335] Y. Liao, E. Hoffman, M. Wimmer, A. Fischer, J. Jacobs, and L. Marks, "CoCrMo metal-on-metal hip replacements," *Physical Chemistry Chemical Physics*, vol. 15, pp. 746-756, 2013.
- [336] J. Cheng, T. Wang, Z. Chai, and X. Lu, "Tribocorrosion study of copper during chemical mechanical polishing in potassium periodate-based slurry," *Tribology Letters*, vol. 58, p. 8, 2015.
- [337] J. Hernandez, P. Wrschka, and G. Oehrlein, "Surface chemistry studies of copper chemical mechanical planarization," *Journal of The Electrochemical Society*, vol. 148, pp. G389-G397, 2001.
- [338] M. Wang, M. Tsai, C. Liu, W. Tseng, T. Chang, L. Chen, *et al.*, "Effects of corrosion environments on the surface finishing of copper chemical mechanical polishing," *Thin Solid Films*, vol. 308, pp. 518-522, 1997.
- [339] Z. Wu, Z. Zhang, and L. Liu, "Electrochemical studies of a Cu (II) □ Cu (III) couple: Cyclic voltammetry and chronoamperometry in a strong alkaline medium and in the presence of periodate anions," *Electrochimica acta*, vol. 42, pp. 2719-2723, 1997.
- [340] L. Jiang, Y. He, X. Niu, Y. Li, and J. Luo, "Synergetic effect of benzotriazole and non-ionic surfactant on copper chemical mechanical polishing in KIO₄-based slurries," *Thin Solid Films*, vol. 558, pp. 272-278, 2014.
- [341] M. Lyvers, D. Bijukumar, A. Moore, P. Saborio, D. Royhman, M. Wimmer, *et al.*, "Electrochemically induced tribolayer with molybdenum for hip implants: Tribocorrosion and biocompatibility study," *Thin Solid Films*, vol. 644, pp. 82-91, 2017.
- [342] A. Iwabuchi, J. Lee, and M. Uchidate, "Synergistic effect of fretting wear and sliding wear of Co-alloy and Ti-alloy in Hanks' solution," *Wear*, vol. 263, pp. 492-500, 2007.

Appendix

Appendix A

Wear Track Roughness

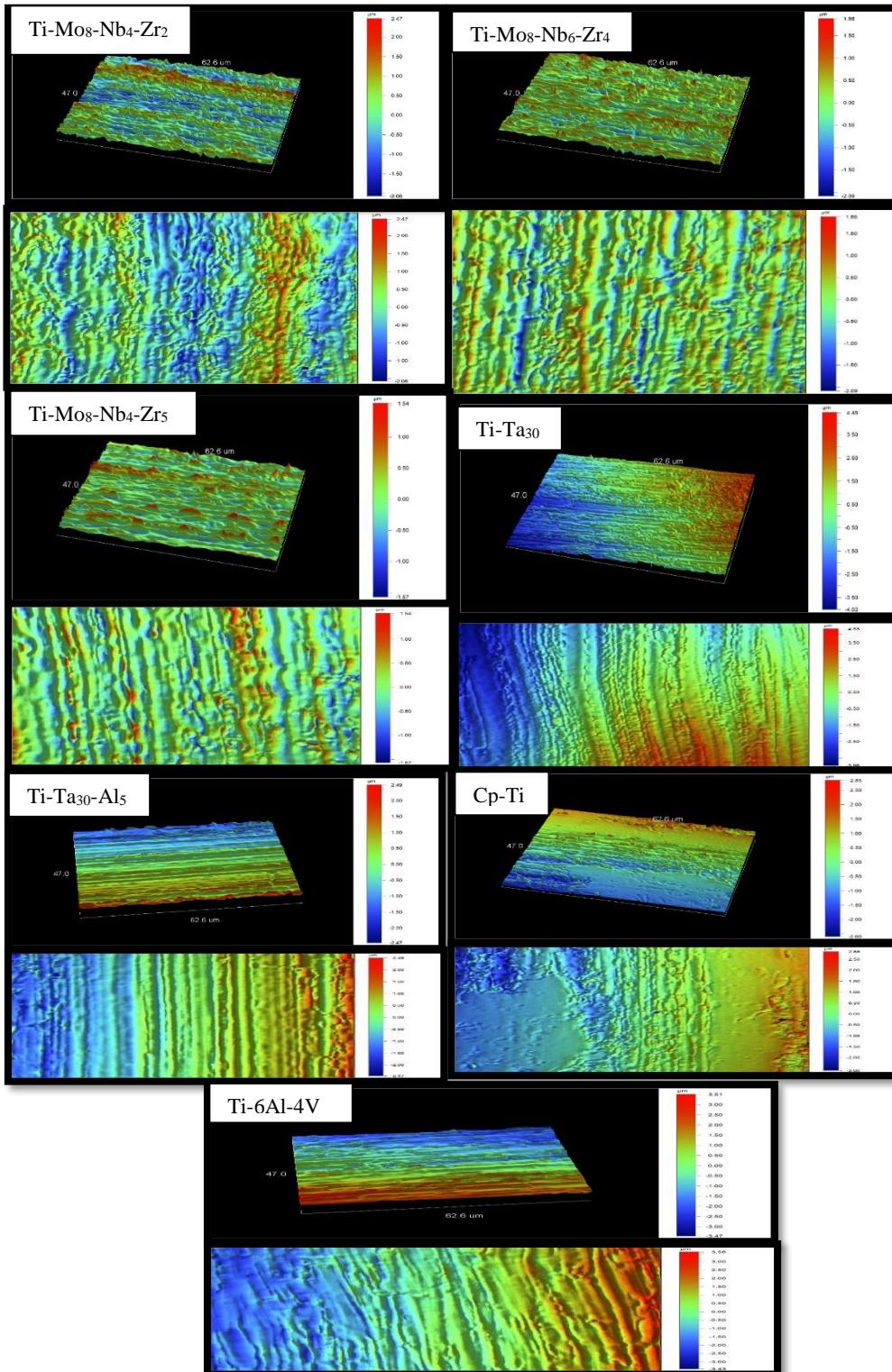


Figure1 Surface roughness, 3D and 2D top view of the wear track at load of 0. 5N

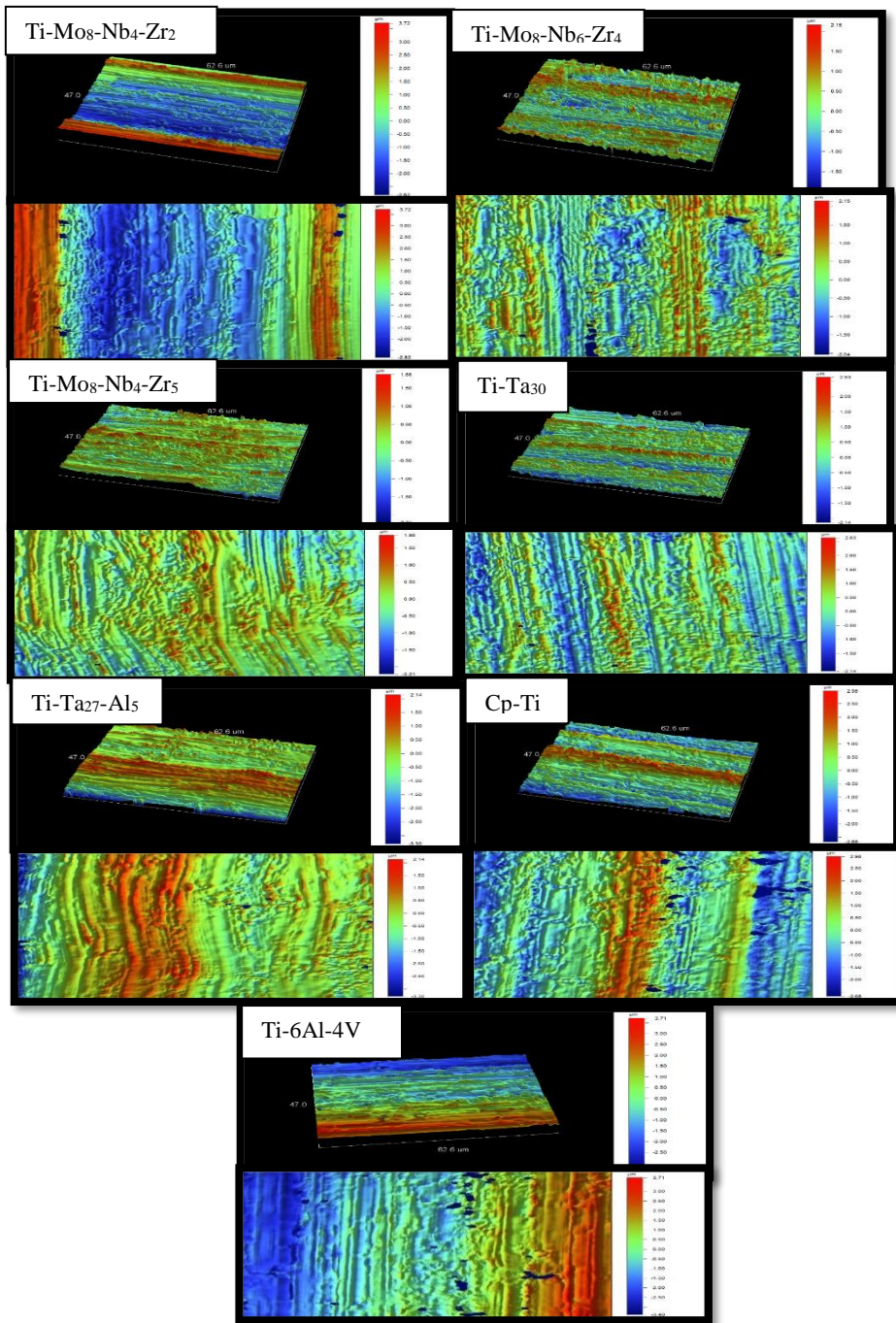


Figure 2: Surface roughness, 3D and 2D top view of the wear track at load of 1N

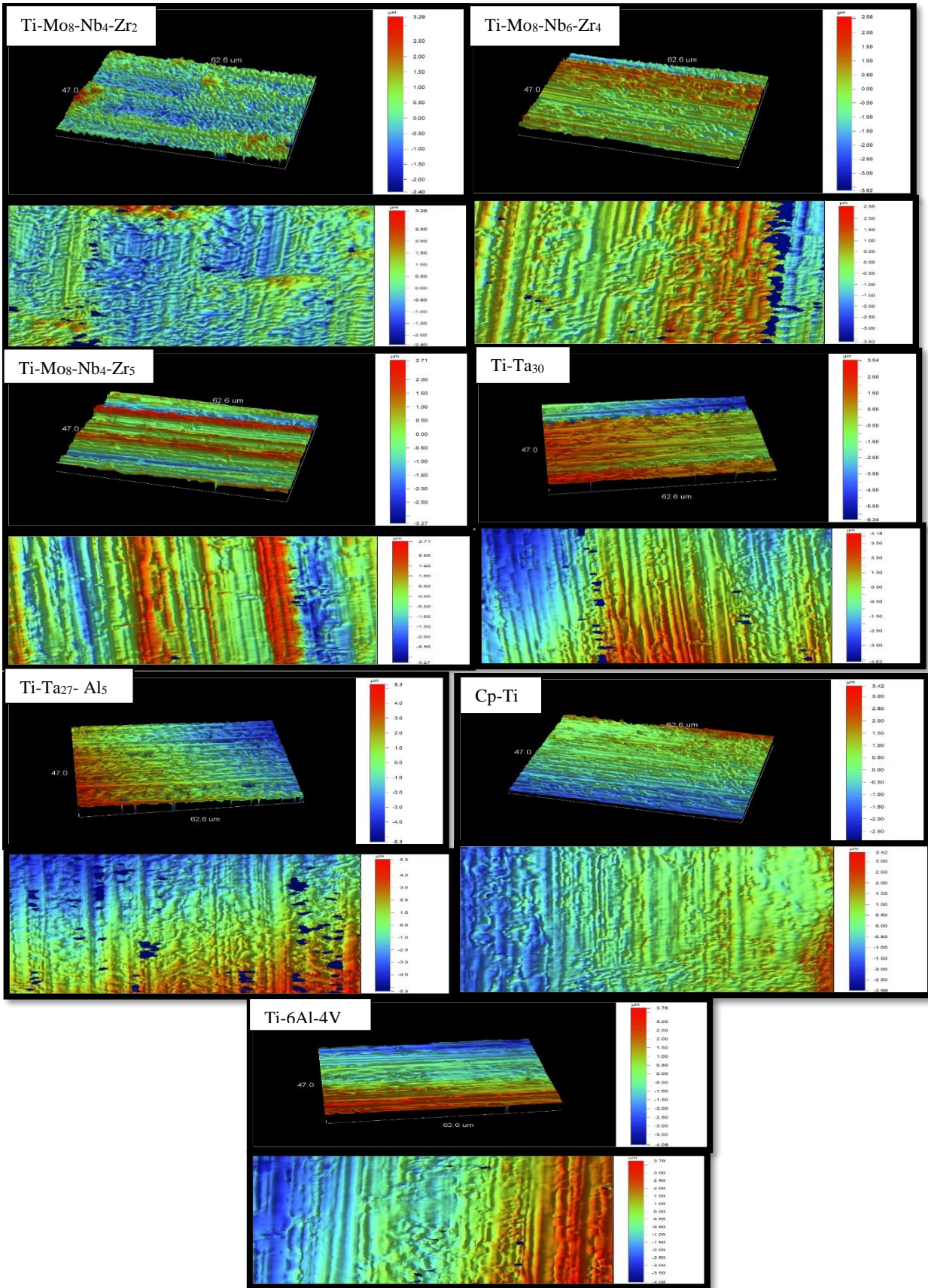


Figure 3 Surface roughness, 3D and 2D top view of the wear track at load of 2N

Appendix B

Wear Track Surface Chemistry

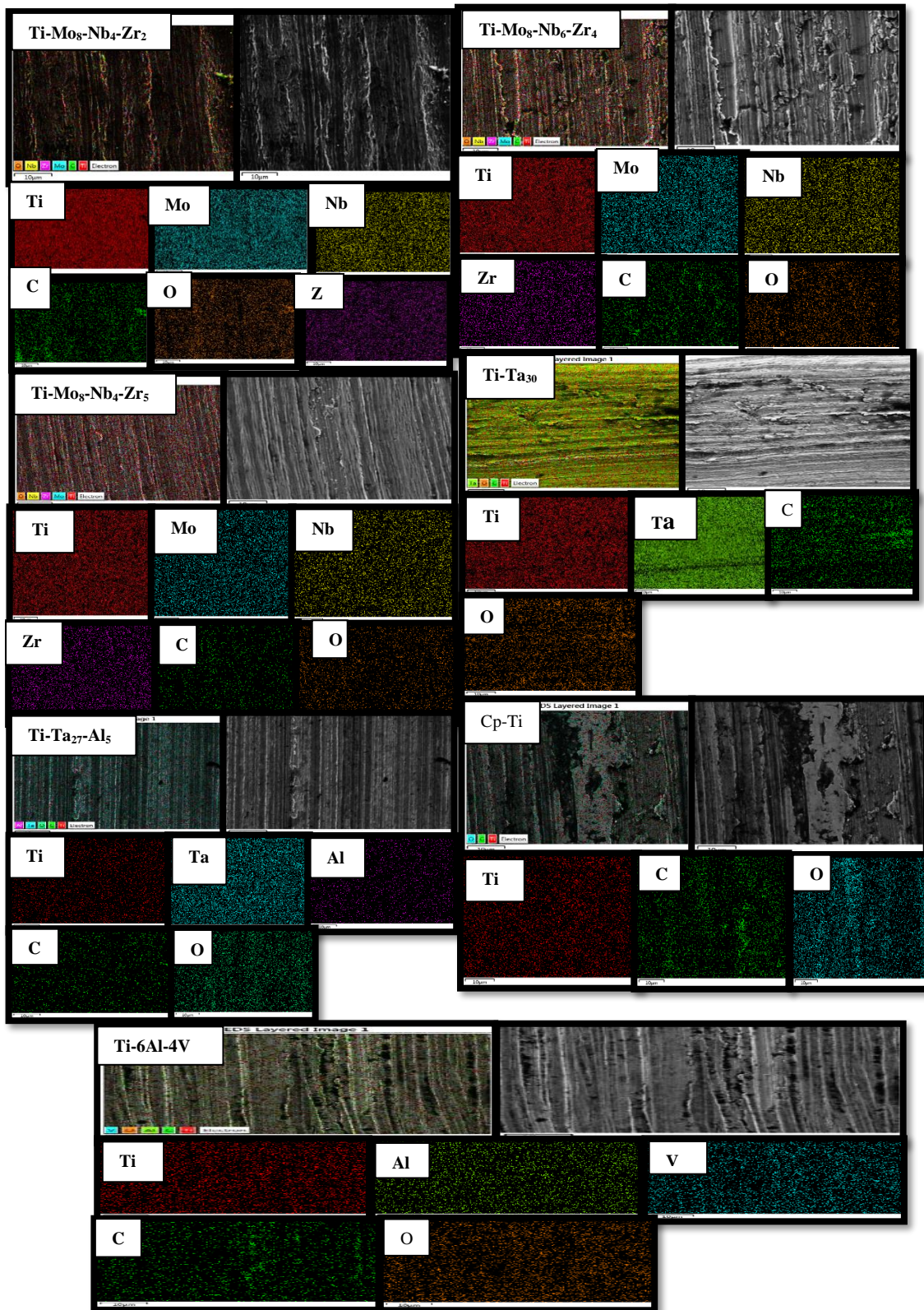


Figure 4 EDX element mapping of the wear track of titanium alloys at load of 0. 5N

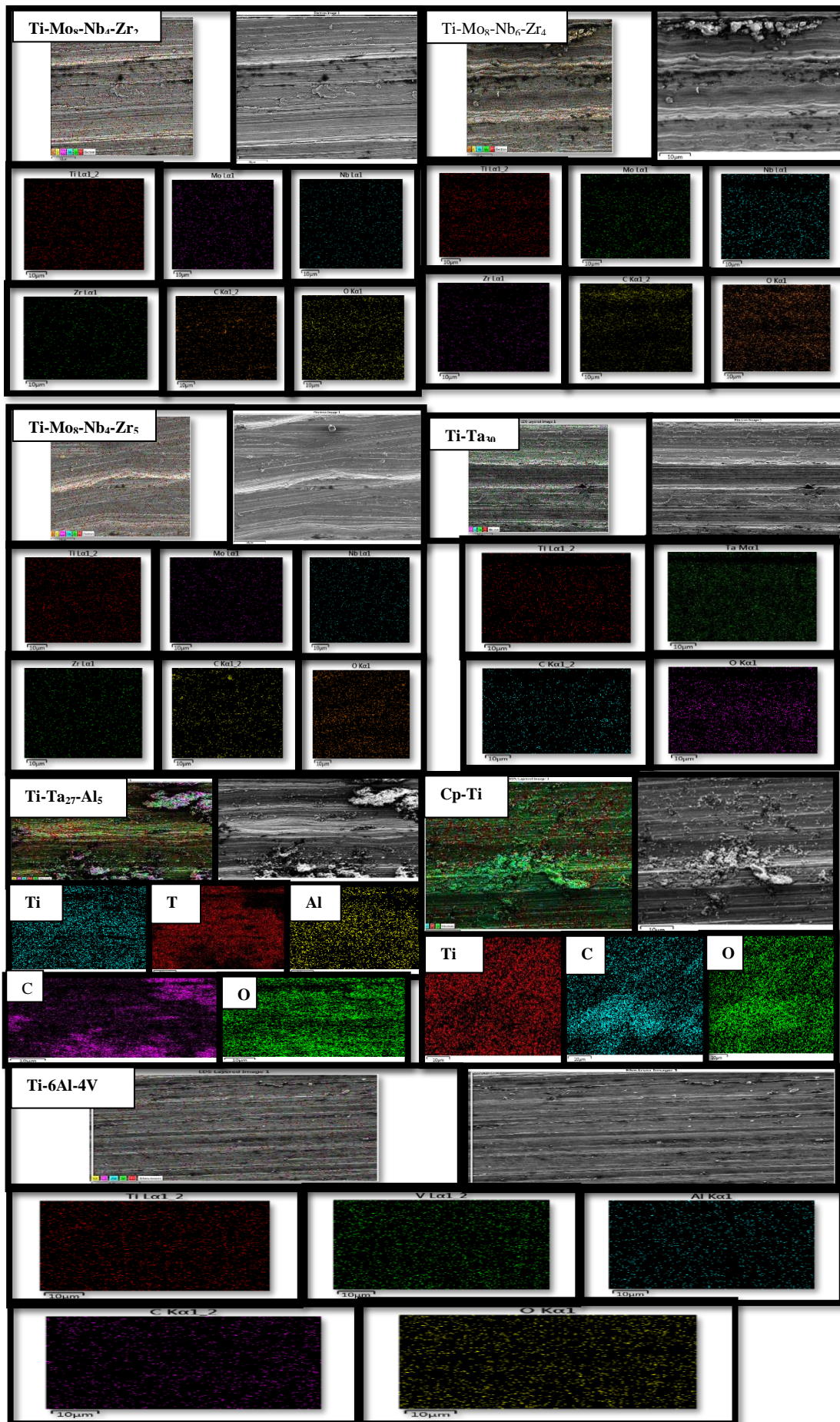


Figure 5: EDX element mapping of the wear track of titanium alloys at load of 1N

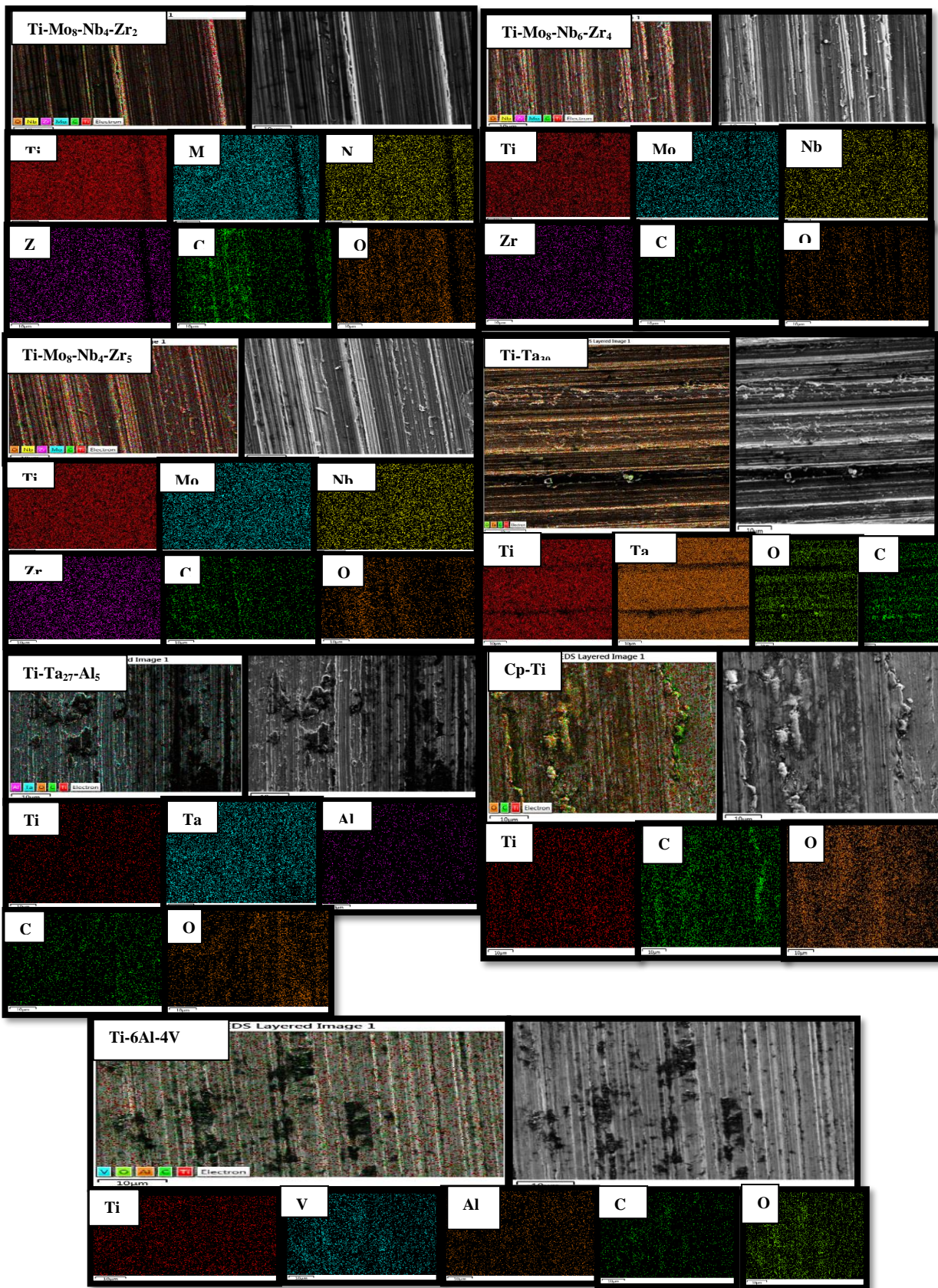


Figure 6: EDX element mapping of the wear track of titanium alloys at load of 2N